JOURNAL OF BIOLOGICAL REGULATORS & HOMEOSTATIC AGENTS
Volume 35, No. 2, March - April, 2021

CONTENTS

Editorials

T.C. Theoharides, D. Lauritano, G. Ronconi, V. Calvisi and P. Conti. Antibodies for COVID-19 - which, when and how long? 417

P. Conti, F.E. Pregliasco, V. Calvisi, A. Caraffa, C.E. Gallenga, S.K. Kritas and G. Ronconi. Monoclonal antibody therapy in COVID-19 induced by SARS-CoV-2 423

Reviews

G. Dipalma, A.D. Inchingolo, F. Inchingolo, I.A. Charitos, M. Di Cosola and A.P. Cazzolla. Focus on the cariogenic process: microbial and biochemical interactions with teeth and oral environment 429

Special article

R. Saggini, G.P. Anastasi, S. Battilomo, P. Maietta Latessa, G. Costanzo, F. Di Carlo, F. Festa, G. Giardinelli, F. Macrì, L. Mastropasqua, M. Nardone, G. Nicoletti, A. Orsini, M. Pastorelli, R. Pellegrino, M. Trevisan, L. La Mesa, A. M. Le Pera, M. G. Privitera, G. Ralli, C. Villani, B. Bricot, R.G. Davidson, A. Hassdenteufel, Z. M. Hawamdeh, GJ. Kleinrensink, E. Matheron, V.L. Stoev, S. Stratulat, S. Tiron, P. Villeneuve, T. Paolucci and R. G. Bellomo. Consensus paper on postural dysfunction: recommendations for prevention, diagnosis and therapy 441

Original articles

A.M. Shamseldeen, M. Hamzawy, N.A. Mahmoud, L. Rashed, S.S. Kamar, I.A. Harb and N. Sharawy. Inhibition of endoplasmic reticulum stress and activation of autophagy-protect intestinal and renal tissues from western diet-induced dysbiosis and abrogate inflammatory response to LPS: role of vitamin E 457

ZB. Li, X. Chen and XJ. Yi. Tumor promoting effects of exosomal microRNA-210 derived from lung cancer cells on lung cancer through the RUNX3/PI3K/AKT signaling pathway axis 473

M. Pietruczuk, L. Kraszula, M. Kupczyk, P. Kuna and M. Eusebio. Dynamics and proliferative capacities of $CD8^{+}CD28^{+}TCR\alpha\beta^{+}CD62L^{high}$ T-cell subsets in healthy and asthmatic subjects 485

Y. Guan, J-Q. Chen, X-Y. Li and S-N. Jiang. ClyA enhances LPS-induced IL-1β secretion in human macrophages through TLR4 and NLRP3 signaling 495

H.-B. Zheng, M. Wu, G. Zhang and K.-L. Chen. MicroRNA-182 inhibits osteogenic differentiation of bone marrow mesenchymal stem cells by targeting Smad1 505

H. Ashraf, S. Nawaz, M. Z. Yousaf, Z. Rashid, A. R. Awan, M. Wasim, M. Tayyab, S. Saeed and S. Firyal. *Fusobacterium necrophorum lktA* gene variants from cow foot rot lesions: molecular characterization, phylogeny and homology modelling analysis 517

P. Cong, C. Yi, X. Wang and Y. Peng. Construction of specific Smo lentivirus and expression of infected pancreatic cancer cells positive for CD24CD44 surface antibody 525

BZ. Li, HH. Bai, FW. Tan, YB. Gao and J. He. Identification of peroxiredoxin 6 as a potential lung-adenocarcinoma biomarker for predicting chemotherapy response by proteomic analysis 537

Y.-X. Qi, X.-J. Su, L.-L. Wei and J. Zhang. Erythropoietin inhibits apoptosis of retinal ganglion cells induced by high glucose through JNK signaling pathway 547

QZ. Li, LP. Sun, HY. Shi, Y. Chen and H. Shen. The new-generation proteasome inhibitor oprozomib increases the sensitivity of cervical cancer cells to cisplatin-induced apoptosis 559

C. Yang, N. Chen, XL. Tang, XH. Qian and CP. Cai. Immunomodulatory effects of IL-33 and IL-25 in an ovalbumin-induced allergic rhinitis mouse model 571

F. Tao, C. Gu, N. Li, Y. Ying, LF. Cao, QF. Xiao, D. Ni, YB. Zhuang and Q. Zhang. New biomarker for lung cancer - focus on circSETD3 583

L.-K. Yu, J. Zhang, Z.-Y. Sun, C.-L. Ruan, H. Li and X.-J. Ruan. Coculture with interleukin-10 overexpressed chondrocytes: a cell therapy model to ameliorate the post-traumatic osteoarthritis development 593

ZH. Liu, DD. Qi, X. Li, SQ. Zhang, Y. Zhao, LX. Fu and LY. Lu. LncRNA SNHG14 promotes osteogenic differentiation of human bone marrow-derived mesenchymal stem cells via regulating miR-185-5p/WISP2 axis 605

Y.-H. Li, M.-F. Lv, M.-S. Lu and J.-P. Bi. Bone marrow mesenchymal stem cell-derived exosomal MiR-338-3p represses progression of hepatocellular carcinoma by targeting ETS1 617

M. Chen, MH. Li, N. Zhang, WW. Sun, H. Wang, YA. Wang, Y. Zhao and W. Wei. Pro-angiogenic effect of exosomal microRNA-103a in mice with rheumatoid arthritis via the downregulation of hepatocyte nuclear factor 4 alpha and activation of the JAK/STAT3 signaling pathway 629

L. Li, J. Bao, M. Wang, B. Chen, B. Luo and F. Yan. High-fat diet exacerbates periodontitis: is it because of dysbacteriosis or stem cell dysfunction? 641

Letters to the Editor

G. Di Giacomo and N. de Gasperis. Glenohumeral osteoarthritis treatment with a single hyaluronic acid administration: clinical outcomes 657

N. Yao, J. Xie, Z-Y. Li , J. Zheng, A. Jiang, Y-F. Wang and M-W. Liu. Effects of kangaroo mother care on immune function and prognosis of premature infants in the neonatal intensive care unit 663

A. Conti, G.J. Burastero, B.J. Hales, D. Breda, M. Alessio and S.E. Burastero. IgE reactivity to house dust mite allergen components in sensitized asymptomatic subjects: a role for Der p 20 669

ZL. Sun, MH. Chen, YN. Guo and ZQ. Liu. LncRNA XIST is elevated in patients with chronic heart failure and has a regulatory role in cardiomyocyte function 677

A. Varricchio, I. La Mantia, FP. Brunese and G. Ciprandi. Smell recovery in patients with COVID-19: an experience with nebulized nasal treatment 683

C. Sun, QT. Shi and HC. Liang. miR-638 serves as an early diagnostic biomarker of acute kidney injury in intensive care units and indicates the clinical outcome of patients 687

JZ. Li, XH. Jin, FM. Zhang and QR. Guo. Dysregulation of lncRNA NRON in diabetic cardiomyopathy protects against high glucose-induced cardiomyocyte injury and inflammation 693

P. Amori, G. Vitiello and T. Lotti. A new Italian chemical peel, based on *Oenanthe crocata* extract 699

YX. Hou, CL. Min and LJ. Ma. miR-520 predicates poor prognosis and inhibits the progression of cervical cancer 703

D. Liu, H. Zhang, D. Liu and T. Peng. Comparison of the effect of regular diet and low-fiber diet on bowel cleansing before colonoscopy 709

M. Ferrillo, M. Migliario, C. Curci, A. Roccuzzo, M. Invernizzi and A. de Sire. Reliability of dental calcification compared to hand-wrist X-ray to evaluate skeletal maturation in growing subjects: a systematic review 717

R. Pulcini, F. Avolio, B. Sinjari, I. Robuffo, V. Flati, L. Pignatelli, S. Martinotti and E. Toniato. Evaluation and efficiency of curcumin against periodontal bacteria: an *in vitro* study 725

W. Arancio, A. Ahmed, C. Basset, A. Jurjus, I. Miletich and A. Leone. Atrial natriuretic peptide differentiates between primary submandibular gland squamous cell carcinoma and oral squamous cell carcinoma: preliminary data 729

M.-F. Zhu, L.-X. Chen, F. Gao, D.-Y. Sheng, M.-J. Xu, J.-R. Zhang and W.-X. Qian. Correlation of STAT6 expression and gene polymorphism with chronic obstructive pulmonary disease 735

F. Rinaldi, A. Trink, A. Sparavigna and D. Pinto. Photo-crosslinking of hyaluronic acid with low-level laser therapy device: a new combined and innovative approach 739

S. Wang, YC. Wang and KL. Dong. Overexpression of miR-522 facilitates gastric cancer progression and predicts poor prognosis 745

D**. Cavagnetto, M. Carossa, A. Deregibus, M. Lacilla, A. Albera, P. Ceruti and S. Carossa.** Efficacy of transcutaneous electrical nervous stimulation in patients with somatosensory tinnitus and cervicofacial myalgia 751

L. Ricciardi, F. Furci and S. Gangemi. Nickel sensitization influence on microbiota in allergic and non-allergic disorders: what's up? 757

RS. Almeida, RI. Ferreira, DAA. Galdino, IGGF. Mariano, NF. Silveira, PL. Almeida and MAP. Andrade. Angiogenic effect of the application of radial shock waves on the integral musculature of the Wistar rat quadriceps - a new perspective for muscle physiology 761

G. Barassi, M. Supplizi, L. Prosperi, G. Irace, A. Younes, M. Della Rovere, A. Rabini, A. Colombo and A. Di Iorio. Dual-wavelength high-power laser therapy and neuromuscular manual therapy in chronic neck pain: a randomized clinical trial 767

R. Rauso, GF. Nicoletti, R. Fragola, N. Zerbinati, E. Nikolli, P. Bove and G. Tartaro. Hyaluronidase use before rhinoplasty in noses previously injected with hyaluronic acid: is it always necessary? 775

K. Lian, J. Cui, L. Li, Y. Li and QH. Zhang. Primary $CD5^+$ diffuse large B-cell lymphoma with hyperlactatemia as the first manifestation 779

I.Z. Sadiq, A. Muhammad, F. Sadiq Abubakar and M.N. Shuaibu. SARS-CoV-2 infection *versus* the body immune defenses: the role of immune responses and mechanism of action of dexamethasone 783

G. Laganà, A. Malara, A. Koumoulis, M. Tepedino, N. Venza and P. Cozza. Bruxism, perceived anxiety and stress in university students 787

N. Logoluso, R. Ciliberto, I. Morelli, G.M. Peretti and A.V. Pellegrini. Custom-made cementless revision total knee arthroplasty in a patient with metal and bone cement hypersensitivity 791

L. Xiao, Z. Yang and G. Li. Factors associated with the synovial membrane thickness of wrist detected by ultrasonography in rheumatoid arthritis patients: a retrospective study 797

L-M. Zhang, L. Chen, Y-J. Chen and M-W. Liu. IL-35 suppresses epileptiform burst activity in primary hippocampal neurons 803

C. Huang, YQ. Xia, L. Xiao, J. Huang and ZM. Zhu. Combining the platelet-to-albumin ratio with serum and pathologic variables to establish a risk assessment model for lymph node metastasis of gastric cancer 811

KH. Tong and J. Qian. Long non-coding RNA FGD5-AS1 is an inducer of cisplatin chemoresistance in gastric cancer cells by sponging miR-195 819

D. Bizzoca, M. T. Rocchetti, S. Scacco, F. Taurino, G. Vicenti, F. Spadaccino, L. Moretti, E. Ranieri, L. Gesualdo, F. Moretti, G. Peretti, G. Banfi, B. Moretti and A. Gnoni. Beyond pre-analytical and analytical concerns in the study of synovial fluid proteome: description of an optimized Gel-based protocol 827

EDITORIAL

Antibodies for COVID-19 - which, when and how long?

T.C. Theoharides[1,2,3], D. Lauritano[4], G. Ronconi[5], V. Calvisi[6] and P. Conti[7]

[1]Laboratory of Molecular Immunopharmacology and Drug Discovery, Department of Immunology, Tufts University School of Medicine, Boston, USA; [2]School of Graduate Biomedical Sciences, Tufts University School of Medicine, Boston, MA, USA; [3]Department of Internal Medicine, Tufts University School of Medicine and Tufts Medical Center, Boston, MA,USA; [4]Medicine and Surgery Department, Centre of Neuroscience of Milan, University of Milan-Bicocca, Italy; [5]Fondazione Policlinico Universitario A. Gemelli IRCCS, Università Cattolica del Sacro Cuore, Rome, Italy; [6]Department of Orthopaedics, School of Medicine, University of L'Aquila, L'Aquila, Italy; [7]Postgraduate Medical School, University of Chieti, Chieti, Italy

Infection with SARS-CoV2 leads to COVID-19, the severity of which derives from the host's immune response, especially the release of a storm of pro-inflammatory cytokines. This coronavirus infects by first binding to the ectoenzyme Angiotensin Converting Enzyme 2 (ACE2), a serine protease acting as the receptor, while another serine protease is necessary for priming the viral spike "S" protein required for entering the cells. Repurposing existing drugs for potential anti-coronavirus activity have failed. As a result, there were intense efforts to rapidly produce ways of providing prophylactic active immunization (vaccines) or abortive passive (convalescent plasma or monoclonal antibodies) neutralizing antibodies. The availability of vaccines for COVID-19 have been largely successful, but many questions still remain unanswered. In spite of the original enthusiasm, clinical studies using convalescent serum or monoclonal antibodies have shown limited benefit. Moreover, the emergence of Long-COVID syndrome in most infected patients necessitates the development of treatment approaches that may prevent viral entry by blocking both serine proteases involved, as with a liposomal blend of the natural flavonoids luteolin and quercetin.

Infection with the recent Coronavirus [severe acute respiratory syndrome (SARS)-CoV2] leads to COVID-19, the severity of which derives from the host's immune response (1) especially the release of a storm of pro-inflammatory cytokines (2-9) mainly IL-6 (10-14), in what has been termed "cytokine storms" (15) or "cytokine release syndrome" (16). This coronavirus infects by first binding to the ectoenzyme Angiotensin Converting Enzyme 2 (ACE2), a serine protease acting as the receptor, while another serine protease is necessary for priming the viral corona spike "S" protein required for entering the cells (17, 18). The S protein is made up of two subunits, S1 containing a receptor-binding domain that binds to ACE2 on the surface of host cells, and the S2 containing a transmembrane anchor that mediates fusion of viral and host cell membranes.

Unfortunately, repurposing existing drugs for potential anti-coronavirus activity have not yielded positive results (19). As a result, there were intense efforts to rapidly produce ways of providing prophylactic active immunization (vaccines) or abortive passive (convalescent plasma or monoclonal antibodies) neutralizing antibodies (20, 21). Early studies used high-throughput methods to identify

Key words: ACE2; antibodies; convalescent serum; corona virus; receptor; S protein

Corresponding Author
Theoharis C. Theoharides, MS, MPhil, PhD, MD
Department of Immunology,
Tufts University School of Medicine,
136 Harrison Avenue, Suite 304, Boston, MA 02111, USA
Tel.; +1 617 636 6866 - Fax: +1 617 636 2456
e-mail: theoharis.theoharides@tufts.edu

0393-974X (2021)
Copyright © by BIOLIFE, s.a.s.
This publication and/or article is for individual use only and may not be further reproduced without written permission from the copyright holder.
Unauthorized reproduction may result in financial and other penalties
DISCLOSURE: ALL AUTHORS REPORT NO CONFLICTS OF INTEREST RELEVANT TO THIS ARTICLE.

antibodies from convalescent plasma using either B cells from patients (22) or a small animal model (23).

How antibodies may work

Neutralizing antibodies could block viral entry by acting in different ways (24): (a) preventing the S protein from binding to ACE2, (b) preventing the S protein conformational changes required for membrane fusion, (c) mimicking ACE2 and prematurely triggering S protein conformational changes before binding ACE2 and thus preventing actual binding, or (d) inhibiting the IL-6 receptor. Such antibodies would be produced after infection, could be present in convalescent serum, made after vaccination, or produced *ex vivo* and administered acutely (25, 26)

Vaccines

A number of vaccines for COVID-19 were developed rapidly using either mRNA or adenovirus vector technology aimed at production of the coronavirus S protein and subsequent innate synthesis of neutralizing antibodies, with apparently minor side-effects so far (27).

However, a number of questions remain unanswered such as the level of antibody titers produced, will they limit transmission, how long will they remain protective, will they prevent asymptomatic disease, whether coronavirus mutations will escape from any antibody neutralizing effect (28), whether the virus will continue to mutate becoming a "recurrent seasonal infection" (29) and requiring the production of new vaccines every year with the realization that such vaccines may have reduced efficacy as is the case for the vaccines against the influenza virus that had only 40% efficacy during 2020 in the US.

Convalescent plasma therapy

Passive immunization with convalescent plasma involves transfusing plasma from patients who have recovered from SARS-CoV2 infection to infected patients with severe disease, assuming that the donors have developed protective antibodies against the coronavirus (30). However, donors may have recovered without production of sufficient neutralizing antibodies. For instance, in one study of 149 convalescent patients whose plasma was collected at 39 days after the onset of symptoms, most did not contain high levels of neutralizing antibodies (only 1% had plasma titers >5000) (31). Moreover, harvesting of such antibodies may have occurred at a time when such antibodies were declining, and any such passive immunity is likely to be short-lived.

A number of studies have reported positive results. In one older study of SARS patients who were treated with high-dose methylprednisolone, the antiviral drug ribavirin and convalescent plasma had shorter duration of hospitalization (32). One uncontrolled study of patients with severe COVID-19, showed convalescent plasma resulted in rapid increase in serum neutralizing antibody titers, no detectable SARS-CoV2 viral RNA nor clinical improvement (33). In another uncontrolled study of five critically ill patients, administration of convalescent plasma led to clinical improvement (34). Three recent studies provided interesting positive results. In the first, administration of convalescent plasma containing high-titer anti-RBD immunoglobulin significantly reduced mortality if given within 44 hours of hospitalization (35) The second showed that convalescent plasma with high but not lower titers reduced risk of death in hospitalized COVID-19 patients not requiring mechanical ventilation (36). The third study reported that early administration of high-titer convalescent serum to mildly ill patients reduced the progression of the diseases (37). However, one randomized clinical trial using convalescent plasma given more than 20 days after viral shedding in patients with severe and life-threatening COVID-19 apparently increased viral clearance but had no effect on mortality (38). Another randomized, placebo-controlled, clinical trial using convalescent plasma in COVID-19 severe pneumonia found no significance in clinical status or overall mortality (39).

Convalescent plasma has several limitations including requirement for blood type matching and screening for blood-borne pathogens, as well as batch-to-batch variability.

Monoclonal antibodies

Passive immunity using human monoclonal antibodies was recognized as potentially serving

as an important abortive treatment for severe COVID-19 patients (40, 41). Such antibodies have been directed against epitopes of the coronavirus receptor-binding domain (RBD) (24, 42). In one instance, the antibody developed could bind potently with RBD, but did not overlap with the ACE2 binding domain (43). In another instance, using more than 1000 purified memory B cells, 11 potent neutralizing antibodies were selected, one of which had the additional ability to enhance the neutralizing ability of the other antibodies (44). There could be additional modifications in the structure of the Fc receptor binding region of the antibodies to increase affinity for Fc receptors.

A number of recent publications have reported on clinical trials using monoclonal antibodies for COVID-19. In one ongoing Phase 2 clinical rial, a single infusion of the neutralizing antibody LY-CoV555 to outpatients with mild to moderate COVID-19, one of the three doses used appeared to accelerate the natural decline of the viral load (45). In another randomized, placebo-controlled, trial administration of LY-CoV555 7000 mg by single infusion to hospitalized COVID-19 patients (who were also on rendemsivir and corticosteroids) did not demonstrate any efficacy (46).

Limitations of antibody use

Several critical questions remain unanswered. What critical epitopes in the S protein are targeted by neutralizing antibodies in convalescent plasma? How many neutralizing antibody epitopes can be targeted simultaneously on the S protein? How easily can the coronavirus develop mutations to allow it to escape neutralizing antibodies? What is the efficacy in different age, sex, or ethnic subpopulations? Are there any undesirable effects, such as antibody-dependent enhancement of infection of immune cells or worsening cytokine storms? Last but not least, antibodies must be given intravenously, even though inhaled delivery has been contemplated. 47

One way to overcome some of the issues raised, at least acutely (abortively) may be the use of a "cocktail" of monoclonal antibodies, rather than a single one, and may decrease the likelihood of rapid mutational escape from neutralization (48, 49). In one instance, the REGN-COV2 neutralizing antibody cocktail reduced viral load and the effect was more pronounced in patients with weak immune response or those with high viral load at baseline.

IL-6 receptor blocking antibodies

In spite of the fact that IL-6, 10-14 has been shown to be increased in the serum of most patients with severe COVID-19 (50), such increases have been mild and two recent clinical trials have also yielded inconsistent results. One study using both tocilizumab and sarilizumab showed better survival than controls, but this clinical study also included treatment with glucocorticoids (51). Another study using only tocilizumab reported no significant improvement in clinical status or death rates (52). Other pro-inflammatory molecules may prove to be better candidates for therapy.

Long-COVID syndrome

COVID-19 survivors experience fatigue and other neuropsychiatric symptoms, especially the presence of mental fatigue known as "brain fog" (53). Such patients have been called "long-haulers" and the illness has been termed "Long COVID syndrome". In addition to the well-known severe respiratory and inflammatory problems discussed above, infection with SARS-CoV-2 can also contribute to neurological (54-57) and mental (58-62) disorders. Increasing publications discuss Long-COVID syndrome (63, 64). A recent paper reported that post-COVID affects over 50% of COVID patients (65). Another showed persistent fatigue that was apparently independent of the severity of the initial symptoms (66). Symptoms experienced by Long-COVID syndrome patients are similar (67) to those present in patients with Mast Cell Activation Syndrome (MCAS) (68, 69).

CONCLUSION

The availability of vaccines for COVID-19 have been largely successful, but many questions still remain unanswered. Despite the original enthusiasm about convalescent serum and monoclonal antibodies, clinical studies have shown limited benefit. Moreover, the emergence of Long-COVID syndrome in most

infected patients necessitates the development of treatment approaches that may prevent viral entry by blocking both serine proteases involved, as with a liposomal blend of the natural flavonoids luteolin and quercetin (e.g., FibroProtek) (70, 71).

REFERENCES

1. Brodin P. Immune determinants of COVID-19 disease presentation and severity. Nat Med 2021; 27(1):28-33.
2. Ye Q, Wang B, Mao J. The pathogenesis and treatment of the `Cytokine Storm' in COVID-19. J Infect 2020; 80(6):607-13.
3. Chen G, Wu D, Guo W et al. Clinical and immunological features of severe and moderate coronavirus disease 2019. J Clin Invest 2020; 130(5):2620-9.
4. Conti P, Ronconi G, Caraffa A et al. Induction of pro-inflammatory cytokines (IL-1 and IL-6) and lung inflammation by Coronavirus-19 (COVI-19 or SARS-CoV-2): anti-inflammatory strategies. J Biol Regul Homeost Agents 2020; 34(2):327-31.
5. Giamarellos-Bourboulis EJ, Netea MG, Rovina N et al. Complex immune dysregulation in COVID-19 patients with severe respiratory failure. Cell Host Microbe 2020; 27(6):992-1000.
6. Zhang C, Baumer A, Mackay IR, Linnane AW, Nagley P. Unusual pattern of mitochondrial DNA deletions in skeletal muscle of an adult human with chronic fatigue syndrome. Hum Mol Genet 1995; 4(4):751-4.
7. Tang Y, Liu J, Zhang D, Xu Z, Ji J, Wen C. Cytokine Storm in COVID-19: The current evidence and treatment strategies. Front Immunol 2020; 11:1708.
8. Paces J, Strizova Z, Smrz D, Cerny J. COVID-19 and the immune system. Physiol Res 2020; 69(3):379-88.
9. Ragab D, Salah EH, Taeimah M, Khattab R, Salem R. The COVID-19 Cytokine Storm; What We Know So Far. Front Immunol 2020; 11:1446.
10. Herold T, Jurinovic V, Arnreich C et al. Elevated levels of IL-6 and CRP predict the need for mechanical ventilation in COVID-19. J Allergy Clin Immunol 2020; 146(1):128-36.
11. Copaescu A, Smibert O, Gibson A, Phillips EJ, Trubiano JA. The role of IL-6 and other mediators in the cytokine storm associated with SARS-CoV-2 infection. J Allergy Clin Immunol 2020; 146(3):518-34.
12. Han H, Ma Q, Li C et al. Profiling serum cytokines in COVID-19 patients reveals IL-6 and IL-10 are disease severity predictors. Emerg Microbes Infect 2020; 9(1):1123-30.
13. Mazzoni A, Salvati L, Maggi L et al. Impaired immune cell cytotoxicity in severe COVID-19 is IL-6 dependent. J Clin Invest 2020; 130(9):4694-703.
14. Liu F, Li L, Xu M et al. Prognostic value of interleukin-6, C-reactive protein, and procalcitonin in patients with COVID-19. J Clin Virol 2020; 127:104370.
15. Canna SW, Cron RQ. Highways to hell: Mechanism-based management of cytokine storm syndromes. J Allergy Clin Immunol 2020; 146(5):949-59.
16. Moore JB, June CH. Cytokine release syndrome in severe COVID-19. Science 2020; 368(6490):473-4.
17. Tai W, He L, Zhang X et al. Characterization of the receptor-binding domain (RBD) of 2019 novel coronavirus: implication for development of RBD protein as a viral attachment inhibitor and vaccine. Cell Mol Immunol 2020; 17(6):613-20.
18. Hoffmann M, Kleine-Weber H, Schroeder S et al. SARS-CoV-2 Cell Entry Depends on ACE2 and TMPRSS2 and Is Blocked by a Clinically Proven Protease Inhibitor. Cell 2020; 181(2):271-80.
19. Rubin EJ, Longo DL. SARS-CoV-2 Vaccination - An Ounce (Actually, Much Less) of Prevention. N Engl J Med 2020; 383(27):2677-8.
20. Abraham J. Passive antibody therapy in COVID-19. Nat Rev Immunol 2020; 20(7):401-3.
21. Sempowski GD, Saunders KO, Acharya P, Wiehe KJ, Haynes BF. Pandemic Preparedness: Developing Vaccines and Therapeutic Antibodies For COVID-19. Cell 2020; 181(7):1458-63.
22. Cao Y, Su B, Guo X et al. Potent Neutralizing Antibodies against SARS-CoV-2 identified by high-throughput single-cell sequencing of convalescent patients' B cells. Cell 2020; 182(1):73-84.
23. Rogers TF, Zhao F, Huang D et al. Rapid isolation of potent SARS-CoV-2 neutralizing antibodies and protection in a small animal model. bioRxiv 2020; 2020.05.11.088674. doi: 10.1101/2020.05.11.088674. Preprint
24. Tai W, Zhang X, He Y, Jiang S, Du L. Identification of SARS-CoV RBD-targeting monoclonal antibodies with cross-reactive or neutralizing activity against SARS-CoV-2. Antiviral Res 2020; 179:104820.

25. Marovich M, Mascola JR, Cohen MS. Monoclonal Antibodies for Prevention and Treatment of COVID-19. JAMA 2020; 324(2):131-2.
26. Sewell HF, Agius RM, Kendrick D, Stewart M. Vaccines, convalescent plasma, and monoclonal antibodies for covid-19. BMJ 2020; 370:m2722.
27. Castells MC, Phillips EJ. Maintaining Safety with SARS-CoV-2 Vaccines. Reply. N Engl J Med 2021; 384(10):e37.
28. Weisblum Y, Schmidt F, Zhang F et al. Escape from neutralizing antibodies by SARS-CoV-2 spike protein variants. Elife 2020; 9:e61312. doi: 10.7554/eLife.61312.
29. Murray CJL, Piot P. The Potential Future of the COVID-19 Pandemic: Will SARS-CoV-2 Become a Recurrent Seasonal Infection? JAMA 2021; 325(13):1249-50.
30. Bloch EM, Shoham S, Casadevall A et al. Deployment of convalescent plasma for the prevention and treatment of COVID-19. J Clin Invest 2020; 130(6):2757-65.
31. Robbiani DF, Gaebler C, Muecksch F et al. Convergent antibody responses to SARS-CoV-2 in convalescent individuals. Nature 2020; 584(7821):437-42.
32. Soo YO, Cheng Y, Wong R et al. Retrospective comparison of convalescent plasma with continuing high-dose methylprednisolone treatment in SARS patients. Clin Microbiol Infect 2004; 10(7):676-8.
33. Duan K, Liu B, Li C et al. Effectiveness of convalescent plasma therapy in severe COVID-19 patients. Proc Natl Acad Sci U S A 2020; 117(17):9490-6.
34. Shen C, Wang Z, Zhao F et al. Treatment of 5 Critically Ill Patients With COVID-19 With Convalescent Plasma. JAMA 2020; 323(16):1582-9.
35. Salazar E, Christensen PA, Graviss EA et al. Significantly decreased mortality in a large cohort of coronavirus disease 2019 (covid-19) patients transfused early with convalescent plasma containing high-titer anti-severe acute respiratory syndrome coronavirus 2 (SARS-CoV-2) spike protein IgG. Am J Pathol 2021; 191(1):90-107.
36. Joyner MJ, Carter RE, Senefeld JW et al. Convalescent plasma antibody levels and the risk of death from Covid-19. N Engl J Med 2021; 384(11):1015-27.
37. Libster R, Perez MG, Wappner D et al. Early high-titer plasma therapy to prevent severe Covid-19 in older adults. N Engl J Med 2021; 384(7):610-8.
38. Li L, Zhang W, Hu Y et al. Effect of convalescent plasma therapy on time to clinical improvement in patients with severe and life-threatening COVID-19: A randomized clinical trial. JAMA 2020; 324(5):460-70.
39. Simonovich VA, Burgos Pratx LD, Scibona P et al. A randomized trial of convalescent plasma in Covid-19 severe pneumonia. N Engl J Med 2021; 384(7):619-29.
40. Watterson WJ, Tanyeri M, Watson AR et al. Droplet-based high-throughput cultivation for accurate screening of antibiotic resistant gut microbes. Elife 2020; 9.
41. Cohen MS. Monoclonal antibodies to disrupt progression of early Covid-19 infection. N Engl J Med 2021; 384(3):289-91.
42. Jahanshahlu L, Rezaei N. Monoclonal antibody as a potential anti-COVID-19. Biomed Pharmacother 2020; 129:110337.
43. Tian X, Li C, Huang A et al. Potent binding of 2019 novel coronavirus spike protein by a SARS coronavirus-specific human monoclonal antibody. Emerg Microbes Infect 2020; 9(1):382-5.
44. Wan J, Xing S, Ding L et al. Human-IgG-Neutralizing Monoclonal Antibodies Block the SARS-CoV-2 Infection. Cell Rep 2020; 32(3):107918.
45. Chen P, Nirula A, Heller B et al. SARS-CoV-2 Neutralizing antibody LY-CoV555 in outpatients with Covid-19. N Engl J Med 2021; 384(3):229-37.
46. Lundgren JD, Grund B, Barkauskas CE et al. A Neutralizing Monoclonal Antibody for Hospitalized Patients with Covid-19. N Engl J Med 2021; 384(10):905-14.
47. Cruz-Teran C, Tiruthani K, McSweeney M, Ma A, Pickles R, Lai SK. Challenges and opportunities for antiviral monoclonal antibodies as COVID-19 therapy. Adv Drug Deliv Rev 2021; 169:100-17.
48. Weinreich DM, Sivapalasingam S, Norton T et al. REGN-COV2, a neutralizing antibody cocktail, in outpatients with Covid-19. N Engl J Med 2021; 384(3):238-51.
49. Baum A, Fulton BO, Wloga E et al. Antibody cocktail to SARS-CoV-2 spike protein prevents rapid mutational escape seen with individual antibodies. Science 2020; 369(6506):1014-8.
50. Aziz M, Fatima R, Assaly R. Elevated interleukin-6 and severe COVID-19: A meta-analysis. J Med Virol

2020; 92(11):2283-85.
51. Gordon AC, Mouncey PR, Al-Beidh F et al. Interleukin-6 Receptor Antagonists in Critically Ill Patients with Covid-19. N Engl J Med 2021; 384(16):1491-1502.
52. Stone JH, Frigault MJ, Serling-Boyd NJ et al. Efficacy of tocilizumab in patients hospitalized with Covid-19. N Engl J Med 2020; 383(24):2333-44.
53. Nalbandian A, Sehgal K, Gupta A et al. Post-acute COVID-19 syndrome. Nat Med 2021; 27(4):601-615.
54. Helms J, Kremer S, Merdji H et al. Neurologic Features in Severe SARS-CoV-2 Infection. N Engl J Med 2020; 382(23):2268-70.
55. Fotuhi M, Mian A, Meysami S, Raji CA. Neurobiology of COVID-19. J Alzheimers Dis 2020; 76(1):3-19.
56. Najjar S, Najjar A, Chong DJ et al. Central nervous system complications associated with SARS-CoV-2 infection: integrative concepts of pathophysiology and case reports. J Neuroinflammation 2020; 17(1):231.
57. Singh AK, Bhushan B, Maurya A, Mishra G, Singh SK, Awasthi R. Novel coronavirus disease 2019 (COVID-19) and neurodegenerative disorders. Dermatol Ther 2020; 33(4):e13591.
58. Ongur D, Perlis R, Goff D. Psychiatry and COVID-19. JAMA 2020; 324(12):1149-50.
59. Vindegaard N, Benros ME. COVID-19 pandemic and mental health consequences: Systematic review of the current evidence. Brain Behav Immun 2020; 89:531-42.
60. Pfefferbaum B, North CS. Mental Health and the Covid-19 Pandemic. N Engl J Med 2020; 383(6):510-2.
61. Xiang YT, Yang Y, Li W et al. Timely mental health care for the 2019 novel coronavirus outbreak is urgently needed. Lancet Psychiatry 2020; 7(3):228-9.
62. Gordon JA, Borja SE. The COVID-19 Pandemic: setting the mental health research agenda. Biol Psychiatry 2020; 88(2):130-1.
63. Huang C, Huang L, Wang Y et al. 6-month consequences of COVID-19 in patients discharged from hospital: a cohort study. Lancet 2021; 397(10270):220-32.
64. Higgins V, Sohaei D, Diamandis EP, Prassas I. COVID-19: from an acute to chronic disease? Potential long-term health consequences. Crit Rev Clin Lab Sci 2020; 1-23.
65. Moreno-Perez O, Merino E, Leon-Ramirez JM et al. Post-acute COVID-19 Syndrome. Incidence and risk factors: a Mediterranean cohort study. J Infect 2021; 82(3):378-383.
66. Townsend L, Dyer AH, Jones K et al. Persistent fatigue following SARS-CoV-2 infection is common and independent of severity of initial infection. PLoS ONE 2020; 15(11):e0240784.
67. Theoharides TC, Conti P. COVID-19 and Multisystem Inflammatory Syndrome, or is it Mast Cell Activation Syndrome? J Biol Regul Homeost Agents 2020; 34(5):1633-6.
68. Akin C, Valent P, Metcalfe DD. Mast cell activation syndrome: Proposed diagnostic criteria. J Allergy Clin Immunol 2010; 126(6):1099-104.
69. Theoharides TC, Tsilioni I, Ren H. Recent advances in our understanding of mast cell activation - or should it be mast cell mediator disorders? Expert Rev Clin Immunol 2019; 15(6):639-56.
70. Theoharides TC. COVID-19, pulmonary mast cells, cytokine storms, and beneficial actions of luteolin. Biofactors 2020; 46(3):306-8.
71. Theoharides TC. Luteolin supplements: All that glitters is not gold. Biofactors 2021 Mar;47(2):242-244. doi: 10.1002/biof.1689. Epub 2020 Nov 7.

EDITORIAL

Monoclonal antibody therapy in COVID-19 induced by SARS-CoV-2

P. Conti[1], F.E. Pregliasco[2], V. Calvisi [3], A. Caraffa[4], C.E. Gallenga [5], S.K. Kritas[6] and G. Ronconi[7]

[1]Postgraduate Medical School, University of Chieti, Chieti, Italy; [2] Istituto Ortopedico Galeazzi, Milano, Italy; [3]Department of Orthopaedics, School of Medicine, University of L'Aquila, L'Aquila, Italy; [4]School of Pharmacy, University of Camerino, Camerino, Italy; [5]Molecular Medicine, Department of Morphology, Surgery, Experimental Medicine, University of Ferrara, Ferrara, Italy; [6]Department of Microbiology, University of Thessaloniki, Thessaloniki, Greece; [7]Fondazione Policlinico Universitario A. Gemelli IRCCS, Università Cattolica del Sacro Cuore, Rome, Italy

Acute severe respiratory syndrome coronavirus-2 (SARS-CoV-2) infection causes coronavirus disease-2019 (COVID-19) which is associated with inflammation, thrombosis edema, hemorrhage, intra-alveolar fibrin deposition, and vascular and pulmonary damage. In COVID-19, the coronavirus activates macrophages by inducing the generation of pro-inflammatory cytokines [interleukin (IL)-1, IL-6, IL-18 and TNF] that can damage endothelial cells, activate platelets and neutrophils to produce thromboxane A2 (TxA2), and mediate thrombus generation. In severe cases, all these phenomena can lead to patient death. The binding of SARS-CoV-2 to the Toll Like Receptor (TLR) results in the release of pro-IL-1β that is cleaved by caspase-1, followed by the production of active mature IL-1β which is the most important cytokine in causing fever and inflammation. Its activation in COVID-19 can cause a "cytokine storm" with serious biological and clinical consequences. Blockade of IL-1 with inhibitory and anti-inflammatory cytokines represents a new therapeutic strategy also for COVID-19. Recently, very rare allergic reactions to vaccines have been reported, with phenomena of pulmonary thrombosis. These side effects have raised substantial concern in the population. Highly allergic subjects should therefore be vaccinated under strict medical supervision. COVID-19 has accelerated vaccine therapy but also the use of drugs and monoclonal antibodies (mABs) which have been used in COVID-19 therapy. They are primarily adopted to treat high-risk mild-to-moderate non-hospitalized patients, and it has been noted that the administration of two mABs gave better results. mABs, other than polyclonal plasma antibodies from infected subjects with SARS-CoV-2, are produced in the laboratory and are intended to fight SARS-CoV-2. They bind specifically to the antigenic determinant of the spike protein, inhibiting the pathogenicity of the virus. The most suitable individuals for mAB therapy are people at particular risk, such as the elderly and those with serious chronic diseases including diabetics, hypertension and obesity, including subjects suffering from cardiovascular diseases. These antibodies have a well-predetermined target, they bind mainly to the protein S (formed by the S1A, B, C and D subtypes), located on the viral surface, and to the S2 protein that acts as a fuser between the virus and the cell membrane. Since mABs are derived from a single splenic immune cell, they are identical and form a cell clone which can neutralize SARS-CoV-2 by binding to the epitope of the virus. However, this COVID-19 therapy may cause several side effects such as mild pain, bleeding, bruising of the skin, soreness, swelling, thrombotic-type episodes, arterial hypertension, changes in heart activity, slowed bone marrow activity, impaired renal function,

Corresponding Author:
Dr. Pio Conti,
Professor of Immunology, Post Graduate School of Medicine,
University of Chieti-Pescara, University Zone,
Viale Unità d'Italia, 73 66013 Chieti, Italy,
Tel./Fax +39 0871 574136
e-mail: piocontieditor@biolifesas.org

0393-974X (2021)
Copyright © by BIOLIFE, s.a.s.
This publication and/or article is for individual use only and may not be further reproduced without written permission from the copyright holder.
Unauthorized reproduction may result in financial and other penalties
DISCLOSURE: ALL AUTHORS REPORT NO CONFLICTS OF INTEREST RELEVANT TO THIS ARTICLE.

diarrhea, fatigue, nausea, vomiting, allergic reaction, fever, and possible subsequent infection may occur at the site of injection. In conclusion, the studies promoting mAB therapy in COVID-19 are very promising but the results are not yet definitive and more investigations are needed to certify both their good neutralizing effects of SARS-CoV-2, and to eliminate, or at least mitigate, the harmful side effects.

Key words: SARS-CoV-2, COVID-19, pro-inflammatory cytokines, anti-phospholipid antibodies, IL-1 family

The infectious SARS-CoV-2 pandemic emerged in 2019 and so far, has rapidly affected millions of people around the world. In coronavirus-19 disease (COVID-19), dyspnoea, progressive respiratory failure, hypoxemia, pulmonary edema, and other symptoms can occur (1). In the severe pathogenesis of COVID-19, anti-phospholipid antibodies are produced which, in conjunction with activated neutrophils and platelets, and pro-inflammatory cytokines, can damage endothelial cells and generate thrombotic events (2). In these cases, the spike protein of the virus by binding to the ACE2 receptor and to CD147 activates platelet PF4 which by binding to endothelial cells generates thrombi (3). Furthermore, SARS-CoV-2 activates granulocytes and platelets to produce thromboxane A2 (TxA2) (detected as TxB2) which also promotes thrombus generation (4). SARS-CoV-2 causes inflammation of tissues and organs, including lungs, with the production of pro-inflammatory cytokines and chemokines that can even cause death (5). Indeed, interleukin (IL)-1, one of the most important cytokines in the inflammatory process, is extensively studied in microbial infections, including viruses. Excessive production of IL-1 causes exaggerated inflammation that triggers pro-inflammatory cytokines that include members of the IL-1 family (such as IL-18), but also IL-6 and TNF, causing a "cytokine storm". Therefore, targeting IL-1 with anti-inflammatory cytokines may represent an interesting therapeutic strategy in inflammatory diseases, including COVID-19.

In a short time, safe and effective COVID-19 vaccines have been generated, representing a true scientific "illuminism" that will save millions of lives (6). However, allergic reactions to the vaccine or monoclonal antibody (mAB) in COVID-19 treatment have raised much concern due to the rare cases, albeit of uncertain origin, occurring globally. Therefore, the doctor must warn people who have a mast cell disorder or who have high allergic reactions before carrying out these therapies, even if serious events rarely occur.

Individuals highly allergic to mRNA or vector (adenovirus) vaccines can undergo allergic phenomena with the risk of an immediate reaction with the production of chemical mediators or delayed response with the generation of pro-inflammatory cytokines. Immediate systemic allergy can occur within the first 2 hours of treatment and can be fatal in some cases. The first allergic reaction can occur at the injection site, but also in tissues and organs, including lungs. After treatment with vaccines or mABs, reactions may be more frequent in highly allergic people and this must be taken into consideration (7). Therefore, before treatment, an anamnesis should be made to assess the pathological risk to which the subject is exposed. The most severe allergic reactions occurred in people who had had a previous life-threatening anaphylactic reaction. Some vaccines have shown life-threatening clotting disorders and have been paused at the present time, although the risk of these potential side effects are very small compared to the risks associated with coronavirus-19 infection. Furthermore, it is not yet certain whether these adverse effects result from vaccination and this should be clarified. In addition, it is recommended not to use these vaccines for people who have a high risk of clotting or a history of anaphylactic reaction. However, failure to use available vaccines could cost many lives.

COVID-19 has accelerated not only the production of vaccines but also the production of drugs and antibodies for the development of clinical therapy. Recently, the FDA approved (not as part of the usual standard review, but with a shorter, simpler, and more incomplete review process) the use of some mABs for COVID-19 therapy in order to reduce the severity and duration of the disease,

as well as hospitalization rates of high-risk patients, improving the chances of recovery (8).

In 1984, Köhler, Milstein and Jerne were awarded the Nobel Prize in Medicine for the discovery of mABs (9). These proteins have previously been generated for the prophylaxis and therapy of viral infections, such as Ebola, HIV, Zika, influenza and MERS-CoV. Officially, only a few mABs have been shown to be very effective in human studies, but they have paved the way for clinical progress, although, a number of mABs are still under study and require wider investigation.

Treatment of COVID-19 patients with mAB used in clinical trials may reduce hospitalization and emergency room visits. mABs were generated for the purpose of fighting the SARS-CoV-2 virus and it is hoped that this treatment represents a new and effective therapeutic strategy against the rapid expansion of COVID-19 which, as we know, can be globally lethal. In SARS-CoV-2 infection, mABs act by specifically binding to the antigenic determinant of the spike protein and inhibiting the pathogenicity of the virus. mABs are proteins produced in the laboratory with the aim of fighting pathogens including SARS-CoV-2. These antibodies have a well-predetermined target and are different from the plasma antibodies from previously infected patients with SARS-CoV-2.

Hence, mABs can be used to treat COVID-19 adult individuals who are not hospitalized and who are at high risk of developing severe symptoms. In particular, the treatment should be administered to patients with mild-to-moderate disease. mABs are recommended to avoid the risk of progression to severe disease and/or hospitalization. In SARS-CoV2 infection, the most suitable subjects for mAB therapy are people at particular risk, such as the elderly and those with serious chronic diseases including diabetes, hypertension and obesity, as well as subjects suffering from cardiovascular diseases. The therapy is directed against the antigenic determinant of the spike protein that the coronavirus uses to enter the host cell. The mABs bind on the receptor domain region of the viral spike protein and carry out its inhibiting action. The antibody binds mainly to the protein S formed by the S1A, B, C and D subtypes located on the viral surface, and to the S2 protein which acts as a fuser between the virus and the cell membrane (10).

The NIH researchers recommend administering 2 mABs in combination for COVID-19 therapy to outpatients with mild-to-moderate disease at high risk of clinical progression. Two different mAbs administered together against the virus can better reduce the effects and symptoms of the disease. In fact, in the therapy with a cocktail of mABs a better functioning was observed compared to the single administration and more effective reduction of the viral load (11). The treatment must be carried out strictly in clinic and lasts about 1 hour.

The mABs against SARS-CoV-2 can be produced by injecting the spike protein into a mouse, causing the formation of reactive splenic immune cells. Genes of the heavy and light chains of antibodies from virus-activated immune cells are isolated to produce mABs. Lymphocytes sensitized and activated by the spike protein are subsequently cloned to produce specific antibodies against this protein, preventing the virus from entering the cells. These antibodies are generated from patient-specific type B immune cells activated against SARS-CoV-2 or from genetically modified mice. Activated immune cells on recognition of the antigenic spike protein are fused with myeloma cells to form a hybridoma, whose reactive positive cells produce mAB against the antigenic spike protein. Since these antibodies are derived from a single splenic immune cell, they are identical and form a cell clone different from the polyclonal antibodies of convalescent patients, therefore, human mAB can neutralize SARS-CoV-2 by binding to an epitope of the virus, offering potential prevention and therapeutic treatment in COVID-19. Thus, mABs can potentially improve disease status by helping to protect the patient and eliminate the virus (12).

Side effects such as mild pain, bleeding, bruising of the skin, soreness, swelling, and possible subsequent infection may occur at the site of injection of the monoclonal antibody. In addition, the most common side effects of mAB therapy are: thrombotic-type episodes, arterial hypertension, changes in heart activity, constipation, slowed bone

marrow activity, impaired renal function, diarrhea, fatigue, nausea, vomiting, pain, allergic reaction and fever. Patients treated with mAB should continue to follow COVID-19 prevention rules such as staying at home, washing hands, disinfecting shared surfaces, and respecting 2 meters of physical distance. Following mAB therapy, individuals can test positive for SARS-CoV-2 for up to three months. COVID-19 vaccination should be performed approximately 90 days after mAB therapy. Therefore, neutralizing mABs are a potential treatment for COVID-19 and therapeutic administration is recommended in the mild or moderate COVID-19 form.

Outpatient treatment should be performed on adult patients at risk of disease progression. These patients include those with chronic diseases e.g., chronic kidney disease, diabetes, cardiovascular disease, hypertension, chronic obstructive pulmonary disease, and other conditions. Patients with a positive SARS-CoV-2 test should be treated with mAB as soon as possible and, if patients have received vaccination, the benefit of monoclonal therapy should be weighed. mAB treatment is a potential effective and novel therapeutic approach in preventing SARS-CoV-2 infection and they represent passive immunotherapy that plays a vital role as a possible treatment for COVID-19. mABs open up new therapeutic hopes that can reduce both the number of hospitalized individuals and mortality, however, this therapy has the disadvantage of being expensive and the effects can be short-lived.

In spite of the therapeutic benefits of mAB, some studies were suspended after finding in several cases that the therapy was ineffective and caused problems. Other studies using mAB were also discontinued because after treatment, hospitalized patients who received oxygen and were on mechanical ventilation had a high risk, greater than the therapeutic benefit.

Moreover, it has been observed that rare cases of immediate, non-fatal hypersensitivity may occur following therapy. In clinical studies, a certain number of excess antibodies that fail to neutralize SARS-CoV-2 can lead to the formation of immune complexes which are subsequently phagocytosed by macrophages within which viruses can replicate inside the cell and increase their virulence. Furthermore, viruses that bind to the gamma Fc fragment of macrophage cells stimulate pro-inflammatory cytokines, causing inflammation.

In conclusion, therapies with anti-SARS-CoV-2 mABs can have side effects aggravating the COVID-19 disease and consequent worsening of respiratory activity. This negative reaction adds to the inflammation due to the "cytokine storm" with deleterious effects that can even be deadly (13).

In light of the observations reported herein, we can say that the studies promoting mAB therapy are very promising but the results are not yet definitive as there are some concerns about their safety, efficacy and use; therefore, research in this field is still under investigation and, based on the potential side effects of this therapy, it should be used with caution also in COVID-19.

REFERENCES

1. Kazi DS, Martin LM, Litmanovich D, Pinto DS, Clerkin KJ, Zimetbaum PJ, Dudzinski DM. Case 18-2020: A 73-year-old man with hypoxemic respiratory failure and cardiac dysfunction. N Engl J Med 2020; 382(24):2354-64.
2. Linnemann B. Antiphospholipid syndrome - an update. Vasa 2018; 47(6):451-64.
3. Düsing R. Pharmacological interventions into the renin-angiotensin system with ACE inhibitors and angiotensin II receptor antagonists: effects beyond blood pressure lowering. Ther Adv Cardiovasc Dis 2016; 10(3):151-61.
4. Conti P, Caraffa A, Gallenga CE, Ross R, Kritas SK, Frydas I, Younes A, Di Emidio P, Ronconi G, Toniato E.IL-1 induces throboxane-A2 (TxA2) in COVID-19 causing inflammation and micro-thrombi: inhibitory effect of the IL-1 receptor antagonist (IL-1Ra). J Biol Regul Homeost Agents 2020; 34(5):1623-7.
5. CORIMUNO-19 Collaborative group. Effect of anakinra versus usual care in adults in hospital with COVID-19 and mild-to-moderate pneumonia (CORIMUNO-ANA-1): a randomised controlled trial. Lancet Respir Med 2021; 9(3):295-304.
6. Krause PR, Gruber MF. Emergency Use Authorization of Covid Vaccines - Safety and Efficacy Follow-up Considerations. N Engl J Med 2020 ; 383(19):e107.
7. Shanmugaraj B, Siriwattananon K, Wangkanont

K, Phoolcharoen W. Perspectives on monoclonal antibody therapy as potential therapeutic intervention for Coronavirus disease-19 (COVID-19). Asian Pac J Allergy Immunol. 2020; 38(1):10-18.

8. Drożdżal S, Rosik J, Lechowicz K, Machaj F, Kotfis K, Ghavami S, Łos MJ. FDA approved drugs with pharmacotherapeutic potential for SARS-CoV-2 (COVID-19) therapy. Drug Resist Updat 2020; 53:100719.
9. Köhler G. The Nobel Lectures in Immunology. The Nobel Prize for Physiology or Medicine, 1984. Derivation and diversification of monoclonal antibodies. Scand J Immunol 1993; 37(2):117-29.
10. He Y, Zhou Y, Liu S, Kou Z, Li W, Farzan M, Jiang S. Receptor-binding domain of SARS-CoV spike protein induces highly potent neutralizing antibodies: implication for developing subunit vaccine. Biochem Biophys Res Commun 2004; 324(2):773-81.
11. Nirula A, Chen P, et al. Effect of Bamlanivimab as monotherapy or in combination with etesevimab on viral load in patients with mild to moderate COVID-19: A Randomized Clinical Trial. Gottlieb RL, JAMA 2021; 325(7):632-44.
12. Wang C, Li W, Drabek D, et al. A human monoclonal antibody blocking SARS-CoV-2 infection. Nat Commun 2020; 11(1):2251.
13. Lee WS, Wheatley AK, Kent SJ, DeKosky BJ. Antibody-dependent enhancement and SARS-CoV-2 vaccines and therapies. Nat Microbiol 2020; 5(10):1185-91.

Focus on the cariogenic process: microbial and biochemical interactions with teeth and oral environment

G. Dipalma[1#], A.D. Inchingolo[1#], F. Inchingolo[1#], I.A. Charitos[2], M. Di Cosola[3*] and A.P. Cazzolla[3*]

[1]Department of Interdisciplinary Medicine, Dentistry Unit, University of Bari, Bari, Italy; [2]Emergency/Urgent Department, National Poisoning Center, Riuniti University Hospital of Foggia, Foggia, Italy; [3]Department of Clinical and Experimental Medicine, Riuniti University Hospital of Foggia, Foggia, Italy

Received January 7, 2021 – Accepted March 22, 2021

# These authors equally served as first co-authors
° These authors equally served as last co-authors

This paper aims to describe the biochemical interactions between teeth and the oral environment that occur during the caries process, hence it covers all the steps related to physico-chemical reactions, including the most up-to-date theoretical basis in the clinical application for the prevention and treatment of caries. The terms 'demineralization' and 'remineralization' that characterise this process were analysed, as well as the role of the microbiota in its interaction with the hard surface of the teeth. The biochemical mechanisms that lead to the onset of carious lesions and those that occur during the healing and repair of such lesions are listed.

Dental caries is the destruction of the dental structure and occurs on any dental surface where dental plaque grows for a long time. The creation of one of the dental plaques is an example of a biofilm that occurs through a natural process and is a community of interacting microbes such as *Lactobacillus* spp, *Candida* spp (1-3). The crown of the teeth can be further divided into separate areas and special ecological sites, each of which are characterized by higher or lower specific risk for the development of caries. Some of these sites host microbial communities that produce acids and can therefore withstand an acid environment. The composition of the dental microbiome is influenced not only by the specific position of each tooth in the mouth and its proximity to the flow of saliva (from neighbouring ducts), but also by the anatomy and physiology of the tooth surface and surrounding teeth (1). Most caries lesions occur in: (a) the cavities and fissures of the chewing surfaces of the posterior teeth; (b) the buccal and palatal cavities of the posterior and anterior teeth; (c) the adjacent surfaces, as well as from the point of contact of the teeth; (d) the cervical area of the teeth near the tooth gap; and (e) in the ossified root surface of the gums from gingivitis (1,4) (Fig. 1).

A change in pH (beyond the physiological value) can affect the integrity of the tooth surface through

Key words: dental diseases, dental caries, microbiota, microbiology, saliva, oral biochemistry

Corresponding Author:
Dr Ioannis Alexandros Charitos,
Ospedali Riuniti Plesso Colonello D'Avanzo,
Viale degli Aviatori, 2,
71122 Foggia, Italy
Tel.: +39 0881731111
e-mail: alexanestesia@hotmail.com

0393-974X (2021)
Copyright © by BIOLIFE, s.a.s.
This publication and/or article is for individual use only and may not be further reproduced without written permission from the copyright holder.
Unauthorized reproduction may result in financial and other penalties
DISCLOSURE: ALL AUTHORS REPORT NO CONFLICTS OF INTEREST RELEVANT TO THIS ARTICLE.

biomolecular mechanisms and physico-chemical reactions. Some oral microbes could produce acids by metabolizing dietary carbohydrates, thus creating a lowering of the pH in the surrounding environment. The humid environment created mainly by the secretions of the oral cavity and maintained through the salivary glands with the secretion of saliva has a protective role, because it has the ability to neutralize acids and increase the pH and recover the ions lost by the teeth (5-7). Furthermore, the part of the teeth exposed to this humid environment causes the formation of a solid-liquid phase system between the hard tissues of the tooth and the saliva, which is governed by biochemical laws, and is in a state of constant dynamic physic-chemical equilibrium. Under

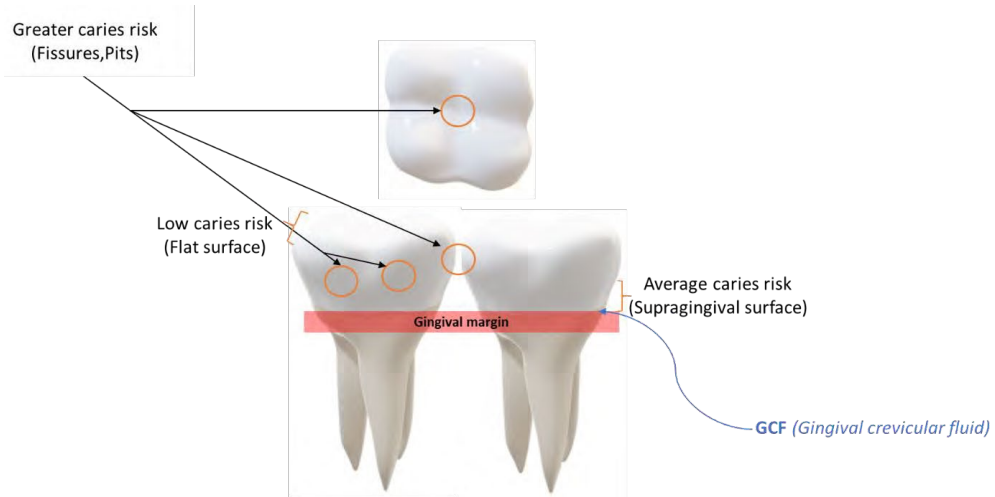


Fig. 1. *The main sites where caries lesion occurs. GCF: Inflammatory exudate of the gingival crevicular fluid is composed of serum that contains degenerated waste tissues from the periodontal areas, inflammatory mediators, and antibodies against dental plaque bacteria.*

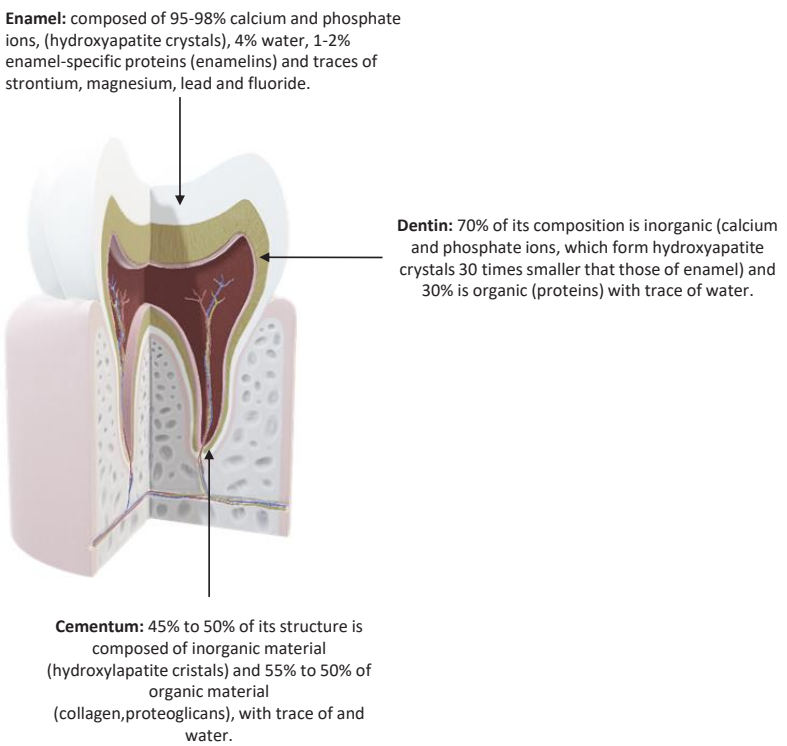


Fig. 2. *Hard tissues of human teeth and their chemical composition*

normal conditions, saliva contains an important number of various ions present also in the salts of the inorganic portion of the hydroxyapatite of the enamel. Thanks to this balance, the hard tissue of the tooth maintains its natural conformation and structural integrity (4, 5, 8) (Fig. 2).

ORAL MICROBIOME AND ITS ROLE IN DENTAL CARIES

The microbial risk factors that develop dental caries

Caries is mainly linked to lifestyle (e.g., diet, alcohol, tobacco, abuse of drugs such as cocaine, methamphetamine and others), socio-economic and behavioural factors such as poor oral hygiene (9, 10). The consumption of large quantities of carbohydrates causes an excessive production of acids that saliva is no longer able to regulate, leading to a continuous decrease in pH. This acidic environment in the oral cavity induces the production of protein enzymes causing changes in the qualitative and quantitative composition of the microbiota, and this also leads to the survival of microorganisms growing in a low pH (acidic) environment (11, 12). Hence, these microorganisms (such as *Streptococcus mutans*, *Lactobacillus* spp) also ferment sugars that produce more lactic acid. This leads to keeping the pH much more lower, thus creating favorable conditions for the damage of hard tissue of the teeth. It has been found that people with or without tooth decay share about 50% of germs. For many decades since the 1950s, *S. mutans* has been held solely responsible for tooth decay, however, several recent studies to determine whether the causative agent of the disease has produced vague results (13). *S. mutans* is often over-represented in white patches but is also present in some healthy people in small colonies, however, it appears to be associated only with the onset of caries and not with the development of caries. Furthermore, it appears to have the characteristics of a pathogen that is affected by dietary changes. In some patients with caries, *Lactobacillus* spp. and *S. mutans* are low or undetectable, suggesting that the onset and progression of lesions cannot be attributed to *S. mutans*. *S. mutans* has several virulence factors that allow it to establish itself in the oral cavity such as the cell surface localized the Ag I/II family proteins (**P1**, SpaP, AgB or **PAc**). Hence, the expression of P1 protein is necessary for the adhesion to hydroxyapatite which occurs during aggregation of **S**. **mutans** to saliva-coated materials. This is the first step towards its colonization in the tooth surface and the formation of dental plaque. During this phase, there is a change in the initial composition of the microbiome with the loss of a part of the microbial populations useful for eubiosis, leading to the development of caries (14, 15). Thus, organic acids derived from the hydrolysis of disaccharides, such as sucrose, and associated with caries also influence enzymatic reactions. Caries, in turn, reduces the diversity of microbes in relation to periodontal disease, possibly due to the acidic environment, thus limiting microbial growth in organisms that do not grow in an acidic environment. The bacteria that cause tooth decay use an enzyme, glucansucrase (or glucosyltransferase), to build long, sticky sugar chains called glucans that use the same sugars we introduce with food as the starting material. These glucans make bacteria adhere to the surface of the teeth, forming and fixing the biofilm. Glucansucrase catalyses two reactions: in the first one the enzyme reacts to sucrose to produce glucose and fructose; and in the second it releases fructose, and the enzyme binds glucose to the glucan chain. Glucan sucrase is a large protein with many sites of action that serve to anchor it to other glucan chains, however, these reactions take place in the central part of the enzyme. It has been noted that the synthesis of extracellular glucan largely depends on the part of *S. mutans*. Hence, glucansucrase catalyses glucan, instead there are proteins that bind glucan known as the glucan-binding proteins (Gbps). The functions of Gpbs include dextran-dependent aggregation, dextranase blockade, plaque adhesion, and possibly cell wall synthesis (16-18). The properties of the GBPs are related to the biological functions of *S. mutans* in the oral cavity. *S. mutans* also has other virulence factors such as collagen binding proteins (CBP) which are the Cnm and Cbm gene. These proteins, along with SpaP and WapA, are important cell surface antigens also linked to its adherence to collagen tissue. Furthermore, CBP + strains of *S.*

mutans have been observed to adhere early and are associated with systemic diseases such as infective endocarditis and others. Finally, other factors associated with the development of caries can be various immune and genetic factors (19-21).

Saliva microbiome and teeth interactions

The oral cavity secretes saliva that contains minerals, organic ingredients (amino acids, mucoproteins, carbohydrates, and others) and antimicrobial action proteins (such as lysozyme, lactose, cysteines, histamines, galactoxin, lactoperoxidase and calicidin). Therefore, the host's defenses against plaque occur through antimicrobial proteins together with immune ones, such as antibodies that reach the oral cavity through the salivary ducts. These factors play an important role in the formation and synthesis of the oral microbiome. The mucous membranes on the surface of the oral cavity and teeth are constantly immersed in saliva. The proteins and glycoproteins present in saliva lubricate, contribute to the sense of taste, facilitate chewing for the formation of the food bolus and support the formation of bio membranes (22). Microorganisms do not directly colonise the surfaces of the teeth. Teeth are always covered with a cell-free protein coating, the pellicle, which forms on the tooth surface. The acquired enamel pellicle formed by selective absorption of glycoproteins, phosphoproteins, lipids and bacterial derivate molecules on the surface of the enamel (23) (Fig. 3).

When there is no food in the oral cavity, microorganisms can break down these specific glycoproteins which are the source of their nutritional needs. The germs of saliva are those that come from the microbiota of the tissues of the oral environment. All epithelial surfaces peel off, releasing relevant germs in the saliva, however, the saliva microbiome is mostly enriched by microorganisms from the biomembrane of the tongue, such as *Prevotella*

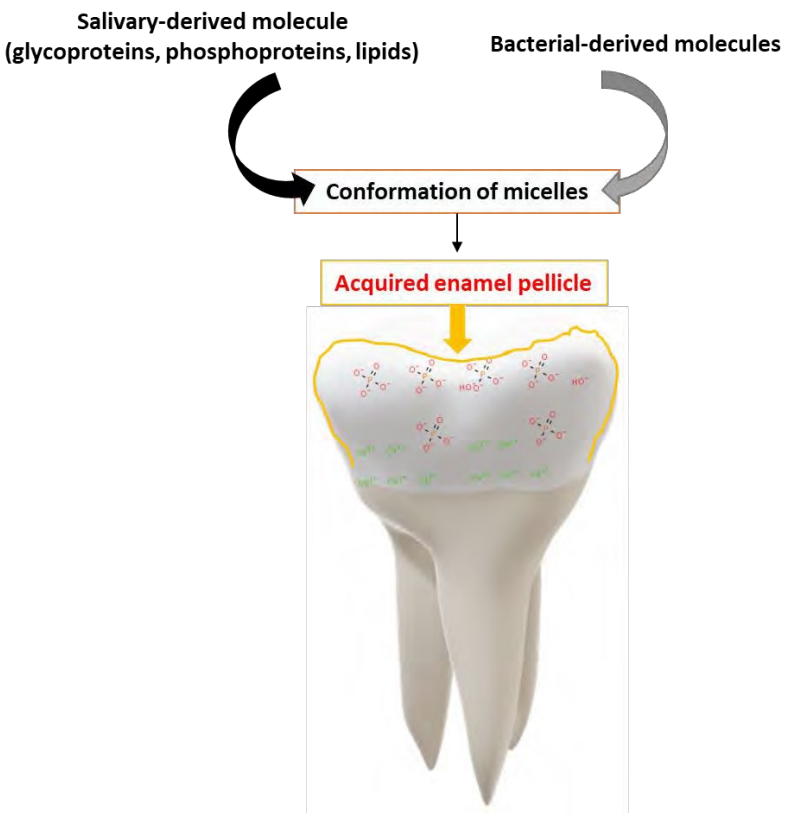


Fig. 3. *Example of the biochemical approach of the adsorption of salivary components to hydroxyapatite crystals and the formation of the enamel pellicle.*

and *Streptococ*cus (24, 25). Bacteria associated with caries, such as *Lactobacillus* spp, *S. mutans*, *Bifidobacterium* spp, *Atopobium* spp., have not been detected in subjects with healthy teeth. If the dental plaque is not removed by frequent brushing, the sugar-eating plaque bacteria release acids that destroy tooth enamel to form caries (26-29). Other genera have a presence of around 1% and are considered in any case transient or non-native microorganisms, thus saliva proteins and glycoproteins influence the formation of the bio membrane. These proteins can promote microbial adhesion because the salivary membrane and its constituent proteins overlap the teeth and mucous membranes. As already mentioned, saliva also contains antimicrobial proteins that can affect bioavailability by limiting the growth of other microorganisms (30). The tooth surfaces provide a stable attachment position for long-term bio membrane development. The tooth enamel is covered with a sialic membrane and the roots are coated with saliva and whey proteins. Consequently, the microbial populations of the plaque formed in the enamel that is supra gingival and above the gum line differs from the community below the gum line. As community development extends along the root and away from the salivary environment, the biofilm contains more serum, the environment becomes more anaerobic and the cleaning of the surface reduced. The microbial community of the tooth surface (crown) has a somewhat different composition from that of the saliva (such as for **Streptococcus** spp. and **Veillonella spp.**) (28, 31, 32).

Oral dysbiosis

As already stated, a disturbance in the balance of the oral and salivary microbiota leads to a condition of eubiosis to an irregular increase in certain bacterial strains that can cause tooth decay. This is the condition of oral microbiota dysbiosis. A community in microbial conditions of dysbiosis can deflect the host's immune response, resulting in local induction of nonspecific inflammatory reactions and subsequent tissue damage. This inflammatory process has as a consequence an increase of Gingival crevicular fluid (GCF) on small local haemorrhagic ulcers that, in turn, will deprive area of oxygen. This encourages the development of anaerobic bacteria (optional and mandatory) present in the gum cracks. This produces a worsening of the microbiota dysbiosis, with a consequent formation of numerous colonies of certain bacterial strains such as *Aggregatibacter actinomycetemcomitans* and *Porphyromonas gingivali*s (associated with periodontitis), *Scardovia* spp., *Actinomyces* spp., *S. mutans*, and *Bacteria mutans,* as well as fungi such as *Candida albicans* (33-36). Finally, oral dysbiosis may have effects on other organs of the human body or even systemic consequences. It has been noted that the increase of some bacterial strains such as *P. gingivalis* have altered the composition of the intestinal microbiota qualitatively and quantitatively, resulting in inflammatory reactions in other parts of the body. This is because the intestinal microbiota is one of the most important metabolic bio-stations and helps the host to an effective immune response. There is not only a relationship between oral and gut but there is also a communication between other organs which are called the cross-talking axes, Gut/lug, Gut/skin, and Gut/brain axes. Oral bacterial natural flora can play an important role in the pathogenesis of various systemic diseases and carcinogenic conditions (e.g., inflammatory bowel diseases, cardiovascular, rheumatoid arthritis, diabetes, colon cancer). The periodontal disease is known to have a negative effect on blood sugar control in diabetes mellitus, and healthy individuals have been found to have a higher risk of developing type II diabetes (37-43).

The use of friendly bacteria called probiotics is recommended. Probiotics fight the spread of pathogens, strengthen the microbiota and contribute to the creation of a strong immune system, which helps to heal a disease in a natural way. The concept of probiotics was first used by Parker (1974) to describe the type of food which has a positive effect on the host thus contributing to the eubiosis of the gut microbiota. The Food and Agriculture Organization/Word Health Association (FAO/WHO) in 2001 identified probiotics as live microorganisms which, when assumed in sufficient quantities as part of a diet, have a beneficial effect on the host (44, 45). The most used probiotic species are *Lactobacillus* and *Bifidobacterium*. Probiotics restore the dysbiosis by introducing good bacteria that fight the bacterial

proliferation of the not-friendly ones. Probiotics help balance the pH in the mouth and protect the microbiota from acids produced by certain bacteria that destroy tooth enamel, and reduce sulphur-producing bacteria found mainly in the back of the tongue, thus preventing bad breath. Finally, probiotics help to restore the natural and healthy production of saliva in the mouth thus preventing xerostomia (46-48).

Regarding the goal of non-invasive caries treatment in addition to probiotics, many strategies have been studied to date in order to prevent caries. Several meta-analyses suggest that sealants or resin infiltrations with 5% sodium fluoride (NaF) toothpaste, or sodium fluoride gel (from 5.000 ppm F = 1.1% NaF) are valid for halting non-cavitated and cavitated carious lesions (9, 49). The use of chlorhexidine in caries prevention, such as a non-invasive management, represents another approach, however, its use for such prevention is controversial and several studies confirm the reduction of persistent plaque from *S. mutans* spp. by chlorhexidine varnish. Since dental caries is a disease with a multifactorial aetiology, it is increasingly appropriate to use evidence-based treatments, such as fluoride applications, complete oral hygiene, and an appropriate diet (50, 51). As already pointed out, chronic oxidative stress, the acidic pH on the enamel surface, together with the dissolution (demineralization) of calcium (Ca) and magnesium (Mg) can contribute to the development and progression of dental caries. It has been noted that zinc (Zn) plays a fundamental role in the bioavailability of Ca and Mg in the oral cavity as it helps the deposition of the two ions in the enamel (remineralization). It has been noted that the use of oral hygiene products such as toothpaste and mouthwash based on zinc salts (zinc chloride, zinc sulphate, zinc citrate, zinc lactate) can reduce the formation of plaque and block the formation of tartar. Finally, several studies are underway to develop vaccines. This means development of antibodies against various *S. mutans* antigens against caries formation (51, 52). Several *S. mutans* cell surface antigens have been pressed to create antibodies such as glucosyltransferase (GTF), AgA/C /D, AgI/II, AgIII, lipoteic acid (LTA), Gbps and dextrasucrase. Dextransacrase antibodies appear to reduce biofilm formation and thus plaque growth in the presence of *S. mutans* (53, 54).

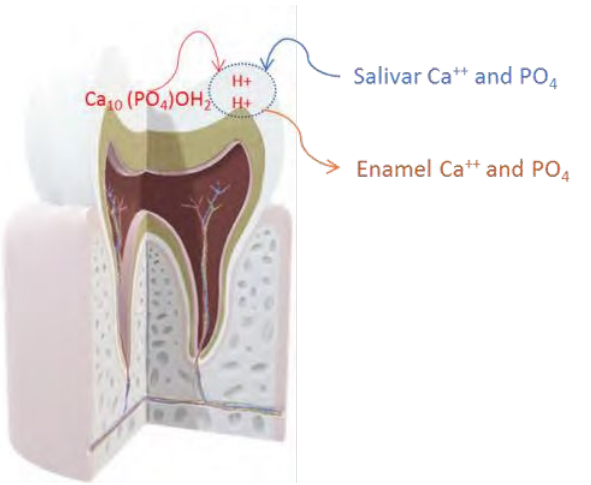


Fig. 4. *In the chemical imbalance of saliva surrounding the enamel (hyper saturation) there is a movement of calcium and phosphorus ions from the enamel into the oral environment (saliva). In restoring the chemical balance of the saliva surrounding the enamel (supersaturation), there is a movement of calcium and phosphorus ions from the oral environment (saliva) to the enamel. In restoring the chemical balance of the saliva surrounding the enamel (supersaturation), there is a movement of calcium and phosphorus ions from the oral environment (saliva) to the enamel.*

PHYSICO-CHEMICAL INTERACTIONS OF TEETH AND THE ORAL ENVIRONMENT

Crystal dissolution process

According to the chemical proprieties, all salt crystals show intrinsic and stable solubility in water at a given temperature. Their dissolution in water is initially rapid, but subsequently slows down when the released ions are concentrated in higher number in the saliva, resulting in the saturation of those ions. In this state of equilibrium, a slow ion exchange remains between the crystals and the solution (Fig. 4) (55).

Water molecules enter the crystallised inorganic surface and release its ions. This is mainly due to the high dielectric constant of the water, which causes a reduction in the forces of attraction between the various ions with opposite charges in the crystal lattice. According to the law of mass action, the rate of a chemical reaction is proportional to products of the masses of the reactive

components elevated to a force equal to the number of molecules participating in the reaction. When a specific mass of a solid hydroxyapatite dissolves, five calcium ions, three phosphate ions and one hydroxyl anion are released ($Ca_5 (PO_4) 3 (OH) \rightleftarrows 5\ Ca_2^{++}\ 3\ PO_4^{3-} + OH-$) (39,40). The main factors that influence the solubility product of a crystalline salt and consequently the dissolution are pH, temperature, and coexistence of other ions. Hence, the solubility of hydroxyapatite is higher in cold water. When hydroxyapatite dissolves, calcium and phosphate ions accumulate in the solution, and the dissolution of hydroxyapatite slows and stops as the solution becomes saturated. If found in an acidic pH environment, PO_4 ions 3- and OH- bind to H^+ and form HPO_4^{2-} and H_2O, respectively, resulting in reduction of PO_4 concentration 3- and OH- (50). The solution becomes saturated, and more hydroxyapatite dissolves to restore the chemical balance. When the solution reaches pH 5 of the solution surrounding the tooth, it is considered non-saturated, but when it reaches pH 7, the solution becomes oversaturated, and hydroxyapatite is formed. Subsequently the pH of a supersaturated solution gradually decreases, and the point where the solution becomes almost saturated is called the critical pH (Fig. 5) (56).

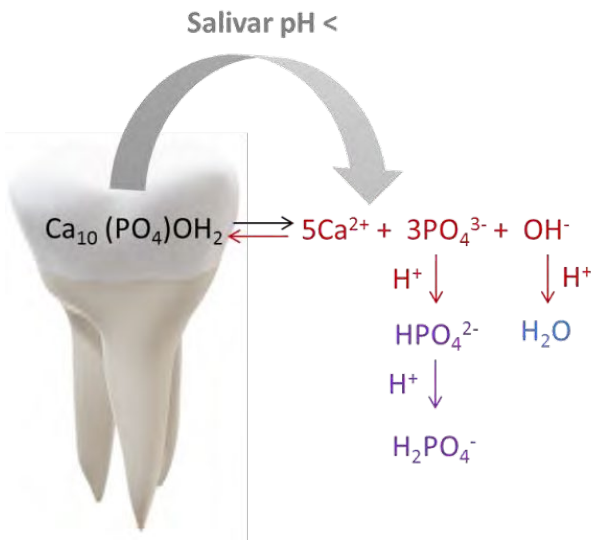


Fig. 5. *The dissolution of hydroxyapatite crystals is not isotropic. According to the equation shown in the figure, if there is an excess of one ion in the solution, less of the other ion is needed to achieve chemical equilibrium (this called the common ion effect). At normal pH (6.7-7.4), hydroxyapatite is the most stable form of calcium phosphate, however, after the eruption of the teeth, the hydroxyapatite of the outer surface of the enamel and dentin is exposed to a wide pH fluctuation due to dietary and metabolic conditions.*

Under favourable conditions, new crystals can therefore precipitate from the solution and these new and small crystals can increase in size in form of soluble salts or increase the pH. However, saliva contains elements that control and inhibit crystalline growth, such as pyrophosphates and various salivary glycoproteins such as statherin (STATH), acidic proline-rich proteins and stereochemical mechanisms e.g., in the enamel the hydroxyapatite crystals are so close together that there is insufficient space to grow and enlarge (4, 56, 57). Indeed, mesenchymal cell (MSC) research can be important for the treatment of various dental diseases. Mesenchymal stem cells of dental origin can be applied for regeneration and replacement of dental or oral tissues against caries, periodontitis, etc. Finally, the use of platelet-rich plasma and fibrin extracts in dental implant surgery may be useful.

Chemical changes in enamel during the caries process

Enamel crystals differ from pure hydroxyapatite as they also contain other inorganic ions. The structure of the enamelled hydroxyapatite allows the flow of external ions to sites that would normally be occupied by calcium ions, phosphates ions and hydroxyl groups. In some crystals, calcium ions are replaced by sodium ions, hydroxyl ions are replaced by fluoride ions, and phosphate ions are replaced by bicarbonate ions. Other ions can be chloride ion (Cl^-) and magnesium ion (Mg^{++}). These elements influence the biochemical properties of the structured crystals such as the solubility of the enamel. The presence of bicarbonate ions causes hydroxyapatite to be more soluble, while fluoride ions cause the opposite effect (62). It is important to mention that fluoride ions, when present in solution, drastically reduce the amount of Ca released by the enamel at acidic pH, so low concentrations of fluoride are effective in reducing tooth decay. Enamel crystals are small and have a relatively large surface area, so they have a high capacity to receive various foreign ions. All ions are absorbed on the surface, or near it, through a layer of water, consequently forming the hydration

zone. Enamel crystals are not only heterogeneous on the surface but also in their mass. Near the outer surface, they contain more fluoride and less carbonate ions than inside and its outer layer is less soluble. Saliva has a significant degree of phosphate (PO_4^{3-}) and calcium (Ca^{++}) ions and is usually also saturated with salts from the enamel (Fig. 6) (4, 63). Enamel does not dissolve at normal oral pH. In supersaturated conditions, the enamel crystals do not continue to grow or form new crystals on the tooth surface because saliva contains proteins that inhibit the growth of hydroxyapatite crystals. These proteins are statherin (a phosphoprotein), a protein with peptides rich in tyrosine and proline, that covers the enamel and protects it from the precipitation of limestone and the consequent crystalline growth. Dental plaque covers the enamel and generally prevents the tooth surface from coming into contact with saliva. This film contains biological fluid of the plaque and its chemical composition differs from saliva (the concentrations of calcium and phosphorus ions are 2-3-fold higher than in saliva). This supersaturated solution is beneficial for the remineralization of the underlying caries lesions but also creates the conditions for the growth of tartar (64-66). The microbial plaque is subjected to significant pH fluctuations, due to the metabolic activities of its microbial flora. When the pH value of the solution surrounding the tooth falls below the critical pH value, the liquid phase ceases to saturate in respect to the surface salts of the enamel with which it comes into contact. This condition involves imbalance between saliva and enamel, so initiating the process of salts from the enamel to the liquid phase (demineralization of the enamel). The average critical pH of the enamel which corresponds to the layer of liquids which are in direct contact with it is around 5.3-5.5. The increase in pH, which occurs with the intake of fermentable carbohydrates, keeps below the critical pH for a period of approximately 19-39 minutes, and the restoration of the pH is achieved by removing acids or neutralizing them from the saliva buffer systems. A certain amount of the acid produced by microbial plaque penetrates the enamel (67, 68). The balance comes about by melting some enamel and reshaping the hydroxyapatite if the supersaturation conditions are suitable. This means that in the tooth surface there is a continuous cycle of demineralization and

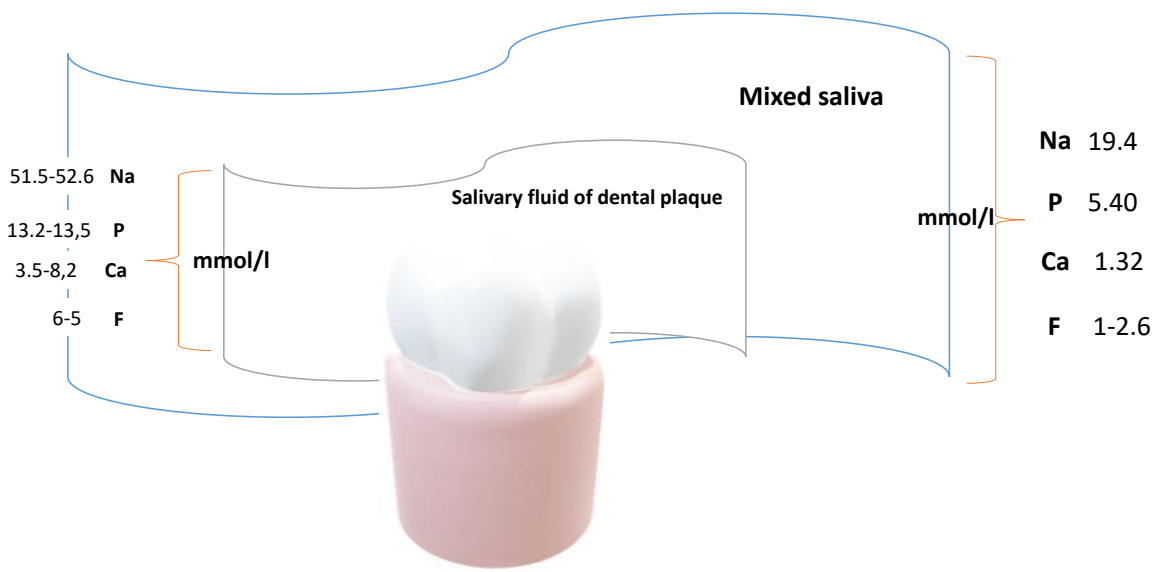


Fig. 6. *During metabolic activity, the salivary fluid of dental plaque has concentrations of minerals higher than in the mixed saliva. It should be noted that the concentrations of Ca and P minerals are 2-3 times higher. Resting mixed saliva is supersaturated compared to pure enamel hydroxyapatite and these concentration levels steadily increase when saliva flow is stimulated.*

remineralization, speed- and duration-dependent. The decrease in pH affects the solubility of the hydroxyapatite crystals and the critical pH of the environment decreases, resulting in in an important modification of its solubility. Hence, the solubility of hydroxyapatite will increase approximately 10 times for each pH unit decrease. During the formation of caries there is partial dissolution of the hard tissue, leaving a sub-superficial lesion body with a loss of 30-50% of minerals (which progresses deep into the enamel or dentin) and a well-defined 20-50 μm-thick calcified layer. When the pH decreases in oral fluids, due to thermodynamic and chemical kinetic properties of the crystals, bruxite appears on the surface of the enamel (67-69). Furthermore, the microbial plaque fluid remains supersaturated for fluor-hydroxyapatite (less soluble) and unsaturated for hydroxyapatite. Under these conditions, hydroxyapatite dissolves on the surface, and bruxite with fluorohydroxyapatite forms a layer on the enamel surface which is responsible for the long-term integrity of the superficial structure. Diffusion of H^+ ions in carious lesions is a slow layering process because the surface of the calcified lesion protects from both demineralization and remineralization. This external enamel layer, after remineralization, presents a disorganized structure (amorph tissue), in opposition to the normal differentiated crystalline structure of hydroxyapatite (65, 66). According to the salivary theory of Leimgruber, endogenous dental tissues are assimilated to a semipermeable membrane, thus dividing the saliva from the blood and interstitial pulp fluids. Bacterial plaque consists of a corpuscular fraction (bacteria, flaking epithelial cells) and an amorphous fraction (deriving from salivary glycoproteins and sugars introduced with the diet) which promotes bacterial adhesion to the tooth surface). We distinguish a supragingival plaque (responsible for caries and influenced by diet) and a subgingival plaque (responsible for periodontal disease). The presence of supragingival plaque exoenzymes, such as glycosyltransferases, glucosidases, pyrophosphatases and amino peptidases, facilitates dental damage. If the plaque is not removed, there is the formation of deposits of calcium and phosphorus salts, which transform it into tartar (70).

Chemical changes in dentin

Dentin has a chemical behaviour like enamel. The difference of dentin lies in the hydroxyapatite crystals, as they are smaller which makes the dentin surface more vulnerable to decay. Dentin has a high percentage of ions in the form of impurities and contains an important percentage of organic matter, mainly collagen. The acid produced by the germs has no effect on the collagen of the dentin. The degradation of its proteins begins with the action of proteolytic enzymes (proteinases or proteases) produced by cariogenic microbes. Another class of proteases that are activated during the caries process are metalloproteinases which are activated at acid pH and cause collagen degradation (64, 69).

CONCLUSION

The approach to dental pathologies such as caries has always concerned prevention, aetiology, histopathology and the diagnostic means, while the treatment has mainly concerned dental surgery. However, tooth decay is a disease with characteristics common to other diseases. It is assumed that an in-depth knowledge of the aetiology of caries and of all the biomolecular/biochemical mechanisms on which the appearance and development of damage depends is required for a better approach. In particular, the microbiota of the teeth and saliva plays an important role because it regulates the health of the hard surface of the teeth and protects it from "bad" bacteria. Probiotics could prevent dental diseases via the beneficial properties of oral cavity commensal bacteria. Prevention and diagnosis in the earliest stages is crucial. Indeed, the treatment of caries, in addition to prevention and restoration of the lesion, now include new approaches with non-invasive therapies

REFERENCES

1. Marsh, PD. Dental plaque as a biofilm and a microbial community - implications for health and disease. BMC Oral Health 2006; 6 (Suppl 1):S14.
2. Monea A, Santacroce L, Marrelli M, Man A. Oral

candidiasis and inflammatory response: A potential synergic contribution to the onset of Type-2 Diabetes Mellitus. AMJ 2017; 10(6):550-6.
3. Man A, Ciurea CN, Pasaroiu D, et al. New perspectives on the nutritional factors influencing growth rate of Candida albicans in diabetics. An in vitro study. Mem Inst Oswaldo Cruz 2017; 112(9):587-92.
4. Santacroce L, Carlaio RG, Bottalico L. Does it make sense that diabetes is reciprocally associated with periodontal disease? Endocr Metab Immune Disord Drug Targets 2010; 10(1):57-70.
5. Barbería E, Maroto M, Arenas M, Silva CC. A clinical study of caries diagnosis with a laser fluorescence system. J Am Dent Assoc 2008; 139(5):572-9.
6. De Benedittis M, Petruzzi M, Pastore L, Inchingolo F, Serpico RJ. Nd:YAG laser for gingivectomy in Sturge-Weber syndrome. Oral Maxillofac Surg 2007; 65(2):314-6.
7. Belibasakis GN, Bostanci N, Marsh PD, Zaura E. Applications of the oral microbiome in personalized dentistry. Arch Oral Biol 2019; 104:7-12.
8. Struzycka I. The oral microbiome in dental caries. Pol J Microbiol 2014;63(2):127-35
9. Inchingolo F, Santacroce L, Ballini A, et al. Oral Cancer: A Historical Review. Int J Environ Res Public Health 2020; 17(9):3168.
10. Chen X, Daliri EB, Kim N, Kim JR, Yoo D, Oh DH. Microbial Etiology and Prevention of Dental Caries: Exploiting Natural Products to Inhibit Cariogenic Biofilms. Pathogens 2020; 9(7):569.
11. Takahashi N, Nyvad B. The role of bacteria in the caries process: ecological perspectives. J Dent Res 2011; 90(3):294-303.
12. Ballini A, Dipalma G, Isacco CG, et al. Oral Microbiota and Immune System Crosstalk: A Translational Research. Biology (Basel) 2020; 9(6):131.
13. Peterson SN, Snesrud E, Liu J, et al. The dental plaque microbiome in health and disease. PLoS One 2013; 8(3):e58487.
14. Gross EL, Leys EJ, Gasparovich SR, et al. Bacterial 16S sequence analysis of severe caries in young permanent teeth. J Clin Microbiol 2010; 48(11):4121-8.
15. Belda-Ferre P, Alcaraz LD, Cabrera-Rubio R, Romero H, Simón-Soro A, Pignatelli M, Mira A. The oral metagenome in health and disease. ISME J 2012; 6(1):46-56.
16. Banas JA, Vickerman MM. Glucan-binding proteins of the oral streptococci. Crit Rev Oral Biol Med 2003; 14(2):89-99.
17. Di Serio F, Lovero R, D'Agostino D, et al. Evaluation of procalcitonin, Vitamin D and C-reactive protein levels in septic patients with positive emocoltures. Our preliminary experience. Acta Med Mediterr 2016; 32:1911–4.
18. Cantore S, Mirgaldi R, Ballini A, et al. Cytokine gene polymorphisms associate with microbiogical agents in periodontal disease: our experience. Int J Med Sci 2014; 11(7):674-9.
19. Nomura R, Ogaya Y, Nakano K. Contribution of the collagen-binding proteins of streptococcus mutans to bacterial colonization of inflamed dental pulp. PLoS One 2016; 11(7):e0159613.
20. Avilés-Reyes A, Miller JH, Lemos JA, Abranches J. Collagen-binding proteins of Streptococcus mutans and related streptococci. Mol Oral Microbiol. 2017; 32(2):89-106.
21. Fejerskov O. Concepts of dental caries and their understanding the disease. Community Dent Oral Epidemiol 1997; 25(1):5-12.
22. Sun F, Ahmed A, Wang L, Dong M, Niu W. Comparison of oral microbiota in orthodontic patients and healthy individuals. Microb Pathog 2018; 123:473-7.
23. Bottalico L, Tatullo M, Marrelli M, Santacroce L. Lights and shadows of dental implants: focus on mucositis and perimplantitis and their biological markers. J Biol Regul Homeost Agents 2016; 30(3):859-61.
24. Vermesan D, Vermesan H, Dragulescu SI, et al. Secondary pathologic fractures in osteosarcoma: prognosis and evolution. Eur Rev Med Pharmacol Sci 2009; 13(2):71-6.
25. Giudice G, Cutrignelli DA, Sportelli P, et al. G. Rhinocerebral Mucormycosis with Orosinusal Involvement: Diagnostic and surgical treatment guidelines. Endocr Metab Immune Disord Drug Targets 2016; 16(4):264-9.
26. Carpenter GH. The secretion, components, and properties of saliva. Annu Rev Food Sci Technol 2013; 4:267-76.
27. Nyvad B, Baelum V. Nyvad criteria for caries lesion activity and severity assessment: a validated

approach for clinical management and research. Caries Res 2018; 52(5):397-405.
28. Wickström C, Herzberg MC, Beighton D, Svensäter G. Proteolytic degradation of human salivary MUC5B by dental biofilms. Microbiology (Reading) 2009; 155(Pt 9):2866-72.
29. Mager DL, Ximenez-Fyvie LA, Haffajee AD, Socransky SS. Distribution of selected bacterial species on intraoral surfaces. J Clin Periodontol 2003; 30(7):644-54.
30. Dewhirst FE, Chen T, Izard J, Paster BJ, Tanner AC, Yu WH, Lakshmanan A, Wade WG. The human oral microbiome. J Bacteriol 2010; 192(19):5002-17.
31. Aas JA, Paster BJ, Stokes LN, Olsen I, Dewhirst FE. Defining the normal bacterial flora of the oral cavity. J Clin Microbiol 2005; 43(11):5721-32.
32. Chen T, Yu WH, Izard J, Baranova OV, Lakshmanan A, Dewhirst FE. The Human Oral Microbiome Database: a web accessible resource for investigating oral microbe taxonomic and genomic information. Database (Oxford) 2010; 2010:baq013.
33. Marsh PD, Head DA, Devine DA. Ecological approaches to oral biofilms: control without killing. Caries Res 2015; 49(Suppl 1):46-54.
34. Hajishengallis G. The inflammophilic character of the periodontitis associated microbiota. Mol Oral Microbiol 2014; 29:248–57.
35. Han YW, Wang X. Mobile microbiome: oral bacteria in extra-oral infections and inflammation. J Dent Res 2013; 92:485-91.
36. Arimatsu K, Yamada H, Miyazawa H et al. Oral pathobiont induces systemic inflammation and metabolic changes associated with alteration of gut microbiota. Sci Rep 2014; 4:4828.
37. Bottalico L, Castellaneta F, Charitos I A. From Hydrotherapy to The Discovery of The Gut Microbiota: The Historical Gastrointestinal Health Concept. Pharmacophore 2020; 11(2):82-90.
38. Santacroce L, Charitos IA, Ballini A, Inchingolo F, Luperto P, De Nitto E, Topi S. The Human Respiratory System and its Microbiome at a Glimpse. Biology (Basel) 2020; 9(10):318.
39. Santacroce L, Inchingolo F, Topi S, et al. Potential beneficial role of probiotics on the outcome of COVID-19 patients: An evolving perspective. Diabetes Metab Syndr 2021; 15(1):295-301.
40. Dewhirst FE. The oral microbiome: critical for understanding oral health and disease. J Calif Dent Assoc 2016; 44(7):409-10.
41. Lis M, Bhatt S, Schoenly NE, Lee AY, Nislow C, Bobek LA. Chemical genomic screening of a Saccharomyces cerevisiae genomewide mutant collection reveals genes required for defense against four antimicrobial peptides derived from proteins found in human saliva. Antimicrob Agents Chemother 2013; 57(2):840-7.
42. Fux CA, Stoodley P, Hall-Stoodley L, Costerton JW. Bacterial biofilms: a diagnostic and therapeutic challenge. Expert Rev Anti Infect Ther 2003; 1(4):667-83.
43. Rendueles O, Ghigo JM. Multi-species biofilms: how to avoid unfriendly neighbors. FEMS Microbiol Rev 2012; 36(5):972-89.
44. Santacroce L, Charitos IA, Bottalico L.A successful history: probiotics and their potential as antimicrobials. Expert Rev Anti Infect Ther 2019; 17(8):635-45.
45. Ballini A, Santacroce L, Cantore S, et al. Probiotics Improve Urogenital Health in Women. Open Access Maced J Med Sci 2018; 6(10):1845-1850
46. Santacroce L, Cagiano R, Del Prete R et al. Helicobacter pylori infection and gastric MALTomas: an up-to-date and therapy highlight. Clin Ter 2008; 159(6):457-62.
47. Nagy-Bota MC, Man A, Santacroce L, et al. Essential oils as alternatives for root-canal treatment and infection control against enterococcus faecalis-a preliminary study. Appl Sci 2021; 11(4):1422
48. Ballini A, Gnoni A, De Vito D, et al. Effect of probiotics on the occurrence of nutrition absorption capacities in healthy children: a randomized double-blinded placebo-controlled pilot study. Eur Rev Med Pharmacol Sci 2019; 23(19):8645-57.
49. Urquhart O, Tampi MP, Pilcher L, et al. Nonrestorative Treatments for Caries: Systematic Review and Network Meta-analysis. J Dent Res 2019; 98(1):14-26.
50. Autio-Gold J. The role of chlorhexidine in caries prevention. Oper Dent 2008; 33(6):710-6.
51. Rahman MT, Hossain A, Pin CH, Yahya NA. Zinc and metallothionein in the development and progression of dental caries. Biol Trace Elem Res 2019; 187(1):51-58

52. Ballini A, Cantore S, Signorini L, et al. Efficacy of sea salt-based mouthwash and xylitol in improving oral hygiene among adolescent population: a pilot study. Int J Environ Res Public Health 2020; 18(1):44.
53. Robinette RA, Oli MW, McArthur WP, Brady LJ. A therapeutic anti-Streptococcus mutans monoclonal antibody used in human passive protection trials influences the adaptive immune response. Vaccine 2011; 29(37):6292-300.
54. Rather SA, Sharma SC, Mahmood A. Antibodies generated against dextransucrase exhibit potential anticariostatic properties in Streptococcus mutans. Appl Microbiol Biotechnol 2020; 104(4):1761-72.
55. Pearce EI. Relationship between demineralization events in dental enamel and the pH and mineral content of plaque. Proc Finn Dent Soc 1991; 87(4):527-39.
56. Larsen MJ. An investigation of the theoretical background for the stability of the calcium-phosphate salts and their mutual conversion in aqueous solutions. Arch Oral Biol. 1986; 31(11):757-61.
57. Robinson C, Shore R.C, Brookes SJ, Strafford S, Wood SR, Kirkhom J. The chemistry of enamel caries. Crit Rev Oral Biol Med 2000; 11(4):481-95.
58. Santacroce L, D'Agostino D, Charitos IA, Bottalico L, Ballini A. A short review about electrophysiology and bioimpedance: history and perspectives. Indian J Public Health Res Dev 2018; 9,587-591.
59. Brown WE. Physicochemical mechanisms in dental caries. J Dent Res 1974; 53(2):204-55.
60. Aoba T. Solubility properties of human tooth mineral and pathogenesis of dental caries. Oral Dis 2004; 10(5):249-57
61. Brown WE, Chow L., Thermodynamics of apatite crystal growth and dissolution. J Cryst Growth 1981; 53(1):31-41.
62. Cantore S, Crincoli V, Boccaccio A, et al. Recent advances in endocrine, metabolic and immune disorders: mesenchymal stem cells (MSCs) and engineered scaffolds. Endocr Metab Immune Disord Drug Targets 2018; 18(5):466-9.
63. Cantore S, Ballini A, De Vito D, et al. Characterization of human apical papilla-derived stem cells. J Biol Regul Homeost Agents 2017; 31(4):901-10.
64. Dohan Ehrenfest DM, Del Corso M, Inchingolo F, Charrier JB. Selecting a relevant in vitro cell model for testing and comparing the effects of a Choukroun's platelet-rich fibrin (PRF) membrane and a platelet-rich plasma (PRP) gel: tricks and traps. Oral Surg Oral Med Oral Pathol Oral Radiol Endod 2010; 110(4):409-11; author reply 411-3.
65. Dohan Ehrenfest DM, Del Corso M, Inchingolo F, Sammartino G, Charrier JB. Platelet-rich plasma (PRP) and platelet-rich fibrin (PRF) in human cell cultures: growth factor release and contradictory results. Oral Surg Oral Med Oral Pathol Oral Radiol Endod 2010; 110(4):418-21; author reply 421-2.
66. Lingström P, van Ruyven FO, van Houte J, Kent R. The pH of dental plaque in its relation to early enamel caries and dental plaque flora in humans. J Dent Res 2000;79(2):770-7.
67. Margolis, HC, Moreno, EC. Kinetic and thermodynamic aspects of enamel demineralization. Caries Res 1985; 19(1):22-35.
68. Fejerskov O, Nyvad B, Kidd E. Dental Caries: The Disease and its Clinical Management, 3rd ed. Wiley-Blackwell, Hoboken (N.Jersey), 2015; pp 2-480
69. Abou Neel EA, Aljabo A, Strange A, Ibrahim S, Coathup M, Young AM, Bozec L, Mudera V. Demineralization-remineralization dynamics in teeth and bone. Int J Nanomedicine 2016; 11:4743-63.
70. Leimgruber C. La carie; textes divers et commentaires critiques [Dental caries; theories and comments]. SSO Schweiz Monatsschr Zahnheilkd 1951; 61(9):948-62.

Consensus paper on postural dysfunction: recommendations for prevention, diagnosis and therapy

R. Saggini[1], G.P. Anastasi[2], S. Battilomo[3], P. Maietta Latessa[4], G. Costanzo[5], F. Di Carlo[3], F. Festa[6], G. Giardinelli[7], F. Macrì[8], L. Mastropasqua[9], M. Nardone[3], G. Nicoletti[3], A. Orsini[10], M. Pastorelli[3], R. Pellegrino[11], M. Trevisan[5], L. La Mesa[8], A. M. Le Pera[8], M. G. Privitera[3], G. Ralli[12], C. Villani[5], B. Bricot[13], R.G. Davidson[14], A. Hassdenteufel[15], Z. M. Hawamdeh[16], GJ. Kleinrensink[17], E. Matheron[18], V.L. Stoev[19], S. Stratulat[20], S. Tiron[19], P. Villeneuve[21], T. Paolucci[1] and R. G. Bellomo[22]

[1]Unit of Physical Medicine and Rehabilitation, Department of Oral, Medical and Biotechnological Sciences, University of G. d'Annunzio of Chieti-Pescara, Italy; [2]Department of Biomedical, Dental Sciences and Morphological and Functional Images, University of Messina, Italy; [3]Italian Ministry of Health, Rome, Italy; [4]Department for Life Quality Studies, University of Bologna, Rimini, Italy; [5]Department of Anatomy, Histology, Legal Medicine, and Orthopaedics, Sapienza, University of Rome, Rome, Italy; [6]Department of Oral, Medical and Biotechnological Sciences, University of G. d'Annunzio of Chieti-Pescara, Italy; [7]National Institute for Occupational Safety and Health, Rome, Italy; [8]Italian Society of Pediatrics, Rome, Italy; [9]Ophthalmic Clinic, SS Annunziata Hospital of Chieti, University of G. d'Annunzio of Chieti-Pescara, Italy; [10]Telematic University "San Raffaele," Rome, Italy; 1[1]UCM-HEI Campus LUDES of Lugano; Switzerland; [12]Otolaryngology Unit, Sapienza, University of Rome, Rome, Italy; [13]CIES, Bandol, France; [14]Comunication Disorders Department ARIEL University, ARIEL, Israel; [15]The International Federation for Proprioceptive and Biomechanical Therapies, Sassenberg, Germany; [16]Physical Medicine and Rehabilitation, School of Rehabilitation Sciences, University of Jordan; [17]Department of Neuroscience and Anatomy, University Medical Center of Rotterdam, Rotterdam. Holland; [18]IRIS Group, "Physiopathologie de la Vision et Motricité Binoculaire" CNRS FR2022, Université Paris Descartes, UFR Biomédicale, Paris, France; [19]Romanian Association of Posturology, Romania; [20]University of Medicine and Pharmacy "Gr. T. Popa," Iasi, Romania; [21]International Posturology Association, University de Valenciennes, Spain; [22]University of Study of Urbino Carlo Bo, Department of Biomolecular Sciences, Urbino, Italy

Received January 7, 2021 – Accepted April 8, 2021

Good fundamentals of posture and balance are essential for the efficient performance of both simple daily tasks and more complex movement patterns. In particular, postural balance is the ability to keep the body in equilibrium and to regain balance after the shift of body segments: postural control mechanisms of integration of the visual, vestibular and foot afferential channels contribute to this. This document provides recommendations based on scientific evidence, clinical practice, and consensus between experts concerning the prevention, diagnosis, and treatment of postural dysfunction at the three stages of life as the developmental age, adult age, and old age > 65 years and follows the "National Guidelines on Classification and Measuring of Posture and its Dysfunctions" per the Italian Ministry of Health (December 2017). The paper answers four main questions: i) "Which measures can be adopted to prevent postural dysfunctions?" ii) "What can we do in order to make a correct diagnosis of postural

Corresponding Author:
Dr Teresa Paolucci,
Physical medicine and Rehabilitation Unit,
Department of Medical and Oral Science and Biotechnology (DSMOB),
G. D'Annunzio University of Chieti-Pescara,
viale Abruzzo 322, 66100 Chieti, Italy
e-mail: teresapaolucci@hotmail.com

0393-974X (2021)
Copyright © by BIOLIFE, s.a.s.
This publication and/or article is for individual use only and may not be further reproduced without written permission from the copyright holder.
Unauthorized reproduction may result in financial and other penalties
DISCLOSURE: ALL AUTHORS REPORT NO CONFLICTS OF INTEREST RELEVANT TO THIS ARTICLE.

dysfunction?" iii) "What are the correct treatment programs for postural dysfunctions?" iv) Which professional competencies and experiences are useful for preventing, diagnosing and treating postural dysfunctions? By the Consensus of the Experts and the scientific evidence, emerge that the approach to postural dysfunctions requires a multidisciplinary and interdisciplinary team. Furthermore, rehabilitation treatment interventions must be specific to the age groups that have been indicated, to consider the integration of the main systems and subsystems of postural control that change with age.

Key words: posture; rehabilitation; exercise; balance; scoliosis; foot; elderly; child

The implementation of appropriate responses and adjustments before and during every movement helps ensure correct postural balance. Anticipatory or compensatory adjustments are appropriate responses to sensory stimuli that are collected primarily by cutaneous receptors and foot receptors, as well as vestibular and musculoarticular proprioceptors (1). Posture can be therefore considered a "multiple-entry" structured system. Somatosensory and vestibular data are transmitted to the cerebellum and cerebral cortex by proprioceptors; specifically, muscular and articular proprioceptors carry information concerning muscle tension and the biomechanical condition of the body, which are critical for selecting the temporal and vectorial properties of mechanical postural responses (2).

As Brosel S. et al. studied (in "The Vestibular System and Ageing", Subcell Biochem 2019), the vestibular system contains the proprioceptors of the saccule and utricle, which supply data on gravity, whereas the receptors of the cristae ampullaris in the semicircular ducts show the speed of head rotation. This information is important for maintaining balance on unstable surfaces and during head movements. The mechano-receptors of the foot sole are some of the most important cutaneous receptors. The 104 foot sole mechanoreceptors are activated following vibrating or stretching pressure on the foot sole (3, 4).

The data that contribute to maintaining balance in the upright position in the static and dynamic state spread from foot sole mechano-receptors to the central nervous system. Stimulation of the primary areas that support the foot activates adaptive postural adjustments. The resulting responses consist of a body incline in the opposite direction of the stimulated area, "faking" a disequilibrium condition. As Buldt AK et al. (in "The relationship between foot posture and plantar pressure during walking in adults: A systematic review", Gait Posture 2018) explained, the information that is conveyed by foot sole mechano-receptors contributes to the awareness of body posture due to the illusory perception of declivity that is induced by tactile pulse trains on the foot sole of a blindfolded person. This hypothesis is supported by the decrease of afferent data as a consequence of the heat reduction in the foot sole due to anesthesia or weariness of the sole muscles which is associated with increasing postural oscillations.

Photoreceptors are involved in the stabilization of posture, as evidenced by the increasing postural instability that results from the reduction in visual activity. Visual stimuli give information about proximity and distance. Sight reduces postural oscillations when the subject is in the upright position, the clinical relevance of which increases in the elderly and in pathological conditions that effect a decline in visual activity (5, 6).

Two core matters are often discussed by studies on postural control with regard to visual problems: the role of the central and peripheral visual fields and that of optical flow i.e., the apparent movement of the elements in a visual area. The central visual field correlates with the focal view, whereas the peripheral visual field is linked to the "overall" view. The former is important for discerning the outline of physical properties, and the latter processes the spatial elements of the surrounding area.

Postural responses differ, depending on the selective provision of visual stimuli in the central or peripheral visual field. Vectorial responses depend on the orientation of the head or the sight in relation to visual stimuli when they are created in the peripheral visual field. These responses are essential for keeping postural stability, whereas if the stimuli are

directed to the middle of the visual field, suggesting the significance of the peripheral visual field in the visual control of posture, it is possible to notice more important postural oscillations. Visual flow determines postural oscillations and, consequently, stabilizing adjustments. According to recent studies, visual flow improves postural responses if both the central stimulation and stimulation of the peripheral visual field are present simultaneously.

In conclusion, we assert that visual data provide cognitive dynamic models in advance concerning potentially destabilizing situations and contribute to orienting the subject in the surrounding area. The central nervous system, through cortical, brain stem, and spinal circuits, controls posture and its adjustments.

With regard to cortical circuits in primates and humans, at the level of the cerebral cortex and, especially, the temporoparietal junction, an area of fundamental importance for the control of posture has been detected. This area harbors multisensory integration processes (somatosensory, vestibular, visual, occlusal, and temporomandibular) that spawn internal models of position of the various parts of the body and the vertical axis in relation to the orientation of the body. These models are fundamental for the organization of the anticipatory responses of the supplementary and presupplementary motor areas, which are conveyed to the spinal cord through the direct pyramidal tract. Contextually, the direct and crossed pyramidal tracts convey movements.

Brain stem circuits integrate sensory data from peripheral areas with movements and cerebellar modulation, originating compensatory responses that are used for maintaining correct posture. These compensatory responses are transmitted to the spinal cord through the extrapyramidal tracts - the reticulospinal, vestibulospinal, and tectospinal tracts. At the level of the cerebral trunk, the trigeminal nerve appears to condition the reticular formation by monitoring all nervous structures along its sensory nucleus (from the superior midbrain colliculi to the first cervical segments of the spinal marrow). This oversight derives from sensory responses that result from the proprioception of the masticatory system, including deglutition.

It must be taken into consideration that the control of posture is a complex mechanism that is activated during most activities that are carried out by a human being over his entire lifetime and this system has great adaptability. This adjustment can occur in the short term i.e., a period of continuous change in conditions of the surrounding environment and during age-related body modifications. These adjustments appear to be exclusively somatic; however, according to recent studies, important connections between the cerebellum and limbic system prove that the nature of these phenomena are also visceral and emotional. We can therefore assert that in the soma, posture represents the manifestation of the sensorimotor and visceral motility of the central nervous system in relation to phylogenetic and ontogenetic aspects.

Purpose of the Consensus

This document provides recommendations on the basis of scientific evidence, clinical practice, and consensus between experts concerning the prevention, diagnosis, and treatment of postural dysfunction at various stages of life developmental age, adult age, and old age > 65 years and follows the "National Guidelines on Classification and Measuring of Posture and its Dysfunctions" per the Italian Ministry of Health (December 2017).

Subjects

Addressees of this document are, in particular, pediatricians, general practitioners, geriatricians, orthopedists, physiatrists, sports doctors, rheumatologists, ophthalmologists, otolaryngologists, odontologists, audiologists, phoniatrics, coroners, occupational doctors, and health care professionals, as well as professionals who are not involved in health care: PhDs in sport sciences, parents, educators, particularly regarding the recommendations for developmental ages (youth and adolescence); and caregivers for every age.

MATERIALS AND METHODS

Bibliographic research

It was considered appropriate to pose clinical questions

that required answers based on evidence pertaining to the most recent literature to compose this document. Some keywords match with these questions per the MeSH (Medical Subject Headings) criteria.

Question 1: "Which measures can be adopted in order to prevent postural dysfunctions?" Related MeSH terms: amblyopia, refractive status, orthoptic defects, strabismus, convergence insufficiency, ocular motility, low vision, erected posture, scoliosis, postural stability, low back pain, physiotherapeutic strategies, flatfoot, plantar foot pain, vascular disease, vascular remodeling, musculoskeletal asymmetries, preventive and adapted motor activity, obesity and quality of life.

Question 2: "What can we do in order to make a correct diagnosis of postural dysfunction?" Related MeSH terms: malocclusions, postural assessment, postural balance (PB), postural clinical evaluation, vestibulo-ocular reflexes, visual field defect, retina diseases, optical coherence tomography, orthoptic evaluation,ophthalmic evaluation, cycloplegia.

Question 3: "What are the correct treatment programs for postural dysfunctions?" Related MeSH terms: rehabilitation, postural re-education, visual rehabilitation, correction of strabismus, refractive error surgery, refractory error correction, asymmetry, orthopedic treatment, scoliosis, Global Postural Reeducation (GPR).

Inclusion criteria: scientific work published between January 1, 2008 and December 31, 2017 was taken into consideration, based on the following research limitations: age from 0 to 65 years; species: human; article type: clinical trial, clinical trial form I to IV, controlled clinical trials, randomized controlled trials; and language: English. The following electronic databases were used: Medline, Embase, Scopus, Google-Scholar, Lilacs, Scielo.

The seven group coordinators autonomously selected every title/abstract and searched for the "full text." Every working group was assigned pertinent publications that were later recorded using a specific form. At least 2 members autonomously evaluated each work. In case of a lack of evidence, the indications above are reported as if based on the consensus of the experts (Tables I and II).

General postural recommendations

Question: "Which procedures can be implemented in order to prevent postural dysfunctions?" Good posture (or neutral spine) refers to the «three natural curves that are present in a healthy spine." Looking directly at the front or back of the body, the 33 vertebrae in the spinal column should appear completely vertical. From a side view, the neck (C1-C7) is bent inward, the thoracic (upper back)

Table I. *Levels of evidence*

I	Evidence obtained by meta-analysis of multiple studies, well outlined and controlled; randomized trials with few false positive and false negative errors (high power).
II	Evidence obtained by at least 1 well-outlined experimental study; randomized trials with many false positive and false negative errors (low power).
III	Evidence obtained by well-outlined semiexperimental studies and non-randomized studies, controlled by a single group, before/after comparison, cohort studies, or case-control sequence.
IV	Evidence obtained by well-outlined studies, non-experimental, such as comparative and descriptive studies on correlation and case studies.
V	Evidence obtained by case report, clinical examples, and experts' points of view.

region (T1-T12) bends outward, and the lumbar (lower back) region (L1-L5) bends inward. The sacrum (tailbone area) (S1-S5 fused) and coccyx (on average, 4 fused) rest between the pelvic bones. A neutral pelvis indicates that the anterior superior iliac spines and pubic symphysis fall in the same vertical line. In contrast, poor posture results from certain muscles tightening up or shortening while others lengthen and become weak, which often occurs due to one's daily activities. There are various factors that influence posture, including occupational activities and biomechanical factors, such as force and repetition. Consequently, postural dysfunction should be prevented throughout life, promoting:

- The adoption of a varied and balanced diet (B)
- The maintenance of an optimal body weight in relation to body mass index (BMI) and waist circumference (B)
- A healthy diet and lifestyle and regular athletic activities that are tailored to individual characteristics (A)
- Good posture, both static and dynamic, during everyday life (B)
- Scrupulous monitoring to preventively identify potential postural dysfunction and diseases that cause it. This monitoring shall first be carried out by the general practitioner (GP) and pediatrician, as well as a specialist (orthopedy and traumatology, physical medicine and rehabilitation, sports medicine, rheumatology, ophthalmology, otorhinolaryngology, odontology, audiology, phoniatrics, geriatrics, forensic medicine, occupational medicine).

Greater circulation of postural evaluation could allow specialists to implement prevention measures, particularly during developmental age (A). An examination of postural assessment can help to identify postural dysfunction in its early stages and implementing the appropriate treatment and most commonly recommended rehabilitation program, if needed. The postural assessment requires a multidisciplinary approach that involves the general practitioner, pediatrician, specialist (physiatrist, orthopedist, otorhinolaryngologist, audiologist, ophthalmologist), and odontologist (consensus of the experts), depending on age and type of case.

Preventive screening examinations that identify postural dysfunction are highly recommended. There is also evidence in favor of the efficacy of treatments, especially conservative ones. Adolescent idiopathic scoliosis is a suitable example: its preventive identification allows to implement adequate conservative therapy to halt the evolution of the pathology and avoid incorrect postures (B).

Postural assessment should be performed with

Table II. *Strength of recommendations (degree)*

A	The implementation of a particular process or diagnostic test is highly recommended. This level suggests a particular recommendation that is supported by scientific evidence of good quality, even if it is not necessarily of type I or II.
B	Doubts about this peculiar process and its recommendation, but its implementation shall be carefully taken into consideration.
C	There is a significant uncertainty in favor of or against the recommendation.
D	The implementation of the procedure is not recommended.
E	The implementation of the procedure is highly advised against.

Strength of Recommendations, Methodological Manual, "How to produce, divulgate and update recommendations for clinical practice", May 2002, National Institute of Health (NIH)

a thorough global clinical examination to exclude complications of another nature, verifying whether the position of the body is in line (in axes) with the ideal position. Taking into consideration the indications in the "National Guidelines on Classification and Measuring of Posture and its Dysfunctions", the global postural assessment should be carried out through (B):

- A complete collection of anamnestic data
- An examination of postural attitude static and dynamic
- An assessment of how the sole of the foot lies on the surface (static and dynamic)
- An evaluation of the masticatory system
- An analysis of potential anomalies that localize to one or more body regions, including vascular alterations
- An analysis of the oculomotor and visual systems
- An analysis of the function of the rachis, cingulum (pelvis and shoulders), and main fulcrum of upper and lower limbs (joint mobility, strength tests, global and segmental muscle length)

In addition to cervical lordosis, dorsal kyphosis, lumbar lordosis, the position of the head, the horizontality of the line of sight, the position of the pelvis (anterior or posterior pelvis tilt), and the position of the knees should be examined on a sagittal plane.

On a coronal plane, it is important to examine: the lines of symmetry in relation to ocular alignment and, thus, the rotation and the inclination of the head in relation to the reference plane; the symmetry of the clavicles; the symmetry of waist "triangles;" the alignment of the anterior superior iliac spine (ASIS); the alignment of the lower limbs; and the potential heterometry of the lower and upper limbs. If there is heterometry, it must be distinguished from functional heterometry through specific clinical and instrument-based examinations. On a rear view of the coronal plane, it is important to evaluate the lines of symmetry of the auricles, head, shoulders, shoulder blades, and axillary creases and the alignment of the posterior superior iliac spine, gluteal creases, lower limbs, and, in particular, the popliteal fosses and malleolus.

A complete, correct, and accurate postural evaluation should include such tests as (C): maneuvers for convergence of the feet; ocular vestibular evoked myogenic potentials (o-VEMPs) and cervical vestibular evoked myogenic potentials (c-VEMPs); march-in-place test; Fukuda stepping test; thumb test; Finkelstein test (thumb test); Nahmani test; Romberg test; head rotation test; video-head impulse test; functional-head impulse test and Meersseman test.

It is recommended that the gap between the coronal plane of the bi-pupillary plane, the coronal plane of the bi-acromial breadth, and that of the iliac crests (C) be verified using specific tools, such as inclinometers and spirit level analyzers. Concerning the sagittal plane, it is recommended that the Frankfurt Plane and Barrè Vertical Axis, per Stagnarà, be used as references, allowing to analyze the following parameters: distance occiput plumb line, fléche cervicale, dorsal plane, fléche lombaire, and gluteal plane (B). When necessary, integration of the evaluation of posture with optoelectronic photogrammetric systems (opto-kinematic evaluation) is recommended to quantitate, analyze, and ease the interpretation of the anthropometric results in the three planes of space — static and dynamic. Also, (B) static and dynamic stabilometry is useful for the evaluation of the oscillations of the mass center in the support polygon(CoM and CoP), under gravity pressure, and in the postural dynamic test (PDT).

Similarly, radiation-free diagnostics of the spinal column with gait and running analysis, raster stereoscopic spinal column measurements, foot pressure analysis, and electromyography of the muscles (also in the static and dynamic condition) have gained prominence in the modern evaluation of posture. Ultimately, clinical experience is a fundamental aspect of the evaluation of correct posture.

Recommendations during developmental age

In developmental age, any postural dysfunction must be preventively individuated, as it could portend problems with psychosomatic development (B). Developmental age is an existential period that is fundamental for postural adjustments, because optimal physical development, with correct static and dynamic posture is essential for a healthy and efficient body, beginning with the musculoskeletal system (by Calvo-Muñoz I et al. in "Preventive physiotherapy interventions for back care in children and adolescents: a meta-analysis." BMC Musculoskelet Disord, 2012). To this end, the pediatrician is a fundamental reference for the evaluation of posture. The other medical experts above can also be references, collaborating with the pediatrician to implement the correct, complete diagnostic-therapeutic pathway (by Hegde AM et al. in "Prevalence of vision defects in a school based population with malocclusion" Int J Dent Med Res 2015 and by Holden S et al. in Sex Differences in Landing Biomechanics and Postural Stability During

Adolescence: A Systematic Review with Meta-Analyses. Sports Med, 2016).

To avoid permanent postural dysfunction, every subject must be monitored from birth until the end of the skeletal growth and the developmental process, at least once a year, with particular attention paid at

Table III. *Conditions to identify and evaluate in developmental age*

Birth - 1 year	- plagiocephaly - craniosynostosis and asymmetries - characteristics of ocular motility and anatomical integrity of eyes - characteristics of the auditory system - congenital muscular torticollis (twisted neck) - axial asymmetries - muscle hypotonia of the frontal and posterior planes - persistence of primitive reflexes - late manifestation (appearance) of parachute reflexes - hip dysplasia - curved knee - clubfoot, talipes valgus deformity, metatarsus adductus - characteristics and properties of the acquisition of motor skills - hearing
1-3 years	- characteristics and properties of motor skills - characteristics and properties of ambulation (on tiptoes, axis deviation of the lower limbs, potential asymmetries in static and dynamics) - analysis of the anatomical integrity of the eyes, potential refractive errors, ocular motility, convergence, strabismus, and nystagmus - evaluation of mouth breathing and bad habits - evaluation of auditory function - craniofacial vascular malformations - control of hearing performance
3-8 years	- mild spinal asymmetries - characteristics and properties of ambulation (on tiptoes, axis deviation of the lower limbs, potential asymmetries in static and dynamics) - analysis of the anatomical integrity of the eyes (potential refractive errors, amblyopia, low vision, congenital disorders, retinal diseases and disorders of the optic nerve, functional alterations of extraocular muscles) - convergence insufficiency, strabismus, and nystagmus - speech - auditory and vestibular function - nasal respiratory function - vascular malformations - maxillary malformations - dysfunctional tongue deglutition - hearing
8-14 years	- anatomical integrity of the eyes (e.g. potential refractive errors, amblyopia, low vision, congenital disorders, retinal diseases and disorders of the optic nerve, functional alterations of extraocular muscles, convergence insufficiency, strabismus, and nystagmus - auditory and vestibular function - nasal respiratory function and night snoring - mild spinal asymmetries - functional and structural disorders of the lower limbs - limb vascular malformations - scarring - potential lymphoedema - characteristics and properties of ambulation (on tiptoes, axis deviation of the lower limbs, potential asymmetries in static and dynamics) - full-body muscle rigidity - integrity of masticatory and swallowing functions - hearing

approximately 6 months of age. In the case of one or more types of dysfunction (e.g., a specific disease: somatic, vestibular, visual, masticatory), the pediatrician should refer the patient to the best expert and verify the outcomes of the specific interventions once or twice yearly (Experts Consensus) (Tables III and IV).

To prevent or limit positional plagiocephaly, it is necessary to provide precise indications that limit

Table IV. *Main prevention measures to avoid postural dysfunction in developmental age*

Early diagnosis and treatment of - musculoskeletal disorders - disorders of the visual system - alterations in vestibular and auditory areas - dysfunction of deglutition and the masticatory system **Promotion of** - an appropriate and supervised physical activity; - an adequate sport activity; - a varied and balanced diet; - balanced head movements in order to avoid deformations and/or rigid positions of the head; - the physiological development of the psychomotor learning in the developmental - age (crawling, prone rolling, straightening). For safety reasons, carriage devices - shall be used for a limited lapse of time **Avoiding** enlarging the hole of the teat and reduce the use of the baby bottle from the 2nd year of the baby
Reduction/limit of asymmetrical loads on the spine (eg, lowering the weight of a backpack and wearing it in a correct and symmetric manner).
Promotion of exercises for the normalization of muscle and myofascial tone in the case of hypotonia and myofascial muscle rigidity.
Correction of dysmorphia, foot dysfunction, and suprasegmental disorders using adequate foot proprioceptive orthoses and implementing rehabilitation programs and pathways per a specialist.

potential problems due to pre- and perinatal plagiocephaly, particularly in subjects aged from 0 to 4 months. It is important to prevent infants from keeping their head on only one side while they are sleeping and not to limit the movement of the muscles of the neck when they are awake. It is preferable to ensure that the infant sleeps in the supine position.

Attention must be paid to the substitution of the maternal breast, especially from age 2 years: prolonged and inappropriate use of a dummy should be disincentivized, whereas an "anatomical" and not "dropped" pacifier should be preferred to effect proper tongue placement. In fact, it is necessary to place the tip against the hard palate (behind the upper front teeth), facilitating phonation and speech, deglutition, breathing, and head movements. It is good practice not to enlarge the hole of the teat to feed a baby more quickly. Furthermore, the administration of solid foods should be incentivized at the appropriate time, as it favors proper development of the maxillary teeth. In the case of persistent tongue dysfunction after the absence of use of a dummy and baby bottle, the expert should make an evaluation. It is not good practice to precociously bring an infant to orthostatic and ambulation, because that negatively affects myofascial and musculoskeletal systems (which have not formed completely yet) and the building of the infant's "step diagram".

Prolonged use of playpens and the use of walkers and other aids are discouraged as they tend to impede the important phase of crawling and promote incorrect habits, such as staying on the tiptoes or developing asymmetric motricity while learning how to stay upright. It is fundamental that an infant who is learning how to stay upright not be given excessive help, favoring the crawling phase. Barefoot ambulation, preferably on non-smooth surfaces, stimulates proprioceptive results and postural balance, promoting a correct "motor and sensory diagram."

Particular attention must be paid to potential alterations in the vestibular and visual systems, especially with regard to the function of oculomotor muscles, which could provoke significant asymmetries in muscle tension bilaterally. Localized deficits modify the natural order of muscle tone between gravity and antigravity muscles. A direct consequence is the incorrect assessment of the position of the body. The vestibular system positively affects the skeletal muscles of the body, maintains balance (decreasing the loss of balance and the risk of falling), and controls movements.

Furthermore, the indirect effects of vestibular deficits on cognitive processes in relation to the near peri-personal space must be considered. The lack of vestibular data often requires the difficult substitution with visual proprioceptive or other types of signals to keep balance, posture, and sight. This replacement decreases attention, limits concentration, and can negatively affect mental processes, compromising other activities, such as multi-tasking, the elaboration of sequences, and the transfer of attention. In these situations, children may encounter difficulties in organizing more than one piece of data and, in particular, in integrating new information while keeping other and previous elements in memory.

Vestibular dysfunction can cause low scholastic results as it provokes oculomotor dysfunction, followed by unavoidable repercussions on reading skills and growing cognitive efforts to maintain balance, which causes emotional disorders. Vestibular and visual disorders have a significant role in determining postural dysfunctions of the head, altering the perception of the subjective visual vertical. Concurrently, dysfunctions of posture, the head, or the masticatory system can affect craniocaudal deficits, with consequent extensive adaptation of the vestibular and visual systems. An eye-muscle imbalance generally alters the perception of one's surroundings. The postural control system can compensate for this anomaly through rotations and slope of the shoulders and pelvis: at the postural level, a visual adjustment affects the underlying structures and muscle chains, and vice versa. When a sensory conflict initially exists, such as from vision, the stomatognathic system, plantar afferences, it can lead to lower motor control and induce asymmetrical postural tone. This asymmetry has the particularity of being labile and organized and should be distinguished from anatomical and behavioral asymmetries, which cannot change immediately.

Matheron E. et al. recommended (in "Impact of a 1-diopter vertical prism on binocular alignment on head rotation: a pilot investigation." Front Neurol, 2016) that for an individual with abnormal position of the head or other types of postural alteration, an eye examination, orthoptic examination, and vestibular evaluation be carried out during the third year of age and no later than the fifth year, to exclude the presence of visual and vestibular system diseases. An adjustment of the visual system by altering the position of the optical axis can determine a loss in parallelism of the eyes, which can lead to heterophoria

and heterotropia. Moreover, a dental examination is suggested to evaluate the harmony of deciduous teeth and maxillary alignment as a potential cause of irregular head positions and non-symmetrical dislocation of the mandibular condyles at the level of the temporal bones. These examinations should be performed to exclude defects in the visual, vestibular, and stomatognathic systems. A low-dose cone beam — only if necessary and diriment — can be implemented for tridimensional diagnosis of the facial bones and cervical segment by age years of 9 (expert consensus). As Korbmacher H et al. studied (in "Correlations between anomalies of the dentition and pathologies of the locomotor system - a literature review. J Orofac Orthop, 2004), it is necessary to monitor the transition of deciduous into permanent teeth, evaluating errors and malocclusions that can occur during this period. Nasal breathing should also be evaluated to permit harmonic growth of the maxillary bases. Informed parental consent is essential for every X-ray examination. The exposure parameters for cone beam CT units for patients in developmental age should be reduced in relation to those for adult patients (C).

Recommendations in adult age

In adult age, posture must be evaluated to identify potential—and asymptomatic—dysfunctions, because preventive interventions and treatments can avoid pathological conditions from arising. It is important to discourage a sedentary lifestyle, whereas moderate and constant physical activity made appropriate for every individual should be promoted to maintain a balanced body weight (B) (Table V).

During everyday activities and in the workplace (use of personal computer, weight lifting, etc.), it is important to maintain proper ergonomics and modify the posture induced from the activity to avoid having an excessively fixed posture for prolonged times. Myofascial, osteoarticular, and muscle stretching exercises are useful in cases of full body inflexibility. For excessive and prolonged upright standing, adequate footwear is recommended to ensure proper biomechanical function of the foot. Shoes should have comfortable heels, cushioned footbeds, stable heel seat linings, and an anatomical and receptive insole. In critical phases, such as pregnancy and menopause, women should pay more attention to monitoring their posture to avoid an imbalance in the sagittal plane with increasing lumbar lordosis during pregnancy and greater dorsal kyphosis during menopause.

In adult age, potential vestibular disorders can often

Table V. *Main preventive actions to avoid postural dysfunctions in adult age (B)*

Preventive interception and treatment for diseases of the: - musculoskeletal system - visual system - auditory and vestibular system - masticatory system
Promotion of: - appropriate and supervised physical activity - sport activities - a varied and balanced diet - global postural reeducation (GPR) methods
Correction of foot and suprasegmental disorders and dysmorphia through adequate proprioceptive foot orthoses and rehabilitation pathways prescribed by an expert.
Correction of body dysmorphic and paramorphic disorders using specific rehabilitation techniques.

be accompanied by extreme symptoms of vertigo. The expert usually focuses on easily controllable symptoms (thanks to the instinctive recovery led by the central system) instead of permanent damage to the vestibular system, which leads to pathology, necessitating careful evaluation and classification. Stochastic vibration therapy could be considered as a rehabilitative approach to create undirected proprioceptive input into the vestibular system.

It is necessary to control masticatory function to avoid the loss of vertical dimensions of the dental arches, which can cause abnormal anteposition of the head. Missing teeth should be replaced with a prosthesis that can avoid improper positioning of the mandible, which can induce adaptation and deviation of the head on the frontal and sagittal plane.

Recommendations age over 65 years

It is also useful to evaluate posture in healthy persons aged over 65 years and with specific symptoms that do not match the pathologies that are outlined by specific diagnostic exams to differentiate potential dysfunctions (C) (7) (Table VI). In this age range, during everyday life, it is necessary to maintain ergonomics and good tone of the myofascial system and muscle chains (by Borel L. et al. in "Posture and cognition in the elderly: interaction and contribution to the rehabilitation strategies." Neurophysiol Clin, 2014). Preventing falls, supported by a re-evaluation and possible readjustment to everyday life framework, is particularly important if signs of altered posture manifest. This phenomenon correlates with a fragile balance, which is common among individuals aged 65 years and over and

Table VI. *Main preventive actions to avoid postural dysfunction at age > 65 years (C)*

Preventive interventions and treatments for: - diseases of the musculoskeletal system - diseases of the visual system - alterations in the auditory and vestibular systems - alterations in the cognitive and psycho-limbic system - loss of proper masticatory function
Promotion of: - appropriate and supervised physical activity - a varied and balanced diet - global postural re-education (GPR) methods and proprioceptive exercises aimed at improving balance and reducing falls
Reduction and limitation of asymmetrical loads on the spine
Correction of postural dysmorphia and paramorphia using specific rehabilitation techniques and, if necessary, specific orthoses that are prescribed by an expert
Correction of foot and suprasegmental disorders and dysmorphia through adequate rehabilitation with proprioceptive foot orthoses prescribed by an expert **Correction** of masticatory function with the replacement of missing teeth that maintain the correct vertical dimension of the dental arches to support the head on the cervical region and promote correct alignment of the cephalic region Mobile prosthetics shall be kept in the mouth during the night to avoid problems with the position of muscle chains.

is intensified by a lack of vestibular function. In particular, the vestibulo-ocular reflex, which can be deficient due to physiological reasons, negatively affects visual activity during movement, eliciting greater cognitive effort, which is not used for other tasks, such as memory and paying attention. This condition worsens in the presence of a permanent vestibular disorder, favoring falls and direct consequences (traumatisms, fractures, disabilities, loss of safety, anxiety of falling again, reduction of motor activity, depression, social isolation). A reduction in visual activity and perception of moving in an environment, especially in this age group, correlates strictly with decreased ability to control balance. Thus, it is important to use adequate footwear and perhaps foot orthoses that are personalized to the anatomical morphology of the feet, deformities (physiological and typical for this age), and the dynamics of the step. Furthermore, postural rehabilitation pathways (with stretching and muscle-strengthening exercises in aquatic or terrestrial microgravity-based environments (8) and cognitive training exercises are especially useful, as they are more effective in preventing postural imbalance. Each activity should be practiced under "safe conditions." (by Pietrangelo T. et al. in " Effects of local vibrations on skeletal muscle trophism in elderly people: mechanical, cellular, and molecular events." Int J Mol Med, 2009 and Saggini R. et al. in " Efficacy of two micro-gravitational protocols to treat chronic low back pain associated with discal lesions: a randomized controlled trial. Eura Medicophys, 2004).

Losses in weight and postural stability might be related to a loss in normal masticatory function i.e., partial edentulism, especially in the molar region, or total edentulism or to the use of a dated prosthesis with a consequent loss in vertical dimension. This occlusal error generates a sensory deficit of the trigeminal nerve, which interacts with the reticular formation of the cerebral trunk, necessitating maintenance of the masticatory system.

WHICH PATHWAYS SHOULD BE UNDERTAKEN TO CORRECTLY DIAGNOSE POSTURAL DYSFUNCTION?

As Nagymáté et al. (in "Reliability analysis of a sensitive and independent stabilometry parameter set. PLoS One, 2018) underlined, postural evaluation (measurement of postural arrows and symmetry, evaluation of balancing) represents the reference procedure for diagnosing postural dysfunction. Also, Petró and colleagues (in "Devices and tasks involved in the objective assessment of standing dynamic balancing. A systematic literature review. PLoS One .2017) reported that, if necessary, the expert should administer more examinations using specific tools (A).

In daily clinical routine, it is good practice to avoid using complex and expensive methods, except when recommended or prescribed by the expert. If necessary, a radiological investigation should be conducted in orthostasis (on graph paper in two projections) of the rachis, with adequate justification. In developmental age, the patient should not undergo standard radiography more than once a year, and if regular checkups are required, a non-invasive optoelectronic instrument should be used. Considering the correlation between posture and the vestibular, visual, odonatological, and somatosensory systems, as discussed, in the case of suspected dysfunction, it is good practice to refer the patient to an expert for in-depth clinical and instrumental analysis (B).

What Are The Clinical Pathways To Undertake For Postural Dysfunction?

Clinical and rehabilitative pathways in children and adolescents

In children and adolescents, motor disorders manifest through postural dysfunction in most cases. Thus, experts recommend global postural re-education (GPR) to recreate the correct synergy between sensory and somatic output, with a readjustment of posture and optimized motor coordination (A).

Ophthalmologists recommend the best achievable correction of ametropia, convergence insufficiency, strabismus, and other pathologies, for which the optimal treatment should be selected. Treatments can be medical and surgical or a simple prescription for corrective lenses. Certain disorders could require rehabilitation techniques.

In children and adolescents, foot sole disorders (flat feet, hollow foot, and pes valgus) and ambulation diseases (on tiptoes or in hyperpronation) can be related to specific postural disorders of the lower

limb, rachis, and pelvis. They can also be the cause, a compensatory response, or a consequence as Saftari LN et al. suggested (in "Ageing vision and falls: a review." J Physiol Anthropol, 2018).

There is no evidence in favor of treatment of the asymptomatic foot, for which clinical monitoring is suggested. To treat the asymptomatic foot, orthopedics and physiatrists recommend rehabilitative therapies and the use of proprioceptive foot orthoses (C). Surgery should be chosen only for specific cases with persistent pain and ambulation diseases, only when suggested by the orthopedic specialist (B). Stretching and muscle-strengthening and proprioceptive exercises (barefoot and with shoes and foot orthoses) are recommended during the rehabilitative therapy. There is no specific evidence on the proper window for treatment with orthoses (it is possible to start at 3 years of age, if suggested by the expert) or on the best model of foot orthoses (C).

Substantial heterometry of the lower limbs (over 5 millimeters) requires periodic evaluation of postural balance (expert consensus). For the compensation of heterometry, experts suggest the use of foot orthoses with adequate correction of the dysmetria. This correction can be clinical and optoelectronic to evaluate the "step dynamic." An individualized treatment plan is recommended to increase the symmetry of static and dynamic posture (C).

In the case of structural dysfunction of the body, e.g., of the rachis (Cobb angle larger than 25° or smaller, during puberty, with confirmed development and presence of hunchback), experts recommend (A) (10):

- individual global rehabilitation to rebalance muscle tone
- increased elasticity and tone of myofascial lines (expert consensus)
- exercises to improve static and dynamic proprioceptive function in aquatic or terrestrial microgravity-based environments
- conservative treatments with an orthopedic corset (A)

There is no scientific evidence of the efficacy of one corset rather than another (expert consensus). The type of corset depends on age and the type of scoliotic curve. A corset is recommended only in global rehabilitation, individualized through: specific muscle- and myofascial chain-stretching exercises, exercises for rebalance of muscle tone of the trunk, proprioceptive exercises, and exercises for self-correcting posture (B).

Stretching exercises are advised in cases of scoliosis that include the pelvis, whereas proprioceptive exercises are suggested for scoliosis that exclude it. Because it is a global developmental disease, treatments should always be personalized, prescribed, and periodically verified (6-8-12 months) by experts and an orthopedist or physiatrist, and should stabilize the correct posture. Health care professionals who are involved in the project must have specific competencies in the treatment of postural dysfunctions and scoliosis. In the case of non-structural dysfunctions, experts recommend: exercises that rebalance muscle tone, specific muscle- and myofascial chain-stretching exercises, exercises for proprioception of the trunk in aquatic or terrestrial microgravity-based environments, and exercises for self-correction of posture during ordinary activities (C). For this purpose, experts advocate therapeutic protocols to optimize posture, re-establishing the space alignment of the body using global postural re-education techniques involving muscle and myofascial chains.

Monitoring the proper change from deciduous to permanent teeth, it is important to pay attention to masticatory function to ensure correct alignment of the head and body, representing the cephalic portion of the scale of static and dynamic balance of the column. The new dental structure is complete between 12 and 14 years of age and should ensure proper masticatory movements of the mandible in relation to the balance of the temporomandibular and atlanto-occipital joints.

To achieve correct alignment of the body, for example, for ensuring optimal reactivation of the postural tone system, experts recommend individualized rehabilitation programs with repetitive training. These rehabilitation approaches emphasize the afferent input and improve movements as a complex function. For this purpose, motor exercises in terrestrial micro-gravity-based environments with three-dimensional body alignment and exercises for functional re-education of the tongue appear to be

useful. These exercises introduce mechanical and proprioceptive changes to the body. The exercise in a micro-gravity-based environment maintains the induced postural optimization, which becomes automatic in relation to the execution of motor exercises (C). Instructions for ergonomics and correct postural hygiene are recommended.

Non-performance-based activities and non-competitive sports are highly recommended. In the literature, there are no univocal data concerning competitive and non-competitive sports with asymmetrical requests; motor activities and sports that require a "global effort" and that respect the morpho-functional characteristics of every individual are useful and recommended (B).

Clinical and rehabilitative pathways in adulthood

In adulthood, postural dysfunction often originates pain symptomatology, carried by the spatial and functional subsystems of the body: craniomandibular, stern-scapulohumeral (acromioclavicular, sternoclavicular, and scapulohumeral joints), pelvic girdle, and foot-ankle complex, related to the lower limb. These functional and spatial entities are connected by the relay subsystem of the spinal column and interact through the myofascial-bone and nervous subsystems. It is therefore necessary to identify the system that compensates for the postural dysfunction through a clinical examination — for implementing rehabilitation programs to recreate postural homeostasis and, in particular, for re-establishing the alignment of the body in space and the flexibility of the posterior, anterior, and crossed myofascial chains. For adults, a diagnosis of postural dysfunction necessitates re-programming with postural optimization (C) (expert consensus).

According to the literature (by Zhang C. et al. in "Efficacy of splint therapy for the management of temporomandibular disorders: a meta-analysis. Oncotarget, 2016 and by Di Pancrazio L. et al. in "Combined rehabilitation program for postural instability in progressive supranuclear palsy. Neuro Rehabilitation, 2013), every patient who is affected by acute, subacute, and chronic unilateral or bilateral vestibulopathy should undergo vestibular rehabilitation. As Sulway S. et al. suggested (in "Advances in Vestibular Rehabilitation." Adv Otorhinolaryngol, 2019) with regard to vestibular rehabilitation, experts recommend motor exercises that recover deficits in function, based on neurophysiological mechanisms according to the principles of addiction, adjustment, and sensory and behavior substitution, for functional recovery of vestibular lesions. Exercises for gaze stabilization (stimulating visual information), correct posture of the tongue, soma, and the body itself (stimulating proprioception), and balance (stimulating vestibular information) are recommended rehabilitative approaches.

Sensory recalibration is an important aspect of vestibular rehabilitation. Repetitive exercises that are guided through head movements that provoke vertigo are useful for examining the progressive reduction in vertigo symptomatology, based on the principle of addiction, according to "vestibular habituation training". The therapeutic approach should be multidisciplinary and include periodic assessments of the objectives of the rehabilitation program. The information above is also recommended for disorders of the visual system.

These exercises aim to re-created the correct synergy between sensory and somatic output, readjusting posture and optimizing motor coordination to better manage the asymmetrical adjustments to locomotion. Exercises that increase static and dynamic proprioception are recommended as Ferreira GE. et al. studied (in "Global Postural Reeducation for patients with musculoskeletal conditions: a systematic review of randomized controlled trials." Braz J Phys Ther, 2016). Experts recommend viscoelastic foot orthoses with support function and viscoelastic proprioceptive foot orthoses, which can be adaptive or compensative. According to the literature, lumbar supports should be used only in the case of acute pain and for short periods (C).

Attention must be paid to a loss in masticatory function due to the parafunctional activity of bruxism, which uses the dental arches to unload psychical and emotional tension. The unconscious tensing of the masticatory muscles activates the alarm system of the reticular system, increasing the muscle tone of the axis. The resulting abrasion of teeth causes

a loss in the vertical dimension and the alignment of the head on the body, causing migraines, cervical dysfunction, and rigidity of the bilateral clavicular subsystems. Hypertonia of the masticatory and hyoid muscles is transmitted to the anterior myofascial chains, causing anterior flexion of the body, with lumbar hypertonia to maintain static balance.

Clinical and rehabilitative pathways in the elderly

In elderly subjects, postural dysfunction is often associated with certain diseases of the nervous and musculoskeletal systems. In the elderly, a postural disease frequently correlates with specific pathologies of the neuro-musculoskeletal system, thus, it is highly recommended that the postural disease be monitored and treated, even when it is an adaptive and non-symptomatic compensation, consistent with the concepts of preventing disability and falls (C). In elderly patients, evaluation and counseling with regard to the adoption of simple precautions to ease postural stability and reduce the risk of falling (e.g., wearing closed instead of open footwear) are recommended (8), also through adaptation of the domestic environment such as shower support bars and removal of carpets (11) (C). Exercise programs are efficient in the elderly only if they are personalized and specific for problems, which should be evaluated and monitored over time, such as hyposthenia, balance and agility disorders, visual deficits, internal pathologies, and pathologies that are related to pharmacological therapies. Furthermore, polyneuropathy and other nervous disorders are common in the elderly, for which a clinical neurological examination and supplementation with vitamins B6 and B12, folic acid, and vitamin D are recommended, because there are huge deficits in this population, which can cause polyneuropathy. This condition then promotes gait and posture insecurity and the tendency to fall. Painful dysfunction of a subsystem has been suggested to be controlled, normalizing the homeostasis of the patient. A multidisciplinary postural program can ensure a specific approach for the system and its correlative for the various subsystems. The priority for a specialistic direction and for the treatment show up in this mechanism (expert consensus).

Safe and low-impact aerobics rehabilitation programs that are easy to execute are recommended, with exercises that strengthen the extensor muscles of the rachis (to prevent and correct dorsal hyper kyphosis) and lower limbs, control static and dynamic balance, and increase the elasticity of the muscle kinetic chains and myofascial system. For this purpose, motor exercises with three-dimensional alignment of the body performed in a terrestrial microgravity-based environment are useful (expert consensus). Once the rehabilitation program is completed, individuals with stable clinical conditions can benefit from adapted physical activities (APAs), preferably supervised by a specialist in motor sciences with significant experience and competencies in posturology. APAs are not part of health services and aim toward regeneration after rehabilitation, contrasting hypomobility and promoting a better lifestyle (expert consensus).

Viscoelastic foot orthoses with adaptive or compensative proprioceptive and supportive purposes are also highly recommended for the elderly (C). Lumbar corsets, anti-gravity or for lumbar support, can be used for pain with obvious postural asthenia (C). The discussion concerning diseases of the visual system is also valid for the elderly. Nevertheless, it is important to take into consideration the limited efficacy of certain therapeutic options, given the reduced recovery due to minor "plasticity" and the potential presence of comorbidities in the visual system (expert consensus). An elderly patient is often edentulous and uses a removable total or partial dental prosthesis, which should be placed properly to balance the maxillary loss due to osteoporosis. Correct positioning of the prosthesis allows to obtain the correct vertical dimension of the dental arches, which is necessary for supporting the head on the body, thus avoiding frequent displacement of the cervical thoracic portion. The improvement in the position of the head assists the visual and vestibular functions, decreasing the feeling of static and dynamic instability.

Which professional competencies and experiences are useful for preventing, diagnosing and treating postural dysfunctions?

The diagnosis of postural dysfunction is a medical

act (B). The prevention of postural dysfunctions includes experts of various age ranges who implement an interdisciplinary approach (expert consensus). When the postural dysfunction requires the intervention of a specialist, implementation of a treatment according to the functional prognosis with short-, medium-, and long-term objectives and programs for specific competencies may be necessary (expert consensus). A specialist in physical medicine and rehabilitation (PM&R) can arrange an *ad personam* therapeutic and rehabilitative program for postural dysfunctions. The team comprises health care professionals who act according to current regulations for their professional profile (B) (12). Among non-health care professions, graduates in motor sciences can contribute through APAs (expert consensus).

REFERENCES

1. Woollacott M, Shumway-Cook A. Attention and the control of posture and gait: a review of an emerging area of research. Gait Posture 2002; 16(1):1-14.
2. Peterka RJ. Sensory integration for human balance control. Handb Clin Neurol 2018; 159:27-42.
3. Buldt AK, Allan JJ, Landorf KB, Menz HB. The relationship between foot posture and plantar pressure during walking in adults: A systematic review. Gait Posture 2018; 62:56-67.
4. Paolucci T, Pezzi L, Mannocci A, La Torre G, Bellomo RG, Saggini R. Flat foot and postural harmony in 6-year-old Caucasians: What is their relationship? Ann Rehabil Med 2020; 44(4):320-6.
5. Mangalam M, Lee IC, Newell KM, Kelty-Stephen DG. Visual effort moderates postural cascade dynamics. Neurosci Lett 2021; 742:135511.
6. Bellomo RG, Iodice P, Di Pancrazio L, Megna M, Saggini R. Visual sensory disability: rehabilitative treatment in an aquatic environment. Int J ImmunopatholPharmacol 2012; 25(1):17S-21S.
7. Pokorski M, Bellomo RG, Saggini R. Bioprogressive paradigm in physiotherapeutic and antiaging strategies: A Review. Adv Exp Med Biol 2018; 1(16):1-9.
8. Bellomo RG, Iodice P, Savoia V, Saggini A, Vermiglio G, Saggini R. Balance and posture in the elderly: an analysis of a sensorimotor rehabilitation protocol. Int J Immunopathol Pharmacol 2009; 22(3 Suppl):37-44.
9. Paolucci T, Morone G, Di Cesare A, et al. Effect of Chêneau brace on postural balance in adolescent idiopathic scoliosis: a pilot study. Eur J Phys Rehabil Med 2013; 49(5):649-57.
10. Negrini S, Donzelli S, Aulisa AG, et al. 2016 SOSORT guidelines: orthopaedic and rehabilitation treatment of idiopathic scoliosis during growth. Scoliosis Spinal Disord. 2018; 10;13:3. doi: 10.1186/s13013-017-0145-8
11. Hijmans JM, Geertzen JH, Dijkstra PU, Postema K. A systematic review of the effects of shoes and other ankle or foot appliances on balance in older people and people with peripheral nervous system disorders. Gait and Posture 2007; 25(2):316-23.
12. Pietilä Holmner E, Fahlström M, Nordström A. The effects of interdisciplinary team assessment and a rehabilitation program for patients with chronic pain. Am J Phys Med Rehabil 2013; 92(1):77-83

Inhibition of endoplasmic reticulum stress and activation of autophagy-protect intestinal and renal tissues from western diet-induced dysbiosis and abrogate inflammatory response to LPS: role of vitamin E

A.M. Shamseldeen[1], M. Hamzawy[1], N.A. Mahmoud[1], L. Rashed[2], S.S. Kamar[3], I.A. Harb[4] and N. Sharawy[1]

[1]Department of Physiology, Faculty of Medicine, Cairo University, Cairo, Egypt; [2]Department of Biochemistry, Faculty of Medicine, Cairo University, Cairo, Egypt; [3]Department of histology, Faculty of Medicine, Cairo University, Cairo, Egypt; [4]Department of Medical Pharmacology, Faculty of Medicine, Cairo University, Cairo, Egypt

Received November 25, 2020 – Accepted March 22, 2021

Diet pattern is an emerging risk factor for renal disease. The mechanism by which high-fat high fructose (western) diet mediates renal injury is not yet fully understood. The objective of the present study was to investigate the relationship between endoplasmic reticulum (ER) stress and autophagy in the development of renal impairment and aggravation of the inflammatory response. Eighty male rats were randomly divided into four groups as follows: a standard diet-fed (ConD), a high-fat high fructose diet fed (HFHF-V), ConD fed and orally supplemented with vitamin E (ConD-E), and HFHF fed and orally supplemented vitamin E (HFHF-E). After 12 weeks, either lipopolysaccharide (LPS) or saline was injected. We found that upregulation of endoplasmic reticulum stress-related proteins rendered the cells susceptible to injury induced by dysbiosis and microbiota-derived metabolites. A downregulation of autophagy and upregulation of caspase-12 resulted in the loss of intestinal integrity and renal tubular injury. Maintained ER stress also increased the inflammatory response to LPS. In contrast, vitamin E effectively ameliorated ER stress and promoted autophagy to protect intestinal and renal tissues. Our results provide insight into the influences of sustained ER stress activation and autophagy inhibition on the development of renal injury, which may contribute also to the enhanced inflammatory response.

Renal diseases continue to carry a high burden of morbidity and mortality. Western diet (WD), an energy-dense high-fat and high-sugar diet, has been recently recognized to be a risk factor for the development of renal disease. In recent years, the dysregulation of gut microbiota and stimulation of inflammation pathways have been implicated in the development of the renal disease (1), however, there is little information available on the molecular mechanism behind this alteration.

The endoplasmic reticulum (ER) is a multifunctional organelle that controls lipid biogenesis, protein folding, and calcium homeostasis. When ER is subjected to harmful stimuli, the ER stress response is activated, with subsequent accumulation of unfolded proteins in the ER lumen. Several pathways linking ER stress to cell survival, inflammation, and autophagy. ER stress activates three transmembrane proteins: inositol-requiring protein 1 (IRE1), PKR [double-stranded-RNA-

Key words; apoptosis; endoplasmic reticulum stress; autophagy; NFκB; kidney disease

Corresponding Author:
Dr Nivin Sharawy,
Kasr El-Aini, Cairo University, AlSaray Street,
11562 Cairo, Egypt
Tel.: +202 01122433182
fax: +202 23628246
e-mail: nivin.sharawi@kasralainy.edu.eg

0393-974X (2021)
Copyright © by BIOLIFE, s.a.s.
This publication and/or article is for individual use only and may not be further reproduced without written permission from the copyright holder.
Unauthorized reproduction may result in financial and other penalties
DISCLOSURE: ALL AUTHORS REPORT NO CONFLICTS OF INTEREST RELEVANT TO THIS ARTICLE.

dependent protein kinase]-like ER kinase (PERK), and activating transcription factor 6 (ATF6), which modulate the expressions of nuclear target genes, including activating transcriptional factor 4 (ATF4), transcriptional factor C/EBP homologous protein (CHOP) and X-box binding protein-1 (XBP1). Recent studies have suggested that numerous diseases are caused by the abnormal expression of ATF4, ATF6, CHOP, and XBP1 in ER stress (2-3). As severe ER stress conditions continue, the apoptosis signaling pathways were reported to be initiated via induction of caspase 12 (4). Furthermore, ER stress intersects with various inflammatory signaling pathways, such as nuclear factor Kappa B (NFκB) signaling, to regulate cytokine production (5-7).

Autophagy is the process by which cytoplasmic components are engulfed into intracellular vesicles (autophagosomes) that fuse with lysosomes to be degraded. Growing evidence supports the idea that autophagy is important in ER quality control. Studies have also strongly indicated that autophagy could be triggered by unfolded proteins to remove damaged endoplasmic reticulum (reticulophagy) (8-9). Furthermore, suppression of autophagy was found to render hepatocytes vulnerable to ER stress (10-11). However, there is no conclusive demonstration of the interplay between ER stress and autophagy in WD-induced renal injury.

Vitamin E has been shown to exert anti-inflammatory effects in different chronic diseases. Accumulating evidence demonstrated the role of vitamin E in determining cell viability under different stress conditions (12, 13). Only a few controversial studies are available on the effect of vitamin E on ER stress. Vitamin E was found to induce ER stress in cancer cells (12), however, ER stress was found to be reduced by vitamin E during atherosclerosis (14). The effects of vitamin E on the various markers for ER stress and autophagy in WD-induced renal impairment are yet to be identified.

In this study, we investigated the effects of high-fat high fructose (HFHF) on the expression of ER stress and autophagy markers in intestinal and renal tissues. We also elucidate the involvement of microbiota-derived metabolites [short-chain fatty acid (SCFA)] in the regulation of renal response to HFHF and LPS. Furthermore, we aimed to determine whether vitamin E supplementation would induce autophagy and ameliorate ER stress to protect against renal injury.

MATERIALS AND METHODS

Experimental protocol

The animal protocol was approved by the research ethics committee at the Faculty of Medicine, Cairo University, and the Institutional Animal Care and use committee, Cairo University (protocol number CU III s5617). Animals were treated following Canadian Council on Animal Care (CCAC) guidelines. Male Wister albino rats were purchased from the animal house of Kasr El Aini, Faculty of Medicine, Cairo University, and housed in individual cages maintained in a temperature-controlled environment, with a 12-h light/dark cycle and allowed ad libitum access to diets and drinking water.

High fat-high fructose (HFHF) diet, containing (gm %): Protein 24; Carbohydrate 41and Fat 24 (Product #D12451; Research Diets, New Brunswick, USA) with an additional 30% of fructose in water was used. The control diet consisted of (gm %): Protein 19.2; Carbohydrate 67.3 and Fat 4.3 (Product #D12450B; Research Diets, New Brunswick, USA).

The rats were randomly fed on ConD or HFHF-diet and were further divided into four subgroups: i. ConD-E: rats were fed a ConD for 3 months in concomitant with the administration of vitamin E dissolved in palm oil orally in a dose of 250 mg/kg/day (15, 16); ii. ConD-V: rats were fed a ConD for 3 months in concomitant with the administration of equal volume of palm oil orally daily; iii. HFHF–E: rats were fed an HFHF for 3 months in concomitant with the administration of vitamin E; iv. HFHF-V: rats were fed an HFHF diet for 3 months in concomitant with the administration of an equal volume of palm oil. After 12 weeks, the rats were given intraperitoneal bolus injections of either 10 mg/kg body weight lipopolysaccharide (LPS) (Sigma Chemical, St Louis, MO) (17) (18) diluted in saline (ConD-LPS, HFHF-LPS, ConD-LPS-E, HFHF-LPS-E) or equal volumes of saline (ConD-V, ConD-E, HFHF-V, HFHF-E).

Animal weight, food and water consumption were measured every other day during the experiment. At the

end of the study, urine, faeces, and blood of each rat were collected, and serum was obtained by centrifugation of blood at 1500× g for 10 min and stored at −80°C until further analysis. The rats were sacrificed by decapitation 24 hours after LPS injection. Intestinal and renal tissues were rapidly removed and stored at −80°C until analysis.

Quantification of firmicutes and bacteroides

Bacterial DNA was amplified based on the amplification of genomic DNA coding 16S ribosomal RNA. Faecal microbiological DNA was analyzed using QIAamp DNA Mini Kit (Qiagen, Valencia, USA). We used the specific forward and reverse primers for Firmicutes phylum and Bacteroidetes phylum: Bacteroidetes (F: 5'-CATGTGGTTTAATTCGATGAT-3'; R: 5'-AGCTGACGACAACCATGC AG-3') and Firmicutes (F: 5'-ATGTGGTTTAATTCGAAGCA-3'; R: 5'-AGCTGACGA CAACCATGCAC-3'). Gut microbiota was quantitatively analyzed using SYBR Green quantitative PCR.

Renal function analysis

Creatinine and blood urea nitrogen (BUN) levels were detected using the conventional colorimetric QuantiChrom TM assay (BioAssay Systems, USA) to measure the absorbency of colour wave, as previously described (18) (19). The Creatinine clearance (CCr) was determined using the following equation: CCr (ml/min/kg of body weight) = [urinary Cr (mg/dl) × urinary volume (mg)/serum Cr (ml/dl)] × [1000/body weight (g)] × [1/1440 (min)].

The expressions of urinary neutrophil gelatinase-associated lipocalin (NGAL) in different groups of rats were quantified using Enzyme-linked immunosorbent assay (ELISA) kits (MyBioSource.com, San Diego, California, USA), as previously reported (20). The mean absorbance was measured spectrophotometrically at 450nm in a microplate reader

Serum LPS and SCFA analysis

Quantitative ELISA was employed to measure the concentration of LPS in the serum. Antibody specific for LPS (CUSABIO Technology LLC; Houston, USA) was pre-coated onto a microplate. 100 µl standard as well as samples were added to the corresponding well. Both sample and buffer were incubated together with LPS-Horseradish Peroxidase (HRP) conjugate in a pre-coated plate for 1 h. After the incubation, the wells were washed and incubated with a substrate for HRP enzyme. The intensity of the developed color was detected at 450 nm on a microplate reader.

The circulating SCFA analysis was performed using gas chromatography-mass spectrometry analysis as previously reported (21, 22). Briefly, derivatized samples were injected in a gas chromatograph (Agilent Technologies) coupled to a mass spectrometer detector. The analysis was performed using a linear temperature gradient at 65°C up to 280°C for 5 min. The injector and transfer line temperatures were kept at 250°C. Serum SCFA was quantified by comparing the spectrum with the internal standard.

Analysis of nuclear *factor-kappa B (NF-κB) protein expression in the intestinal and renal tissues*

The concentration of NF-kB p65 in intestinal and renal tissues supernatants was evaluated using the rat NF-kB p65 (ELISA) kit (MyBioSource.com, San Diego, California, USA). The intensity of color was spectrophotometrically detected at 450 nm using a 96-well plate reader. The NF-κB concentration was estimated by comparing the optical densities of the samples with the standard curve.

Quantitative Real-Time PCR analysis

Total cellular RNA was isolated from intestinal and renal tissues using the Qiagen tissue extraction kit (Qiagen, USA) according to the manufacturer's instructions. 0.5–2 µg of extracted RNA was inversely transcribed into cDNA using a high-capacity cDNA reverse transcription kit. Real-time qPCR amplification and analysis were performed using an Applied Biosystem with software version 3.1 (StepOne™, USA). Gene expression was normalized to the internal standard basic transcription beta-actin. The following primer pairs were used for amplification: occludin, ZO-1, TLR4, caspase-12, Vamp8, LAMP, ATF 4, ATF 6, CHOP, XBP1, Beta-actin (Table I).

mTOR, Beclin-1, and LC3 protein analysis by Western blot

Western blot was used to quantify autophagy biomarkers in the intestinal and renal tissues. Renal and intestinal tissues were lysed in RIPA buffer (Marhham, Ontario L3R 8T4, Canada). Thereafter, supernatant fluids were collected to measure the protein levels, using

Bradford Protein Assay Kit (BIO BASIC INC. Markham Ontario L3R 8T4 Canada). 5-20 ug protein concentration of each sample was loaded with an equal volume of 2x Laemmli sample buffer, and the mixture was boiled at 95°C for 5 min to ensure denaturation of protein before polyacrylamide gel electrophoresis. The samples were transferred onto a PVDF membrane followed by the addition of primary antibodies against mTOR (1:1000; Thermofisher, USA); beclin-1 (1:1000; Thermofisher, USA), and LC3 (1:1000; Thermofisher, USA).

Table I. *Sequences of primers used in real-time polymerase chain reaction (Real-time PCR)*

Gene	**Primer sequences (5′-3′)**	
occludin	Forward	5’-GCTATGAAACCGACTACACGACA-3’
	Reverse	5’-ACTCTCCAGCAACCAGCATCT-3’
ZO-1	Forward	5’-AGGCTATTTCCAGCGTTTTGA-3’
	Reverse	5’-AATCCTGGTGGTGGTACTTGC-3’
TLR4	Forward	5′-TCATCCAGGAAGGCTTCCA-3′
	Reverse	5′-GCTGCCTCAG CAAGGACTTCT-3′
caspase-12	Forward	5′-TTCATTATTCAGGCCTGCCGAGG -3′
	Reverse	5′ TTCTGACAGGCCATGTCATCCTCA-3′
Vamp8	Forward	5′-CCCTCTCCTGTCCTCCTCCA-3′
	Reverse	5′-TCTCCTCCCAGGGGATCAAG-3′
LAMP	Forward	5′-TGCTGGCTACCATGGGGCTG-3′
	Reverse	5′-GCAGCTGC CTGTGGAGTGAGT-3′
ATF 4	Forward	5′-GCCGGTTTAAGTTGTGTGCT-3′
	Reverse	5′-CTGGATTCGAGGAATGTTGCT-3′
ATF 6	Forward	5′-GATGCAGCACATGAGGCTTA-3′
	Reverse	5′-CAGGAACGTGCTGAGTTGAA-3′
CHOP	Forward	5′-GAAAGCAGAAACCGGTCCAAT-3′
	Reverse	5′-GGATGAGATATAGGTGCCCCC-3′
XBP1	Forward	5′-AAACAGAGTAGCAGCGCAGACTGC-3′
	Reverse	5′-GGATCTCTAAAACTAGAGGCTTGGTG-3′
BETA ACTIN	Forward	5′-AGGCATCCTCACCCTGAAGTA-3′
	Reverse	5′CACACG-CAGCTCATTGTAGA-3′

Chemiluminescent substrate (Clarity™ Western ECL substrate - BIO-RAD, USA cat#170-5060) was used to the blot according to the manufacturer's recommendation.

Histological analysis

The kidneys and jejuna tissues of each rat were dissected, fixed in formaldehyde, and embedded in paraffin. Sections of 6 μm thickness were obtained and stained with hematoxylin and eosin (H&E). The morphological changes were analyzed using a light microscope equipped with (Leica Qwin 500 C; Cambridge) image analysis software.

Histological changes in renal tissue were evaluated at 10 randomly selected fields and scored as illustrated in a previous study (23). The tubular injury was defined as cellular degeneration and vacuolization, tubular dilatation, and cast formation. According to the aforementioned criteria, 0 = normal renal architecture, 1 = renal damage involved less than 25% of the tubular area, 2 = renal damage between 25% and 50% of the tubular area, 3 = renal damage between 50% and 75% of the tubular area, and 4 = renal damage between 75% and 100% of the tubular area. Jejuna samples were analyzed for the inflammatory cell infiltration, epithelial damage, and mucosal architecture, as illustrated previously (24) and summarized in Table II.

Statistical analysis

The data were analyzed using Graph Pad Prism software (version 5.0; San Diego, California USA). One-way ANOVA plus Newman-Keuls's post hoc multiple comparison tests were used to analyze differences between the groups. Two-way ANOVAs (subject factors: Time and diet) were used to analyze data from the total water and food consumption. Pearson's correlation coefficient was used to estimate the relationship between variables. In this study, the value of r was used to represent the strength of the correlationship. In all cases, $\mathbf{P}<0.05$ was taken to indicate significance. All data are expressed as mean ± SEM.

RESULTS

Bodyweight and food and water consumption

The results showed that the body weight gain was significantly increased ($\mathbf{P} < 0.05$) in all HFHF fed rats when compared to their respective counterparts on control diets. There was no significant difference in average fluid intake yield by diet ($F=5.9$, $P<0.0001$) and time ($F=4.9$, $P<0.0001$), however, diet ($F=4.4$, $P<0.0001$), but not time ($F=0.18$, $P=0.99$), had a significant effect on food consumption, and no significance was found in the interaction between both factors (Fig. 1).

Table II. *Intestinal injury scoring system*

Findings	Definition	Scoring
Inflammatory infiltrates	Minimal (less than 10%)	1
	Mild (10-25%)	2
	Moderate (26-50%)	3
	Marked (more than 51%)	4
Epithelial damage	Focal erosions	1
	Multiple erosions	2
	Villous denudation	3
Mucosal architecture:		
- Villous shortening	Mild: villous/crypt ratio of 2:1 to 3:1.	2
	Moderate: villous/crypt ratio of 1:1 to 2:1.	
	Non-parallel crypts, variable crypt diameters	3
- Irregular crypts		4

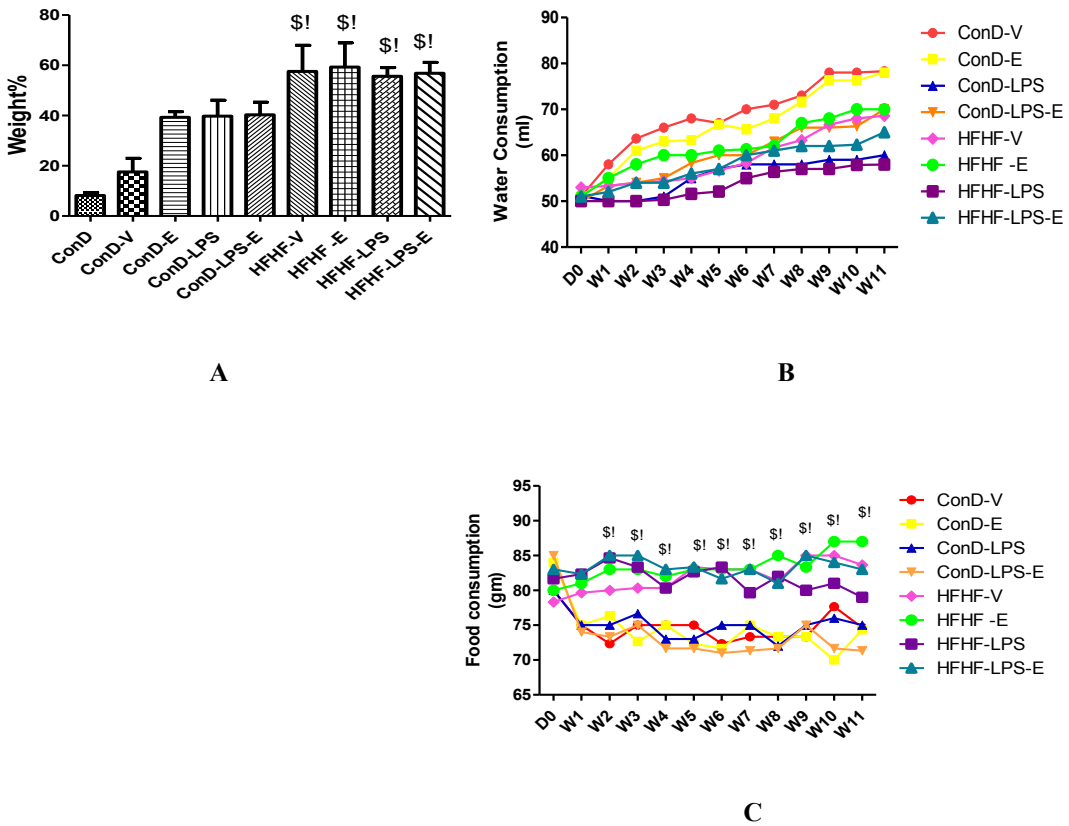
HFHF **acted synergistically with LPS to** *increase Firmicutes and intestinal injury score and reduce occludin and vitamin E reversed the effects of HFHF and LPS*

HFHF-fed rats (with and without LPS) and ConD-LPS elicited a significant increase ($P < 0.05$) in Firmicutes and a significant decrease ($P < 0.05$) in Bacteroides, compared with rats on the control diet and not subjected to LPS (ConD-V and ConD-E). Small intestinal gene expressions revealed that HFHF, HFHF-LPS, and ConD-LPS rats had lower ($P < 0.05$) levels of occludin and ZO-1 compared with ConD-V and ConD-E rats. Furthermore, rats fed HFHF and challenged with LPS showed a significant increase ($P < 0.05$) in Firmicutes and a decrease in occludin, when compared to HFHF-V and ConD-LPS groups (Fig. 2 A-D). Moreover, intestinal histological score and caspase-12 were significantly increased ($P < 0.05$) in rats receiving HFHF-LPS than other rats receiving either HFHF or LPS. The rats of control groups (ConD-V and ConD-E) showed no intestinal injury (Fig. 2 E-G).

Compared with the vehicle-treated groups (HFHF-V, HFHF-LPS and ConD-LPS), Firmicutes, caspase-12, and intestinal injury scores were significantly decreased ($P < 0.05$) in the vitamin E-treated groups (HFHF-E, HFHF-LPS-E, and ConD-LPS-E). Moreover, all vitamin E-treated rats (HFHF-E, HFHF-LPS-E, and ConD-LPS-E) showed significantly increased ($P < 0.05$) gene expressions of occludin and ZO-1 (Fig. 2).

HFHF **acted synergistically with LPS to** *increase serum LPS and SCFA and promote renal injury and vitamin E reversed the effects of HFHF and LPS*

We assumed that the increased serum LPS and SCFA, produced by gut microbiota, would



A **B** **C**

Fig. 1. *Evaluation of body weight gain and food and water consumption of rats on different dietary regimens and challenged with lipopolysaccharide (LPS). Data are expressed as the percentage (%) of body weight gain relative to the initial body weight. ConD: control diet; HFHF: High-fat-High-Fructose diets; LPS: lipopolysaccharide; E: vitamin E; V: vehicle. Data are expressed as mean ± SEM. $ p<0.05 vs ConD-V, ! p<0.05 vs ConD-E.*

enhance the development of acute kidney injury after endotoxin injection. To validate this, we examined the relationship of serum LPS and SCFA to the development of renal impairment. Detailed analysis of kidney function and structure revealed a significant increase (**P** < 0.05) in renal caspase-12 and renal impairment in ConD-LPS as well as untreated HFHF feeding rats (HFHF-V and HFHF-LPS). In the renal morphological analysis, the bowman's space in the rats on an HFHF and/or LPS tended to be dilated. Furthermore, tubular hyaline casts, apoptotic degeneration, and inflammatory cell infiltrations were observed in LPS, HFHF as well as HFHF-LPS groups (Table III, Fig. 3).

Concomitantly, serum levels of LPS and SCFA were significantly increased (**P** < 0.05) in untreated HFHF feeding rats (with and without LPS) and ConD-LPS, when compared to rats on the control diet (Conn-V and ConD-E). Moreover, HFHF acted synergistically to significantly increase (**P** < 0.05) serum LPS and SCFA, and to significantly enhance (**P** < 0.05) LPS induced renal injury. Compared to untreated rats (HFHF-V, HFHF-LPS, and ConD-LPS), rats subjected to HFHF and/or LPS and treated with Vitamin E showed a significant reduction (**P** < 0.05) in renal injury as well as serum levels of SCFA and LPS, as shown in Fig. 3. Increased levels of SCFA and LPS were found significantly correlated

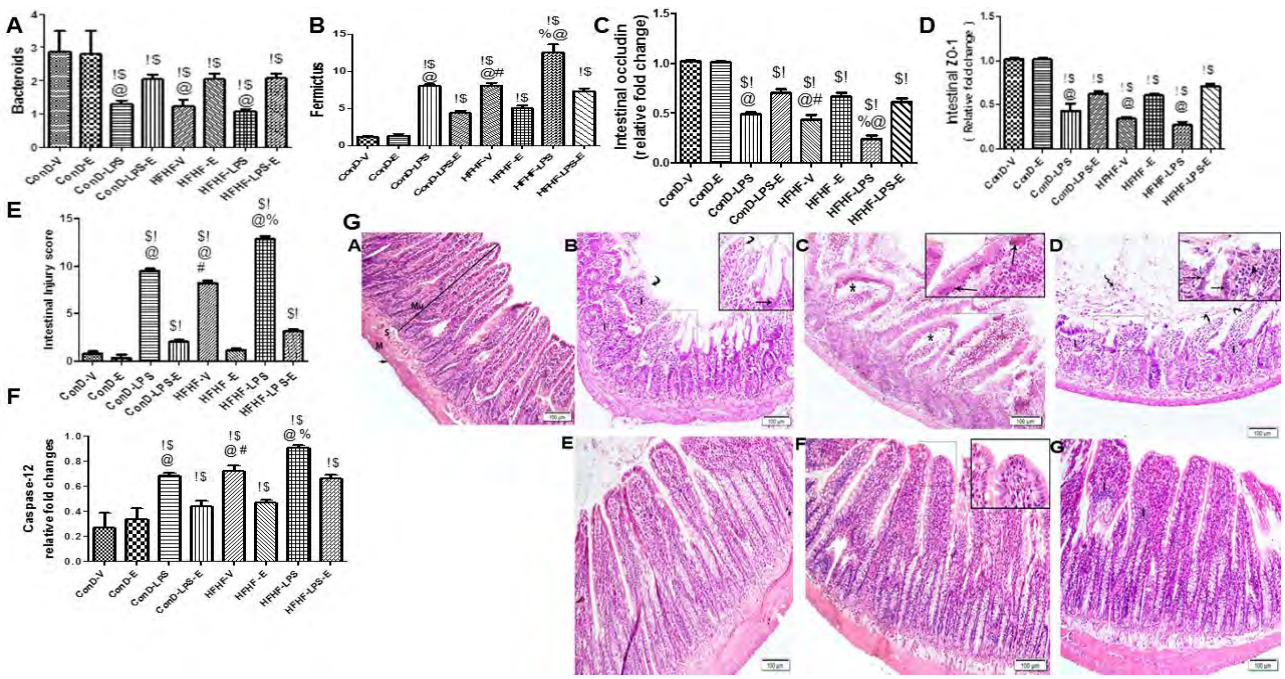


Fig. 2. *A high-fat high fructose diet modified the microbiota composition and enhanced endotoxin-induced intestinal injury and vitamin E reversed the effects. Alterations in the intestinal Bacteroides (A) and Firmicutes (B) were associated with modulations of the intestinal occludin (C) and ZO-1. (D) mRNA expression levels. E, F) Quantifications of intestinal injury and caspase-12 mRNA level. G) Representative hematoxylin and eosin (H&E) stained images of intestinal tissue at 100 × and 400 x magnification for Control group (A) showing the normal structure of intestinal layers; ConD-LPS group (B) with distortion of the villi with the sloughed epithelium of some parts (curved arrow)and the inflammatory cells infiltration (I), HFHF-V(C) showing brooding and distortion of the villi and oedema (star) in lamina propria, HFHF-LPS (D) with substantial distortion of most of the villi with obvious denudation and the inflammatory cells infiltration in the intestinal mucosa (I) and the lumen of the intestine (wavy arrow). Vitamin E preserved the morphological structure of the intestinal mucosa, submucosa, musculosa, and serosa in ConD-LPS-E (E) and HFHF-E (F). Some inflammatory infiltrations (I) were noted in some villi in HFHF-LPS-E (G). ConD: control diet; HFHF: High-fat-High-Fructose diet; LPS: lipopolysaccharide; E: vitamin E; V: vehicle. Data are expressed as mean ± SEM. $ p<0.05 vs ConD-V, ! p<0.05 vs ConD-E, @ p<0.05 vs respective vitamin E treated group, % p<0.05 vs ConD-LPS, # p<0.05 vs HFHF-LPS.*

with renal damage. Creatinine, NGAL, and renal injury score values were positively and significantly correlated with serum LPS and SCFA levels (Table IV).

HFHF **acted synergistically with LPS to** *increase TLR4 and NFKB expressions in intestinal and renal tissues and vitamin E reversed the effects of HFHF and LPS*

In intestinal and renal tissues, the data revealed a significant increase (**P** < 0.05) of TLR4 and NF-κB expressions in ConD-LPS, HFHF, and HFHF-LPS. Additionally, HFHF combined with LPS significantly aggravated (**P** < 0.05) the effect of LPS or HFHF on TLR4 and NFKB expressions. In contrast, vitamin E significantly reduced (**P** < 0.05) TLR4 and NF-κB levels compared with untreated groups (HFHF-V, HFHF-LPS, and ConD-LPS) (Fig. 4).

HFHF **acted synergistically with LPS to promote ER stress** *in intestinal and renal tissues and vitamin E reversed the effects of HFHF and LPS*

ConD-LPS, HFHF, and HFHF-LPS were found to induce the activation of ER stress in intestinal as well as renal tissues. As shown in Fig. 5, the expression levels of the ER stress-related proteins ATF 4, ATF6, CHOP, and XBP1 were all significantly enhanced ($p<0.05$) after LPS or HFHF compared with control groups (ConD-V and ConD-E), with the highest increase observed in HFHF-LPS. However, vitamin E significantly decreased ($p<0.05$) the ER stress both

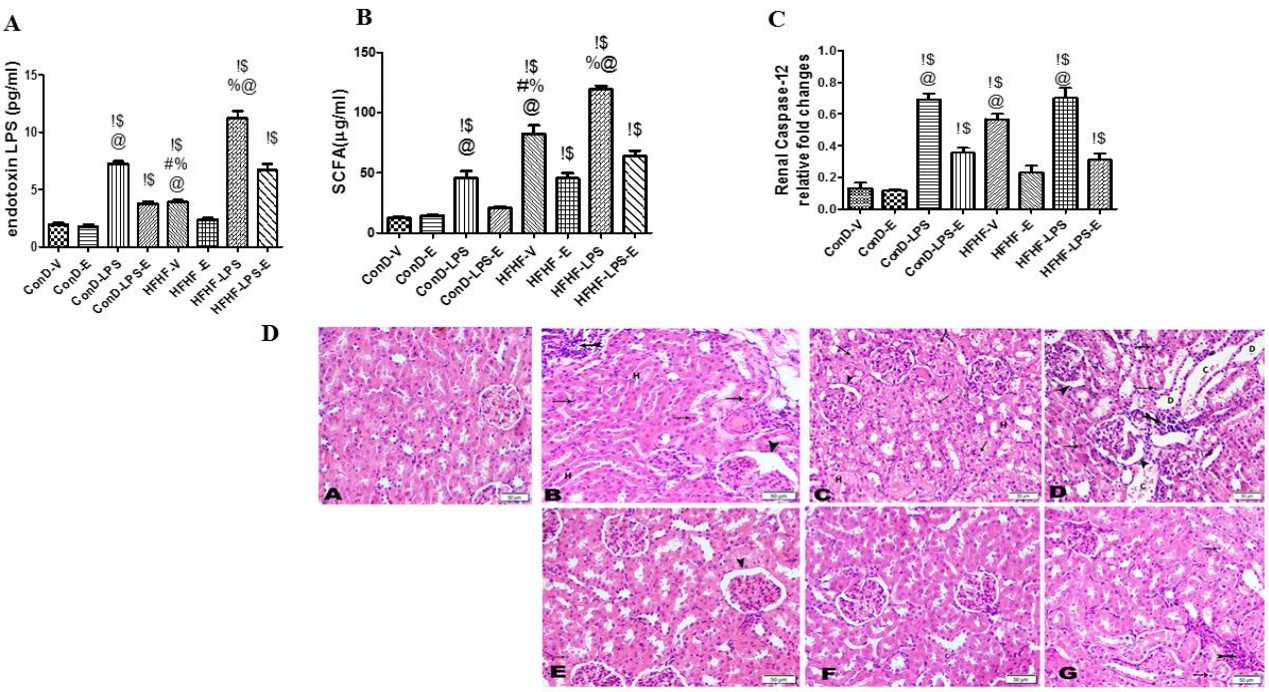


Fig. 3. *The relationship between serum short-chain fatty acids (SCFA) and lipopolysaccharide (LPS) and the degree of renal injury. A, B) Quantifications of LPS and SCFA in the serum. E) Quantifications of renal caspase-12 mRNA level. D) Representative photomicrographs for hematoxylin and eosin staining (at 200×magnification) of kidney sections of rats fed a control diet (ConD) (A), ConD and subjected to LPS (B), high-fat high fructose (HFHF) diets (C), and HFHF diet and subjected to LPS (D). HFHF diet as well as LPS induced an obvious dilatation of Bowman's space (arrowheads), hyaline casts (H), inflammatory cells infiltrations (bifid arrow), and dilatation of the renal tubules (D) and the blood vessels (C). The tubular epithelium showed multiple degenerated cells with cytoplasmic vacuolation and pyknotic nuclei (arrows). E-G) Vitamin E almost preserved the normal architecture of the kidney. Data are expressed as mean ± SEM. $ p<0.05 vs ConD-V, ! p<0.05 vs ConD-E, @ p<0.05 vs respective vitamin E treated group, % p<0.05 vs ConD-LPS, # p<0.05 vs HFHF-LPS.*

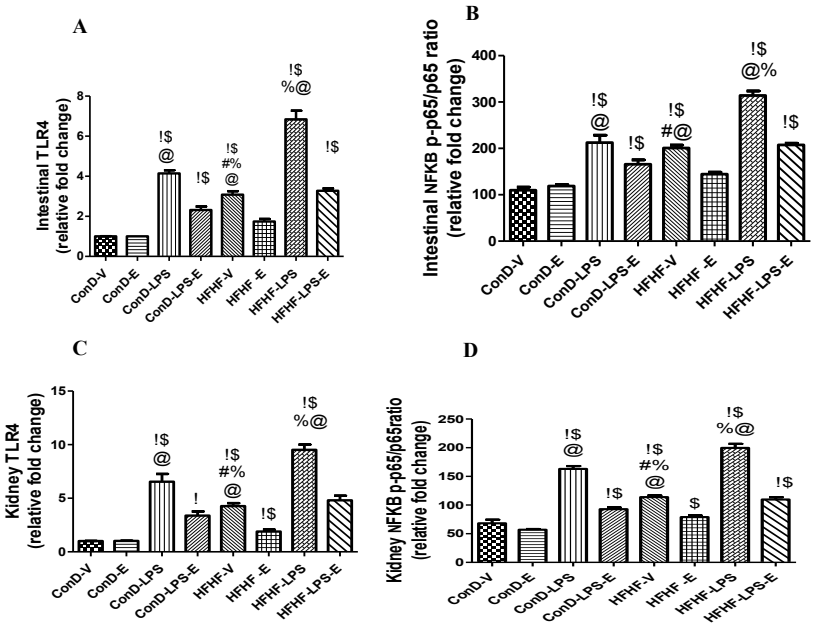


Fig. 4. *A high-fat high fructose diet upregulated toll-like receptor 4 (TLR4) and enhanced endotoxin-induced nuclear factor kappa B (NFkB) expression in renal and intestinal tissues and vitamin E reversed the effects. ConD: control diet; HFHF: High-fat-High-Fructose diet; LPS: lipopolysaccharide; E: vitamin E; V: vehicle. Data are expressed as mean ± SEM. $ p<0.05 vs ConD-V, ! p<0.05 vs ConD-E, @ p<0.05 vs respective vitamin E treated group, % p<0.05 vs ConD-LPS, # p<0.05 vs HFHF-LPS.*

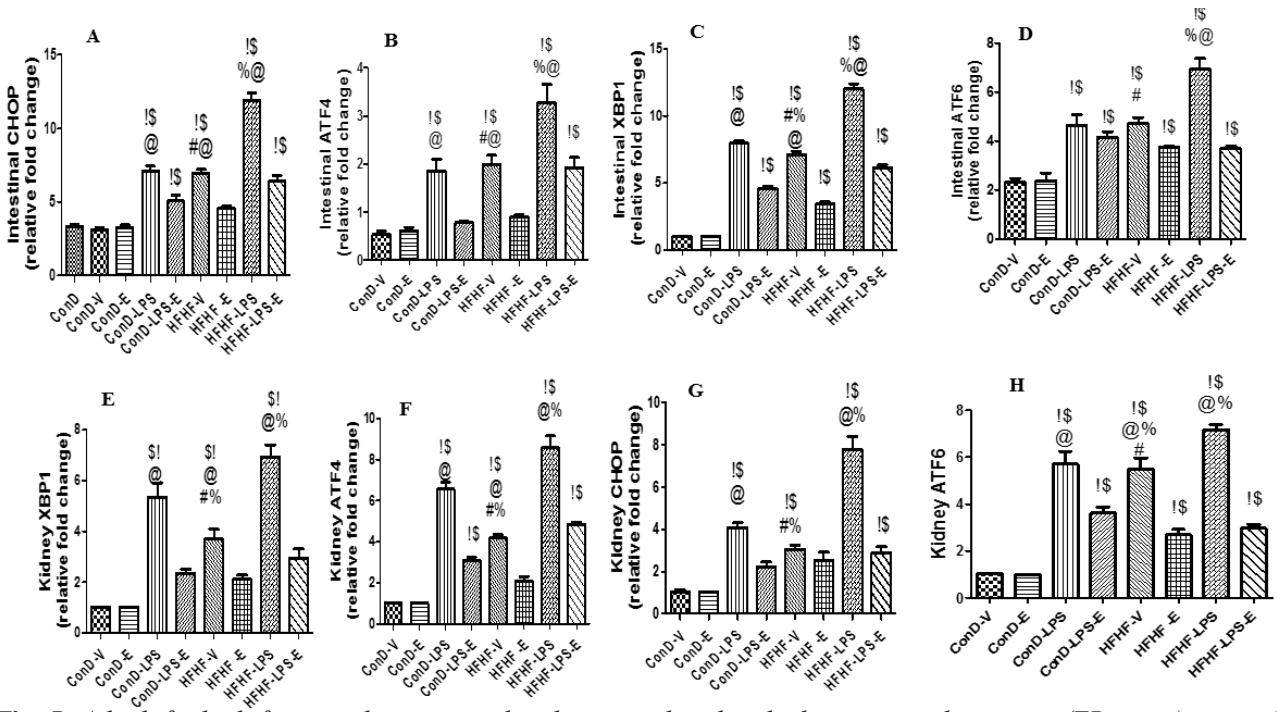


Fig. 5. *A high-fat high fructose diet promoted endotoxin-induced endoplasmic reticulum stress (ER stress) in renal and intestinal tissues and vitamin E reversed the effects. Intestinal (A-D) and renal (E-H) tissues RT-PCR analysis for XBP-1 (A&F), ATF4 (B&G), CHOP (C& H), and ATF6 (E&I) mRNA relative expression normalized to the beta-actin housekeeping gene from rats fed on control diet (ConD) or high-fat high fructose (HFHF) diets (with and without vitamin E) and subjected to LPS or vehicle (V). Data are expressed as mean ± SEM. $ p<0.05 vs ConD-V, ! p<0.05 vs ConD-E, @ p<0.05 vs respective vitamin E treated group, % p<0.05 vs ConD-LPS, # p<0.05 vs HFHF-LPS.*

in renal and intestinal tissues in ConD-LPS, HFHF and HFHF-LPS, as illustrated in Fig. 5.

***HFHF* acted synergistically with LPS to upregulate mTOR and downregulate autophagy** *in intestinal and renal tissues and vitamin E reversed the effects of HFHF and LPS*

Consistent with an increased ER stress, the results showed a significant upregulation ($p<0.05$) of mTOR and downregulation ($p<0.05$) of the autophagy response (beclin 1, LC3, LAMP, and VMAP) in ConD-LPS, HFHF, and HFHF-LPS. Levels of previous parameters were significantly altered ($p<0.05$) in the rats with combined LPS and HFHF. However, vitamin E significantly decreased ($p<0.05$) the ER stress and augmented ($p<0.05$) the autophagy in ConD-LPS, HFHF, and HFHF-LPS, as illustrated in Fig. 6.

DISCUSSION

A high-fat high fructose diet (HFHF, western diet) induced renal priming of the immune response (TLR4 and NFKB) and aggravated the inflammatory response to LPS. The previous findings could be attributed to a change in Bacteroid/Firmicutes ratio (dysbiosis) and elevated serum levels of SCFA and LPS. The data also suggest that the primed inflammatory response could be possibly due to persistent upregulation of ER stress responses (ATF6/CHOP/XBP1). The results indicate also that downregulation of autophagy (beclin 1, LC3, Vamp8, and LAMP) and upregulation of caspase 12 rendered intestinal and renal cells vulnerable to ER stress. Moreover, downregulation of autophagy could be involved in the intestinal barrier and proximal tubular renal injuries. Vitamin E supplementation dampened

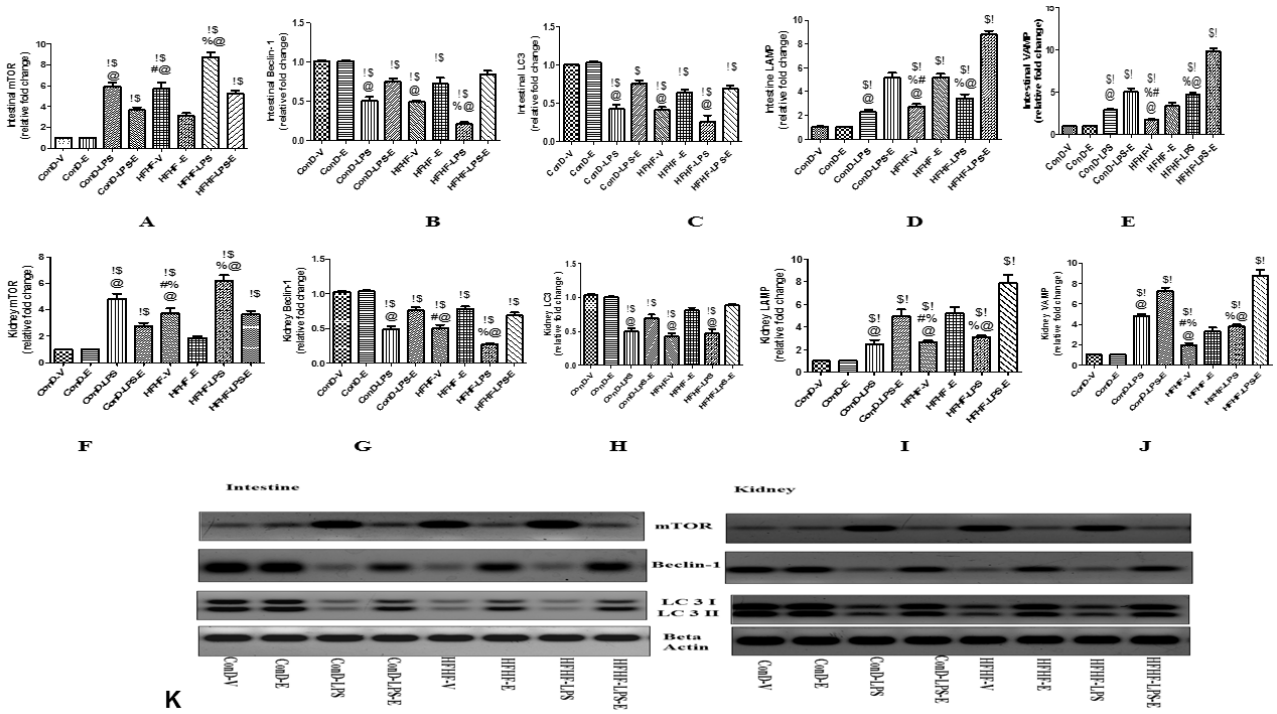


Fig. 6. *A high-fat high fructose diet and lipopolysaccharide acted synergistically to dampen the autophagy-related markers in renal and intestinal tissues and vitamin E reversed the effects. Intestinal (A-E) and renal (F-J) tissues RT-PCR and western blot analysis for Mtor (A & F), beclin-1 (B & G), LC 3 (C & H), LAMP (D &I), and VAMP (E & J) mRNA relative expression normalized to the beta-actin housekeeping gene from rats fed on a control diet (ConD) or high-fat high fructose (HFHF) diets (with and without vitamin E) and subjected to LPS or vehicle (V). (K) Western blot indicated protein expression of mTOR, beclin-1, and LC3 . Data are expressed as mean ± SEM. $ $p<0.05$ vs ConD-V, ! $p<0.05$ vs ConD-E, @ $p<0.05$ vs respective vitamin E treated group, % $p<0.05$ vs ConD-LPS, # $p<0.05$ vs HFHF-LPS.*

Table III. *Impact of high fat-high fructose (HFHF), lipopolysaccharide (LPS), and vitamin E on renal function and structure*

	ConD-V	ConD-E	ConD-LPS	ConD-LPS-E	HFHF-V	HFHF -E	HFHF-LPS	HFHF-LPS-E
KWI	0.7±0.0	0.9±0.1	1.4±0.3	1.3±0.1	1.1±0.3	0.9±0.1	1.1±0.2	1.1±0.2
Creatinine (mg/dl)	0.2 ± 0.0	0.1 ± 0.0	1.1 ± 0.3$^{!\$@}$	0.4 ± 0.2	0.7 ± 0.2$^{!\$@\#\%}$	0.3 ± 0.0	1.8 ± 0.2$^{!\$@\%}$	0.6±0.1$^{\$}$
BUN (mg/dl)	34.8±14.2	34.7±5.9	80.7±9.7$^{!\$@}$	51.8±8.4	74.6±12.9$^{!\$@\#}$	42.4±4.4	112.2±4.9$^{\$!@\%}$	76.9±17.5$^{\$}$
Cr clearance (ml/min/kg)	37.3±40.9	38.6±20.7	1.0±0.9$^{!\$@}$	25.6±19.4	2.2 ±2.0$^{\$\ @\#}$	11.4±12.9	0.7±0.6$^{\$@\%}$	5.7±1.3
NGAL (ng/ml)	0.4±0.2	0.5±0.1	1.9±0.6$^{!\$@}$	0.9±0.0	1.0±0.2 $^{\#\%@}$	0.6±0.1	2.8±0.5$^{\$@\%}$	1.1±0.2
Renal Injury Score	0.6±0.3	0.6±0.3	3.7±0.1$^{!\$@}$	1.0±0.3	2.5±0.2 $^{\$@\%\#}$	0.5±0.2	4.5±0.2$^{\$@\%}$	0.8±0.3
MBP (mmHg)	85±7.5	73±1.8	80±5.1	96±12.0	117±3$^{\$!}$	111±10.3$^{\$!}$	113±11.0$^{\$!}$	104±7.2$^{\$!}$

Data are expressed as mean ± SD. ConD: control diet; LPS: lipopolysaccharide; HFHF: high fat-high fructose; KWI: Kidney weight index; BUN: Blood urea nitrogen; Cr clearance: creatinine clearance; NGAL: neutrophil gelatinase-associated lipocalin; MBP: mean blood pressure. ! P< 0.05 vs ConD-V ; $P< 0.05 vs ConD-E; # P< 0.05 vs HFHF-LPS; @ P< 0.05 vs the corresponding group treated with vitamin E and % P< 0.05 vs ConD-LPS

Table IV. *Relationship between* ***serum LPS and SCFA and*** *biochemical and* **morphological** *changes in kidney*

	Biochemical & morphological parameters	**Pearson's correlationship**	
		r	*P*
LPS	**Creatinine**	0.85	< 0.0001
	CCr	-0.49	0.0006
	NGAL	0.88	< 0.0001
	Renal score injury	0.56	< 0.0001
SCFA	**Creatinine**	0.78	< 0.0001
	CCr	-0.43	0.0032
	NGAL	0.66	< 0.0001
	Renal score injury	0.70	< 0.0001

LPS: lipopolysaccharide; SCFA: short-chain fatty acids; CCr: creatinine clearance; NGAL: neutrophil gelatinase-associated lipocalin

ER stress, enhanced autophagy, and ameliorated the inflammatory response.

In this study, HFHF-induced dysbiosis (decreased Bacteroides and increased firmicutes) was observed to provoke the intestinal leakage leading to a systemic release of LPS and SCFAs (short-chain fatty acids produced by fermentation of undigested carbohydrates via intestinal microbiota). The relationship between microbiota composition and the circulating levels of SCFAs and LPS was previously reported (25, 26). High levels of serum LPS and SCFAs could affect other distant organs (27-29). Concurrently, we found that chronic intake of HFHF acts synergistically with injected endotoxin to increase systemic LPS and SCFAs secretions, and to induce TLR4 and NFKB expressions in the renal tissue. Our data revealed also that serum levels of LPS and SCAFs were strongly related to the observed renal alterations.

Based on the emerging evidence, the inflammatory response is commonly triggered as a result of ER stress. In intestinal and renal tissues, we found that the increased TLR4 and NFKB expressions in parallel accompanied by upregulation of ER stress (ATF6/CHOP/XBP1), and these findings are inconsistent with previous studies (30, 31). Recent data revealed that NFKB activation is linked to ER stress activation in the liver (32) and adipose tissue (33). This finding coincides with a significant decrease in the IL-1β level after LPS injection in CHOP-/-mice, signifying that inhibition of ER stress reduces inflammation. Inflammation activates a positive feedback mechanism involving ER stress to induce pro-inflammatory cytokine release leading to a vicious cycle (34, 35).

In this study, upregulation of caspase 12 simultaneously with ER stress biomarkers supports the strong relationship between ER-stress and apoptotic pathways. ER stress could be invoked to explain caspase upregulation in renal and intestinal tissues. Sustained ER stress stimulates several pro-apoptotic events leading to apoptosis. ATF4/ATF6-CHOP axis activation was found to stimulate caspase 12 in parallel with inhibition of anti-apoptotic proteins of the Bcl-2 family (36). Moreover, cells were found to resist apoptosis in CHOP knockout mice (37). In atherosclerosis, suppression of the ER stress was found to reduce apoptosis of endothelial cells (38).

Maintaining basal levels of autophagic activity is crucial for cell survival. Consistent with previous results (39-42), we found that dampening of autophagy is accompanied by a reduced expression of both occludin and ZO-1 and enhanced renal tubular injury. We proposed that inhibition of autophagy contributes to prolonged ER stress after HFHF and LPS. Autophagy and endoplasmic reticulum may work independently or synergistically to relieve stress and protect cells, but they could induce cell death with extreme stress (43). In chronic neurodegenerative diseases, sustained ER stress frequently causes activation of the autophagic pathway to alleviate ER stress; however, impaired autophagy leads to inefficient clearance of the accumulated proteins (44). Prolonged ER stress inhibits autophagy via activation of the ER-resident protein RTN3, which enhances the interaction between beclin1 and Bcl-2 (45). Furthermore, ER stress-induced autophagy inhibition may be mediated by NFKB activation (46). Growing evidence implicates NFKB in autophagy inhibition through the activation of mTOR (47, 48). Synergistic effects of HFHF and LPS on the ER stress response support the role of the insult strength on the degree of ER stimulation and the ability of autophagy to attenuate ER stress (49).

Vitamin E was found to protect cells against oxidative stress and display anti-inflammatory properties. We found that vitamin E could ameliorate the effects of HFHF on the kidney by reducing the release of LPS and SCFA. Vitamin E restored the disruption of the barrier function of the intestine, a result similar to few other studies (13, 50-52). Similarly to Nighot and Ma (40), we found that vitamin E alleviated the decrease of occludin and ZO-1 expressions. Furthermore, we found that concomitant intake of vitamin E restored intestinal bacterial homeostasis. This means that part of the impact of vitamin E on the intestinal wall could be due to the gut microbiota's community changes. Previous findings are further supported by a study conducted in pregnant women, which showed that higher intake of vitamin E was associated with a decrease in Firmicutes and an increase in Bacteroides (53).

Vitamin E can influence intestinal and renal cell viability through modulating ER stress in parallel with the autophagy pathway. Our data, consistent with previous reports on various cancer cells (54-56), indicate that vitamin E may induce autophagy and dampen ER stress. Vitamin E is a strong inducer of autophagy via Akt/AMPK/mTOR signaling (57-58). Previous effects of vitamin E on the expression of ER stress markers could explain its ability to ameliorate inflammation and enhance autophagy (16, 59, 60).

Our findings suggest that the western diet persistently increased serum concentrations of LPS and SCFA to induce priming of the immune response in the renal tissue. There is a cross-talk between the NFKB pathway, ER stress, apoptosis, and autophagy that determines the fates of intestinal and renal cells. Vitamin E supplementation restores intestinal junction integrity and protects the kidney via suppression of ER stress and enhancement of autophagy. Our results are interesting as they provide a mechanistic explanation for diet style being an independent risk factor for renal disease progression.

ACKNOWLEDGEMENTS

The authors would like to thank Afaf Ahmed and Tarek Mamdouh for their skilful technical assistance. This study was supported by the Cairo University Research Funds

REFERENCES

1. Zhang J, Ankawi G, Sun J, Digvijay K, Yin Y, Rosner MH, Ronco C. Gut-kidney crosstalk in septic acute kidney injury. Crit. Care 2018; 22(1):117.
2. Delbrel E, Soumare A, Naguez A, et al. HIF-1α triggers ER stress and CHOP-mediated apoptosis in alveolar epithelial cells, a key event in pulmonary fibrosis. Sci Rep 2018; 8(1):17939.
3. Zhou L, Tan J hui, Cao R chang, et al. ATF6 regulates the development of chronic pancreatitis by inducing p53-mediated apoptosis. Cell Death Dis 2019; 10(9):662.
4. Tan JH, Cao RC, Zhou L, et al. ATF6 aggravates acinar cell apoptosis and injury by regulating p53/AIFM2 transcription in severe acute pancreatitis. Theranostics 2020; 10(18):8298-314.
5. Aslani MR, Ghobadi H, Panahpour H, Ahmadi M, Khaksar M, Heidarzadeh M. Modification of lung endoplasmic reticulum genes expression and NF-kB protein levels in obese ovalbumin-sensitized male and female rats. Life Sci 2020; 247:117446.
6. Kumar A, Singh PK, Zhang K, Kumar A. Toll-like receptor 2 (TLR2) engages endoplasmic reticulum stress sensor IRE1α to regulate retinal innate responses in Staphylococcus aureus endophthalmitis. FASEB J 2020; 34(10):13826-38.
7. Stengel S, Fazio A, Lipinski S, et al. Activating Transcription Factor 6 mediates inflammatory signals in intestinal epithelial cells upon endoplasmic reticulum stress. Gastroenterology 2020; 159(4):1357-74.
8. Zhao D, Du L-L. Epr1, a UPR-upregulated soluble autophagy receptor for reticulophagy. Autophagy 2020; 16(11):2112-3.
9. Yin J, Gu L, Wang Y, Fan N, Ma Y, Peng Y. Rapamycin improves palmitate-induced ER stress/NF B pathways associated with stimulating autophagy in adipocytes. Mediators Inflamm 2015; 2015:272313.
10. Yang L, Li P, Fu S, Calay ES, Hotamisligil GS. Defective hepatic autophagy in obesity promotes ER stress and causes insulin resistance. Cell Metab 2010; 11(6):467-78.
11. Zhou X, Fouda S, Li D, Zhang K, Ye J-M. Involvement of the Autophagy-ER stress axis in high fat/carbohydrate diet-induced nonalcoholic fatty liver disease. Nutrients 2020; 12(9):2626.
12. Montagnani Marelli M, Marzagalli M, et al. Vitamin E δ-tocotrienol triggers endoplasmic reticulum stress-mediated apoptosis in human melanoma cells. Sci Rep 2016; 6(1):30502.
13. Tahan G, Aytac E, Aytekin H, et al. Vitamin E has a dual effect of anti-inflammatory and antioxidant activities in acetic acid-induced ulcerative colitis in rats. Can J Surg 2011; 54(5):333-8.
14. Bozaykut P, Ekren R, Sezerman OU, Gladyshev VN, Ozer NK. High-throughput profiling reveals perturbation of endoplasmic reticulum stress-related genes in atherosclerosis induced by high-cholesterol diet and the protective role of vitamin E. BioFactors 2020; 46(4):653-64.
15. Karabulut-Bulan O, Bolkent S, Yanardag R, Bilgin-Sokmen B. The role of vitamin C, vitamin E, and selenium on cadmium-induced renal toxicity of

rats. Drug Chem Toxicol 2008; 31(4):413-26.
16. Xu C, Sun R, Qiao X, Xu C, Shang X, Niu W, Chao Y. Effect of vitamin e supplementation on intestinal barrier function in rats exposed to high altitude hypoxia environment. Korean J Physiol Pharmacol 2014; 18(4):313-20.
17. Liu X, Lu J, Liao Y, et al. Dihydroartemisinin attenuates lipopolysaccharide-induced acute kidney injury by inhibiting inflammation and oxidative stress. Biomed Pharmacother 2019; 117:109070.
18. Sabry MM, Ahmed MM, Maksoud OMA, et al. Carnitine, apelin and resveratrol regulate mitochondrial quality control (QC) related proteins and ameliorate acute kidney injury: role of hydrogen peroxide. Arch Physiol Biochem 2020; 13:1-10.
19. Hamzawy M, Gouda SAA, Rashid L, Attia Morcos M, Shoukry H, Sharawy N. The cellular selection between apoptosis and autophagy: roles of vitamin D, glucose and immune response in diabetic nephropathy. Endocrine 2017; 58(1):66–80.
20. Han M, Li Y, Liu M, Li Y, Cong B. Renal neutrophil gelatinase associated lipocalin expression in lipopolysaccharide-induced acute kidney injury in the rat. BMC Nephrol 2012; 13(1):25.
21. Kristensen NB. Quantification of whole blood Short-chain fatty acids by gas chromatographic determination of plasma 2-chloroethyl derivatives and correction for dilution space in erythrocytes. Acta Agric Scand A Anim Sci 2000; 50(4):231-6.
22. Niibo M, Shirouchi B, Umegatani M, et al. Probiotic Lactobacillus gasseri SBT2055 improves insulin secretion in a diabetic rat model. J Dairy Sci 2019; 102(2):997-1006.
23. Chen Y, Jin S, Teng X, et al. Hydrogen sulfide attenuates LPS-induced acute kidney injury by inhibiting inflammation and oxidative stress. Oxid Med Cell Longev 2018; 2018:6717212.
24. Erben U, Loddenkemper C, Doerfel K, et al. A guide to histomorphological evaluation of intestinal inflammation in mouse models. Int J Clin Exp Pathol 2014; 7(8):4557-76.
25. Ban-Tokuda T, Maekawa S, Miwa T, Ohkawara S, Matsui H. Changes in faecal bacteria during fattening in finishing swine. Anaerobe 2017; 47:188-93.
26. Lobo LA, Benjamim CF, Oliveira AC. The interplay between microbiota and inflammation: lessons from peritonitis and sepsis. Clin Transl Immunol 2016; 5(7):e90.
27. Singh V, Yeoh BS, Chassaing B, et al. Dysregulated microbial fermentation of soluble fiber induces cholestatic liver cancer. Cell 2018; 175(3):679-94.e22.
28. Park J, Goergen CJ, HogenEsch H, Kim CH. Chronically elevated levels of short-chain fatty acids induce T cell-mediated ureteritis and hydronephrosis. J Immunol 2016; 196(5):2388-400.
29. Wieland A, Frank DN, Harnke B, Bambha K. Systematic review: microbial dysbiosis and nonalcoholic fatty liver disease. Aliment Pharmacol Ther 2015; 42(9):1051-63.
30. Schmitz M, Shaban M, Albert B, Gökçen A, Kracht M. The crosstalk of endoplasmic reticulum (ER) stress pathways with NF-κB: Complex mechanisms relevant for cancer, inflammation and infection. Biomedicines 2018; 6(2):58.
31. Kilberg MS, Balasubramanian M, Fu L, Shan J. The transcription factor network associated with the amino acid response in mammalian cells. Adv Nutr 2012; 3(3):295-306.
32. Zhao M, Zang B, Cheng M, Ma Y, Yang Y, Yang N. Differential responses of hepatic endoplasmic reticulum stress and inflammation in diet-induced obese rats with high-fat diet rich in lard oil or soybean oil. PLoS One 2013; 8(11).
33. Garfinkel BP, Hotamisligil GS. ER stress promotes inflammation through Re-wIREd macrophages in obesity. Mol. Cell 2017; 66(6):731-3.
34. Kim S, Joe Y, Surh Y-J, Chung HT. Differential regulation of Toll-like receptor-mediated cytokine production by unfolded protein response. Oxid Med Cell Longev 2018; 2018:9827312.
35. Masson GS, Nair AR, Dange RB, Silva-Soares PP, Michelini LC, Francis J. Toll-Like Receptor 4 promotes autonomic dysfunction, inflammation and microglia activation in the hypothalamic paraventricular nucleus: role of endoplasmic reticulum stress. PLoS One 2015; 10(3):e0122850.
36. Schönthal AH. Endoplasmic reticulum stress: its role in disease and novel prospects for therapy. Scientifica (Cairo) 2012; 2012:1-26.
37. Jung SY, Kim SS, Yeo SG. Impact of endoplasmic reticulum stress in otorhinolaryngologic diseases. Int J Mol Sci 2020; 21(11):1-23.

38. Kim S, Woo CH. Laminar flow inhibits ER stress-induced endothelial apoptosis through PI3K/Akt-dependent signaling pathway. Mol Cells 2018; 41(11):964-70.
39. Wong M, Ganapathy AS, Suchanec E, Laidler L, Ma T, Nighot P. Intestinal epithelial tight junction barrier regulation by autophagy-related protein ATG6/beclin 1. Am J Physiol Physiol 2019; 316(5):C753-65.
40. Nighot P, Ma T. Role of autophagy in the regulation of epithelial cell junctions. Tissue barriers 2016; 4(3):e1171284.
41. Sunahara S, Watanabe E, Hatano M, et al. Influence of autophagy on acute kidney injury in a murine cecal ligation and puncture sepsis model. Sci Rep 2018; 8(1):1050.
42. Hsiao HW, Tsai KL, Wang LF, Chen YH, Chiang PC, Chuang SM, Hsu C. The decline of autophagy contributes to proximal tubular dysfunction during sepsis. Shock 2012; 37(3):289-96.
43. Cybulsky A V. Endoplasmic reticulum stress, the unfolded protein response and autophagy in kidney diseases. Nat Rev Nephrol 2017; 13(11):681-96.
44. Cai Y, Arikkath J, Yang L, Guo ML, Periyasamy P, Buch S. Interplay of endoplasmic reticulum stress and autophagy in neurodegenerative disorders [Internet]. Autophagy. 2016; 12(2):225-44.
45. Wilkinson S. Emerging Principles of Selective ER Autophagy. J. Mol. Biol 2020; 432(1):185-205.
46. Zhu X, Huang L, Gong J, et al. NF-κB pathway link with ER stress-induced autophagy and apoptosis in cervical tumor cells. Cell Death Discov 2017; 3:17059.
47. Trocoli A, Djavaheri-Mergny M. The complex interplay between autophagy and NF-κB signaling pathways in cancer cells. Am J Cancer Res 2011; 1(5):629-49.
48. Dhingra R, Gang H, Wang Y, et al. Bidirectional regulation of nuclear factor-κB and mammalian target of rapamycin signaling functionally links Bnip3 gene repression and cell survival of ventricular myocytes. Circ Heart Fail 2013; 6(2):335-43.
49. Luchetti F, Crinelli R, Cesarini E, et al. Endothelial cells, endoplasmic reticulum stress and oxysterols. Redox Biol 2017; 13:581-7.
50. Liu F, Cottrell JJ, Furness JB, et al. Selenium and vitamin E together improve intestinal epithelial barrier function and alleviate oxidative stress in heat-stressed pigs. Exp Physiol 2016; 101(7):801-10.
51. Li L, Krause L, Somerset S. Associations between micronutrient intakes and gut microbiota in a group of adults with cystic fibrosis. Clin Nutr 2017; 36(4):1097-104.
52. Pierre JF, Hinterleitner R, Bouziat R, et al. Dietary antioxidant micronutrients alter mucosal inflammatory risk in a murine model of genetic and microbial susceptibility. J Nutr Biochem 2018; 54:95-104.
53. Mandal S, Godfrey KM, McDonald D, et al. Fat and vitamin intakes during pregnancy have stronger relationships with a proinflammatory maternal microbiota than does carbohydrate intake. Microbiome 2016; 4(1):55
54. Fontana F, Moretti RM, Raimondi M, et al. δ□ Tocotrienol induces apoptosis, involving endoplasmic reticulum stress and autophagy, and paraptosis in prostate cancer cells. Cell Prolif 2019; 52(3):e12576.
55. Comitato R, Guantario B, Leoni G, Nesaretnam K, Ronci MB, Canali R, Virgili F. Tocotrienols induce endoplasmic reticulum stress and apoptosis in cervical cancer cells. Genes Nutr 2016; 11:32.
56. Tiwari R V., Parajuli P, Sylvester PW. γ-Tocotrienol-induced endoplasmic reticulum stress and autophagy act concurrently to promote breast cancer cell death. Biochem Cell Biol 2015; 93(4):306-20.
57. Yu Y, Hou L, Song H, Xu P, Sun Y, Wu K. Akt/AMPK/mTOR pathway was involved in the autophagy induced by vitamin E succinate in human gastric cancer SGC-7901 cells. Mol Cell Biochem 2017; 424(1-2):173-83.
58. Yang P, Zhao J, Hou L, Yang L, Wu K, Zhang L. Vitamin E succinate induces apoptosis via the PI3K/AKT signaling pathways in EC109 esophageal cancer cells. Mol Med Rep 2016; 14(2):1531-7.
59. Ilçe F, Gök G, Pandir D. Acute effects of lipopolysaccharide (LPS) in kidney of rats and preventive role of vitamin E and sodium selenite. Hum Exp Toxicol 2019; 38(5):547-60
60. Jiang Q. Natural forms of vitamin E: metabolism, antioxidant, and anti-inflammatory activities and their role in disease prevention and therapy. Free Radic Biol Med 2014; 72:76-90.

Tumor promoting effects of exosomal microRNA-210 derived from lung cancer cells on lung cancer through the RUNX3/PI3K/AKT signaling pathway axis

ZB. Li*, X. Chen* and XJ Yi

Department of Oncology, Jiangxi Chest Hospital, Nanchang, Jiangxi, P.R. China

Received September 23, 2020 – Accepted February 9, 2021

*These Authors contributed equally to this work

Exosomes are involved in a range of processes in lung cancer such as cell proliferation, metastasis, and angiogenesis. Tumor-derived exosomes participate in the formation and progression of lung cancer by delivering functional biomolecules, including microRNAs (miRNA). The purpose of the present study was to determine the role of lung cancer cell-derived exosomal miR-210 in the proliferation and invasion of lung cancer cells and its underlying mechanism. Initially, exosomes were isolated from A549 cells and characterized by transmission electron microscopy and assessment of exosomal marker expression. RT-qPCR determined that miR-210 expression was elevated in exosomes as well as lung cancer cells. As reflected by dual-luciferase reporter assay, miR-210 negatively regulated RUNX3 expression. Following loss- and gain- function assay, it was found that miR-210 inhibition suppressed biological properties of A549 and H460 cells, which could be reversed by the silencing of RUNX3. miR-210 elevation induced the p-PI3K/PI3K and p-AKT/AKT levels, suggesting the activation of PI3K/AKT signaling pathway. Collectively, exosomal miR-210 targeted and negatively regulated RUNX3 expression to promote malignant properties of lung cancer cells by potentiating PI3K/AKT signaling pathway.

Lung cancer, as a severe malignancy, claims more lives worldwide than any other cancers (1). Typical cases with mass or nodule can be easily recognized, whereas the diagnosis with unusual manifestations, such as pneumonia, lung abscess and postinfectious scarring, is far more challenging (2), consequently its high mortality rate is largely attributed to delayed detection (3). Cell apoptosis, proliferation, angiogenesis and metastasis serve as hallmarks for lung cancer (4). Targeting different pathways associated with these hallmarks are prevalent therapies for lung cancer (5), and identification of reliable markers would be conductive to improve the survival rates.

Exosomes, extracellular vesicles secreted by most cells, could mediate cell-to-cell communication physiologically and pathologically, and cancer-derived exosomes could help recruit and reprogram constituents engaged in tumor microenvironment, including that of lung cancer (6). Exosomal microRNAs (miRNAs or miRs) may serve as diagnostic and prognostic biomarkers in lung cancer (7). miRNAs, small 20-24 nucleotides molecules, could regulate the biological properties of cells to serve as pivotal players in tumorigenesis, including lung cancer (8). In a prior study, miR-210 was transferred by lung cancer cell-derived exosomes (9). Moreover,

Key words: lung cancer cells; exosomes; microRNA-210; RUNX3; PI3K/AKT signaling pathway

Corresponding Author:
Dr Xiangjun Yi,
Department of Oncology, Jiangxi Chest Hospital,
No.346, Dieshan Road, Donghu District,
Nanchang 330044, Jiangxi, P.R. China
Tel./Fax: +86 86781433
e-mail: yixiangjun4222@163.com

0393-974X (2021)
Copyright © by BIOLIFE, s.a.s.
This publication and/or article is for individual use only and may not be further reproduced without written permission from the copyright holder.
Unauthorized reproduction may result in financial and other penalties
DISCLOSURE: ALL AUTHORS REPORT NO CONFLICTS OF INTEREST RELEVANT TO THIS ARTICLE.

lung cancer stem cell-derived exosomes contributed to a pro-metastatic phenotype in lung cancer cells via miR-210-3p transfer (10). In addition, miR-210 level was elevated in lung cancer tissues relative to normal control tissues (11). However, whether lung cancer cell-derived exosomes are also tumor-supporting in lung cancer by transferring miR-210 has yet to be established. Intriguingly, the targeting relationship between runt-related transcription factor-3 (RUNX3) and miR-210 has been revealed in the context of toluene diisocyanate (12). RUNX3, a transcription factor, is involved in the beginning of cartilage mineralization and chondrocyte maturation (13). RUNX3 suppression regulated by miR-301a is associated with facilitated tumor microenvironment antitumor immunity in lung cancer (14). The elevation of RUNX3 could impair the phosphatidylinositol-3-kinase protein kinase B (PI3K/AKT) signaling pathways to attenuate Caco2 cell inflammatory injury (15). The abnormal activation of this PI3K/Akt signaling pathway results in the excessive proliferation of cancer cells (16). Moreover, the inhibition of lung cancer cell proliferation is correlated with the PI3K/AKT signaling pathway blockage (17). Based on the above-mentioned studies, we can presume that there may be effects of exosomal miR-210 on lung cancer via the PI3K/Akt signaling pathway by interacting with RUNX3. Therefore, in the current study, we aim to elucidate the specific mechanism, with the intention of presenting a theoretical foundation for an enhanced understanding of lung cancer treatment.

MATERIALS AND METHODS

Cell culture

A549 and H460 (lung cancer cell lines) were obtained from Institute of Biochemistry and Cell Biology, Shanghai Institutes for Biological Sciences, Chinese Academy of Sciences (Shanghai, China). Cells were maintained in Roswell Park Memorial Institute (RPMI)-1640 medium containing 10% fetal bovine serum (FBS), 100 U/mL penicillin and 100 mg/mL streptomycin in a 5% CO_2 incubator (DHP-9162, Czech, Shanghai, China) at 37°C. The medium was renewed every 1~2 days, and at cell confluence of 80~90% the cells were passaged.

Isolation, culture and identification of exosomes

The exosomes were collected using ultracentrifugation. After A549 cells were cultured for 72 h, they were cultured in a medium containing 10% exosomes. The conditioned medium was collected after 48 h of culture, and the cells were centrifuged at 800 g for 15 min, 10,000 g for 30 min, and ultracentrifuged at 1×10^6 g for 70 min. Exosomes were separated with Beckman Optima L-100XP. The morphology of exosomes was observed with a transmission electron microscope (TEM) HT7700, and exosomal markers CD63, heat shock protein 90 (Hsp90), tumor suppressor gene 101 (Tsg101) expression was determined by immunoblotting.

A549 and H460 cells were cultured with 50 μg exosomes or dimethyl sulfoxide (DMSO, as control) for a 48-h culture at 37°C with 5% CO_2.

Table I. *Primer sequences for RRT-qPCR*

Target gene	Sequence (5'-3')
miR-210	F: ACACTCCAGCTGG-GCTGTGCGTGTG
	R: CAACTGGT-GTCGTGGAGTCG
RUNX3	F: GGCAATGACGAGAACTAC
	R: GGAGAATGGGTTCAGTTC
U6	F: CAAATTCGTGAAGCGTTCCATAT
	R: AACGCTTCACGAATTTGCGT
GAPDH	F: CATGTTCCAATATGATTCCA
	R：CCTGGAAGATGGTGATG

miR-210: microRNA-210; RUNX3: runt related transcription factor 3; GAPDH: glyceraldehyde 3 phosphate dehydrogenase

Cell transfection

A549 and H460 cells were treated with NC inhibitor, miR-210 inhibitor, NC mimic, or miR-210 mimic (all designed and synthesized by Ribobio, Guangzhou, Guangdong, China), si-NC or si-RUNX2 (both from Thermo Fisher, Austin, TX, USA). Remaining vectors were designed and constructed by VectorBuilder Inc. (Guangzhou, Guangdong, China). A549 and H460 cells were seeded in a 6-well plate (1×10^6 cells/well) overnight and transfected with Lipofectamine 2000 transfection reagent (Invitrogen, Carlsbad, CA, USA). After an overnight culture, cells were treated with LY29400 (PI3K/AKT signaling pathway inhibitor; MCE) at a concentration of 20 μm. At different time periods after transfection, cells were collected for subsequent experiments.

RT-qPCR

Total RNA was extracted with Trizol as per the manufacturer's instructions and reversely transcribed into complementary DNA (cDNA) as per TaqMan MicroRNA Assays Reverse Transcription primer (4427975, Applied Biosystems, NY, USA)/PrimeScript™ RT kit (Takara, Tokyo, Japan). RT-qPCR was performed on diluted cDNA using SYBR Premix Ex Taq II kit (Takara). Primers are shown in Table I. Relative expression of mRNA or miR-210 was calculated using $2^{-\Delta\Delta Ct}$ method with glyceraldehyde-3-phosphate dehydrogenase (GAPDH) or snRNA U6 expression as loading controls.

Immunoblotting

After 24 h of transfection, cells were lysed on ice with radio-immunoprecipitation assay, and then centrifuged at 20,000 g at 4°C for 10 min, and supernatants were collected. For each sample, 15 μg total protein was electrophoresed on 12% sodium dodecyl sulfate polyacrylamide gel electrophoresis and transferred to membrane. Protein concentration was determined using a bicinchoninic acid kit (Abcam, Cambridge, MA, USA). The membrane was probed overnight with diluted primary anti-rabbit antibodies to CD63 (55051, Cell Signaling Technology, Beverly, MA, USA), Hsp90 (4877, CST), Tsg101 (ab125011, Abcam), RUNX3 (9647, CST), PI3K (ab32089, Abcam), phosphorylated (p)-PI3K (ab182651, Abcam), AKT (ab8805, Abcam), p-AKT (ab38449, Abcam) and GAPDH (ab8245, Abcam). The membrane was re-probed with secondary goat anti-rabbit antibody to immunoglobulin G (IgG; ab97051, Abcam). All bands were detected using an enhanced chemiluminescence kit (Thermo Fisher).

Dual-luciferase reporter gene assay

Target genes of miR-210 were predicted using a biological prediction website (http://www.targetscan.org/vert_72/). Dual-luciferase reporter gene assay was performed. Complementary mutated (MUT) sequence was designed on RUNX3 wild-type (WT) in synthetic pGL3-RUNX3 3'-UTR plasmids (Huayueyang, Beijing, China). After digestion with restriction enzymes, target fragment was inserted into pGL3 reporter plasmid using T4 DNA ligase. Correctly sequenced luciferase reporter plasmids WT and MUT were co-transfected with miR-210 into HEK-293T cells (Beinuo Life Science, Shanghai, China), respectively. After 48 h of transfection, cells were collected and lysed, and luciferase activity was detected using luciferase detection kit (K801-200, Biovision, Exton, PA, USA) Glomax20/20 luminometer (Promega, Madison, WI, USA).

Cell counting kit-8 (CCK-8)

Cell proliferation was determined with CCK-8 kits (Bimake, Houston, TX, USA). Briefly, 24-h post transfection, cells were re-seeded on 96-well plates (3000 cells/well). Optical density (OD) value was measured with a microplate reader at 450 nm. Each test was performed in triplicates.

Transwell assay

After 24 h of cell transfection, cells were detached, centrifuged, resuspended into 5×10^5 cells/mL with serum-free medium. The apical chamber of Transwell (Thermo Fisher) was added with 200 μL cell suspension, while basolateral chamber with 500 μL RPMI-1640 medium containing 10% FBS at 37°C for 48 h. The basolateral chamber was removed and stained with crystal violet (Solarbio, Beijing, China) for 10 min. After the dyeing solution was washed off, the migrated cells were observed and counted under a microscope (CX33, Olympus, Tokyo, Japan). Cell invasion was determined with Matrigel invasion assay. The bottom of the apical chamber was pre-coated with Matrigel (BD Biosciences, Sparks, MD, USA) in advance and allowed to stand for 30 min at room temperature prior to the addition of cell suspension and culture medium. The invaded cells were counted under 5 randomly selected fields.

Tumorigenicity in nude mice

All animal experiments were performed in compliance with the authenticated animal protocols of the Institutional Animal Care and Use Committee of Jiangxi Chest Hospital. Efforts were made to avoid all unnecessary distress to the animals. Twenty-four 4-week-old BALB/c female nude mice (weight 20 ± 2g) were from Beijing Vital River Laboratory Animal Technology Co., Ltd. (Beijing, China). A 12-12 h lights on-off cycle was maintained in an environmentally controlled room (25°C, 45% humidity). The animals were allowed standard chow pellets and water ad libitum. All animals were randomly divided into 8 groups (n = 3, the DMSO, EXO, NC inhibitor, miR-210 inhibitor, miR-210 inhibitor + si-NC, miR-210 inhibitor + si-RUNX3, si-RUNX3 + DMSO, si-RUNX3 + LY294002 groups). Logarithmically growing A549 cells were adjusted to 1×10^7 cells/mL and then inoculated into the armpits of nude mice. The tumor volume was recorded every 7 days according to tumor volume = $(a \times b^2)/2$ (where a is the longest diameter of tumor, b is the shortest diameter of tumor) to plot the growth curve.

Statistical analysis

All data, representative of three independent experiments in triplicate, are summarized by mean ± standard deviation and analyzed by SPSS 21.0 (IBM, Armonk, NY, USA). Independent sample *t*-test was used for data comparison between two groups, and two-way analysis of variance (ANOVA) was utilized for data comparison among multiple groups. $p < 0.05$ referred to statistically significant difference.

RESULTS

Lung cancer cells-encapsulated exosomes enhance biological properties of lung cancer cells

Initially, we cultured A549 cells and separated exosomes from the A549 cell supernatant. The morphology of exosomes under a TEM is presented in Fig. 1A. Afterwards, the expression of exosomal markers CD63, Hsp90, and Tsg101 was determined with immunoblotting revealing the positive expression of these markers (Fig. 1B). We treated A549 and H460 cells with the exosomes and adopted CCK-8 and Transwell assays to determine the cell proliferation (Fig. 1C), migration (Fig. 1D) and invasion (Fig. 1E). Results revealed that exosomes markedly elevated the proliferation, migration and invasion of A549 and H460 cells relative to DMSO treatment, indicating that lung cancer cells-secreted exosomes could promote malignant properties of lung cancer cells.

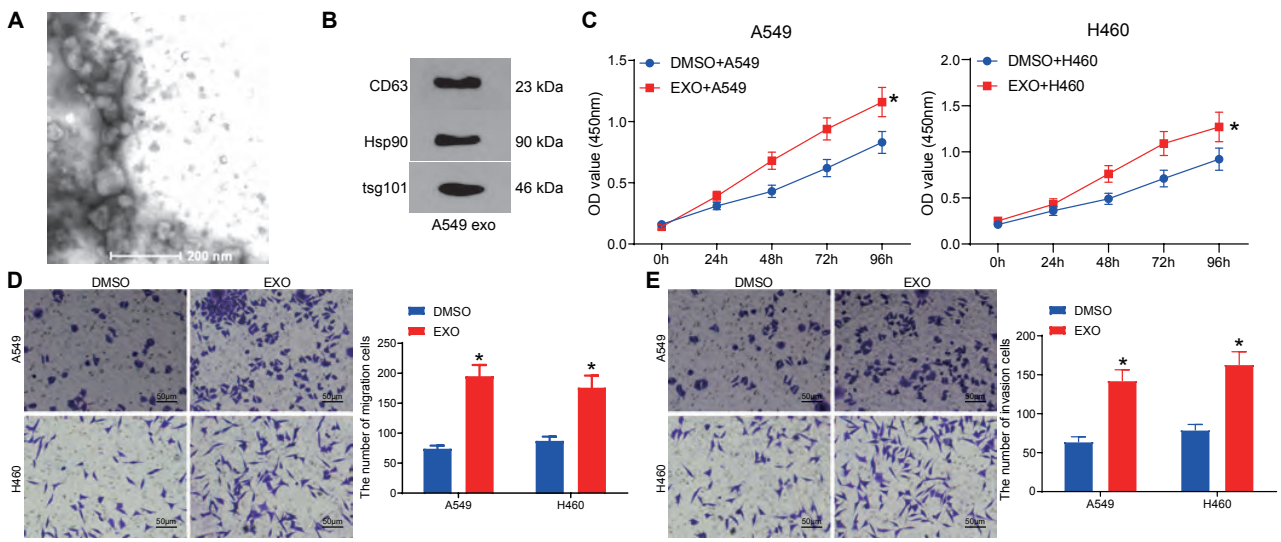


Fig. 1. *Lung cancer cell-derived exosomes promote biological properties of lung cancer cells. **A)** Morphology of A549 cell-derived exosomes under a TEM. **B)** Exosomal markers expression determined with immunoblotting. **C)** Cell proliferation determined with CCK-8 assays in response to DMSO or exosomes. **D)** Cell migration assayed with Transwell assays. **E)** Cell invasion assessed using Transwell assays. * $p < 0.05$ vs DMSO treatment. The experimental data are expressed as the mean ± SD of three independent replicates. Two-way ANOVA was utilized for data comparison among multiple groups.*

miR-210 inhibition suppresses biological properties of lung cancer cells

As revealed by a prior study, miR-210 could be transferred by lung cancer cell-derived exosomes (9) and miR-210 level was elevated in lung cancer tissues (11). We measured miR-210 expression in A549 and H460 cells after co-culture by RT-qPCR, demonstrating that exosomes promoted miR-210 level (Fig. 2A). We silenced miR-210 expression in A549 and H460 cells co-cultured with exosomes (Fig. 2B), and CCK-8 (Fig. 2C) and Transwell (Fig. 2 D, E) assays revealed reduced cell proliferation, migration and invasion in response to miR-210 inhibitor *vs* NC inhibitor.

Exosomal miR-210 inversely regulates the expression of RUNX3

To explore the downstream genes of miR-210, we performed Kyoto Encyclopedia of Genes and Genomes (KEGG) pathway enrichment analysis on the target genes of miR-210. The analysis showed that the RUNX3-mediated pathway was the most abundant among the downstream genes of miR-210, and the target genes of miR-210 were mainly enriched in the PI3K/AKT pathway (Fig. 3A). We found the binding sites between miR-210 and RUNX3 through the bioinformatics website, and confirmed by dual-luciferase reporter analysis that the luciferase activity was significantly lowered after co-transfection of miR-210 mimic and RUNX3-WT compared to NC mimic (Fig. 3B), thus confirming that miR-210 can target RUNX3. RT-qPCR results displayed that compared with DMSO treatment, RUNX3 mRNA expression was markedly downregulated in response to GW4869 treatment (Fig. 3C). Meanwhile, miR-210 inhibition also increased RUNX3 mRNA levels relative to NC inhibitor (Fig. 3D), suggesting that exosomal miR-210 inversely regulates the expression of RUNX3.

miR-210 inhibition suppresses biological properties of lung cancer cells by negatively targeting RUNX3

A549 and H460 cells were transfected with si-NC, si-RUNX3, miR-210 inhibitor + si-NC, and miR-210 inhibitor + si-RUNX3. As revealed by RT-qPCR (Fig. 4A), cells transfected with si-RUNX3 exhibited reduced RUNX3 and unchanged miR-210 expression. Meanwhile, miR-210 inhibitor + si-

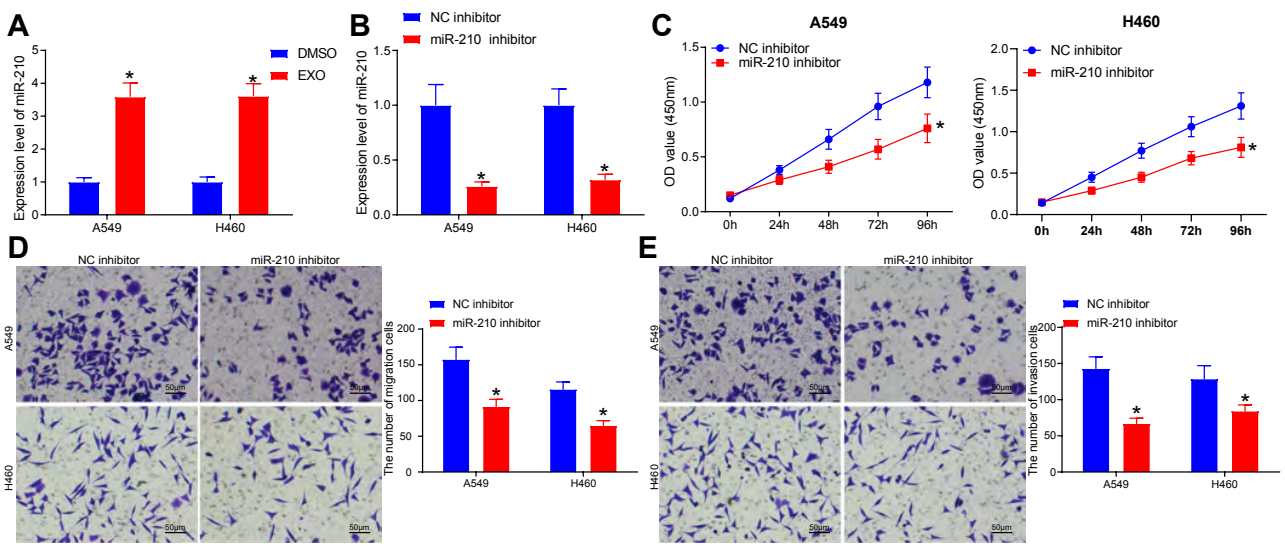


Fig. 2. *miR-210 silencing inhibits biological properties of lung cancer cells. **A**) miR-210 expression in A549 and H460 cells after co-culture assessed by RT-qPCR. **B**) miR-210 expression in A549 and H460 cells after transfection examined by RT-qPCR. **C**) cell proliferation determined with CCK-8 assays in response to miR-210 inhibitor or NC inhibitor. **D**) Cell migration assayed with Transwell assays. **E**) Cell invasion assessed using Transwell assays. * $p < 0.05$ vs NC inhibitor or DMSO. The experimental data are expressed as the mean ± SD of three independent replicates. Two-way ANOVA was utilized for data comparison among multiple groups.*

RUNX3 treatment reduced RUNX3 expression *vs* miR-210 inhibitor + si-NC treatment, accompanied by unchanged miR-210 level. CCK-8 (Fig. 4B) and Transwell (Fig. 4 C, D) assays demonstrated that si-RUNX3-treated cells exhibited marked increases in cell proliferation, migration and invasion in comparison with cells treated with si-NC. Meanwhile, reduced biological properties by miR-210 inhibitor were abrogated by the further treatment of si-RUNX3.

RUNX3 elevation suppresses malignant properties of lung cancer cells by impairing the PI3K/AKT signaling pathway

A549 and H460 cells were treated with si-NC + DMSO, si-RUNX3 + DMSO or si-RUNX3 + LY294002 (a PI3K/AKT signaling pathway inhibitor). Immunoblotting (Fig. 5A) exhibited that silencing of RUNX3 reduced RUNX3 expression as well as increased p-PI3K/PI3K and p-AKT/AKT levels in A549 cells. LY294002 administration rescued the effects of RUNX3 silencing on p-PI3K/PI3K and p-AKT/AKT levels, accompanied by unchanged RUNX3 level. As reflected by CCK-8 (Fig. 5B) and Transwell (Fig. 5 C, D), silencing of RUNX3 induced cell proliferation, migration and invasion, while LY294002 administration reversed these trends.

miR-210 negatively mediates RUNX3 expression to promote biological properties of lung cancer cells by activating PI3K/AKT signaling pathway

A549 and H460 cells were treated with NC mimic + DMSO, miR-210 mimic + DMSO or miR-210 mimic + LY294002. RT-qPCR was adopted to determine miR-210 expression (Fig. 6A), while immunoblotting to assess the RUNX3, p-PI3K/PI3K and p-AKT/AKT levels in A549 cells (Fig. 6B). Results revealed that miR-210 elevation induced miR-210, p-PI3K/PI3K and p-AKT/AKT levels as well as diminished RUNX3 expression, while LY294002 treatment reversed the effects of miR-210 mimic on p-PI3K/PI3K and p-AKT/AKT levels

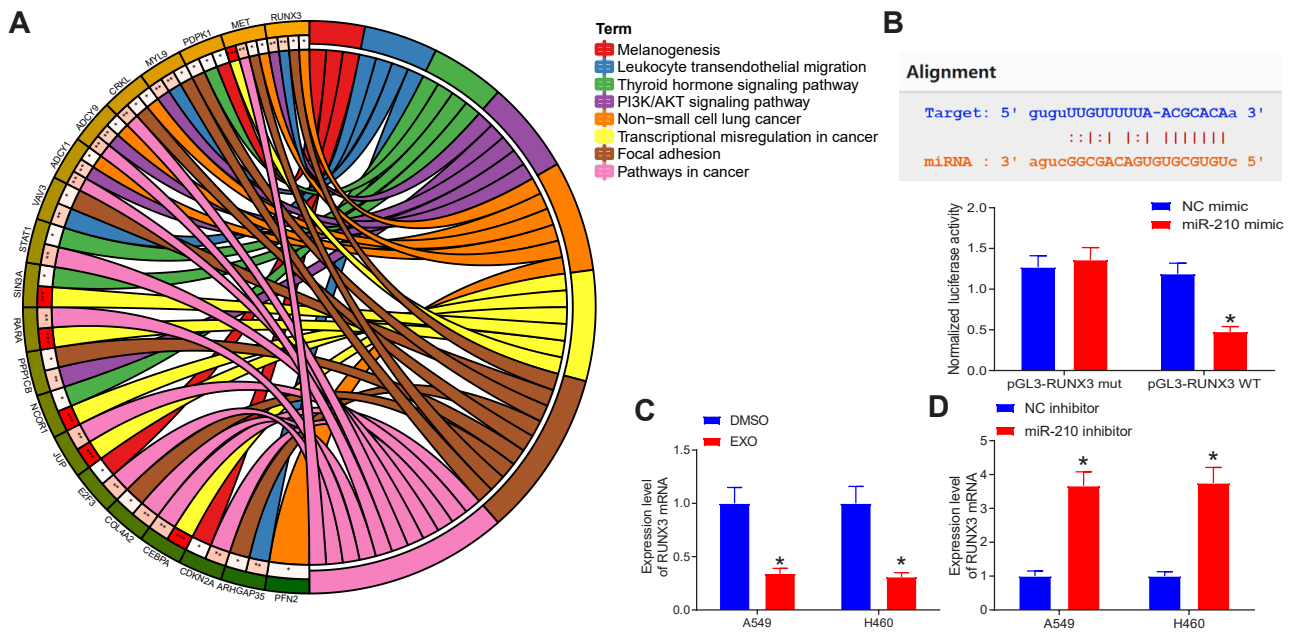


Fig. 3. *miR-210 inversely regulates RUNX3 expression. **A**) miR-210 downstream genes and mediating pathways probed by KEGG pathway enrichment analysis; **B**) Targeting relationship between miR-210 and RUNX3 determined using dual-luciferase reporter gene assay. **C, D**) mRNA levels of RUNX3 assayed with RT-qPCR in response to DMSO or exosomes (C) and NC inhibitor or miR-210 inhibitor (D). * $p < 0.05$ vs NC mimic, DMSO or NC inhibitor. The experimental data are expressed as the mean ± SD of three independent replicates. Two-way ANOVA was utilized for data comparison among multiple groups.*

accompanied by unchanged expression of miR-210 and RUNX3. CCK-8 (Fig. 6C) and Transwell (Fig. 6 D, E) assays demonstrated that miR-210 elevation augmented cell proliferation, migration and invasion, while LY294002 administration reversed these trends.

miR-210 activates PI3K/AKT signaling pathway by targeting RUNX3 and promotes tumor growth in vivo in lung cancer

To verify the exosome-mediated effects of miR-210 and RUNX3 *in vivo*, A549 cells were injected into mice and tumor volume changes were detected. By examining the tumor volume, we found that exosome treatment increased the tumor volume significantly, while miR-210 downregulation decreased the tumor volume. By contrast, si-RUNX3 inhibited the effect of miR-210 inhibitor to increase the tumor volume, and PI3K/AKT pathway inhibitor treatment reversed the effect of si-RUNX3 to decrease the tumor volume again. We also found that exosome treatment increased cell tumorigenicity by tumor weight assay, whereas miR-210 downregulation decreased cell tumorigenicity. RUNX3 downregulation reversed miR-210 inhibitor to increase cell tumorigenicity, and PI3K/AKT pathway activity reduction decreased cell tumorigenicity (Fig. 7).

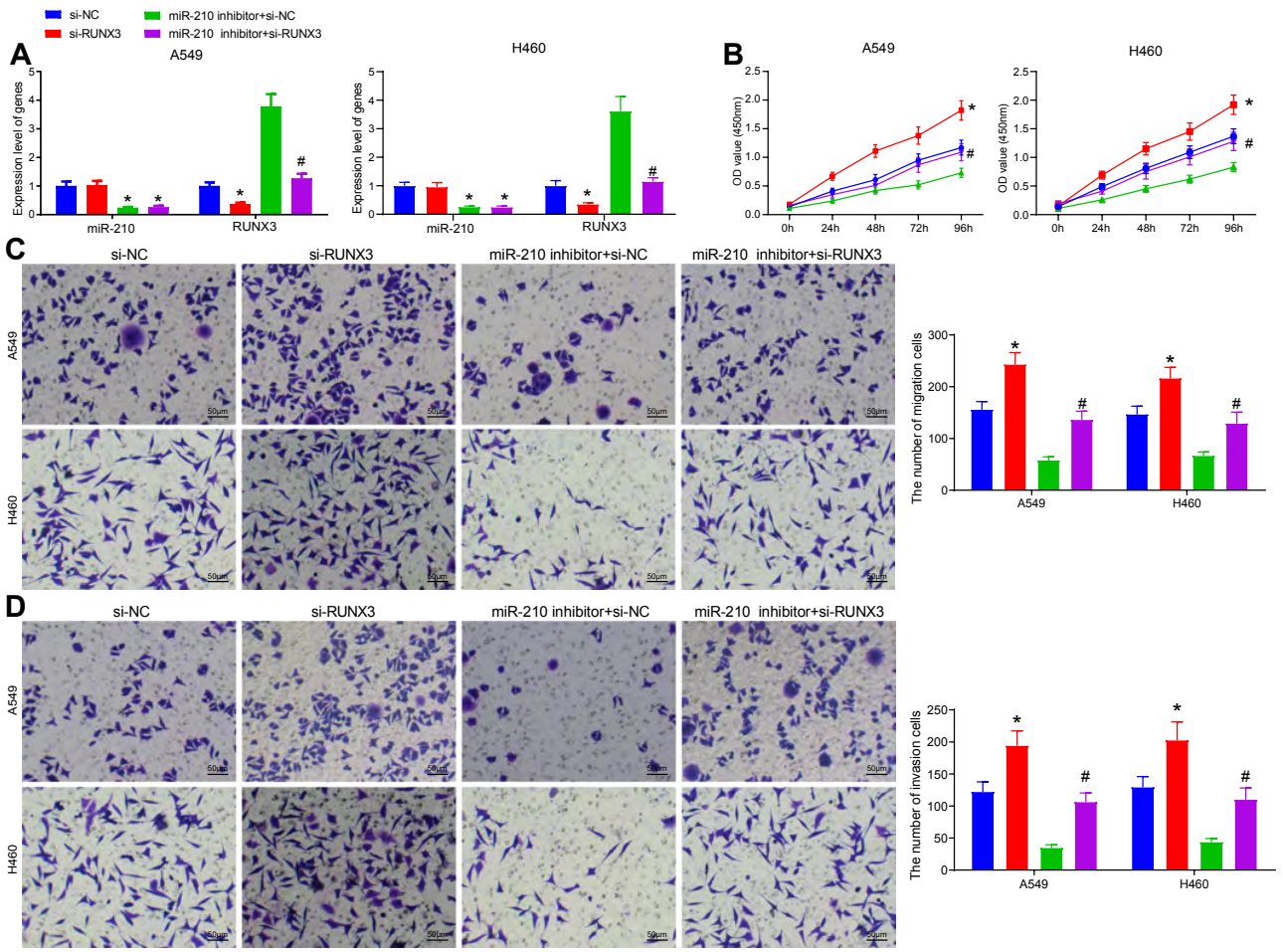


Fig. 4. *miR-210 inhibition suppresses biological properties of lung cancer cells by targeting RUNX3. A549 and H460 cells were treated with si-NC, si-RUNX3, miR-210 inhibitor + si-NC or miR-210 inhibitor + si-RUNX3.* ***A****) miR-210 and RUNX3 mRNA expression determined with RT-qPCR.* ***B****) Cell proliferation determined with CCK-8 assays.* ***C****) Cell migration assayed with Transwell assays.* ***D****) Cell invasion assessed using Transwell assays. * $p < 0.05$ vs si-NC; # $p < 0.05$ vs miR-210 inhibitor + si-NC. The experimental data are expressed as the mean ± SD of three independent replicates. Two-way ANOVA was utilized for data comparison among multiple groups.*

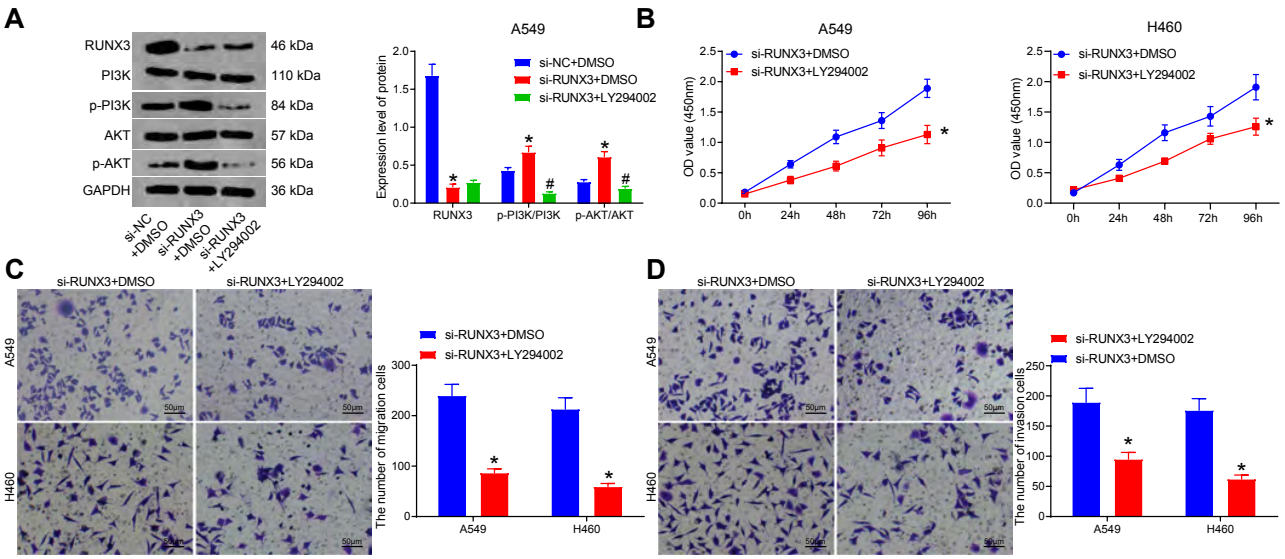


Fig. 5. *RUNX3 inhibits biological properties of lung cancer cells by inactivating PI3K/AKT signaling pathway. A549 and H460 cells were treated with si-NC + DMSO, si-RUNX3 + DMSO or si-RUNX3 + LY294002 (PI3K/AKT signaling pathway inhibitor). **A**) RUNX3, p-PI3K/PI3K and p-AKT/AKT levels determined with immunoblotting (* $p < 0.05$ vs si-NC + DMSO; # $p < 0.05$ vs si-RUNX3 + DMSO). **B**) Cell proliferation determined with CCK-8 assays. **C**) Cell migration assayed with Transwell assays. **D**) Cell invasion assessed using Transwell assays. In panels B-D, * $p < 0.05$ vs si-RUNX3 + DMSO. The experimental data are expressed as the mean ± SD of three independent replicates. Two-way ANOVA was utilized for data comparison among multiple groups.*

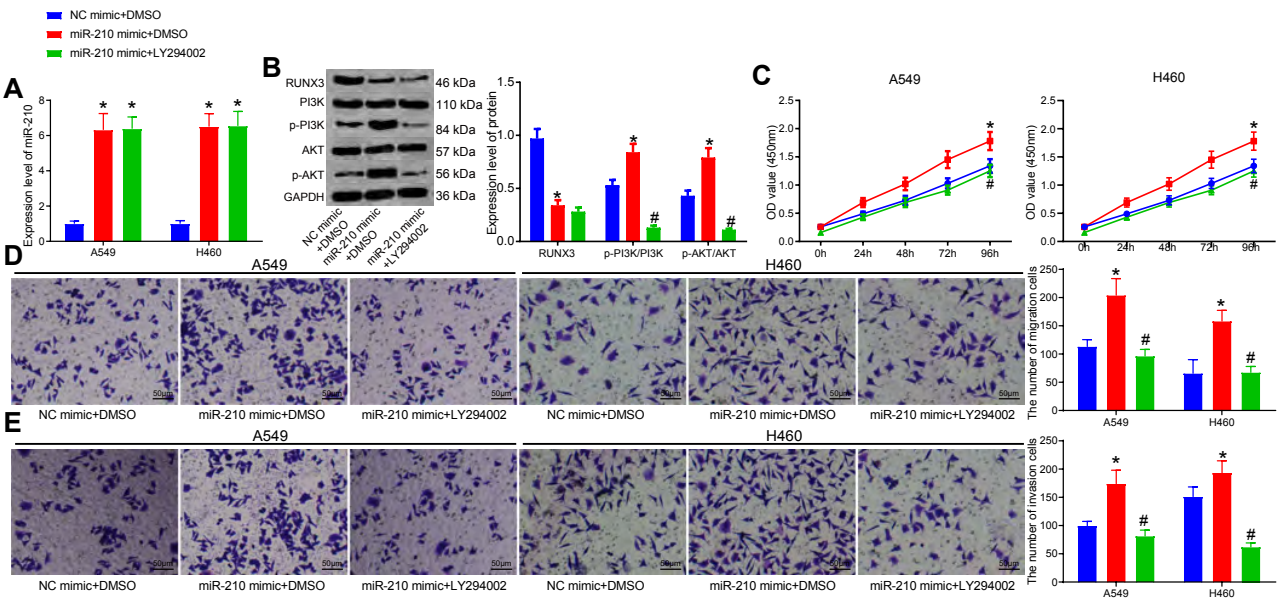


Fig. 6. *miR-210 knockdown inversely mediates RUNX3 expression to suppress biological properties of lung cancer cells by inactivating PI3K/AKT signaling pathway. A549 and H460 cells were treated with NC mimic + DMSO, miR-210 mimic + DMSO or miR-210 mimic + LY294002. **A**) miR-210 expression determined with RT-qPCR. B) RUNX3, p-PI3K/PI3K and p-AKT/AKT levels measured with immunoblotting. **C**) Cell proliferation determined with CCK-8. **D**) Cell migration assayed with Transwell. **E**) Cell invasion assessed using Transwell. * $p < 0.05$ vs NC mimic + DMSO; # $p < 0.05$ vs miR-210 mimic + DMSO. The experimental data are expressed as the mean ± SD of three independent replicates. Two-way ANOVA was utilized for data comparison among multiple groups.*

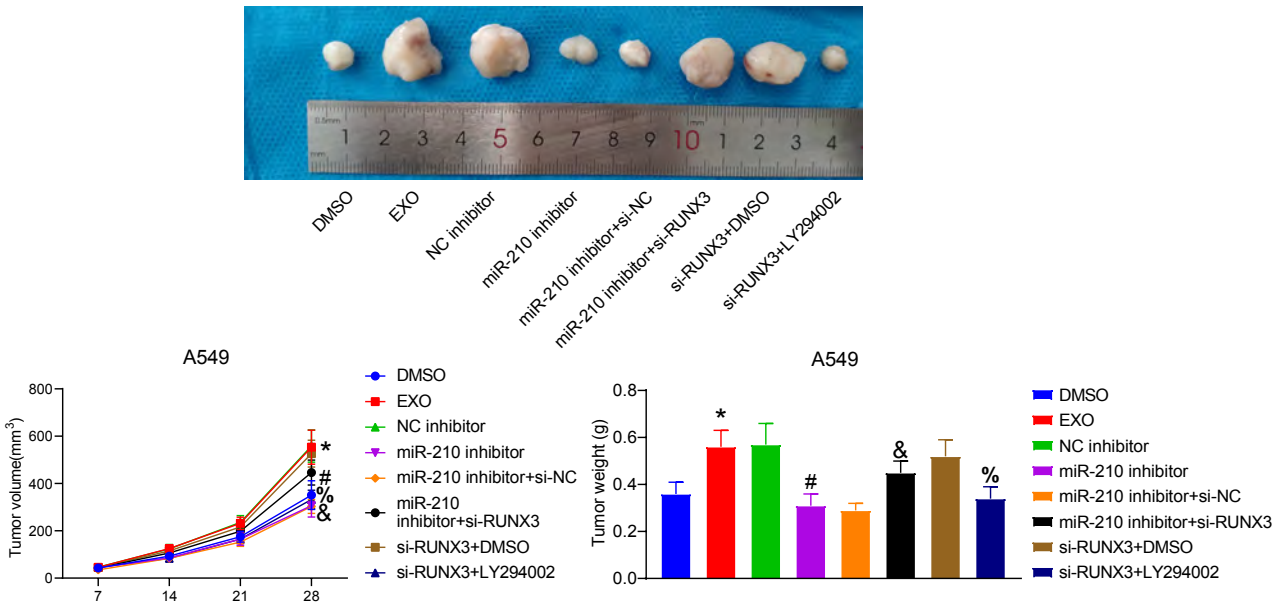


Fig. 7. *Exosomal miR-210 mediates the RUNX3/PI3K/AKT axis to regulate lung cancer cell activity in vivo. A549 cells treated with DMSO, EXO, NC inhibitor, miR-210 inhibitor, miR-210 inhibitor + si-NC, miR-210 inhibitor + si-RUNX3, si-RUNX3 + DMSO or si-RUNX3 + LY294002 were injected into nude mice (n = 3). Tumorigenesis of A549 cells in nude mice. * $p < 0.05$ vs DMSO; # $p < 0.05$ vs NC inhibitor; & $p < 0.05$ vs miR-210 inhibitor + si-NC; % $p < 0.05$ vs si-RUNX3 + DMSO. The experimental data are expressed as the mean ± SD of three independent replicates. Two-way ANOVA was utilized for data comparison among multiple groups.*

DISCUSSION

Lung cancer claims more lives worldwide than any other cancer and remains a challenge for patients, with a low rate of survival following diagnosis (18). Delayed diagnosis, restricted therapeutic tools, relapse and drug resistance hinders the success of lung cancer-targeted therapies (8). Many recent reports established that exosomal miRNAs might be applied for lung cancer diagnosis and prognosis (19, 20). Intriguingly, exosomal miR-210-3p is predicted to enhance lung cancer cell invasion by activating STAT3 signaling-induced epithelial-mesenchymal transition, acting as a biomarker for lung cancer (21). The present study provides evidence that exosomal miR-210 inversely regulates RUNX3 expression to promote malignant phenotype of lung cancer cells by activating the PI3K/AKT signaling pathway.

Exosomes could serve as efficient drug delivery vehicles, making them a suitable diagnostic modality for the treatment of lung cancer (22). Cancer-secreted exosomes help to recruit and reprogram constituents associated with lung cancer microenvironment, including initiation, progression and metastasis (6). In the current study, we revealed that lung cancer cell-encapsulated exosomes enhanced malignant phenotype of lung cancer cells, and miR-210 was contained in these exosomes. As shown in a prior study, elevated miR-210 expression was detected in pancreatic cancer stem cells and their derived exosomes (23). More relevantly, miR-210 could be transferred by lung cancer cell-derived exosomes, and the exosomes with elevated miR-210 exerted pro-angiogenesis effects (9). Moreover, we found that miR-210 inhibition reverted the malignant phenotype of lung cancer cells. Recent evidence presented that miR-210 expression was remarkably elevated in lung cancer samples *versus* benign (non-neoplastic) pleural effusion (24). Likewise, exosomes derived from lung cancer stem cells exerted pro-metastatic effects on lung cancer cells via miR-210-3p transfer (10). Cancer-associated fibroblasts (CAF)-derived exosomes contain miR-210, and miR-210 elevation enhances the malignant phenotype of non-small cell

lung cancer (NSCLC) cells (25). Moreover, miR-210 was overexpressed in exosomes *in vitro* and *in vivo* after tissue inhibitor of metalloproteinase-1 was overexpressed in tumor cells (26). Therefore, more mechanistical studies will be carried out in the near feature to expound the detailed mechanism of miR-210 overexpression in exosomes derived from lung cancer cells.

In the subsequent study, miR-210 inversely regulated the expression of RUNX3 based on biological prediction and dual-luciferase reporter gene assay. RUNX3 is directly targeted by miR-210 in pulmonary fibrosis (27). Furthermore, our finding also demonstrated that RUNX3 depletion is correlated with the promoted malignant biological properties of lung cancer cells. RUNX3 serves as a prognostic factor for the poor outcome in NSCLC, accompanied by a reduction in apoptotic index and shorter overall survival (28). Enlarged tumor size and severe osteolytic lesions were observed in the calvaria and tibiae of mice injected with RUNX3-silencing cells (29). At the same time, miR-210 inhibition suppressed biological properties of lung cancer cells by negatively targeting RUNX3. The similar mechanism was proposed by another study related to the biological properties of human umbilical vein endothelial cells (HUVECs), demonstrating the promotion effects of microvesicle-secreted miR-210 released by adipose-derived stem cells on the aggressive phenotype of HUVECs by regulating RUNX3 (30).

Our results further revealed that the RUNX3 elevation could block the PI3K/AKT signaling pathway, which was correlated with the suppressed biological properties of lung cancer cells. Therapeutic approaches focused on the cross-talk between RUNX3 and PI3K/AKT may contribute to improve gastric cancer control (31). Since RUNX3 is a well-known transcription factor, we postulated that it regulates the PI3K/AKT pathway by modulating the transcription of a certain gene in this pathway, however, the detailed mechanism awaits further elucidation. Another study has also highlighted the preclinical and clinical significance of PI3K pathway inhibitors in NSCLC, alone or in combination with chemotherapy and other drugs (32). Meanwhile, CAF-derived exosomal miR-210 could activate the PTEN/PI3K/AKT pathway to promote the malignant phenotype of NSCLC (25). In the present study, LY294002, the PI3K/AKT signaling pathway inhibitor, reversed the effects of miR-210 mimic on biological properties of lung cancer cells. Likewise, administration of the PI3K inhibitor LY294002 also reduced A549 cell viability rate induced by lappaconitine sulfate (33).

In conclusion, our study revealed the role of exosomal miR-210/RUNX3/PI3K/AKT pathway in the regulation of a malignant phenotype of lung cancer cells. miR-210 was expressed in the lung cancer cell-derived exosomes and miR-210 knockdown negatively modulated RUNX3 expression to suppress biological properties of lung cancer cells by blocking the PI3K/AKT signaling pathway. Exosomal miR-210 might offer a promising biomarker for treatment of lung cancer. However, we only adopted a single dose of exosomes in our experiments. Identification of dose and times of injection should be optimized in the future.

REFERENCES

1. Bray F, Ferlay J, Soerjomataram I, Siegel RL, Torre LA, Jemal A. Global cancer statistics 2018: GLOBOCAN estimates of incidence and mortality worldwide for 36 cancers in 185 countries. CA Cancer J Clin 2018; 68:394-424.
2. Snoeckx A, Dendooven A, Carp L, et al. Wolf in Sheep's Clothing: Primary Lung Cancer Mimicking Benign Entities. Lung Cancer 2017; 112:109-17.
3. Thawani R, McLane M, Beig N, Ghose S, Prasanna P, Velcheti V, Madabhushi A. Radiomics and radiogenomics in lung cancer: a review for the clinician. Lung Cancer 2018; 115:34-41.
4. Hammad A, Namani A, Elshaer M, Wang XJ, Tang X. "NRF2 addiction" in lung cancer cells and its impact on cancer therapy. Cancer Lett 2019; 467:40-9.
5. Bearz A, Cecco S, Francescon S, Re FL, Corona G, Baldo P. Safety profiles and pharmacovigilance considerations for recently patented anticancer drugs: lung cancer. Recent Pat Anticancer Drug Discov 2019; 14:242-57.

6. Chen R, Xu X, Qian Z, et al. The biological functions and clinical applications of exosomes in lung cancer. Cell Mol Life Sci 2019; 76:4613-33.
7. Wu J, Shen Z. Exosomal miRNAs as biomarkers for diagnostic and prognostic in lung cancer. Cancer Med 2020; 9(19):6909-6922.
8. Iqbal MA, Arora S, Prakasam G, Calin GA, Syed MA. MicroRNA in lung cancer: role, mechanisms, pathways and therapeutic relevance. Mol Aspects Med 2019; 70:3-20.
9. Fan J, Xu G, Chang Z, Zhu L, Yao J. miR-210 transferred by lung cancer cell-derived exosomes may act as proangiogenic factor in cancer-associated fibroblasts by modulating JAK2/STAT3 pathway. Clin Sci (Lond) 2020; 134:807-25.
10. Wang L, He J, Hu H, Tu L, Sun Z, Liu Y, Luo F. Lung CSC-derived exosomal miR-210-3p contributes to a pro-metastatic phenotype in lung cancer by targeting FGFRL1. J Cell Mol Med 2020; 24:6324-39.
11. He RQ, Cen WL, Cen JM, et al. Clinical Significance of miR-210 and its Prospective Signaling Pathways in Non-Small Cell Lung Cancer: Evidence from Gene Expression Omnibus and the Cancer Genome Atlas Data Mining with 2763 Samples and Validation via Real-Time Quantitative PCR. Cell Physiol Biochem 2018; 46:925-52.
12. Long CM, Lukomska E, Marshall NB, Nayak A, Anderson SE. Potential inhibitory influence of miRNA 210 on regulatory t cells during epicutaneous chemical sensitization. Genes (Basel) 2016; 8(1):9
13. Zhou Z, Yao B, Zhao D. Runx3 regulates chondrocyte phenotype by controlling multiple genes involved in chondrocyte proliferation and differentiation. Mol Biol Rep 2020; 47:5773-92.
14. Li X, Zhong M, Wang J, et al. miR-301a promotes lung tumorigenesis by suppressing Runx3. Mol Cancer 2019; 18:99.
15. Qiao CX, Xu S, Wang DD, et al. MicroRNA-19b alleviates lipopolysaccharide-induced inflammatory injury in human intestinal cells by up-regulation of Runx3. Eur Rev Med Pharmacol Sci 2018 ;22:5284-94.
16. Wei J, Gou Z, Wen Y, Luo Q, Huang Z. Marine compounds targeting the PI3K/Akt signaling pathway in cancer therapy. Biomed Pharmacother 2020; 129:110484.
17. Gu JJ, Qiao KS, Sun P, Chen P, Li Q. Study of EGCG induced apoptosis in lung cancer cells by inhibiting PI3K/Akt signaling pathway. Eur Rev Med Pharmacol Sci 2018; 22:4557-63.
18. Cheung CHY, Juan HF. Quantitative proteomics in lung cancer. J Biomed Sci 2017; 24:37.
19. Fortunato O, Gasparini P, Boeri M, Sozzi G. Exo-miRNAs as a New Tool for Liquid Biopsy in Lung Cancer. Cancers (Basel) 2019; 11(6):888.
20. Vanni I, Alama A, Grossi F, Dal Bello MG, Coco S. Exosomes: a new horizon in lung cancer. Drug Discov Today 2017; 22:927-36.
21. Zhang X, Sai B, Wang F, et al. Hypoxic BMSC-derived exosomal miRNAs promote metastasis of lung cancer cells via STAT3-induced EMT. Mol Cancer 2019; 18:40.
22. Srivastava A, Amreddy N, Razaq M, et al. Exosomes as Theranostics for Lung Cancer. Adv Cancer Res 2018; 139:1-33.
23. Yang Z, Zhao N, Cui J, Wu H, Xiong J, Peng T. Exosomes derived from cancer stem cells of gemcitabine-resistant pancreatic cancer cells enhance drug resistance by delivering miR-210. Cell Oncol (Dordr) 2020; 43:123-36.
24. Tamiya H, Mitani A, Saito A, et al. Exosomal MicroRNA Expression profiling in patients with lung adenocarcinoma-associated malignant pleural effusion. Anticancer Res 2018; 38:6707-14.
25. Yang F, Yan Y, Yang Y, et al. MiR-210 in exosomes derived from CAFs promotes non-small cell lung cancer migration and invasion through PTEN/PI3K/AKT pathway. Cell Signal 2020; 73:109675.
26. Cui H, Seubert B, Stahl E, et al. Tissue inhibitor of metalloproteinases-1 induces a pro-tumourigenic increase of miR-210 in lung adenocarcinoma cells and their exosomes. Oncogene 2015; 34:3640-50.
27. Zhu Y, Wang J, Meng X, et al. A positive feedback loop promotes HIF-1alpha stability through miR-210-mediated suppression of RUNX3 in paraquat-induced EMT. J Cell Mol Med 2017; 21:3529-39.
28. Chen X, Deng Y, Shi Y, et al. Loss of expression rather than cytoplasmic mislocalization of RUNX3 predicts worse outcome in non-small cell lung cancer. Oncol Lett 2018; 15:5043-55.
29. Kim HJ, Park J, Lee SK, Kim KR, Park KK, Chung WY. Loss of RUNX3 expression promotes cancer-

associated bone destruction by regulating CCL5, CCL19 and CXCL11 in non-small cell lung cancer. J Pathol 2015; 237:520-31.
30. Zheng Z, Liu L, Zhan Y, Yu S, Kang T. Adipose-derived stem cell-derived microvesicle-released miR-210 promoted proliferation, migration and invasion of endothelial cells by regulating RUNX3. Cell Cycle 2018; 17:1026-33.
31. Vogiatzi P, De Falco G, Claudio PP, Giordano A. How does the human RUNX3 gene induce apoptosis in gastric cancer? Latest data, reflections and reactions. Cancer Biol Ther 2006; 5:371-4.
32. Fumarola C, Bonelli MA, Petronini PG, Alfieri RR. Targeting PI3K/AKT/mTOR pathway in non-small cell lung cancer. Biochem Pharmacol 2014; 90:197-207.
33. Qu D, Ma J, Song N, Hui L, Yang L, Guo Y, Sang C. Lappaconitine sulfate induces apoptosis and G0/G1 phase cell cycle arrest by PI3K/AKT signaling pathway in human non-small cell lung cancer A549 cells. Acta Histochem 2020; 122:151557.

Dynamics and proliferative capacities of $CD8^+CD28^+TCR\alpha\beta^+CD62L^{high}$ T-cell subsets in healthy and asthmatic subjects

M. Pietruczuk[1*], L. Kraszula[1], M. Kupczyk[2], P. Kuna[2] and M. Eusebio[1*]

[1]Department of Laboratory Diagnostics, Medical University of Lodz, Poland; [2]Department of Internal Medicine, Medical University of Lodz, Poland

Received November 11, 2020 – Accepted April 14, 2021

*These Authors contributed equally to this work

Adhesion molecules, as such, play essential roles in T-cell transendothelial extravasation during inflammation. A better understanding of the mechanisms underlying this process may be of value in the management of asthma. The present study employed Magnetic-Activated Cell Sorting (MACS) to isolate human $CD8^+$ T lymphocytes from peripheral blood of asthma patients and controls. The cells were flow cytometrically assessed to evaluate surface expression of an adhesion molecule, L-selectin (CD62L) on the surface of $CD8^{FoxP3-/bright}$ T cell subsets and its response to inflammatory cytokines. We showed that $CD8^+CD28^+TCR\alpha\beta^+CD62L^{high}FoxP3^{bright}$ T cells were deficient in blood of some asthma patients but abundant in others. After co-stimulation of $CD8^+$ T cells with anti-CD3/CD28 in combination with IL-2 and IL-10 or TGF-β, the frequencies of $CD8^+CD28^+TCR\alpha/\beta^+CD62L^{high}$ T cells in the group of patients were lower than at baseline. Our data indicate that L-selectin expression is regulated by inflammatory cytokines. Overall, these data reveal that asthma phenotypes may be further stratified into micro subtypes with distinct cellular and molecular characteristics, supporting the concept of asthma endotypes.

The pathogenesis of asthma is thought to be mediated by the migration of T cells from the regional lymph nodes into the airways. Antigen processing and presentation is primordial for the initiation of the inflammatory cascade. A literature review revealed that T-cell receptor (TCR) activation dictates the differentiation of naive T cells into various cell lineages. It has been shown that TCR harbors two protein chains (α /β and γ/δ) which lodge on the surface of circulatory T cells (1). Increasing evidence suggest that $TCR\alpha\beta^+$ T cells play a significant role in immune homeostasis (2). While some studies suggest that TCR activation alone is sufficient for the initiation of T-cell mediated immune response, other reports indicate that CD28 signaling may provide an additional signal for T-cell activation and expansion (3). $CD8^+$ T cells have been broadly divided into two major subsets according to CD28 expression. There has been increasing interest in the role of $CD8^+$ T cells in health and illness (4, 5). The emigration of immune cells such as lymphocytes to target sites plays a main role in inflammatory response. There is scarce data on the role of adhesion molecules, namely L-selectin (CD62L) in lymphocyte recycling and recruitment to the inflamed tissues. T cells have been categorized into central memory ($CD62L^{high}$) and effector memory

Key words: $CD8^+CD28^+$ T cells; selectin; Foxp3; cytokines; anti-CD3/CD28; asthma

Corresponding Author:
Makandjou-Ola Eusebio, MD, PhD
Department of Laboratory Diagnostics,
II Chair of Internal Medicine,
Medical University of Lodz, Kopcinski 22 str.,
90-153 Lodz, Poland
Tel.: +48 42 677 69 83 Fax: +48 42 678 28 33
e-mail: eusemak@yahoo.com

0393-974X (2021)
Copyright © by BIOLIFE, s.a.s.
This publication and/or article is for individual use only and may not be further reproduced without written permission from the copyright holder.
Unauthorized reproduction may result in financial and other penalties
DISCLOSURE: ALL AUTHORS REPORT NO CONFLICTS OF INTEREST RELEVANT TO THIS ARTICLE.

($CD62L^{low}$) subsets (6) according to the pattern of L-selectin expression. To the best of our knowledge the role of the expression of an adhesion molecule, L-selectin (CD62L) on the surface of $CD8^+$ T-cell subsets in the pathogenesis of asthma has not yet been studied and the effects of cytokines on L-selectin expression is not fully understood. We explored whether anti-CD3/CD28 activation in combination with IL-10 or TGF-β could enrich and expand $CD62L^{high}$ T-cell subsets within $CD8^+$ T cells *ex vivo*. The present study demonstrates the implication of L-selectin expression on the mechanisms underlying the influx of $CD8^+$ T cells from the periphery to the airways. Furthermore, our data indicate that L-selectin expression is controlled by inflammatory cytokines. Overall, these data reveal that asthma phenotypes may be further stratified into micro subtypes with distinct cellular and molecular characteristics, supporting the concept of asthma endotypes. This study may have clinical implications for cellular therapy.

MATERIALS AND METHODS

Study population

Twenty-five individuals with severe asthmatics (SA), 25 with mild-to-moderate asthmatics (MA), and 25 healthy individuals (NC) were studied. The study participants underwent physical examination followed by spirometry and skin prick tests. The diagnosis of asthma was based on history of periodic wheeze and reversible airway obstruction, as previously described in GINA guidelines. The severity distribution of asthma was based on the European Network for Understanding Mechanisms of Severe Asthma (ENFUMOSA) classification. Patients were in clinically stable condition and had no recent history of an upper respiratory tract infection. The study was approved by the Ethics Committee of our institution. All participants provided written consent before enrollment.

$CD8^+$ T-cell purification

Peripheral blood samples were obtained from study participants. Peripheral blood mononuclear cells (PBMCs) were isolated by ficoll-hypaque gradient centrifugation. Naïve $CD8^+$ T cells were enriched according to the manufacturer's instructions. $CD8^+$ T cells were sorted by Magnetic-Activated Cell Sorting (MACS). Cells were assessed on a FACS CANTO II flow cytometer using the appropriate panel of fluorescent antibodies. The purity of the enriched $CD8^+$ T-cell fraction was always higher than 97%.

In-vitro cell cultivation

Freshly isolated $CD8^+$ T cells were cultured in RPMI-1640 medium supplemented with 10% heat inactivated fetal bovine serum (FBS), L-glutamine (40 mmol/l), penicillin (100 U/ml) and streptomycin (100 μg/ml). The cells were activated with anti-CD3 (10 μg/ml), anti-CD28 (1 μg/ml), and IL-2 (20 U/mL) and cultivated with IL-2 in the presence of 10 ng/ml of IL-10 or TGF-β. A sample of enriched cells was plated in a 96-well plate and incubated for 3 days at 37C° in a fully humidified atmosphere with 5% CO_2 in air.

Flow cytometry analysis

Blood collected in EDTA tubes was used to enrich $CD8^+$ T cells. Briefly, 100 μL of cells was incubated for 30 min with the following cell surface markers: CD3 (fluorescein isothiocyanate (FITC)) (clone UCHT1, IgG1, κ), CD8 (American Cyanamid (Am Cyan)) (Clone SK1, IgG_1, κ), CD28 (peridinin chlorophyll protein- Cy5 (PerCP-Cy5)) (Clone CD28.2, IgG_1, κ), CD62L (phycoerythrin cyanine-5 (PE-Cy™ 5)) (Clone DREG-56, IgG_1, κ), and TCRα/β (Pacific blue) (Clone T10B9.1A-31, IgG_1, κ). Intracellular protein staining was performed using FoxP3 (allophycocyanin (APC)) (clone 259D/C7, IgG_1, κ) and staining buffer set. Stained cells were acquired on a FACS CANTO II cytometer (BD Biosciences, USA) using a FACS Diva software software (Becton Dickinson, USA). Flow cytometry analysis was performed using analysis gates for $CD8^+$ T cells from typical forward and side angle light scattering. Specific subsets were identified by comparison to isotype and fluorescent-minus-one (FMO) controls. Scatter profiles were used to exclude dead cells. $CD8^+$ T lymphocytes were gated based on the co-expression of CD28, TCRαβ, CD62L and FoxP3. Quadrants show staining of populations gated according to fluorescence-minus-one (FMO) control technique (Fig. 1). Gates were standardized within individual samples to ensure a fully comparative data. All experiments were carried out in triplicate. The same gate specifications were used for each sample.

Statistical analyses

Demographic and clinical data are expressed as the

mean ± SD. Cell frequencies are expressed as medians ± IQ. Statistical analysis was performed with Stat Soft's software (z o.o., Krakow, Poland). Differences between groups were tested for statistical significance using Mann-Whitney U test. Associations between the cell frequencies were analyzed with Spearman's rank correlation test. A p value <0.05 was considered statically significant.

RESULTS

Characteristics of study participants

Clinical and demographic data of study participants are shown in Table I. A total of 50 patients and 25 healthy controls were studied. Subjects in all groups were matched for age and sex. Lung function parameters such as $\%FEV_1$ and PEF differed among the asthma groups and controls.

Comparative analysis of the proportions of isolated $CD8^+$ T lymphocyte subsets

The peripheral blood of patients with severe asthma had almost similar proportions of $CD8^+CD28^+TCR\alpha/\beta^+CD62L^{high}$ T cell subsets, namely, $CD8^+CD28^+TCR\alpha\beta^+CD62L^{high}FoxP3^{bright}$ cells (SA 12.5±[6.8-22.5]); $CD8^+CD28^+TCR\alpha\beta^+CD62L^{high}FoxP3^-$ (SA12.3±[8-18.1]). In contrast, cells with $CD8^+CD28^+TCR\alpha/\beta^+CD62L^{high}Foxp3^{bright}$ phenotype predominated in the blood of mild-to-moderate asthma

Table I. *Clinical and demographic characteristics of the cases and controls*

Parameters	SA (n=25)	NC (n=25)	MA (n=25)
Sex ♂/♀	13/12	12/13	12/13
Age (Yr±SD)	49 SD±14.5	47 SD±16.0	42 SD±13.5
Disease duration	16 y SD±8.7	14y±7.2	10 y SD±6.3
Atopy	Yes	N/A	Yes
Predicted FEV_1	67 SD±15.98	96.6 SD±4	87.71 SD±16.12
ICS	800-1.600 µg	N/A	200-800 µg

SA: severe asthma; MA: Mild-to-moderate asthma; NC: Healthy controls; FEV_1: Forced expiratory volume in 1 second; y: years ICS: inhaled glucocorticosteroids; N/A: Not applicable.

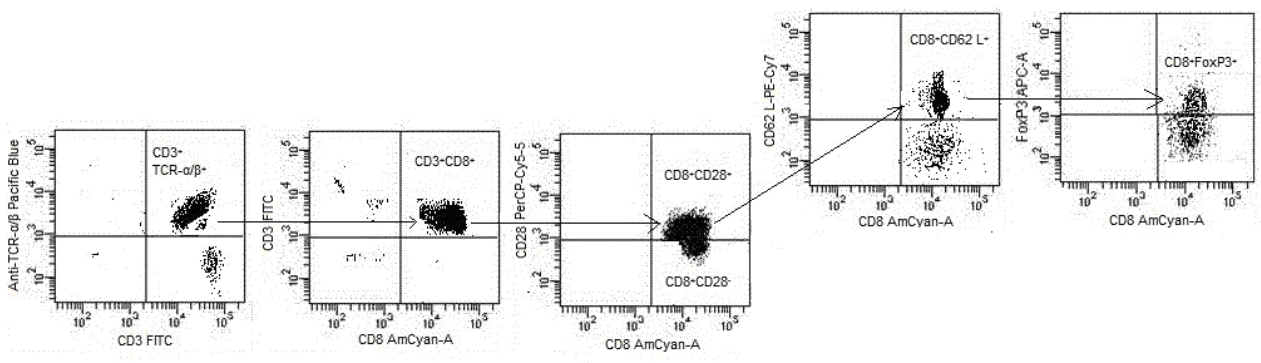


Fig. 1. *Representative flow cytometry dot plots in each group are shown. $CD8^+$ T population were evaluated for co-expression of CD28, TCRαβ, CD62L and FoxP3. Quadrants show staining of populations gated according to fluorescence-minus-one (FMO) control technique.*

patients whereas their counterparts were abundant in the blood of controls (Fig. 2).

$CD8^+CD28^+TCR\alpha\beta^+CD62L^{high}FoxP3^{bright}$ T cells were deficient in blood of some asthma patients but abundant in others

The frequency of both $CD8^+CD28^+TCR\alpha/\beta^+CD62L^{high}$ T-cell subsets were significantly lower in blood samples from severe asthma subjects compared with those with mild-to-moderate asthma and controls. We observed a remarkable deficiency of $CD8^+CD28^+TCR\alpha\beta^+CD62L^{high}FoxP3^{bright}$ T cells in severe asthmatic patients (SA 12.5±[6.8-22.5]) compared with mild-to-moderate (MA33.2±[32-48.6]) ($p<0.01$), and controls NC (22.4[19.7-24.1]) ($p<0.05$). In contrast we observed a significant abundance of $CD8^+CD28^+TCR\alpha\beta^+CD62L^{high}FoxP3^{bright}$ T cells in mild-to-moderate asthma patients (MA 33.2± [32-48.6]) ($p<0.01$) compared with controls (NC 22.4[19.7-24.1]) ($p<0.05$) (Fig. 2).

$CD8^+CD28^+TCR\alpha\beta^+CD62L^{high}FoxP3^-$ T cells were deficient in blood of asthma patients

We observed a remarkable deficiency of $CD8^+CD28^+TCR\alpha\beta^+CD62L^{high}FoxP3^-$ T cells in severe asthmatic patients (SA 12.3±[8-18.1]) compared with mild-to-moderate (MA 25.5[20-28.3]), ($p<0.01$), and controls (NC 31.8[26.7-34.5]) ($p<0.001$) (Fig. 2).

IL-10 or TGF-β decreased the proportion of $CD8^+CD28^+TCR\alpha/\beta^+CD62L^{high}$ T cells

To determine the effect of anti-inflammatory cytokines, namely IL-10 or TGF-β, on the expansion of $CD8^+$ T cells, $CD8^+$ T cells were stimulated by anti-CD3/CD28-coated beads and exogenous IL-2 along with either IL-10 or TGF-β. After 72 h, a marked decrease was noted in the frequencies of $CD8^+CD28^+TCR\alpha/\beta^+CD62L^{high}$ T cell subsets. Co-stimulation with IL-10 remarkably decreased the percentage of $CD8^+CD28^+TCR\alpha/\beta^+CD62L^{high}Foxp3^{bright}$ T cells in the group of allergic asthma subjects [(SA (12.5± [6.8-22.5] to 9.06± [6.9-19]), and MA (33.2± [32-48.6] to 3.3± [0.4-4.5)] and healthy controls (22.4[19.7-24.1] to 6[3.4-8]) (Fig. 3). There was a statistically significant difference between severe asthma patients and controls in respect to the frequencies of $CD8^+CD28^+TCR\alpha/\beta^+CD62L^{high}$ T cells that express ($p<0.05$) or lack ($p<0.01$) $Foxp3^{bright}$ (Fig. 3). Similarly, T-cell activation in combination with TGF-β stimulation decreased the frequencies of $CD8^+CD28^+TCR\alpha/\beta^+CD62L^{high}Foxp3^{bright}$ T cells in allergic asthma subjects [(SA (12.5± [6.8-22.5] to 11.3 [4.5-45.8]), and MA (33.2± [32-48.6] to 13.5[5-14.6]) and healthy controls (22.4[19.7-24.1] to 5.5[4.3-10]) (Fig. 4).

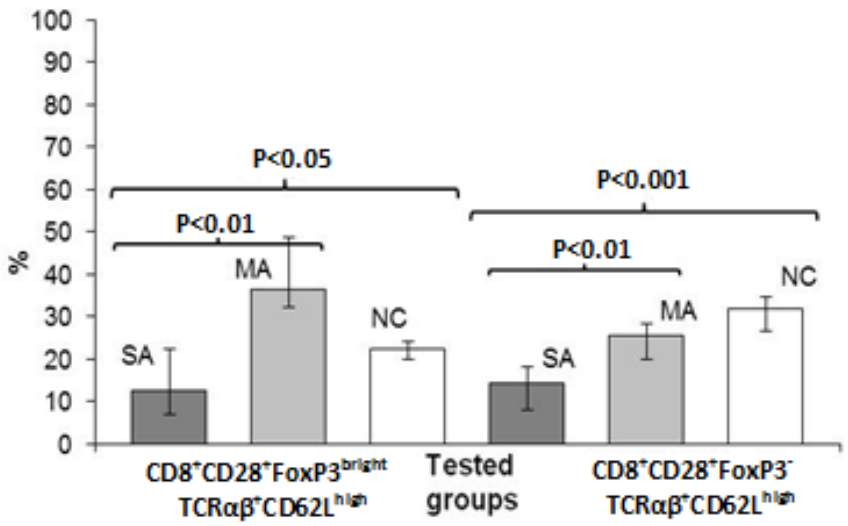


Fig. 2. *CD28, TCRαβ, CD62L and FoxP3 co- expression within circulatory $CD8^+$ T cells at baseline. The bar graph shows the median ± Interquartile (IQ). P values of 0.05 or less were considered statistically significant.*

IL-10 or TGF-β decreased the proportion of $CD8^+CD28^+TCR\alpha/\beta^+CD62L^{high}FoxP3^-$ T cells

T cell activation in combination with IL-10 remarkably decreased the percentage of $CD8^+CD28^+TCR\alpha/\beta^+CD62L^{high}Foxp3^-$ T cells in asthma subjects [(SA (12.3 [8-18.1] to 5.5[4.6-15.3]), MA (25.5[20-28.3] to 3.3[0.4-4.5]) and controls [(31.8[26.7-34.5] to 1[0.5-1.5])] (Fig.3). There were statistically significant differences in the frequency of $CD8^+CD28^+TCR\alpha/\beta^+CD62L^{high}Foxp3^-$ T cells between asthma groups ($p<0.01$) and between severe asthma and control groups ($p<0.01$) (Fig.3). Similarly, TGF-β decreased the percentage of $CD8^+CD28^+TCR\alpha/\beta^+CD62L^{high}Foxp3^-$ T cells in mild-to-moderate asthma group 25.5[20-28.3] to 3.8[0.6-5.6 and healthy controls 31.8[26.7-34.5] to 0.7 [0.5-1.3]. After stimulation with TGF-β, there was a statistically significant difference between the two asthma groups ($p<0.05$) and between severe asthma and control groups ($p<0.001$) (Fig. 4).

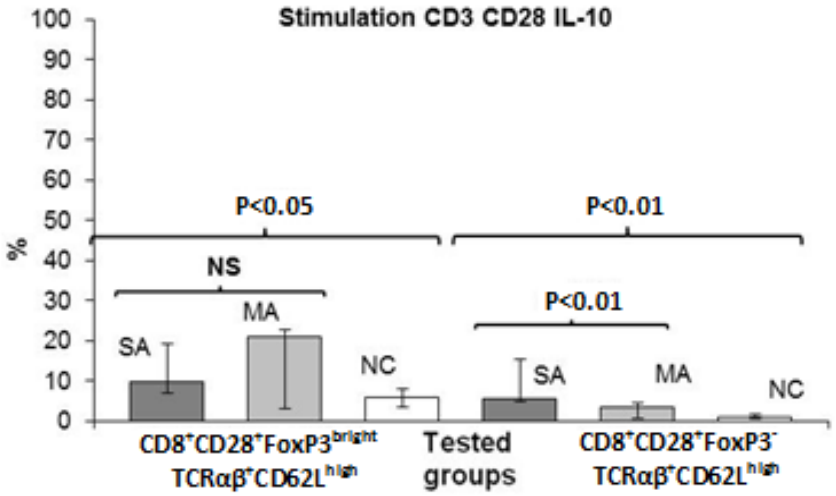


Fig. 3. *The effects of anti-CD3/CD28 and IL-10 co-stimulation on the co-expression of CD28, TCRαβ, CD62L and FoxP3 on circulatory $CD8^+$ T cells. The bar graph shows the median ± Interquartile (IQ). P values of 0.05 or less were considered statistically significant.*

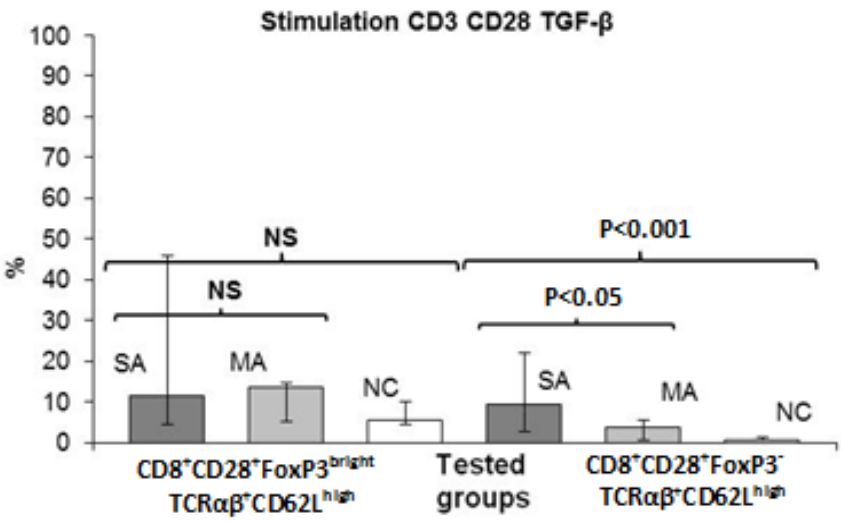


Fig. 4. *The effects of anti-CD3/CD28 and TGF-β co-stimulation on the co-expression of CD28, TCRαβ, CD62L and FoxP3 on circulatory $CD8^+$ T cells. The bar graph shows the median ± Interquartile (IQ). P values of 0.05 or less were considered statistically significant.*

DISCUSSION

Airway hyperresponsiveness (AHR) is associated with airway inflammation and bronchoconstriction upon exposure to nonspecific stimuli and is a key finding in chronic airways disorders. Forced expiratory volume (FEV1) is routinely used to evaluate the degree of airway obstruction during asthma exacerbation. The percentage of predicted FEV_1 (% FEV_1) levels were lower in asthmatic than in controls. Our data corroborate previous studies suggesting a reduced FEV1 in asthma (7) and complement previous studies on the role of lung function assessment in the diagnosis and management of asthma. The results contradict other studies reporting normal lung functions in asthma patients, suggesting the need for other tests to confirm airways hyperresponsiveness (AHR), a key component of chronic airway illness, namely asthma. Since severe asthma subjects had the lowest FEV1, our findings are consistent with other studies suggesting the use of the % of FEV_1 for assessing the severity of airflow obstruction, namely in lung disease (8, 9), however, they seem to contradict findings from previous studies suggesting normal FEV1 in asthma without exacerbation and suggest the need of additional parameter to detect and manage airways obstruction (10). In recent years, there has been a great deal of effort to isolate lymphocytes by density gradient methods and FACS- or MACS-activated cell sorting, for functional analysis, engineering, and cell-based applications. The present study employed MACS to isolate human $CD8^+$ T lymphocytes from peripheral blood. Several studies have demonstrated the the ability of this invention to isolate cells with high-yield and throughput (11) and higher reproducibility (12) without structural, phenotypic or functional alteration. Compared to other methods of enrichment, namely FACS which is the gold standard for cell separation, this technology is time/cost effective and has clinical application.

We therefore reasoned that such technology is suitable for high-throughput and selective isolation of $CD8^+$ T lymphocytes from peripheral blood. Our data provide further support to previous reports indicating that L-selectin (CD62L) is one of the surface markers of leukocytes (13) such as $CD8^+$ T cells. Based on the expression level of this marker, $CD8^+$ T cells can be divided into $CD62L^{low}$ (effector/effector memory) and $CD62L^{high}$ (central memory) subgroups as previously mentioned by previous reports (14). Chronic airway inflammation is associated with the cell migration towards the inflammatory microenvironment. Nevertheless, the mechanisms that oversee this movement to the airways are not fully understood. The precise effects of allergic response on L-selectin expression have not been yet extensively examined. We therefore wanted to examine the effects of allergic response on L-selectin expression. To this end, we compared the frequency of circulatory $CD62L^{high}$ T cells between asthma patients and healthy individuals. Our study supports previous studies reporting the role of adhesion molecule expression on T cells in chronic inflammation (15). A novel finding from our study was the differences in the frequencies of circulatory $CD8^+CD28^+TCR\alpha/\beta^+CD62L^{high}$ T-cell subsets between asthma subjects and control groups. Our results further replicate and extend the few existing data suggesting the implications of adhesion molecule expression for chronic airway inflammation. Our data further identified the proportion of $CD8^+CD28^+TCR\alpha/\beta^+CD62L^{high}$ T cell-subsets as markers of asthma phenotypes and as predictors of airway inflammation. Severe asthma is characterized by a more potent airway inflammation and remodeling than mild-to-moderate phenotype, as evidenced by the need of higher doses of anti-inflammatory drugs to manage its symptoms. Another important finding from our study was the inverse correlation between the proportion of $CD8^+CD28^+TCR\alpha/\beta^+CD62L^{high}$ T cells and the degree of airway inflammation. An alternative explanation for that finding is that the decrease of $CD8^+CD28^+TCR\alpha/\beta^+CD62L^{high}$ T cells may have evolved from activation-induced apoptosis of these subsets or their aggressive influx from peripheral blood to the airways. Further studies are required to better elucidate the mechanisms responsible for these changes. Our data provide additional evidence to support the effects of IgE-mediated immune response on the expression of adhesion molecules on

T lymphocytes (16). The decrease in the proportion of $CD8^+CD28^+TCR\alpha/\beta^+CD62L^{high}$ T cells in severe asthma patients compared to controls provides evidence to support their implication in the pathogenesis of severe asthma. Thus, we reasoned that that a high level expression of CD62L might represent a candidate surrogate marker for the assessment of the level of airflow obstruction. Our findings may have important diagnostic and therapeutic implications for the management of asthma if confirmed by independent large cohort multicenter case control studies. Previous studies have shown that the anti-inflammatory property of corticosteroids is mediated through interaction between glucocorticosteroid receptors (17) along with inhibition of adhesion molecules. Our study corroborates data from previous studies showing the role of allergen mediated CD62L expression in chronic airway inflammation (18). The effects of allergy-mediated inflammatory response on L-selectin expression might have contributed to the decreased proportion of $CD8^+CD28^+TCR\alpha/\beta^+CD62L^{high}$ T cells. One could argue that the down-regulatory effects of glucocorticoid on L-selectin mRNA and protein expression in blood of human and animal models (19) and the recruitment of leukocytes into inflammatory sites (20, 21) may seem a plausible explanation for the decreased frequencies of $CD8^+CD28^-TCR\alpha\beta^+CD62L^{high}FoxP3^{bright}$ T cells in severe asthma. In contrast, the alleged inhibitory effect of ICS on adhesion molecules were not seen in mild-to-moderate asthma patients who had increased frequencies of the selected subset. The quantitative deficiency of $CD8^+CD28^+TCR\alpha\beta^+CD62L^{high}FoxP3^{bright}$ T cells in the blood of severe asthma patients parallel to its abundance in samples from the other asthma subgroup provides evidence to support the claim that our findings are related rather to cell extravasation from the systemic to the local compartment during airflow obstruction, as previously mentioned elsewhere (22). In recent years, there has been an increasing interest in the *in-vitro* engineering of T cells for therapeutic and diagnostic purposes. A better understanding of the conditions that mediate T-cell proliferation and evasion is required to improve or boost clinical efficacy of currently on-going trials. Various assays, namely mitogens and antibodies directed against CD3/CD28, have been used successfully to design efficient *i- vitro* T-cell expansion assays. Specifically, CD3/CD28 monoclonal antibodies have been previously employed to expand various subsets of T cells without the contribution of antigen presenting cells (23). The role of IL-2 in T-cell growth and differentiation (24) has also been debated in the literature. Additional data suggest that TCR, CD28, and IL-2 influence T-cell proliferation in an independent manner (25). In contrast, other studies suggest that these mediators mutually govern T-cell fate *in vivo*. Indeed, one study revealed the therapeutic potential of anti-CD3/CD28-mediated T-cell expansion. Although the effects of various assays on T-cell proliferation have been previously debated, the molecular mechanisms underlying this process have not yet been fully elucidated. Another aim of our study was to assess the effects of IL-10 or TGF-β in the regulation of $CD62L^{high}$ T cell subset responses to anti-CD3/CD28 and IL-2 stimulation in asthma. IL-10 or TGF-β decreased the frequencies of $CD8^+CD28^+TCR\alpha/\beta^+CD62L^{high}$ T cells subsets, regardless of FoxP3 expression after short-term cultivation with anti-CD3/CD28 and IL-2. The decrease proportion of these subsets after *in-vitro* co-stimulation may be partially explained by the down regulation of L-selectin expression. This explanation is based on previous findings suggesting the loss of this cell surface molecule after cell activation (26). These findings are in agreement with previous studies highlighting the inhibitory capacity of TGF-β on IL-2/anti-CD3/CD28 driving T-cell expansion (27). One may hypothesize that the inhibitory effects of the selected cytokines (28) have prevailed over the effect of anti-CD3/CD28 stimulation. However, our data contradict previous data suggesting the stimulatory effects of IL-10 (29), (30) and TGF-β on T cells. It has been shown that *in-vitro* stimulation with anti-CD3/CD28 is not suitable for $CD8^+$ T-cell expansion (31). Furthermore, additional lines of evidence suggest the impact of IL-2 mediated loss of CD28 expression and T cell apoptosis (32). We therefore hypothesize that the low frequency of $CD8^+CD28^+TCR\alpha/\beta^+CD62L^{high}$ T-cell subsets may have been caused by the loss of

CD28 expression. The changes in T-cell frequencies could be linked to altered T-cell proliferation or enhanced apoptosis, or both. Indeed, CD28 has been previously shown to mediate the expression of Bcl-xL, Bcl-2 (33). The mutual interaction between these molecules is known to inhibit both apoptosis and proliferation (34). We therefore suggested that the alteration in CD28 signaling may have led to the decreased in the proportion of $CD8^+CD28^+TCR\alpha/\beta^+CD62L^{high}Foxp3^{high}$ T-cell defects observed in asthma patients. It has further been demonstrated that apoptosis plays a compensatory or pathogenic role in lung diseases (35). Our findings may also be explained by a previous study, suggesting that cell division switches $CD62L^{high}$ cell phenotype into $CD62L^{low}$ phenotype (8). Previous studies indicate that T-cell activation after challenge with IL-10 enhances the expression of lymph node homing marker CD62L and promotes central memory development (36xx38x). Moreover, it has been demonstrated that IL-2 mediates induced IL-10 expression in $CD8^+$ T cells (37). The present study contradicts these data by demonstrating an inhibitory effect of IL-10 or TGF-β in anti-CD3/CD28 and IL-2-mediated $CD62L^{high}$ T-cell subset differentiation and/or activation in healthy and asthmatic subjects. Our study also supports previous studies suggesting the role of TGF-β signaling to $CD8^+$ T cells is critical for the formation and maintenance of memory T cells (38), however, it contradicts previous reports indicating that exogenous Transforming-growth factor-beta (TGF-β) signaling enhances the expression of the lymph-node homing receptors, L-selectin (CD62L) expressing cells, promoting memory phenotype after anti-CD3 and anti-CD28 stimulation in the presence of exogenous IL-2 (39). It has also been shown that isolated $CD8^+$ T cells produce TGF-β following cognate peptide recognition (40xx42x). A previous study suggests that prolonged *in-vitro* co-stimulation decreases the expression of memory markers such as CD62L, causing a shift to more differentiated T lymphocytes (41, 33). The short duration of *in-vitro* stimulation may be a major explanation for the difference between our findings and others. Our data corroborate those of previous reports suggesting that the duration and strength of stimulation of environmental signals upon antigen presentation determines the extent of proliferation of naïve CD8 T cells (42). A short-term cultivation of $CD8^+$ T cells results in down regulation of high level CD62L expression. This finding contradicts previous studies that have linked reduced duration of antigenic stimuli and up regulation of CD62L expression on naïve CD8 T cells (43). Whether IL-10 or TGF-β modulates the expression of this adhesion molecule during the course of anti-CD3/CD28 and IL-2-mediated $CD8^+$ T-cell activation remains to be elucidated in further study with a larger cohort. One of the limitations of our study was that it did not examine whether the observed effect of IL-10 or TGF-β is influenced by *in-vitro* secretion of the selected cytokines by T cells. A blockade of endogenous secretion of IL-10 and TGF-β would provide a better assessment of the effects of exogenous cytokine on CD62L expression. Our data indicate that L-selectin expression is somehow mediated by inflammatory cytokines. Overall, these data reveal that asthma phenotypes may be further stratified into micro subtypes with distinct cellular and molecular characteristics, supporting the concept of asthma endotypes.

ACKNOWLEDGEMENTS

This work was supported by grant from the Polish Academy of Sciences grant KBN nr N N402 517339. The funders had no influence on study design, data collection and interpretation, or the decision to publish the manuscript.

REFERENCES

1. Scott CS, Richards SJ, Roberts BE. Patterns of membrane TcR alpha beta and TcR gamma delta chain expression by normal blood CD4+CD8-, CD4-CD8+, CD4-CD8dim+ and CD4-CD8- lymphocytes. Immunology 1990; 70 (3):351-6.
2. Thome M, Hirt W, Pfaff E, Reddehase MJ, Saalmüller A. Porcine T-cell receptors: molecular and biochemical characterization. Vet Immunol Immunopathol 1994; 43(1-3):13-8.
3. Vacchio MS, Hodes RJ. CD28 Costimulation

Is Required for In Vivo Induction of Peripheral Tolerance in CD8 T Cells. J Exp Med. 2003; 197(1):19-26.
4. Batliwalla F, Monteiro J, Serrano D, Gregersen PK. Oligoclonality of CD8+ T cells in health and disease: Aging, infection, or immune regulation? Hum Immunol 1996; 48(1-2):68-76.
5. Eusebio M, Kraszula L, Kupczyk M, Kuna P, Pietruczuk M. The effects of interleukin-10 or TGF-beta on anti-CD3/CD28 induced activation of CD8+CD28- and CD8+CD28+ T cells in allergic asthma. J Biol Regul Homeost Agents. 2013; 27 (3):681-92.
6. Kedzierska K, Stambas J, Jenkins MR, Keating R, Turner SJ, Doherty PC. Location rather than CD62L phenotype is critical in the early establishment of influenza-specific CD8+ T cell memory. Proc Natl Acad Sci U S A 2007; 104(23):9782-7.
7. Dijkstra A, Vonk JM, Jongepier H, et al. Lung function decline in asthma: association with inhaled corticosteroids, smoking and sex. Thorax 2006; 61(2):105-10.
8. Eschenbacher WL. Defining Airflow Obstruction. Chronic Obstr Pulm Dis 2016; 3(2):515-518,
9. Quanjer PH, Pretto JJ, Brazzale DJ, Boros PW. Grading the severity of airways obstruction: new wine in new bottles. Eur Respir J 2014; 43(2):505-11.
10. Grzelewski T, Stelmach W, Stelmach R, et al. Spirometry-adjusted fraction of exhaled nitric oxide allows asthma diagnosis in children, adolescents, and young adults. Respir Care 2016; 61(2):162-72.
11. Sutermaster BA, Darling EM. Considerations for high-yield, high-throughput cell enrichment: fluorescence versus magnetic sorting. Sci Rep; 9(1):227.
12. Gunzer M, Weishaupt C, Planelles L, Grabbe S. Two-step negative enrichment of CD4+ and CD8+ T cells from murine spleen via nylon wool adherence and an optimized antibody cocktail. J Immunol Methods 2001; 258(1-2):55-63.
13. Yang S, Liu F, Wang QJ, Rosenberg SA, Morgan RA. The shedding of CD62L (L-Selectin) regulates the acquisition of lytic activity in human tumor reactive T lymphocytes. PLoS One 2011; 6(7):e22560.
14. Schlub TE, Badovinac VP, Sabel JT, Harty JT, Davenport MP. Predicting CD62L expression during the CD8+ T cell response in vivo. Immunol Cell Biol 2010; 88(2):157-64.
15. Filep JG, Zouki C, Petasis NA, Hachicha M, Serhan CN. Anti-inflammatory actions of lipoxin A (4) stable analogs are demonstrable in human whole blood: modulation of leukocyte adhesion molecules and inhibition of neutrophil-endothelial interactions. Blood 1999; 94(12):4132-42.
16. Monteseirín J, Llamas E, Sánchez-Monteseirín H, Bonilla I, Camacho MJ, Conde J, Sobrino F. IgE-mediated downregulation of L-selectin (CD62L) on lymphocytes from asthmatic patients Allergy 2001; 56(2):164-8.
17. Eusebio M, Grzelewski T, Pietruczuk M, Lewandowska B, Stelmach I. The patents on glucocorticosteroids and selected new therapies for the management of asthma in children. Recent Pat Inflamm Allergy Drug Discov 2011; 5(1):57-65.
18. Monteseirín J, Chacón P, Vega A, et al. L-selectin expression on neutrophils from allergic patients. Clin Exp Allergy 2005; 35(9):1204-13.
19. Weber PS, Toelboell T, Chang LC, Tirrell JD, Saama PM, Smith GW, Burton JL. Mechanisms of glucocorticoid-induced down-regulation of neutrophil L-selectin in cattle: evidence for effects at the gene-expression level and primarily on blood neutrophils. J Leukoc Biol 2004; 75 (5): 815-27.
20. Strausbaugh HJ, Rosen SD. A potential role for annexin 1 as a physiologic mediator of glucocorticoid-induced l-selectin shedding from myeloid cells. J Immunol 2001; 166(10):6294-300.
21. Nakagawa M, Bondy GP, Waisman D, Minshall D, Hogg JC, van Eeden SF. The Effect Of Glucocorticoids On The Expression Of L-Selectin On Polymorphonuclear Leukocyte. Blood 1999; 93(8):2730-7.
22. Stockfelt M, Christenson K, Andersson A, et al. Increased CD11b and decreased CD62L in blood and airway neutrophils from long-term smokers with and without COPD. J Innate Immun 2020; 12(6):480-489.
23. Riddell SR, Greenberg PD. The use of anti-CD3 and anti-CD28 monoclonal antibodies to clone and expand human antigen-specific T cells. J Immunol Methods 1990; 128 (2):189-201.
24. Wakamatsu E, Omori H, Tabata Y, Akieda Y, Watanabe S, Ogawa S, Abe R. CD28 co-stimulation is dispensable for the steady state homeostasis of

intestinal regulatory T cells. Int Immunol 2018; 30 (4):171-80.
25. Dela Peña-Ponce MG, Rodriguez-Nieves J, Bernhardt J, et al. Increasing JAK/STAT signaling function of infant CD4+ T Cells during the first year of life. Front Pediatr 2017; 5:15.
26. Díaz-González F, González-Alvaro I, Campanero MR, et al. Prevention of in vitro neutrophil-endothelial attachment through shedding of L-selectin by nonsteroidal antiinflammatory drugs. J Clin Invest 1995; 95(4):1756-65.
27. Koberda J, Grimm EA, Moser RP. Effect of anti-CD3/anti-CD28/interleukin-2 stimulation of mononuclear cells on transforming growth factor beta inhibition of lymphokine-activated killer cell generation. J Cancer Res Clin Oncol 1993; 119(3):131-6.
28. Vignali DA, Collison LW, Workman CJ. How regulatory T cells work. Nat Rev Immunol 2008; 8(7): 523-32.
29. Groux H, Bigler M, de Vries JE, Roncarolo MG. Inhibitory and stimulatory effects of IL-10 on human CD8+ T Cells. J Immunol 1998; 160 (7):3188-93.
30. Bagheri Y, Babaha F, Falak R, et al. IL-10 induces TGF-β secretion, TGF-β receptor II upregulation, and IgA secretion in B cells. Eur Cytokine Netw 2019; 30(3):107-13.
31. Li Y, Kurlander RJ. Comparison of anti-CD3 and anti-CD28-coated beads with soluble anti-CD3 for expanding human T cells: differing impact on CD8 T cell phenotype and responsiveness to restimulation. J Transl Med 2010; 8:104.
32. Borthwick NJ, Lowdell M, Salmon M, Akbar AN. Loss of CD28 expression on CD8+ T cells is induced by IL-2 receptor chain signalling cytokines and type I IFN, and increases susceptibility to activation-induced apoptosis. Int Immunol 2000; 12(7):1005-13.
33. Di Renzo M, Zhou Z, George I, Becker K, Cunningham-Rundles C. Enhanced apoptosis of T cells in common variable immunodeficiency (CVID): role of defective CD28 co-stimulation. Clin Exp Immunol 2000; 120(3):503-11.
34. Janumyan YM, Sansam CG, Chattopadhyay A, et al. Bcl-xL/Bcl-2 coordinately regulates apoptosis, cell cycle arrest and cell cycle entry. EMBO J 2003; 22(20):5459-70.
35. White SR. Apoptosis and the airway epithelium. J Allergy (Cairo) 2011; 2011:948406.
36. Reiser J, Sadashivaiah K, Furusawa A, Banerjee A, Singh N. Eomesodermin driven IL-10 production in effector CD8+ T cells promotes a memory phenotype. Cell Immunol 2019; 335:93-102.
37. Jiang L, Yao S, Huang S, Wright J, Braciale TJ, Sun J. Type I IFN signaling facilitates the development of IL-10-producing effector CD8(+) T cells during murine influenza virus infection. Eur J Immunol 2016; 46(12):2778-88.
38. Ma C, Zhang N. Transforming growth factor-β signaling is constantly shaping memory T-cell population. Proc Natl Acad Sci U S A 2015;112(35):11013-7.
39. Dahmani A, Janelle V, Carli C, et al. TGFβ Programs central memory differentiation in ex vivo-stimulated human T cells. Cancer Immunol Res 2019; 7(9):1426-39.
40. Takai S, Schlom J, Tucker J, Tsang KY, Greiner JW. Inhibition of TGF-β1 signaling promotes central memory T cell differentiation. J Immunol 2013; 191(5):2299-307.
41. Teschner D, Wenzel G, Distler E, et al. In vitro stimulation and expansion of human tumour-reactive CD8+ cytotoxic T lymphocytes by anti-CD3/CD28/CD137 magnetic beads. Scand J Immunol 2011; 74:155-64.
42. Khan SH, Martin MD, Starbeck-Miller GR, Xue HH, Harty JT, Badovinac VP. The timing of stimulation and IL-2 signaling regulate secondary CD8 T cell responses. PLoS Pathog 2015; 11(10):e1005199.
43. van Faassen H, Saldanha M, Gilbertson D, Dudani R, Krishnan L, Sad S. Reducing the stimulation of CD8+ T cells during infection with intracellular bacteria promotes differentiation primarily into a central (CD62LhighCD44high) subset. J Immunol 2005; 174(9):5341-50.

ClyA enhances LPS-induced IL-1β secretion in human macrophages through TLR4 and NLRP3 signaling

Y. Guan[1*], J-Q. Chen[2*], X-Y. Li[2] and S-N. Jiang[2]

[1]Department of Ultrasound, The first affiliated Hospital of Hainan Medical University, Hainan, China; [2]Department of Radiology, Central South University Xiangya School of Medicine affiliated Haikou Hospital, Hainan, China

Arrived August 7, 2020 – Accepted February 9, 2021

[*]These authors contributed equally to this work

Lipopolysaccharide (LPS) plays an important role in tumor suppression by activating macrophages. After macrophages activation, a trail of cytokines was secreted, including IL-1β. Previous studies reported that the anti-tumor function of IL-1β is concentration-dependent, and increasing the level of IL-1β will enhance its anti-tumor effect. Cytolysin A (ClyA), a member of the protein family called pore-forming toxins (PFTs), is secreted by Gram-negative bacteria, which has a potential role in enhancing the secretion of IL-1β. In this study, the function of Cytolysin A was evaluated by investigating its ability to induce innate immune responses in macrophages and the signaling pathway(s) involved in LPS-induced production of IL-1β. The production of IL-1β was highly enhanced when the macrophages were treated with LPS and ClyA together. The production of IL-1β was regulated by TLR4-MyD88-IL-1β pathway and NLRP3-ASC-Caspase1-IL1β pathway. By treating the colon cancer cell line CT26 with the conditioned medium, the proliferation of CT26 cells was inhibited and the apoptosis of CT26 cells was increased. In conclusion, this study indicated that ClyA enhances the production of IL-1β induced by LPS in human macrophages. The proliferation of CT26 cells was inhibited and the apoptosis was increased when being treated with the macrophage-conditioned media, which provides a feasible treatment for colon tumor.

Macrophages are the main cell population of the innate immune system, which can be activated by bacterial endotoxins and cytokines, for example, LPS and IFN-γ. Accumulating evidence has demonstrated that activated macrophages release proinflammatory mediators, such as nitric oxide (NO), proinflammatory cytokines, and chemokines, contributing to nonspecific immunity. These mediators can regulate the maturation and differentiation of innate and adaptive immune system cells, and further enhance inflammation (1-3). According to previous studies, among the cytokines produced by the macrophages, interleukin (IL)-1β has an important role in the anti-tumor process (4-9). IL-1β belongs to the IL-1 family, which contains 11 distinct cytokines (10, 11), some of which are involved in inflammatory pathways, while others have anti-inflammatory properties (3, 11).

The production of IL-1β is closely related to both Toll-like receptor 4 (TLR4) and NOD-like receptor (NLRP3) signaling pathways (12-16).

Key words: Cytolysin A; lipopolysaccharide; macrophages; colon cancer

Corresponding Author:
Prof. Sheng-nan Jiang,
Department of Radiology, Central South University,
Xiangya School of Medicine affiliated Haikou Hospital,
Hainan, 570208China
Tel.: +86 13707577955 - Fax: +86 898 66189725
e-mail: 2669253486@qq.com

0393-974X (2021)
Copyright © by BIOLIFE, s.a.s.
This publication and/or article is for individual use only and may not be further reproduced without written permission from the copyright holder.
Unauthorized reproduction may result in financial and other penalties
DISCLOSURE: ALL AUTHORS REPORT NO CONFLICTS OF INTEREST RELEVANT TO THIS ARTICLE.

The TLR4 pathway can be activated by MyD88-dependent and independent regulation (17, 18). Previous studies confirmed that lipopolysaccharide (LPS), the main component of the outer membrane of gram-negative bacteria, was the natural ligand of TLR4. LPS binds specifically to TLR4 expressed in various immune and non-immune cells and induces a robust immune reaction through production of proinflammatory cytokines such as TNFα, IL-1β, IL-6, and chemokines (19-21).

The NLRP3 complex is the best characterized inflammasome, which comprises the NLR protein (NLRP3), the adapter ASC and pro-caspase-1. NLRP3 was triggered and activated by a wide range of pathogen-associated molecular patterns (PAMPs) and damage-associated molecular patterns (DAMPs). Upon activation, NLRP3 undergoes self-oligomerization, and then ASC and Pro-caspase-1 are recruited to form NLRP3 inflammasome (16, 22, 23). Pro-caspase-1 is auto-catalyzed to generate Caspase-1, thus promoting the secretion of IL-lβ. It was reported that K^+ efflux was also a necessary signal for the activation of NLRP3 inflammasome. Extracellular ATP binds to the ion channel P2X7, which leads to the opening of the ion channel Pannexin-1 and accelerates K+ efflux. However, the pores formed on the cell membrane are closed rapidly after the external stimulations is removed, therefore, it is difficult to maintain the sustained release of IL-1β (24-28). It is worth noting that Cytolysin A (ClyA), a pore-forming toxin, can act on the mammalian cell membrane to form a permanent pore, which leads to massive outflow of K^+ from cells, thus activating the NLRP3 inflammasome (29, 30).

LPS and ClyA are therefore important regulators to activate TLR4 and NLRP3 pathways, respectively, however, whether they can promote the production of IL-1β in human macrophages is still elusive. In the present study, the production was evaluated of IL-1β and its tumor suppression capacity in human macrophages by introducing LPS and ClyA, and the production of IL-1β was highly enhanced when treating macrophages with LPS and ClyA together, and the generation of IL-1β was regulated by TLR4-MyD88-IL-1β pathway and NLRP3-ASC-Caspase-1-IL-1β pathway. By treating the colon cancer cell line CT26 with the conditioned medium of human macrophages, the proliferation of CT26 cells was suppressed and the apoptosis of CT26 cells was increased. This study, for the first time, indicates that ClyA could enhance the IL-1β secretion induced with LPS in human macrophages, and then suppress the proliferation of CT26 tumor cells, providing a feasible treatment for colon tumor.

MATERIALS AND METHODS

Human macrophage differentiation

Human monocyte-like cell line THP-1 was purchased from ATCC and maintained in DMEM supplemented with 10% fetal calf serum (FCS), penicillin, and streptomycin sulfate. Human macrophages were induced from THP-1 cells with phorbol-12-myristate 13-acetate (PMA, Sigma-Aldrich). PMA was added to the final concentration of 100 nM. After 24 h of incubation at 37°C, most of the cells transformed from suspension to adhesion, indicating the successful induction of macrophages. Then, RPMI-1640 medium (serum-free) containing 10% fetal calf serum (FCS), penicillin, and streptomycin sulfate was used for further incubation.

Macrophage treatment and experimental design

For ELISA analysis, 10^5 cells of macrophages were planted in 24-well plates; 10^6 cells of macrophages were planted in 6-well plates for Western-blot assay. The experiments were designed as follows. Ctrl: only fresh medium was added. LPS treatment: fresh medium with LPS (100 ng/ml, Sigma-Aldrich, L2630) was included. ClyA treatment: ClyA (Catlog No.2784) was purchased from Shanghai Youke Biotechnology Co., Ltd. fresh medium containing ClyA protein (10 ng/ml) was included. LPS+ClyA treatment: fresh medium containing LPS (100 ng/ml) and ClyA protein (10 ng/ml) were added. For each treatment, triple biological repeats were conducted. IL-1β Antibody treatment: After culture for 24 h of the above groups, anti-IL-1β Ab (1 μg/ml, Abcam, ab9722) was added to the medium to neutralize the expression of IL-1β. MyD88 and NLRP3 inhibitor treatment: inhibitor to MyD88 (NBP2-29328, Novus Biologicals) and to NLRP3 (MCC950, Selleck) was added to the culture medium along with LPS, ClyA, and LPS+ClyA in the LPS treatment, ClyA treatment and LPS+ClyA treatment, respectively.

Tumor suppression detection

Cancer cell lines (CT26 cells) were cultured in RPMI-1640 supplemented with 10% FBS, penicillin, and streptomycin under standard conditions. After 48 h, the supernatant from different treatments (with or without IL-1β Ab) was collected by centrifugation at 12,000× g for 10 min. When the CT26 cells were in logarithmic growth phase, half of the culture medium was replaced with the supernatant of THP-1 derived macrophages (with or without IL-1β Ab treatment).

The cell proliferation was detected by Cell counting kit-8 (Abcam, ab228554). Briefly, 4 h before the end of culture, 10 μl of CCK-8 (5mg/ml) was added into each well (100 μL of medium). At the end of the experiment, the supernatant was carefully collected and incubated with DMSO at 150μl/well for 10 min at 37°C. OD 460 was measured with a microplate reader (Biorad M-550), and the cell proliferation rate was calculated. According to the manufacturer's instructions, Annexin V-7AAD (Abcam, ab214663) and flow cytometry were used to examine the apoptosis of CT26 cells.

ELISA

The secretion level of cytokine IL-1β in the supernatant of cell culture medium was detected by ELISA. THP-1-derived macrophages were inoculated into a 24-well plate, with $1x10^5$ cells in each well. After being treated with LPS, ClyA and LPS+ClyA, the cells were incubated at 37°C for 48 h, and the supernatant was collected. The secretion level of IL-1β was detected by ELISA according to the instructions.

Western-blot

The expression of TLR4-MyD88-IL-1β and NLRP3-ASC-Caspase-1-IL-1β signaling pathways were detected by Western-blot analysis. The cultured macrophages were lysed in SDS-RIPA lysis buffer and protease inhibitor cocktail after 48 h. Proteins were separated by SDS–PAGE and transferred onto a PVDF membrane. After being blocked with 5% milk for 1 h at room temperature, the membranes were probed with primary antibodies overnight at 4°C, followed by incubation with secondary antibodies for 1 h at room temperature, and visualized with enhanced chemiluminescence reagent (Thermo Scientific). The gray value of each target band was analyzed by Bio-RAD gel imaging system. The antibodies used in this article were as follows: NLRP3 (Adipogen, AG-20B-0014, 1:1000), ASC (Adipogen, AG-25B-006, 1:1000), Caspase-1 (CST, #4199, 1:500), IL-1β (R&D Systems, AF-201-NA, 1:300), TLR4 (R&D Systems, AF1478, 1:1000), MyD88 (R&D Systems, AF2928,1;500), β-Actin (R&D Systems, 1:500). Secondary antibodies for western blot were from Sigma-Aldrich (St. Louis, MO, USA).

Statistical analysis

Statistical analysis was performed using GraphPad Prism version 7.0 software package (GraphPad Software, San Diego, CA, USA). Unpaired two-tailed *t*-tests were used to compare two data sets. One-way ANOVA followed by Dunnett's multiple comparison tests were used for experiments with three or more data sets. For each comparison, numbers from at least 3 individual experiments were averaged. All data is expressed as the mean±SD, and data were considered significant at $p < 0.05$.

RESULTS

Effects of LPS and ClyA on the proliferation of CT26 cells

To examine whether LPS-, ClyA-, and LPS+ClyA-treated human macrophages can influence the proliferation of CT26 cells, LPS, ClyA, and LPS+ClyA were added to THP-1 derived macrophage cells. Then, as described in Materials and Methods, the supernatant was collected and added to CT26 culture medium. First, we detected CT26 cell proliferation at 12h, 24h, and 48h after treatment. The results are shown in Fig. 1A-C. A clear proliferation inhibition of CT26 cells was detected in all groups, which indicated that these media had an anti-proliferative effect. Moreover, the apoptosis of CT26 cells was also examined with flow cytometry. The results showed that macrophage conditioned media treated with LPS, ClyA, and LPS+ClyA promoted the apoptosis of CT26 cells, and the LPS+ClyA group had a stronger effect (Fig. 1 D-H).

To test whether the anti-tumor function of the conditioned media is caused by the residual LPS and ClyA in the media, we checked whether there was any LPS left in the supernatant of the conditioned media by ELISA. The results showed that there is no LPS left in the conditioned media, while in the

newly prepared media, LPS was easy to detect (Fig. 2A). We proposed that the LPS be degraded and/or consumed after 48 h of incubation with macrophages.

Because of the un-availability of antibodies to ClyA, it is not feasible to detect the residual ClyA. In order to test whether ClyA and LPS can affect CT26 cells, LPS, ClyA and LPS+ClyA were directly added into the culture medium of CT26. The results showed that the proliferation and apoptosis of CT26 cells were not changed compared to the control group after 48-h incubation (Fig. 2 B-G). Therefore, we proposed that some factors in the supernatant of macrophage culture media led to the decrease of cell proliferation and the increase of apoptosis.

Apoptosis and proliferation of CT26 cells were affected by IL-1β produced in macrophages

Previous studies indicated that IL-1β is the key regulator for tumor suppression, therefore we wondered whether the anti-tumor phenotypes observed in CT26 cells were triggered by IL-1β produced from the macrophages. To address this question, the expression level of IL-1β with was detected ELISA in the conditioned media. As shown in Fig. 3A, the expression level of IL-1β was significantly upregulated in the groups treated with LPS and ClyA compared to the blank group, the combination of LPS+ClyA had a more significant effect after 48-h incubation. Next, to discover

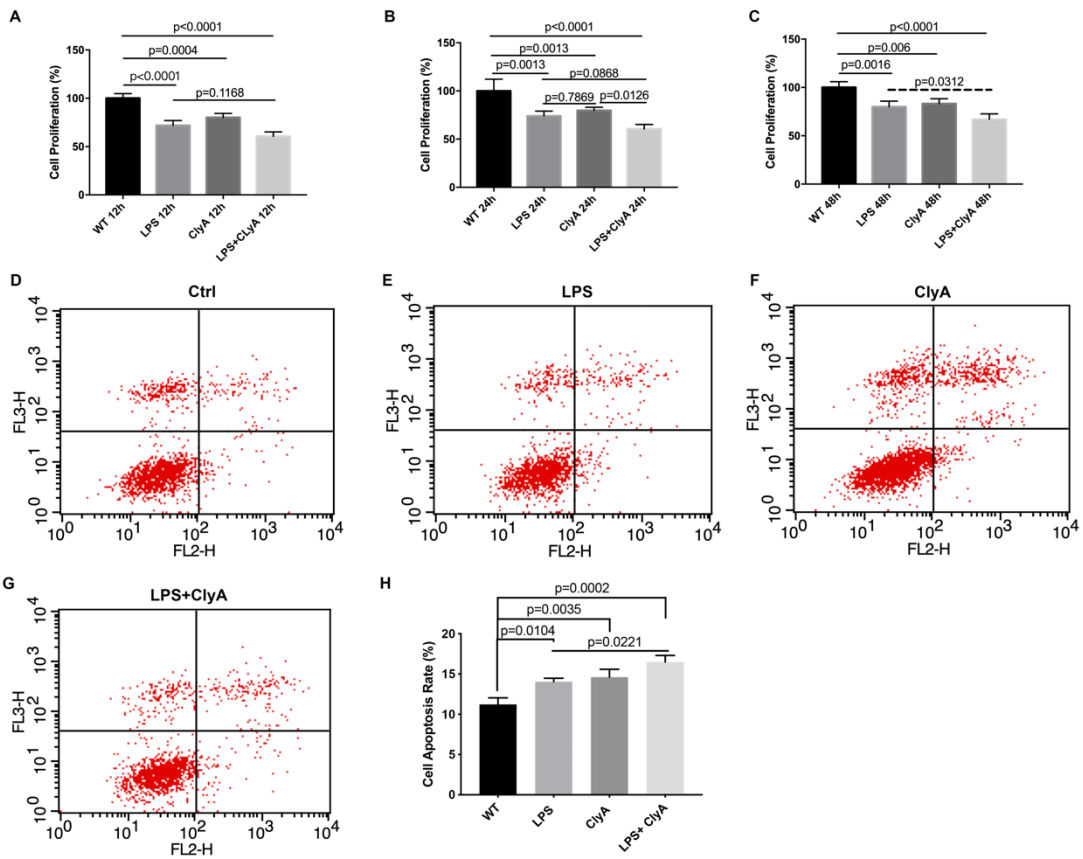


Fig. 1. *The proliferation of CT26 cells was suppressed and the apoptosis was increased after incubating the cells with the conditioned media of macrophages.* ***A-C****) The proliferation of CT26 cells was detected after 12h, 24h and 48h incubation. A constant decrease was observed of proliferation compared with the Control group, indicating a clear anti-proliferation effect in the supernatant of macrophage conditioned medium.* ***D-H****) A strong apoptosis was detected after treating CT26 cells with macrophage conditioned medium (E, F, G) compared with the Control group (D).*

whether the increase of apoptosis and the decrease of proliferation were mediated by IL-1β, given that macrophages can produce many cytokines, the IL-1β protein was neutralized with anti-IL-1β antibody in the conditioned medium collected from macrophages. Then, the apoptosis and proliferation of CT26 were examined. As shown in Fig. 3 B, C, after incubation with anti-IL-1β antibody, the proliferation suppression effect observed in the LPS-treated group had returned to normal ($p>0.05$), and the apoptosis rate was comparable to that of the control group (Fig. 3 D-H). Likewise, a similar result was detected in the ClyA and LPS+ClyA treatment groups (Fig. 3). Taken together, these results indicate the increase of apoptosis and suppression of proliferation of the CT26 cells was mediated by the IL-1β from the conditioned media of THP-1-derived macrophages.

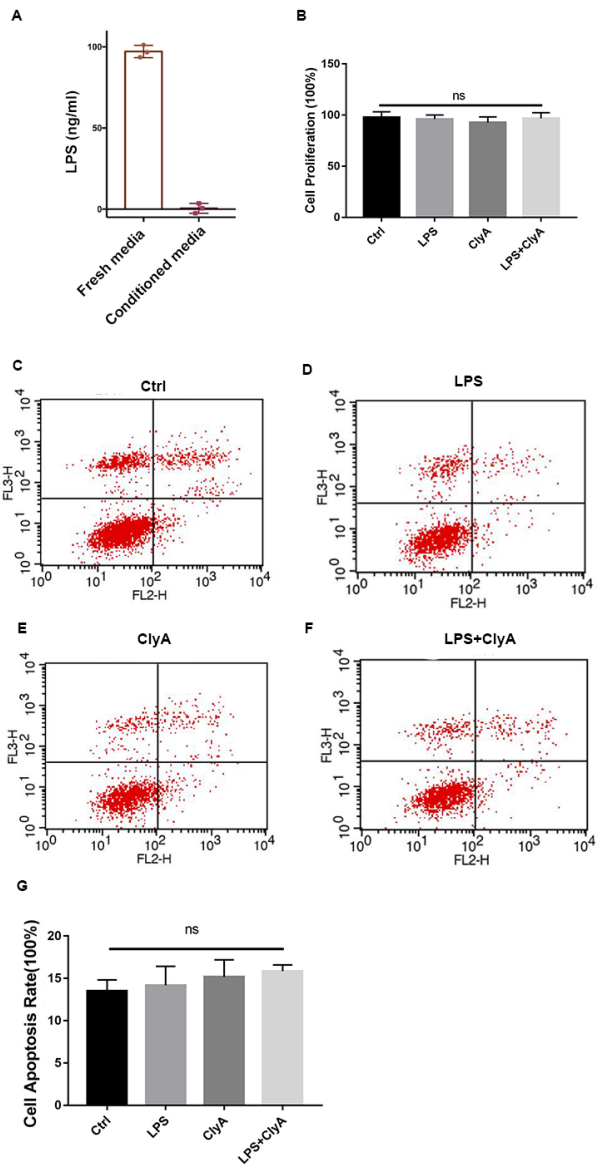


Fig. 2. *LPS and ClyA have no effect on CT26 cells.* ***A)*** *No LPS was detected in the conditioned media.* ***B)*** *No significant decrease of proliferation of CT26 cell was examined when treated with LPS, ClyA and LPS+ClyA;* ***C-G)*** *The cell apoptosis is normal compared with the control group when CT26 cells were treated with LPS, ClyA and LPS+ClyA.*

LPS, ClyA, and LPS+ClyA treatment activated TLR4-MyD88-IL-1β pathway and NLRP3-ASC-Caspase-1-IL-1β pathway

Previous studies have demonstrated that the production of IL-1β is closely related to the Toll-like receptor 4 and the NLRP3 signaling pathway. To test whether the upregulation of IL-1β is modulated by TLR4 and NLRP3 signaling pathway after LPS, ClyA, and LPS+ClyA treatment, the expression and the activation of key components of the two pathways were examined by Western-blot. As shown in Fig. 4, an apparent upregulation of NLRP3, ASC, MyD88, Caspase-1, TRL4 as well as IL-1β in the LPS, ClyA, and LPS+ClyA groups, respectively, were detected.

Next, we wondered whether the expression of IL-1β would be suppressed if these two pathways were blocked, and whether the proliferation of CT26 cells would be restored when CT26 cells were treated with THP-1-derived macrophage conditioned media. To address this question, the small molecule inhibitors to MyD88 and to NLRP3 were applied to THP-1-derived macrophages. The expression of IL-1β was detected by ELISA, the result is presented in Fig. 5. A drop of the expression of IL-1β was observed when the inhibitors were introduced in the cultured cells. Additionally, the proliferation of CT26 cells incubated with the conditioned medium was examined. As shown in Fig. 5B, the proliferation of CT26 cells was also suppressed when incubated with the supernatant of the LPS+ClyA-treated groups, a clear restoring of the proliferation of CT26 cells was observed when inhibitors to MyD88 and NLRP3 signaling pathways were included in the conditioned media (Fig. 5).

DISCUSSION

Colon cancer is one of the most common malignant tumors in the world (31). It ranks third in morbidity and mortality, and is growing rapidly at the rate of over 1 million new cases every year (32-34). According to the national cancer registration data in 2015, the incidence and mortality of colon cancer in China were 27.3/100,000 and 13.9/100,000, respectively.

In our previous study, by using genetically engineered *Salmonella typhimurium* (*S.t-ΔpG* $^{lux/pT\text{-}ClyA}$), we found that *S.t-ΔpG* inhibits colon tumor growth and recurrence in CT26 tumor mice model. We also detected the increased production of IL-1β in the mice serum (35). However, which cells contribute to the production of IL-1β and the underlying mechanisms are not clear, especially in humans. In this study, LPS and ClyA were introduced to the THP-1 derived macrophages, and the production of IL-1β and its tumor suppression capacity were evaluated. We observed that when human macrophages were treated with LPS and ClyA together, the production of IL-1β was highly enhanced, and the production of IL-1β was regulated by TLR4-MyD88-IL-1β pathway and NLRP3-ASC-Caspase-1-IL-1β pathway. After incubation of CT26

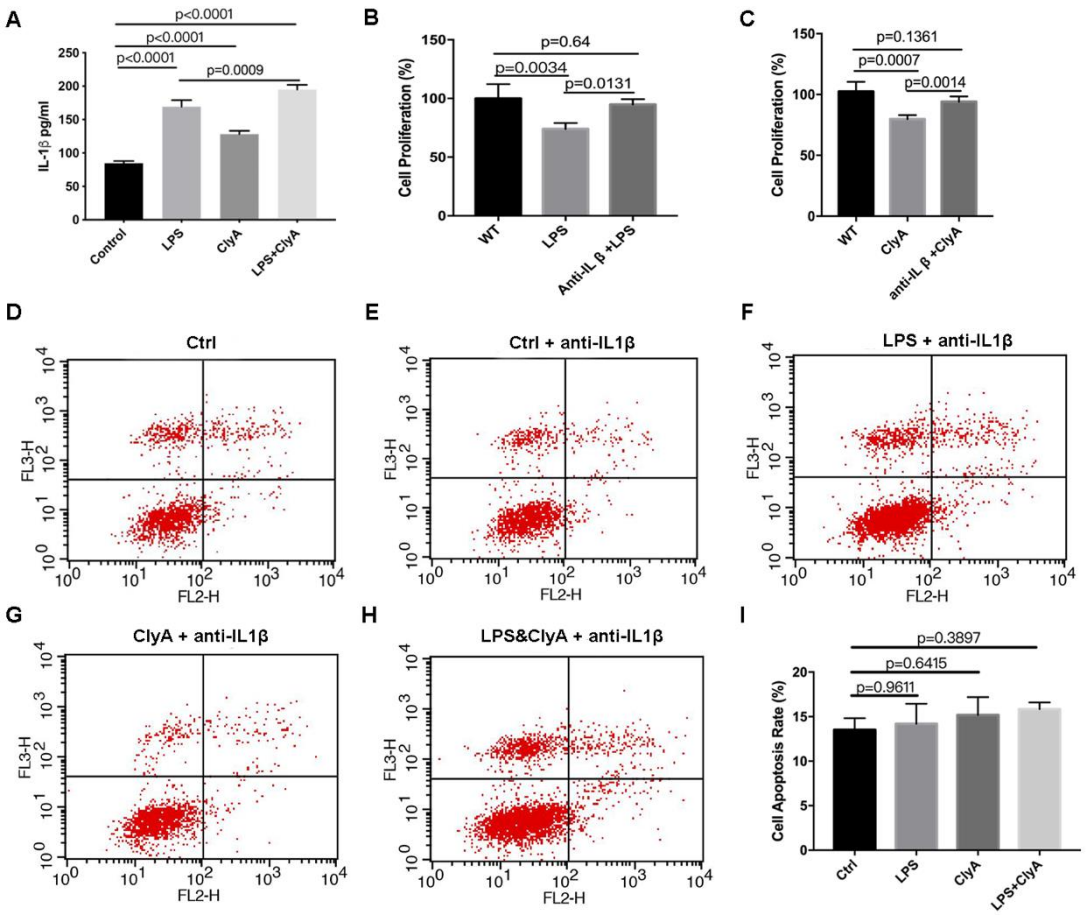


Fig. 3. *IL-1β is the key effector of the anti-tumor effect of conditioned medium from different treatments of macrophage. The expression level of IL-1β was significantly upregulated in the macrophages treated with LPS, ClyA, and LPS+ClyA (**A**). The proliferation of CT26 was not affected when antibody to IL-1β was added in the conditioned medium (**B** and **C**). The apoptosis of CT26 was not increased when treated with macrophage-conditioned medium containing IL-1β antibody (**D-I**).*

cells with the supernatant of macrophages conditioned medium, the proliferation of CT26 cells was suppressed and the apoptosis of CT26 cells was increased.

Regarding the function of IL-1β, some studies, including ours, indicated that it plays an important role in the anti-tumor process. On the contrary, it was reported that IL-1β can promote the growth and invasion of colon tumors. Li et al. reported the effects of IL-1β on cancer stem cell development and epithelial-mesenchymal transition (EMT) in human primary colon cancer cells and colon cancer cell line HCT-116. They found that IL-1β can increase the sphere-forming capability of colon cancer cells in serum-free medium (36). Therefore, we believe that the different functions of IL-1 in the two different situations are attributed to its concentration. Previous studies also showed that low

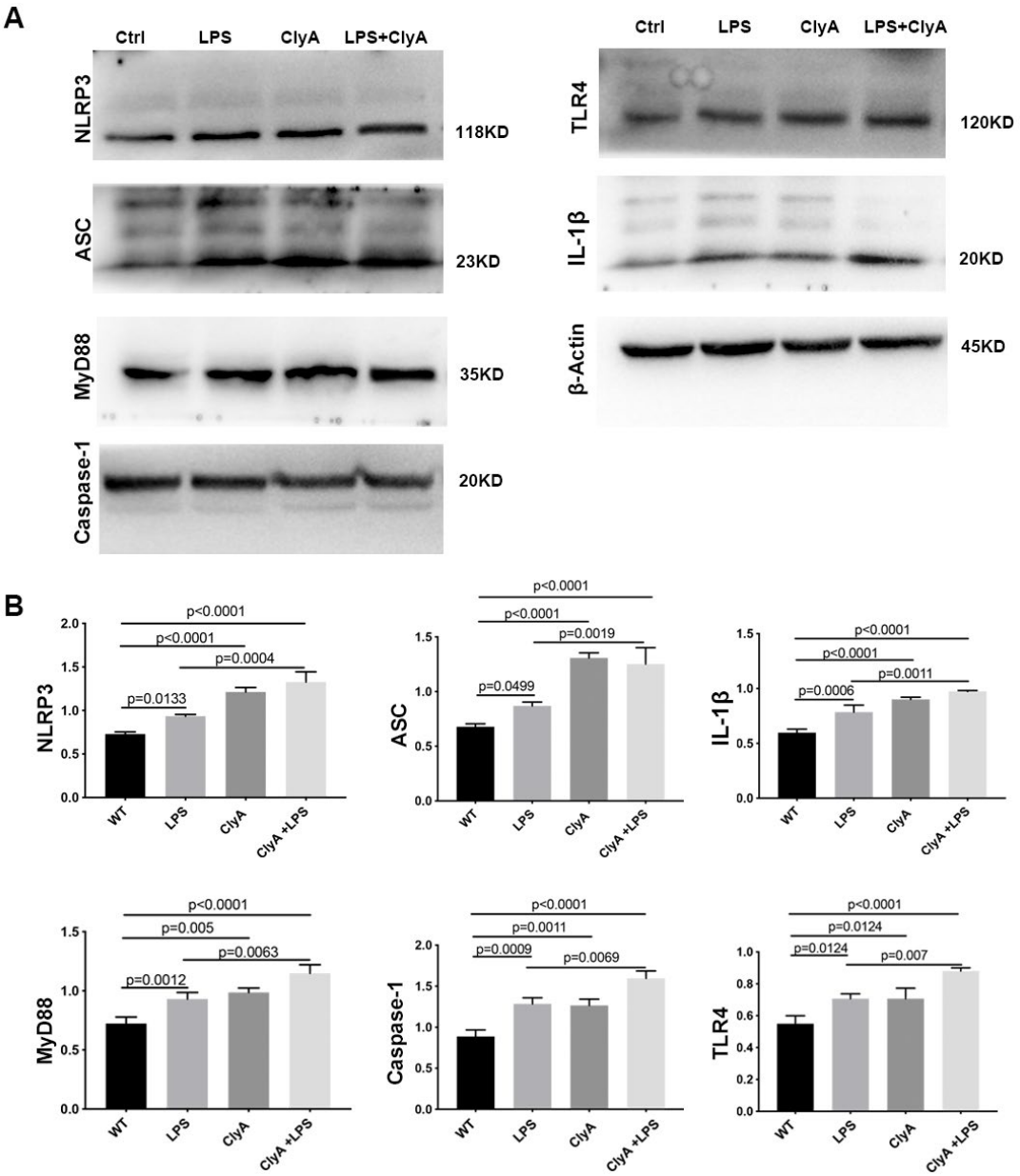


Fig. 4. *TRL4 and NLRP3 signaling pathways were activated in LPS, ClyA, and LPS+ClyA-treated macrophages. The expression of key components of TRL4 and NLRP3 signaling was detected with Western-blot (**A**); a significant increase of the expression of these components was detected (**B**).*

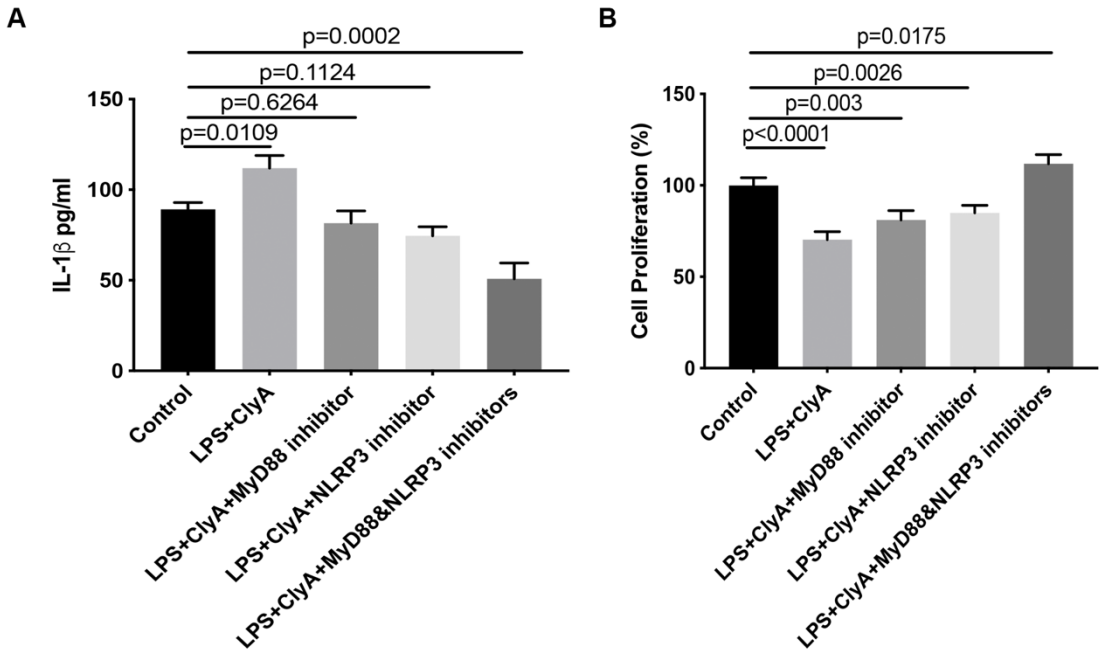


Fig. 5. *Inhibitors to MyD88 and NLRP3 suppressed the up-regulation of IL-1β in THP-1 derived macrophages and the anti-tumor property of the conditioned media was inhibited. The expression of IL-1β was decreased when the inhibitor to MyD88 or NLRP3 was added (**A**). When MyD88 inhibitor or NLRP3 inhibitor was introduced, the anti-proliferation effect of macrophage-conditioned medium on CT26 cells was suppressed (**B**).*

concentration of IL-1β can promote the secretion of IL-17 by $CD4^+$ T cells and inhibit the anti-tumor effect of the body. High concentration of IL-1β activates $CD8^+$ T cells and promotes anti-tumor effects, which suggests that the anti-tumor function of IL-1β is concentration-dependent, and increasing the level of IL-1β will enhance its anti-tumor effect (4, 37). Therefore, by introducing ClyA and LPS together, we observed that the release of IL-1β in human macrophages was enhanced, and then had a strong ability of tumor inhibition, as observed in mice models (35).

In contrast to anti-tumor activity, IL-1β is also an important mediator in local and systemic inflammation (3, 10). Recent studies reported COV-19, also known as SARS-COV-2, can bind to TLR receptors and cause the release of pro-IL-1β which is cleaved by caspase-1, followed by inflammasome activation and production of active mature IL-1β which is a mediator of lung inflammation, fever and fibrosis (38, 39).

IL-1β is not the only cytokines that are produced by macrophages after LPS treatment. We also detected the increase of TNF-α, TNF-β, and IL-12 (data not shown). However, compared with LPS treatment, the expression of these cytokines did not increase after ClyA treatment. Moreover, the expression of IL-1β increased after treatment with LPS and/or ClyA.

In conclusion, in this study, we tested the ability of the combination of ClyA and LPS on the release of IL-1β on human macrophages. The results showed that the production of IL-1β was highly enhanced when human macrophages were treated with LPS and ClyA together, which provides a new experimental and theoretical basis for further understanding the tumor immune function of human macrophages. The analysis of the relationship between the expression level of IL-lβ and the prognosis of patients will also provide a powerful reference for its clinical application.

ACKNOWLEDGEMENTS

This work was supported by the National Natural Science Foundation of China (NSFC:81760515,

81960556) and Finance science and technology project of Hainan Province (No. ZDYF2018175) and Hainan Provincial Health and Family Planning Industry Research Project (No.16A200107).

REFERENCES

1. Liu Y, Cao X. The origin and function of tumor-associated macrophages. Cell Mol Immunol 2015; 12(1):1-4.
2. Wynn TA, Chawla A, Pollard JW. Macrophage biology in development, homeostasis and disease. Nature 2013; 496(7446):445-55.
3. Dinarello CA. Overview of the IL-1 family in innate inflammation and acquired immunity. Immunol Rev 2018; 281(1):8-27.
4. Ghiringhelli F, Apetoh L, Tesniere A, et al. Activation of the NLRP3 inflammasome in dendritic cells induces IL-1beta-dependent adaptive immunity against tumors. Nat Med 2009; 15(10):1170-8.
5. Hazuda DJ, Strickler J, Kueppers F, Simon PL, Young PR. Processing of precursor interleukin 1 beta and inflammatory disease. J Biol Chem 1990; 265(11):6318-22.
6. Netea MG, Nold-Petry CA, Nold MF, et al. Differential requirement for the activation of the inflammasome for processing and release of IL-1beta in monocytes and macrophages. Blood 2009; 113(10):2324-35.
7. Dinarello CA. Biologic basis for interleukin-1 in disease. Blood 1996; 87(6):2095-147.
8. Dinarello CA. Immunological and Inflammatory Functions of the Interleukin-1 Family. Annual Rev Immunol 2009; 27(1):519-50.
9. Garlanda C, Dinarello CA, Mantovani A. The Interleukin-1 family: back to the future. Immunity 2013; 39(6):1003-18.
10. Dinarello CA. Interleukin-1 in the pathogenesis and treatment of inflammatory diseases. Blood 2011; 117(14):3720-32.
11. Franza L, Carusi V, Altamura S, et al. Interrelationship between inflammatory cytokines (IL-1, IL-6, IL-33, IL-37) and acquired immunity. J Biol Regul Homeost Agents 2019; 33(5):1321-6.
12. Basith S, Manavalan B, Yoo TH, Kim SG, Choi S. Roles of toll-like receptors in cancer: a double-edged sword for defense and offense. Arch Pharm Res 2012; 35(8):1297-316.
13. Jimenez-Dalmaroni MJ, Gerswhin ME, Adamopoulos IE. The critical role of toll-like receptors--From microbial recognition to autoimmunity: A comprehensive review. Autoimmun Rev 2016; 15(1):1-8.
14. Lee CC, Avalos AM, Ploegh HL. Accessory molecules for Toll-like receptors and their function. Nat Rev Immunol 2012; 12(3):168-79.
15. Phongsisay V. The immunobiology of Campylobacter jejuni: Innate immunity and autoimmune diseases. Immunobiology 2016; 221(4):535-43.
16. Ungerback J, Belenki D, Jawad ul-Hassan A, et al. Genetic variation and alterations of genes involved in NFkappaB/TNFAIP3- and NLRP3-inflammasome signaling affect susceptibility and outcome of colorectal cancer. Carcinogenesis 2012; 33(11):2126-34.
17. Mariathasan S, Newton K, Monack DM, et al. Differential activation of the inflammasome by caspase-1 adaptors ASC and Ipaf. Nature 2004; 430(6996):213-8.
18. Shcheblyakov DV, Logunov DY, Tukhvatulin AI, Shmarov MM, Naroditsky BS, Gintsburg AL. Toll-Like receptors (TLRs): the role in tumor progression. Acta Naturae 2010; 2(3):21-9.
19. Fitzgerald KA, Rowe DC, Golenbock DT. Endotoxin recognition and signal transduction by the TLR4/MD2-complex. Microbes Infect 2004; 6(15):1361-7.
20. Kawai T, Akira S. The role of pattern-recognition receptors in innate immunity: update on Toll-like receptors. Nat Immunol 2010; 11(5):373-84.
21. Ryoo S, Lee S, Jo S, et al. Effect of lipopolysaccharide (LPS) on mouse model of steroid-induced avascular necrosis in the femoral head (ANFH). J Microbiol Biotechnol 2014; 24(3):394-400.
22. Conforti-Andreoni C, Ricciardi-Castagnoli P, Mortellaro A. The inflammasomes in health and disease: from genetics to molecular mechanisms of autoinflammation and beyond. Cell Mol Immunol 2011; 8(2):135-45.
23. Strowig T, Henao-Mejia J, Elinav E, Flavell R. Inflammasomes in health and disease. Nature 2012; 481(7381):278-86.
24. Albalawi F, Lu W, Beckel JM, Lim JC, McCaughey SA, Mitchell CH. The P2X7 receptor primes IL-1beta and the NLRP3 inflammasome in astrocytes

exposed to mechanical strain. Front Cell Neurosci 2017; 11:227.
25. Franceschini A, Capece M, Chiozzi P, et al. The P2X7 receptor directly interacts with the NLRP3 inflammasome scaffold protein. FASEB J 2015; 29(6):2450-61.
26. Karmakar M, Katsnelson MA, Dubyak GR, Pearlman E. Neutrophil P2X7 receptors mediate NLRP3 inflammasome-dependent IL-1beta secretion in response to ATP. Nat Commun 2016; 7:10555.
27. Quan JH, Huang R, Wang Z, et al. P2X7 receptor mediates NLRP3-dependent IL-1beta secretion and parasite proliferation in Toxoplasma gondii-infected human small intestinal epithelial cells. Parasit Vectors 2018; 11(1):1.
28. Salaro E, Rambaldi A, Falzoni S, et al. Involvement of the P2X7-NLRP3 axis in leukemic cell proliferation and death. Sci Rep 2016; 6:26280.
29. Wallace AJ, Stillman TJ, Atkins A, et al. E. coli hemolysin E (HlyE, ClyA, SheA): X-ray crystal structure of the toxin and observation of membrane pores by electron microscopy. Cell 2000; 100(2):265-76.
30. Gupta R, Ghosh S, Monks B, et al. RNA and beta-hemolysin of group B Streptococcus induce interleukin-1beta (IL-1beta) by activating NLRP3 inflammasomes in mouse macrophages. J Biol Chem 2014; 289(20):13701-5.
31. Siegel RL, Miller KD, Jemal A. Cancer statistics, 2019. CA Cancer J Clin 2019; 69(1):7-34.
32. Cavestro GM, Zuppardo RA, Mannucci A. Early-onset colorectal cancer: trends and challenges. Lancet Gastroenterol Hepatol 2019; 4(7):491-2.
33. Dekker E, Tanis PJ, Vleugels JLA, Kasi PM, Wallace MB. Colorectal cancer. Lancet 2019; 394(10207):1467-80.
34. The Lancet Gastroenterology H. The shifting epidemiology of colorectal cancer. Lancet Gastroenterol Hepatol 2019; 4(7):489.
35. Wu Y, Feng Z, Jiang S, Chen J, Zhan Y, Chen J. Secreting-lux/pT-ClyA engineered bacteria suppresses tumor growth via interleukin-1beta in two pathways. AMB Express 2019; 9(1):189-94.
36. Li Y, Wang L, Pappan L, Galliher-Beckley A, Shi J. IL-1beta promotes stemness and invasiveness of colon cancer cells through Zeb1 activation. Mol Cancer 2012; 11:87.
37. Bruchard M, Mignot G, Derangere V, et al. Chemotherapy-triggered cathepsin B release in myeloid-derived suppressor cells activates the Nlrp3 inflammasome and promotes tumor growth. Nat Med 2013; 19(1):57-64.
38. Conti P, Gallenga CE, Tetè G, et al. How to reduce the likelihood of coronavirus-19 (CoV-19 or SARS-CoV-2) infection and lung inflammation mediated by IL-1. J Biol Regul Homeost Agents 2020;34(2):333-38.
39. Conti P, Ronconi G, Caraffa A, et al. Induction of pro-inflammatory cytokines (IL-1 and IL-6) and lung inflammation by Coronavirus-19 (COVI-19 or SARS-CoV-2): anti-inflammatory strategies. J Biol Regul Homeost Agents 2020; 34(2):327-31.

MicroRNA-182 inhibits osteogenic differentiation of bone marrow mesenchymal stem cells by targeting Smad1

H.-B. Zheng, M. Wu, G. Zhang and K.-L. Chen

Department of Orthopaedics, Yongjia People's Hospital, Wenzhou, China

Received November 23, 2020 – Accepted February 9, 2021

The present study aimed to screen abnormally expressed microRNAs (miRs/miRNAs) in patients with postmenopausal osteoporosis (POP) and explore their mechanisms via functional verification. Bone marrow mesenchymal stem cells (BMSCs) were extracted from healthy controls and patients with POP. Differences in osteogenic differentiation and proliferation of human BMSCs were compared between the two groups using Cell Counting Kit-8 (CCK-8) assay and alizarin red staining. A rat model of POP was established. Compared with patients with POP, human BMSCs in healthy controls had significantly enhanced viability at 24, 36, 48 and 72 h. The results of alizarin red staining revealed that the deposition of calcium minerals in human BMSCs were significantly lower in patients with POP. Based on miRNA microarray and reverse transcription-quantitative polymerase chain reaction (PCR) results, the expression levels of miR-7010 and miR-467c decreased, while miR-132 and miR-182 expression increased in the human BMSCs of patients with POP. Alizarin red staining showed that miR-182 markedly suppressed the osteogenic differentiation of primary rat BMSCs in rats. Western blotting and immunofluorescence assay revealed that miR-182 inhibited the expression of osteogenesis markers runt-related transcription factor 2, osterix and actinin-associated LIM protein. The results of the luciferase reporter assay showed that Smad1 is the direct target of miR-182. In rat primary BMSCs, Smad1 overexpression abolished the inhibitory effect of miR-182 on osteogenesis, indicating that miR-182 inhibits osteogenic differentiation of primary rat BMSCs in rats by targeting Smad1. Finally, *in vivo* experimental results showed that the biomechanical characteristics of bone tissues in POP rats were significantly enhanced by miR-182 inhibition, while they were significantly weakened by miR-182 overexpression. MiR-182 inhibits osteogenic differentiation of rat BMSCs, thus aggravating POP in rats.

Bone tissues are composed of bone marrow mesenchymal stem cells (BMSCs), osteoblasts, osteoclasts, osteocytes, extracellular matrix and minerals. Under physiological conditions, bone metabolic balance is regulated by osteoblast-mediated bone formation and osteoclast-mediated bone metabolism (1). Once such balance is broken, osteoporosis (OP) and osteosclerosis may be caused. OP is a chronic degenerative disease mainly manifested as decline in bone mass and degradation of bone tissue microstructure (2). OP can raise the disability and mortality rates, and lower the quality of life of patients around the world. In general, primary OP is classified into postmenopausal OP (POP) and senile OP.

POP is characterized by enhanced bone resorption,

Key words: microRNA-182; Smad1; bone marrow mesenchymal stem cells; postmenopausal osteoporosis; osteogenic differentiation

Corresponding Author:
Kangle Chen, BM.
Department of Orthopaedics, Yongjia People's Hospital,
37 Yongzhong Road, Beicheng Street,
Shangtang Town, Yongjia, Wenzhou,
Zhejiang 325100, China
Tel.: +86 013736968650
e-mail: mas11s@163.com

0393-974X (2021)
Copyright © by BIOLIFE, s.a.s.
This publication and/or article is for individual use only and may not be further reproduced without written permission from the copyright holder.
Unauthorized reproduction may result in financial and other penalties
DISCLOSURE: ALL AUTHORS REPORT NO CONFLICTS OF INTEREST RELEVANT TO THIS ARTICLE.

different from an obvious decline in osteogenic ability in senile OP. According to epidemiological studies, the incidence rate of OP in menopausal women is directly related to the decrease in the circulating estrogen level. In subsequent research, it was confirmed that estrogen deficiency is the most important cause of OP (3). The therapeutic methods for POP include estrogen replacement therapy and bisphosphonates (4). Estrogen replacement therapy reduces bone mass loss mainly through inhibiting bone resorption, but various complications may result, therefore it has been gradually abandoned. In addition, the long-term application of bisphosphonates may raise the incidence of esophageal ulcers (5). As the only drug approved by the FDA used to promote bone formation, parathyroid hormone may increase the risk of bone resorption in the case of long-term administration (6). Therefore, a deeper understanding of the pathogenesis of POP and exploring the prevention and treatment methods have become a clinical problem demanding prompt solution.

Micro ribonucleic acids (miRNAs) are non-coding RNAs composed of 18-22 nucleic acids, and they play crucial roles in a series of important pathophysiological processes. MiRNAs induce mRNA degradation through binding to the mRNA 3' untranslated region (3' UTR), ultimately inhibiting protein synthesis at the post-transcriptional level. The development, proliferation and metabolism of bone tissues have a significant correlation with miRNA functions (7). Moreover, the abnormal expression of miRNAs related to bone metabolism can lead to bone metabolic disorders, ultimately causing OP. In addition, the changes in expressions of key miRNAs may also exert a potential therapeutic effect. Although the exact regulatory mechanism is yet to be determined, miRNAs playing important roles in bone metabolism may become a potential means of treatment for OP.

MATERIALS AND METHODS

Tissue samples of patients

OP tissue samples were obtained from the bone marrow of 68-year-old females at 19 years after menopause. The patients were diagnosed with OP via bone densitometry and X-ray examination. Tissue samples of healthy controls were obtained from 66-year-old females with traumatic femoral fractures but no OP. In the total hip arthroplasty on the affected side, 10 ml of iliac bone marrow was extracted with a syringe after heparinization in both patients and healthy controls. The bone marrow tissues of patients were centrifuged at 600 × g, and the human BMSCs at the bottom of the tube were extracted. There was no statistical difference in baseline data (age) between the two groups. This study was approved by the Ethics Committee of Yongjia People's Hospital. Signed written informed consent was obtained from all participants prior to the study.

Isolation and culture of primary rat BMSCs in rats

Three-week-old male Sprague-Dawley rats weighing 140±20 g were purchased from Yongjia People's Hospital Animal Center. The rats were fed in a specific pathogen-free (SPF) animal room at 22±2°C, 60±10% humidity and 12/12 h light/dark cycle (light on from 6:00 a.m.) and had free access to food and water. The rats were fasted for 12 h before extraction of primary rat BMSCs. The present study was approved by the Animal Ethics Committee of Yongjia People's Hospital Animal Center.

The rats were sacrificed via cervical dislocation after anesthesia with peritoneal administration of 40 mg/kg pentobarbital sodium and sterilized with 75% ethanol. The bone marrow was aseptically extracted from the femur and tibia and mixed with Dulbecco's modified eagle medium (DMEM) (Gibco, Rockville, MD, USA) supplemented with 10% fetal bovine serum (FBS) (Gibco, Rockville, MD, USA), followed by gradient centrifugation at 900 × g to extract rat BMSCs. Cells were cultured with DMEM at 37°C and 5% CO_2. The media was replaced with fresh media every 3 days. The cells were passaged every 6-7 days. To ensure the purity, third generation rat BMSCs (purity >95%) were used for subsequent experiments.

Determination of cell viability via cell counting kit-8 (CCK-8) assay

Human BMSCs were collected from both groups, and inoculated into a 96-well plate (1×10^4 cells/mL). After incubation for 12, 24, 36, 48 and 72 h, 10 µL of CCK-8 solution (Dojindo Molecular Technologies, Inc., Kumamoto, Japan) was added into each well, followed by incubation at 37°C for 2 h in the dark. Finally, the absorbance was measured at a wavelength of 490 nm

using a microplate reader (Bio-Rad Laboratories, Inc., Hercules, CA, USA). Human BMSCs not co-cultured with Ophiopogonin D were used as the control group. Each assay was repeated 3 times.

Induction of osteogenic differentiation and alizarin red staining

Human BMSCs were inoculated into a 24-well plate (5×10^4 cells/mL) (Corning Costar, Corning, NY, USA) in both groups. When the cell density was 70-80%, the osteogenic induction medium already prepared (10% FBS, 10 nmol/L dexamethasone, 10 mmol/L β-glycerophosphate, 50 μg/mL ascorbic acid, 1% penicillin-streptomycin and 1% HEPES) was added, and replaced every 3 days. After 2 weeks, human BMSCs were fixed with 95% ethanol at room temperature for 10 min, and stained with 40 mM alizarin red solution (pH 4.2) at room temperature for 10 min. Then human BMSCs were treated with 10 mM sodium phosphate solution containing 10% cetylpyridinium chloride at room temperature for 15 min, and washed with phosphate buffered saline (PBS) for 15 min.

MiRNA microarray assay

The third-generation rat BMSCs were inoculated into a 6-well plate (1×10^5 cells/mL). Upon reaching 80-85% confluency, the total RNA was extracted in both groups using the reagent (Invitrogen, Carlsbad, CA, USA) according to the manufacturer's instructions. Then miRNA microarray analysis was performed by Guangzhou Ribo Biological Co., Ltd. (Guangzhou, China) The differentially expressed miRNAs were verified via reverse transcription-quantitative polymerase chain reaction (RT-qPCR).

Reverse transcription-quantitative PCR

The expression of differentially expressed miRNAs in bone marrow tissues were detected via RT-qPCR. A total of 500 ng RNA were divided into three different pools for RT. Total RNA was diluted (10-fold) and 3 μl total RNA was used for PCR amplification. The amplification levels of the target gene was verified via 5% agarose gel electrophoresis. The data were quantified and processed using image acquisition and analysis software (LabWorks 4.0, Cambridge, UK). U6 and GAPDH were used as internal references. miR-182 primers were purchased from ABM (Peterborough, Camb, Canada). Experiments in each group were repeated three times. The relative expression levels of target genes were analyzed using the $2^{-\Delta\Delta Cq}$ method. The primer sequences used are shown in Table I.

Luciferase reporter assay

Wild-type and mutant-type Smad1 3'-untranslated region (3'-UTR) were amplified and cloned into psiCHECK-2 luciferase plasmids (Promega Corporation, Madison, WI, USA). Primary rat BMSCs were cultured in a 24-well plate and co-transfected with miR-182 mimic or miR-con and wild-type or mutant-type plasmids. Luciferase activity was determined at 48 h after transfection using dual-luciferase reporter reagent (Promega Corporation, Madison, WI, USA).

Cell transfection

miR-182 mimic, miR-con, miR-182 inhibitor and pcDNA 3.1-Smad1 were all synthesized by Shanghai Genetic Pharmaceutical Co., Ltd. Prior to transfection, rat BMSCs were seeded into a six-well plate (2×10^6 cells/ml) until 60-80% confluence. Rat BMSCs were then transfected with 100 nM miR-182 mimic, miR-182 inhibitor, miR-con and pcDNA 3.1-Smad1 for 6 h using Lipofectamine® 2000 (Invitrogen, Carlsbad, CA, USA). Following digestion with 0.025% trypsin for 24 h, the cells were collected for RT-qPCR, Western blotting, luciferase reporter assays and immunofluorescence assays.

Western blotting

An appropriate amount of radioimmunoprecipitation assay (RIPA) lysis buffer was prepared, which was evenly mixed with and the protease inhibitor phenylmethylsulfonyl fluoride (PMSF) (RIPA:PMSF = 100:1) (Beyotime Institute of Biotechnology, Shanghai, China). Following digestion with trypsin, the cells were lysed with lysis buffer, and the lysate was collected and transferred into an Eppendorf (EP) tube, followed by centrifugation at 10,500 × g at 4°C for 30 min. Subsequently, the protein supernatant was collected and heated at 95°C for 10 min for protein denaturation. The protein samples were stored at -80°C for later use and quantified using a bicinchoninic acid kit (Pierce, Rockford, IL, USA). Sodium dodecyl sulphate-polyacrylamide electrophoresis (SDS-PAGE)

gels were then prepared, and protein samples were loaded into each well for electrophoresis at 80 V for 2.5 h. Proteins were then transferred onto a polyvinylidene fluoride (PVDF) membrane using a semi-dry transfer method (EMD Millipore, Billerica, MA, USA). PVDF membranes were blocked with TBS-Tween-20 (TBS-T) containing 5% skim milk powder on an orbital shaker for 1 h under gentle rotation. Subsequently, membranes were incubated with primary antibody diluted in 5% skim milk powder and rinsed with TBS-T three times for 10 mins each time. Following primary antibody incubation, membranes were incubated with secondary antibody for 2 h at room temperature. Membranes were then rinsed with TBS-T twice and with TBS once (10 mins each time). Finally, protein signals were detected using ECL reagent, followed by exposure in a dark room. The relative expressions of proteins were analyzed using Image-Pro Plus v6 (Media Cybernetics, Inc.).

Immunofluorescence assay

Rat BMSCs were fixed with 4% paraformaldehyde at room temperature for 20 min, permeabilized with 0.25% Triton X-100 (Sigma-Aldrich, St. Louis, MO, USA) and blocked with 0.1% BSA (Roche Diagnostics, Basel, Switzerland) at room temperature for 30 min. Cells were incubated with primary antibodies against Runx2 (cat. no. ab114133; 1:500; Abcam, Cambridge, MA, USA), osterix (cat. no. ab209484; 1:500; Abcam, Cambridge, MA, USA) and ALP (cat. no. ab83259; 1:500; Abcam, Cambridge, MA, USA) overnight at 4°C. Once rat BMSCs were

Table I. *Primer sequences*

Primer		Sequence (5'-3')
MiR-182	Forward	5'-GGGTTTACGTTGGGAGA-3'
	Reverse	5'-GAACATGTCTGCGTATCTC-3'
MiR-132	Forward	5'-CCTGAACTCTGCACCAAGTCCT-3'
	Reverse	5'-TCATCTGGCTCAGATAGGAGGG-3'
MiR-7010	Forward	5'-AACACCGTGCGCAGCTTCCATC-3'
	Reverse	5'-CGGAAGATCTGGAGTTCTGCAG-3'
MiR-467c	Forward	5'-TAGGCCACAGCCACCCATG-3'
	Reverse	5'- GAACATGTCTGCGTATCTC-3'
ALP	Forward	5'-ATTCTCTCTGGATCCCATGG-3'
	Reverse	5'-GAACATGTCTGCGTATCTC-3'
Smad1	Forward	5'-CCCATTGCATATCGGAG-3'
	Reverse	5'- GAACATGTCTGCGTATCTC-3'
Runx2	Forward	5'-GAGCTTATTCATAAAAGTGC-3'
	Reverse	5'-GAACATGTCTGCGTATCTC-3'
Osterix	Forward	5'-GAGCTTAGCTGATTGGTGA-3'
	Reverse	5'-GAACATGTCTGCGTATCTC-3'
U6	Forward	5'-CCCTGAGACCCTTTAACC-3'
	Reverse	5'-GAACATGTCTGCGTATCTC-3'
GAPDH	Forward	5'-AGGTCGGTGTGAACGGATTTG-3'
	Reverse	5'-TGTAGACCATGTAGTTGAGGTCA-3'

washed with PBS three times, they were then incubated with corresponding secondary antibodies (cat. nos. PV-0024 and PV-0023; 1:100; BIOSS, Wuhan, China) at 37°C for 30 min. Rat BMSCs were observed under an optical microscope (×200 magnification; Leica Microsystems GmbH, Wetzlar, Germany) to compare the degree of osteogenic differentiation between the two groups.

Establishment of a POP rat model

All the rats were randomly divided into a sham group (n=15), model group (n=15), agomiR-182 group (n=15) and antagomir-182 group (n=15) using a random number table. Rats were routinely fed and had free access to water under a 12/12 h light/dark cycle. After adaptive feeding for 7 days, bilateral oophorectomy was performed as previously described (8). After being anesthetized using peritoneal administration of pentobarbital sodium at a dose of 40 mg/kg, rats in the model, agomiR-182 and antagomir-182 groups underwent bilateral ovariectomy. In the sham group, bilateral ovaries were exposed but not removed. After successful modeling, 5 µl agomiR-182 (40 nmol/ml; Shanghai GenePharma Co., Ltd., Shanghai, China), 5 µl antagomir-182 (40 nmol/ml; Shanghai GenePharma Co., Ltd., Shanghai, China) and 5 µl agomiR-NC (40 nmol/ml) were intraperitoneally injected into rats in the agomiR-182 group, antagomir-182 group and model group, respectively, once every 3 days for 1 month (9).

Three-point bending test

At 1 month after treatment in each group, the damaged part of the femoral shaft was removed, and the femoral shaft was placed on two saddle supports in a span of 20 mm. The three-point bending test was conducted at the distal end (one-third) of femoral shaft using a Shimadzu universal testing machine. The pressure was applied to the midpoint between the two saddle supports at a loading rate of 1 mm/min using a saddle head connected to the sensor, until the femur fractured. Experimental data were analyzed using Trapezium2 software (Version 2.2, Shimazu Production Company, Japan), based on mechanical structure parameters (maximum load, fracture load, structural stiffness, energy absorption and maximum bending moment) and material mechanical parameters (elastic modulus, ultimate strength, fracture strength, maximum strain and fracture strain).

Statistical analysis

Data were analyzed using Statistical Product and

Table II. *MiR-182 reduces biomechanical characteristics of osteoporosis in rats*

	Sham group	Model group	agomiR-182 group	antagomir-182 group
Maximum load (N)	133.45±6	107.54±8.86**	90.79±7.31$^{\&\&}$	119.49±7.14
Fracture load (N)	109.69±6.06	78.9±8.69**	59.09±5.35$^{\&\&}$	94.98±6.23
Energy absorption (N.mm)	93.45±6.66	58.22±6.74**	36.93±4.11$^{\&\&}$	78.74±7.21
Structural stiffness (N.mm^{-1})	226.3±12.77	174.41±12.1**	128.05±7.47$^{\&\&}$	201.47±12.29
Maximum bending moment (N.mm)	806.8±58.23	600.41±50.04**	511.07±31.32$^{\&\&}$	719.04±45.04
Elastic modulus (N.mm^{-1})	6800.71±194.25	5371.19±174.52**	4145.6±149.12$^{\&\&}$	6086.4±179.63$^{\&\&}$
Ultimate strength (N.mm^{-2})	200.0±13.51	147.15±16.11**	123.4±11.15$^{\&\&}$	176.04±15.1$^{\&\&}$
Fracture strength (N.mm^{-2})	191.2±15.12	132.81±16.1**	109.67±9.99$^{\&\&}$	159.16±15.22$^{\&\&}$
Maximum strain (%)	6.41±0.64	3.06±0.28**	2.23±0.65$^{\&\&}$	4.01±0.39$^{\&\&}$
Fracture strain (%)	9.03±1.02	5.16±0.85**	3.74±0.4$^{\&\&}$	6.62±1.47$^{\&\&}$
Maximum load (N)	133.45±6	107.54±8.86**	90.79±7.31$^{\&\&}$	119.49±7.14$^{\&\&}$
Fracture load (N)	109.69±6.06	78.9±8.69**	59.09±5.35$^{\&\&}$	94.98±6.23$^{\&\&}$
Energy absorption (N.mm)	93.45±6.66	58.22±6.74**	36.93±4.11$^{\&\&}$	78.74±7.21$^{\&\&}$
Structural stiffness (N.mm^{-1})	226.3±12.77	174.41±12.1**	128.05±7.47$^{\&\&}$	201.47±12.29$^{\&\&}$

$^{**}P<0.01$: model group vs sham group, $^{\&\&}P<0.01$: model group vs agomiR-182 group or antagomir-182 group

Service Solutions (SPSS) 13.0 (SPSS, Inc., Chicago, IL, USA). Data were expressed as the mean ± SD (standard deviation). Comparison of pairwise differences between groups was carried out using the Student's *t*-test. Comparison between multiple groups was made using One-way analysis of variance (ANOVA) test followed by Post Hoc Test (Bonferroni). $P<0.05$ was considered to indicate a statistically significant difference.

RESULTS

Proliferation and osteogenic differentiation of human BMSCs are significantly lower in patients with OP

Alizarin red staining results revealed that the deposition of calcium minerals in human BMSCs was significantly higher in healthy controls compared with patients with OP (Fig. 1A). CCK-8 assay results revealed that human BMSCs in healthy controls had significantly enhanced viability at 24, 36, 48 and 72 h compared with patients with OP (Fig. 1B).

Expression of miR-182 in human BMSCs is higher in patients with OP

To investigate the possible pathogenesis of OP at the miRNA level, human BMSCs were extracted from patients with OP and healthy controls, and were subjected to miRNA microarray analysis. A total of 584 miRNAs were screened (FC >1, $P<0.05$). Compared with healthy controls, patients with OP had 293 upregulated miRNAs and 271 downregulated miRNAs (Fig. 2A and B). Subsequently, to verify the reliability of the high-throughput screening results, the differences in the expression of miR-7010, miR-467c, miR-132 and miR-182 were detected via RT-qPCR. The expression levels of miR-7010 and miR-467c were significantly higher, while those of miR-132 and miR-182 were significantly lower in the human BMSCs of healthy controls compared with patients with OP ($P<0.01$) (Fig. 2C). Among them, miR-182 had the most obvious decreasing trend.

Isolation and identification of rat BMSCs in rats

The number of red blood cells and other suspended cells markedly declined after 18 days of culture. The morphology of cultured primary rat BMSCs is shown in Fig. 3A. Rat BMSCs were distinguished from blood cells and other monocytes using two specific markers for rat BMSCs. Flow cytometry results showed that the CD44-positive rate and CD45-positive rate of cultured rat BMSCs were 99.8% and only 2.4%, respectively (Fig. 3B), indicating that cultured rat BMSCs were highly purified and could be used for further experiments.

MiR-182 inhibits osteogenic differentiation of rat BMSCs

To investigate the function of miR-182 in osteogenic differentiation of rat BMSCs, rat BMSCs were transfected with miR-182 mimic or miR-182 inhibitor. Fig 4A shows that the transfections were successful by RT-qPCR. The expression of Runx2,

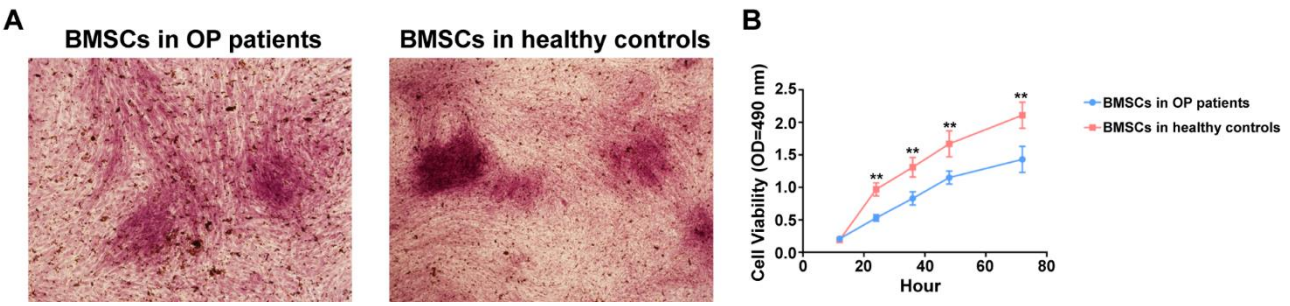


Fig. 1. *Proliferation and osteogenic differentiation of human BMSCs significantly decline in osteoporosis patients.* ***A)*** *The results of alizarin red staining revealed that the deposition of calcium minerals in human BMSCs obviously declines in OP patients compared with that in healthy controls. (magnification: 200×).* ***B)*** *Results of CCK-8 assay reveal that human BMSCs in healthy controls significantly enhanced viability at 24 h, 36 h, 48 h and 72 h compared with those in OP patients.* $^{**}P<0.01$*: Human BMSCs in OP patients vs Human BMSCs in healthy controls*

osterix and ALP in rat BMSCs were determined using immunofluorescence assay and Western blotting. The results showed that the mRNA and protein expression of Runx2, osterix and ALP were markedly lower in miR-182 mimic group and markedly higher in the miR-182 inhibitor group compared with the control group (Fig. 4B and C). Additionally, the deposition of calcium minerals was

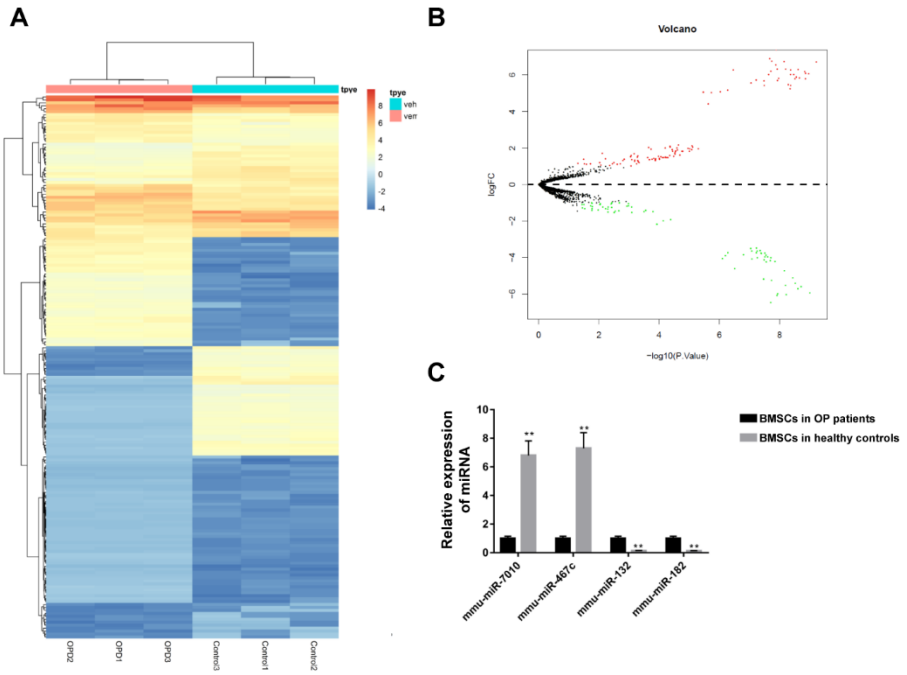


Fig. 2. *Expression of miR-182 in human BMSCs rises in OP patients. **A**,**B**) According to the heat map and volcano plot, there are 584 differentially expressed miRNAs in human BMSCs in OP patients compared with healthy controls. Red: up-regulated miRNAs, blue: down-regulated miRNAs. **C**) It is found via RT-qPCR that the expressions of miR-7010 and miR-467c evidently decline, while those of miR-132 and miR-182 evidently rise in OP patients compared with those in healthy controls. **P<0.05: vs healthy controls*

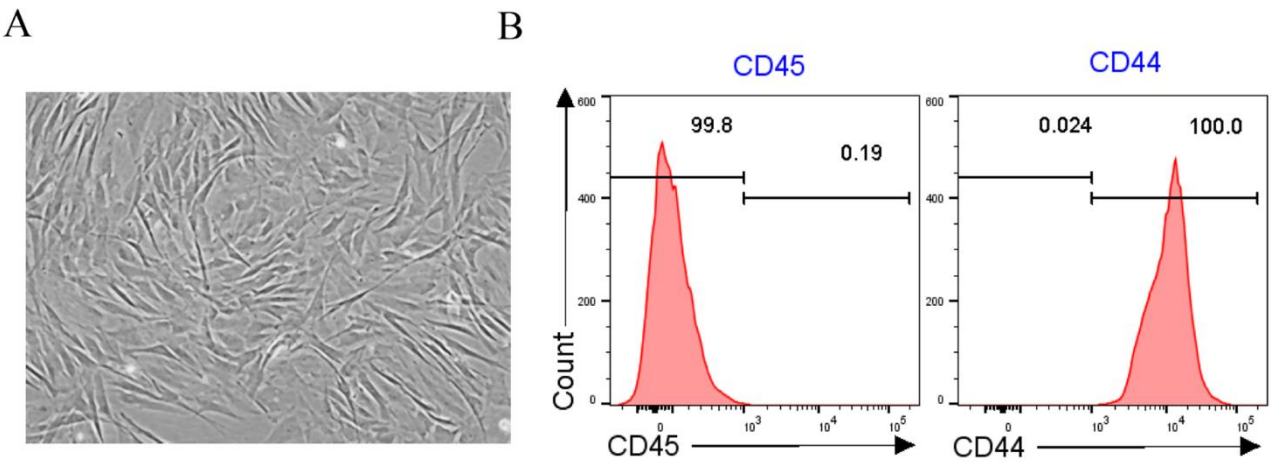


Fig. 3. *Isolation and identification of rat BMSCs in rats. **A**) Morphology of primary rat BMSCs. (magnification: 200×). **B**) The results of flow cytometry show that the CD44-positive rate and CD45-positive rate of cultured rat BMSCs are 99.8% and only 2.4%, respectively, indicating that cultured rat BMSCs are highly purified.*

higher in the miR-182 inhibitor group compared with control and miR-182 mimic groups (Fig. 4D). These results suggest that the osteogenic differentiation of rat BMSCs is significantly inhibited by the increased expression of miR-182.

miR-182 negatively regulates Smad1 expression via binding to the Smad1 mRNA 3'-UTR

TargetScan analysis predicted that Smad1 may be a potential target of miR-182 (Fig. 5A). To further confirm the interaction between miR-182 and Smad1, the response of wild-type and mutant-type Smad1 in primary rat BMSCs to miR-182 and miR-con was detected via luciferase reporter assay. The results revealed that the fluorescence response intensity significantly declined in miR-182-transfected primary rat BMSCs with wild-type Smad1, while no significant difference was observed in rat BMSCs with mutant-type Smad1 (Fig. 5B). RT-qPCR and Western blotting were then performed for further evidence. miR-182 transfection significantly decreased both mRNA and protein levels of Smad1, while knockdown of miR-182 increased Smad1 expression (Fig. 5 C, D). To summarize, miR-182 negatively regulates Smad1 expression via binding to the Smad1 mRNA 3'-UTR.

Smad1 overexpression abolishes the inhibitory effect of miR-182 on osteogenic differentiation of rat BMSCs

Smad1 was overexpressed using pcDNA 3.1-Smad1 in order to further investigate whether miR-182 can inhibit osteogenic differentiation of

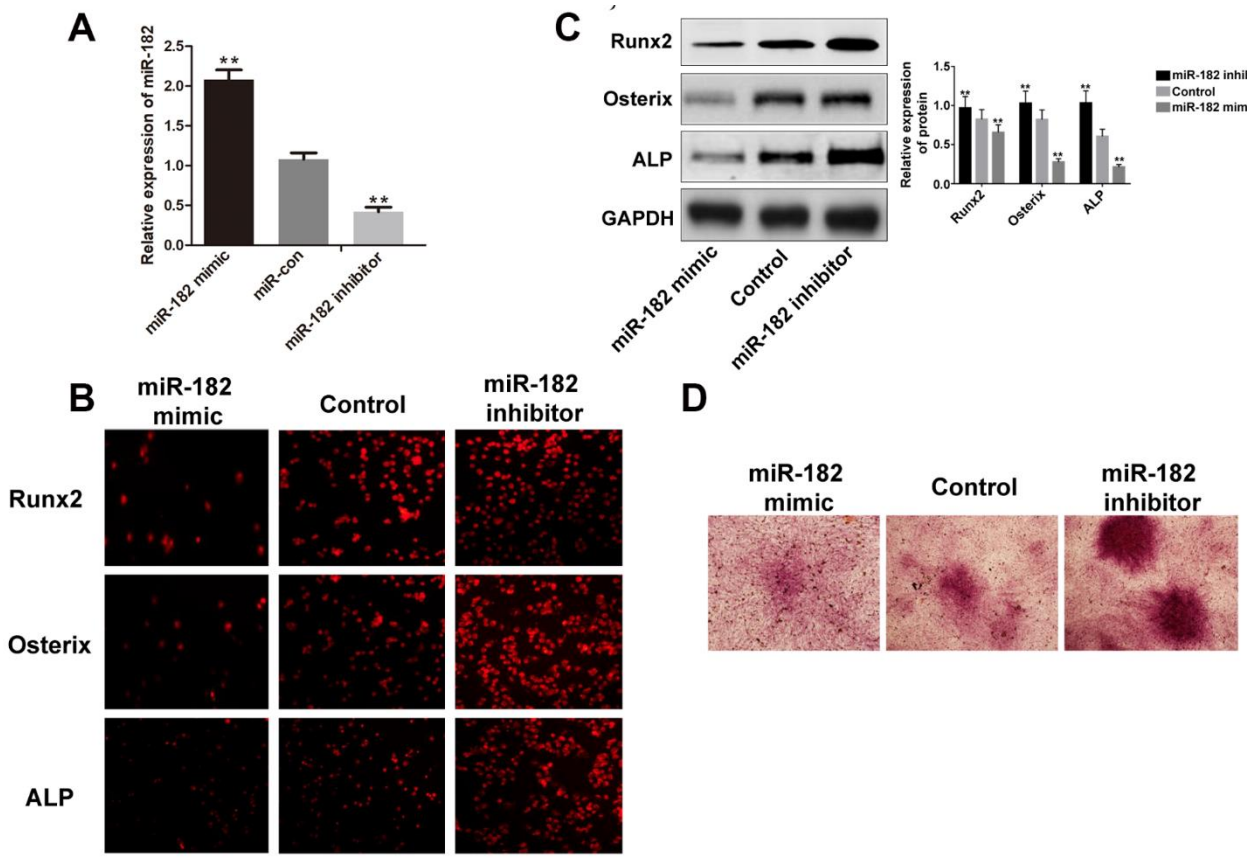


Fig. 4. *Effect of miR-182 expression on osteogenic differentiation of rat BMSCs. **A**) The expression of miR-182 was increased in cells transfected with miR-182 mimic while decreased in cells transfected with miR-182 inhibitor. **B**) Effect of miR-182 on osteogenic differentiation of rat BMSCs detected using alizarin red staining (magnification: 200×). **C**) Effects of miR-182 on expressions of osteogenesis markers Runx2, Osterix and ALP detected using RT-qPCR. **D**) The deposition of calcium minerals was stronger in miR-182 inhibitor group than that in control group and miR-182 mimic group (magnification: 200×) $^{**}P<0.05$: vs control group*

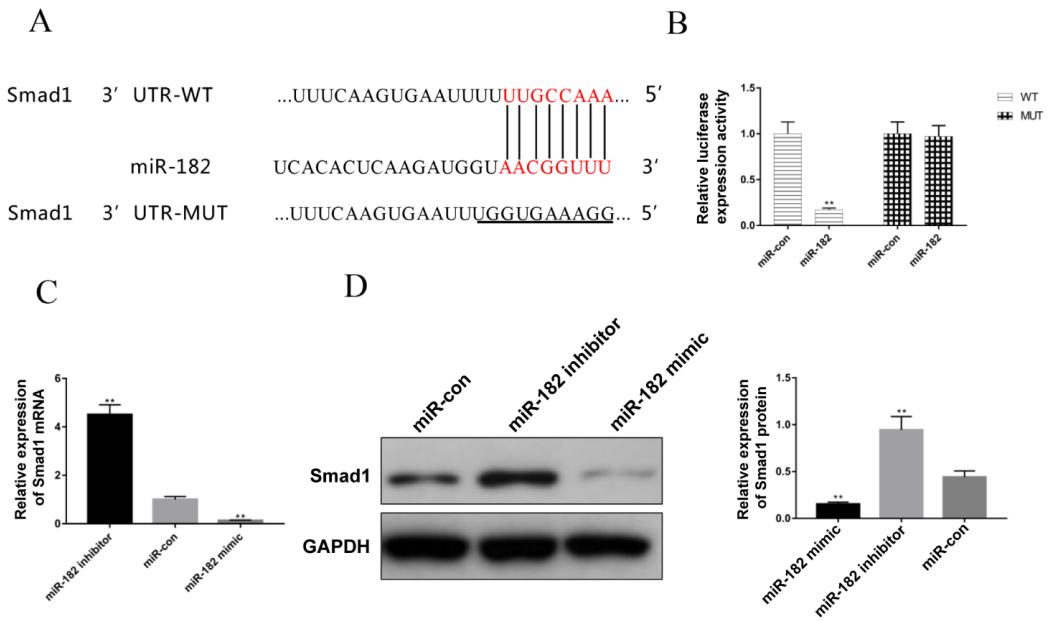


Fig. 5. *MiR-182 negatively regulates Smad1 expression via directly binding to Smad1 mRNA 3'UTR.* ***A****) According to prediction results using TargetScan, miR-182 binds directly to the Smad1 mRNA 3'UTR.* ***B****) The response of wild-type and mutant-type Smad1 in primary rat BMSCs to miR-182 and miR-con was detected via luciferase reporter assay.* ***C, D****) The effects of transfection of miR-con, miR-182 and miR-182 inhibitor on Smad1 mRNA and protein levels were determined using Western blotting and RT-qPCR. $^{**}P<0.01$: miR-182 group vs miR-con group, $^{\&\&}P<0.01$: miR-182 inhibitor group vs miR-con group*

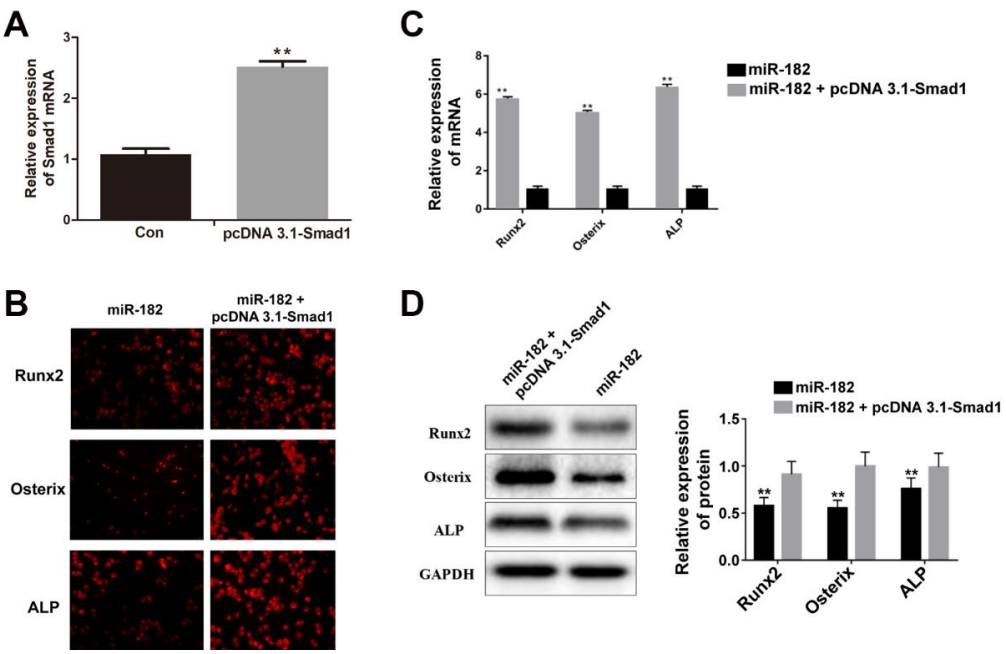


Fig. 6. *Overexpression of Smad1 abolishes the inhibitory effect of miR-182 on osteogenic differentiation of primary rat BMSCs.* ***A****) The expression of Smad1 mRNA was increased in cells transfected with pcDNA 3.1-Smad1.* ***B****) Effects of Smad1 and miR-182 overexpression on protein expressions of Runx2, Osterix and ALP detected via immunofluorescence assay.(****C****) Effects of Smad1 and miR-182 overexpression on mRNA expressions of Runx2, Osterix and ALP detected via RT-qPCR.* ***D****) Effects of Smad1 and miR-182 overexpression on protein expressions of Runx2, Osterix and ALP detected via Western blotting. $^{**}P<0.01$: miR-182 group vs miR-182 + pcDNA 3.1-Smad1 group*

primary rat BMSCs of rats via targeting Smad1. Fig. 6A shows that the transfections were successful by RT-qPCR. RT-qPCR. Western blotting and immunofluorescence assay showed that the mRNA and protein levels of Runx2, osterix and ALP were significantly higher in the miR-182 + pcDNA 3.1-Smad1 group compared with the miR-182 mimic group ($P<0.01$) (Fig. 6 A-C).

miR-182 reduces the biomechanical characteristics of POP rats

To evaluate the effect of miR-182 expression on POP rats *in vivo*, the effects of agomiR-182 and antagomir-182 on biomechanical characteristics were determined using the three-point bending test. Compared with the sham group, the model group presented with significantly decreased mechanical structure parameters (maximum load, fracture load, structural stiffness, energy absorption and maximum bending moment) and material mechanical parameters (elastic modulus, ultimate strength, fracture strength, maximum strain and fracture strain), indicating successful modeling. In addition, mechanical structure parameters and material mechanical parameters were significantly lower in the agomiR-182 group ($P<0.01$), but significantly higher in the antagomir-182 group compared with the model group ($P<0.01$). miR-182 decreased the biomechanical characteristics of POP rats (Table II).

DISCUSSION

Numerous studies have shown that the osteogenic differentiation of BMSCs is weakened in patients with POP (10, 11). The present study found that both osteogenic differentiation and proliferation of human BMSCs significantly declined in patients with OP compared with healthy controls. However, the role of miR-182 in osteogenic differentiation of BMSCs is poorly understood. To investigate the mechanism of strong osteogenic differentiation in the BMSCs of healthy controls at the miRNA level, the differences in miRNA expression profiles were detected using miRNA microarray analysis. miRNA microarray and RT-qPCR results showed that human BMSCs in patients with OP had higher miR-182 expression. However, the potential mechanism of miR-182 in osteogenic differentiation of BMSCs remains to be elucidated.

Each miRNA can bind to hundreds of different mRNAs, and miRNAs can be assembled with argonaute proteins into miRNA-induced silencing complexes, thus inducing post-transcriptional silencing of complementary mRNAs (12). Based on previously published studies, miR-182 has been identified to be associated with a variety of diseases, such as non-small cell lung cancer (13), cisplatin-resistance gastric cancer (14) and acute stroke (15). In addition, several studies have demonstrated that miR-182 expression is significantly associated with bone homeostasis (16). For example, Pan et al. (17) pointed out that the decreased miR-182 expression in OP can help alendronate promote the proliferation and differentiation of osteoblasts via the Rap1 GTPase-activating protein 1/MAPK pathway. The present study revealed that miR-182 inhibited the osteogenic differentiation of primary rat BMSCs in rats by directly targeting Smad1. As an essential transcription factor for skeletal development, Smad1 serves as a signaling hub and transcription regulator to regulate the expression of target genes, thereby controlling bone formation (18, 19). For example, Fu et al. (20) showed that miR-100 can suppress bone morphogenetic protein-induced osteogenic differentiation by targeting Smad1. However, to the best of our knowledge, there has been no evidence about the role of miR-182 targeting Smad1 in osteogenic differentiation of BMSCs in the literature.

The present study evaluated whether Smad1 is a direct target of miR-182 and whether miR-181 regulates osteogenic differentiation of BMSCs by targeting Smad1. Additionally, the response of wild-type and mutant-type Smad1 in primary rat BMSCs to miR-182 and miR-con was detected via luciferase reporter assay. The results revealed that the fluorescence response intensity significantly declined in miR-182-transfected primary rat BMSCs with wild-type Smad1, while no significant changes were observed in rat BMSCs with mutant-type Smad1. RT-qPCR and Western blotting were then performed for further evidence, and it was found that miR-182 transfection significantly decreased both mRNA and

protein levels of Smad1, while knockdown of miR-182 increased Smad1 expression.

To further confirm whether miR-181 regulates osteogenic differentiation of BMSCs by targeting Smad1, rat BMSCs were transfected with miR-182 mimic and miR-182 inhibitor. mRNA and protein expression of osterix, ALP and Runx2 were determined via Western blotting and immunofluorescence assays. The protein expression of osterix, ALP and Runx2 were lower in the miR-182 mimic group but significantly higher in the miR-182 inhibitor group compared with the control group. Moreover, alizarin red staining showed that the deposition of calcium minerals was stronger in the miR-182 inhibitor group compared with control and miR-182 mimic groups. It was revealed that miR-182 inhibitor activates bone turnover. Furthermore, Smad1 overexpression reversed the inhibitory effect of miR-182 on osteogenic differentiation. Finally, the biomechanical characteristics were determined to evaluate the effects of miR-182 expression on POP rats *in vivo*. The results showed that miR-182 reduced the biomechanical characteristics of POP rats. It should be noted that the deposition of calcium minerals was observed only using alizarin red staining, and precise quantification was nor performed. Despite this limitation, the present study validated the hypothesis that miR-182 targeted Smad1 and may directly inhibit osteogenic differentiation of BMSCs. The clinical significance of findings of the present study is that miR-182/Smad1 may be used as a therapeutic target for OP. In addition, inhibiting the overexpression of miR-182 may be a novel therapeutic method for OP. MiR-182 also inhibited osteogenic differentiation of rat BMSCs, thus aggravating POP in rats. miR-182 suppressed osteogenic differentiation of BMSCs by targeting Smad1, and miR-182/Smad1 may be a new treatment strategy for OP.

In conclusion, miR-182 inhibits the osteogenic differentiation of rat BMSCs, thus aggravating POP in rats.

REFERENCES

1. Orimo H, Hayashi Y, Fukunaga M, et al. Diagnostic criteria for primary osteoporosis: year 2000 revision. J Bone Miner Metab 2001; 19:331-37.
2. Zhao Y, Wang HL, Li TT, Yang F, Tzeng CM. Baicalin ameliorates dexamethasone-induced osteoporosis by regulation of the RANK/RANKL/OPG signaling pathway. Drug Des Devel Ther 2020; 14:195-206.
3. Xu L, Shen L, Yu X, Li P, Wang Q, Li C. Effects of irisin on osteoblast apoptosis and osteoporosis in postmenopausal osteoporosis rats through upregulating Nrf2 and inhibiting NLRP3 inflammasome. Exp Ther Med 2020; 19:1084-90.
4. Cosman F, Crittenden DB, Adachi JD, et al. Romosozumab treatment in postmenopausal women with osteoporosis. N Engl J Med 2016; 375:1532-43.
5. Liu H, Zhao H, Lin H, et al. Relationship of COL9A1 and SOX9 genes with genetic susceptibility of postmenopausal osteoporosis. Calcif Tissue Int 2020; 106:248-55.
6. Xiao Y, Wei R, Yuan Z, et al. Rutin suppresses FNDC1 expression in bone marrow mesenchymal stem cells to inhibit postmenopausal osteoporosis. Am J Transl Res 2019; 11:6680-90.
7. Kocijan R, Muschitz C, Geiger E, et al. Circulating microRNA signatures in patients with idiopathic and postmenopausal osteoporosis and fragility fractures. J Clin Endocrinol Metab 2016; 101:4125-34.
8. Xi G, Wai C, Rosen CJ, Clemmons DR. A peptide containing the receptor binding site of insulin-like growth factor binding protein-2 enhances bone mass in ovariectomized rats. Bone Res 2018; 6:23.
9. Cai W, Zhao Q, Shao J, et al. MicroRNA-182 Alleviates neuropathic pain by regulating Nav1.7 following spared nerve injury in rats. Sci Rep 2018; 8:16750.
10. Ma XY, Wen XX, Yang XJ, et al. Ophiopogonin D improves osteointegration of titanium alloy implants under diabetic conditions by inhibition of ROS overproduction via Wnt/beta-catenin signaling pathway. Biochimie 2018; 152:31-42.
11. Huang Q, Gao B, Wang L, et al. Ophiopogonin D: A new herbal agent against osteoporosis. Bone 2015; 74:18-28.
12. Sarshad AA, Juan AH, Muler A, et al. Argonaute-

miRNA complexes silence target mRNAs in the nucleus of mammalian stem cells. Mol Cell 2018; 71:1040-50.
13. Gao L, Yan SB, Yang J, et al. MiR-182-5p and its target HOXA9 in non-small cell lung cancer: a clinical and in-silico exploration with the combination of RT-qPCR, miRNA-seq and miRNA-chip. Bmc Med Genomics 2020; 13:3.
14. Huang XX, Zhang Q, Hu H, et al. A novel circular RNA circFN1 enhances cisplatin resistance in gastric cancer via sponging miR-182-5p. J Cell Biochem 2020; doi: 10.1002/jcb.29641.
15. Qi R, Liu H, Liu C, Xu Y, Liu C. Expression and short-term prognostic value of miR-126 and miR-182 in patients with acute stroke. Exp Ther Med 2020; 19:527-34.
16. Inoue K, Deng Z, Chen Y, et al. Bone protection by inhibition of microRNA-182. Nat Commun 2018; 9:4108.
17. Pan BL, Tong ZW, Li SD, et al. Decreased microRNA-182-5p helps alendronate promote osteoblast proliferation and differentiation in osteoporosis via the Rap1/MAPK pathway. Biosci Rep 2018; 38(6):BSR20180696.
18. Luzi E, Marini F, Sala SC, Tognarini I, Galli G, Brandi ML. Osteogenic differentiation of human adipose tissue-derived stem cells is modulated by the miR-26a targeting of the SMAD1 transcription factor. J Bone Miner Res 2008; 23:287-95.
19. Skarzynska J, Damulewicz M, Filipowska J, Madej W, Leboy PS, Osyczka AM. Modification of Smad1 linker modulates BMP-mediated osteogenesis of adult human MSC. Connect Tissue Res 2011; 52:408-14.
20. Fu HL, Pan HX, Zhao B, et al. MicroRNA-100 inhibits bone morphogenetic protein-induced osteoblast differentiation by targeting Smad1. Eur Rev Med Pharmacol Sci 2016; 20:3911-19.

Fusobacterium necrophorum lktA gene variants from cow foot rot lesions: molecular characterization, phylogeny and homology modelling analysis

H. Ashraf[1], S. Nawaz[1], M. Z. Yousaf[2], Z. Rashid[3], A. R. Awan[1], M. Wasim[1], M. Tayyab[1], S. Saeed[1] and S. Firyal[1]

[1]Institute of Biochemistry and Biotechnology, University of Veterinary and Animal Sciences, Lahore, Pakistan; [2]School of Life Sciences, Forman Christian College University Lahore, Pakistan; [3]Department of Biomedical Engineering, Faculty of Engineering, Science, Technology and Management, Ziauddin University, Karachi, Pakistan

Received December 18, 2020 – Accepted February 11, 2021

Foot rot is a necrotic, infectious, and debilitating disease of hooves in ruminants caused by the concordant effect of *Dichelobacter nodosus* and *Fusobacterium necrophorum.* This work aimed for identification and prevalence of leukotoxin gene, *lktA*, variant strains of *F. necrophorum* in cow foot rot lesions. A total of twenty samples were collected from the feet of foot rot-affected cattle. Bacterial DNA was extracted and amplification of *lktA* was performed through polymerase chain reaction (PCR) followed by direct DNA sequencing. The sequencing data was subjected to homology search, multiple sequence alignment and phylogenetic tree reconstruction using respective software for taxonomic characterization. This study revealed the presence of JKS-F3, JKS-F2 and JKS-F1 in the foot rot-affected cattle in the local isolates of Punjab, Pakistan, with high prevalence of *F. necrophorum* JKS-F3 strain (80%) with a lesion score of 3 and 4. The 3D structure of protein was performed using comparative homology modeling with I-TASSER. The accuracy of the predicted 3D structure was checked using Ramachandran plot analysis and showed that 85.4% amino acids were in the favored region i.e., extended conformation of β-sheets are clustered in the right hand-region. These findings suggest that early and accurate identification and characterization of the causative agent of foot rot is a preliminary requirement to control the infection.

Foot rot (Interdigital phlegmon) is a necrotic, infectious, and debilitating disease of hooves in ruminants including cattle, goats, and sheep. It is one of the common reasons of weakness in cows and sheep (1), and is an acute disease which produces lesions on the subcutaneous tissues of ruminants (2). *D. nodosus* is considered as a primary agent and an important component for causing foot rot, whereas *F. necrophorum* is an auxiliary component involved in predisposition to foot rot (3). *F. necrophorum* contributes toward the duration and intensity of the disease (4). The virulent strains of *F. necrophorum* produce hemolysin, endotoxin, haemagglutinin, adhesion and leukotoxin. Among all these factors leukotoxin is the most virulent, and its structural protein is encoded by *lktA* gene. The higher transcription of *lktA* gene of *F. necrophorum* subsp. *necrophorum* at exponential growth describes the virulence of the species (5). Hence, *lktA* gene is highly useful for the detection of *F. necrophorum* and helpful

Key words: foot rot; Fusobacterium necrophorum; lktA gene; cow; phylogenetic analysis

Corresponding Author:
Sehrish Firyal,
Assistant Professor,
Institute of Biochemistry and Biotechnology,
University of Veterinary and Animal Sciences,
Lahore, Pakistan
Tel.: +924299211449 450
e-mail: sehrishfiryal@uvas.edu.pk

0393-974X (2021)
Copyright © by BIOLIFE, s.a.s.
This publication and/or article is for individual use only and may not be further reproduced without written permission from the copyright holder.
Unauthorized reproduction may result in financial and other penalties
DISCLOSURE: ALL AUTHORS REPORT NO CONFLICTS OF INTEREST RELEVANT TO THIS ARTICLE.

in determination of variation among its strains (6). The *lktA* gene has four variant strains present in the *F. necrophorum* subsp. *necrophorum,* namely JKS-F1, JKS-F2, JKS-F3 and JKS-F4, in foot rot lesions, which have been submitted to the National Centre for Biotechnology Information (NCBI). Recently, for the reduction of prevalence and severity of foot rot disease in cattle, a vaccine consisting of fusion of *F. necrophorum* leukotoxoid and pyrogen of bacteria was used, but failed to prove effectively against the disease (7), therefore there is an urgent need to find an effective method. The occurrence of variant strains of *F. necrophorum* in foot rot lesions vary greatly among the breeds of different regions. PCR-based techniques are the rapid molecular technique for the identification of *F. necrophorum* and its variant strains (8).

In Pakistan, foot rot is endemic in the Punjab province. Recently, its severity has increased and attained significant importance in animal husbandry. Little is known about the *lktA* variant(s) associated with severe foot rot in cow (lesion score of 4) and no study has described the distribution and predominance of *lktA* variant(s) of *F. necrophorum* in foot rot lesions. The current work aimed to investigate the prevalence and identification of *lktA* variants of *F. necrophorum* linked to severe foot rot in cow.

MATERIALS AND METHODS

Sample collection

A total of 20 swab samples were randomly collected from clinically-diagnosed foot rot-affected cows (Holstein Friesien) from the lesions formed between the horn of the hoof and the underlying skin tissues. The samples were collected from one foot of each cow using sterile cotton swabs and were transported to the laboratory in thioglycolate broth which is an enriched and differential media for the growth of anaerobic microorganisms. This study was approved by the Institutional ethics review board of the University of Veterinary and Animal Sciences Lahore, Pakistan.

Isolation and identification of bacteria from clinical samples

For microbiological analysis, initially samples were plated on blood agar media (Oxoid CM0331) with the addition of antibiotics vancomycin and neomycin at 5 mg and 100 mg/ml of medium, respectively, for the growth of *F. necrophorum* bacteria. Bacterial growth media plates were incubated anaerobically at 37°C for 48 h. Anaerobic environment was created using an appropriate catalyst (Oxoid™ AnaeroGen™ AN0025A) and an anaerobic gas jar (Oxoid, AG0025A). The suspected irregular, flat, grayish colonies showing β-hemolysis zone were restreaked to obtain pure culture. Species confirmation of the isolates was made through observation of typical cellular morphology of *F. necrophorum* on gram-stained smear and detection of *lktA* gene fragments by PCR.

DNA extraction and amplification of lktA Gene

Bacterial DNA was extracted from the cultured media by standard procedure for anaerobic bacterium. Extracted DNA was checked for qualitative and quantitative analysis using 1% gel electrophoresis and Nanodrop spectrophotometer (IMPLEN, Germany). For amplification of *lktA* gene, specific primers for three strains (JKS-F1, F2 and F3) were used (Table I). The composition of 25 µL reaction mixture included 50 ng of 2 uL DNA, forward primer 0.25 uL (10pMol), reverse primer 0.25 uL (10pMol), PCR buffer 2.5 uL, $MgCl_2$ 2.5

Table I. *Primer sequence of lktA gene variants*

Strain	Sequence	Amplicon size
JKS-F1	F: AGTAGGTTCTGTCGGTGTTGG R: CTTTGGTAACTGCCACTGCTG	404 bp
JKS-F2	F: TCGGAGTAGTAGGTTCTGTTGG R: CTTTGGTAACTGCCACTGCTG	401 bp
JKS-F3	F: GGAGTAGTAGGTTCTGTCGGTGTT R: CTTTGGTAACTGCCACTGCTG	404 bp

uL, dNTPs 2.5 uL, *Taq polymerase* 0.25 uL and deionized water 13.75uL. The conditions of PCR included initial denaturation for 5 min at 95ºC followed by 35 cycles of 30s denaturation at 94ºC, annealing at 54-64°C for 30 s and 45 s extension at 72ºC. The cycles were followed by a final extension of 10 min at 72ºC.

DNA sequencing and bioinformatics analysis

Successfully amplified PCR products were sequenced subject to forward and reverse orientation sequencing PCR reactions followed by Sanger's chain termination chemistry Applied Biosystems®3130 Genetic Analyzer. The ab1 sequencing results of *lktA* gene were trimmed manually before loading for homology search in Basic Local Alignment Tool (BLASTn), and multiple sequence alignment was performed against previously reported sequences of *F. necrophorum* in NCBI using CLUSTAL X followed by construction of phylogenetic tree in MEGA X by using neighbor-joining method. The cladogram was validated by generating 1000 bootstrap trees and each branch represented a bootstrap value in the final tree.

Homology modelling and protein prediction analysis of lktA gene

The findings of the present study were further validated by translating nucleotide sequences into putative amino acid and performing multiple sequence alignment through EMBOSS-TransSeq and CLUSTAL Omega (EMBL-EBI) software, respectively. The amino acid sequence of *lktA* were analyzed by I-TASSER to predict 3D protein structure and function. The 3D structure was refined and checked for accuracy using Ramachandran plot analysis in GalaxyWEB online tool.

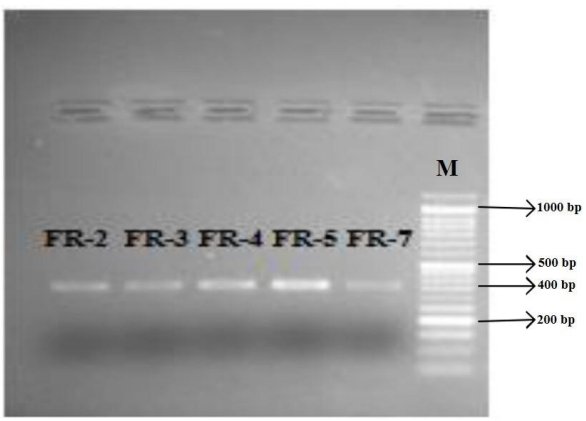


Fig. 1. *Leukotoxin (lktA) gene fragment (400bp) detection of Fusobaterium necrophorum through polymerase chain reaction. Lane 1-5 (left to right): test samples lane. Lane M: 100 bp DNA ladder.*

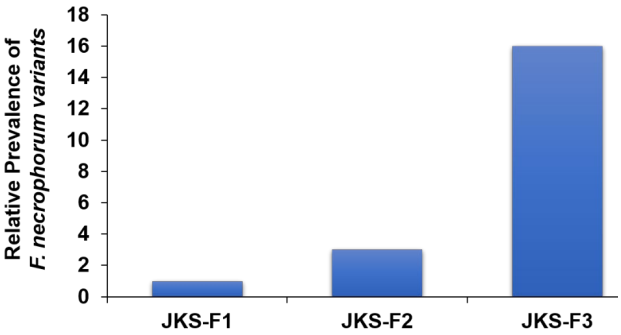


Fig. 2. *Bar graph showing the relative prevalence of JKS-F1, JKS-F2 and JKS-F3 strains in the foot rot samples of cattle.*

RESULTS

Prevalence and distribution of lktA variants in foot rot-affected cows

The samples collected from lesions of foot rot-affected cows were positive for *F. necrophorum,* as revealed by successful amplification of *lktA* (400 bp) gene fragment (Fig. 1). Sixteen (80%) out of twenty isolates carried JKS-F3 *lktA* variant, while JKS-F1 and JKS-F2 variants were noticed in one (5%) and three (15%) samples, respectively (Fig. 2). Samples of the foot rot disease were detected based on lesion score from 1 to 4 which describes disease severity. Score 1 was given to moderate inflammation, score 2 was provided to necrotic inflammation, score 3 was given to necrotic inflammation extended to abaxial wall of hoof, and score 4 was given to the condition of hoof structure disrupted extending to sensitive laminae. Out of twenty positive samples, 15 (75%) samples carried JKS-F3 *lktA* variant of *F. necrophorum* with lesion score 4 and 3, while the rest belonged to JKS-F2 variant with lesion scores of 2 and 1, respectively. Hence, *lktA* variant (JKS-F3)

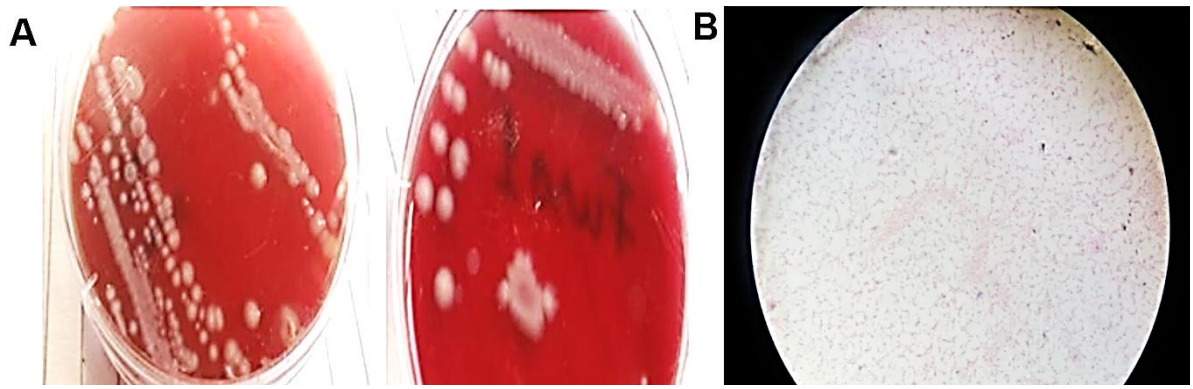


Fig. 3. *Morphological analysis of Fusobacterium necrophorum.* ***A****) Growth of Fusobacterium necrophorum on blood agar media.* ***B****) Gram staining images showing gram-negative rods at 100X lens.*

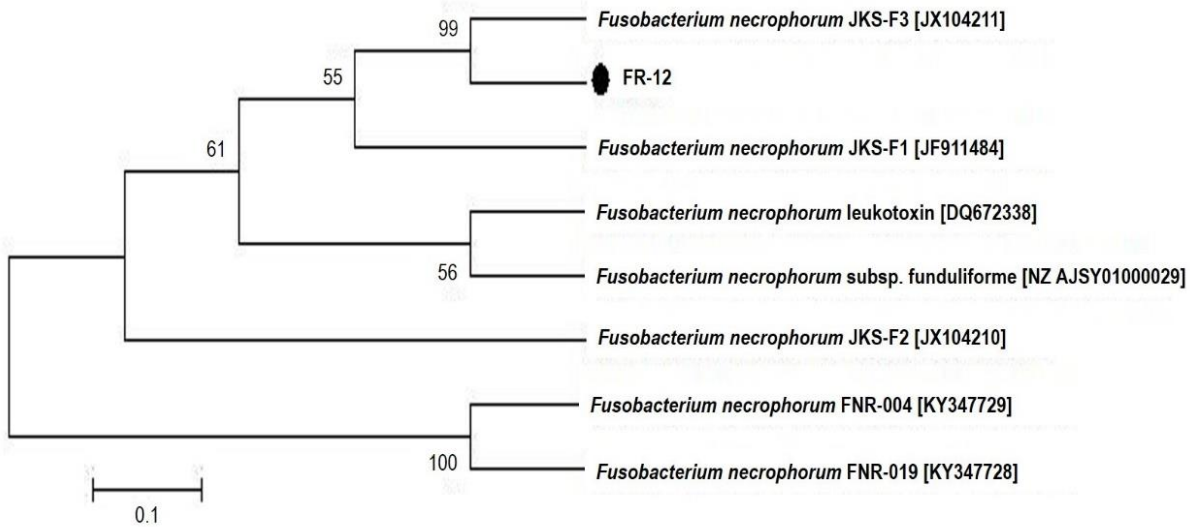


Fig. 4. *Cladogram of leukotoxin (lktA) gene sequences. The tree was constructed through neighbor-joining method using lktA nucleotide sequences identified from cow foot rot lesion sample (FR-12) showing genetic similarity with Fusobacterium necrophorum JKS-F3 [JX104211] strain.*

of *F. necrophorum* is associated with severe foot rot and ultimately contributes towards the severity and duration of this disease.

Isolation of F. necrophorum from clinical samples

All the twenty isolates showed characteristic morphological features peculiar to bacterium *F. necrophorum* when grown on blood agar media (Fig. 3A). The colony characteristics on Gram's staining revealed gram-negative pink rods (Fig. 3B).

Phylogenetic analysis of lktA variants of F. necrophorum

The nucleotide sequences of *lktA* variants (JKS-F1/F2 and F3) of *F. necrophorum* from foot rot lesions of affected cows of Punjab, Pakistan were compared against already submitted *lktA* variants of *F. necrophorum*. A phylogenetic tree of each *lktA* variant (JKS-F1/F2 and F3) was created based on minimum evolutionary distance to give a well-resolved tree. It was found that the newly identified sequence of *F. necrophorum* of this study, FR-12, was the consensus sequence of sixteen aligned and verified sequences of JKS-F3 strain of *lktA* gene of *F. necrophorum* by using BLASTn and Clustal X. FR-12 showed strong sequence similarity of 99% branch value with *F. necrophorum* strain JKS-F3 [JX104211] compared to the other previously

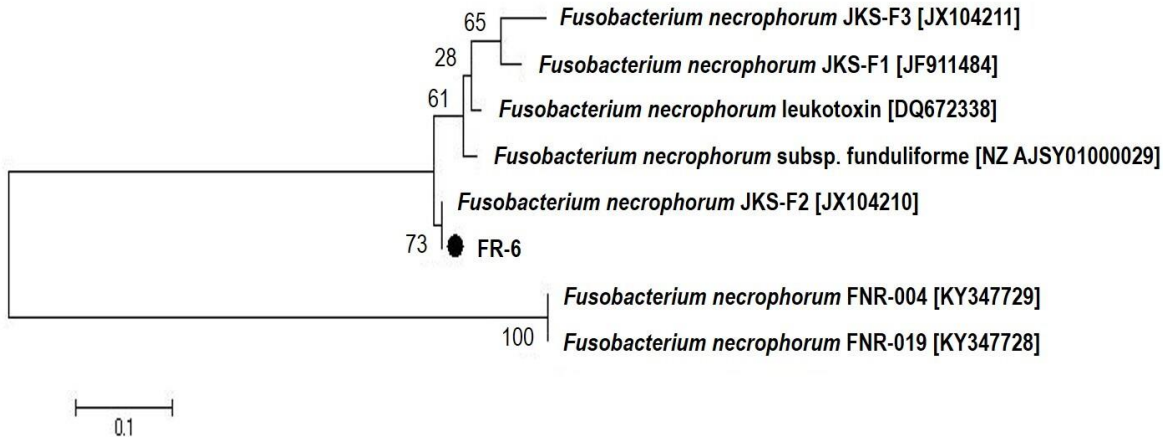


Fig. 5. *Cladogram of leukotoxin (lktA) gene sequences. The tree was constructed through neighbor-joining method using lktA nucleotide sequences identified from cow foot rot lesion sample (FR-6) showing genetic similarity with Fusobacterium necrophorum JKS-F2 [JX104210] strain.*

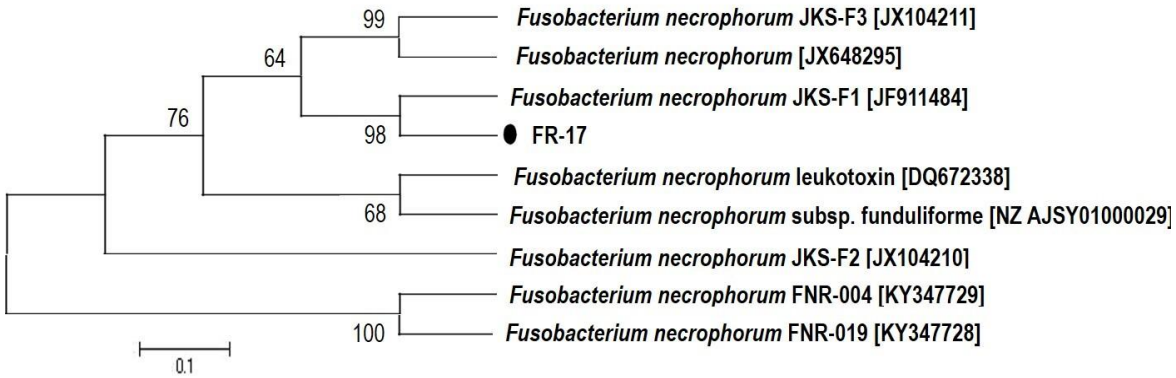


Fig. 6. *Cladogram of leukotoxin (lktA) gene sequences. The tree was constructed through neighbor-joining method using lktA nucleotide sequences identified from cow foot rot lesion sample (FR-17) showing genetic similarity with Fusobacterium necrophorum JKS-F1 [JF911484] strain.*

reported sequences of *F. necrophorum* variants (JKS-F1 and F2) (Fig. 4). The sequence of sample FR-6 was the consensus sequence of three aligned and verified sequences of JKS-F2 strain of *F. necrophorum*. FR-6 was the consensus sequence of three aligned and verified sequences of JKS-F2 strain of *F. necrophorum* by using BLAST and Clustal W. FR-6 showed maximum sequence similarity (73%) with *F. necrophorum* strain JKS-F2 [JX104210] (Fig. 5). The newly identified sequence of *F. necrophorum* of this study (FR-17) showed maximum sequence homology (98%) with *F. necrophorum* strain JKS-F1 [JF911484] compared to the other previously reported sequences of JKS-F2 strain (Fig. 6). Based on phylogenetic analysis, *lktA* variants JKS-F1 and JKS-F3 were placed in a similar branch which revealed genetic similarity between them.

In silico leukotoxin protein sequence and structure analysis

Amino acid sequence alignment of *lktA* variants (FR-12/6 and17) from Punjab, Pakistan revealed ~99% between FR-12 (JKS-F3) and FR-17 (JKS-F1) strains. In contrast, the sequence identity with FR-6

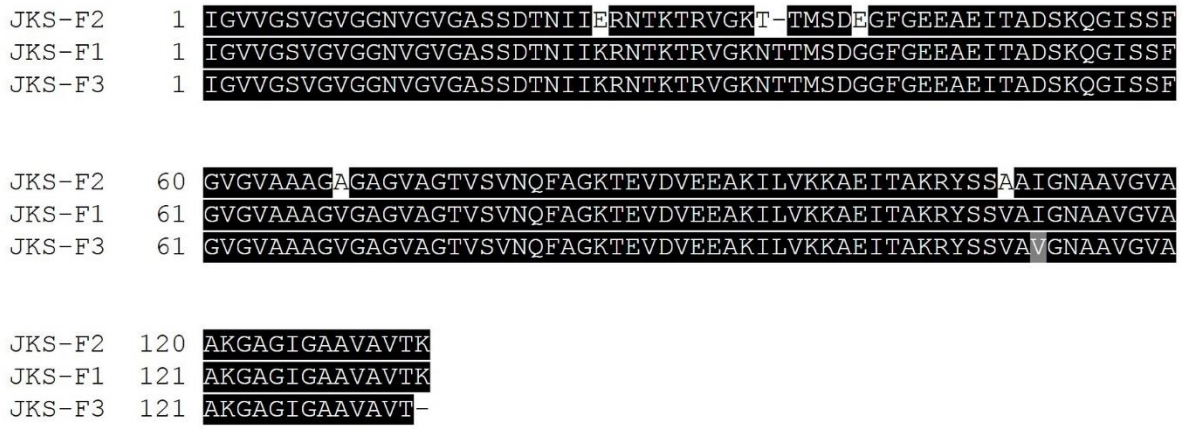


Fig. 7. *Alignment of putative amino acid sequence of lktA gene variants (JKF-F1/F2/F3) of Fusobacterium necrophorum. Grey and black boxes indicate similar and identical residues. The alignment was generated using CLUSTAL Omega and shaded with BoxShade.*

(JKS-F2) was only ~70% (Fig. 7). The product of JKS-F3 *lktA* variant is 135 amino acid protein with molecular weight 12,750 Da. This sequence was utilized to predict the 3D structure of the protein. I-TASSER predicted the structure of lktA protein with a C-score of -1.63 which signifies a structure with good confidence. The estimated TM-score of the predicted protein structure was 0.32±0.10, indicating the better value of similarity between the predicted model and the template protein used for modeling (Fig. 8). There is not much information available about the biological, cellular and molecular function of leukotoxin protein, the COACH database predicted 2qiaA URIDINE-5'-DIPHOSPHATE-3-O-(R-3-HYDROXYMYRISTOYL)-N-ACETYL-D-GLUCOSAMINE and 4k6rA (N-ACETYL-ALPHA-D-GLUCOSAMINE 1-PHOSPHATE as ligand of leukotoxin with 0.50 and 0.44 C-score, respectively. The COACH database was also used to predict the biological process of leukotoxin protein and its location inside the cell. It is predicted to be the cellular component of cytoplasm and is involved in the lipid A biosynthetic process

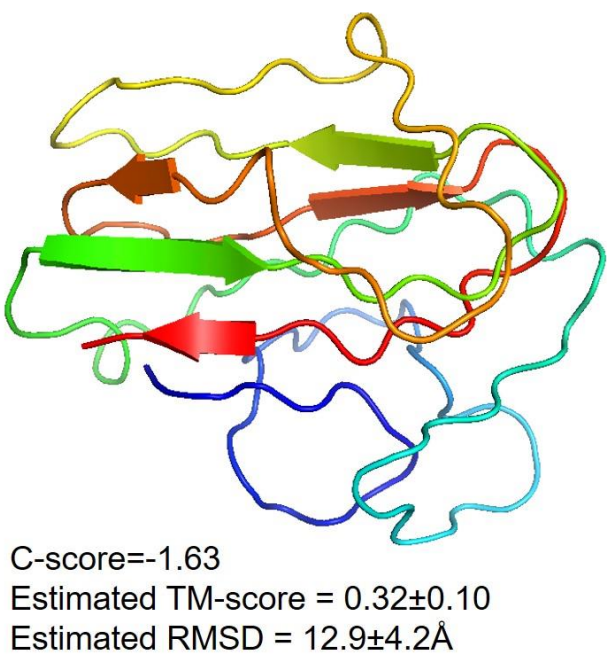


Fig. 8. *The three-dimensional predicted structure of JKS-F3 lktA protein by I-TASSER. The C-score and estimated TM and RMSD values depicted structure accuracy against template from protein data bank.*

Accession codes

The bacterial sequences were deposited at the National Center for Biotechnology Information (NCBI), and GenBank accession numbers were assigned for samples FR-17, FR-6 and FR-12 as *Fusobacterium necrophorum* JKS-F1 [MW266034], *Fusobacterium necrophorum* JKS-F2 [MW266035] and *Fusobacterium necrophorum* JKS-F3 [MW266036], respectively.

DISCUSSION

This study describes the identification and

prevalence of *F. necrophorum* in foot rot-affected cows through molecular characterization of *lktA* gene variants. The overall prevalence of foot rot disease in infected feet of cattle in Punjab, Pakistan showed high ~86% frequency of *F. necrophorum* JKS-F3 strain compared to the other variants (JKS-F2 and F1). The prevalence of *F. necrophorum* in foot rot is mainly linked with favorable conditions in soil because of contamination of manure. *F. necrophorum* is a commensal bacterium of the ruminant's alimentary canal and is mostly shed in feces (9). The identification of *F. necrophorum* was performed using culture-based and molecular techniques to elucidate the concordance between these two techniques. The high detection rate of leukotoxin variants of *F. necrophorum* through PCR, using *lktA* genetic marker, revealed the accuracy of PCR which is in agreement with previous studies (10), demonstrating PCR as a useful and predominant technique for detecting low concentrations of *F. necrophorum*. The current study reports the three most common variants of *F. necrophorum* in the lesions formed between the horn of the hoof and underlying skin tissues of foot rot-affected cows. Moreover, it was noticed that single strain infection is prevalent in individual samples; these findings correlate with the work of Zhou et al. (2009), on identification of foot rot in cattle, sheep and goats in New Zealand. However, another study reported detection of multiple strain infection of *F. necrophorum* (JKS-F1,F2 and F30 in a single sample of foot rot-affected sheep (11). It has been reported that multiple strain/serotype infections were common in *D. nodosus* in which up to seven serotypes were detected in a single sample of sheep hoof (12).

In the present work, JKS-F3 strain was detected at a high rate (80%) associated with severe foot rot showing lesion score of 3 and 4. The high occurrence of this *lktA* variant in cows is due to high adaptation according to environmental conditions compared to other *lktA* variants (JKS-F1, F2 and F3). It was also observed that presence of *lktA* variant JKS-F3 is associated to a higher level of virulence and adaptation in cow, which depicted disease severity compared to other strains. The reason behind this is still uncertain and further studies based on higher sample size of herds from different geographical areas are required to validate the findings.

The three indigenously isolated *lktA* variants *F. necrophorum* (FR-6, 12 and 17) from foot rot lesions of cows in the present study may represent different species of *Fusobacterium* as described previously (13). A similar report also illustrated the phenomenon of reclassification of "*Fusobacterium strains*" from horses based on phylogenetic analysis of 16S rRNA gene, phenotype, and DNA-DNA hybridization (14). To develop preventive measures and appropriate treatment for foot rot, these findings may be helpful in understanding the pathogenesis.

In conclusion, the local isolates of foot rot-infected feet of cattle showed higher prevalence of JKS-F3 strain of *F. necrophorum* compared to other strains. *lktA* gene can be used as a genetic marker for molecular characterization of variant strains of *F. necrophorum* recovered from foot rot lesions. Phylogenetic analysis has shown that JKS-F3 strain from indigenous isolates has maximum similarity with the JKS-F3 strain of Kashmir, India. These findings may further contribute towards our understanding the pathogenesis of ovine foot rot, and for the development of appropriate treatment and prevention measures. Therefore, this *lktA* variant of *F. necrophorum* needs to be considered in outbreak management or maintaining quarantine or in future strategies to combat foot rot.

REFERENCES

1. Abbott KA, Lewis CJ. Current approaches to the management of ovine foot rot. Vet J 2005; 169:28-41.
2. Van Metre DC. Pathogenesis and treatment of bovine foot rot. Vet Clin Food Anim Pract 2017; 33:183-94.
3. Bennett G, Hickford J, Sedcole R, Zhou H. Dichelobacter nodosus, Fusobacterium necrophorum and the epidemiology of foot rot. Anaerobe 2009; 15:173-76.
4. Witcomb LA, Green LE, Calvo-Bado LA, et al First study of pathogen load and localisation of ovine foot rot using fluorescence in situ hybridisation (FISH). Vet Microbiol 2015; 176:32-27.
5. Tadepalli S, Stewart GC, Nagaraja TG, Narayanan SK. Human Fusobacterium necrophorum strains have a leukotoxin gene and exhibit leukotoxic activity. J Med Microbiol 2008; 57:225-31.

6. Nagaraja TG, Narayanan SK, Stewart GC, Chengappa MM. Fusobacterium necrophorum infections in animals: pathogenesis and pathogenic mechanisms. Anaerobe 2005; 11:23-246.
7. Jones G, Jayappa H, Hunsaker B, et al. Efficacy of an Arcanobacterium pyogenes-Fusobacterium necrophorum bacterin-toxoid as an aid in the prevention of liver abscesses in feedlot cattle. Bov Pract 2004; 36-44.
8. Ozgen EK, Cengiz S, Ulucan M, et al. Isolation and identification of Dichelobacter nodosus and Fusobacterium necrophorum using the polymerase chain reaction method in sheep with foot rot. Acta Vet Brno 2015; 84:97-104.
9. Clifton R, Giebel K, Liu NLBH, et al. Sites of persistence of Fusobacterium necrophorum and Dichelobacter nodosus: a paradigm shift in understanding the epidemiology of foot rot in sheep. Sci Rep 2019; 9:1-11.
10. Saleh MA, Muhammed HA, Alnasrawi AA. A concordance study between polymerase chain reaction assay and conventional culture-based methods for detection of Fusobacterium necrophorum. Indian J Forensic Med Toxicol 2020; 14:827-33.
11. Farooq S, Wani SA, Hassan MN, et al. The detection and prevalence of leukotoxin gene variant strains of Fusobacterium necrophorum in foot rot lesions of sheep in Kashmir, India. Anaerobe 2018; 51:36-41.
12. Zhou H, Hickford JGH. Novel fimbrial subunit genes of Dichelobacter nodosus: recombination in vivo or in vitro? Vet Microbiol 2000; 76:163-74.
13. Holm K, Collin M, Hagelskjær-Kristensen L, et al. Three variants of the leukotoxin gene in human isolates of Fusobacterium necrophorum subspecies funduliforme. Anaerobe 2017; 45:129-32.
14. Dorsch M, Lovet DN, Bailey GD. Fusobacterium equinum sp. nov., from the oral cavity of horses. Int J Syst Evol Microbiol 2001; 51:1959-63.

Construction of specific Smo lentivirus and expression of infected pancreatic cancer cells positive for CD24CD44 surface antibody

P. Cong[1], C. Yi[2], X. Wang[2] and Y. Peng[1]

[1]Department of Hepatobiliary and Pancreatic Surgery, Nanchong Central Hospital, Sichuan, P.R. China; [2]Department of Hepato-Pancreato-Biliary Surgery, Cancer Hospital Affiliated to Xinjiang Medical University, Urumqi, Xinjiang, P.R. China

Received September 11, 2020 – Accepted February 23, 2021

This study aimed to construct a vector lentivirus carrying the Smo gene and transfect pancreatic cancer cells positive for CD24CD44 surface antibody and detect the infectivity. A lentivirus carrying a specific Smo fragment was designed and synthesized, and its functionality was tested. An overexpression group, inhibitory group, and negative control group were used for subsequent experimental research and comparison. A virus was successfully designed and produced. The best viral load was the $1X10^6$ TU virus, where the cell growth and fluorescence effect of culture wells with polybrene dilution were the best. These are the transfection conditions and transfection parameters for subsequent experiments. This plasmid was detected with a flag antibody by Western blot. The result was that it had a large specific 250kD band, and the membrane protein was overexpressed successfully. The expression results of Smo in five groups of cells after virus transfection detected by RT-PCR: blank group were 1.0038±0.0344, CON238 negative group: 1.0276±0.2944d, CON077 negative group: 0.8793±0.0402; LV-SMO15570-2 overexpression group: 2.7479±0.8308, and LV-SMO-RNAi37304-1 inhibition group: 0.2386±0.0481. There were differences among the overexpression group and inhibition group with the other three groups. Homogeneity of variance: Bartlett F = 4.3530, P = 0.0016 < 0.05, heterogeneous. K-W test: $c^2 = 10.9905$* P = 0.0267, and there was a statistically significant difference. The designed virus achieved the goal requirements. An sRNA fragment was designed for the key gene Smo of the Hh signaling pathway, and a vector lentivirus carrying this fragment was successfully constructed. The expression of Smo was analyzed after transfecting SW1990CD24CD44 positive cells, suggesting that the function of the RNA fragment designed for the key gene Smo in this experiment was successful.

Smo is an important member of the Hh signaling pathway, playing a bridge role in the process of signal transmission. The Hedgehog signal pathway receptor Smo gene is located on chromosome 7q31-7q32 (1). Under normal conditions, it maintains normal metabolism and function in normal tissues and cells. Smo protein is low expressed or not expressed; if Smo is overexpressed, it transmits the Hh signal to the cells. The downstream Gli protein factor is transcriptionally activated, resulting in modification and transformation, then Gli enters the nucleus, and the expressions of multiple target genes are then activated. In this way, cell differentiation, proliferation, and apoptosis are regulated, and results in induction of tumorigenesis (2, 3).

Small interfering RNA (siRNA) is the key link in the intermediate interference process of RNA interference (RNAi) (4, 5). Because of a specific ability that can be targeted to control gene expression, it can provide expectations in the treatment of genetic diseases and malignant tumors. As an anti-tumor strategy, it has been the focus in the field of inhibition of Hh signaling pathways. A variety of materials have been reported. For example, catechin, an active

Key words: pancreatic cancer; Smo-carrying gene; retrovirus; transfection; vector lentivirus

Corresponding Author:
Dr Yong Peng,
Department of Hepatobiliary and Pancreatic Surgery,
Nanchong Central Hospital,
No. 97 of Renmin South Road, Shunqing District,
Sichuan 637000, P.R. China
Tel.: +86 18181112175 - Fax: +86 0817 2793010
e-mail: yomgpemg@163.com

0393-974X (2021)
Copyright © by BIOLIFE, s.a.s.
This publication and/or article is for individual use only and may not be further reproduced without written permission from the copyright holder.
Unauthorized reproduction may result in financial and other penalties
DISCLOSURE: ALL AUTHORS REPORT NO CONFLICTS OF INTEREST RELEVANT TO THIS ARTICLE.

substance in green tea discovered by Tang et al. (6), inhibits the ability of pancreatic CSC self-renewal by inhibiting members of the Hh signaling pathway, including Smo, Ptch, Gli1, and Gli2. Sulforaphane, an antioxidant in *Decidaceae* plants, can reduce pancreatic cancer stem cells self-renewal by inhibiting Smo, Gli1, and Gli2 in the Hh signaling pathway (7, 8). Resveratrol 3, 4, 5-trihydroxystilbene can inhibit proliferation and induce apoptosis by inhibiting the Hh signaling pathway in pancreatic cancer (9). Erismodegib (LDE225), an Smo antagonist, can inhibit tumor growth and prolong survival rate in mice with islet cell tumors (10). Although the clinical efficacy of the combination therapy with Hh inhibitors is controversial, effective strategies will surely be found to treat pancreatic cancer.

When targeting the inhibitors of Hh signaling pathways, targeted gene technology has attracted extensive attention. In the present study, a lentivirus that can affect Smo in the Hh signaling pathway was constructed. The quality and function of lentivirus were detected, and it was confirmed that the constructed lentivirus was functional. The expression of Smo, a member of the Hh signaling pathway in pancreatic cancer CD24CD44 double-positive cells transfected with the virus, was detected by real-time polymerase chain reaction (PCR) and Western blot, to have a deeper understanding of its biological characteristics, the maintenance of tumor characteristics, and the interaction of various signal pathways.

MATERIALS AND METHODS

Vector cleavage and target gene amplification

The human Smo (NM_005631) was carried by GV358 (Shanghai Jikai Gene Co., Ltd., China). The sequence was Ubi-MCS-3FLAG-SV40-EGFP-IRES-puromycin. The clone site was AgeI/AgeI (Shanghai Jikai Gene Chemical Technology Co., Ltd., China). The carrier map is shown in Fig. 1. The control number is CON238.

The 50-μL restriction cleavage system was prepared, and the following added in turn according to the reagent system sequence: 42 μL of ddH_2O, 5 μL of 10 × Cut Smart Buffer2, 2 μL of purified plasmid DNA (1 μg/μL), 1 μL of Age I (10 U/μL), and 1 μL of ddH_2O (10 U/μL), respectively. Reagents were shaken to mix in a pipette, pipetted gently, centrifuged temporarily, and placed at 37°C for 3 h or overnight. Restriction enzyme cleavage product of vectors was subjected to agarose gel electrophoresis (SBS Genetech Co., Ltd.), and objective bands were recovered. The restriction enzymes (NEB, Ipswich, MA, USA) were selected according to the required restriction enzyme reaction. The restriction enzymes should reach at least 50% of the reaction activity under the specified Buffer conditions. The specific reaction activities of various restriction enzymes under different Buffer conditions were introduced from their respective instructions.

Primer description contained an exchange pair base, restriction site, and 5' end sequence of the target gene, which

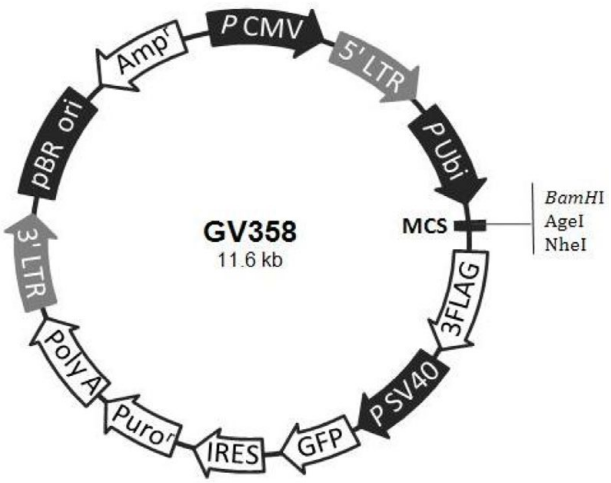


Fig. 1. *Vector map*

Table I. *Primers used in target gene fragment acquisition experiment*

ID	seq
SMO (15570-2) - P1	GAGGATCCCCGGGTACCGGTCGCCACCATGGCCGCTGCCCGCCCAG
SMO (15570-2) - P2	TCCTTGTAGTCCATACCGAAGTCCGAGTCTGCATCCATG

was used to catch the target gene through PCR (Table I). The reaction systems listed were prepared as follows: 32.5 μL of ddH_2O, 10 μL of 5 × PS Buffer, 4 μL of dNTP Mix (2.5 mM each; cat no. D4030A, Takara, Tokyo, Japan), 1 μL of upstream primer (10 μM), 1 μL of downstream primer (10 μM), 1 μL of template 1 (10 ng/μL), 0.5 μL of PrimeSTAR H DNA polymerase (cat no. R010B, Takara). Reagents were pipetted gently, and mixed evenly, centrifuged temporarily, and placed in a PCR machine for reactions. The source of the template was plasmid or bacterial liquid. The dosage of the plasmid template was usually less than 200 ng, and the dosage of the bacterial liquid template was routinely 1 μL, referring to the supporting instructions of PrimeSTAR H DNA polymerase. The extension time was determined according to the length of the PCR products. PrimeSTAR H DNA polymerase extension time was calculated according to 1 KB/min.

The reaction system was prepared (Table II). An EP tube was placed in an ice-water bath, reagents were shaken to mix in a pipette, pipetted gently, centrifuged temporarily to avoid bubbles as much as possible, placed at 37°C for 30 min, then placed again in an ice-water bath, cooled for 5 min, and then transformed immediately.

Transformation

In 100 μl of competent cells (Genechem, Shanghai, China), 10 μl of exchange reaction products were added, then mixed evenly. The tube wall was gently flicked several times, then the tube was placed on ice for 30 min, underwent heat shock at 42°C for 90 s, incubated in an ice-water bath for 2 min, added with 500 μl of medium LB, and cultured on a shaking table at 37°C for 1 h. An appropriate amount of bacterial liquid was extracted, applied evenly on the plate containing the corresponding antibiotics, and finally invertedly cultured in a constant-temperature incubator for 12–16 h.

PCR and sequencing

In the present study, one of the primers was located on the vector and the other in the target gene, which was used to identify the transformants by colony PCR (Table III). It was prepared according to the following reaction system (BIO-RAD, Hercules, CA, USA): 9.2 μL of ddH_2O, 10 μL of 2 × Taq Plus Master Mix (Vazyme, Nanjing, China), 0.4 μL of upstream primer (10 μM; GeneRay, Shanghai, China), 0.4 μL of downstream primer (10 μM; GeneRay), single colony. Reagents were shaken to mix, then centrifuged temporarily. In the clean bench test, a single colony was selected and transferred with a sterile pipette tip into a 20-μl identification system, pipetted and shaken to mix in a pipette, then placed in a PCR machine for reactions.

The identified positive clone transformants were inoculated in a suitable LB liquid medium containing corresponding antibiotics and cultured at 37°C for 12–16 h. Then the bacterial solution was sequenced, and the target gene sequences and sequencing results were compared, analyzed, and processed.

Plasmid extraction and lentivirus packaging

The correctly sequenced bacterial solution was

Table II. *PCR products and vector exchange reaction system*

Reaction system	Positive control (μL)	Self-connected control (μL)	Experimental group (μL)
ddH2O	2.5	4.5	3.5
5×CE II Buffer	2	2	2
Vector DNA after enzymatic digestion	2.5	2.5	2.5
Purified PCR product fragment	2	0	1
Exnase TM II	1	1	1
Total	10	10	10

transferred, placed in 10 ml of LB liquid medium containing corresponding antibiotics, and cultured at 37°C overnight. The plasmids were then extracted using a Tiangen endotoxin-free plasmid small- and medium-dose kit (cat no. A1460, Promega, Madison, WI, USA).

The 293T cells were cultured in DMEM (cat no. 12800-017, Gibco, Waltham, MA, USA) containing 10% fetal bovine serum (Gibco). Cells were digested with trypsin and prepared into cell suspension. The cell suspension was inoculated into a 24-well plate, and the cells were counted ahead of time (the number of cells was about 4×10^5), placed in an incubator for culture at 37°C with 5% CO_2, and cell fusion was observed under a microscope until about 80%. Transfection was carried out according to Invitrogen Lipofectamine 2000 instructions. A fluorescence microscope (Olympus, Tokyo, Japan) was used to observe the expressions of fluorescent-labeled genes on the plasmid after 24 h of transfection. The infection efficiency was determined by fluorescence expression. After taking fluorescence photos, 500 µl of complete medium was added. After 36 h of transfection, the cells were collected for Western blot.

Western blot

The cell culture bottle was taken out of the incubator, the culture medium was removed, and cells were washed with phosphate-buffered saline (PBS) two times. Then PBS was removed, and the appropriate amount of precooled 2 × lysis Buffer (2% mercaptoethanol, 20% glycerol, 4% sodium dodecyl sulfate (SDS)) was added. Cells were extracted, placed into an EP tube, then placed on ice for cleavage for 10–15 min. The cells were broken by a sonicator (200 W, 5 s each time, the interval was 2 s, 4 times in total), centrifuged at 12000 g at 4°C for 15 min. The supernatant was extracted, and the protein concentration was measured. The final concentration of protein was adjusted to 2 µg/µl in each sample and kept at −80°C for future use. The same amount of total protein was extracted from each sample, added with sample loading buffer, added with the same volume of 2X loading buffer (2% mercaptoethanol, 0.02% bromophenol blue, 20% glycerol, 4% SDS), mixed evenly, underwent a boiling water bath for 5–10 min and placed in a refrigerator at 4°C. The 10% sodium dodecyl sulfate-polyacrylamide gel electrophoresis (SDS-PAGE, BIO-RAD) separation gel was prepared,

Table III. *PCR identification primers*

ID	seq
KL15570-P3	CTGCGGCATCCAGTGCCAGAAC
FLAG-R-2	CCTTATAGTCCTTATCATCGTC

Table IV. *Reverse transcription system*

No.	Reactants	Dose
1	The total DNA samples	5µl (1µg)
2	oligDT	0.5µl
3	Random Hexamor	0.5µl
4	10* dNTP	2µl
5	RiAidRT	1µl
6	DEPC	6µl
7	RiLockRNoseInhibtor	1µl
8	5*Reactimbuffer	4µl
9	The total volume	20µl

and electrophoresis was carried out at 30 mA for two h. At the end of electrophoresis, electroporation transfection was carried out for 120 min at 4°C and 400 mA constant current. The protein was then transferred to polyvinylidene fluoride (PVDF) membrane. Tris-Buffered Saline and Tween 20 (TBST) solution containing 5% skimmed milk was used and placed on the shaker with a blocking solution at room temperature. PVDF membrane was sealed at 4°C for 1 h or overnight. After the primary anti-FLAG antibody (Sigma, Cat#F1804) was diluted with a blocking solution (dilution ratio: 1:3000), the sample was placed on a concussion instrument with a sealed PVDF membrane and incubated at room temperature for 2 h or at 4°C overnight. The membrane was washed with TBST 3 times for 10 min each time. An anti-mouse secondary antibody (Santa Cruz, Cat#sc2005) was diluted with a blocking solution (dilution ratio: 1:4000), and the PVDF membrane was incubated on a shaker at room temperature for 2 h. The membrane was washed with TBST 3 times for 10 min each time. The ECL + PlusTM Western blotting system kit (cat no. RPN2232, Amersham, Little Chalfont, UK) was used for color development. For X-ray development, the membrane with bands were added with enhanced chemiluminescence (ECL; Shanghai Guanlong Photographic Materials Factory, China), exposed, developed, and fixed in the darkroom.

Lentivirus purification

According to the status of cells, the supernatant of 293T cells was collected at 48 h after transfection and centrifuged at 4000 g and 4°C for 10 min. The fragments of cells were removed. The supernatant was filtered with a 0.45-μm filter, then transferred to a 40-ml ultracentrifugation tube. The samples were balanced separately. The ultracentrifuge tubes with virus supernatant were placed into a Beckman ultracentrifuge one by one. Then the centrifugal parameters were set at 2 h and 25,000 rpm. After the end of centrifugation, the supernatant was removed, the liquid remaining on the pipe wall was removed, added with a virus preservation solution, and pipetted gently. The precipitant was resuspended, then dissolved sufficiently and centrifuged at 10,000 rpm for 5 min. The supernatant was separated and extracted according to the requirements. These were samples to be prepared for testing.

Detection of lentivirus quality

For the physical index detection, the color was observed with the naked eye. The clear pink liquid was the lentivirus preservation solution developed by Jikai company. Fifty μl of lentivirus preservation liquid was drawn slowly with a 20–200 μl Standard pipette, and there was no obvious sense of stickiness or absorption lag. Sterility tests: The 293T cells were verified, and the virus added. Microscopic examination: after 24 h of normal culture, no bacteria and fungi were found, and a blank cell group was set up. The titer was determined by the fluorescence method. The infection conditions and parameters of the target cells were confirmed by the effect of cell infection.

Detection of the expression of Smo virus by PCR

The following groups were analyzed: Blank group (SW1990CD24CD44 double-positive cells); CON238 (SW1990CD24CD44 double-positive cells were transfected with negatively overexpressed control virus); CON077 (SW1990CD24CD44 double-positive cells were transfected with negatively inhibition control virus); LV-SMO15570-2 (SW1990CD24CD44 double-positive cells were transfected with overexpressed control virus); LV-SMO-RNAi37304-1 (SW1990CD24CD44 double-positive cells were transfected with inhibition virus)

The lysed cells were extracted, placed at room temperature for 5 min, and left to dissolve completely. Two-phase separation: Every 1 ml of samples lysed by Trizol reagent was added with 0.2 ml of chloroform, the pipe cover was closed, a manual violent oscillation of tube body was carried out for 15 s until the solution was emulsified, incubated at 15-30°C for 2–3 min, centrifuged at 12,000 rpm and 4°C for 15 min, left standing for 10 min, and centrifuged at 12,000 rpm and 4°C for 10 min. At this time, RNA precipitation will form gelatinous precipitation on the sidewall and the bottom of the tube. RNA cleaning: The supernatant was removed (without touching the precipitation). At least 1 ml of 75% ethanol was added to every 1 ml of sample lysed by Trizol reagent. The RNA precipitation was cleaned, the wall of the centrifugal tube was washed gently upside down, then the sample was mixed evenly and centrifuged at 7,500 rpm and 4°C for 5 min. The supernatant was then carefully removed, and again the precipitation was not touched. For RNA drying, the test tube was inverted on the filter paper, allowing the RNA to be air-dried at room temperature for about 10 min. Dissolution of RNA precipitation: When RNA was dissolved, an appropriate amount of RNase-free water was

added to dissolve the precipitation. The dosage was about 20–50 μL. The RNA solution obtained was stored at −80°C for future use. Finally, the total RNA concentration was tested on a machine.

Detection of RNA quality

The reading value at A260 was 1, which represents 40 μg RNA/ml. The calculation formula of RNA concentration (μg/ml) of the sample was A260 × dilution rate × 40 μg/ml. The ratio of A260/A280 of RNA solution is the purity of RNA, and the range of ratio is 1.8–2.1, which was determined by denatured agarose gel electrophoresis (SBS Genetech Co., Ltd., Beijing, China). Four μl of DNA buffer (5:1) was added to 20 μl sample system, and then the sample was placed carefully in the sample well (added with 5 μL of Mark and 10 μL of the sample). Electrophoresis parameters: V = 110V, I = 90Am, P = 015W, T = 00:15, (constant pressure) electrophoresis was performed until the indicator infiltrated the gel by at least 2–3 cm. Observation and photography were carried out under ultraviolet transmission light, and the electrophoretic results were recorded with a digital camera.

Reverse transcription

The rReaction system is shown in Table IV. The samples were tested on a machine at 25°C for 5 min, and then at 42°C for 60 min, and stored at −20°C for future use. The prepared samples and positive samples to be tested were tested at the same time. The reaction conditions were: 95°C for 5 min, 95°C for 10 s, and 60°C for 30 s. A total of 40 cycles were performed. The results were obtained and analyzed according to the formula.

Statistical analysis

All data were analyzed using SASjmp10.0. Quantitative data of Smo were expressed as mean±standard deviation (X±SD). Comparisons were made between the five groups: blank group, CON238, CON077, LV-SMO15570-2, LV-SMO-RNAi37304-1, and LV-SMO-RNAi37304-1. A variance homogeneity test among the groups was conducted. In cases of homogeneity of variance, data were compared using a one-way analysis of variance. In cases of heterogeneity of variance, data were compared using Kruskal–Wallis rank-sum tests, and intergroup pairwise comparison was conducted using *t*-tests. Inspection level was $\alpha = 0.05$.

RESULTS

Transfection

The results of electrophoresis of restriction enzyme cleavage vector are shown in Fig. 2A. The results showed that for 10-kb Marker, restriction enzyme cleavage products and non-restriction enzyme cleavage vectors were obtained. PCR product size: 2401 (Fig. 2B). PCR results revealed that the

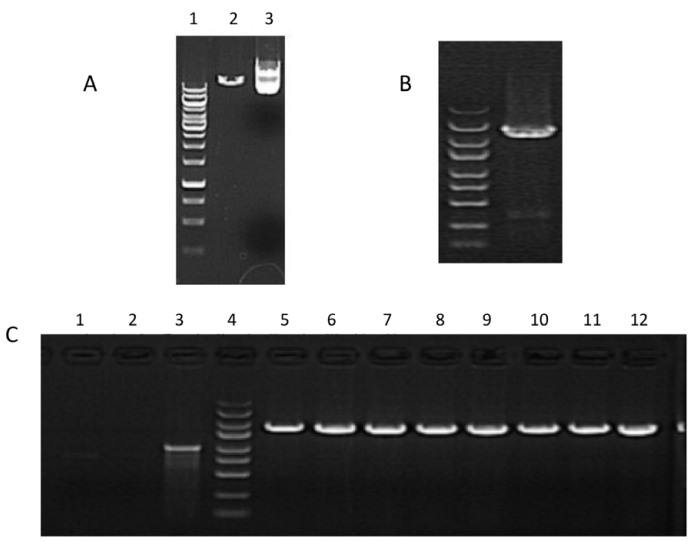


Fig. 3. *Plasmid transfection and Western blot. **A)** Transformation of 293T cells with plasma and Western blot map; **B)** The marker band size is shown in the figures. 1. Positive: WB standard SURVIVIN-3FLAG-GFP (molecular size: 48 KD); 2. Con: 293T cells; 3. OE: sample of 293T cells transfected with target gene plasmid.*

Table V. *Sequencing comparison results*

GGCTTTTTTGTTAGACGAAGCTTGGGCTGCAGGTCGACTCTAGAGGATCCCCGG
GTACCGGTCGCCACCATGGCCGCTGCCCGCCCAGCGCGGGGGCCGGAGCTCCCGCTC
CTGGGGCTGCTGCTGCTGCTGCTGCTGGGGGACCCGGGCCGGGGGGCGGCCTCGAG
CGGGAACGCGACCGGGCCTGGGCCTCGGAGCGCGGGCGGGAGCGCGAGGAGGAGC
GCGGCGGTGACTGGCCCTCCGCCGCCGCTGAGCCACTGCGGCCGGGCTGCCCCCTGC
GAGCCGCTGCGCTACAACGTGTGCCTGGGCTCGGTGCTGCCCTACGGGGCCACCTCC
ACACTGCTGGCCGGAGACTCGGACTCCCAGGAGGAAGCGCACGGCAAGCTCGTGCT
CTGGTCGGGCCTCCGGAATGCCCCCCGCTGCTGGGCAGTGATCCAGCCCCTGCTGTG
TGCCGTATACATGCCCAAGTGTGAGAATGACCGGGTGGAGCTGCCCAGCCGTACCCT
CTGCCAGGCCACCCGAGGCCCCTGTGCCATCGTGGAGAGGGAGCGGGGCTGGCCTG
ACTTCCTGCGCTGCACTCCTGACCGCTTCCCTGAAGGCTGCACGAATGAGGTGCAGA
ACATCAAGTTCAACAGTTCAGGCCAGTGCGAAGTGCCCTTGGTTCGGACAGACAACC
CCAAGAGCTGGTACGAGGACGTGGAGGGCTGCGGCATCCAGTGCCAGAACCCGCTC
TTCACAGAGGCTGAGCACCAGGACATGCACAGCTACATCGCGGCCTTCGGGGCCGTC
ACGGGCCTCTGCACGCTCTTCACCCTGGCCACATTCGTGGCTGACTGGCGGAACTCG
AATCGCTACCCTGCTGTTATTCTCTTCTACGTCAATGCGTGCTTCTTTGTGGGCAGCAT
TGGCTGGCTGGCCCAGTTCATGGATGGTGCCCGCCGAGAGATCGTCTGCCGTGCAGA
TGGCACCATGAGGCTTGGGGAGCCCACCTCCAATGAGACTCTGTCCTGCGTCATCATC
TTTGTCATCGTGTACTACGCCCTGATGGCTGGTGTGGTTTGGTTTGTGGTCCTCACCTA
TGCCTGGCACACTTCCTTCAAAGCCCTGGGCACCACCTACCAGCCTCTCTCGGGCAA
GACCTCCTACTTCCACCTGCTCACCTGGTCACTCCCCTTTGTCCTCACTGTGGCAATC
CTTGCTGTGGCGCAGGTGGATGGGGACTCTGTGAGTGGCATTTGTTTTGTGGGCTACA
AGAACTACCGATACCGTGCGGGCTTCGTGCTGGCCCCAATCGGCCTGGTGCTCATCGT
GGGAGGCTACTTCCTCATCCGAGGAGTCATGACTCTGTTCTCCATCAAGAGCAACCA
CCCCGGGCTGCTGAGTGAGAAGGCTGCCAGCAAGATCAACGAGACCATGCTGCGCC
TGGGCATTTTTGGCTTCCTGGCCTTTGGCTTTGTGCTCATTACCTTCAGCTGCCACTTC
TACGACTTCTTCAACCAGGCTGAGTGGGAGCGCAGCTTCCGGGACTATGTGCTATGTC
AGGCCAATGTGACCATCGGGCTGCCCACCAAGCAGCCCATCCCTGACTGTGAGATCA
AGAATCGCCCGAGCCTTCTGGTGGAGAAGATCAACCTGTTTGCCATGTTTGGAACTG
GCATCGCCATGAGCACCTGGGTCTGGACCAAGGCCACGCTGCTCATCTGGAGGCGTA
CCTGGTGCAGGTTGACTGGGCAGAGTGACGATGAGCCAAAGCGGATCAAGAAGAGC
AAGATGATTGCCAAGGCCTTCTCTAAGCGGCACGAGCTCCTGCAGAACCCAGGCCAG
GAGCTGTCCTTCAGCATGCACACTGTGTCCCACGACGGGCCCGTGGCGGGCTTGGCC
TTTGACCTCAATGAGCCCTCAGCTGATGTCTCCTCTGCCTGGGCCCAGCATGTCACCA
AGATGGTGGCTCGGAGAGGAGCCATACTGCCCCAGGATATTTCTGTCACCCCTGTGGC
AACTCCAGTGCCCCCAGAGGAACAAGCCAACCTGTGGCTGGTTGAGGCAGAGATCT
CCCCAGAGCTGCAGAAGCGCCTGGGCCGGAAGAAGAAGAGGAGGAAGAGGAAGAA
GGAGGTGTGCCCGCTGGCGCCGCCCCCTGAGCTTCACCCCCCTGCCCCTGCCCCCAG
TACCATTCCTCGACTGCCTCAGCTGCCCCGGCAGAAATGCCTGGTGGCTGCAGGTGC
CTGGGGAGCTGGGGACTCTTGCCGACAGGGAGCGTGGACCCTGGTCTCCAACCCATT
CTGCCCAGAGCCCAGTCCCCCTCAGGATCCATTTCTGCCCAGTGCACCGGCCCCCGT
GGCATGGGCTCATGGCCGCCGACAGGGCCTGGGGCCTATTCACTCCCGCACCAACCT
GATGGACACAGAACTCATGGATGCAGACTCGGACTTCGGTATGGACTACAAGGATGA
CGATGACAAGGA

PCR product size of the positive transformant was 1164 (Fig. 2C). The sequencing results are shown in Table V. At the yellow fluorescent marker, GGG was replaced synonymously by GGC. After transfection, cell fluorescence observation revealed that the fluorescence expression was strong (Fig. 3A). The results of Western blot are shown in Fig. 3B. The size of the target gene fusion protein was 89 kD. This result revealed that when this plasmid was detected with a flag antibody, it had a large specific 250kD band, and the membrane protein was overexpressed successfully.

Virus titer detection, virus infection conditions, and infection parameters

SW1990CD24CD44 double-positive pancreatic cancer cells were transfected with lentivirus for 3–4 days. The result revealed that the viral load was $1X10^6$ TU virus, and the cell growth and fluorescence effect of culture wells with polybrene dilution were the best (Table VI). Therefore, these were the transfection conditions and transfection parameters for subsequent experiments.

RT-PCR to detect the expression of Smo, a member of the Hedgehog signaling pathway in cells in 5 groups

The 5 groups were as follows: blank group; CON238, CON077, LV-SMO15570-2, LV-SMO-RNAi37304-1, and LV-SMO-RNAi37304-1. Expressions in the five groups of cells are shown in Fig. 4. The relative expression levels calculated with β-actin as internal controls are shown in Table VI. The results revealed that the expression of Smo in the blank group, CON238, CON077, LV-SMO15570-2, and SMO-RNAi37304-1 groups were 1.0038±0.0344, 1.0276±0.2944, 0.8793±0.0402, 2.7479±0.8308abce, and 0.2386±0.0481, respectively.

DISCUSSION

In January 2012, the Smo inhibitor, vismodegib, was first clinically approved by the FDA for the treatment of unresectable or metastatic skin basal cell tumors (11). Hh signaling pathway inhibitors can be used as single therapy, molecular targeted drugs, or radiotherapy, or in combination therapy. All these explained that inhibitors of the Hh signaling pathway

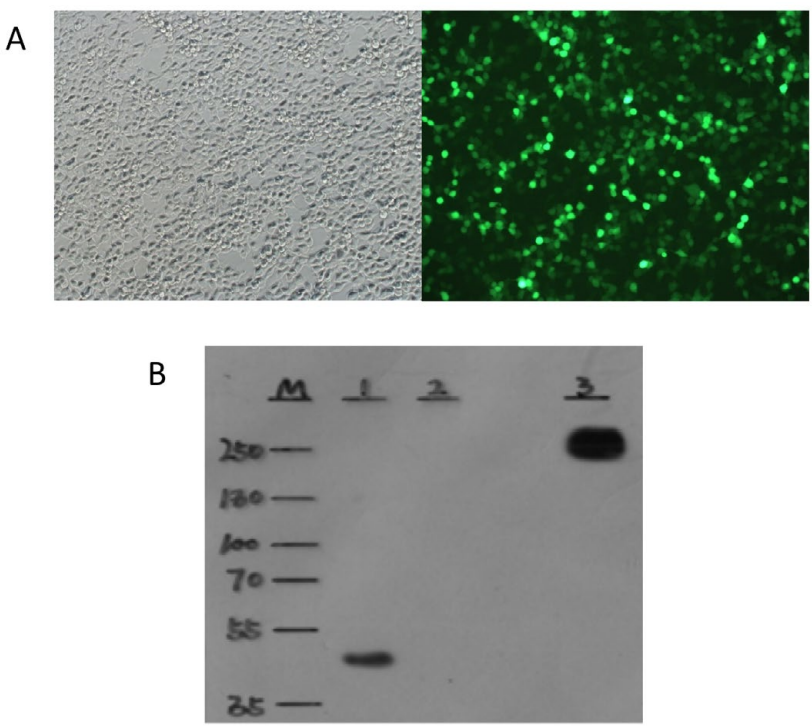


Fig. 4. *Detection of the expression of Smo, a member of the Hedgehog signaling pathway in cells in five groups by RT-PCR.*

Table VI. *Virus titer detection*

ID	Titer(TU/ml)
LV-SMO(15570-2)	1E+8
LV-SMO-RNAi(37303-1)	5E+8
LV-SMO-RNAi(37304-1)	1E+9
LV-SMO-RNAi(37305-1)	8E+8
Negative control virus CON238	2E+9
Negative control virus CON077	1E+9

Table VII. *Comparison of the relative expression levels calculated with β actin as internal control*

Smo	mean ±SD
Blank group	1.0038±0.0344d
CON238	1.0276±0.2944d
CON077	0.8793±0.0402d
LV-SMO15570-2	2.7479±0.8308abce
SMO-RNAi37304-1	0.2386±0.0481d

Homogeneity of variance: BartlerttF= 10.243.P =0.002 < 0.05
K w test: =10.99 P=0.027 is different*
vs blank group difference a; vs CON238 different b; vs CON077 there is a difference c; vs LV SMO15570 2 Has difference d; vs SMO RNAI37304 1 have difference e

had been gradually recognized in clinical practice. Small interfering RNA (siRNA) is the key link in the intermediate interference process of RNA interference (RNAi) (4, 5) and is the core of the RNAi process. It is also an effective tool for interference. Zeng et al. (12) revealed that when the related genes were inhibited by siRNA in pancreatic cancer cells, it was found that the proliferation and *in vitro* invasion and migration were inhibited in Panc-1 cells, a pancreatic cancer cell line. However, *in vitro* experiments of previous studies conducted by Zhang et al. confirmed the relationship between siRNA and vascular endothelial growth factor (VEGF) (13). A later study on *in vitro* experiments further proved that siRNA could inhibit the angiogenesis of transplanted tumors of pancreatic

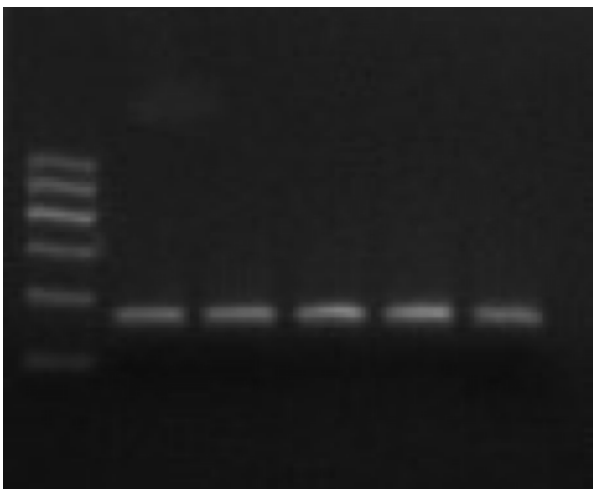


Fig. 4. *Detection of the expression of Smo, a member of the Hedgehog signaling pathway in cells in five groups by RT PCR*

cancer cells in mice (14). Other *in vivo* and *in vitro* studies confirmed the related mechanism of siRNA inhibits pancreatic cancer cells (15, 16).

In the present study, a small RNA fragment targeting Smo (17–19), an important member of the Hh signaling pathway, was designed. The vector lentivirus was successfully constructed to carry this fragment and included 15570-2, which took the experimental production method as an example, then an identification experiment was conducted in the overexpression vector virus constructed. Whether or not there was an effect on the expression of Smo, the key gene of the Hh signaling pathway in pancreatic cancer cells after transfection with SW1990CD24CD44 double-positive cells was observed. The results of RT-PCR showed: blank group: 1.0038±0.0344; CON238: 1.0276±0.2944d; CON077: 0.8793±0.0402. The differences among groups were not statistically significant. LV-SMO15570-2: 2.7479±0.8308 and LV-SMO-RNAi37304-1: 0.2386±0.0481, were statistically significantly different from the other three groups. Homogeneity of variance: Bartlett $F = 10.243$, $P = 0.002 < 0.05$, heterogeneity of variance. In the Kruskal–Wallis test, $\chi^2 = 10.99^*$ $P = 0.027$, there was statistically significant difference. It was further indicated that the designed and constructed RNA fragment is specially targeted for the key gene Smo in the Hh signaling pathway. The expression of Smo, the key gene of the Hh signaling pathway, was affected by the vector virus in SW1990CD24CD44 double-positive cells after transfection. The expression level of RNA in the overexpression group was 2.7479±0.8308, which was significantly higher than that in the blank and negative control groups. The expression level of RNA in the inhibition group was 0.2386±0.0481, which was significantly lower than that in the blank and negative control groups.

In summary, these results suggest that the function of the RNA fragment designed for the key gene Smo in this study was successful. Real-time quantitative PCR and Western blot can be further conducted to detect the expression of SHh, Patch-1, Patch-2, Smo, Gli1, Gli2, Gli3, Bcl-2, and Sufu, to understand the relationship between other members of the Hh signaling pathway after affecting Smo, a member of the Hh signaling pathway, and to further understand the relationship between the Hh signaling pathway and biological characteristics of pancreatic cancer cells.

REFERENCES

1. Chen X, Tukachinsky H, Huang CH, et al. Processing and turnover of the Hedgehog protein in the endoplasmic reticulum. J Cell Biol 2011; 5:825-38.
2. Narayanan R. Phenome-genome association studies of pancreatic cancer: new targets for therapy and diagnosis. Cancer Genomics Proteomics 2015; 1:9-19.
3. Goodell MA, Brose K, Paradis G, Conner AS, Mulligan RC. Isolation and functional properties of murine hematopoietic stem cells that are replicating in vivo. J Exp Med 1996; 4:1797-806.
4. Tuschl T. Expanding small RNA interference. Nat Biotechnol. 2002; 205:446-8.
5. Sperti C, Moletta L, Patanè G. Metastatic tumors to the pancreas: The role of surgery. World J Gastrointest Oncol 2014; 10:381-92.
6. Tang SN, Fu J, Nall D, Rodova M, Shankar S, Srivastava RK. Inhibition of sonic hedgehog pathway and pluripotency maintaining factors regulate human pancreatic cancer stem cell characteristics. Int J Cancer 2012; 1:30-40.
7. Li SH, Fu J, Watkins DN, Srivastava RK, Shankar S. Sulforaphane regulates self-renewal of pancreatic cancer stem cells through the modulation of Sonic hedgehog-GLI pathway. Mol Cell Biochem 2013; 373:217-27.
8. Rodova M, Fu J, Watkins DN, Srivastava RK, Shankar S. Sonic hedgehog signaling inhibition provides opportunities for targeted therapy by sulforaphane in regulating pancreatic cancer stem cell self-renewal. PLoS One 2012; 7: e46083.
9. Mo W, Xu X, Xu L, Wang F, Ke A, Wang X, Guo C. Resveratrol inhibits proliferation and induces apoptosis through the hedgehog signaling pathway in pancreatic cancer cell. Pancreatology 2011; 11:601-9.
10. Fendrich V, Wiese D, Waldmann J, Lauth M, Heverhagen AE, Rehm J, Bartsch DK. Hedgehog inhibition withthe orally bioavailable Smo antagonist LDE225 repressestumor growth and prolongs survival in a transgenicmouse model of islet cell neoplasms. Ann Surg 2011; 254:818-23;
11. Atwood SX, Chang AL, Oro AE. Hedgehog pathway inhibition and the race against tumor evolution. Cell

Biol 2012; 199:193-7.
12. Zeng W, He JT. Effect of THOC1 siRNA on biological behavior of humanpancreatic cancer Panc-1 cells. China Journal of Modern Medicine 2015; 6:38-42.
13. Li SP, Liu HW, Cheng L, Zhang H, Cao D, Li Z. Suppression of VEGF siRNA on growth of human pancreatic cancer cells in vitro. China General Surgical Basic and Clinical 2010; 58:651-4.
14. Zhang H, Liu HW, Lv F, Cheng L, Cao D. The influence of VEGF siRNA on the angiogenesis of human pancreatic cancer(PANC-1) cells transplantation tumor. Chin J Surg Onco 2014; 1:31-4.
15. Wang K, Demir IE, D'Haese JG, et al. The neurotrophic factor neurturin contributes toward an aggressive cancer cell phenotype, neuropathic pain and neuronal plasticity in pancreatic cancer. Carcinogenesis 2014; 1:103-13.
16. Liu SH, Lu TH, Su CC, et al. Lotus leaf (Nelumbo nucifera)and its active constituents prevent inflammatory responses in macrophages via JNK/NF-κB signaling pathway. American Journal of Chinese Medicine 2014; 4:9671-6.
17. Abula Y, Yi C, Wang XY, et al. Gli1 expression in pancreatic ductal adenocarcinoma and its clinical significance. Genet Mol Res 2015; 4:12323-9.
18. Abula Y, Li DW, Yi C, Li HJ. The expression and significance of Hedgehog signaling pathway genes Shh, Ptch1, Smo, and Gli1 in pancreatic cancer. World Chinese Digestive Journal 2015; 18:2894-900.
19. Cong P, Yi C, Wang XY. Expression of Smo in pancreatic cancer CD44+CD24+cells and construction of a lentiviral expression vector to silence Smo. Oncol Lett 2018; 4:4855-62.

Identification of peroxiredoxin 6 as a potential lung-adenocarcinoma biomarker for predicting chemotherapy response by proteomic analysis

BZ. Li[1], HH. Bai[2], FW. Tan[3], YB. Gao[3] and J. He[3]

[1]Department of Thoracic Surgery, Beijing Shijitan Hospital, Capital Medical University, Beijing, P.R. China;
[2]Phase I Clinical Trial Center, Beijing Shijitan Hospital, Capital Medical University, Beijing, P.R. China;
[3]Department of Thoracic Surgery, National Cancer Center/National Clinical Research Center for Cancer/ Cancer Hospital, Chinese Academy of Medical Sciences and Peking Union Medical College, Beijing, China

Received November 23, 2020 – Accepted February 4, 2021

The prognosis of lung cancer remains poor due to the limited biomarker selection for treating patients with optimal chemotherapy. The aim of this study is to discover and identify new biomarkers with the value of predicting chemotherapy responses in a lung adenocarcinoma (AD) specimen. In this study, six pairs of pre-treatment fresh primary lung AD-cancer tumors with varied chemotherapy responses were used to discover new biomarkers by two-dimensional difference gel electrophoresis (2D DIGE). Among the matched protein spots, 19 were up-regulated and 18 were down-regulated in chemo-sensitive tumors *versus* chemo-resistant tissues. These differentially expressed proteins could be divided into five classes: redox regulation protein, the cytoskeletal protein, cell metabolism enzymes or proteins, apoptosis, signal transduction mediated molecules, and other functional proteins. Proteins of interest, including PRDX2, PRDX6, and Gelsolin, were differentially expressed in chemo-sensitive tumors *versus* chemo-resistant tissues and these observations were validated by immunohistochemistry in 92 formalin-fixed and paraffin-embedded (FFPE) specimens. Our results demonstrated that PRDX6 protein expression was closely related to tumor response ($\chi^2 = 5.57$, $P < 0.05$), whereas no relationship of PRDX2 and Gelsolin were obtained with tumor response ($\chi^2 = 0.51$ $P > 0.05$, $\chi^2 = 0.41$ $P > 0.05$). This tissue proteomics study provides evidence that PRDX6 may be regarded as a predictive biomarker for poor chemotherapy response, which can be helpful in guiding pretreatment protocols.

Lung cancer is the leading cause of cancer death in men and women worldwide with over a million deaths annually (1). Lung adenocarcinoma (AD) is the predominant type of non-small cell-lung cancer (NSCLC) with increased incidence in recent years (2). Although great advances have taken place in the treatment of this disease, especially with new agents targeted to certain genes and the utilization of anti-PD-1 immunotherapy, platinum-based (cisplatin or carboplatin) double-agent chemotherapies remain as the standard first-line treatment for patients with advanced NSCLC without sensitive *EGFR* mutations (NCCN guidelines; http://www.nccn.org/professionals/), which contribute to improved survival outcomes. Unfortunately, chemotherapy efficacy is deficient because the response rate in most clinical trials has been less than 40% (3). Chemotherapy has reached the therapeutical plateau with few advances in recent years and only a few patients benefiting (4). There is therefore an urgent

Key words: 2D DIGE; PRDX6; cisplatin; chemotherapy response; lung adenocarcinoma

Corresponding Author:
Dr Yibo Gao,
No. 17 South Panjiayuan Lane,
Chaoyang District, Beijing,
100021, P.R. China
Tel.: +86 10 87788863
e-mail: gaoyibo@cicams.ac.cn

0393-974X (2021)
Copyright © by BIOLIFE, s.a.s.
This publication and/or article is for individual use only and may not be further reproduced without written permission from the copyright holder. Unauthorized reproduction may result in financial and other penalties
DISCLOSURE: ALL AUTHORS REPORT NO CONFLICTS OF INTEREST RELEVANT TO THIS ARTICLE.

need for clinicians to select optimal patients who might benefit from chemotherapy to participate in this toxic therapy.

The biomarker discovery and identification are promising methods for solving this problem. Numerous translational studies have explored the usefulness of proteomics studies related to chemotherapy-specific biomarkers for different cancers (5). Two-dimensional difference gel electrophoresis (2D-DIGE) continues to be one of the most versatile and widely used techniques for studying a biological system's proteome (6, 7). The proteomic approach has improved understanding of the biology of cancers and contributed to the potential identification of protein biomarkers for this disease (8).

In the present study, to discover new biomarkers and accurately identify their functions in predicting chemotherapy responses, proteomic methods and technologies were used to quantitate differences between chemo-sensitive and chemo-resistant samples. The up-regulated or down-regulated spots were further analyzed by mass spectrometry to identify the protein structure. Then, three proteins of interest were selected for further validation by immunohistochemistry (IHC) in a larger group of patients who had taken cisplatin-based regime chemotherapy. More importantly, the relationship of chemotherapy responses with the three newly discovered biomarkers were analyzed.

MATERIALS AND METHODS

Sample collection

All of the tissues were collected from patients in the Cancer Institute and Hospital of the Chinese Academy of Medical Sciences. None of these patients had received antineoplastic therapy prior to chemotherapy. All of the tissue samples were taken by experienced physicians through bronchoscopy and examined independently by two experienced pathologists. For 2D-DIGE, six pairs of pre-treatment fresh primary lung AD tumors with varied chemotherapy responses were obtained during 2007-2008 (Table I). Necrotic tissue confirmed by histopathologic evaluation was excluded. The samples were snap frozen in liquid nitrogen immediately after resection and stored at –80°C until use. For immunohistochemistry analysis, 92 paraffin-embedded pretreated lung-tumor tissues were obtained by bronchoscopy during 1999-2008. All selected patients had not accepted anti-neoplasm treatment before chemotherapy. Chemotherapy for all selected patients was cisplatin-based regimens (two drugs). For all participants, clinicopathological information (age, gender, pathology, differentiation, smoking history, TNM stage, and chemotherapy response) was available. The study was approved by the medical ethics committee of the Cancer Institute and Hospital of the Chinese Academy of Medical Sciences. All procedures performed in studies involving human participants were in accordance with the ethical standards of the institutional research board. All participants understood and signed the informed consent.

2D-DIGE

Approximately 0.5 g of tissue was ground into powder in liquid nitrogen with a precooled mortar and pestle. The samples were then homogenized on ice in 1 ml of lysis buffer (7 M urea, 2 M thiourea, 4% CHAPS, 30 mM Tris-HCl, pH 8.5, protease inhibitor mixture) using a glass homogenizer. After sonication on ice for 10 s using an ultrasonic processor, the samples were centrifuged for 30 min (40,000 × g) to remove particulate materials. Protein concentrations were determined in duplicate by the Bradford method (Bio-Rad) and confirmed by SDS-PAGE.

The protein pH was adjusted to 8.5 by 50 mM NaOH, and the concentration was adjusted to 5 mg/mL with lysis buffer. Equal amounts of proteins from the six sample pairs were pooled together as the internal standard. Tumors from each patient were randomly labeled with Cy3 or Cy5, whereas internal standards were labeled with Cy2 using 400 pmol of fluorochrome/50 μg of protein. Labeling was performed for 30 min on ice in the dark. The reactions were then quenched by the addition of 1 μL of lysine (10 mM) for 10 min on ice in the dark.

The DIGE experimental design is shown in Table I. Fifty-microgram Cy3- and Cy5-labeled samples from each patient were combined before mixing with 50 μg of Cy2-labeled internal standard. Then an equal volume of 2 × sample buffer (7 M urea, 2 M thiourea, 4% CHAPS, 1% Bio-Lyte, pH 3–10, 20 mg/mL DTT) was added to the sample, and the total volume was adjusted to 410 μL with rehydration buffer (7 M urea, 2 M thiourea, 4% CHAPS, 0.5% Bio-Lyte, 10 mg/mL DTT).

The samples were actively rehydrated into 24-cm pH 3–10 IPG strips (Bio-Rad) at 17°C for 12 h using a Protean IEF cell (Bio-Rad). Isoelectric focusing was performed for a total of 80 kV-h (ramped to 250 V in 30 min, held at 1000 V for 1 h, ramped to 10,000 V in 5 h, and held at 10,000 V for 60 kV-h). The IPG strips were equilibrated in equilibration buffer (6 M urea, 2% SDS, 50 mM Tris-HCl, pH 8.8, 30% glycerol) and supplemented with 0.5% DTT for 15 min at room temperature followed by incubation in 4.5% iodoacetamide in equilibration buffer for another 15 min at room temperature.

IPG strips were placed on the top of 12% homogeneous polyacrylamide gels that had been precast with low fluorescence glass plates using an Ettan DALT 12-gel caster. The second dimension SDS-PAGE was carried out using the Protean Plus system (Bio-Rad). After two-dimensional electrophoresis, the gels were scanned on the Typhoon 9410 scanner with Ettan DALT gel alignment guides using excitation/emission wavelengths specific for Cy2 (488/520 nm), Cy3 (532/580 nm), and Cy5 (633/670 nm). The intensity was adjusted to ensure that the maximum volume of each image was within 60,000–90,000.

Analysis of 2D-DIGE was carried out using DeCyder 6.5 software (GE Healthcare) according to the manufacturer's recommendations. Briefly, the DeCyder biological variation analysis module was used to detect spots (the estimated number of spots was 2500) and simultaneously match all 36 protein spot maps from 6 gels. All matches were also confirmed manually. The paired *t*-test with false discovery rate correction was used for statistical analysis of the data. Protein spots that were differentially expressed in PR and PD tissues (ratio ≤ -1.5 or ratio ≥ 1.5, $p \leq 0.05$) were selected. Only spots altered in the same direction with their average ratio in at least 5 of the 12 patients were chosen for identification.

In-gel digestion

Spot picking was carried out with preparative gels. Two-dimensional electrophoresis was performed as described under "2D-DIGE" except that the IPG strips were loaded with 1000 μg of protein, and the gels were stained with Coomassie Brilliant Blue. Protein spots of interest were excised and destained with 25 mM ammonium bicarbonate, 50% ACN. The gels were then dried completely by centrifugal lyophilization. In-gel digestion was performed with 0.01 μg/μL trypsin (Promega) in 25 mM ammonium bicarbonate for 15 h at 37°C. The supernatants were collected, and the tryptic peptides were extracted from the gel sequentially with 5% TFA at 40°C for 1 h and with 2.5% TFA, 50% ACN at 30°C for 1 h. The extracts were pooled and dried completely by centrifugal lyophilization.

Protein identification

Peptide mixtures were redissolved in 0.5% TFA, and 1 μL of peptide solution was mixed with 1 μL of matrix (4-hydroxy-α-cyanocinnamic acid in 30% ACN, 0.1% TFA) before spotting on the target plate. Matrix-assisted laser desorption ionization tandem time-of-flight mass spectrometry (MALDI-TOF/TOF MS) was carried out on a 4800 Proteomics Analyzer (Applied Biosystems). Peptide mass maps were acquired in positive reflection mode, averaging 1500 laser shots/MALDI-TOF spectrum and 3000 shots/TOF/TOF spectrum (the resolution was 20,000). The 4800 calibration mixtures (Applied Biosystems) were used to calibrate the spectrum to a mass tolerance within 0.1 Da. Parent mass peaks with a mass range of 600 - 4000 Da and minimum signal to noise ratio of 15 were picked out for tandem TOF/TOF analysis. Combined mass and mass/mass spectra were used to interrogate human sequences in the IPI human database v3.23 (which contains 66,619 protein entries) using the MASCOT database search algorithms (version 2.1). Searches were performed to allow for carbamidomethylation, oxidation, and a maximum of one missed trypsin cleavage. Peptide tolerance and MS/MS tolerance were both 0.2 Da. All of the automatic data analysis and database searches were fulfilled by the GPS Explorer software (version 3.6; Applied Biosystems). Known contaminant ions (keratin) were excluded. The confident identification had a statistically significant ($p \leq 0.05$) protein score (based on combined mass and mass/mass spectra). Protein redundancy that appeared in the database under different names and accession numbers was eliminated. Spots in which more than one protein was identified were excluded.

Immunohistochemistry staining

In total, 92 paired AD tumors with different chemotherapy responses were used to examine PRXD2, PRXD6, Gelsolin, and Rab2a expression. Routine

immunohistochemical SP staining was carried out according to the manufacturer's protocol with anti-PRXD2 antibody (diluted 1:600; Proteintech), PRXD6 (diluted 1:250; Abcam), and Gelsolin (diluted 1:250; Abcam). The slide-microscopic analysis was independently performed by two experienced pathologists in a blind fashion without knowledge of the patient information. The cell-immunostaining intensity was scored as 0, 1, 2, and 3, and the percentage of positive cells was assigned as following categories: 0 (0–5%), 1 (6–25%), 2 (26–50%), 3 (51–75%), or 4 (76–100%). The sections' final scores were recorded as – (negative), + (weakly positive), ++ (positive), and +++ (strongly positive); the scores were based on the intensity and the number of stained cells. In this study, scores of negative (-) and weakly positive (+) were considered as negative, whereas positive (++) and strongly positive (+++) were considered as positive.

Evaluation of the therapeutic effect

One week after chemotherapy, all patients underwent a further pulmonary computed tomography (CT) scan. The therapeutic effect was evaluated based on Response Evaluation Criteria in Solid Tumors (RECIST) (9): (i) complete response (CR), all detectable symptoms faded away; (ii) partial response (PR), ≥ 30% shrinkage in the sum of linear tumor measurements; (iii) progressive disease (PD), new lesions faded away and ≥ 20% increase in the sum of target lesions; and (iv) stable disease (SD), neither enough of a decrease for PR nor enough of an increase for PD. CR and PR were considered effective responses, and SD and PD were considered ineffective responses. Patients with PR were considered as chemo-sensitive by CT scans after two treatment cycles by RECIST (version 1.1), whereas patients with PD were considered as chemo-resistant. The objective response rate (ORR) and disease control rate (DCR) were calculated by (CR+PR)/total cases × 100% and (CR+PR+SD)/total cases × 100%, respectively.

Statistical analysis

The differences between chemo-sensitive and chemo-resistant tumor tissues were evaluated by Wilcoxon matched pairs test, whereas the associations between protein expression and chemotherapy responses were evaluated by the χ^2 test using SPSS 21.0 software. Statistical significance was defined as $p < 0.05$.

RESULTS

Differentially expressed proteins in chemo-sensitive lung AD tumors and chemo-resistant lung AD tissues by 2D-DIGE

To detect the differentially expressed proteins, chemo-sensitive and chemo-resistant fresh-tumor tissues from lung AD patients through bronchoscopy

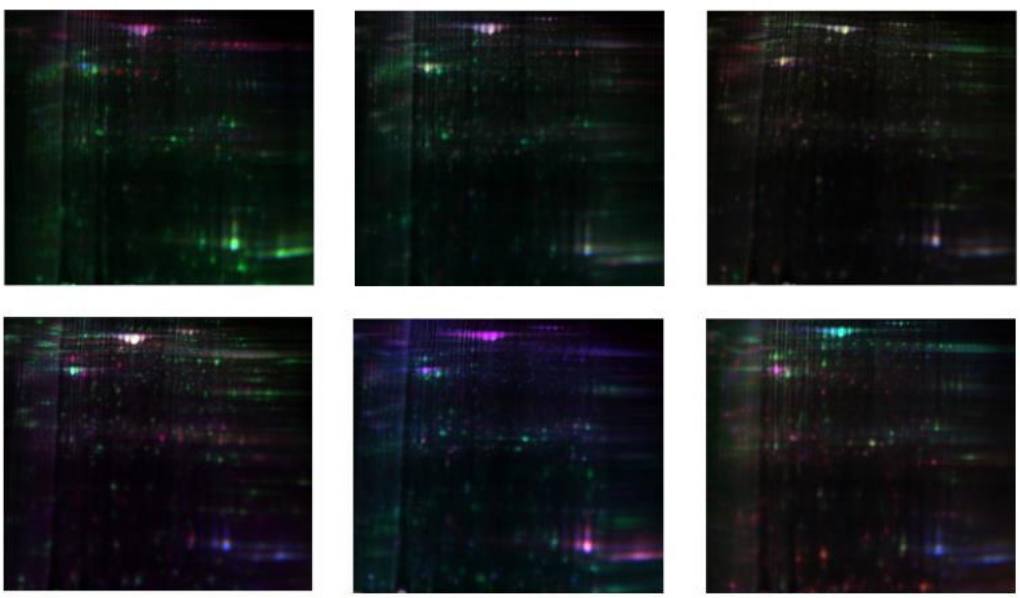


Fig. 1. *Differentially expressed protein spots in human lung adenocarcinoma marked with master numbers and displayed in representative 2D-DIGE images.*

or pre-chemotherapy were analyzed by 2D-DIGE. These 6 patients' characteristics are shown in Table I. Twelve lung AD samples labeled with Cy3 or Cy5 were run in 6 gels along with a pooled standard that was labeled with Cy2, and the images were analyzed by Decyder 6.5 software (Fig. 1). Among 2067 matched protein spots, 37 were up-regulated (ratio chemo-sensitive/chemo-resistant ≥ 1.5, $p \leq 0.05$; paired *t* test with false discovery rate correction), and 32 were down-regulated (ratio chemo-sensitive/chemo-resistant ≥ -1.5, $p \leq 0.05$) in chemo-sensitive tumors *versus* chemo-resistant tissues (Fig. 2).

Identification of differentially expressed proteins

To identify the above-mentioned differentially expressed proteins, mass spectrometry technology was applied to compare the characters of known proteins. Fifty-two differentially expressed protein spots exhibiting sufficient intensity, clear separation from surrounding spots, and consistent spot shape and size were excised and subsequently in-gel digested by trypsin and then successfully analyzed by MALDI-TOF/TOF. After the peptide mass fingerprinting (PMF), Mascot Distiller software was applied to calculate mass load ratio (m/z) values of peptide fragment through analyzing single isotope PMF. Through searching Mascot query system, SWISS-PROT, and NCBInr protein databases, the corresponding proteins were identified. The five spots identified as known contaminants (keratin 1, 2, and 10) and the 10 spots with multiple protein identities were excluded from further analysis. Among the remaining, 37 spots (19 up-regulated spots and 18 down-regulated spots shown in Fig. 1, A and B, respectively) representing 19 up-regulated and 18 down-regulated non-redundant proteins in tumor samples were identified. The corresponding proteins included PRDX 2, PRDX 6, and Gelsolin (Fig. 3). Based on functional annotation in SWISS-PORT and NCBInr databases, these differentially expressed proteins can be classified into six classes: (i) redox regulation protein, (ii) the cytoskeletal protein, (iii) cell metabolism enzymes or proteins, (iv) apoptosis, (v) signal transduction mediated molecules, and (vi) other functional proteins (Fig. 4). The results indicated that chemotherapy-related proteins may be included in cell metabolism, apoptosis, redox regulation, transcription, and signaling transduction.

Immunohistochemical staining of interested proteins in validated specimen

To validate the results from proteomics analysis, PRD2, PRD6, and Gelsolin were selected for further validation by IHC in a larger group of pretreatment

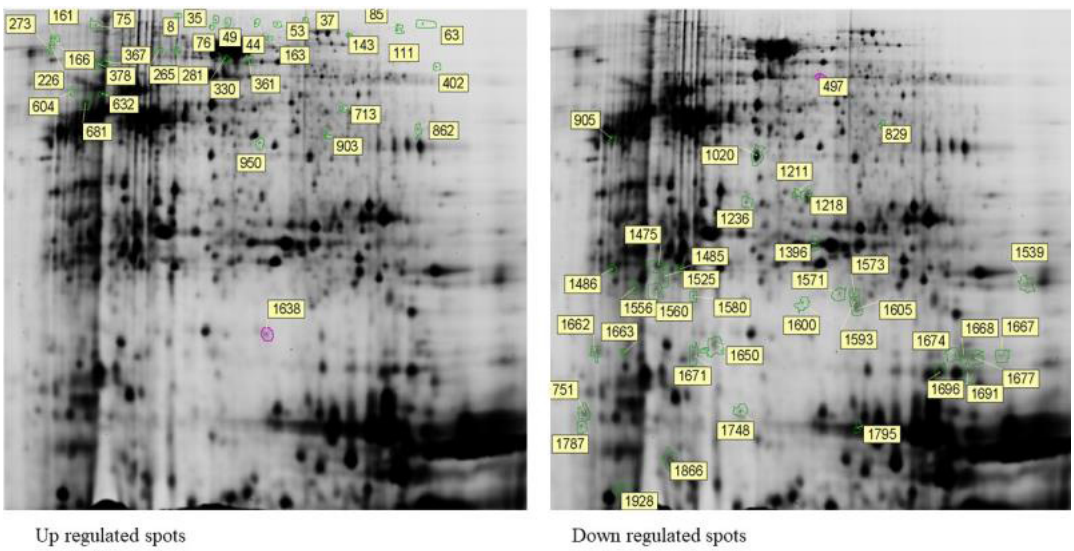


Fig. 2. *The up-regulated (left) and down-regulated (right) spots between chemo-sensitive tumors and chemo-resistant tissues as analyzed by DeCyder 6.5 software.*

Table I. *The basic clinical information of the lung AD patients enrolled in this study*

Sample no.	Age	Gender	Differentiation	Chemo-response
1	67	M	M	PR
2	71	F	M	PR
3	63	F	L	PR
4	65	M	L	PR
5	50	M	M	PR
6	44	M	M	PR
7	69	F	M	PD
8	46	F	M	PD
9	51	M	M	PD
10	56	F	L	PD
11	61	M	M	PD
12	51	M	M	PD

specimens (Table II). It was found that PRDX2 protein expression was negative in 73 (79.3%) patients and positive in 9 (21.0%) patients according to the score method above. As for PRDX6, the staining results were negative in 77 (83.6%) patients and positive in 15 (16.2%) patients. We also found that Gelsolin was negative in 83 (90.2%) patients and positive in 9 (9.6%) patients (Table III, Fig. 5).

Associations between PRDX2, PRDX6, and gelsolin with chemotherapy response

To understand the relationship of chemotherapy response with AD-lung expression of PRDX2, PRDX6, the χ^2 method was applied to analyze the relationship in 92 patients. As shown in Table IV, PRDX6 protein expression was closely related

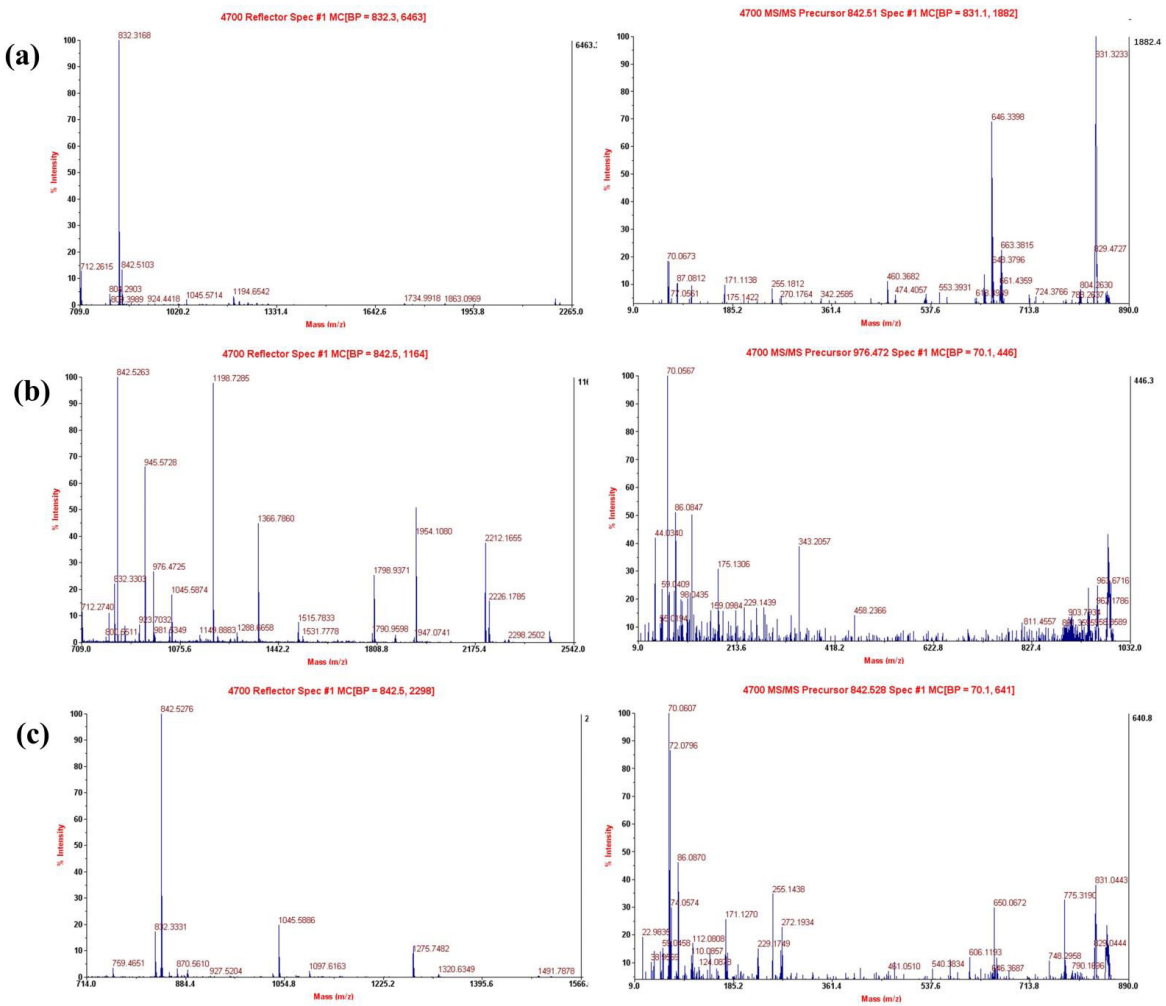


Fig. 3. *MALDI-TOF MS spectra of PRDX 2 (a), PRDX 6 (b) and Gelsolin (c) after digestion by trypsin (left) and the correspond MS/MS spectra (right).*

to tumor response ($\chi^2 = 5.57$, $P < 0.05$), whereas the relationship with disease control rate was insignificant ($\chi^2 = 2.19$, $P > 0.05$). Furthermore, PRDX2 had no relationship with tumor response ($\chi^2 = 0.51$, $P > 0.05$) and disease control rate ($\chi^2 = 1.37$, $P > 0.05$). Likewise, the correlation with tumor response ($\chi^2 = 0.41$, $P > 0.05$) and disease control rate ($\chi^2 = 1.25$, $P > 0.05$) also indicated a weak implication of Gelsolin in lung AD. In summary, it was concluded that highly expressed PRDX6 is a potential biomarker of chemotherapy response in lung AD patients.

Table II. *The experimental design of the samples classification for 2D-DIGE*

Characteristics	Percentage (%)	Number of patients
Sex		
Male	58.7	54
Female	41.3	38
Age		
Median	55	
Range	29-74	
Stage		
IIIA	5.4	5
IIIB	21.7	20
IV	72.8	67
Response		
CR	1.1	1
PR	31.1	28
SD	47.8	43
PD	20.0	18
Unknown	2.2	2
Tumor response rate (CR+PR/CR+PR+SD+PD)	32.2	29
Disease control rate (CR+PR+SD/CR+PR+SD+PD)	80.0	72

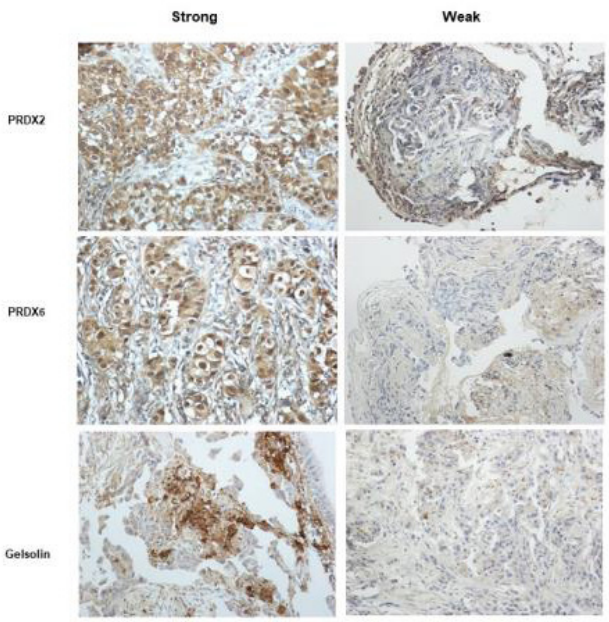


Fig. 5. *Results (a) and the statistical analysis (b) of immunohistochemical staining of PRDX 2, PRDX 6 and Gelsolin.*

Table III. *The expression of PRDX2, PRDX6 and Gelsolin in specimen by IHC*

	0	1+	2+	3+
PRDX2	51 (55.4)	22 (23.9)	12 (13.4)	7 (7.6)
PRDX6	50 (54.3)	27 (29.3)	13 (14.1)	2 (2.1)
Gelsolin	60 (65.2)	23 (25.0)	5 (5.4)	4 (4.3)

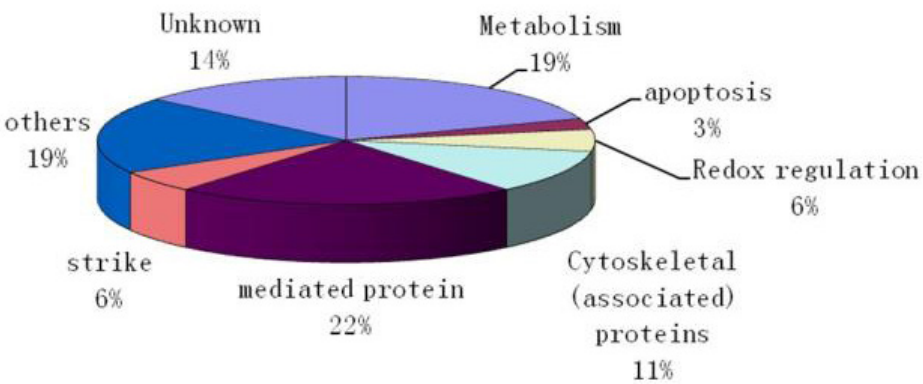


Fig. 4. *Classification of the differentially expressed proteins based on functional annotations in SWISS-PORT and NCBInr databases.*

DISCUSSION

The 2D-DIGE technique is a frequently used and highly reliable bioanalytical method for the systematic discovery of new biomarkers (10). As traditional two-dimensional gel electrophoresis runs on different gels, the difference between gels creates difficulties in distinguishing system errors with sample differences, which limits its application. The 2D-DIGE can isolate and analyze multiple samples on the same gel to eliminate systematic errors, which is particularly suitable for identifying differences in proteomics research. Simultaneously, 2D-DIGE technology adds a third fluorescent color as an internal standard, which can effectively reduce the system error and greatly improve the accuracy, reliability, and reproducibility of quantitative results (11). In this study, we obtained differentially expressed-protein profiles by 2-D DIGE and MALDI-TOF/TOF-MS mass spectrometry technologies in lung AD specimens before chemotherapy. Afterwards, three proteins of interest were then selected to be validated in a larger series of specimens by IHC analysis in order to find their potential value as biomarkers for predicting chemotherapy response in lung AD patients.

In this study**,** 37 differentially expressed proteins were identified between chemo-sensitive and chemo-resistant lung AD specimens, which were mainly redox regulation proteins, the cytoskeletal proteins, cell metabolism enzymes, apoptosis-related proteins, signal transduction mediated molecules, and other functional proteins. The results indicated that multiple protein types and signal pathways may be involved in the complex chemotherapy-response process. Among the identified proteins, PRDX6 2, PRDX 6, and Gelsolin were identified in a larger series of patients by IHC. The results demonstrated that PRDX6 overexpression was associated with poor chemotherapy response, whereas no relationship was obtained between the expression of PRDX2 and Gelsolin with chemotherapy response. The results demonstrated that PRDX6 may be regarded as a potential biomarker for predicting chemotherapy response in lung AD.

PRDX6 protein is a known member of the peroxiredoxin family, which is involved in the process of cellular antioxidant. Six members of the peroxiredoxin family exist in mammals, and are classified into three groupings based on the number and position of active site cysteines: the 2-Cys type (*Prdx1–4*), the atypical 2-Cys Prdx (*Prdx5*), and the 1-cys member (*Prdx6*) (12, 13). Peroxiredoxins have a role in preventing ROS-induced cell damage and apoptosis and can also modulate peroxide-induced signal transduction. Besides assisting in the protection of cells against oxidative stress, PRDX6 uniquely possesses calcium-independent phospholipase A2 (PLA2) activity and glutathione peroxidase activity that can assist in oxidative stress prevention (14). Moreover, numerous studies have proven that PRDX6 has an essential role in tumor maintenance and cell survival by protecting cells from OS-induced apoptosis (15). There is mounting evidence that PRDX 6 is overexpressed in multiple cancer types and is involved in the process of carcinogenesis (16).

Recently, there has been increasing interest in cell oxygen sense and cancer due to their influence on cellular survival or apoptosis (17). due to their

Table IV. *The correlation between the chemotherapy response and the expression of PRDX2, PPRDX6 as well as Gelsolin*

	Tumor Response χ^2 value	*P* value	Disease Control χ^2 value	*P* value
PRDX2	0.51	0.50	1.37	0.29
PRDX6	5.57	0.02	2.19	0.19
Gelsolin	0.41	0.63	1.25	0.28

influences on cellular survival or apoptosis (17). Pak et al. studied whether PRDX 6 overexpression attenuates cisplatin-induced apoptosis in providing chemoprotection in human ovarian cancer cells. PRDX6 protein overexpression reversed the apoptotic effect of cisplatin by reducing ROS levels and suppressing the caspase signaling pathway. The results indicated that targeting PRDX6 may sensitize cancer cells to ROS-producing therapeutic treatments, such as anticancer drugs and radiation (15). Moreover, another study found that PRDX6 promoted cisplatin resistance in human lung cancer cells by promoting the stem-like properties of cancer cells, which suggested PRDX6 as a target for treating cisplatin resistant NSCLC (18). However, these findings are all based on the data from cell lines. To the best of our knowledge, the results are the first evidence that reveals the relationship between PRDX6 and chemo-resistant effects in lung AD specimens, which further indicates a potentially new, therapeutic strategy for targeting PRDX6 during lung AD treatment. These findings suggest a potential value of PRDX6 as a tissue biomarker for chemotherapy response prediction and in guiding personalized therapy for patients with AD.

It is indicated that patients with PRDX6-positive tumors may need more active follow-up and other treatment options instead of chemotherapy. However, more clinical specimens are needed for testing, including samples from patients of squamous cell cancer, large cell lung cancer, small cell lung cancer, and other cancers to understand the potential value of this new biomarker. If PRDX 6 could be detected and is found elevated significantly in the specimens of AD patients, it will be considered as a biomarker for chemotherapy-response prediction in lung cancer.

In summary, by applying 2D DIGE proteomics analysis, 37 differentially expressed proteins were identified in chemo-resistant and chemo-sensitive lung AD specimens, of which 19 were up-regulated and 18 were down-regulated. PRDX6, one of the 19 up-regulated proteins in tumors, was further confirmed by IHC in a larger series of patients, and then proved to be an independently unfavorable prognostic biomarker for the survival of NSCLC patients in further immunohistochemical study and statistical analysis. Based on further investigation, we found that PRDX6 may be regarded as a novel biomarker for poor chemotherapy response, even a potentially novel target for diagnosis and treatment of lung AD. However, larger-scale and further studies on lung AD are required before developing the applicability of PRDX6 in clinical practice.

ACKNOWLEDGEMENTS

This study was supported by the National Key R&D Program of China 2018YFC1312100, 2017YFC1311000); R&D Program of Beijing Municipal Education commission KJZD20191002302). We would also like to thank TopEdit (www.topeditsci.com) for English language editing of this manuscript.

REFERENCES

1. Bray F, Ferlay J, Soerjomataram I, Siegel RL, Torre LA, Jemal A. Global cancer statistics 2018: GLOBOCAN estimates of incidence and mortality worldwide for 36 cancers in 185 countries. CA Cancer J Clin 2018; 68:394-424.
2. Nakamura H, Saji H. Worldwide trend of increasing primary adenocarcinoma of the lung. Surg Today 2014; 44:1004-12.
3. Yang ZY, Liu L, Mao C, Wu XY, Huang YF, Hu XF, Tang JL. Chemotherapy with cetuximab versus chemotherapy alone for chemotherapy-naive advanced non-small cell lung cancer. Cochrane Database Syst Rev 2014; 11:CD009948.
4. Lee DH, Tsao MS, Kambartel KO, et al. Molecular testing and treatment patterns for patients with advanced non-small cell lung cancer: PIvOTAL observational study. PLoS One 2018; 13:e0202865, 2018.
5. Peng H, Chen R, Brentnall TA, Eng JK, Picozzi VJ, Pan S. Predictive proteomic signatures for response of pancreatic cancer patients receiving chemotherapy. Clin proteomics 2019; 16:31.
6. Ciereszko A, Dietrich MA, Slowinska M, et al. Identification of protein changes in the blood plasma of lung cancer patients subjected to chemotherapy using a 2D-DIGE approach. PLoS One 2019; 14:e0223840.

7. Rong Z, Fan T, Li H, et al. Differential proteomic analysis of gender-dependent hepatic tumorigenesis in Hras12V transgenic mice. mol cell proteomics 2017; 16:1475-90.
8. Chen R, Yi EC, Donohoe S, et al. Pancreatic cancer proteome: the proteins that underlie invasion, metastasis, and immunologic escape. Gastroenterology 2005; 129:1187-97.
9. Eisenhauer EA, Therasse P, Bogaerts J, et al. New response evaluation criteria in solid tumours: revised RECIST guideline (version 1.1). Eur J Cancer 2009; 45:228-47.
10. Murphy S, Dowling P, Ohlendieck K. Comparative skeletal muscle proteomics using two-dimensional gel electrophoresis. Proteomes 2016; 4:27.
11. Shen SH, Gu LJ, Liu PQ, Ye X, Chang WS, Li BS. Comparative proteomic analysis of differentially expressed proteins between K562 and K562/ADM cells. Chin Med J (Engl) 2008; 121:463-8.
12. Lu D, Wang W, Liu J, et al. Peroxiredoxins in inflammatory liver diseases and ischemic/reperfusion injury in liver transplantation. Food Chem Toxicol 2018; 113:83-9.
13. Tu DD, Zhou YL, Gu WB, et al. Identification and characterization of six peroxiredoxin transcripts from mud crab Scylla paramamosain: The first evidence of peroxiredoxin gene family in crustacean and their expression profiles under biotic and abiotic stresses. Mol Immunol 2018; 93: 223-35.
14. Ho JN, Lee SB, Lee SS, Yoon SH, Kang GY, Hwang SG, Um HD. Phospholipase A2 activity of peroxiredoxin 6 promotes invasion and metastasis of lung cancer cells. Mol Cancer Ther 2010; 9:825-32.
15. Pak JH, Choi WH, Lee HM, et al. Peroxiredoxin 6 overexpression attenuates cisplatin-induced apoptosis in human ovarian cancer cells. Cancer Invest 2011; 29:21-28.
16. Hirota Y, Acar N, Tranguch S, et al. Uterine FK506-binding protein 52 (FKBP52)-peroxiredoxin-6 (PRDX6) signaling protects pregnancy from overt oxidative stress. Proc Natl Acad Sci U S A 2010; 107:15577-82.
17. Zhang Q, Yan Q, Yang H, Wei W. Oxygen sensing and adaptability won the 2019 Nobel Prize in Physiology or medicine. Genes Dis 2019; 6:328-32.
18. Xu J, Su Q, Gao M, Liang Q, Li J, Chen X. Differential expression and effects of peroxiredoxin-6 on drug resistance and cancer stem cell-like properties in non-small cell lung cancer. Onco Targets Ther 2019; 12:10477-86.

Erythropoietin inhibits apoptosis of retinal ganglion cells induced by high glucose through JNK signaling pathway

Y.-X. Qi[1*], X.-J. Su[1*], L.-L. Wei[2] and J. Zhang[1]

[1]Department of Ophthalmology, The First Affiliated Hospital of Jiamusi University, Jiamusi, China; [2]Department of Pediatrics, The First Affiliated Hospital of Jiamusi University, Jiamusi, China

Received November 4, 2020 – Accepted March 2, 2021

[*]These Authors contributed equally to this work

The aim of this study was to investigate the effect of erythropoietin (EPO) on the apoptosis of retinal ganglion cells (RGCs) induced by high glucose and its mechanism. Rat primary RGCs were extracted to establish high glucose-induced apoptosis models using a 30 mM high-glucose medium. Then flow cytometry, cell counting kit-8 (CCK-8) assay and Western blotting assay were performed to detect the effects of high-, medium- and low-dose EPO on the apoptosis of RGCs induced by high glucose. Next, the molecular mechanism by which EPO suppressed the high glucose-induced apoptosis of RGCs was explored via gene array assay and bioinformatics analysis. The results and mechanism of bioinformatics analysis were verified by Western blotting assay. Finally, the small interfering ribonucleic acid (siRNA) experiment was applied to knock down tyrosine-protein phosphatase non-receptor type 1 (PTPN1) and PTPN11 to verify their roles in the inhibition of EPO on the apoptosis of RGCs triggered by high glucose. Flow cytometry-Annexin V/propidium iodide (PI) staining and CCK-8 assay confirmed that the high-, medium- and low-dose EPO inhibited the apoptosis of RGCs induced by high glucose in a dose-dependent manner ($P<0.05$). Subsequently, Western blotting assay results manifested that the high-, medium- and low-dose EPO reduced the expression levels of apoptosis-related proteins active-cysteinyl aspartate specific proteinase 3 (Caspase 3) and active-Caspase 9 in a dose-dependent manner ($P<0.05$). Moreover, according to gene array assay and bioinformatics analysis results, the c-Jun N-terminal kinase (JNK) signaling pathway, PTPN1 and PTPN11 might exert crucial effects in the inhibition of EPO on the apoptosis of RGCs induced by high glucose. Western blotting assay results also demonstrated that, compared with the high-glucose treatment, the high-dose EPO treatment decreased the protein expression level of phosphorylated (p)-JNK1/JNK but increased the protein expression levels of PTPN1 and PTPN11 ($P<0.05$). Moreover, flow cytometry-Annexin V/PI staining and CCK-8 assay results revealed that in EPO-treated cells, knocking down PTPN1 and PTPN11 significantly reversed the protective effect of EPO against high glucose-induced retinal ganglion cell apoptosis ($P<0.05$). Lastly, Western blotting assay illustrated that knocking down PTPN1 and PTPN11 significantly abolished the inhibition of high-dose EPO on the JNK signaling pathway. EPO may suppress the JNK signaling pathway by raising the expression levels of PTPN1 and PTPN11, so as to inhibit the apoptosis of RGCs triggered by high glucose.

Key words: erythropoietin; diabetic retinopathy; rat retinal ganglion cell apoptosis; JNK signaling pathway

Corresponding Author:
Jian Zhang, MM.
Department of Ophthalmology,
The First Affiliated Hospital of Jiamusi University,
No. 348, Dexiang Street, Xiangyang District,
Jiamusi, Heilongjiang 154002, China
Tel.: +86 015694548255
e-mail: ieut96@163.com

0393-974X (2021)
Copyright © by BIOLIFE, s.a.s.
This publication and/or article is for individual use only and may not be further reproduced without written permission from the copyright holder.
Unauthorized reproduction may result in financial and other penalties
DISCLOSURE: ALL AUTHORS REPORT NO CONFLICTS OF INTEREST RELEVANT TO THIS ARTICLE.

According to the results of an epidemiological study, as life expectancy extends, the number of patients with diabetes will increase dramatically in the next decade, which is expected to reach 592 million by 2035 (1). Diabetic retinopathy (DR) is the most common complication of diabetes, leading to blindness. In the population with diabetes from 1990 to 2010, the incidence rates of DR-related visual impairment and blindness were 64% and 27%, respectively (2). With a high blindness rate, DR severely threatens the quality of life of patients, therefore is an urgent issue to be solved in the contemporary medical field. Currently, hypoglycemic therapy, laser therapy, VEGF-targeted therapy and surgical therapy are the main treatment methods for DR, but there is still an urgent need for new treatment.

Current research has shown that the specific pathological mechanism of DR is relatively complex. In the aspect of microvasculature, its pathological mechanism primarily includes peripheral cell loss (3), capillary basement membrane thickening (4), microangioma (5) and blood retinal barrier damage (6). At present, however, increasingly more evidence proves that DR is a neurodegenerative disease. In the early stage of DR, when the apoptosis of nerve cells occurs earlier than the injury of vascular endothelial cells, retinal ganglion cells (RGCs) undergo apoptosis, indicating that RGCs play a crucial role in DR, therefore, it may be an effective strategy to treat DR by regulating apoptosis-related signaling pathways and inhibiting the apoptosis of nerve cells.

Erythropoietin (EPO), a glycoprotein composed of 165 amino acids, exerts a vital role in the process of erythropoiesis (7). Numerous studies have pointed out that EPO is an effective inhibitor of apoptosis that can be utilized for diverse nerve injuries, including traumatic brain injury (8), cerebral apoplexy (9) and spinal cord injury (10). Besides, studies have illustrated that the serum EPO level in patients with type 1 and type 2 diabetes mellitus obviously declines, and EPO is able to suppress the pathological process of DR by inhibiting oxidative stress and resisting apoptosis and inflammation. However, the action mechanism of EPO in inhibiting DR remains unclear. In the present study, the effect of EPO on the apoptosis of primary RGCs induced by high glucose was detected *in vitro*, and the potential action mechanism by which EPO represses DR was investigated through gene array assay and knockout experiments in order to provide an experimental basis for the treatment of DR.

MATERIALS AND METHODS

Cell culture methods

This study was approved by the Animal Ethics Committee of Jiamusi University. Primary RGCs were extracted from neonatal Sprague-Dawley (SD) rats according to the extraction method shown in the literature (11), briefly described below. Firstly, neonatal SD rats aged 1-3 days were dissected under aseptic conditions to obtain their retinal tissues which were then digested at 37°C for 30 min in HBSS equilibrium buffer containing 70 U/mL collagenase and 15 U/mL papain. Subsequently, the digested tissues were added into Dulbecco's modified eagle medium (DMEM) (Gibco, Rockville, MD, USA) containing 1 mg/mL bovine serum albumin (BSA), 2 mg/mL ovomucoid, and 0.004% deoxyribonuclease, and carefully ground using Pasteur tubes to obtain suspended cells. After that, the cells were collected by centrifugation and then washed again with phosphate-buffered saline (PBS). Next, macrophages were removed using macrophage antibodies, and RGCs were selectively screened using anti-Thy1.1 antibody. RGCs were then cultured in Neurobasal medium containing 1 mM glutamine, 10mg/mL gentamicin, 5ng/mL forskolin and 5 ng/mL brain-derived neurotrophic factors. Finally, the cells were cultured at 37°C in a humid incubator containing 5% CO_2.

In this study, models of RGC apoptosis induced by high glucose were established using 30 mM high-glucose medium. EPO-treated cells were divided into low-dose group (2 U/mL), medium-dose group (20 U/mL) and high-dose group (200 U/mL).

Small interfering ribonucleic acid (siRNA) transfection

When the density reached about 70%, the RGCs cultured were transfected with non-targeted siRNA (siRNA Neg), siRNA tyrosine-protein phosphatase non-receptor type 1 (PTPN1) and siRNA PTPN11 using

Lipofectamine RNAimax (Invitrogen, Carlsbad, CA, USA) in strict accordance with the manufacturer's instructions, and the siRNA concentration was 100 nM. Finally, real-time quantitative polymerase chain reaction (RT-qPCR) and Western blotting assays were carried out to verify the transfection. Each assay was repeated at least 3 times.

The transfected cells were assigned into 4 groups, namely, EPO + si-PTPN1 group, EPO + si-PTPN11 group and their corresponding negative control groups.

Gene array assay

Total RNAs were extracted from RGCs and quantified using a NanoDrop kit (Thermo Fisher Scientific, Waltham, MA, USA). Then the integrity of RNAs was evaluated using Bioanalyzer 2100 (Agilent, USA). Complementary ribonucleic acids (cRNAs) were prepared using the Affymetrix 3'IVT Express kit and 100 ng of total RNAs. According to the user's manual of GeneChip 3'Array (Affymetrix, Santa Clara, CA, USA), the cRNAs were hybridized on Affymetrix Primeview Human array at 45°C for 16 h. In addition, the array was processed on the Affymetrix FS-450 fluid station for washing and dyeing and scanned on the Affymetrix GeneChip scanner according to the manufacturer's protocol (Affymetrix, Santa Clara, CA, USA). The original data of the .CEL file were imported into the Partek Genomics Suite 6.6 software and the probe set was standardized using the Robust Multiarray Average method. Thereafter, the significance of differentially expressed genes was determined by one-way analysis of variance, and *p* was corrected by FDR.

Gene set enrichment analysis (GESA) and protein interaction network

In this study, GSEA was conducted to annotate data of high-throughput proteomics to explore the function of differentially expressed genes (12). The differential expression tags were derived from KEGG and GO databases.

To extract the key genes among differentially expressed genes, the online search tool STRING was utilized to analyze the protein interaction in differentially expressed genes. String (version 11.0) covers 5214,234 proteins from 1133 organisms. In this study, the protein interaction score was greater than 0.9, which represented interactive significance. Then the key modules in the network were screened using the MCODE (molecular complex detection) plug-in in the Cytocape software.

Cell counting kit-8 (CCK-8) assay

Firstly, the cells were inoculated into 96-well plates, and those in the transfection group were cultured overnight before transfection. Secondly, all the cells were stimulated by 30 mM glucose for 48 h, and different doses of EPO (2 U/mL in low-dose group, 20 U/mL in medium-dose group and 200 U/mL in high-dose group) were simultaneously administered. Thirdly, the cells in each well were treated with 10 μL of CCK-8 solution and incubated at 37°C for 2 h. Finally, the optical density (OD) at 450 nm was detected using a microplate reader (Bio-Rad, Hercules, CA, USA).

Flow cytometry

Apoptosis was detected by flow cytometry combined with Annexin V-fluorescein isothiocyante (FITC)/ propidium iodide (PI) staining. The cells were stimulated by high glucose (30 mM) for 48 h and treated with different concentrations of EPO. Then the collected cells were washed by PBS at 4°C and resuspended using binding buffer in the kit. Next, Annexin V-FITC/PI staining solution was added to stain the cells in the dark for 15 min. Subsequently, FACS flow cytometry (BD Biosciences, San Jose, CA, USA) was performed for cell sample loading and analysis.

Western blotting assay

In the first place, the cells were digested with trypsin and lysed using RIPA lysis buffer containing protease inhibitors (Beyotime Biotechnology, Shanghai, China). Then the supernatant was collected after centrifugation in a low-temperature high-speed centrifuge, and the protein concentration was determined using a bicinchoninic acid (BCA) protein quantification kit (Beyotime Biotechnology, Shanghai, China). The proteins were then separated via sodium dodecyl sulphate-polyacrylamide gel electrophoresis (SDS-PAGE) and transferred onto a polyvinylidene fluoride (PVDF) membrane by semi-dry transfer method (Millipore, Billerica, MA, USA), after which the PVDF membrane was sealed with 5% skim milk. Thereafter, the proteins were incubated with primary antibodies overnight in a 4°C environment, and rinsed by tris-buffered saline with Tween-20 (TBST) for 3 times (15 min/time). After that, the proteins were incubated with

secondary antibodies coupled with horseradish peroxidase at room temperature for 2 h, washed with TBST, and detected using an Amersham ECL Western Blotting detection kit (GE Healthcare, Chicago, IL, USA). Finally, Image-Pro Plus 6.0 software was adopted to quantify the proteins.

RT-qPCR assay

Firstly, total RNAs were extracted from the cells digested with trypsin using TRIzol reagent (Invitrogen, Carlsbad, CA, USA) and transcribed into complementary deoxyribose nucleic acids (cDNAs) using a PrimeScript RT kit. Then PCR amplification of cDNAs was carried out according to SYBR Green PCR Master Mix (Applied Biosystems, Foster City, CA, USA) and Applied Biosystems 7500 RT-PCR System under the following conditions: 40 cycles of reaction at 95°C, with 15 s each, and reaction at 60°C for 1 min. With glyceraldehyde-3-phosphate dehydrogenase (GAPDH) as an internal reference, the target gene expression was standardized. The primer sequences used in are shown in Table I.

Statistical analysis

Statistical analysis was conducted using Statistical Product and Service Solutions (SPSS) Statistics Version 16 (SPSS Inc., Chicago, IL, USA) and GraphPad Prism v5.0 (Graphpad Software Inc., La Jolla, CA, USA), and *t*-test and univariate analysis were performed. $P<0.05$ represented statistically significant differences, and $P<0.001$ substantially statistically significant differences.

RESULTS

EPO inhibited RGCs apoptosis induced by high glucose in a dose-dependent manner

CCK-8 assay results showed that at 48 h after EPO treatment, EPO reduced the apoptosis of RGCs induced by high glucose in a dose-dependent manner, and the difference was statistically significant ($P<0.001$) (Fig. 1A). Subsequently, it was discovered from the flow cytometry-Annexin V/PI staining results that the apoptosis rate of RGCs was 6.8% in the control group, 51.2% in the model group, 41.3% in the low-dose group, 30.9% in medium-dose group and 19.8% in the high-dose group (Fig. 1B). Finally, Western blotting assay results revealed that EPO decreased the protein expression levels of active-cysteinyl aspartate specific proteinase (Caspase 3) and active-Caspase 9 in RGC apoptosis induced by high glucose in a dose-dependent manner ($P<0.05$) (Fig. 1C).

Screening of differentially expressed genes

Three cases of cells treated with EPO + high glucose and 3 cases of cells treated with high glucose were detected by gene array assay. Then with $P<0.05$ and fold change = 2 as the standard, a total of 1203 differentially expressed genes were screened out, of which 567 exhibited an obviously increased expression level and 636 showed a significantly decreased expression level. The heat maps of differentially expressed genes are shown in Fig. 2A. Subsequently, GSEA manifested that the differentially expressed genes in the high-dose EPO + high-glucose treatment group were significantly enriched in the negative regulatory pathway of apoptosis, c-Jun N-terminal kinase (JNK) signaling pathway, nuclear factor kappa-B (NF-κB) signaling pathway and Janus kinase/signal transducer and activator of transcription (JAK/STAT) signaling pathway (Fig. 2B).

Protein interaction network

As shown in Fig. 3, the protein interaction network consisted of 186 nodes and 1828 sides, among which, through screening with closeness centrality as an index, it could be concluded that PTPN11, PTPN1, STAT3, mitogen-activated protein kinase 8 (MAPK8), EP300 and Crebbp occupied a central position in the protein interaction network, which revealed that these nodes may exert a crucial effect in EPO inhibition on the apoptosis of RGCs induced by high glucose.

EPO suppressed the JNK signaling pathway in a dose-dependent manner

According to the results of bioinformatics analysis, PTPN1, PTPN11 and JNK signaling pathways probably play vital roles in EPO inhibition on the apoptosis of RGCs triggered by high glucose. The results of RT-qPCR assay illustrated that EPO increased the messenger RNA (mRNA) expression

levels of PTPN1 and PTPN11 in a dose-dependent manner, which was consistent with the results of bioinformatics analysis (Fig. 4A). Afterwards, Western blotting assay demonstrated that high-dose EPO raised the protein expression levels of PTPN1 and PTPN11. Additionally, it was discovered from Western blotting assay that EPO significantly repressed the phosphorylation level of JNK in the high-dose group, showing a statistically significant difference (P<0.05) (Fig. 4B).

EPO inhibited the JNK signaling pathway by

Table I. *Primer sequences*

Primer name	Primer direction	Primer sequence
GAPDH	Forward	CATCACTGCCACCCAGAAGACTG
	Reverse	ATGCCAGTGAGCTTCCCGTTCAG
PTPN1	Forward	TCACAACGGGAAGTGCAAGGAG
	Reverse	CGTCTCCTAACTTCAGTGTCTGG
PTPN11	Forward	TGACTTCTGGCGGATGGTGTTC
	Reverse	GACGTTCCTAACACGCATGACC

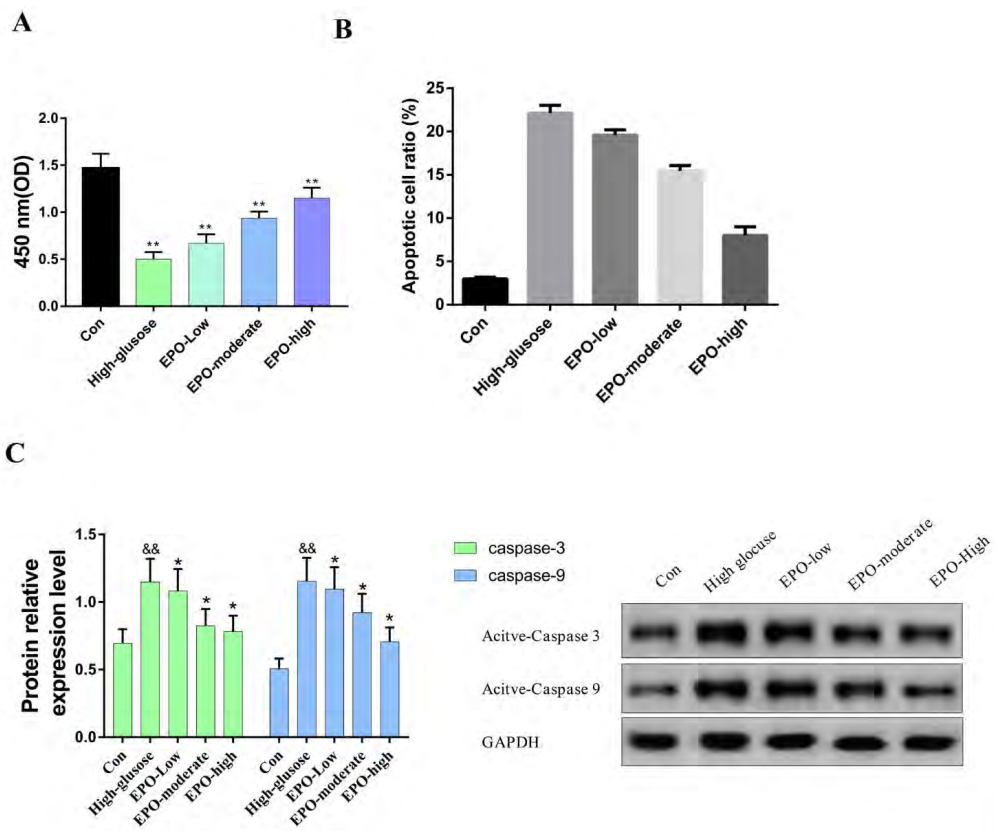


Fig. 1. *EPO inhibited RGC-5 apoptosis induced by high glucose in a dose-dependent manner.* ***A****) Effect of EPO on the activity of RGCs induced by high glucose detected via CCK-8 assay.* ***B****) Impact of EPO on the apoptosis of RGCs induced by high glucose detected via flow cytometry-Annexin V/PI staining.* ***C****) Effects of EPO on the expressions of apoptosis-related proteins active-Caspase 3 and active-Caspase 9 examined via Western blotting assay.* $^{\&\&}P<0.001$ *vs control group,* $^{*}P<0.05$ *vs model group,* $^{**}P<0.001$ *vs model group, showing a statistically significant difference.*

activating PTPN11

CCK-8 assay results manifested that the cell activity in the EPO + si-PTPN11 treatment group was significantly weakened compared with that in the EPO treatment group at 48 h, and the difference was statistically significant (P<0.001) (Fig. 5A). Moreover, RT-qPCR assay showed that in comparison with that in the EPO treatment group, the mRNA expression level of PTPN11 in cells in the EPO + si-PTPN11 treatment group was significantly reduced, displaying a statistically significant difference (P<0.001) (Fig. 5B). Furthermore, the flow

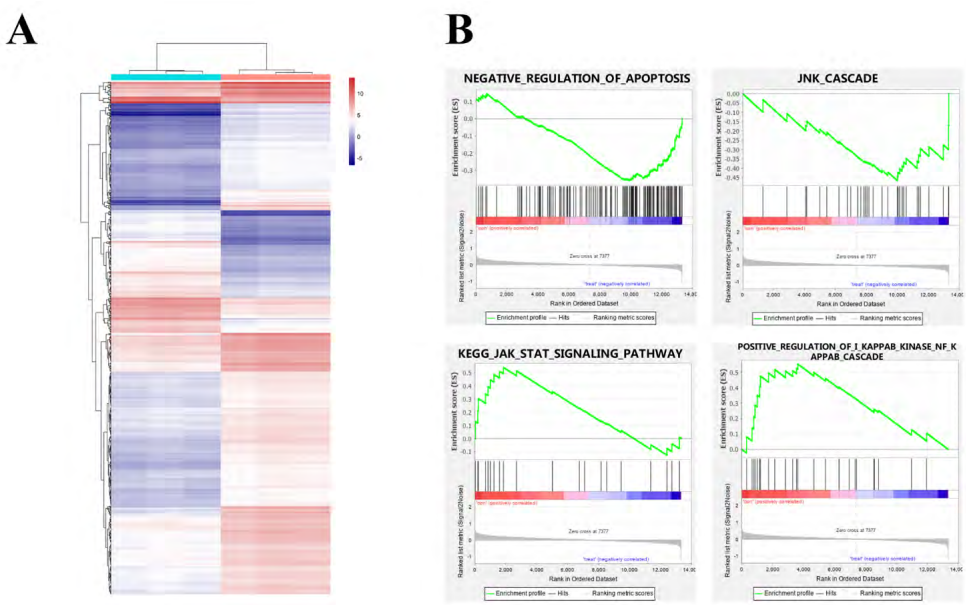


Fig. 2. *Heat maps of differentially expressed genes. **A**) Red: up-regulated genes, and green: down-regulated genes. **B**) Signaling pathways of significantly enriched and differentially expressed genes explained by GSEA.*

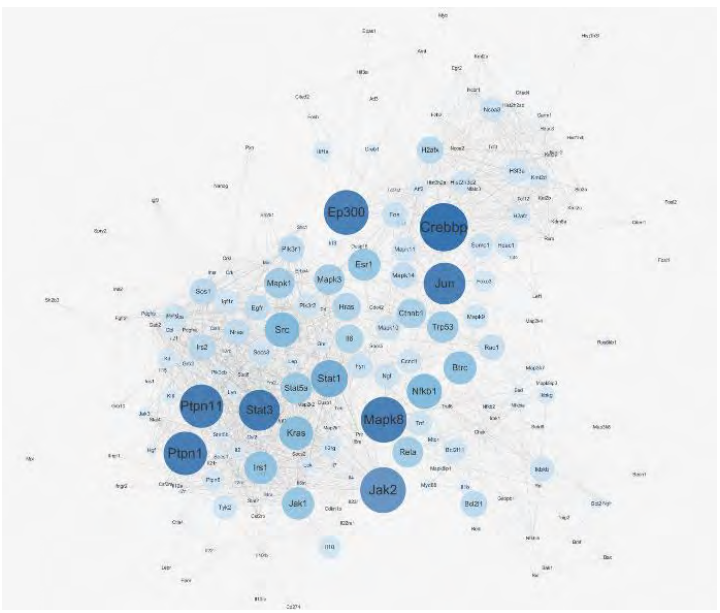


Fig. 3. *Key genes explored via the protein interaction network. The network consisted of 186 nodes and 1828 sides. The larger the area of the node was, the darker the color would be, representing a higher betweenness centrality in the network.*

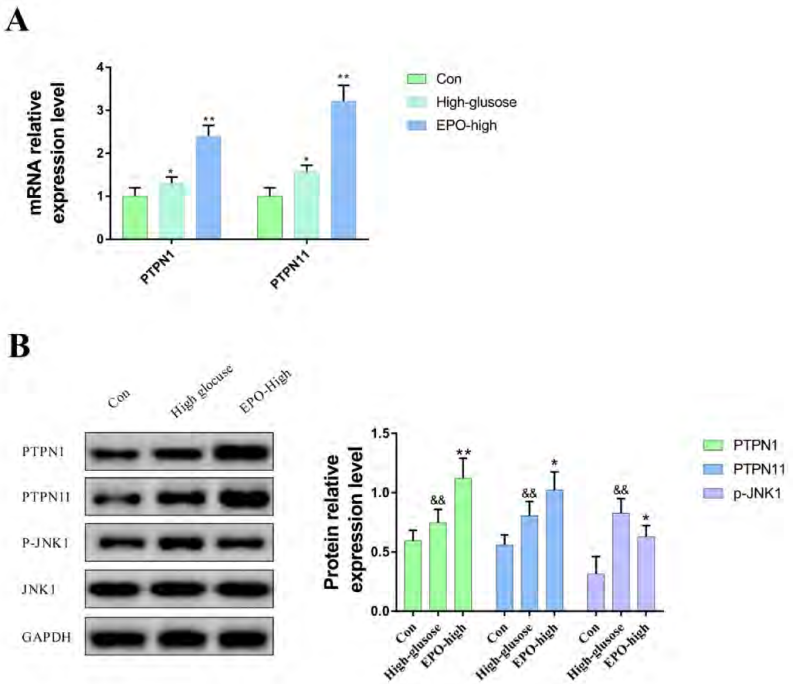


Fig. 4. *EPO repressed the JNK signaling pathway in a dose-dependent manner.* ***A****) Impacts of EPO on the messenger RNA (mRNA) levels of PTPN1 and PTPN11 detected via RT-qPCR.* ***B****) Effects of EPO on the protein expression levels of PTPN1 and PTPN11 as well as the JNK signaling pathway.* $^{\&\&}P<0.001$ *vs control group,* $^{*}P<0.05$ *vs model group,* $^{**}P<0.001$ *vs model group, displaying a statistically significant difference.*

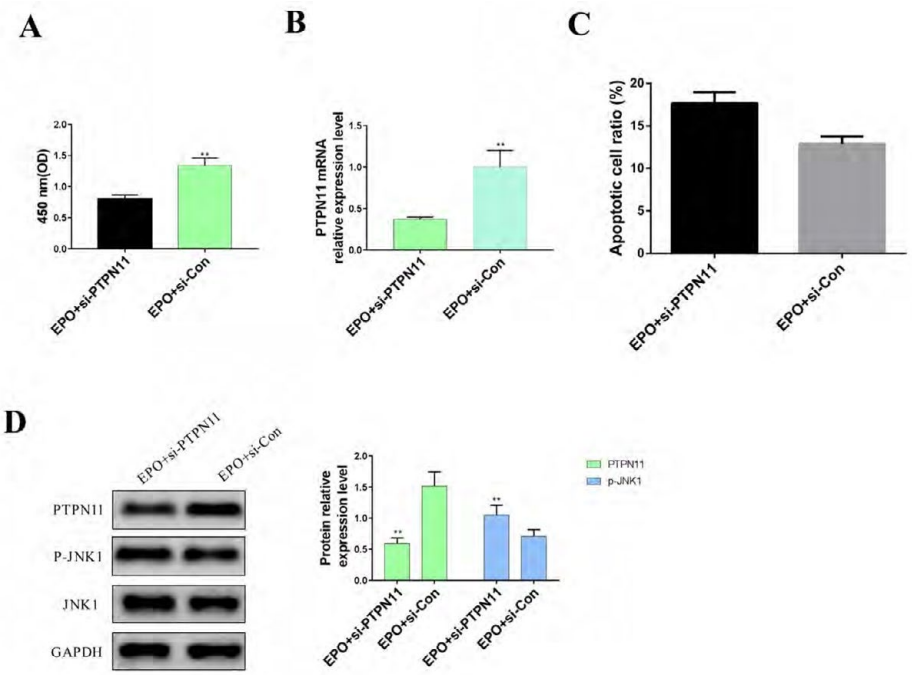


Fig. 5. *EPO inhibited the JNK signaling pathway by activating PTPN11.* ***A****) Differences in the mRNA expression level of PTPN11 in cells between EPO treatment group and EPO + si-PTPN11 treatment group detected via RT-qPCR.* ***B****) Protective effect of EPO against RGCs by knocking down PTPN11 examined via CCK-8 assay.* ***C****) Influence of knocking down PTPN11 on the inhibitory effect of EPO on apoptosis detected via flow cytometry-Annexin V/PI staining.* ***D****) Effect of knocking down PTPN11 on the JNK signaling pathway examined via Western blotting assay.* $^{**}p<0.001$ *vs model group.*

cytometry-Annexin V/PI staining results denoted that the apoptosis rate was 29.8% in the EPO treatment group and 43.5% in the EPO + si-PTPN11 treatment group (Fig. 5C). Finally, it was found from the results of Western blotting assay that in contrast to that in the EPO treatment group, the protein expression level of phosphorylated (p)-JNK1 in the cells was significantly increased, but the protein expression level of PTPN11 was significantly reduced in the EPO + si-PTPN11 treatment group, with statistically significant differences (P<0.001) (Fig. 5D). The above results indicate that EPO may inhibit the JNK signaling pathway and further suppress the apoptosis of RGCs induced by high glucose through activating and increasing the PTPN11 expression.

EPO inhibited the JNK signaling pathway by activating PTPN1

RT-qPCR assay revealed that in contrast to that in EPO treatment group, the mRNA expression level of PTPN1 in cells in the EPO + si-PTPN1 treatment group was decreased, and the difference was statistically significant (P<0.001) (Fig. 6A). Subsequently, it was discovered from CCK-8 assay results that the cell activity in the EPO + si-PTPN1 treatment group was significantly repressed compared with that in the EPO treatment group at 48 h, showing a statistically significant difference (P<0.001) (Fig. 6B). Moreover, the flow cytometry-Annexin V/PI staining results denoted that the apoptosis rate was 31.3% in the EPO treatment group and 45.6% in the EPO + si-PTPN1 treatment group (Fig. 6C). Lastly, Western blotting assay results indicated that the protein expression level of p-JNK1 in the cells was significantly increased, but the protein expression level of PTPN1 was significantly reduced in the

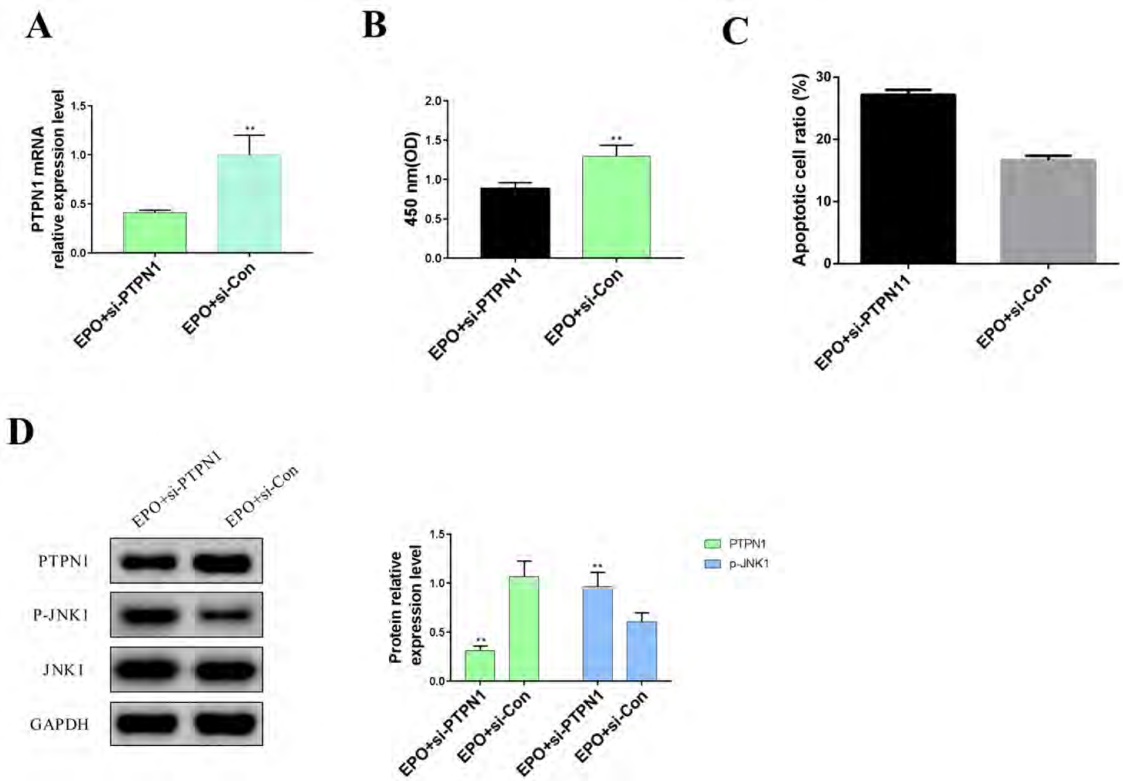


Fig. 6. *EPO inhibited the JNK signaling pathway by activating PTPN1.* ***A)*** *Differences in the mRNA expression level of PTPN1 in cells between EPO treatment group and EPO + si-PTPN1 treatment group detected via RT-qPCR.* ***B)*** *Protective effect of EPO against RGCs by knocking down PTPN1 examined via CCK-8 assay.* ***C)*** *Influence of knocking down PTPN1 on the inhibitory effect of EPO on apoptosis detected via flow cytometry-Annexin V/PI staining.* ***D)*** *Effect of knocking down PTPN1 on the JNK signaling pathway examined via Western blotting assay.* $^{**}P$*<0.001 vs model group.*

EPO + si-PTPN1 treatment group in comparison with that in the EPO treatment group, displaying a statistically significant difference (P<0.001) (Fig. 6D). It can be seen that EPO probably suppresses the JNK signaling pathway to inhibit the apoptosis of RGCs induced by high glucose through activating and increasing the PTPN1 expression.

DISCUSSION

In the present research, the efficacy and mechanism of EPO in inhibiting the apoptosis of RGC cells induced by high glucose were explored. In the first place, flow cytometry-Annexin V/PI staining, CCK-8 and Western blotting results manifested that EPO repressed the high glucose-triggered apoptosis of RGCs in a dose-dependent manner. Next, gene array assay results confirmed that the differentially expressed genes in EPO treatment group were significantly enriched in the negative regulatory pathway of apoptosis, JNK signaling pathway, NF-κB signaling pathway and JAK/STAT signaling pathway. Through the protein interaction network, it was discovered that MAPK8, PTPN1 and PTPN11 may play crucial roles in EPO inhibition on the apoptosis of RGCs induced by high glucose. Moreover, Western blotting results revealed that EPO inhibited the JNK signaling pathway, which was accompanied by the elevated expression levels of PTPN1 and PTPN11. Finally, the protein expression levels of PTPN1 and PTPN11 were knocked down using siRNA experimental method, and EPO's inhibitory effect on the apoptosis of RGCs triggered by high glucose was weakened accordingly. The above results of this study indicate that EPO may suppress the JNK signaling pathway by activating PTPN11/PTPN1, thus inhibiting high glucose-induced apoptosis of RGCs.

EPO probably exerts a pivotal effect in the apoptosis of RGCs in DR. In the first place, some studies have shown that EPO is a vital neuroprotective factor in DR, but its serum level in patients with type I and type II diabetes mellitus markedly declines. This significant reduction is associated with DR, microangiopathy and the impairment of renal autonomic nerve function during diabetes.

Furthermore, EPO may be applied to inhibit the apoptosis of RGCs triggered by high glucose. The results of this study denoted that EPO repressed the high glucose-triggered apoptosis of RGCs in a dose-dependent manner. In consistency with the results of this research, some studies have pointed out that EPO can inhibit oxidative stress level and the apoptosis of RGCs by increasing glutathione content and reducing the levels of intracellular reactive oxygen species (ROS) and AGEs in streptozotocin-induced diabetic rat models (13). Additionally, other studies have shown that EPO is able to reduce the expressions of IL-4, IL-1β, IFN-γ and tumor necrosis factor-alpha (TNF-α) in the serum of rats and inhibit the apoptosis of RGCs in DR rat models, and its effect on inflammatory factors probably has an association with the NF-κB signaling pathway (14). It is well known that inflammation and oxidative stress are important causes of RGC apoptosis, which is consistent with the results of this research.

As is well-known, the MAPK signaling pathway is obviously correlated with cell proliferation and apoptosis modulated by ROS and inflammation. The MAPK signaling pathway includes the ERK1/2 signaling pathway, JNK signaling pathway, and p38-MAPK signaling pathway, among which the JNK signaling pathway is generally believed to be correlated with apoptosis-promoting signals modulated by inflammation, hypoxia and oxidative stress. Stimulated by inflammatory factors and oxidative stresses, the JNK signaling pathway is activated to facilitate apoptosis through the transcription-dependent pathway. The transcription-dependent pathway is to phosphorylate transcription factors AP-1 and ATF-2 after JNK enters the nucleus, thus inducing the expressions of apoptosis-related factors such as FasL and TNF to facilitate apoptosis. Moreover, numerous studies have shown that inflammation, hypoxia and oxidative stresses are vital ways to promote the apoptosis of RGCs in retinal neuropathy. Hence, the JNK signaling pathway may be a core target for RGC apoptosis in the treatment of DR. Liu et al. (15) pointed out that hesperidin can inhibit RGC-5 cell apoptosis induced by high glucose through suppressing the JNK signaling pathway, which is consistent with the

results of the present research.

Gene array assay was conducted to further explore the molecular mechanism by which EPO inhibited the apoptosis of RGCs induced by high glucose through repressing the JNK signaling pathway. The results pointed out that PTPN1 and PTPN11 were core molecules in the network, so they probably exert a vital effect in the apoptosis of RGCs induced by high glucose. Some studies have indicated that PTPN1 and PTPN11 are negative regulators of the JNK signaling pathway. For instance, a study by Moon et al. (16) revealed that PTPN1 is able to specifically suppress the activation of the JNK signaling pathway in 77 mammalian tissues or cell lines, and it can reduce TNF-α-induced apoptosis through negatively modulating the JNK signaling pathway. Additionally, a study by Xu et al. (17) showed that miR-125a-5p can lower the expression level of PTPN1 by targeting it, so as to activate the JNK signaling pathway, thus inhibiting the proliferation of liver cancer cells and promoting their apoptosis. Nasimian et al. (18) demonstrated that repressing the PTPN1 expression in macrophages increases the phosphorylation level of JNK. As for the relationship between the JNK signaling pathway and PTPN11, Tibbles et al. (19) pointed out that PTPN11 can remarkably result in the inactivation of the JNK/SAPK signaling under cell stresses. Moreover, Bhattacharyya et al. (20) confirmed that inhibiting the PTPN11 expression can markedly increase the phosphorylation level of JNK and the transportation of c-JUN and c-FOS into the nucleus in CRL-2887 cell line. These results suggest that PTPN1 and PTPN11 have negative regulatory effects on the JNK signaling pathway.

In the current research, it was found that EPO up-regulated the protein expressions of PTPN1 and PTPN11 in a dose-dependent manner. Meanwhile, knocking down PTPN1 and PTPN11 prominently activated the JNK signaling pathway and abrogated EPO's protection against the high glucose-triggered apoptosis of RGCs to some extent. With regard to the correlations of EPO with PTPN1 and PTPN11, some studies have denoted that EPO can facilitate the expressions or activation of PTPN1 and PTPN11 by binding to its receptor EPO receptors (EPORs). For example, Tauchi et al. (21) indicated that the phosphorylation level of PTPN11 was elevated in DA-3 cell line but obviously reduced in DA-3 cell line with EPOR mutation. In addition, Thomas et al. (22) highlighted that activating EPORs can raise the phosphorylation level of PTPN11. Concerning the correlation between PTPN1 and the EPO/EPOR signaling pathway, research has manifested that EPO can raise the protein expression level and tyrosine phosphorylation level and enhance the tyrosinase activity of PTPN1 through the JAK2 and PI3K signaling pathways in EPO-dependent UT-7 cell line. It can be seen from all these studies that EPO may increase the expression and enhance the activity of PTPN1 and PTPN11, which is in consistency with the results of the present research. However, this experiment is also associated with some limitations, the exact mechanism of EPO inhibiting the JNK signaling pathway is still unclear, especially the roles of PTPN1 and PTPN11 in it, which seem to require more rescue experiments to further clarify.

To sum up, the research results indicate that EPO may suppress the JNK signaling pathway by raising the expression levels of PTPN1 and PTPN11, thus inhibiting the apoptosis of RGCs induced by high glucose.

ACKNOWLEDGEMENTS

Scientific research project of Heilongjiang Health Commission (2020-337).

REFERENCES

1. Seferovic PM, Petrie MC, Filippatos GS, et al. Type 2 diabetes mellitus and heart failure: a position statement from the Heart Failure Association of the European Society of Cardiology. Eur J Heart Fail 2018; 20:853-72.
2. Gardner GG, Keating D, Williamson TH, Elliott AT. Automatic detection of diabetic retinopathy using an artificial neural network: a screening tool. Br J Ophthalmol 1996; 80:940-4.
3. Hammes HP. Pericytes and the pathogenesis of diabetic retinopathy. Horm Metab Res 2005; 37 Suppl 1:39-43.
4. Greenwood MD, Ressler MJ, Audette JL, et al.

Significant retinal capillary basement membrane thickening in hyperglycemic and normoglycemic diabetic-prone (DP) BB Wistar rats. Ultrastruct Pathol 2011; 35:97-105.
5. Mitchell P, Wong TY. DIRECT new treatments for diabetic retinopathy. Lancet 2008; 372:1361-3.
6. Jampol LM, Odia I, Glassman AR, et al. Panretinal photocoagulation versus ranibizumab for proliferative diabetic retinopathy: comparison of peripapillary retinal nerve fiber layer thickness in a randomized clinical trial. Retina 2019; 39:69-78.
7. Meng R, Zhu D, Bi Y, Yang D, Wang Y. Erythropoietin inhibits gluconeogenesis and inflammation in the liver and improves glucose intolerance in high-fat diet-fed mice. Plos One 2013; 8:e53557.
8. Brines ML, Ghezzi P, Keenan S, et al. Erythropoietin crosses the blood-brain barrier to protect against experimental brain injury. Proc Natl Acad Sci U S A 2000; 97:10526-31.
9. Ehrenreich H, Hasselblatt M, Dembowski C, et al. Erythropoietin therapy for acute stroke is both safe and beneficial. Mol Med 2002; 8:495-505.
10. Celik M, Gokmen N, Erbayraktar S, et al. Erythropoietin prevents motor neuron apoptosis and neurologic disability in experimental spinal cord ischemic injury. Proc Natl Acad Sci U S A 2002; 99:2258-63.
11. Kim D, Lim S, Park M, et al. Ubiquitination-dependent CARM1 degradation facilitates Notch1-mediated podocyte apoptosis in diabetic nephropathy. Cell Signal 2014; 26:1774-82.
12. Subramanian A, Kuehn H, Gould J, Tamayo P, Mesirov JP. GSEA-P: a desktop application for Gene Set Enrichment Analysis. Bioinformatics 2007; 23:3251-3.
13. Zheng DH, Han ZQ, Wang XX, Ma D, Zhang J. Erythropoietin attenuates high glucose-induced oxidative stress and inhibition of osteogenic differentiation in periodontal ligament stem cell (PDLSCs). Chem Biol Interact 2019; 305:40-47.
14. Ozkurt M, Uzuner K, Erkasap N, et al. Erythropoietin Protects the Kidney by Regulating the Effect of TNF-alpha in L-NAME-Induced Hypertensive Rats. Kidney Blood Press Res 2018; 43:807-19.
15. Liu WY, Liou SS, Hong TY, Liu IM. Protective Effects of Hesperidin (Citrus Flavonone) on High Glucose Induced Oxidative Stress and Apoptosis in a Cellular Model for Diabetic Retinopathy. Nutrients 2017; 9:1312.
16. Moon J, Ha J, Park SH. Identification of PTPN1 as a novel negative regulator of the JNK MAPK pathway using a synthetic screening for pathway-specific phosphatases. Sci Rep 2017; 7:12974.
17. Xu X, Tao Y, Niu Y, et al. miR-125a-5p inhibits tumorigenesis in hepatocellular carcinoma. Aging (Albany NY) 2019; 11:7639-62.
18. Nasimian A, Taheripak G, Gorgani-Firuzjaee S, Sadeghi A, Meshkani R. Protein tyrosine phosphatase 1B (PTP1B) modulates palmitate-induced cytokine production in macrophage cells. Inflamm Res 2013; 62:239-46.
19. Tibbles LA, Woodgett JR. The stress-activated protein kinase pathways. Cell Mol Life Sci 1999; 55:1230-54.
20. Bhattacharyya S, Feferman L, Han X, et al. Decline in arylsulfatase B expression increases EGFR expression by inhibiting the protein-tyrosine phosphatase SHP2 and activating JNK in prostate cells. J Biol Chem 2018; 293:11076-87.
21. Tauchi T, Damen JE, Toyama K, Feng GS, Broxmeyer HE, Krystal G. Tyrosine 425 within the activated erythropoietin receptor binds Syp, reduces the erythropoietin required for Syp tyrosine phosphorylation, and promotes mitogenesis. Blood 1996; 87:4495-501.
22. Thomas SM, Brugge JS. Cellular functions regulated by Src family kinases. Annu Rev Cell Dev Biol 1997; 13:513-609.

The new-generation proteasome inhibitor oprozomib increases the sensitivity of cervical cancer cells to cisplatin-induced apoptosis

QZ. Li[1,2#], LP. Sun[1#], HY. Shi[3], Y. Chen[1] and H. Shen[1*]

[1]Department of Pathology, School of Basic Medical Sciences, Southern Medical University, Guangzhou, China; [2]Department of Pathology, The Fifth People's Hospital of Foshan Nahai District, Foshan, China; [3]Department of Pathology, The first People's Hospital of Foshan, Foshan, China

Received August 23, 2020 – Accepted March 10, 2021

[#] These authors contributed equally to this study.

This study aimed to evaluate the anti-tumor effect of a new generation of protease inhibitor, oprozomib (OPZ), used alone and in combination with cisplatin, also called CDDP, on cervical cancer. Five different types of cervical cancer cell lines - HeLa, Caski, HeLa-CDDP, C33a, and SiHa - and one nontransformed cervical cell line – HaCaT -were treated with OPZ alone or in combination with cisplatin. The inhibitory effects of OPZ and cisplatin on the proliferation of cervical cancer cells were then analyzed using cytotoxicity tests, flow cytometry, and Western blotting. It was found that OPZ alone or in combination with cisplatin can reduce the proliferation of the five types of cancer cells by enhancing the lysis of caspase-3 and PARP and inducing cancer cell apoptosis. In the combined treatment, OPZ was found to inhibit the degradation of inhibitory factor κB alpha induced by cisplatin, thereby inhibiting the activation of NF-κB, which causes cisplatin resistance, and enhancing the sensitivity of the tumor cells to cisplatin. Moreover, OPZ promoted the phosphorylation of the apoptosis signaling pathway JNK that was activated by cisplatin, thereby inducing tumor cell apoptosis. These findings provide a theoretical basis for the clinical use of OPZ alone and in combination with cisplatin in the treatment of cervical cancer.

Cervical cancer is one of the most common malignant tumors of the female reproductive system and is highly progressive and metastatic in nature. Its morbidity and mortality are second only to breast and ovarian cancer (1), and the five-year survival rate of locally advanced or recurrent cervical cancer patients is only 30–50%. Thestandard treatment is combined chemotherapy based on cisplatin (2–5).

Cisplatin is the most common chemotherapy drug used in the treatment of cervical cancer. It can interfere with target cell apoptosis and survival-related pathways but can also produce a large number of protein substrates, such as unfolded proteins, misfolded proteins, and peptides, that greatly change the quantity, quality, and location distribution of protein substrates in the cells. The two main obstacles that affect the clinical efficacy of cisplatin are the side effects associated with chemotherapy and the inherent drug resistance to cisplatin - it has been reported that approximately 50% of patients with

Key words: cervical cancer; proteasome inhibitor; oprozomib; chemotherapy; cisplatin

**Corresponding Author:*
Dr Hong Shen,
Department of Pathology,
School of Basic Medical Sciences, Southern Medical University,
No. 1023-1063 of Shatai South Street,
Baiyun District, Guangzhou 510515, China
Tel.: +86 10 61648227 - Fax: +86 10 61648227
e-mail: shenhong99_dr@163.com

0393-974X (2021)
Copyright © by BIOLIFE, s.a.s.
This publication and/or article is for individual use only and may not be further reproduced without written permission from the copyright holder.
Unauthorized reproduction may result in financial and other penalties
DISCLOSURE: ALL AUTHORS REPORT NO CONFLICTS OF INTEREST RELEVANT TO THIS ARTICLE.

cervical cancer develop resistance to the drug (5). The ideal treatment plan to overcome this resistance and improve the drug's anti-tumor effect is to combine it with sensitizer factors (6). Finding new, safe, and effective sensitizers that can be combined with cisplatin has therefore become an urgent challenge in the clinical treatment of cervical cancer.

The ubiquitin-proteasome system (UPS) is the main pathway of protein degradation in eukaryotic cells. It regulates important processes, such as apoptosis, survival, the cell cycle, DNA damage, and antigen presentation (7, 8), and plays a central role in the cell's regulatory network (9). When cisplatin is used to treat cervical cancer, intracellular protein increases; the UPS cannot completely degrade this increased protein, which inhibits the protein homeostasis. The imbalanced protein homeostasis means the newly synthesized protein is unable to fold effectively to form a functional conformation or to induce apoptosis of cancer cells and exert the chemotherapeutic effect of cisplatin, and it may activate cell survival pathways while inducing apoptosis of cancer cells (10). Protease inhibitors (PIs), however, can prevent the aggregation of substrate proteins and induce this apoptosis. In the past few decades, first- and second-generation PIs have been extensively studied in clinical trials as selective anti-tumor treatments (11). PIs have been found to have several anti-tumor activity mechanisms: they can block the degradation of nuclear transcription factor inhibitor (I-kB), down-regulate the NF-κB signaling pathway, promote the production of apoptosis factor (tumor necrosis factor), induce tumor cell apoptosis, stabilize the P53 gene, and interfere with many different cell signaling pathways, including AKT, MAPK, and c-Jun (12).

The first-generation PI bortezomib and the second-generation PI carfilzomib were approved by the Food and Drug Administration of the United States (FDA) for the treatment of multiple myeloma and mantle cell lymphoma in 2003 and 2012, respectively. These PIs inhibit the activity of the 20S proteasome through reversible and irreversible binding with β5 subunits, thereby inhibiting tumor cells (13, 14). Ixazomib, a bortezomib analog, became the first oral PI to enter clinical trials by reversibly binding to the β5 subunit; it was approved by the FDA to treat myeloma in 2016. Another biologically effective oral PI is oprozomib (OPZ), an analog of carfilzomib that has been approved by the FDA as a treatment drug for relapsed multiple myeloma (15, 16), which irreversibly binds to the β5 subunit. OPZ can selectively inhibit the activity of protease and reduce its toxic effect on peripheral nerve tissue (17). Unlike these analogs, bortezomib and carfilzomib are administered intravenously. The affinity with high concentrations of proteases and very low dissociation in the blood, however, limits their entry into the surrounding tissues, including solid tumors; therefore, their therapeutic effect on solid tumors is limited. Oral PIs can be dissociated from the proteasome more quickly and more evenly distributed in the body tissues (18). Although the use of PIs has been successful in the treatment of malignant tumors of the hematopoietic system, their clinical efficacy as a single drug in the treatment of solid tumors is limited (19–21). In recent years, however, the effect of PIs combined with conventional cytotoxic drugs in the treatment of solid tumors has been confirmed in many clinical trials. For example, the combination of bortezomib, camptothecin, and adriamycin in the treatment of oral cancer can improve the efficacy of the treatment and reduce its toxicity (22).

OPZ has potential significance in the treatment of hematopoietic malignancies and other solid tumors, such as breast cancer (23), head and neck malignancies, and hepatocellular carcinoma (24–26). However, the mechanism of OPZ alone or in combination with cytotoxic drugs on the proliferation of cervical cancer cells remains unclear. The present study therefore aims to evaluate the inhibitory effect of OPZ alone and in combination with cisplatin on the proliferation of cervical cancer cells.

MATERIALS AND METHODS

Cell lines and cell culture

Five molecular subtypes of cervical cancer cell, SiHa, C33a, HeLa, HeLa-CDDP (a type of cisplatin-resistant HeLa cell), and Caski (Guangzhou Ougini Biotechnology Co., Ltd.), and one nontransformed cervical cell line,

HaCaT, were selected and frozen in the Southern Medical University's National Pathology Laboratory.

All cells were routinely cultured in Dulbecco's modified Eagle's medium (DMEM) (Lonza, Walkersville, MD, USA), which was supplemented with 10% fetal bovine serum (Sigma-Aldrich Co. LLC., St. Louis, MO, USA), 100 units/ml penicillin, and 100 mg/ml streptomycin at 37°C in a humidified atmosphere of 5% CO_2.

The antibodies against IκBα (9242), phosphor SAPK/JNK (Thr183/Tyr185) (9251), SAPK/JNK (9258), PARP (9532), and caspase-3 (9662) and an antibody against α-tubulin (10D8) (#2148) were purchased from Cell Signaling Technology (Danvers, MA, USA). OPZ (ONX-0912) and cisplatin (A8321) were obtained from APExBIO Technology LLC (Houston, TX, USA).

The cell cytotoxicity assays were conducted using MTT (MKBH9792V; Sigma-Aldrich Co. LLC., St. Louis, MO, USA) according to the manufacturer's instructions. SPC cells were seeded in 96-well plates at a density of 5 × 103 cells per well and treated with increasing concentrations of OPZ (0.003, 0.01, 0.03, 0.1, 0.3, 1, 3, and 10 *μm*), or with 0.03 μm OPZ in combination with increasing concentrations of cisplatin (0, 1, 2, 4, 8, 16, 32, and 64 *μm*), for 72 h. After incubating at 37°C for 72 h, the cells were observed and photographed with an optical microscope. A total of 100 μl medium containing 10 μl of MTT was added to each well and incubated for another 4 h. A total of 50 μL DMSO was then added to each well, and the cells were incubated for another 10 min. The absorbance of each well was measured at 540 nm, and the cell viability curve was plotted.

Flow cytometry

Apoptosis was simulated using an Annexin V staining kit (Boehringer Mannheim, Indianapolis, IN, USA) according to the manufacturer's instructions. The cells, diluted with 500 μL buffer, were rinsed and suspended in 5 μL of FITC-annexin V/propidium iodide stain for 15 min at 2–8°C, after which 10 ul of PI was mixed with the cells for 5 min at 2–8°C. The fluorescence of 104 cells was measured using a FACScan analyzer (Becton Dickinson, Franklin Lakes, NJ, USA) by the Arizona Cancer Center Flow Cytometry Core Service. Viable cells were determined by subtracting the apoptotic fraction (Annexin VFITC positive).

Western blotting assay

After treatment, the cells were rinsed twice with cold phosphate buffer solution. They were then collected into Eppendorf tubes and centrifuged for 5 min at 4,000 rpm, before being lysed on ice for 30 min in cooled radioimmunoprecipitation assay buffer (50 mM (0.001mol/L) Tris-HCl at pH 7.4, 150 mM NaCl, 1 mM EDTA, 1% NP-40, 0.25% sodium deoxycholate) with protease inhibitors (50 mM Tris-HCl at pH 7.4, 150 mM NaCl, 1 mM EDTA, 1% NP-40, 0.25% sodium deoxycholate) and phosphatase inhibitors at 4°C. This was followed by centrifuging for 15 min at 12,000 rpm at 4°C to collect the supernatants as cell lysates. Protein concentration was measured using Bradford reagent (Bio-Rad Laboratories,USA), and the samples were mixed with 4 × loading buffer and heated at 100°C for 7 min. Cell lysates were separated by 10% SDS-PAGE, transferred to polyvinylidene fluoride membranes (Bio-Rad Laboratories, USA), and blocked with 5% milk at 25°C for 1 h. The membranes were then probed with appropriate dilutions of indicated primary antibodies overnight at 4°C. Over the following days, the membranes were incubated with horseradish peroxidase-conjugated secondary antibodies against rabbit or mouse immunoglobulin with anti-mouse or rabbit IgG at 25°C for 1 h. The membranes were developed using the ECL-Plus Western detection system (GE Health Care, Buckinghamshire, UK). In all cell samples, membranes were reprobed with α-tubulin antibodies as a loading control for whole-cell extracts.

RESULTS

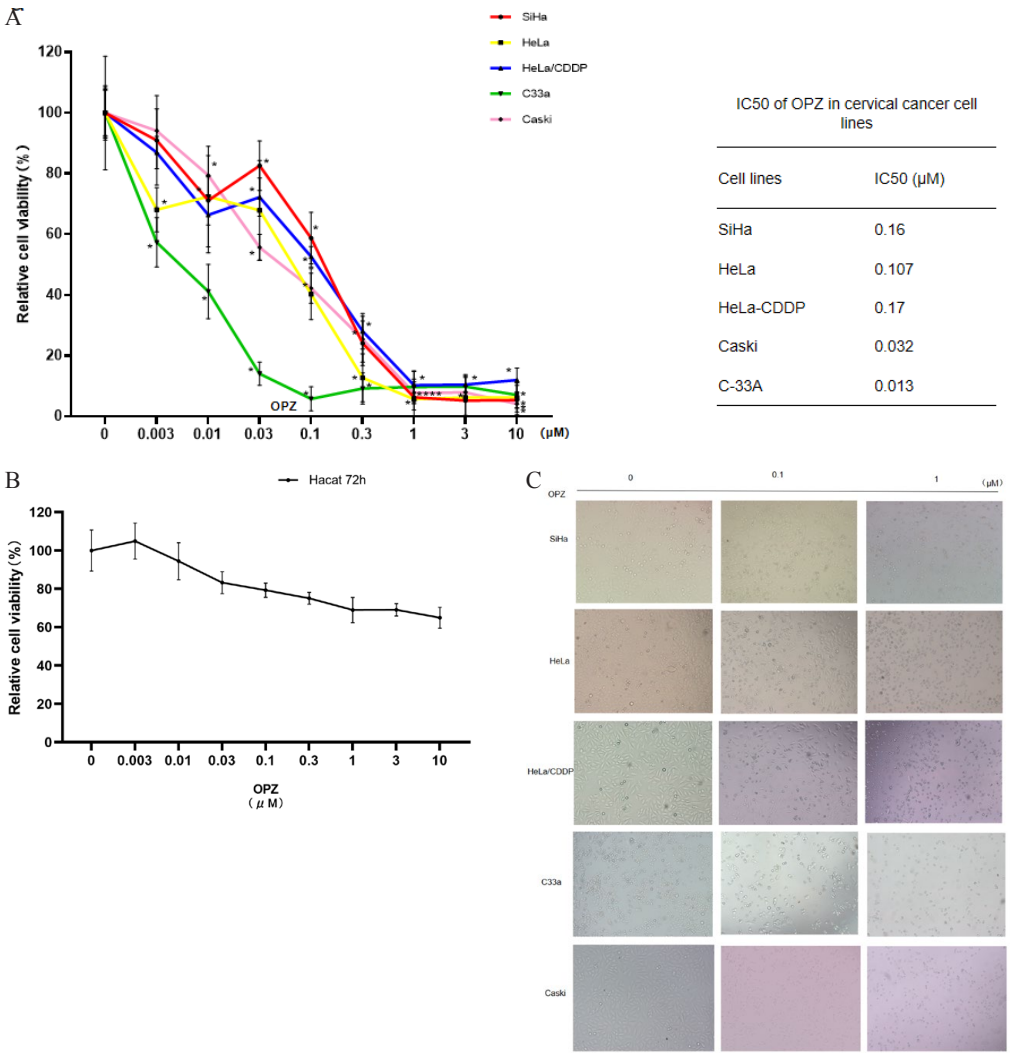
Inhibitory effect of OPZ on the activity of cervical cancer cells

SiHa, HeLa, HeLa-CDDP, Caski, C33a, and HaCaT cells were treated with 0.003 μm to 10 μm OPZ for 72 h, then tetrazolium salt colorimetry assay (MTT) was performed. The results revealed that OPZ could reduce the activity of all subtypes of cervical cancer cells in a dose-dependent manner. The half-maximal inhibitory concentration (IC50) of OPZ was between 13 nm and 170 nm (Fig. 1a), in which HPV-negative C33a was the most sensitive to OPZ, and the IC50 values of other cells were similar. The inhibitory effect of OPZ on HaCaT, a type of nontransformed cervical cell line, was significantly lower than that on other cervical cancer cell lines (Fig. 1b). The morphological changes of five

subtypes of cervical cancer cells could be observed under the microscope after 72 h of treatment with OPZ alone (Fig. 1c).

Apoptosis of cervical cancer cells induced by OPZ

It has been reported that OPZ can induce apoptosis of different tumor cells, including acute childhood leukemia, hepatocellular carcinoma, and head and neck squamous cell carcinoma (23, 24–26). In order to detect the apoptosis of tumor cells induced by OPZ, in this study, 0 μm, 0.1 μm, 0.3 μm, 1.0 μm and 3 μm concentrations of OPZ were used to treat different cervical cancer cell lines. After 24 h of treatment, the cells were collected, then Western blot was performed for quantitative detection. The results revealed that OPZ could induce expressions of cleaved PARP and cleaved caspase-3 in different cell lines (Fig. 2a–e). With the increase in drug concentration, the cleavage of PARP was increased. The results revealed that OPZ alone could induce apoptosis of cervical cancer cells in a dose-dependent manner.



IC50 of OPZ in cervical cancer cell lines

Cell lines	IC50 (μM)
SiHa	0.16
HeLa	0.107
HeLa-CDDP	0.17
Caski	0.032
C-33A	0.013

Fig. 1. *OPZ exhibits anti-cell proliferation effects on cervical cancer cell lines.* ***a)*** *The effects of OPZ on the proliferation of a panel of five cervical cancer cell lines were determined by MTT assay.* ***b)*** *The effects of OPZ on the proliferation a nontransformed cervical cell line (Hacat) were detected by using MTT assay.* ***c)*** *OPZ caused cell morphological changes and decreased cell proliferation in indicated cervical cancer cells. ***P <0.001.*

OPZ could improve the toxicity of cisplatin to cervical cancer cells

In order to further detect the synergistic effect of OPZ combined with cisplatin on cervical cancer cells, the cells were divided into two groups for controlled experiments. Cells in one group were treated with different concentrations (0 μm, 0.3 μm, 0.6 μm, 5 μm, 10 μm, 20 μm, and 40 μm) of cisplatin alone, while cells in the other group were treated with different concentrations of cisplatin combined with 0.03 μm OPZ. After 72 h, MTT was performed for detection. The results (Fig. 3a-e) revealed that the index in the combined group was far lower than 1.0. This indicates that the combination of drugs has a synergistic effect on the inhibition of cervical cancer cells. This suggests that OPZ can increase the cytotoxicity of cisplatin on cervical cancer cells.

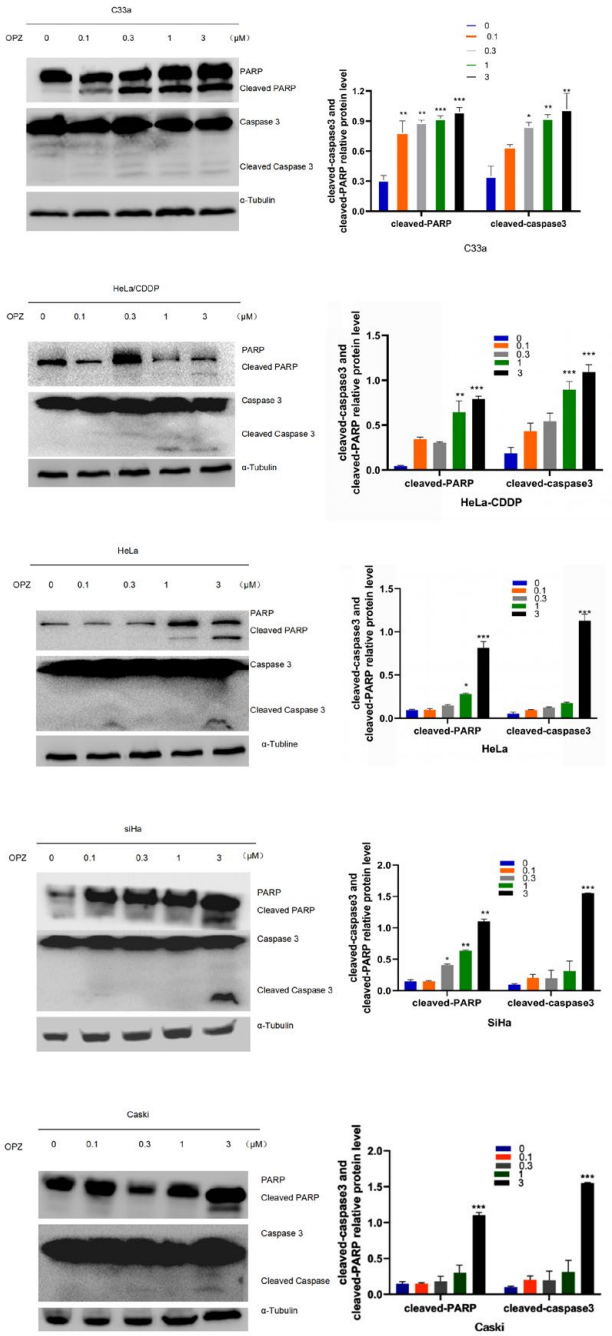


Fig. 2. *OPZ induces apoptosis of cervical cancer cells via the caspase 3 pathway. The expressions of cleaved PARP and caspase 3 in all five cervical cancer cells after treatment with four increasing doses of OPZ increased, as measured by Western blot analysis.*

Apoptosis effect of cisplatin on cervical cancer cells induced and enhanced by OPZ

In order to detect the induction effect of OPZ combined with cisplatin on cervical cancer cells, in this study, the cells were treated with cisplatin alone (80 μm) or in combination with 1 μm OPZ for 12 h. Then Western blot revealed that OPZ enhanced the apoptosis effect of cisplatin on cervical cancer cells by inducing cleavage of PARP and caspase-3 (Fig. 4a–e). In order to further verify the combined effect of OPZ and cisplatin, in this study the most sensitive C33a cells were used and treated with 0.1 μm OPZ, 10 μm cisplatin and the combination of the two drugs for 24 h, respectively, then cell apoptosis rate was detected by flow cytometry. The results revealed that the apoptosis rate significantly increased after the combination of the two drugs compared with that of the two drugs alone (Fig. 5a–d).

OPZ inhibited the degradation of inhibition factor IκBα induced by cisplatin and enhanced the activation of c-Jun N-terminal kinase (JNK) pathway induced by cisplatin

In the present study, HeLa and cisplatin-resistant HeLa/CDDP cells were selected for the experiment. They were treated with 80 μm cisplatin alone or 80 μm cisplatin combined with 10 μm OPZ, respectively. The action time was 0, 4, and 8 h, and then Western blot was performed to detect the changes in NF-κB and c-Jun N-terminal kinase (JNK), two signaling pathways closely related to a variety of cancer progression (Fig. 6a–b). The results revealed that when cisplatin was combined

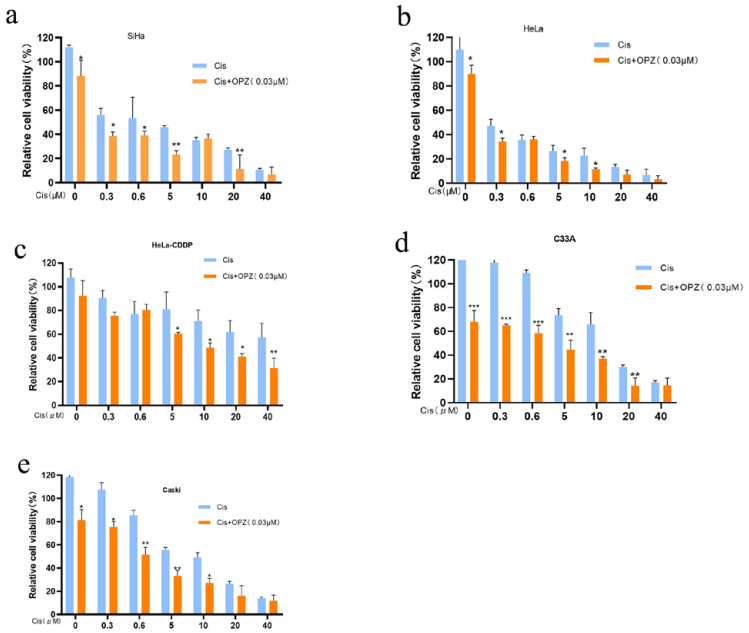


Fig. 3. *OPZ enhances cisplatin-induced cytotoxicity. Based on MTT analysis, OPZ combined with cisplatin has significantly stronger toxic effects on 5 types of cervical cells than cisplatin alone.*

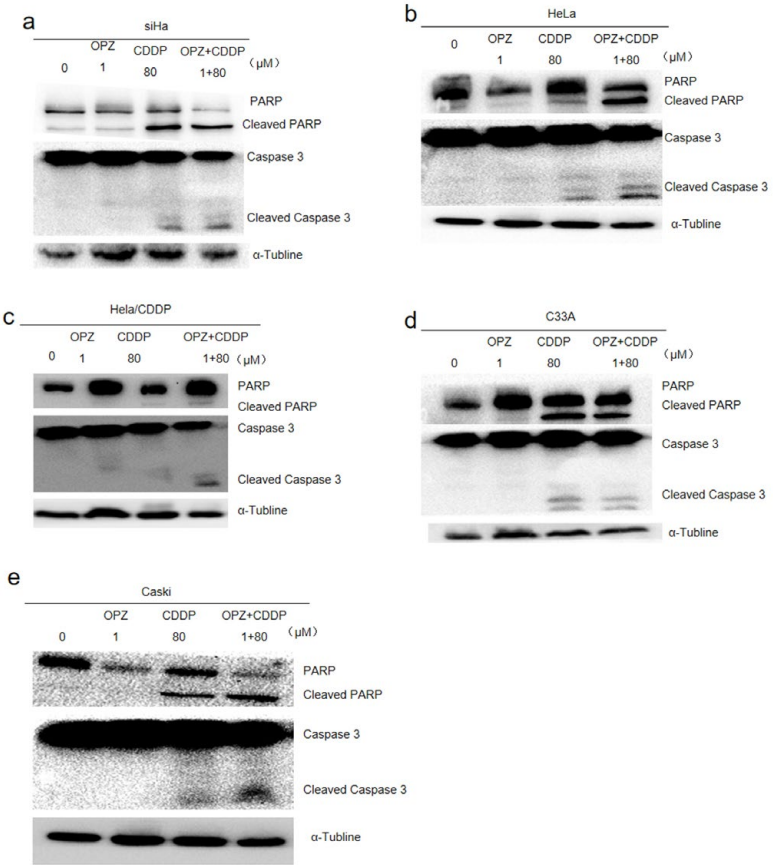


Fig. 4. *OPZ strengthens cisplatin-induced apoptosis in cervical cancer cells. Then whole cell lysates were subjected to SDS-PAGE and immunoblotted with antibodies against PARP and Caspase 3 to detect apoptosis.*

with OPZ, the expression of IκBα, an inhibitor of NF-κB, significantly increased, and the expression of phosphorylated JNK also significantly increased. Furthermore, the expression of phosphorylated JNK was increased in HeLa/CDDP cells induced by OPZ. This suggests that OPZ can significantly enhance the sensitivity of tumor cells to cisplatin.

DISCUSSION

Inhibition of proteasomes in the UPS can promote protein accumulation in cells, leading to the accumulation of cancer cell substrates and cell apoptosis (27). As a new-generation PI, OPZ has an inhibitory effect on lung cancer, breast cancer, multiple myeloma, and head and neck solid tumor cells (28–31). In the present study, the cytotoxicity of OPZ on five types of cervical cancer cell, including cisplatin-resistant HeLa-CDDP cells, was detected. The results revealed that OPZ had high cytotoxicity and dose- and time-dependence. The IC50 values of OPZ in different cervical cancer cells ranged from 13 nm to 170 nm, with the highest value being more than ten times greater than the lowest. These results are similar to those reported in other cell lines (32, 33), suggesting that the sensitivity of different types of cervical cancer cell to OPZ varies.

OPZ was also found to have weak cytotoxicity to a nontransformed cervical cell line (HaCaT, OD value = 0.5–1.5), suggesting that the cytotoxicity of drugs that inhibit proteasome activity is greater in cancer cells than in nontransformed cells (34). The reason for this is that more than 90% of solid tumors in humans contain aneuploid cells (35), in which protein synthesis is disordered, meaning excess protein cannot reach stable conformation and is degraded by the UPS. This makes tumor cells more sensitive to OPZ than nontransformed cells. OPZ alone can inhibit cervical cancer cell proliferation, induce cancer cell apoptosis, enhance cleavage of PARP and caspase-3 in cervical

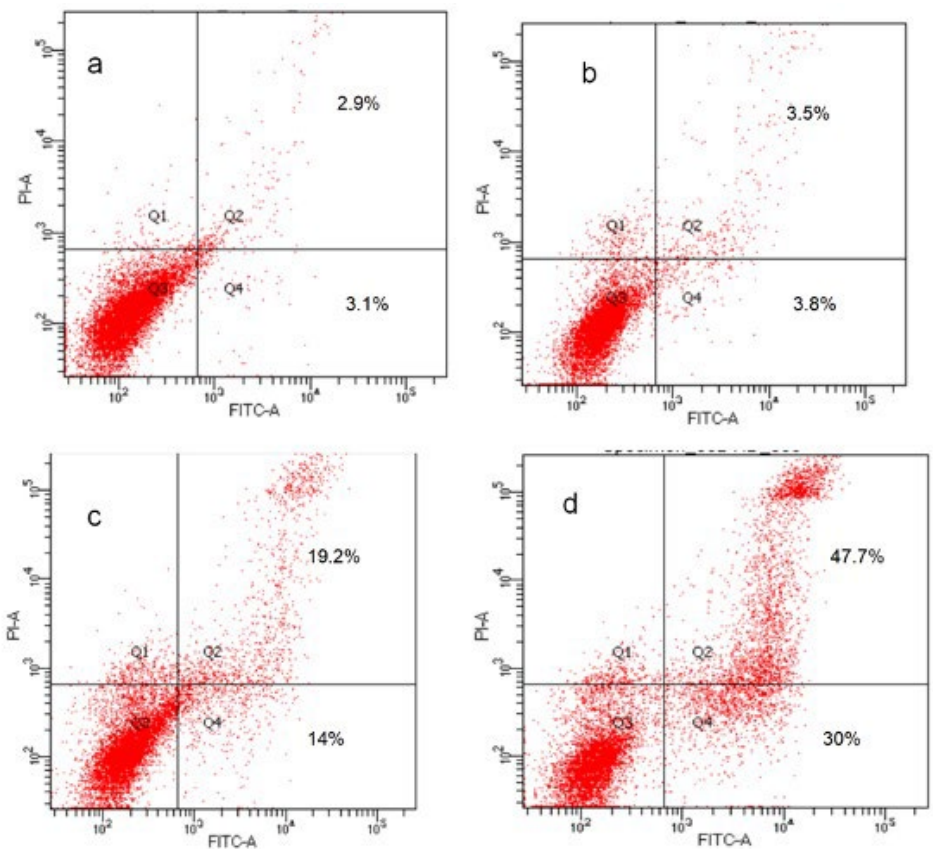


Fig. 5. *Effect of oprozomib combined with cisplatin on C33a cells early apoptosis in vitro detected by flow cytometry after 24 h treated.* ***a****) normal control;* ***b****) oprozomib 0.1um;* ***c****) cisplatin10 um;* ***d****) oprozomib 0.1 um combined with cisplatin 10 um.*

cancer cells, and act in a dose-dependent manner. However, in SiHa cells, cleaved PARP is observed even in the absence of treatment, which could be due to the nature of this cell line.

In the present study, OPZ combined with cisplatin was used to treat cervical cancer cells. The results showed that this combination led to significantly higher proliferation inhibition rates in the various cervical cancer cell lines than the use of cisplatin alone. Furthermore, OPZ was found to enhance both the chemosensitivity of cervical cancer cells to cisplatin and the apoptosis-inducing effect of cisplatin on tumor cells. This was particularly significant in the apoptosis of HeLa-CDDP cells induced by OPZ combined with cisplatin, suggesting that the two drugs have a synergism in cervical cancer cells and that combination therapy can inhibit the proliferation of tumor cells, improving the apoptosis ability of different types of cervical cancer cell.

Cisplatin binds with DNA to form a cisplatin–DNA complex, which activates a variety of intracellular signaling pathways and induces tumor cell apoptosis; the JNK signaling pathway is an important mechanism of cisplatin inducing the apoptosis of tumor cells. The mechanism for the resistance of tumor cells to cisplatin is the reduction of cisplatin's anti-tumor effect through the up-regulation of the expression of apoptosis proteins like myeloid leukemia-1 (Mcl-1) and B-lymphoma-xL (Bcl XL), stimulating the activity of NF-κB and inhibiting the activation of the JNK pathway. The activation of NF-κB is the main cause of drugs missing the target and treatment discontinuity; it is also involved in tumor formation and drug resistance (36–38), as it has the ability to induce the proliferation and transcription of survival genes, such as cyclin D1, c-IAP-2, and Bcl XL (39, 40).

The results of the present study show that the

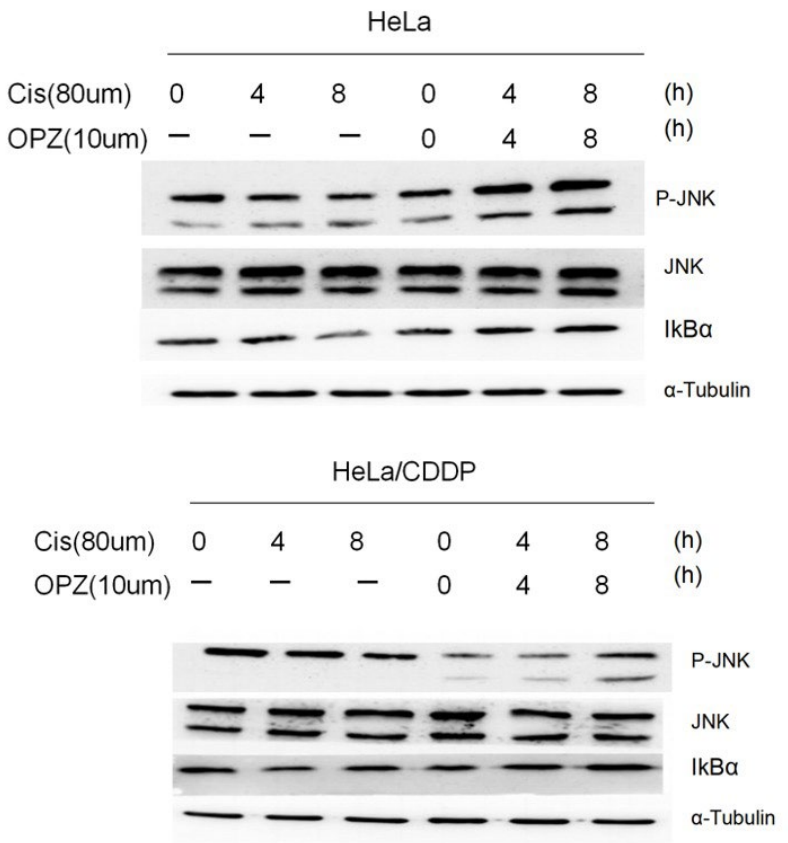


Fig. 6. *OPZ enhances cisplatin-induced SAPK/JNK phosphorylation and inhibits cisplatin-induced IκBα degradation in cervical cancer cells.*

combination of OPZ and cisplatin could enhance the sensitivity of cervical cancer cells to cisplatin by increasing the expression of IκBα, an NF-κB inhibiting factor, and inhibiting the transcription and expression of NF-κB. In addition, OPZ was found to promote the phosphorylation of JNK in the cisplatin pathway and the apoptosis of cervical cancer cells. The combination of OPZ and cisplatin in treatment was also found to be time dependent.

The present study provides key evidence that, although OPZ on its own can inhibit tumor cell proliferation and induce apoptosis, its combined use with cisplatin enhances the cytotoxicity of cisplatin, induces apoptosis, and increases the sensitivity of cervical cancer cells to cisplatin. The apoptosis of cervical cancer cells induced by this combination treatment is realized by inhibiting NF-κB inhibitor degradation and activating JNK apoptosis signals. The study therefore suggests that OPZ may be an effective combination drug for patients with cisplatin-resistant cervical cancer. Animal studies and studies of the pathological tissues of patients with cisplatin-resistant cervical cancer will be conducted in the future to further explore the mechanism of the combination of OPZ and cisplatin and provide an experimental basis for clinical combined chemotherapy in patients with cervical cancer.

ACKNOWLEDGEMENTS

We are particularly grateful to all the people who have given us help on our article.

This study was funded by the Natural Science Foundation of Xinjiang Uygur Autonomous Region (No.2015211C007) and Medical research project of Foshan Health Bureau (No.20200167). The funding body had no role in the design of the study and collection, analysis, and interpretation of data and in writing the manuscript.

REFERENCES

1. Torre LA, Bray F, Siegel RL, Ferlay J, Lortet-Tieulent J, Jemal A. Global cancer statistics, 2012. CA Cancer J Clin 2015; 65:87-108.
2. Lukka H, Johnston M. Concurrent cisplatin-based chemotherapy plus radiotherapy for cervical cancer: a meta-analysis. Clin Oncol (R Coll Radiol) 2004; 16:160-1.
3. Martín-Martínez A, Molano F, Lloret M, Falcón-Vizcaino O, García-Hernández JA. Concurrent chemotherapy and radiotherapy for cervical cancer. Eur J Gynaecol Oncol 2003; 24:160-2.
4. Thomas GM. Improved treatment for cervical cancer--concurrent chemotherapy and radiotherapy. N Engl J Med 1999; 340:1198-200.
5. Green JA, Kirwan JM, Tierney JF, et al. Survival and recurrence after concomitant chemotherapy and radiotherapy for cancer of the uterine cervix: a systematic review and meta-analysis. Lancet 2001; 358:781-6.
6. Koh WJ, Greer BE, Abu-Rustum NR, et al. Cervical Cancer, Version 2.2015. J Natl Compr Canc Netw 2015; 13:395-404.
7. Manasanch EE, Orlowski RZ. Proteasome inhibitors in cancer therapy. Nat Rev Clin Oncol 2017; 14:417-33.
8. Chowdhury M, Enenkel C. Intracellular dynamics of the ubiquitin-proteasome-system. F1000Res 2015; 4:367.
9. Labbadia J, Morimoto RI. The biology of proteostasis in aging and disease. Annu Rev Biochem 2015; 84:435-64.
10. Stark AL, Madian AG, Williams SW, et al. identification of novel protein expression changes following cisplatin treatment and application to combination therapy. J Proteome Res 2017; 16:4227-36.
11. Zhang J, Wu P, Hu Y. Clinical and marketed proteasome inhibitors for cancer treatment. Curr Med Chem 2013; 20:2537-51.
12. Driscoll JJ, Woodle ES. Targeting the ubiquitin+proteasome system in solid tumors. Semin Hematol 2012; 49:277-83.
13. Arastu-Kapur S, Anderl JL, Kraus M, et al. Nonproteasomal targets of the proteasome inhibitors bortezomib and carfilzomib: a link to clinical adverse events. Clin Cancer Res 2011; 17:2734-43.
14. Jakubowiak AJ. Evolution of carfilzomib dose and schedule in patients with multiple myeloma: a historical overview. Cancer Treat Rev 2014; 40:781-90.
15. Irene M. Ghobrial, Michael R. Savona, Ravi Vij, et al. Final results from a multicenter, open-label, dose-escalation phase 1b/2 study of single-

agent oprozomib in patients with hematologic malignancies. Blood 2016; 128:2110.
16. Deshaies RJ. Proteotoxic crisis, the ubiquitin-proteasome system, and cancer therapy. BMC Biol 2014; 12:94.
17. Merin NM, Kelly KR. Clinical use of proteasome inhibitors in the treatment of multiple myeloma. Pharmaceuticals (Basel) 2014; 8:1-20.
18. Sonneveld P, Goldschmidt H, Rosiñol L, et al. Bortezomib-based versus nonbortezomib-based induction treatment before autologous stem-cell transplantation in patients with previously untreated multiple myeloma: a meta-analysis of phase III randomized, controlled trials. J Clin Oncol 2013; 31:3279-87.
19. Roeten MSF, Cloos J, Jansen G. Positioning of proteasome inhibitors in therapy of solid malignancies. Cancer Chemother Pharmacol 2018; 81:227-43.
20. Huang Z, Wu Y, Zhou X, et al. Efficacy of therapy with bortezomib in solid tumors: a review based on 32 clinical trials. Future Oncol 2014; 10:1795-807.
21. Infante JR, Mendelson DS, Burris HA 3rd, et al. A first-in-human dose-escalation study of the oral proteasome inhibitor oprozomib in patients with advanced solid tumors. Invest New Drugs 2016; 34:216-24
22. Ding X, Matsuo K, Xu L, Yang J, Zheng L. Optimized combinations of bortezomib, camptothecin, and doxorubicin show increased efficacy and reduced toxicity in treating oral cancer. Anticancer Drugs 2015; 26:547-54.
23. Shi Y, Yu Y, Wang Z, et al. Second-generation proteasome inhibitor carfilzomib enhances doxorubicin-induced cytotoxicity and apoptosis in breast cancer cells. Oncotarget 2016; 7:73697-710.
24. Vandewynckel YP, Coucke C, Laukens D, et al. Next-generation proteasome inhibitor oprozomib synergizes with modulators of the unfolded protein response to suppress hepatocellular carcinoma. Oncotarget 2016; 7:34988-5000.
25. Niewerth D, Franke NE, Jansen G, et al. Higher ratio immune versus constitutive proteasome level as novel indicator of sensitivity of pediatric acute leukemia cells to proteasome inhibitors. Haematologica 2013; 98:1896-904.
26. Zang Y, Thomas SM, Chan ET, et al. Carfilzomib and ONX 0912 inhibit cell survival and tumor growth of head and neck cancer and their activities are enhanced by suppression of Mcl-1 or autophagy. Clin Cancer Res 2012; 18:5639-49.
27. Johnson DE. The ubiquitin-proteasome system: opportunities for therapeutic intervention in solid tumors. Endocr Relat Cancer 2015; 22:T1-T17.
28. Hari P, Paba-Prada CE, Voorhees PM, et al. Efficacy and safety results from a phase 1b/2, multicenter, open-label study of oprozomib and dexamethasone in patients with relapsed and/or refractory multiple myeloma. Leuk Res 2019; 83:106172.
29. Shi Y, Bieerkehazhi S, Ma H. Next-generation proteasome inhibitor oprozomib enhances sensitivity to doxorubicin in triple-negative breast cancer cells. Int J Clin Exp Pathol 2018; 11:2347-55.
30. Zhu H, Wang T, Xin Z, et al. An oral second-generation proteasome inhibitor oprozomib significantly inhibits lung cancer in a p53 independent manner in vitro. Acta Biochim Biophys Sin (Shanghai) 2019; 51:1034-40.
31. Hurchla MA, Garcia-Gomez A, Hornick MC, et al. The epoxyketone-based proteasome inhibitors carfilzomib and orally bioavailable oprozomib have anti-resorptive and bone-anabolic activity in addition to anti-myeloma effects. Leukemia 2013; 27:430-40.
32. Teicher BA, Tomaszewski JE. Proteasome inhibitors. Biochem Pharmacol 2015; 96:1-9.
33. Zang Y, Kirk CJ, Johnson DE. Carfilzomib and oprozomib synergize with histone deacetylase inhibitors in head and neck squamous cell carcinoma models of acquired resistance to proteasome inhibitors. Cancer Biol Ther 2014; 15:1142-52.
34. Cancer Genome Atlas Research Network. Electronic address: andrew_aguirre@dfci.harvard.edu; Cancer Genome Atlas Research Network. Integrated Genomic Characterization of Pancreatic Ductal Adenocarcinoma. Cancer Cell 2017; 32:185-203.e13.
35. Weaver RL, Limzerwala JF, Naylor RM, Jeganathan KB, Baker DJ, van Deursen JM. BubR1 alterations that reinforce mitotic surveillance act against aneuploidy and cancer. Elife 2016; 5:e16620.
36. DiDonato JA, Mercurio F, Karin M. NF-κB and the link between inflammation and cancer. Immunol Rev 2012; 246:379-400.

37. Zhang J, Xin X, Chen Q, et al. Oligomannurarate sulfate sensitizes cancer cells to doxorubicin by inhibiting atypical activation of NF-κB via targeting of Mre11. Int J Cancer 2012; 130:467-77.
38. Karin M. Nuclear factor-kappaB in cancer development and progression. Nature 2006; 441:431-6.
39. Karin M, Greten FR. NF-kappaB: linking inflammation and immunity to cancer development and progression. Nat Rev Immunol 2005; 5:749-59.
40. Infante JR, Mendelson DS, Burris HA 3rd, et al. A first-in-human dose-escalation study of the oral proteasome inhibitor oprozomib in patients with advanced solid tumors. Invest New Drugs 2016; 34:216-24.

Immunomodulatory effects of IL-33 and IL-25 in an ovalbumin-induced allergic rhinitis mouse model

C. Yang[1*], N. Chen[1*], XL. Tang[2], XH. Qian[2] and CP. Cai[1]

[1]Department of Otolaryngology & Head and Neck Surgery, Ruijin Hospital, Shanghai Jiao Tong University School of Medicine, Huangpu District, Shanghai, China; [2]School of Biomedical Engineering, Shanghai Jiao Tong University, Xuhui District, Shanghai, China

Received October 21, 2020 – Accepted March 10, 2021

[*]These authors contributed equally to this work

Both interleukin (IL)-33 and IL-25 induce Th2-type cytokine production by various cell types, suggesting that they may contribute to development of allergic disorders, however, the immunomodulatory effects of IL-33 and IL-25 in ovalbumin (OVA)-induced allergic rhinitis (AR) remain unclear. In the present study, anti-IL-33 and anti-IL-25 Abs were administrated intranasally during rechallenge in OVA-induced AR. Immunomodulatory effects were evaluated by measuring nasal rubbing, sneezing occurrence, serum OVA-specific antibodies, Th2 immune responses, neutrophil, eosinophil and mast cell recruitment into the nasal mucosa. We found that treatment with anti-IL-33 Ab markedly reduced nasal rubbing, sneezing events, Th2 immune responses, serum OVA-specific IgE and IgG1 levels, mucosal neutrophil, eosinophil and mast cell infiltration. In contrast, the effect of IL-25 antagonism was limited to attenuating the Th2 immune responses, and neutrophil and eosinophil infiltration. These observations indicate that IL-33 and IL-25 play a pathogenic role in an established AR mouse model, with a greater contribution of IL-33 than IL-25. Our findings suggest that IL-33 neutralization may be a potential approach for treatment of AR.

Allergic rhinitis (AR) is one of the most common allergic diseases, the pathogenesis of which is considered to be the result of the interplay among environmental, immunological and genetic factors (1, 2). A large number of studies on pathophysiological mechanism of AR have focused on proinflammatory cytokines, while immunomodulatory effect cytokines have received less attention.

IL-33 and IL-25 are thought to share several roles in immune responses, such as induction of Th2-type cytokines by Th2 cells, suggesting that these cytokines contribute to the development of allergic diseases (3). IL-33, which is a cytokine of the IL-1 family, is a ligand for IL-33 receptors (IL-33R), which comprise two IL-1R families, ST2 and IL-1R accessory protein. IL-33 is produced by epithelial cells, endothelial cells, macrophages and mast cells (4, 5), while ST2 is expressed on various types of cells, including both non-immune cells (epithelial cells, endothelial cells, fibroblasts and smooth muscle cells) and immune cells (Th2 cells, B-1 cells, NKT cells, NK cells, natural helper cells,

Key words: IL-33; IL-25; allergic rhinitis; ovalbumin

Corresponding Author:
Dr Changping Cai,
Department of Otolaryngology & Head and Neck Surgery, Ruijin Hospital,
Shanghai Jiao Tong University School of Medicine,
197 Ruijiner Road, Huangpu District,
Shanghai 200025, China
e-mail: drcaichangping@163.com

0393-974X (2021)
Copyright © by BIOLIFE, s.a.s.
This publication and/or article is for individual use only and may not be further reproduced without written permission from the copyright holder.
Unauthorized reproduction may result in financial and other penalties
DISCLOSURE: ALL AUTHORS REPORT NO CONFLICTS OF INTEREST RELEVANT TO THIS ARTICLE.

mast cells, basophils, eosinophils, macrophages and dendritic cells) (4, 5). IL-33 potently induces production of Th2 cytokines such as IL-4, IL-5 and/or IL-13 by Th2 cells, mast cells, basophils, NKT cells and natural helper cells (4-6). Similar to IL-33, IL-25 (also called IL-17E) can induce Th2-type cytokine production by various types of cells, such as Th2 cells, NKT cells and natural helper cells, via IL-25R (composed of IL-17RA and IL-17RB) and TSLPR (composed of IL-7Rα and TSLPR) (7-10). Thus, IL-33 and IL-25 are considered to be involved in host defense against nematodes and development of Th2-associated disorders, such as allergy (11). Indeed, treatment of mice with exogenous IL-33 and IL-25 results in development of intestinal and/or pulmonary inflammation accompanied by accumulation of eosinophils and/or increased levels of IgG1, IgE and/or Th2 cytokines in sera (12, 13). Moreover, elevated levels of IL-33 and IL-25 were observed in the inflamed skin of patients with atopic dermatitis, in lung smooth muscle cells and epithelial cells from patients with asthma, and/or in sera from patients with AR (14, 15). In particular, genetic polymorphism at the IL-33 loci was identified in patients with Japanese cedar pollinosis, suggesting IL-33 involvement in the development of pollen-mediated AR (16). In support of this, IL-33 is known to be important for induction of AR by OVA and ragweed pollen in mice (17, 18). However, immunomodulatory effects IL-33 and IL-25 in the pathogenesis of AR induced by OVA remains unclear. Therefore, the aim of this study was to investigate the immunomodulatory effects of IL-33 and IL-25 in a mouse model of AR, through administration of IL-33 and IL-25 Abs.

MATERIALS AND METHODS

Mice

Female BALB/c mice (6-8 weeks old) were purchased from Shanghai SLAC Laboratory Animal Co., Ltd. (Shanghai, China) and were housed in the Animal Resource Facility. All procedures and experiments involving animals in this study were performed in accordance with the National Institutes of Health Guide for Care and Use of Laboratory Animals. The study protocol was approved by the Animal Ethics Committee of the Shanghai Jiao Tong University School of Medicine.

Experimental protocol

BALB/c mice were divided into six treatment groups of six mice each as follows: (i) control group mice sensitized and challenged with saline; (ii) OVA group mice sensitized and challenged with OVA; (iii) isotype1 group mice treated with isotype Abs for anti-IL-33; (iv) anti-IL-33 group mice treated with anti-IL-33 Ab; (v) isotype2 group mice treated with isotype Abs for anti-IL-25; (vi) anti-IL-25 group mice treated with anti-IL-25 Ab. The sensitization challenge for the murine model of AR was performed as previously described with slight modification (19). Under pathogen-free conditions, mice were sensitized using OVA (Sigma-Aldrich, St. Louis, MO, USA) as follows. OVA (40 μg/kg) diluted in sterile normal saline was administered along with aluminum hydroxide gel (alum adjuvant, 40 mg/kg) by intraperitoneal injection on days 1 and 7. After a week, the animals were challenged by nasal instillation of 40 μg OVA in 20 μL 0.9% saline per mouse, using a micropipette, on three successive days a week for three consecutive weeks (between day 14 to day 35). After a further 2 weeks, the animals were re-challenged with intranasal OVA for 7 days (from day 49 to day 55). The isotype1, anti-IL-33, isotype2 and anti-IL-25 group mice were given intranasal instillation of goat IgG (isotype antibody for anti-IL-33), anti-IL-33 Ab, rat IgG2a (isotype antibody for anti-IL-25) and anti-IL-25 Ab thirty min prior to OVA re-challenge, 10 μg in 20 μL saline per mouse, respectively. All antibodies were purchased from R&D Systems Inc. (Minneapolis, MN, USA). Control group mice were sensitized and challenged with saline instead of OVA at all stages. Two h after the last challenge on day 55, the animals were sacrificed and the nasal mucosa, blood and superficial cervical lymph nodes (LNs), which drain the nasal mucosa, were harvested from each animal for further analyses. One half of the nasal mucosa samples were used for RNA isolation and the other half were fixed overnight for histocytochemical analysis. Serum was analyzed for antigen-specific-antibody. Superficial cervical LNs were analyzed for the number of IL-4+ CD4+ T cells and IL-4 secretion after OVA stimulation.

Nasal symptom scores

After the final intranasal allergen challenge with OVA, the frequencies of sneezing and nose scratching were

counted for 20 min by three blinded observers to evaluate early allergic responses.

Measurement of OVA-Specific IgE and total IgE

Serum levels of total IgE and OVA-specific IgE were measured by solid-phase enzyme-linked immunosorbent assay (ELISA). Serum samples were harvested 2 h after the last nasal OVA challenges and plated on 10 μg/mL of OVA-coated microtiter plates. Bound immunoglobulin isotypes were detected with specific secondary antibody (biotin-conjugated rat anti-mouse IgE Ab was purchased from BD Pharmingen, San Jose, CA, USA). Total serum IgE was measured by standard ELISA using anti-mouse IgE capture mAb (BD Pharmingen).

Measurement of cytokines

The levels of IL-33 and IL-25 in serum were determined using ELISA kits obtained from BioLegend or Peprotech Inc. (Rocky Hill, NJ) according to the manufacturer's instructions. For measurement of IL-4 cytokine production, single-cell suspensions of LNs were cultured with OVA (200 μg/mL) in 48-well plates in duplicate for 48 h and at the end of incubation, the supernatants were collected for analysis of IL-4.

Real-time polymerase chain reaction (PCR)

Total RNA was prepared from the nasal mucosa with TriZolreagent (Invitrogen, Carlsbad, CA, USA). Complementary DNA (cDNA) was synthesized using superscript reverse transcriptase (Invitrogen) and oligo (20) primers (Fermentas, Burlington, ON, Canada). For the analysis of IL-33, IL-25, IL-4, IL-5, IL-13, Ear1, Ear11, Fcer1g, Mcpt1 and Mcpt2. PDAR (Pre-Developed AssayReagent) kits of primers, and probes were purchased from Applied Biosystems (Foster City, CA, USA). Amplification of IL-33, IL-25, IL-4, IL-5, IL-13, Ear1, Ear11, Fcer1g, Mcpt1, Mcpt2 and GAPDH cDNA was carried out on MicroAmp optical 96-well reaction plates (Applied Biosystems). The reaction was performed using an ABI prism 7000 Sequence Detection System (Applied Biosystems). The average transcript levels of genes were then normalized to GAPDH. The primer sequences used were as follows. GAPDH: forward CGGATTTGGCCGTATTGGG, reverse CTCGCTCCTGGAAGATGG. IL-33: forward CCAGCAGCTCTCTCGGAATC, reverse TCATATGTCCCGCTGGTGC. IL-25: forward TCTCTGATGCTGTTGCTGCT, reverse CGTGGAACGGTTGAGGTAGT. IL-4: forward tcttgataaacttaattgtctctcgtcac, reverse GCAGGATGACAACTAGCTGGG. IL-5: forward AGCACAGTGGTGAAAGAGACCTT, reverse TCCAATGCATAGCTGGTGATTT. IL-13: forward CAGCTTCCCTGGTTCTCTCAC, reverse GGAATCCAGGGCTACACAGA. Ear1: forward AATGCTGTTGGTGTGTGTGGAAAT, reverse CACTGGATACATGGGACTGTCCTG. Mcpt1: forward AAGAGGCCTGTAAAATGTATAAGCA, reverse AGAAGAGGTCCCCCAGAGTC. Mcpt2: forward CCTTTCGGGTTTCTATGACATC, reverse CACATCTTCCCAGGCTTGAT. QuantiTect Primer Assay QT00266959 (Qiagen, Hilden, GmbH, Germany) for Ear11 and QT00115717 (Qiagen) for Fcer1g.

Flow cytometry assay

Single-cell suspensions of superficial cervical LNs were prepared and cultured in RPMI-1640 with 10% FCS at a concentration of 5 × 106 cells/mL. For detection of IL-4+ CD4+ T cells, the cells were then stimulated with 0.1 μg/ml PMA (Sigma-Aldrich) and 1 μg/ml ionomycin (Sigma-Aldrich) in the presence of 1 μM Monensin (Sigma-Aldrich) at 37°C for 4 h. After washing, the cells were incubated with anti-mouse-CD4. Intracellular staining for IL-4 was performed using BD Cytofix/Cytoperm Kit. After fixation and permeabilization, the cells were stained intracellularly with Alexa Fluor 647-conjugated anti-mouse-IL-4. Isotype-matched antibodies conjugated with PerCP-CyTM5.5 and Alexa Fluor 647 were used as negative controls. All antibodies were purchased from BD Pharmingen. Samples were assessed flow cytometry (FACSCalibur; Becton Dickinson, San Jose, CA, USA) and data were analyzed using the CellQuest software (BD Biosciences).

Histology

At 2 h after the last treatment, mouse heads were harvested, fixed in 10% neutral buffered formalin at room temperature for 7 days and decalcified in 10% EDTA (pH 7.0) for 14 days. The head tissues were then embedded in paraffin, and 4-μm coronal sections were stained for assessment of eosinophil infiltration, mast cell infiltration, or stained by immunohistochemistry for assessment of IL-25, IL-23 and neutrophils.

Immunohistochemistry

For detection of IL-33 and IL-25, paraffin sections

were prepared as described above, and the slides were placed in 0.01 M citric buffer (pH 6.0) and autoclaved at 121°C for 20 min. The sections were then incubated with 5 μg/ml goat anti-mouse IL-33 polyclonal Ab (AF3626; R&D Systems Inc., Minneapolis, MN) or anti-rabbit-IL-25 (Santa Cruz Biotechnology, Santa Cruz, CA), washed and incubated with Alexa 594-conjugated donkey anti-goat IgG Ab (Invitrogen). The stained sections were mounted in VECTASHIELD mounting medium with DAPI (Vector Laboratories, Burlingame, CA). The specimens were scanned with a fluorescent microscope (BX51, DP72 CCD camera; Olympus Optical Co., Tokyo, Japan). Eosinophils, mast cells and neutrophils numbers in the nasal mucosa in five randomly selected tissue sections from each animal were counted using microscopy at ×400 magnification, by two observers who were blinded to the treatment. The mean values of counts made by the two observers were used for statistical analysis.

Statistical analysis

Data were presented if not indicated elsewhere as Mean ± SD. All statistical analyses were performed using SPSS 22.0 (SPSS Inc., Chicago, IL, USA), and the Mann-Whitney U test was used for mean analysis.

RESULTS

Expression of IL-33 and IL-25 in OVA-induced AR mouse model

To elucidate the roles of IL-33 and IL-25 in the development of OVA-induced AR, mice were repeatedly treated with an OVA intranasally. As shown in Fig. 1A. 2 h after the last challenge on day 55, the concentration of serum IL-33 and IL-25 was significantly increased in OVA-treated mice compared to control group. Moreover, the mRNA (Fig. 1B) levels of IL-33 and IL-25 in the nasal mucosa was increased in OVA mice. Furthermore, histological analysis found infiltration of leukocytes and hyperplasia of goblet cells in the nasal mucosa of OVA treatment mice, but not control mice (Fig. 1C). These findings suggest that IL-33 and IL-25 may contribute to the development of OVA-induced AR.

Effect of IL-33 and IL-25 blockade on nasal symptoms in the AR mouse model

To determine the effect of IL-33 and IL-25 blockade on nasal symptoms, the number of nasal rubbings and sneezes was counted after the final intranasal allergen challenge with OVA. As shown in Fig. 1D, the number of nasal rubbings and sneezes was

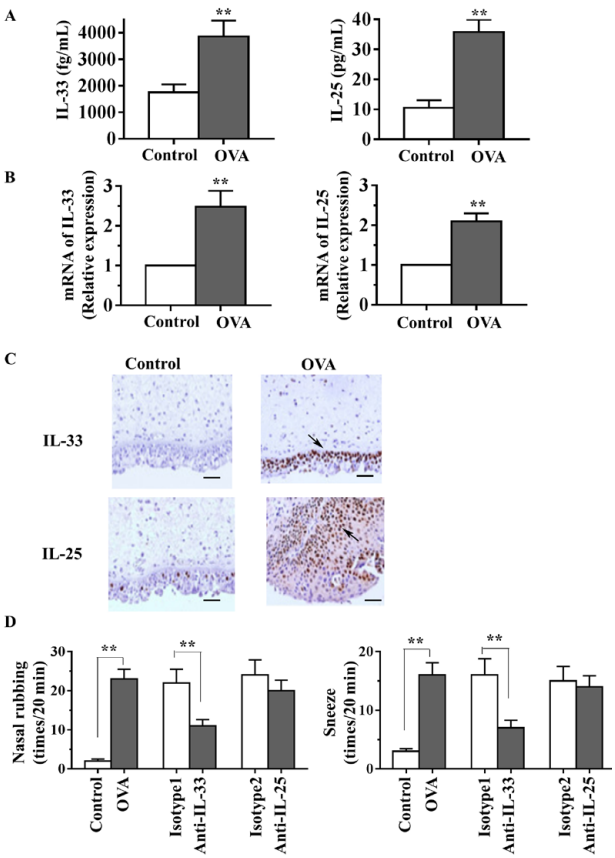


Fig. 1. *The roles of IL-33 and IL-25 in the development of OVA-induced AR. A, B) Up-regulation of IL-33 and IL-25 in the mouse model of AR. Blood and nasal mucosa were collected 2 h after the last challenge at day 55 and analyzed for serum IL-33 and IL-25 levels (A), relative mRNA level of IL-33 and IL-25 (B) in nasal mucosa. C) The sections were stained with anti-rabitt-IL-33 or anti-rabitt-IL-25 Abs. IL-33 and IL-25 were detected in the cytoplasm of epithelial cells (brown) from OVA-treated mice. Arrowheads indicate IL-33-positive or IL-25-positive epithelial cells. Scale bars, 100 μm. D) Effect of IL-33 and IL-25 blockade on nasal rubbings and sneezes. Control: sensitized and challenged with saline; ovalbumin (OVA): sensitized and challenged with OVA; isotype1: treated with control Abs for anti-IL-33; anti-IL-33: treated with anti-IL-33; isotype2: treated with control Ab for anti-IL-25; anti-IL-25: treated with anti-IL-25. The number of nasal rubbings and sneezes was counted for 20 min immediately after the last challenge. Data are presented as the mean ± SD (n=6). **p < 0.01, vs control.*

significantly increased in OVA and isotypes 1 and 2 group compared to the control group. Interestingly, blockade of IL-33 significantly reduced the nasal rubbing and sneezing, whereas no significant decrease was observed after IL-25 blockade (Fig. 1D). These results suggest that Anti-IL-33 antibody is more effective than Anti-IL-25 antibody for experimental AR.

Inhibition of Th2 responses by IL-33 and IL-25 blockade

To evaluate the effects of anti-IL-33 and anti-IL-25 Abs on Th2 responses in OVA-induced allergic rhinitis, Real-time polymerase chain reaction (RT-PCR) was used to test the mRNA level of Th2 cytokines (IL-4, IL-5 and IL-13) in nasal mucosa. We observed that the gene expression of IL-4, IL-5 and IL-13 were significantly up-regulated in OVA, isotypes 1 and 2 groups. In addition, the increase of these genes was inhibited by treatment with IL-33 or IL-25 antibody (Fig. 2A). Moreover, blockade of IL-33 and IL-25 inhibited IFN-γ + T cells, as shown by flow cytometry assay (Fig. 2B). Furthermore, IL-4 levels in superficial cervical LNs in OVA and isotypes 1 and 2 groups were also decreased by IL-33 and IL-25 blockade (Fig. 2C). These observations suggest that IL-33 and IL-25 antibodies may inhibit Th2 responses in OVA-induced AR mouse model.

Effects of IL-33 and IL-25 blockade on serum OVA-specific antibodies and neutrophil infiltration

To investigate the effect of IL-33 and IL-25 blockade on serum OVA-specific antibodies in OVA-induced AR mouse model, the level of OVA-specific IgE, IgG1 and IgG2a were tested by ELISA assay. As shown in Fig.3 A, the IgE, IgG1 and

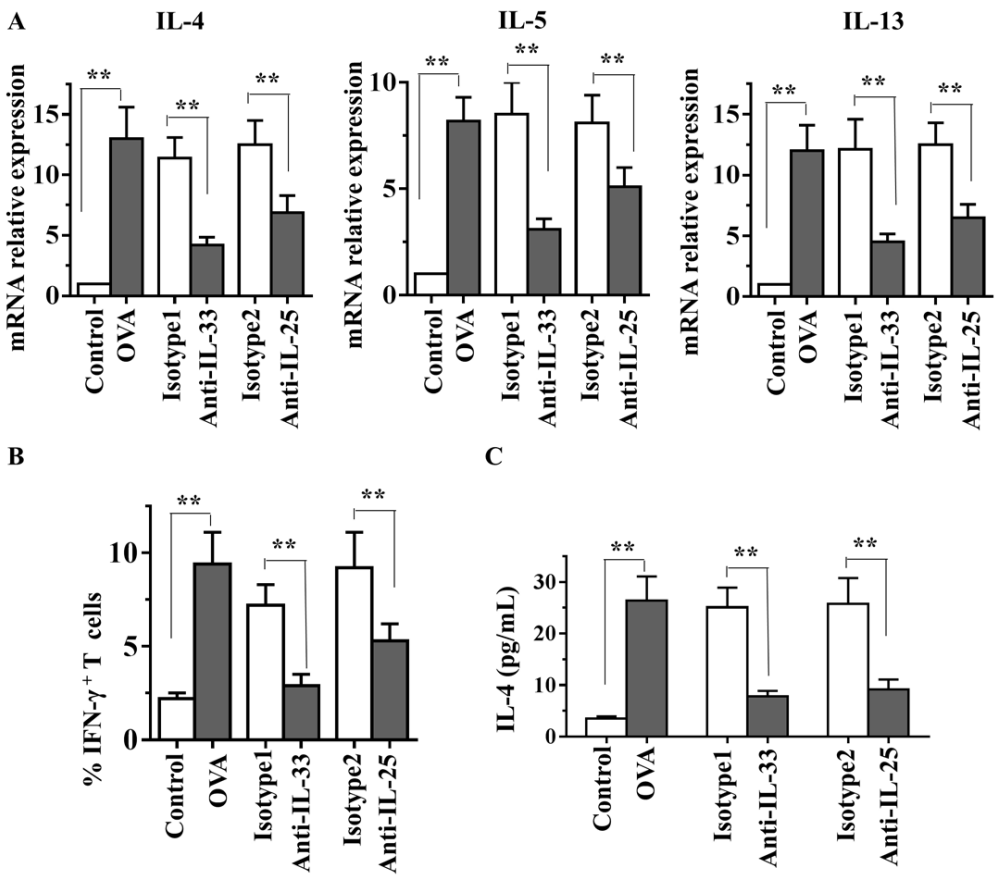


Fig. 2. *Effects of IL-33 and IL-25 Abs on Th2 responses in OVA-induced AR. A) Expression of IL-4, IL-5 and IL-13 genes in nasal mucosa of OVA-induced AR mice. B) Quantitative analysis of IFN-γ + T cells for each treatment group measured by flow cytometry. C) IL-4 secretion by LN cells stimulated with OVA in vitro. Data are presented as the mean ± SD. **p < 0.01, vs control.*

IgG2a levels were significantly increased in OVA and isotypes 1 and 2 group compared to control mice. Interestingly, blockade of IL-33 significantly reduced the levels of OVA-specific IgE, IgG1 and IgG2a. In contrast, there is no significant effect on OVA-specific IgE, IgG1 or IgG2a by blockade of IL-25. Furthermore, neutrophil infiltration was tested by histological analysis. The results showed that the number of neutrophils were significantly increased in nasal mucosa of OVA and isotypes 1 and 2 mice compared with the control group. Notably, the number of neutrophils were significantly attenuated by treatment with anti-IL-33 or anti-IL-25 Abs (Fig. 3 B, C). These data suggest that IL-33 and IL-25 may regulate serum OVA-specific antibodies and neutrophil infiltration of OVA-induced AR, with a more pronounced contribution of IL-33 than IL-25.

Inhibition of eosinophil infiltration by treatment with anti-IL-33 and anti-IL-25 Abs

The number of eosinophil cells were measured in nasal mucosa collected from sacrificed mice. In the present study, we found that the eosinophil cells were significantly increased in nasal mucosa of OVA and

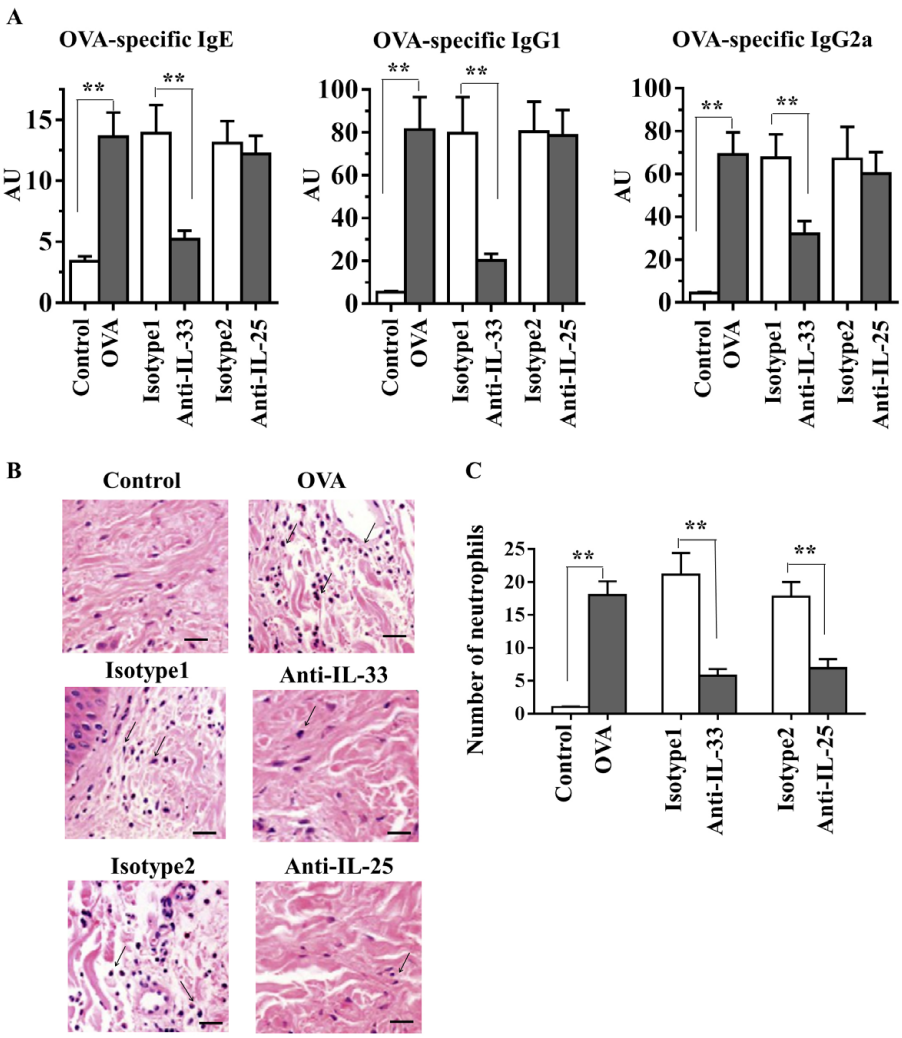


Fig. 3. *Effect of IL-33 and IL-25 antibodies on serum OVA-specific antibodies and neutrophil infiltration. A) Estimation of serum antigen-specific-antibody responses. Serum was collected two h after the last challenge, and the OVA-specific IgE, IgG1 and IgG2a levels were analyzed by ELISA. Levels of OVA-specific antibodies were expressed as arbitrary unit (AU). B) Representative images of neutrophil infiltration of each group. Positive neutrophil cells are stained brown. Scale bars, 100 μm. C) Quantitative analysis of neutrophils. Six fields from five sections of individual mice were counted. Data are presented as the mean ± SD (n=6). **p < 0.01, vs control.*

isotypes 1 and 2 group compared with control mice. In addition, this increase was significantly attenuated by blockade with anti-IL-33 or anti-IL-25 Abs (Fig. 4 A, B). Moreover, the expression of eosinophil-associated ribonuclease (Ear)1 and Ear11 genes were significantly increased in OVA and isotypes 1 and 2 mice, and inhibited by treated with anti-IL-33 or anti-IL-25 Abs (Fig. 4C). These results suggest that IL-33 and IL-25 antibodies may decrease eosinophil cells infiltration in OVA-induced AR mouse model.

Inhibition of mast cell infiltration by IL-33 and IL-25 blockade

To further evaluate the immunomodulatory effects of IL-33 and IL-25 Abs in OVA-induced allergic rhinitis, we measured the number of mast cells in nasal mucosa by histological analysis. As shown in Fig. 5 A, B, the numbers of mast cells

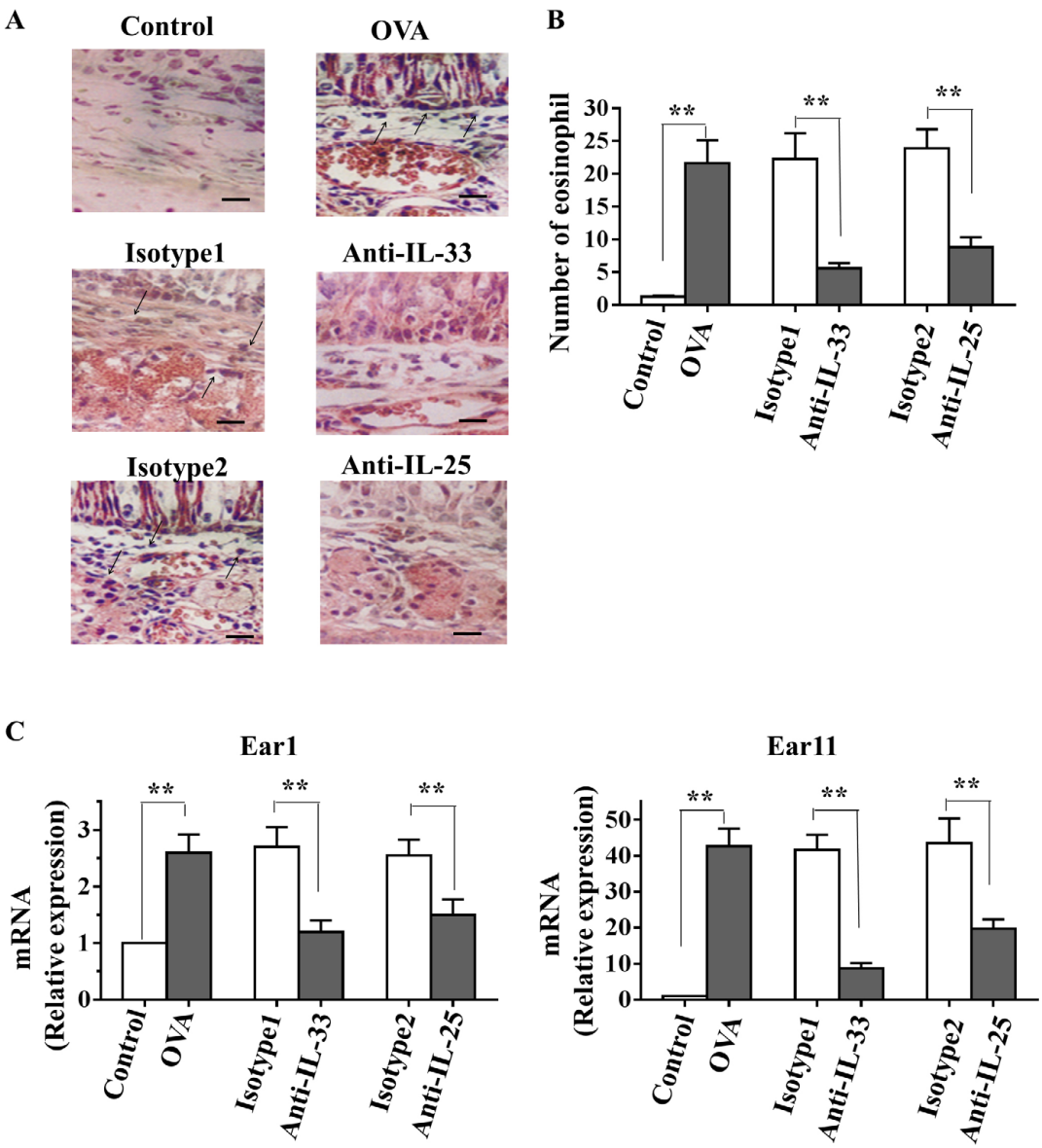


Fig. 4. *Effect of IL-33 and IL-25 blockade on eosinophil infiltration in nasal mucosa. A) Representative images of eosinophil infiltration in nasal mucosa of each group are shown. Scale bars, 100 μm. B) Quantitative analysis of eosinophils. Six fields from five sections of individual mice were counted. C) Expression of eosinophil-related genes, Ear1 and Ear11, in the nasal mucosa. Data are presented as the mean ± SD. **p < 0.01, vs control.*

in nasal mucosa were significantly increased in OVA and isotypes 1 and 2 mice, and significantly decreased by anti-IL-33 Ab treatment, but not by anti-IL-25 Ab treatment. In agreement with mast cell recruitment in nasal mucosa, expression of Mcpt1 and Mcpt2 genes was significantly increased in OVA and isotypes 1 and 2 mice compared to control mice. However, blockade of IL-33 significantly inhibited the expression of Mcpt1 and Mcpt2 genes, IL-25 blockade had no significant effect on the expression of these genes (Fig. 5C). Furthermore, we found that the increased expression of Fcer1g gene in OVA and isotypes 1 and 2 mice was decreased by IL-33 blockade, but not by IL-25 blockade (Fig. 5C). Together, these findings show the evidence that IL-33 and IL-25 are associated with immune function of OVA-induced AR, with a more pronounced contribution of IL-33 than IL-25.

DISCUSSION

IL-33 and IL-25 are produced by epithelial cells, and have a shared biological activity to induce Th2 cytokines, suggesting involvement in the development of allergic diseases (21). Indeed, expression of these cytokines and/or their receptors is known to be increased in specimens from patients with allergies such as AR and asthma. Some

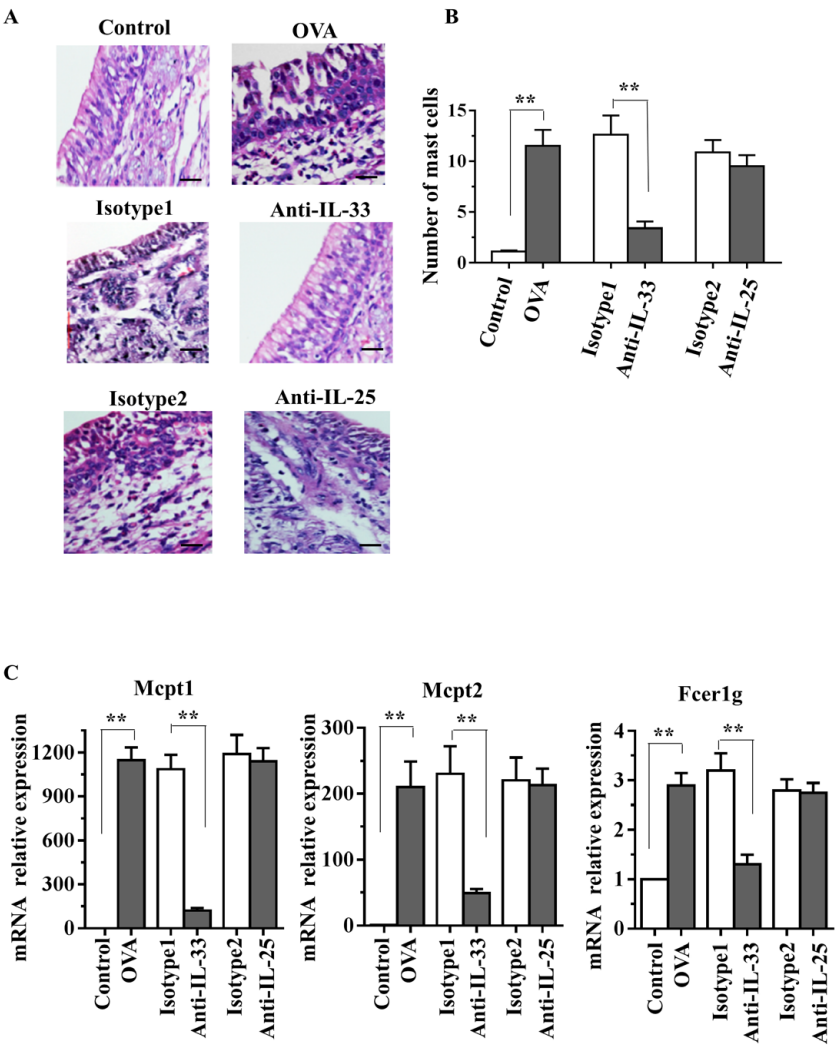


Fig. 5. *Effect of IL-33 and IL-25 blockade on mast cell infiltration in nasal mucosa. A) Representative images of mast cell infiltration of each group in nasal mucosa are shown. Scale bars, 100 μm. B) Quantitative analysis of mast cells. Six fields from 5 sections of individual mice were counted. C) Expression of mast cell-related genes, Mcpt1, Mcpt2 and Fcer1g, in the nasal mucosa. Data are presented as the mean ± SD (n=6). **p < 0.01, vs control.*

investigators demonstrated that IL-33 and IL-25 are crucial for development of OVA-induced "acute" airway inflammation and/or hypersensitivity, which are widely considered to be models for asthma, using mice deficient in those cytokines or mice treated with neutralizing antibodies/reagents for them (22-26). Mast cells play a very important role in allergic diseases, and constitutively express the IL-33 receptor ST2. In addition, followed by IL-33 stimulation, mast cells can produce a variety of cytokines (6, 27, 28). It was indicated that IL-33 could stimulate mast cells and induce asthma diseases, however, the potential pathogenic mechanisms associated with these mediators are largely unknown. The goal of this study was to explore the immunoregulatory effect of IL-33 and IL-25 in an OVA-induced AR mouse model. In this study, we observed the increase of IL-33 and IL-25 in AR mouse model. We also found that anti-IL-33 Ab and anti-IL-25 Ab treatment had different effects. Anti-IL-33 treatment was effective in alleviating allergic symptoms, accompanied by decreased Th2 responses, serum OVA-specific IgE, as well as nasal neutrophil, eosinophil and mast cell infiltration. However, anti-IL-25 Ab treatment only inhibited the Th2 responses and nasal neutrophil and eosinophil infiltration. Considering that AR is accompanied with several symptoms which significantly impair the quality of life, anti-IL-33 antibody treatment has the potential to improve the quality of lives of AR patients.

In the present study, we found that both IL-33 and IL-25 blockade inhibited the increased nasal neutrophil infiltration, suggesting that IL-33 and IL-25 may contribute to neutrophil recruitment into the nasal mucosa. Our findings for neutrophil recruitment into the nasal mucosa in AR are consistent with previous studies, which showed the involvement of IL-33 and IL-25 in neutrophil infiltration (29-31). Eosinophil infiltration is a hallmark of allergic airway inflammation. In this study, we observed that anti-IL-33 and anti-IL-25 Abs inhibited both eosinophil numbers and eosinophil-associated gene expression in the nasal mucosa, supporting an enhancing role of these two cytokines in eosinophil recruitment. Moreover, eosinophil infiltration is related to Th2 responses, especially IL-5 secreted by Th2 cells (32). Moreover, we found that the titers of IL-4, IL-5, and IL-13 were all significantly decreased after anti-IL-33 or anti-IL-25 antibody treatment. These cytokines play important roles in the initiation and maintenance of allergic inflammation (8). IL-4 promotes Th2 cell differentiation, synthesis of IgE and up-regulation of receptors for IgE, and secretion of mucus (33, 34). IL-5 increases eosinophilic inflammation and airway infiltration (35). IL-13 induces differentiation of B cells and isotype change to IgE (36). Murdaca et al. has reported that IL-33 and IL-31 are involved in most autoimmune and allergic diseases. Furthermore, Th2 cells could produce IL-31, and IL-33 promotes IL-31 in Th2 cells (37). Through the inhibition of these actions, anti-IL-33 and anti-IL-25 antibody exerts its therapeutic effects on allergic inflammation and AR. However, there is still controversy about the role of IL-33 on neutrophils. Cherry et al. (38) argued that neutrophils do not express the ST2 receptor and so do not respond to IL-33. On the other hand, Liu et al. (39) reported that the number of neutrophils was slightly decreased after the treatment, although without significance. Therefore, further studies designed to elucidate the effect of IL-33 on neutrophils are needed to clarify the issue.

There is evidence that mast cell recruitment is often accompanied by eosinophil infiltration and that there is an interaction between mast cells and eosinophils (40, 41). Our study showed that treatment with anti-IL-33 or anti-IL-25 Abs decreased allergen-induced mast cell infiltration in the nasal mucosa. In agreement with this, previous studies have demonstrated that mast cell migration and activation are related to IgE levels (20, 42). Our findings support the notion that mast cell infiltration in AR is predominantly related to IgE. Moreover, our study indicated that although IL-25 has a pathogenic role in this well-established mouse model of AR, its effects are limited to the Th2 responses and nasal neutrophil and eosinophil infiltration. The failure of anti-IL-25 Ab to inhibit OVA-specific Ig-E and mast cell infiltration in our study may contribute to its failure to alleviate nasal symptoms, because IgE levels are related to mast cell migration and

activation (20) and secretion of histamine, which is the main mediator that stimulates nasal rubbing and sneezing (43). The limited effects of anti-IL-25 Ab in our study indicate that IL-25 may not be a crucial pathogenic mediator in this mouse model of AR.

In summary, we demonstrate t a pathogenic role of IL-23 and IL-25 in OVA-induced AR mice, with a greater contribution of IL-33 than IL-25. Our findings suggest that IL-33 neutralization may be a potential approach for treatment of AR in humans.

ACKNOWLEDGEMENT

This work was supported by the Shanghai Jiao Tong University Med-X Interdisciplinary Research Funding (Grant No. YG2019QNB25).

REFERENCES

1. Kauffmann F, Demenais F. Gene-environment interactions in asthma and allergic diseases: challenges and perspectives. J Allergy Clin Immunol 2012; 130:1229-40; quiz 41-2.
2. Liu JX, Liao B, Yu QH, et al. The IL-37-Mex3B-Toll-like receptor 3 axis in epithelial cells in patients with eosinophilic chronic rhinosinusitis with nasal polyps. J Allergy Clin Immunol 2020; 145:160-72.
3. Nagata Y, Maruoka S, Gon Y, et al. Expression of IL-25, IL-33, and thymic stromal lymphopoietin in nasal polyp gland duct epithelium in patients with chronic rhinosinusitis. Am J Rhinol Allergy 2019; 33:378-87.
4. Oboki K, Ohno T, Kajiwara N, Saito H, Nakae S. IL-33 and IL-33 receptors in host defense and diseases. Allergol Int 2010; 59:143-60.
5. Ohno T, Morita H, Arae K, Matsumoto K, Nakae S. Interleukin-33 in allergy. Allergy 2012; 67:1203-14.
6. Mukai K, Tsai M, Saito H, Galli SJ. Mast cells as sources of cytokines, chemokines, and growth factors. Immunol Rev 2018; 282:121-50.
7. Iwakura Y, Ishigame H, Saijo S, Nakae S. Functional specialization of interleukin-17 family members. Immunity 2011; 34:149-62.
8. Shao JB, Yang G, Zhang YY, et al. Mal-deficiency impairs the tolerogenicity of dendritic cell of patients with allergic rhinitis. Cell Immunol 2019; 344:103930.
9. Omori-Miyake M, Ziegler SF. Mouse models of allergic diseases: TSLP and its functional roles. Allergol Int 2012; 61:27-34.
10. Patel NN, Kohanski MA, Maina IW, Workman AD, Herbert DR, Cohen NA. Sentinels at the wall: epithelial-derived cytokines serve as triggers of upper airway type 2 inflammation. Int Forum Allergy Rhinol 2019; 9:93-99.
11. Nasiri Kalmarzi R, Fakhimi R, Manouchehri F, et al. The relationship between B7 homologous 1 with interleukin-4, interleukin-17 and interferon gamma in patients with allergic rhinitis. Expert Rev Clin Immunol 2019; 15:897-901.
12. Seshasayee D, Lee WP, Zhou M, et al. In vivo blockade of OX40 ligand inhibits thymic stromal lymphopoietin driven atopic inflammation. J Clin Invest 2007; 117:3868-78.
13. Van Dyken SJ, Nussbaum JC, Lee J, et al. A tissue checkpoint regulates type 2 immunity. Nat Immunol 2016; 17:1381-87.
14. Reynolds JM, Angkasekwinai P, Dong C. IL-17 family member cytokines: regulation and function in innate immunity. Cytokine Growth Factor Rev 2010; 21:413-23.
15. Ziegler SF. The role of thymic stromal lymphopoietin (TSLP) in allergic disorders. Curr Opin Immunol 2010; 22:795-9.
16. Katoh S, Ikeda M, Matsumoto N, et al. Possible role of IL-25 in eosinophilic lung inflammation in patients with chronic eosinophilic pneumonia. Lung 2017; 195:707-12.
17. Haenuki Y, Matsushita K, Futatsugi-Yumikura S, et al. A critical role of IL-33 in experimental allergic rhinitis. J Allergy Clin Immunol 2012; 130:184-94 e11.
18. Kim YH, Yang TY, Park CS, et al. Anti-IL-33 antibody has a therapeutic effect in a murine model of allergic rhinitis. Allergy 2012; 67:183-90.
19. Wang M, Zhang W, Shang J, Yang J, Zhang L, Bachert C. Immunomodulatory effects of IL-23 and IL-17 in a mouse model of allergic rhinitis. Clin Exp Allergy 2013; 43:956-66.
20. Mathias CB, Freyschmidt EJ, Caplan B, et al. IgE influences the number and function of mature mast cells, but not progenitor recruitment in allergic pulmonary inflammation. J Immunol 2009; 182:2416-24.

21. Salter BM, Oliveria JP, Nusca G, et al. IL-25 and IL-33 induce Type 2 inflammation in basophils from subjects with allergic asthma. Respir Res 2016; 17:5.
22. Ballantyne SJ, Barlow JL, Jolin HE, et al. Blocking IL-25 prevents airway hyperresponsiveness in allergic asthma. J Allergy Clin Immunol 2007; 120:1324-31.
23. Liu YJ, Soumelis V, Watanabe N, et al. TSLP: an epithelial cell cytokine that regulates T cell differentiation by conditioning dendritic cell maturation. Annu Rev Immunol 2007; 25:193-219.
24. Oboki K, Ohno T, Kajiwara N, et al. IL-33 is a crucial amplifier of innate rather than acquired immunity. Proc Natl Acad Sci U S A 2010; 107:18581-6.
25. Suzukawa M, Morita H, Nambu A, et al. Epithelial cell-derived IL-25, but not Th17 cell-derived IL-17 or IL-17F, is crucial for murine asthma. J Immunol 2012; 189:3641-52.
26. Ferreira MAR, Vonk JM, Baurecht H, et al. Eleven loci with new reproducible genetic associations with allergic disease risk. J Allergy Clin Immunol 2019; 143:691-99.
27. Galli SJ, Gaudenzio N, Tsai M. Mast cells in inflammation and disease: recent progress and ongoing concerns. Annu Rev Immunol 2020; 38:49-77.
28. Theoharides TC, Leeman SE. Effect of IL-33 on de novo synthesized mediators from human mast cells. J Allergy Clin Immunol 2019; 143:451.
29. Divekar R, Kita H. Recent advances in epithelium-derived cytokines (IL-33, IL-25, and thymic stromal lymphopoietin) and allergic inflammation. Curr Opin Allergy Clin Immunol 2015; 15:98-103.
30. Roussel L, Farias R, Rousseau S. IL-33 is expressed in epithelia from patients with cystic fibrosis and potentiates neutrophil recruitment. J Allergy Clin Immunol 2013; 131:913-6.
31. Swaidani S, Bulek K, Kang Z, et al. The critical role of epithelial-derived Act1 in IL-17- and IL-25-mediated pulmonary inflammation. J Immunol 2009; 182:1631-40.
32. Takatsu K, Nakajima H. IL-5 and eosinophilia. Curr Opin Immunol 2008; 20:288-94.
33. Dabbagh K, Takeyama K, Lee HM, Ueki IF, Lausier JA, Nadel JA. IL-4 induces mucin gene expression and goblet cell metaplasia in vitro and in vivo. J Immunol 1999; 162:6233-7.
34. Pawankar R, Okuda M, Yssel H, Okumura K, Ra C. Nasal mast cells in perennial allergic rhinitics exhibit increased expression of the Fc epsilonRI, CD40L, IL-4, and IL-13, and can induce IgE synthesis in B cells. J Clin Invest 1997; 99:1492-9.
35. Foster PS, Hogan SP, Ramsay AJ, Matthaei KI, Young IG. Interleukin 5 deficiency abolishes eosinophilia, airways hyperreactivity, and lung damage in a mouse asthma model. J Exp Med 1996; 183:195-201.
36. Cocks BG, de Waal Malefyt R, Galizzi JP, de Vries JE, Aversa G. IL-13 induces proliferation and differentiation of human B cells activated by the CD40 ligand. Int Immunol 1993; 5:657-63.
37. Murdaca G, Greco M, Tonacci A, Negrini S, Borro M, Puppo F, Gangemi S. IL-33/IL-31 Axis in Immune-Mediated and Allergic Diseases. Int J Mol Sci 2019; 20.
38. Cherry WB, Yoon J, Bartemes KR, Iijima K, Kita HA. novel IL-1 family cytokine, IL-33, potently activates human eosinophils. J Allergy Clin Immunol 2008; 121:1484-90.
39. Liu X, Li M, Wu Y, Zhou Y, Zeng L, Huang T. Anti-IL-33 antibody treatment inhibits airway inflammation in a murine model of allergic asthma. Biochem Biophys Res Commun 2009; 386:181-5.
40. Minai-Fleminger Y, Elishmereni M, Vita F, Soranzo MR, Mankuta D, Zabucchi G, Levi-Schaffer F. Ultrastructural evidence for human mast cell-eosinophil interactions in vitro. Cell Tissue Res 2010; 341:405-15.
41. Wong CK, Ng SS, Lun SW, Cao J, Lam CW. Signalling mechanisms regulating the activation of human eosinophils by mast-cell-derived chymase: implications for mast cell-eosinophil interaction in allergic inflammation. Immunology 2009; 126:579-87.
42. Sly LM, Kalesnikoff J, Lam V, et al. IgE-induced mast cell survival requires the prolonged generation of reactive oxygen species. J Immunol 2008; 181:3850-60.
43. Shamji MH, Layhadi JA, Achkova D, et al. Role of IL-35 in sublingual allergen immunotherapy. J Allergy Clin Immunol 2019; 143:1131-42 e4.

New biomarker for lung cancer - focus on circSETD3

F. Tao, C. Gu, N. Li, Y. Ying, LF. Cao, QF. Xiao, D. Ni, YB. Zhuang and Q. Zhang

Department of Respiratory Medicine, The Affiliated Hospital of Jiaxing University, Jiaxing, Zhejiang, China

Received November 12, 2020 – Accepted February 22, 2021

In order to explore the mechanism of gefitinib-acquired resistance in lung cancer, a new biomarker has been developed for early clinical diagnosis and intervention; human NSCLC (Non-Small Cell Lung Cancer) cell lines H292 (denoted as H292S) and PC9 (denoted as PC9S) were used to establish gefitinib-resistant NSCLC cell lines H292 and PC9 models. CCK-8 (Cell Counting Kit-8) method was used to test the drug resistance of the cells. circRNAs (circular RNAs) that were differentially expressed before and after resistance were screened by RNA sequencing technology. The effects of circSETD3 overexpression and interference on the sensitivity of gefitinib was observed to analyze the nuclear localization of circSETD3 and verify the interaction between circSETD3-miR-520h-ABCG2. The results showed that the most significant change in differential expression of human NSCLC cell lines before and after drug resistance was hsa_circ_0000567, that is, circSETD3, which is mainly present in the cytoplasm. In H292S and PC9S, compared with the negative control group, the cell proliferation ability of the overexpression group was significantly increased, and the apoptosis ability was significantly decreased. In H292R and PC9R, compared with the negative control group, the proliferation ability of the interference group was significantly decreased, and the apoptosis ability was significantly increased. Overexpression of circSETD3 to H292S and PC9S, the expression of ABCG2 increased significantly. Also, the expression of ABCG2 decreased significantly after transfection with miR-520h mimics. H292R and PC9R interfered with circSETD3, the expression of ABCG2 decreased significantly. Moreover, the expression of ABCG2 increased significantly after transfection with miR-520h inhibitor. In conclusion, circSETD3 can be used as a novel biomarker for lung cancer. It relieves miR-520h degradation of the transporter ABCG2 by down-regulating the miR-520h expression, causing gefitinib to be pumped out of the cell.

Lung cancer continues to be the most malignant tumor, with the fastest increase in morbidity and mortality (1). Non-small cell lung cancer (NSCLC) is the most frequent type of lung cancer, characterized by a relatively high spread rate and increased metastasis potential (2). Chemotherapy and radiotherapy are the main therapeutic options (3, 4). Gefitinib, an oral epithelial growth factor receptor tyrosine kinase (EGFR-TK) inhibitor, is currently the first therapeutical option for NSCLC because of its high efficacy and mild side effects (5). However, clinical investigations have shown that the vast majority of patients develop acquired resistance after using gefitinib for 6-12 months. This resistance limits the efficacy of treatment and promotes the progression of the disease (6). CircRNAs are non-coding RNA molecules that are not affected by RNA exonucleases due to their closed-loop structure, making them hard to degrade and more

Key words: circSETD3; lung cancer; marker; gefitinib; acquired resistance

Corresponding Author:
Dr Qi Zhang,
Department of Respiratory Medicine,
The Affiliated Hospital of Jiaxing University,
Jiaxing, 314001, Zhejiang, China
e-mail: dr_zhangqi2001@163.com

0393-974X (2021)
Copyright © by BIOLIFE, s.a.s.
This publication and/or article is for individual use only and may not be further reproduced without written permission from the copyright holder.
Unauthorized reproduction may result in financial and other penalties
DISCLOSURE: ALL AUTHORS REPORT NO CONFLICTS OF INTEREST RELEVANT TO THIS ARTICLE.

stable (6). The advancement in sequencing technology determines an increased interest in studying circRNAs functions in the occurrence, development, treatment, and prognosis of several pathologies, including also malignant tumors (7). Several circRNAs have been identified as biomarkers of drug resistance in different types of cancers. For example, down-regulation of has_circ_0000258 in bladder cancer is implicated in cisplatin resistance (8), while up-regulation of circKDM4C decreases doxorubicin resistance in breast cancer (9). To date, few studies have evaluated the mechanism of gefitinib-acquired resistance. This study aimed to investigate human NSCLS cell line *in vitro* to discover whether circRNAs are involved in the pathogenesis of NSCLS and in gefitinib-acquired resistance.

MATERIALS AND METHODS

Cells and cell culture

Human NSCLC cell lines H292 (Shanghai Kanglang Biological Technology Co., Ltd., China) and PC9 (Shanghai Kanglang Biological Technology Co., Ltd., China) were stored in liquid nitrogen tanks (Wuxi ASC Instrument Co., Ltd., China). The frozen H292 and PC9 cells were warmed in a thermostatic water bath at 37°C under continued shaking until they dissolve completely. Then the cells were culture in a complete medium containing RPMI-1640 (Roswell Park Memorial Institute-1640) medium (Wuhan Chundu Biotechnology Co., Ltd., China) and fetal bovine serum (Zhejiang Tianhang Biotechnology Co., Ltd., China) in a 9:1 ratio at 37°C in a 5% CO_2 cell incubator (Thermo Electron Corporation, USA). The new complete medium was replaced periodically.

Establishment of the gefitinib-resistant NSCLC cell line model

Human NSCLC cell lines H292 (named H292S) and PC9 (named PC9S) were cultured in a complete medium: RPMI-1640 with 1% penicillin-streptomycin mixed solution (Qingdao Jisskang Biotechnology Co., Ltd., China), and 12% Bioind serum (Shanghai Yaji Biotechnology Co., Ltd., China) at 37°C in a 5% CO_2 cell incubator. A method of gradually increasing concentration proposed by AstraZeneca (UK) was used. Briefly, cells were treated with a low concentration (0.1μmol/L gefitinib) for 3 days, then digested with 0.25% trypsin and passaged. Finally, after 13 months, the cells were stably and tolerantly grown in complete medium at a gefitinib concentration of 1.5μmol/L. Based on this model, gefitinib-resistant NSCLC cell lines H292 (H292R) and PC9 (PC9R) models were established.

CCK-8 (Cell Counting Kit-8) – cell viability assay

H292S, H292R, PC9S, and PC9R cells in the logarithmic growth phase were selected and inoculated into a 96-well plate at a concentration of 4.0×10^4/mL after digestion and centrifugation. 100 μL of cell suspension was added to each well, and 5 replicate wells were worked. The cells were cultured in the incubator for 48 h. CCK-8 reagent (Shanghai Jingke Chemical Technology Co., Ltd., China) was slowly added in a concentration of 10μL/well and cultured for 2 h at 37°C in 5% CO_2 atmosphere in the dark. The absorbance of each well was measured by a microplate reader (Illumina, USA). The mean maximal inhibitory concentration (IC_{50}) value and the resistance index of gefitinib were calculated.

RNA sequencing and RT-qPCR (Real-time Quantitative polymerase chain reaction) method for verification of differentially expressed circRNAs

HiSeq 2500 sequencer (Illumina, USA) was used for RNA sequencing of H292S *vs* H292R and PC9S *vs* PC9R. RIN (RNA integrity number) ≥ 7 and 28S/18S> 0.7 were used as the library building standard for RNA library building. FC (Fold change) ≥ 2 and P <0.05 circRNAs were used as differentially expressed circRNAs.

Extraction of RNA: H292S, H292R, PC9S, and PC9R cells in the logarithmic growth phase were selected. After digestion and centrifugation, the cell precipitate was transferred to an EP (Eppendorf) tube, and 1 mL of Trizol reagent (Wuhan Chundu Biotechnology Co., Ltd., China) was added. After mixing, the cells were kept at room temperature for 10 min, 200μL chloroform was added and shaken vigorously for 15 s, and then the samples were kept at room temperature for 5 min. After centrifuging (12000 rpm/min, 4°C) for 10 min, the upper water phase was discarded, and the same amount of isopropanol was added, shaking vigorously for 15 s and left for 10 min. Then, the cells were centrifuged (12000 rpm/min, 4°C) for 10 min, and the supernatant was discarded. One mL of 75% ethanol was added and centrifuged (12,000 rpm/min, 4°C) for 5 min. The precipitate was dried

at room temperature for 20 min, and 20 μL of DEPC (diethylpyrocarbonate) water was added to dissolve it and the cells were then stored at -80°C for further analysis.

Reverse transcription reaction: The reverse transcription reaction was performed on the total RNA extracted to obtain the cDNA. A reverse transcription kit (Takara, Japan) was used to operate according to the instruction system. The reaction system was: 2 μL 5×Prime Script Buffer, 0.5 μL PrimeScript RT Enzyme Mix, 0.5 μL Oligo dT Primer (50 μM), 0.5 μL Random hexamer primer (100 μM), 0.5 μg Total RNA (500 ng), and RNase Free dH2O (Shanghai Kemin Biotechnology Co., Ltd. China). These were supplemented to the total volume of 10 μL. The reverse transcription reaction was performed at 37°C for 15 min, and the inactivation reaction of reverse transcriptase was performed at 85°C for 5 s.

Amplification reaction: The primer sequences of the target gene and the reference gene were designed. The reaction system was: 5 μL SYBR Premix enzyme, 0.5 μL Forward Primer (10 μM), 0.5 μL Reverse Primer (10 μM), 0.5 μL cDNA template, and DEPC (diethylpyrocarbonate) water was added to the total volume of 10 μL. The pre-denaturation was performed at 95°C for 30 s. Then the samples were denatured at 95°C for 5 s, and the reaction was repeated for 39 cycles. It was annealed and extended at 60°C for 30 s. The calculation was performed using ΔCt, and the final result was expressed by the $2^{-\Delta Ct}$ method.

Cell transfection

H292S, H292R, PC9S, and PC9R cells in the logarithmic growth phase, after digestion were selected and inoculated into a 6-well plate at a concentration of at 3.0×10^5/well with 2 mL complete medium and cultured overnight at 37°C in 5% CO_2 atmosphere. Cells were transfected with 1.0 μg of circSETD3 overexpression (the gene was over transcribed and translated, and the final gene expression product exceeded the normal level) or interference plasmid (siRNA or shRAN targeting the target gene was introduced into the plasmid to degrade the mRNA of the target gene and change the phenotype) diluted with 200 μL of serum-free RPMI-1640 medium using Lipofectamine 2000 as a transfection reagent according to the manufacturer's instructions. The 6-well plate was rinsed twice with PBS and 2 mL of the serum-free medium was added. The reaction complex was slowly added dropwise, shaken well, and placed in an incubator for 48 h at 37°C in 5% CO_2 atmosphere. The transfection efficiency was observed under a fluorescence microscope (OLYMPUS, Japan) and was stored for photographing.

Effect of circSETD3 on cells resistance to gefitinib

The cell proliferation was tested by the CCK-8 method (the same method as previously described), and the cell apoptosis was tested by flow cytometry. The logarithmic growth phase cells were taken to resuspend in PBS at a concentration of 1×10^5/mL. The cells were cultured in an incubator at 37°C in 5% CO_2 atmosphere until the degree of cell fusion exceeded 80%. Cells were transfected with circSETD3 overexpression (overexpression group) and interference plasmid (interference group) as well as its negative control vector plasmid. After 4 h, the cells were rinsed 3 times with PBS, the media was replaced with a complete culture solution, and cultured for 72 h at 37°C in 5% CO_2 atmosphere. Then, the cells were rinsed 3 times with PBS, and the supernatant was discarded after digestion and centrifugation. 500 μL of pre-chilled PBS was added to resuspend the cells and transfer to the EP tube. 100 μL binding buffer was used to resuspend and transfer to a flow test tube. 5μL Annexin V (Wuhan ChunDu Biotechnology Co., Ltd., China) was added to the cells and incubated for 15 min at room temperature in the dark, then centrifuged at 800 rpm/min for 20 min. The staining solution was discarded. 100 μL binding buffer was used to resuspend, and 5 μL PI (Propidium iodide) (Beijing Zhongsheng Ruitai Technology Co., Ltd., China) staining solution was added in the dark. The solution was filtered using a 0.45-μm filter (Shanghai Yiyan Biotechnology Co., Ltd., China) and tested using a flow cytometer (BD Corporation, USA). The samples were worked in triplicates. Cells stained only by Annexin V were considered apoptotic cells, while cells stained only by PI were considered necrotic cells.

Nuclear localization of circSETD3

Extraction of cytoplasmic RNA: The digested cells were resuspended with PBS and transferred to the EP tube on ice. The cells were centrifuged at low speed and PBS was discarded. 3 μL of pre-chilled Cell Fractionation Buffer (Shanghai Binzhi Biotechnology Co., Ltd., China) was added to resuspend the cells, incubated on ice for 10 min and centrifuged at 500 rpm/min and 4°C for 3 min. The supernatant was discarded and placed in an enzyme-

free EP tube. Equal volumes of absolute ethanol and 2×Lysis/Binding (Shanghai Binzhi Biotechnology Co., Ltd., China) solution were added in sequence and mixed. 700 μL of the sample was put into a filter cartridge with 700 μL wash solution, centrifuged for 1 min and then the liquid was discarded. Following, 500 μL wash solution 2/3 was added successively for 2 times to filter, then the liquid was discarded and the filter was placed in a new collection tube and 40 μL of 95°C elution solution (Beijing Zhongsheng Ruitai Technology Co., Ltd., China) was added and centrifuged for 30 s to recover the RNA. 10μL of 95°C elution solution was added for a second wash, and the RNA was stored at -80°C.

Extraction of nuclear RNA: The digested cells were resuspended with PBS and transferred to the EP tube on ice. The cells were centrifuged at low speed and PBS was discarded. 3μL of pre-chilled Cell Fractionation Buffer was added to resuspend the cells, incubated on ice for 10 min, and centrifuged at 500rpm/min and 4°C for 3 min. The supernatant was discarded, and 300 μL Cell Disruption Buffer (Shanghai Binzhi Biotechnology Co., Ltd., China) was added, shaking vigorously. Equal volumes of absolute ethanol and 2×Lysis/Binding solution were added in sequence and mixed. The subsequent steps were the same as the extraction of cytoplasmic RNA.

RNaseR digestion: 1μL of RnaseR diluted to 10ng/mL with Dilution Buffer (Shanghai Binzhi Biotechnology Co., Ltd., China) was mixed with 1 μg of RNA and left to react at 37°C for 1 h. GAPDH (glyceraldehyde-3-phosphate dehydrogenase) was used as a cytoplasmic localization marker. U6 (A class of snRNA transcribed from RNA polymerase III) was used as the nuclear localization marker. The expression level of the target gene was tested by the qPCR method as previously described.

ABCG2 (ATP binding cassette subfamily G member 2) as a target for circSETD3-miR-520h

The identification of ABCG2 as a target for circSETD3-miR-520h was obtained through STRING database (https://string-db.org/). Dual-luciferase reporting assay and qPCR method were used to verify this relationship. The transfection reagent was prepared in advance and the cells with a fusion of 60% were used for transfection. 10 μL DMEM (Dulbecco's modified eagle medium) (Beijing Zhongsheng Ruitai Technology Co., Ltd., China) was mixed with 0.16 μg circSTED3/Mut and circSTED3/WT target plasmids as well as 5 pmol of miR-520h/negative control. Then, the cells were kept at room temperature for 5 min (solution A). 10 μL DMEM was mixed with 0.3 μL transfection reagent (solution B) and placed at room temperature for 5 min. Solution A and solution B were mixed uniformly and placed at room temperature for 20 min. The fresh medium was changed after transfection for 6 h, and cells were collected for testing after transfection for 48 h.

1×Pasive Lysis Buffer was added to the 96-well plate at 100 μL/well. After shaking for 15 min on a room temperature shaker, the cells were centrifuged at 12,000rpm/min for 10 min. The supernatant was

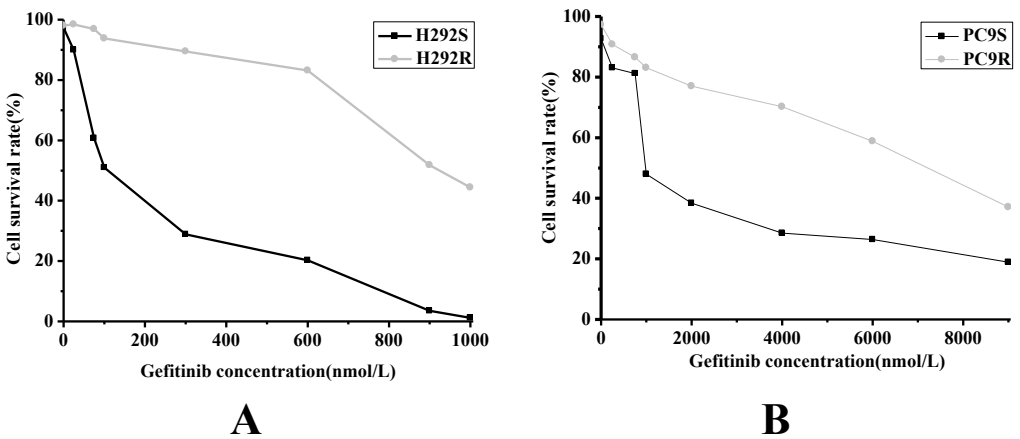


Fig. 1. *Cell survival rates at different gefitinib concentrations.* ***A)*** *H292S and H292R cells;* ***B)*** *PC9S and PC9R cells.*

separated and transferred to the 96-well plate with 100 μL Luciferase Assay Reagent I (Shanghai Binzhi Biotechnology Co., Ltd., China) working solutionand mixed, and Firefly luciferase value (reference value) was measured and recorded. Then 100 μL Stop&GloReagent (Beijing Zhongsheng Ruitai Technology Co., Ltd., China) was added and mixed, and Renilla luciferase value (reporting gene luminescence value) was measured and recorded. The ternary relationship of circSETD3-miR-520h-ABCG2 was verified by the qPCR method.

Statistical analysis

The data analysis was performed using SPSS22.0 statistical software (IBM, USA). Data were expressed as mean ± standard deviation ($\bar{x}\pm s$). The *t*-test was used for comparison of the two samples' means. The *chi*-squared test was used for the comparison of the enumeration data. The difference of $P < 0.05$ was considered statistically significant.

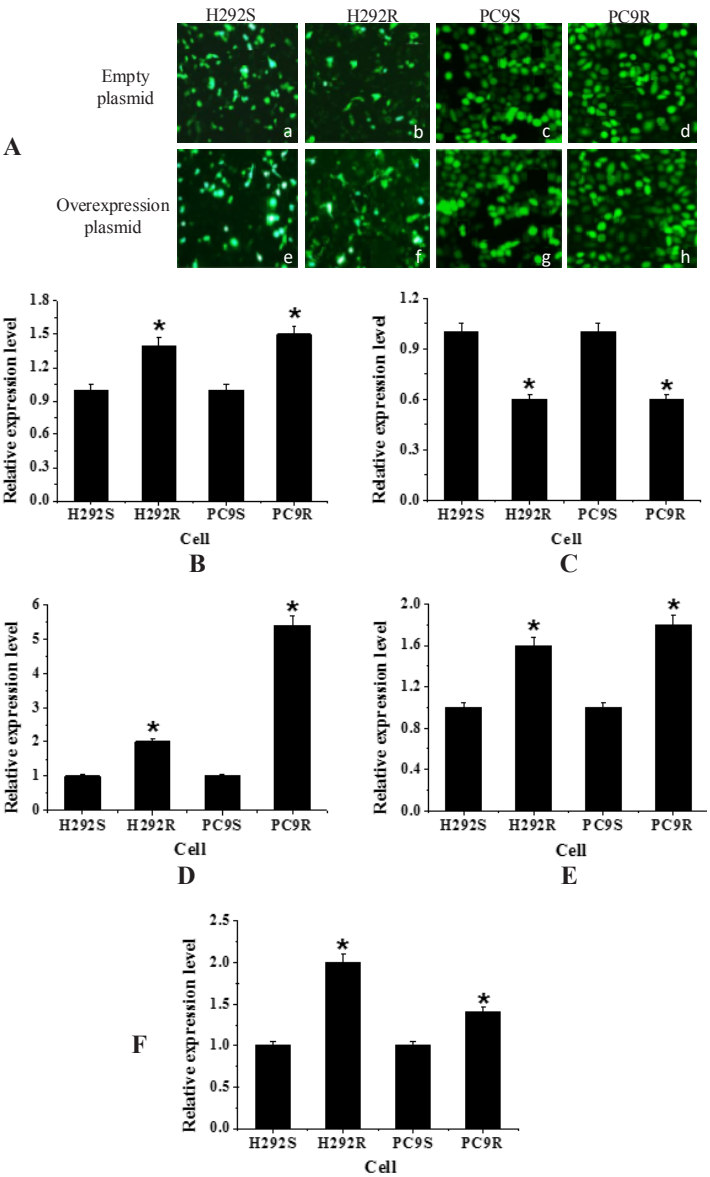


Fig. 2. *Results of cell transfection and verification of RNA sequencing by qPCR.* ***A****) Cell transfection experiment (a-d were fluorescence microscope images of H292S, H292R, PC9S and PC9R empty plasmids; e-h were fluorescence microscope image of H292S, H292R, PC9S and PC9R overexpression plasmids);* ***B****) Expression of hsa_circ_0006867;* ***C****) Expression of hsa_circ_0001147;* ***D****) Expression of hsa_circ_0000655;* ***E****) Expression of hsa_circ_0000620;* ***F****) Expression of hsa_circ_0000567. *Compared with sensitive cell lines, P < 0.05.*

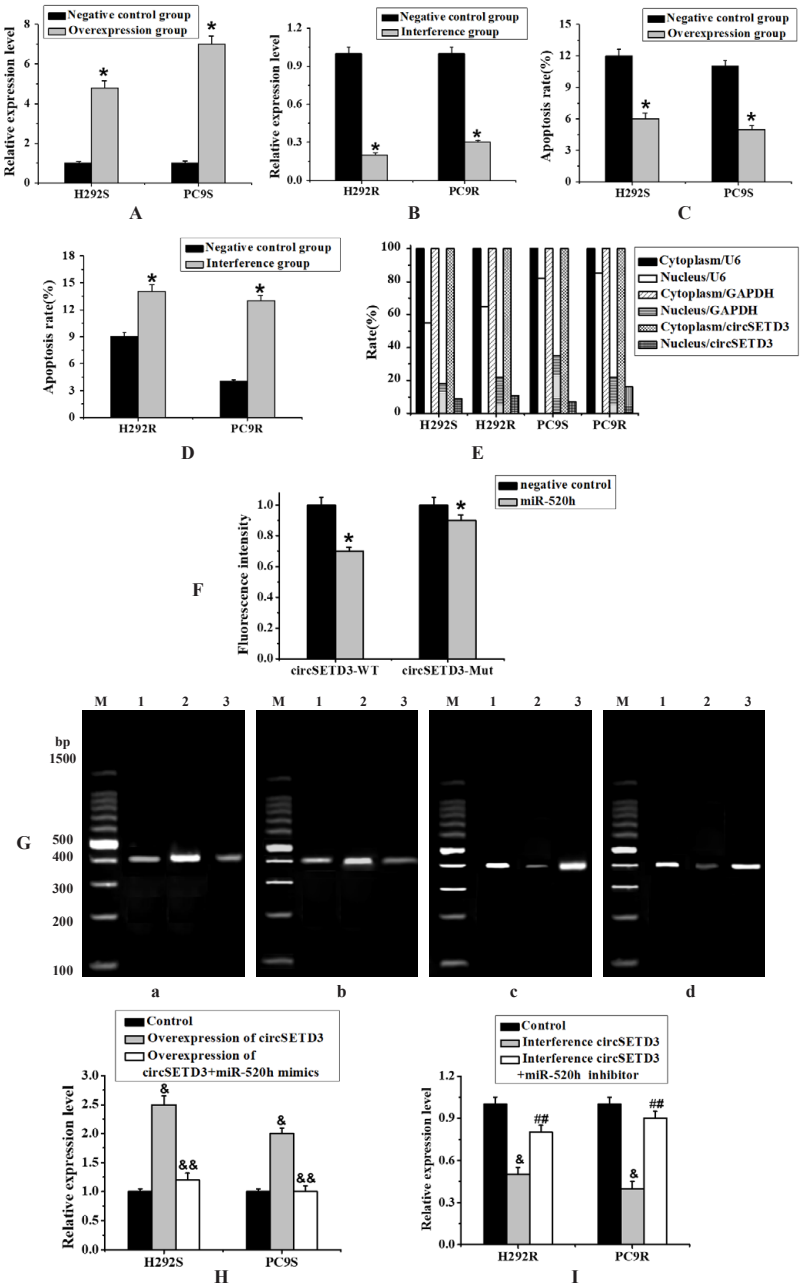


Fig. 3. Experimental results of circSETD3. A) Effect of circSETD3 on cell gefitinib sensitivity detected by CCK-8 assay on H292S and PC9S; B) the effect of circSETD3 on cell gefitinib sensitivity detected by CCK-8 assay on H292R and PC9R; C) Effect of circSETD3 on cell gefitinib sensitivity detected by flow cytometry on H292S and PC9S; D) Effect of circSETD3 on cell gefitinib sensitivity detected by flow cytometry on H292R and PC9R; E) The nucleocytoplasmic localization of circSETD3; F) Results of double luciferase experiment, *P <0.05 compared with negative control; G) qPCR electrophoresis results for evaluating the relation between circSETD3-miR-520h-ABCG2 (a. H292S□M. marker, 1: Control, 2: overexpression of circSETD3, 3: overexpression of circSETD3+miR-520h mimics; b. PC9S, M: marker, 1: Control, 2: overexpression of circSETD3, 3: overexpression of circSETD3+miR-520h mimics; c. H292R, M: marker, 1: Control, 2: interfering circSETD3, 3: interfering circSETD3+miR-520h inhibitor; d. PC9R, M: marker, 1: Control, 2: interfering circSETD3, 3: interfering circSETD3+miR-520h inhibitor); H) the mutual effect of overexpression of H292S and PC9S on circSETD3-miR-520h-ABCG2 detected by qPCR; I) the mutual effect of interference of H292S and PC9S on circSETD3-miR-520h-ABCG2 detected by qPCR. *Compared with negative control, P < 0.05; compared with Control, &P < 0.05; &&compared with overexpression of circSETD3, P < 0.05; ## compared with interfering circSETD3, P < 0.05.

RESULTS

Gefitinib cell resistance

Cell survival rates at different gefitinib concentrations are shown in Fig. 1. The IC_{50} values for gefitinib on the growth and proliferation of H292S and H292R cells were 111.15 nmol/L and 979.64 nmol/L, respectively. The drug resistance index was 8.81. The IC_{50} values for gefitinib on the growth and proliferation of PC9S and PC9R cells were 768.87 nmol/L and 7881.01 nmol/L, respectively. The drug resistance index was 10.25.

circRNAs expression before and after gefitinib-acquired resistance in human NSCLC cell lines

In the cell transfection experiment, the fluorescence microscope images of the empty plasmids and the overexpression plasmids are shown in Fig. 2A. Compared with the empty plasmids, the fluorescence expression of the overexpression plasmids was not significantly different (P> 0.05), and the transfection efficiency was more than 40%, which met the requests of *in vitro* cell experiments.

By RNA sequencing, there were 22 differentially expressed circRNAs in H292S *vs* H292R, and 23 differentially expressed circRNAs in PC9S *vs* PC9R. There were 5 common circRNAs: hsa_circ_0006867, hsa_circ_0001147, hsa_circ_0000655, hsa_circ_0000620, and hsa_circ_0000567.

The qPCR method was used to verify the results of RNA sequencing. The results are shown in Fig. 2 B-F. The expression of hsa_circ_0001147 was down-regulated in H292R and PC9R. The expression of hsa_circ_0006867, hsa_circ_0000655, hsa_circ_0000620, and hsa_circ_0000567 were all up-regulated in H292R and PC9R. Among them, the differential expression of hsa_circ_0000567 changed significantly. Further analysis by searching the circBase database found that hsa_circ_0000567 is derived from the SETD3 gene and it is a circular molecule, namely circSETD3.

Effect of circSETD3 on gefitinib sensitivity in cells

In H292S and PC9S cells (NSCLC cell lines sensitive to gefitinib), the cell proliferation ability of the overexpression group was significantly increased compared with the negative control group (P <0.05) (Fig. 3A). In H292R and PC9R (NSCLC cell lines resistant to gefitinib), the proliferation ability of the interference group was significantly decreased compared with the negative control group, (P <0.05) (Fig. 3B). In H292S and PC9S, the apoptosis ability of the overexpressed group was significantly decreased compared with the negative control group (P <0.05) (Fig. 3C). In H292R and PC9R, the apoptosis ability of the interference group was significantly increased compared with the negative control group (P <0.05) (Fig. 3D).

Nuclear localization of circSETD3

qPCR was used to test the expression level of the target gene. It can be seen that circSETD3 is mainly present in the cytoplasm (Fig. 3E).

Relationship between circSETD3-miR-520h-ABCG2

The results of the double luciferase experiment are shown in Fig. 3F. It can be seen that when circSETD3-WT and miR-520h were co-transfected into cells, the fluorescence intensity was significantly reduced (P <0.05). When circSETD3-Mut and miR-520h were co-transfected into the cells, the fluorescence intensity changed little, with no statistical significance (P> 0.05).

qPCR was used to verify the interaction relationship between circSETD3-miR-520h-ABCG2, as shown in Fig. 3 G-I. After circSETD3 overexpression in H292S and PC9S cells, the expression of ABCG2 increased significantly (P <0.05). Transfecting miR-520h mimics on overexpression of circSETD3, determined a significantly decrease of ABCG2 expression (P <0.05). When H292R and PC9R interfered with circSETD3, the expression of ABCG2 decreased significantly (P <0.05). Transfecting miR-520h inhibitor on interfering with circSETD3, the expression of ABCG2 increased significantly (P <0.05).

DISCUSSION

Gefitinib-acquired resistance is a major problem in the treatment of lung cancer. The development of new biomarkers that can predict the sensitivity

of anticancer drugs and the explanation of the drug resistance mechanism of tumor cells have guiding significance for overcoming gefitinib resistance in lung cancer. In this study, H292S and PC9S cell lines were used to establish a model of gefitinib-resistant NSCLC cell line. It has been shown that from all circRNAs screened before and after drug resistance, circSETD3 plays an important role by promoting cell proliferation and inhibiting cell apoptosis.

CircRNAs play different roles in different cellular localizations. For example, the circRNA in the nucleus directly or indirectly affects the expression of target genes through interaction with proteins or DNA (10). The circRNA in the cytoplasm exerts its biological functions mainly through competitive endogenous RNA mechanisms (11). In this paper, through the nuclear localization test of circSETD3, it was found that circSETD3 mainly exists in the cytoplasm. Therefore, it is considered that circSETD3 exerts biological functions through competitive endogenous RNA. The interaction relationship of circSETD3-miR-520h-ABCG2 is obtained through bioinformatics analysis and confirmed by dual-luciferase reporting assay and qPCR. It has been shown that circSETD3 can be directly combined with miR-520h. Overexpression of circSETD3 in H292S and PC9S cells, leads to up-regulation of ABCG2 expression, while the transfection of the cells with miR-520h mimics down-regulate the ABCG2 expression. These findings are consistent with other studies that showed that miR-520h could down-regulate the ABCG2 expression (11). ABCG2 is an adenosine triphosphate binding cassette transporter associated with chemotherapeutics resistance. It has been previously reported that high expression of ABCG2 in tumor cells is an important cause of gefitinib-acquired resistance. (12).

In conclusion, circSETD3 can be used as a new biomarker for lung cancer. It relieves miR-520h degradation of the transporter ABCG2 by down-regulating miR-520h expression, causing gefitinib to be pumped out of the cell.

ACKNOWLEDGEMENT

This work was supported by the Project of Jiaxing Science and Technology Bureau (Project No.: 2019AD32264).

REFERENCES

1. Zhang Y, Ren JS, Huang HY, Shi JF, Li N, Zhang Y, Dai M. International trends in lung cancer incidence from 1973 to 2007. Cancer Med 2018; 7(4):1479-89.
2. Zhang Y, Cai Y. Expression and clinical significance of lincRNA-EPS in NSCLC. Journal of Practical Oncology 2017; 32:349-51.
3. Patcas A, Mogosan C, Alexescu TG, Bordea IR, Buzoianu AD, Todea DA. The challenges of using pd-l1 as a predictive biomarker and the therapeutic approach in non-small cell lung cancer immunotherapy. Farmacia 2020; 68(3):390-5.
4. Sani TA, Mohammadpour E, Mohammadi A, et al. Cytotoxic and apoptogenic properties of dracocephalum kotschyi aerial part different fractions on calu-6 and mehr-80 lung cancer cell lines. Farmacia 2017; 65(2):189-99.
5. Solassol I, Pinguet F, Quantin X. FDA- and EMA-Approved Tyrosine Kinase Inhibitors in Advanced EGFR-Mutated Non-Small Cell Lung Cancer: Safety, Tolerability, Plasma Concentration Monitoring, and Management. Biomolecules 2019; 9(11):668.
6. Ma Y, Zhang X, Wang YZ, Tian H, Xu S. Research progress of circular RNAs in lung cancer. Cancer Biol Ther 2019; 20(2):123-9.
7. Tang W, Ji M, He G, Yang L, Niu Z, Jian M, Wei Y, Ren L, Xu J. Silencing CDR1as inhibits colorectal cancer progression through regulating microRNA-7. Onco Targets Ther 2017; 10:2045-56.
8. Chi BJ, Zhao DM, Liu L, et al. Downregulation of hsa_circ_0000285 serves as a prognostic biomarker for bladder cancer and is involved in cisplatin resistance. Neoplasma 2019; 66(2):197-202.
9. Liang Y, Song X, Li Y, et al. circKDM4C suppresses tumor progression and attenuates doxorubicin resistance by regulating miR-548p/PBLD axis in breast cancer. Oncogene 2019; 38(42):6850-66.
10. Jin X, Guan Y, Sheng H, Liu Y. Crosstalk in competing endogenous RNA network reveals the complex molecular mechanism underlying lung cancer. Oncotarget 2017; 8(53):91270-80.
11. Kaehler M, Ruemenapp J, Gonnermann D, et

al. MicroRNA-212/ABCG2-axis contributes to development of imatinib-resistance in leukemic cells. Oncotarget 2017; 8(54):92018-31.
12. Vlaming ML, Läppchen T, Jansen HT, et al. PET-CT imaging with [(18)F]-gefitinib to measure Abcb1a/1b (P-gp) and Abcg2 (Bcrp1) mediated drug-drug interactions at the murine blood-brain barrier. Nucl Med Biol 2015; 42(11):833-41.

Coculture with interleukin-10 overexpressed chondrocytes: a cell therapy model to ameliorate the post-traumatic osteoarthritis development

L.-K. Yu[1*], J. Zhang[1*], Z.-Y. Sun[1], C.-L. Ruan[2], H. Li[1] and X.-J. Ruan[3]

[1]Department of Orthopaedic Surgery, Liaocheng People's Hospital, Liaocheng, China; [2]Department of Anesthesiology, Liaocheng People's Hospital Dongchangfu District, Liaocheng, China; [3]Department of Surgery, Liaocheng People's Hospital Dongchangfu District, Liaocheng, China

Received January 29, 2021 - Accepted March 29, 2021

[*]These Authors contributed equally to this work

Autologous chondrocyte (CH) transplantation is a novel strategy to treat post-traumatic osteoarthritis (PTOA). In this study, an *in vitro* coculture model was used to explore the effects of interleukin (IL)-10 overexpressed CHs on degenerated CHs. The original CHs were isolated from the patients' knee joint cartilage and pretreated with IL-1β to get degenerated CHs. Moreoer, CHs were transfected with a lentivirus vector to overexpress IL-10. After coculture with the degenerated CHs, the apoptosis, collagen X, IL-6, and TNF-α of original CHs were increased, and the collagen II and IL-10 were decreased compared to the separated culture condition. Coculture with original CHs did not alleviate the degeneration of the IL-1β-pretreated CHs. **However, coculture with the IL-10-overexpressed CHs rescued the proliferation, collagen II, aggrecan, SOX9, and IL-10 expression, and suppressed the apoptosis, collagen X, RUnx2, IL-6, and TNF-α levels in the IL-1**β pretreated **CHs. Additionally, the IL-10-overexpressed CHs also maintained a healthy state when cocultured with the degenerated CHs. Therefore, transplanting the IL-10-overexpressed CHs in the treatment of PTOA would obtain a more durable and visible effect in alleviating the CH degeneration.**

Post-traumatic osteoarthritis (PTOA) is osteoarthritis secondary to joint trauma, often accompanied by pathological changes such as cartilage destruction, inflammation infiltration, and subchondral bone changes (1). The main clinical manifestations are pain in the affected joints, joint mobility disorders of varying degrees, and severe deformities (2). Different degrees of trauma can cause various degrees of joint damage. Severe trauma can cause intra-articular fractures, joint dislocations, rupture of the joint capsule and ligaments, intra-articular haemorrhage, and even massive tissue necrosis and defects. Mild injuries may be asymptomatic at the time, but after a certain period, the affected joints become painful, and their mobility is reduced. High energy damage destroys the integrity of joint tissues, directly leads to necrosis of cartilage tissue, and forms the pathological basis of PTOA (3). Newberry et al. (4) found that when the articular load exceeds a critical value, the cartilage

Key words: IL-10; chondrocyte transplantation; post-traumatic osteoarthritis; inflammation

Corresponding Author:
Xingju Ruan, BM,
Department of Surgery, Liaocheng People's Hospital,
Dongchangfu District, No. 67, Dongchang West Road,
Dongchangfu District, Liaocheng, Shandong 252000, China
Tel./Fax: +86 013563006106
e-mail: vkey85@163.com

0393-974X (2021)
Copyright © by BIOLIFE, s.a.s.
This publication and/or article is for individual use only and may not be further reproduced without written permission from the copyright holder.
Unauthorized reproduction may result in financial and other penalties
DISCLOSURE: ALL AUTHORS REPORT NO CONFLICTS OF INTEREST RELEVANT TO THIS ARTICLE.

will undergo irreversible damage, with a significant proteoglycan loss and then chondrocyte (CH) necrosis, cartilage thinning, and gradual subchondral bone thickening. The rate of apoptotic CHs in patients with intra-articular fractures is significantly higher than that in patients with OA, and up to 90% in fracture fragments. This can explain to some extent why PTOA occurs in the later stages, even if an intra-articular fracture is anatomically reduced (5, 6). Additionally, injured CHs bring high-oxygen active substances, damaged mitochondria DNA, low cell proliferation, and less extracellular matrix (ECM) secretion, which affects the function of the cartilage (7).

Articular cartilage is a unique connective tissue without blood vessels, lymph, and nerves; its nutritional source mainly depends on the synovial fluid in the joint cavity and the blood supply of the subchondral bone. Therefore, it has limited self-repair ability, and it is difficult to recover once injured (8). With the rapid development of molecular biology and gene technology, the research and application of gene introduction and other methods in tissue engineering are becoming increasingly widespread. The genetic modification in autologous CH transplantation (ACT) is to introduce the target gene into the CH through vector transfection (9). The modified CHs can continuously and efficiently secrete growth factors locally in the process of cartilage regeneration, thereby promoting cartilage repair. Che et al. (10) transplanted CHs overexpressing bone morphogenetic protein-7 (BMP-7) gene to rabbit knee joints for repair. After 12 weeks, the content of hyaline cartilage and aggrecan was significantly higher than that in the control group, indicating CHs transfected with BMP-7 can promote the repair of cartilage damage. Moreover, the preliminary result of transforming growth factor β1 (TGF-β1)-transfected CHs for treating arthritis patients shows no obvious safety issues (11).

During *in vitro* culture, CHs proliferate faster and are prone to undergo dedifferentiation, which would increase the uncontrollability during transplantation. Therefore, many problems remain to be solved before the method is applied in the clinic, for example, which appropriate gene to choose. The chondroprotective effects of interleukin (IL)-10 with the inhibition of inflammatory, catabolism, and apoptosis in cartilage were previously described (12, 13), which caught our attention. IL-10 may be a promising target of genetic modification in autologous CH transplantation to treat the damaged CHs of PTOA. In this study, CH injury was caused by IL-1**β pretreatment, and** coculture with IL-10-overexpressed CHs was found to rescue the injured CHs. These results may provide a new option for the cartilage repair of PTOA by genetically-modified autologous CH transplantation.

MATERIALS AND METHODS

Samples source and CHs isolation

Three patients (1 male and 2 females, age: 45, 52, and 54, respectively) undergoing total knee arthroplasty due to the diagnose of osteoarthritis donated their joints to our study (other underlying diseases such as heart disease, high blood pressure, diabetes, were excluded). The patients signed written informed consent before the surgery. This research project was approved by the Ethics Committee of Liaocheng People's Hospital. The samples were washed three times with PBS to remove the blood, and the part with a smooth and flat surface was minced into small pieces before digestion. The fragment was incubated for 1 hwith 0.25% type II collagenase at 37°C overnight. Then, the cell solution was filtrated with a 100-μm pore size cell strainer, and resuspend with Dulbecco's modified eagle medium (DMEM) medium (Thermo Fisher, Waltham, MA, USA) containing 10% fetal bovine serum (FBS) (Gibco, Rockville, MD, USA).

Coculture model and cell treatment

After isolation, CHs of passage one were used for the following experiments, and a 10-cm petri dish was used for cell culture. A total number of 1.5×10^5 CHs per dish were pretreated with 15ng/ml IL-1β medium to induce the degeneration and another group of CHs (with or without IL-10 transfection) were prepared at the density of 3×10^5/dish on the coverslip without IL-1β. To prepare the co-cultivated CHs, the bottom of one side of the dish was raised, and the IL-1β-pretreated CHs just attached to the bottom half. After two days, the medium without IL-1β was changed and put in the non-injured CHs on the

coverslip for another 3-day coculture. After coculture, CHs on the coverslip were taken out and analyzed**.**

Reverse transcription-polymerase chain reaction (RT-PCR)

The relative gene expressions of the mRNA level were analyzed by the RT-PCR method. Total RNA of each group was isolated from CHs with TRIzol reagent (Invitrogen, Carlsbad, CA, USA) according to the manufacturer's instructions. The quality of RNA was detected by the nucleic acid-protein analyzer. RNA was reverse-transcribed into complementary deoxyribose nucleic acid (cDNA) with PrimeScript™ RT Master Mix (Applied Biosystems, Foster City, CA, USA), and RT-PCR was performed to analyze collagen II, aggrecan, collagen X, IL-10, IL-6, and tumor necrosis factor-α (TNF-α) expression using SYBR Green Master Mix (Applied Biosystems, Foster City, CA, USA). The RNA expression level of glyceraldehyde 3-phosphate dehydrogenase (GAPDH) was used for normalization by $2^{-\Delta\Delta Ct}$. The primers used for RT-PCR are listed in Table I.

Immunofluorescence

The collagen II, SOX9, and Runx2 expression in CHs were determined using immunofluorescence (IF). Briefly, CHs were fixed and permeabilized after treatments. Then, cells were incubated with primary antibody: anti-collagen II, anti-SOX9, or anti-Runx2 (Abcam, Cambridge, UK) overnight at 4°C. The following day, CHs were incubated with Donkey anti-rabbit or anti-mouse IgG (Abcam, Cambridge, UK) and DAPI (Beyotime, Shanghai, China) for 1 h. The staining intensity was measured using Image-J software (National Institutes of Health).

IL-10 overexpression

Lentivirus vector-IL-10 (sapiens, human) was purchased from Kewei Biological Technology Company (Xi'an, Shaanxi, China). CHs were transfected with Lentivirus vector-IL-10 to upregulate the IL-10 expression using Lipofectamine 2000 (Invitrogen, Carlsbad, CA, USA). After 48 h, transfection efficacy was evaluated by RT-PCR.

Flow cytometry

The proliferation and apoptosis of CHs in each group were detected by flow cytometry with 5-Ethynyl-2'- deoxyuridine (EdU) or annexin V-FITC (fluorescein isothiocyanate)/ Propidium Iodide (PI) kit (Beyotime, Shanghai, China) according to the manufacturer's instructions. Briefly, 1×10^5 CHs in each group were incubated with EdU or Annexin V-FITC/PI solution for 20 min in the dark. Then, the processed cells were subjected to flow cytometry.

Enzyme-linked immunosorbent assay (ELISA)

Human IL-10, IL-6, and TNF-α Quantikine ELISA Kit (R&D Systems, Minneapolis, MN, USA) were used to analyze the IL-10, IL-6, and TNF-α protein contents of the medium after co-culture according to the manufacturer's instructions.

Statistical analysis

Data were analyzed by GraphPad Prism (La Jolla, USA,

Table I. *Primers for RT-PCR*

Name	Forward (5'>3')	Reverse (5'>3')
Collagen II	TGGACGATCAGGCGAAACC	GCTGCGGATGCTCTCAATCT
Aggrecan	ACTCTGGGTTTTCGTGACTCT	ACACTCAGCGAGTTGTCATGG
Collagen X	GAGGGCCAAGACGAAGACATC	CAGATCACGTCATCGCACAAC
IL-10	GACTTTAAGGGTTACCTGGGTTG	TCACATGCGCCTTGATGTCTG
IL-6	ACTCACCTCTTCAGAACGAATTG	CCATCTTTGGAAGGTTCAGGTTG
TNF-α	CCTCTCTCTAATCAGCCCTCTG	GAGGACCTGGGAGTAGATGAG
GAPDH	ACAACTTTGGTATCGTGGAAGG	GCCATCACGCCACAGTTTC

USA) and presented by the means ± standard deviations. Differences between the two groups were analyzed by using the Student's *t*-test. Comparison between multiple groups was carried out using one-way ANOVA test followed by Post Hoc Test (Least Significant Difference). P-value <0.05 was considered statistically significant.

RESULTS

Degenerated CHs aggravate the apoptosis of original CHs

CHs were pretreated by IL-1β (10 mg/ml) for 3 days to induce cell degeneration. Then the number of 1.5×10^5 degenerated CHs and original CHs (without any intervention) were cultured in 5 ml media, respectively. For coculture, original CHs (1.5×10^5) on the coverslip were put beside the degenerated CHs (1.5×10^5) in 10 ml media for an extra 3 days (Fig. 1A). After three days of coculture, the degenerated CHs on the bottom of the petri dish and the original CHs on the coverslip were harvested, respectively (Fig. 1B). The activity of the CHs was valued via proliferation and apoptosis by flow cytometry. In addition to the coculture, the degenerated and original CHs were also cultured as a comparison for three days, separately. Compared to the degenerated CHs, the original CHs presented a highly proliferative ability, whether co-cultured or not (Fig. 1C). Meanwhile, IL-1β-pretreated CHs had a more significant number of apoptotic cells than the original CHs, and the apoptosis of the original CHs increased after coculture with degenerated

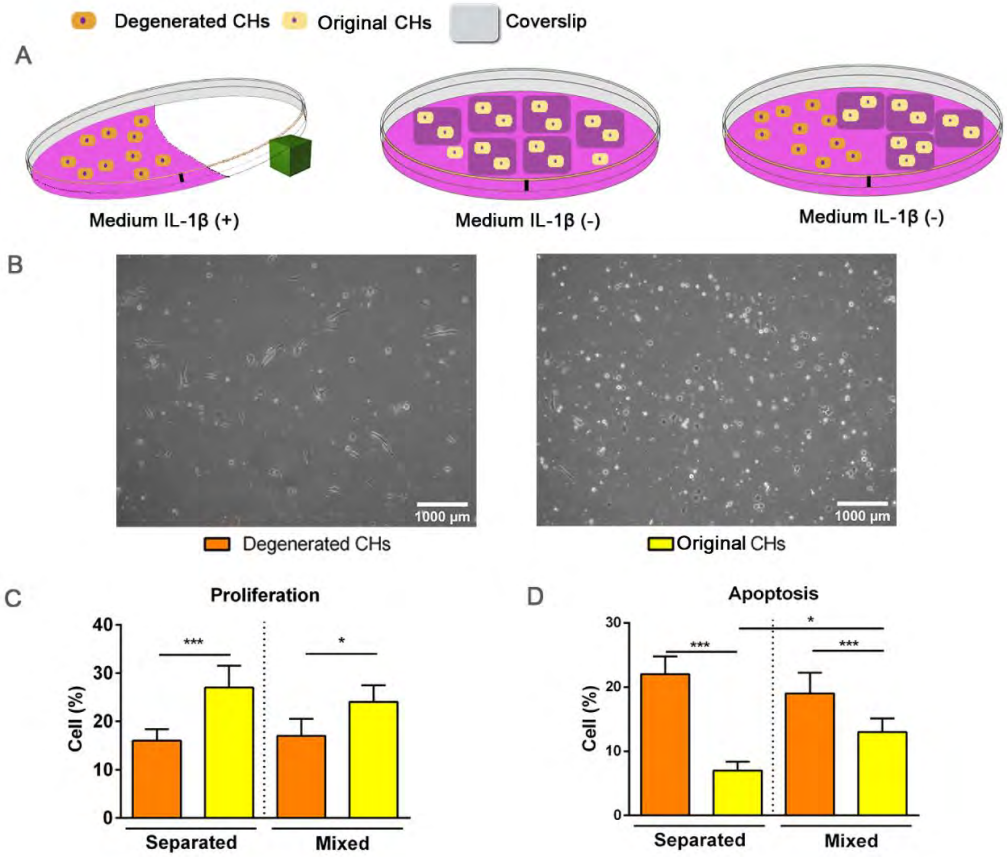


Fig. 1. *Degenerated CHs aggravate the apoptosis of original CHs. **A**) Schematic diagram of the coculture model. The bottom of the CHs pretreated with IL-1β was raised on one side to make CHs attach just on the bottom half. The original CHs were seeded on the coverslip for coculture. **B**) Degenerated and original CHs of the co-cultured dish 3 days later (magnification 200×). **C**) The proliferative cell rate and the (**D**) apoptotic cell rate were determined by flow cytometry. Separated means the CHs were cultured alone without mix, and mixed means the CHs were cocultured. Statistically significant differences P < 0.05 are marked as*, P < 0.001 are marked as***.*

CHs. However, coculture with original CHs did not significantly affect the apoptosis of the degenerated CHs compared to the separated culture condition (Fig. 1D). Therefore, coculture had no positive effect on the degenerated CHs but aggravated the apoptosis of original CHs.

Degenerated CHs accelerate the ECM degradation and inflammation of original CHs

In addition to the cell activity, the ECM components synthesized by CHs also changed with the process of degeneration. Hence, the mRNA levels of the chondrogenic gene, containing collagen II and

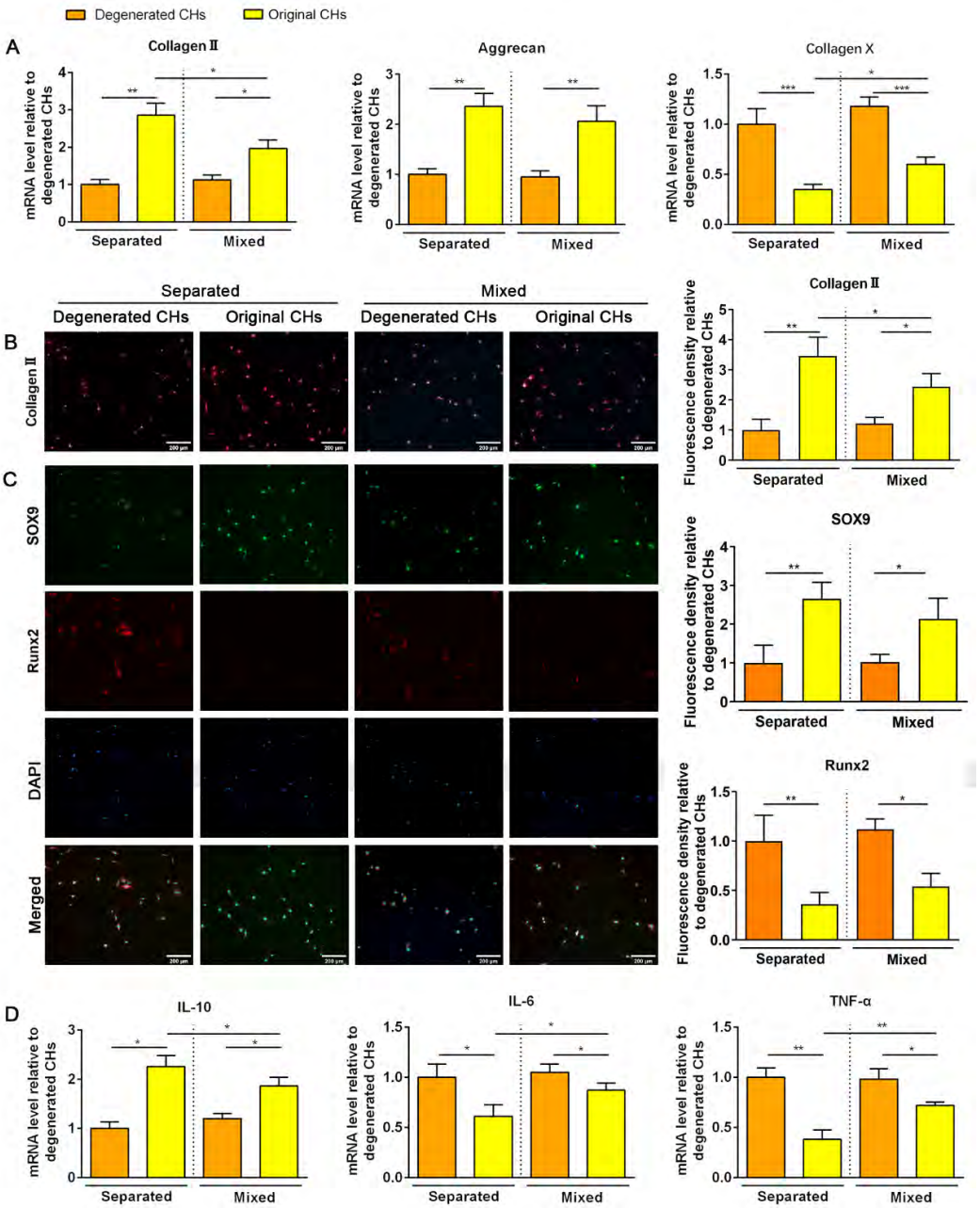


Fig. 2. *Degenerated CHs accelerate the ECM degradation and inflammation of original CHs. The mRNA expression level of (**A**) collagen II, aggrecan, collagen X was assayed by RT-PCR. IF staining of (**B**) collagen II, (**C**) SOX9, and Runx2, and quantitative analysis. The mRNA expression level of (**D**) IL-10, IL-6, and TNF-α was assayed by RT-PCR. Separated means the CHs were cultured alone without mix, and mixed means the CHs were cocultured. Statistically significant differences P < 0.05 are marked as*, P < 0.01 are marked as**, P < 0.001 are marked as***.*

aggrecan, and the hypertrophic marker collagen X of each condition, were analyzed. The results showed that the collagen II and aggrecan mRNA expression of the original CHs were significantly higher than the IL-1β-pretreated CHs, and the collagen X level was lower than the IL-1β-pretreated CHs. However, coculture with degenerated CHs led to decreased collagen II and increased collagen X expression of original CHs. Moreover, the ECM production of the degenerated CHs was not improved after coculture with the original CHs (Fig. 2A). Additionally, the collagen II expression was also verified with IF staining which was consistent with the PCR result (Fig. 2B). SOX9 is a pivotal transcription factor that expresses stably in cartilage and decreases in OA condition. On the contrary, Runx2 overexpression usually leads to more severe articular cartilage degeneration and accelerates the OA progression. Therefore, the degeneration of CHs was also shown by the SOX9 and Runx2 expression in the present study. The data indicated that original CHs presented a higher level of SOX9 and lower level of Runx2 than the degenerated CHs, and coculture did not significantly affect SOX9 and Runx2 expression (Fig. 2C). Furthermore, the mRNA expression regarding the inflammatory factor was also explored. The anti-inflammatory factor IL-10 expression of the original CHs was higher than the degenerated

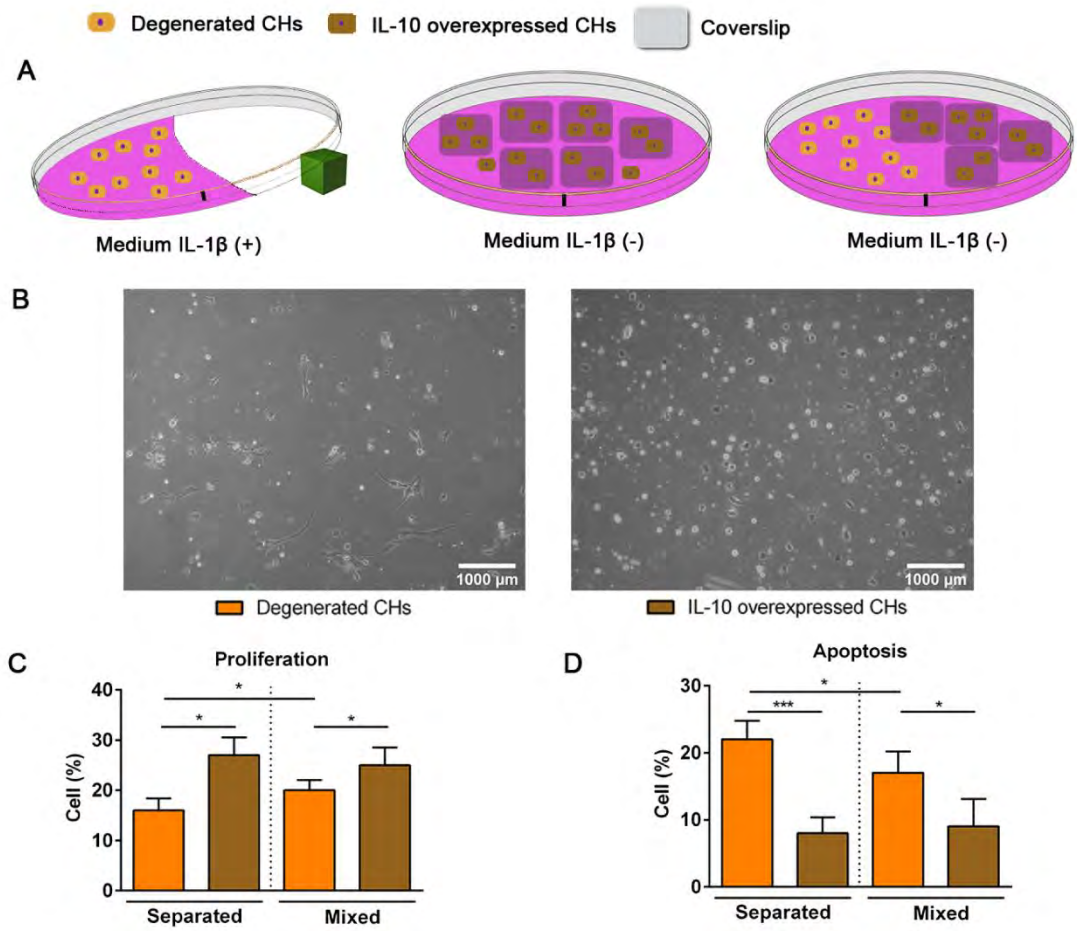


Fig. 3. *IL-10-transfected CHs improve the activity of degenerated CHs.* ***A****) Schematic diagram of the coculture model. The bottom of the CHs pretreated with IL-1β was raised to one side to make CHs just attach on the bottom half. The IL-10-transfected CHs were seeded on the coverslip for coculture.* ***B****) Degenerated and IL-10-transfected CHs of the co-cultured dish 3 days later. (magnification 200×).* ***C****) The proliferative cell rate and the (****D****) apoptotic cell rate was determined by flow cytometry. Separated means the CHs were cultured alone without mix, and mixed means the CHs were cocultured. Statistically significant differences P < 0.05 are marked as*, P < 0.001 are marked as***.*

CHs, but it was decreased after coculture with the degenerated CHs. Additionally, the IL-6 and TNF-α mRNA of the original CHs was upregulated, caused by the degenerated CHs (Fig. 2D).

IL-10-transfected CHs improve the activity of degenerated CHs

The original CHs cannot enhance the function of the degenerated CHs, what about the IL-10-

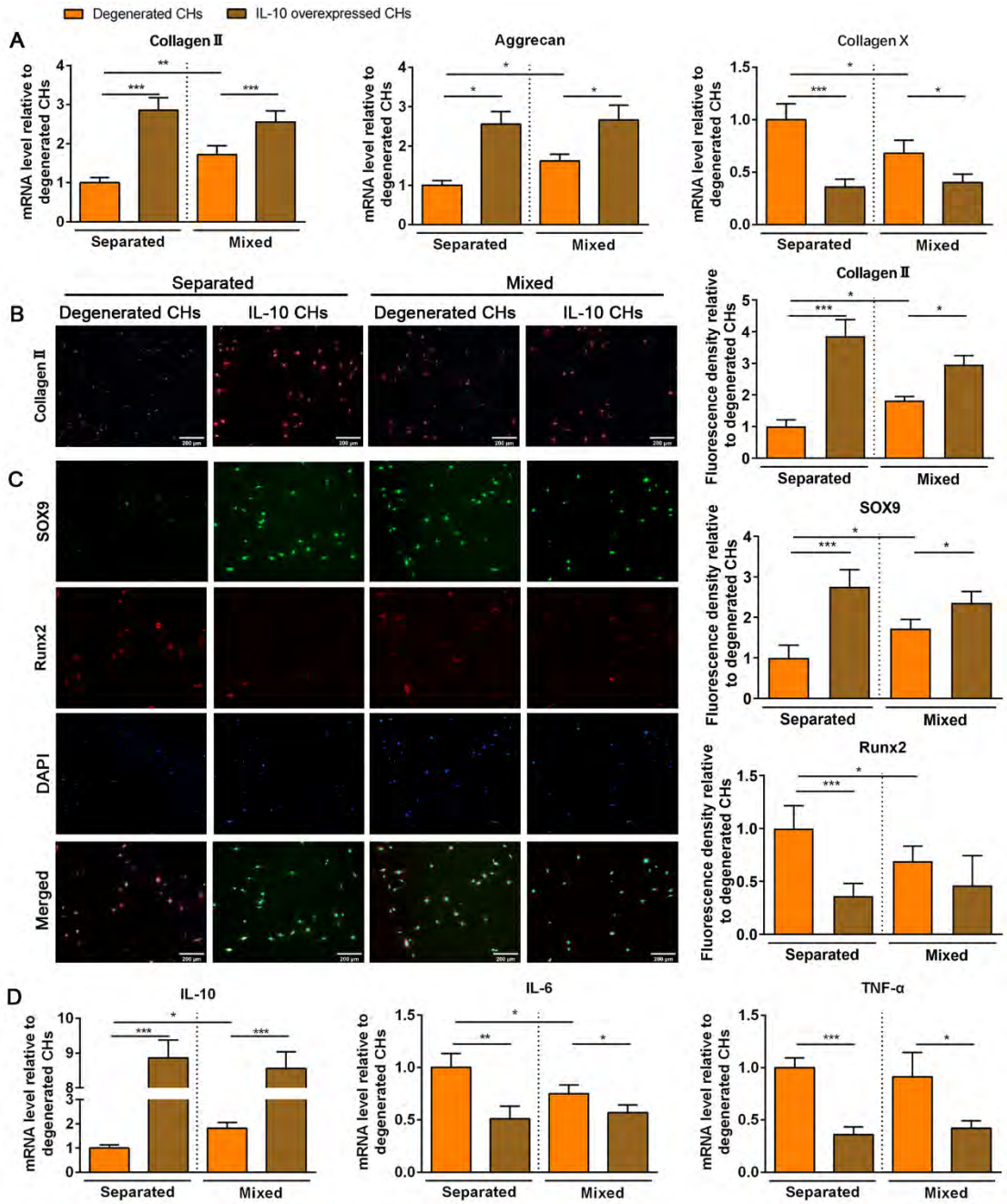


Fig. 4. *IL-10-transfected CHs alleviates the ECM degradation and inflammation of degenerated CHs. The mRNA expression level of (**A**) collagen II, aggrecan, collagen X was assayed by RT-PCR. IF staining of (**B**) collagen II, (**C**) SOX9, and Runx2, and quantitative analysis. The mRNA expression level of (**D**) IL-10, IL-6, and TNF-α was assayed by RT-PCR. Separated means the CHs were cultured alone without mix, and mixed means the CHs were cocultured. Statistically significant differences P < 0.05 are marked as*, P < 0.01 are marked as**, P < 0.001 are marked as***.*

overexpressed CHs? To answer this question, the original CHs were transfected on the coverslip with a lentivirus vector via inserting IL10 to upregulate the IL-10 expression. After 48 h of infection, the IL-10-overexpressed CHs (1.5×10^5) were cocultured with the IL-1***β-pretreated CHs*** (*1.5×10^5*) in 10 ml media for three days (Fig. 3A). After 3 days' coculture, the degenerated CHs on the bottom of the petri dish and the IL-10-overexpressed CHs on the coverslip were harvested, respectively (Fig. 3B). Similarly to the original CHs, the IL-10-overexpressed CHs had a higher proliferative population compared to the degenerated CHs. After coculture, the proliferation of the degenerated CHs increased compared to the separated culture group, and the proliferation of the IL-10 group was not affected by the degenerated CHs (Fig. 3C). Moreover, coculture with the IL-10-overexpressed CHs also suppressed the apoptosis of IL-1β-pretreated CHs compared to the separated culture group, and the apoptosis of the IL-10-overexpressed CHs still stayed at a low level as the separated culture group (Fig. 3D).

IL-10-transfected CHs alleviate the ECM degradation and inflammation of degenerated CHs

The IL-10-overexpressed CHs had a higher amount of collagen II and aggrecan mRNA expression, and a lower collagen X expression than the degenerated CHs. Under the coculture condition, IL-10-overexpressed CHs rescued the collagen II and aggrecan mRNA expression and suppressed the collagen X mRNA expression in the degenerated CHs. Unlike the original CHs, IL-10-overexpressed CHs can still maintain proper ECM secretion in the presence of degenerated CHs (Fig. 4A). The same result of collagen II protein expression was obtained via IF staining (Fig. 4B). In addition, coculture with IL-10-overexpressed CHs improved the SOX9 expression and suppressed the Runx2 expression of the degenerated CHs, which did not affect their own level (Fig. 4C). Furthermore, the IL-10 mRNA expression was much higher in the transfected CHs, and coculture also resulted in the upregulation of the IL-10 level of the degenerated CHs. Additionally, the IL-6 and TNF-α mRNA level of the IL-10-

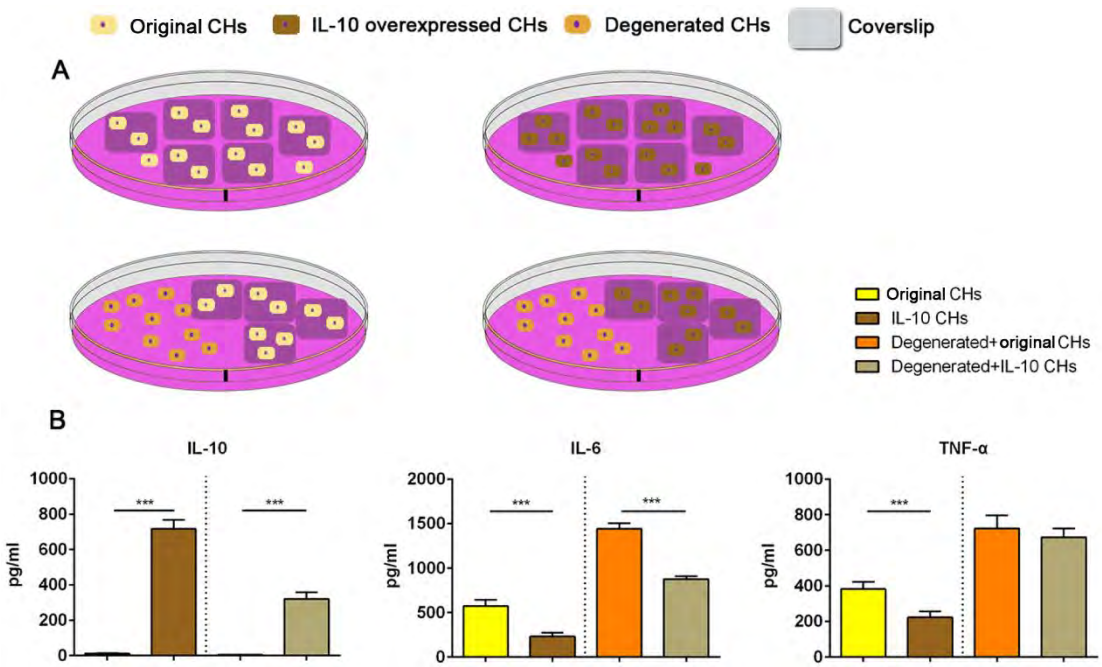


Fig. 5. *IL-10-transfected CHs suppresses the inflammatory factors in the medium.* ***A)*** *The 3-day culture medium from the original CHs, IL-10-overexpressed CHs, coculture of degenerated and original CHs, coculture of degenerated and IL-10-overexpressed CHs were collected for ELISA.* ***B)*** *The protein level of IL-10, IL-6, and TNF-α in the medium was measured by ELISA. Statistically significant differences $P < 0.001$ are marked as***.*

overexpressed CHs was downregulated compared to the degenerated CHs. After coculture, the IL-6 expression of the degenerated CHs was suppressed compared to the separated culture group, but not the TNF-α expression (Fig. 4D). Therefore, gene-edited CHs can effectively inhibit CH degeneration and also protect ECM, and these may be related to the powerful anti-inflammatory effects of IL-10.

IL-10-transfected CHs suppresses the inflammatory factors in the medium

Transplanted CHs play a role in stabilizing ECM and orthotopic CHs metabolism through paracrine effects. Therefore, under the conditions of co-culture, the exchange of biologically active substances between the CHs should also be performed through the culture medium. Therefore, the 3-day culture medium of four groups was collected: original CHs, IL-10-overexpressed CHs, coculture of degenerated and original CHs, coculture of degenerated and IL-10-overexpressed CHs (Fig. 5A), and the protein contents of three inflammatory factors in the medium were measured with the ELISA. The results indicated that the IL-10 content of the transfected group was much higher than the original group, and the coculture group with IL-10-transfected CHs also maintained a higher IL-10 level compared to the coculture with original CHs. Additionally, the IL-10-transfected CHs also suppressed the production and release of IL-6 in both separated culture and coculture conditions. However, a significant difference was only found in the TNF-α between the original and IL-10-transfected CHs, not in the coculture with the degenerated CHs (Fig. 5B). In this part, the IL-10-transfected CHs might mediate the inflammatory response of the degenerated CHs through the culture medium. Of course, more possible mechanisms need to be further explored.

DISCUSSION

In the present study, we provided a feasible way to rescue degenerated CHs via coculture with autologous IL-10-overexpressed CHs. In this way, the number of functional CHs is increased not only by reducing the already degenerated-CHs, but also by supplying more ectogenous CHs. It is a theoretical basis for CH transplantation to treat cartilage defects. At present, cartilage defects of PTOA patients are usually treated conservatively, and patients with severe symptoms need artificial joint replacement. For young patients with excellent joint stability and mobility, cartilage defects, and proper joint alignment, ACT is another way used to repair local cartilage defects. Since the launch of the ACT technology in 1994, it has undergone three upgrades (14, 15). Briefly, the first generation of ACT (16) is to take the proximal tibial periosteum to cover the common defect area. A suspension containing autologous CHs is injected into the gap between the periosteum and the defected area, and CH growth repairs cartilage defects. The second-generation (17) uses collagen membranes (usually type I/III double-layer collagen membranes) instead of periosteum sheets to seal and fix CHs. The third-generation technology is based on the use of biomaterials as the cartilage seed cell carrier, and matrix-induced ACT. At present, many scholars in different countires have reported on the technique of ACT, and the follow-up shows that the effect is stable (15, 18).

In addition to cartilage defects, in the long-term course of PTOA, changes in the microenvironment of the joint cavity are also a chronic injury to CHs. Decreased joint stability increases the shear stress on the articular cartilage during weight loading, causing CHs to produce excessive oxides. CHs undergo persistent oxidative damage and premature aging, and even die (19). After trauma, various MMPs can be produced by articular CHs, synovial cells, fibroblasts, and macrophages in the form of the zymogen, which accelerates the destruction of the ECM. Apart from this, many cytokines such as IL-1β, IL-6, and TNF-α produced by synovial cells are also widely involved in PTOA joint degeneration. Fujita et al. (20) found that IL-1β, IL-6, TNF-α, and MMP-3 were increased in synovial fluid of dog knees after ACLT, with increased aggrecan loss, and that IL-1β and MMP-3 and the limp time are closely related. The levels of IL-1β and TNF-α in the synovial fluid of patients with chronic anterior cruciate ligament injury were significantly increased, which was consistent with the severity of articular

cartilage damage (21). Therefore, after PTOA, the joint cavity is usually in a harsh environment with high oxidative stress and active inflammation. The role of transplanted seed CHs in this environment is limited and even loses vitality. In the present study, coculture with the degenerated CHs accelerated the original CH degradation. However, the efficiency of rescuing the degenerated CHs was limited. If the cells degenerate rapidly after seeding, the effect of cell transplantation is uncertain. Therefore, these data suggest that if it is simply implanted with healthy CHs, it will not delay the degeneration process of the degenerated cells. On the contrary, the degenerated cells can accelerate the degeneration of healthy cells, which may be related to inflammation. Thus, we aimed to explore an improvement that can achieve better effects on transplantation.

Inflammation is involved in the pathological process of PTOA and promotes its development, therefore finding effective anti-inflammatory methods has become the core issue of our research, and IL-10 is an attractive candidate. CHs and synovial fibroblasts synthesize IL-10 and express the IL-10 receptor on their cellular surface (22, 23). IL-10 suppresses matrix-degrading enzymes, and the pro-inflammatory cytokines triggered IL-1β expression in OA (24). Apart from that, IL-10 improved the activity of CHs, promoted the ECM synthesis in the inflammatory environment during cartilage explants of joints (25). CHs overexpressed with IL-10 not only can stimulate the collagen II gene expression but also have anti-apoptotic effects by inhibiting the caspase activities in the articular CHs (26). In this study, we, fortunately, observed that the IL-10-overexpressed CHs exhibited influence in rescuing the cell viability, ECM production, and inflammation of the degenerated CHs. Meanwhile, coculture with degenerated CHs did not affect the activity of the IL-10-overexpressed CHs. Overexpression of IL-10 in CHs may not be able to reverse the degenerated CH; we believe its effect on delaying the degeneration of CHs can be concluded from the present experiments. By genetic modification, the introduced IL-10 in autologous CHs can continuously and efficiently secrete anti-inflammatory factors after transplantation, maintaining the local microenvironment stability and thus facilitating cartilage repair. In contrast to direct IL-10 gene editing of CHs in the human body, fabricating the IL-10-overexpressed CHs *in vitro* ensures an adequate source of cells and allows to test the efficiency of IL-10 overexpression in advance, which is more controllable and efficient.

To summarize, this study elucidated that coculture with IL-10-overexpressed CHs protects the activity and prevents the ECM degradation of degenerated CHs. The novelty of this study is to provide a cell therapy option in ACT treatment of PTOA via combining autologous CH transplantation with IL-10 gene transfection, which not only benefits the repair of cartilage, but also ameliorates the inflammatory microenvironment.

REFERENCES

1. Riegger J, Brenner RE. Evidence of necroptosis in osteoarthritic disease: investigation of blunt mechanical impact as possible trigger in regulated necrosis. Cell Death Dis 2019; 10:683.
2. Coughlin TR, Kennedy OD. The role of subchondral bone damage in post-traumatic osteoarthritis. Ann N Y Acad Sci 2016; 1383:58-66.
3. Schenker ML, Mauck RL, Ahn J, Mehta S. Pathogenesis and prevention of posttraumatic osteoarthritis after intra-articular fracture. J Am Acad Orthop Surg 2014; 22:20-28.
4. Newberry WN, Garcia JJ, Mackenzie CD, Decamp CE, Haut RC. Analysis of acute mechanical insult in an animal model of post-traumatic osteoarthrosis. J Biomech Eng 1998; 120:704-9.
5. Kim HT, Lo MY, Pillarisetty R. Chondrocyte apoptosis following intraarticular fracture in humans. Osteoarthritis Cartilage 2002; 10:747-9.
6. Cho H, Pinkhassik E, David V, Stuart JM, Hasty KA. Detection of early cartilage damage using targeted nanosomes in a post-traumatic osteoarthritis mouse model. Nanomedicine-Uk 2015; 11:939-46.
7. Cinque ME, Dornan GJ, Chahla J, Moatshe G, LaPrade RF. High rates of osteoarthritis develop after anterior cruciate ligament surgery: an analysis of 4108 patients. Am J Sports Med 2018; 46:2011-9.
8. Blaker CL, Clarke EC, Little CB. Adding insult

to injury: synergistic effect of combining risk-factors in models of post-traumatic osteoarthritis. Osteoarthritis Cartilage 2019; 27:1731-4.
9. Ogura T, Bryant T, Merkely G, Minas T. Autologous chondrocyte implantation for bipolar chondral lesions in the patellofemoral compartment: clinical outcomes at a mean 9 years' follow-up. Am J Sports Med 2019; 47:837-46.
10. Che JH, Zhang ZR, Li GZ, Tan WH, Bai XD, Qu FJ. Application of tissue-engineered cartilage with BMP-7 gene to repair knee joint cartilage injury in rabbits. Knee Surg Sports Traumatol Arthrosc 2010; 18:496-503.
11. Ha CW, Noh MJ, Choi KB, Lee KH. Initial phase I safety of retrovirally transduced human chondrocytes expressing transforming growth factor-beta-1 in degenerative arthritis patients. Cytotherapy 2012; 14:247-56.
12. Mrosewski I, Jork N, Gorte K, et al. Regulation of osteoarthritis-associated key mediators by TNFalpha and IL-10: effects of IL-10 overexpression in human synovial fibroblasts and a synovial cell line. Cell Tissue Res 2014; 357:207-23.
13. Steen-Louws C, Popov-Celeketic J, Mastbergen SC, et al. IL4-10 fusion protein has chondroprotective, anti-inflammatory and potentially analgesic effects in the treatment of osteoarthritis. Osteoarthritis Cartilage 2018; 26:1127-35.
14. Rai V, Dilisio MF, Dietz NE, Agrawal DK. Recent strategies in cartilage repair: A systemic review of the scaffold development and tissue engineering. J Biomed Mater Res a 2017; 105:2343-54.
15. Zaslav K, Cole B, Brewster R, et al. A prospective study of autologous chondrocyte implantation in patients with failed prior treatment for articular cartilage defect of the knee: results of the Study of the Treatment of Articular Repair (STAR) clinical trial. Am J Sports Med 2009; 37:42-55.
16. Henderson I, Gui J, Lavigne P. Autologous chondrocyte implantation: natural history of postimplantation periosteal hypertrophy and effects of repair-site debridement on outcome. Arthroscopy 2006; 22:1318-24.
17. Haddo O, Mahroof S, Higgs D, et al. The use of chondrogide membrane in autologous chondrocyte implantation. Knee 2004; 11:51-5.
18. Browne JE, Anderson AF, Arciero R, et al. Clinical outcome of autologous chondrocyte implantation at 5 years in US subjects. Clin Orthop Relat Res 2005; (436):237-45.
19. Martin JA, Brown TD, Heiner AD, Buckwalter JA. Chondrocyte senescence, joint loading and osteoarthritis. Clin Orthop Relat Res 2004; 427S:96-S103.
20. Fujita Y, Hara Y, Nezu Y, Schulz KS, Tagawa M. Proinflammatory cytokine activities, matrix metalloproteinase-3 activity, and sulfated glycosaminoglycan content in synovial fluid of dogs with naturally acquired cranial cruciate ligament rupture. Vet Surg 2006; 35:369-76.
21. Han PF, Wei L, Duan ZQ, et al. Contribution of IL-1beta, 6 and TNF-alpha to the form of post-traumatic osteoarthritis induced by "idealized" anterior cruciate ligament reconstruction in a porcine model. Int Immunopharmacol 2018; 65:212-20.
22. Schulze-Tanzil G. Activation and dedifferentiation of chondrocytes: implications in cartilage injury and repair. Ann Anat 2009; 191:325-38.
23. Iannone F, De Bari C, Dell'Accio F, et al. Interleukin-10 and interleukin-10 receptor in human osteoarthritic and healthy chondrocytes. Clin Exp Rheumatol 2001; 19:139-45.
24. Schulze-Tanzil G, Zreiqat H, Sabat R, et al. Interleukin-10 and articular cartilage: experimental therapeutical approaches in cartilage disorders. Curr Gene Ther 2009; 9:306-15.
25. John T, Muller RD, Oberholzer A, et al. Interleukin-10 modulates pro-apoptotic effects of TNF-alpha in human articular chondrocytes in vitro. Cytokine 2007; 40:226-34.
26. Muller RD, John T, Kohl B, et al. IL-10 overexpression differentially affects cartilage matrix gene expression in response to TNF-alpha in human articular chondrocytes in vitro. Cytokine 2008; 44:377-85.

LncRNA SNHG14 promotes osteogenic differentiation of human bone marrow-derived mesenchymal stem cells via regulating miR-185-5p/WISP2 axis

ZH. Liu[1*], DD. Qi[1*], X. Li[2], SQ. Zhang[2], Y. Zhao[3], LX. Fu[2] and LY. Lu[4]

[1]Department of Spinal Surgery, East Hospital, Tongji University School of Medicine, Shanghai, China; [2]Department of Orthopedics, South of Guang'anmen Hospital, China Academy of Chinese Medical Sciences, Beijing, China; [3]Department of Nursing, South of Guang'anmen Hospital, China Academy of Chinese Medical Sciences, Beijing, China; [4]Department of Joint and Sports Medicine, East Hospital, Tongji University School of Medicine, Shanghai, China

Received June 22, 2020 – Accepted March 29, 2021

*Co-first authors

Osteogenic differentiation of human bone marrow-derived mesenchymal stem cells (hBMSCs) is vital for bone formation, and its dysfunction is linked to osteoporosis (OP). In this work, we explored the function of long non-coding RNA (lncRNA) small nucleolar RNA host gene 14 (SNHG14) in regulating osteogenic differentiation of hBMSCs. In the present study, the expression of SNHG14 in hBMSCs obtained from OP patients was measured by quantitative real-time polymerase chain reaction (qRT-PCR). SNHG14 was over-expressed or knocked down in hBMSCs, and the expression levels of OP-related genes (ALP, OCN, and OPN) in hBMSCs were detected by qRT-PCR and Western blot. StarBase database and miRanda database were used to predict the binding sites between SNHG14 and miR-185-5p, and between miR-185-5p and 3'UTR of WNT1 inducible signaling pathway protein 2 (WISP2), respectively. Luciferase reporter gene assay was used to validate the binding relationship between SNHG14 and miR-185-5p, and miR-185-5p and 3'UTR of WISP2, respectively. Here, we report that SNHG14 was significantly down-regulated in hBMSCs obtained from patients with OP. Overexpression of SNHG14 promoted osteogenic differentiation, while knockdown of SNHG14 worked oppositely. Mechanistically, miR-185-5p was demonstrated to be a target of SNHG14, and could reverse the function of SNHG14. Additionally, WISP2 was identified as a target gene of miR-185-5p in hBMSCs and could be indirectly regulated by SNHG14. Taken together, down-regulation of SNHG14 in hBMSCs accelerated the progression of OP via regulating miR-185-5p/WISP2 axis.

Osteoporosis (OP) is a common bone metabolic disease that threatens the health of middle-aged and elderly people (1, 2). It is featured with decreased bone mass, microstructural changes in bone tissue and increased fracture frequency. According to statistics, 1/3 of women with fractures over the age of 50 in the world suffer from OP, compared with 1/5 in males (3, 4). Anti-reabsorption drugs, bone-forming drugs and bone mineralization drugs are widely used to treat OP. Although these treatment strategies have certain effects, there are many side effects, therefore, it is imperative to explore the mechanism of osteogenesis

Key words: SNHG14; miR-185-5p; WISP2; hBMSCs.

Corresponding Author:
Dr Lu Liangyu,
Shanghai East Hospital,
Tongji University School of Medicine
150 # Jimo Rd,Pudong New Area,
200120 Shanghai, China
e-mail: 1310657@tongji.edu.cn

0393-974X (2021)
Copyright © by BIOLIFE, s.a.s.
This publication and/or article is for individual use only and may not be further reproduced without written permission from the copyright holder.
Unauthorized reproduction may result in financial and other penalties
DISCLOSURE: ALL AUTHORS REPORT NO CONFLICTS OF INTEREST RELEVANT TO THIS ARTICLE.

to develop new options for the treatment of OP.

LncRNA is a non-coding RNA with more than 200 *nt* in length (5). Increasing studies have demonstrated that it can regulate biological processes despite its inability to encode proteins (6). In recent years, the dysregulation or dysfunction of lncRNA has been linked to bone diseases. For example, the aberrant expression of lncRNA H19 can induce the activation of hedgehog signaling pathway and up-regulation of yes-associated protein 1, which lead to the excessive and abnormal proliferation of osteoblasts (7). The expression of proliferating cell nuclear antigen, matrix metalloproteinase-9, PI3K p85 α and Akt in osteoblasts were inhibited after MALAT1 knockdown, which decreased the proliferation of osteoblasts (8). In mice bone marrow-derived mesenchymal stem cells (BMSCs), after lncRNAp21 was silenced, the expression levels of vascular endothelial growth factor, basic fibroblast growth factor and insulin-like growth factor were promoted by the activation of Wnt/β-catenin signaling, and the differentiation of BMSCs into osteoblasts was facilitated (9). LncRNA small nucleolar RNA host gene 14 (SNHG14) is reported to be involved in cancer progression (10-12). However, its role in the pathogenesis of OP is rarely reported.

MicorRNAs (miRNAs) can regulate the expression levels of multiple target genes by binding to the 3'UTR of mRNA, and about 60% genes in human genome can be regulated by them (13, 14). MiRNAs are abundant in human cells and can regulate various physiological and pathological processes (15, 16). MiRNAs play crucial functions in the osteogenic differentiation of human bone marrow-derived mesenchymal stem cells (hBMSCs). For instance, miR-130a promotes the osteoblastic differentiation of hBMSCs by repressing the expression of Smurf2 and blocks the adipogenic differentiation of hBMSCs by inhibiting PPARγ (17). MiR-185-5p is involved in the development of various diseases, such as asthma, and clear cell renal cell carcinoma (18, 19). Recently, miR-185-5p is linked to cleidocranial dysplasia, suggesting its important role in regulating the balance between bone formation and resorption (20). However, how miR-185-5p regulates the osteoblast differentiation of hBMSCs is still not clear.

In the present study, we found that SNHG14 was downregulated in hBMSCs isolated from OP patients. Interestingly, it was found through bioinformatics that there was a binding site between SNHG14 and miR-185-5p, and between miR-185-5p and the 3'UTR of WNT1 inducible signaling pathway protein 2 (WISP2). This study explored the function of SNHG14/miR-185-5p/WISP2 axis in osteogenic differentiation of hBMSCs, aiming to provide a new theoretical basis for the treatment of OP.

MATERIALS AND METHODS

Clinical samples and cell culture

The study was approved by the Research Ethics Committee of the Chinese Academy of Medical Sciences (Approval number: 201908A015). Bone marrow was obtained from the femoral head of the patients (with or without OP) receiving total hip arthroplasty. All subjects gave informed and signed consent to participate in the study. Exclusion criteria: patients with rheumatoid arthritis, cancer, diabetes, hyperthyroidism, hyperparathyroidism or kidney disease. There were 30 patients in each group. Primary hBMSCs were isolated by density gradient centrifugation, and were cultured in phenol red-free α-MEM medium (HyClone, Logan, UT, USA) with 10% fetal bovine serum (FBS) (Gibco, Grand Island, NY, USA), 100U/mL penicillin and 100μg/mL streptomycin (HyClone, Logan, UT, USA). Notably, the cells were placed in a saturated humidity incubator with 5% CO_2 at 37°C. The medium was replaced every two days, with the unattached cells discarded. When the primary cell reached 80-90% confluence, cells were subcultured and the cells in logarithmic phase were used for subsequent experiments. For osteogenic induction of hBMSCs, medium containing 1% FBS was adopted, so as to avoid possible proliferation and differentiation, and 50μg/mL ascorbic acid (Sigma-Aldrich, St.Louis, MO, USA), 10 mM β-glycerophosphate (Sigma-Aldrich, St.Louis, MO, USA) and 0.1μg/mL dexamethasone (Sigma-Aldrich, St.Louis, MO, USA) were subsequently added. The medium was replaced every 3 days.

Quantitative real-time polymerase chain reaction (qRT-PCR)

Total RNA was extracted using TRIzol reagent (Invitrogen, Carlsbad, CA, USA). After RNA purity was determined, complementary DNA (cDNA) was obtained by reverse transcription of RNA utilizing PrimeScript RT Reagent Kit (Thermo Fisher Scientific, Waltham, MA,

USA). With cDNA as template, qPRC was performed by SYBR Premix Ex Taq Kit (Takara Biotechnology, Dalian, China). GAPDH and U6 were used as the internal parameters. The relative expression of the target gene was calculated by $2^{-\Delta\Delta CT}$ method. The primers were synthesized by Sangon Biotech Co., Ltd (Shanghai, China). The primer sequences are shown in Table 1.

Western blot

The cells were collected and washed 3 times with pre-cooled PBS, and radioimmunoprecipitation (RIPA) lysate (Sigma-Aldrich, St.Louis, MO, USA) was used to extract the total protein from the cells in ice water. The protein concentration was determined by the bicinchoninic acid (BCA) kit (Beyotime Institute of Biotechnology, Haimen, China). Total protein (30 μg in each group) was separated by sodium dodecyl sulfate polyacrylamide gel electrophoresis (SDS-PAGE) and then transferred to a polyvinylidene difluoride (PVDF) membrane. The membrane was blocked with 5% skim milk for 1 h, and incubated with primary antibodies including anti-osteocalcin (OCN) antibody (1:500; ab93876, Abcam, UK), anti-osteopontin (OPN) antibody (1:1000; ab8448; Abcam, UK), anti-alkaline phosphatase (ALP) antibody (1:1000; ab83259; Abcam, UK) and anti-GAPDH antibody (1:5000, ab9484, Abcam, UK) at 4°C overnight. Next day, the membrane was rinsed with TBST and incubated with horseradish peroxidase-labeled seconday antibody at 37°C for 1 h. Ultimately, ECL chemiluminescent reagent (Millipore, Bedford, MA, USA) was added onto the membrane to develop the protein bands.

ALP activity measurement

To determine ALP activity, an ALP assay kit (Njjcbio, Nanjing, China) was used. The cells were lysed with 1% Triton X-100 for 30 min at 4°C and then the lysate was dripped into the reaction buffer. Following incubation at 37°C for 15 min, the color developing agent was loaded, and the absorbance of each sample was measured at 520 nm with a microplate reader.

Cell transfection

SNHG14 overexpression plasmid pcDNA3.1-SNHG14, short hairpin RNA (shRNA) targeting SNHG14 (sh-SNHG14) or WISP2 (sh-WISP2) were synthesized by RiboBio (Guangzhou, China). The miR-185-5p mimics, miR-185-5p inhibitors and miRNA negative control (miR-NC) were purchased from GenePharma (Shanghai, China). The above vectors or miRNAs were transfected into hBMSCs employing Lipofectamine 2000 (Invitrogen, Carlsbad, CA, USA).

Luciferase reporter assay

Luciferase reporter gene assay was conducted using a dual-luciferase reporter assay system (Promega, Madison, WI, USA). Wild-type SNHG14 (SNHG14-WT) and WISP2 3'-UTR (WISP2-WT) and mutant types (SNHG14-MUT, WISP2-MUT) were constructed and integrated into pGL3vector (Promega, Madison, WI, USA). HEK-293T cells were co-transfected with the luciferase reporter plasmids mentioned above and miR-185-5p mimics or control mimics. After 48 h of transfection, the luciferase activity was determined in compliance with the manufacturer's protocol.

RNA binding protein immunoprecipitation (RIP) assay

RIP analysis was performed utilizing the Magna RIP kit (Millipore, Bedford, MA, USA) according to the manufacturer's protocol. hBMSCs were lysed in the RIP lysis buffer and the mixture was incubated with the antibody against Ago2 (Millipore, Bedford, MA, USA) or normal immunoglobulin G (IgG) (Millipore, Bedford, MA, USA). After that, the samples were mixed with proteinase K, and RNA was extracted by TRIzol reagent. Subsequently, the expressions of SNHG14 and miR-185-5p in the pellet were detected by qRT-PCR.

Statistics analysis

Statistical analyses were performed using SPSS 17.0 statistical software (SPSSInc., Chicago, IL, USA). All measurement data are expressed as mean ± standard deviation (x±s). A multivariate comparison was performed by one-way ANOVA. The independent sample *t*-test was used for comparison between two groups. The difference was statistically significant at $P<0.05$.

RESULTS

Expression levels of SNHG14 and miR-185-5p in hBMSCs

First of all, the expression levels of SNHG14 and miR-185-5p in hBMSCs isolated from patients with or without OP were detected by qRT-PCR. As shown,

the expression of SNHG14 in the hBMSCs isolated from the patients with OP was much lower than that in the control group (Fig. 1A). Conversely, compared with that in the control group, the expression of miR-185-5p in OP group was significantly increased (Fig. 1B). Interestingly, in the OP group, the expression of SNHG14 was negatively correlated with the expression of miR-185-5p (Fig. 1C). Then osteogenic medium (OM) was employed to induce osteogenic differentiation of hBMSCs for 21 consecutive days. qRT-PCR results manifested that the osteogenesis-related genes ALP, OPN and OCN were significantly upregulated in a time-dependent manner (Fig. 1D-F). As expected, the expression of SNHG14 was increased by osteogenic induction (Fig. 1G), while the expression of miR-185-5p was remarkably reduced by osteogenic induction (Fig. 1H).

SNHG14 promotes the osteogenic differentiation of hBMSCs

To detect the functional role of SNHG14 in osteogenic differentiation of hBMSCs, the SNHG14 knockdown model with SNHG14 shRNA was established (Fig. 2A). ALP activity assay showed that knockdown of SNHG14 reduced osteogenic differentiation of hBMSCs (Fig. 2B). Furthermore, qPCR results displayed that mRNA expression levels of ALP, OPN and OCN were significantly reduced in hBMSCs with SNHG14 knockdown (Fig. 2 C-E).

SNHG14 targets miR-185-5p in hBMSCs

To study how SNHG14 regulates the osteogenic differentiation of hBMSCs, we predicted the targets of SNHG14. Given the negative correlation between the expression of SNHG14 and miR-185-5p in OP

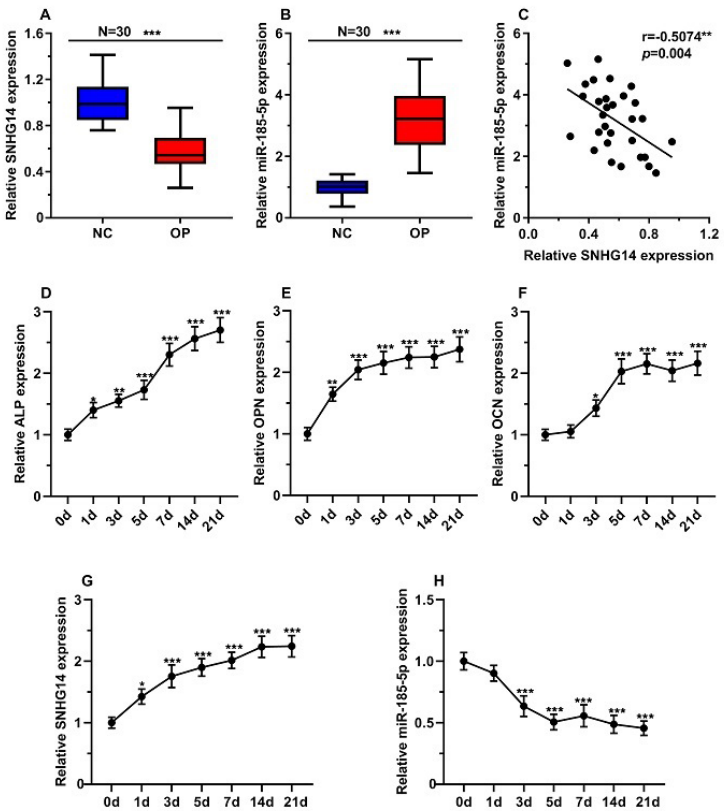


Fig. 1. *Expression levels of SNHG14 and miR-185-5p in hBMSCs.* ***A, B****) The relative expression levels of SNHG14 and miR-185-5p in hBMSCs isolated from patients was detected by qRT-PCR (n=30 in each group).* ***C****) Correlations between the expression levels of SNHG14 and miR-185-5p in hBMSCs (n=30).* ***D-F****) The expression of osteogenic genes ALP, OPN and OCN in hBMSCs treated with OM was detected by qRT-PCR. G, H) qRT-PCR was performed to detect the expression levels of SNHG14 and miR-185-5p in hBMSCs treated with OM. hBMSCs, human bone marrow-derived mesenchymal stem cells; qRT-PCR, quantitative real-time polymerase chain reaction; ALP, alkaline phosphatase; OPN, osteopontin; OCN, osteocalcin; OM, osteogenic medium. *P<0.05, *P<0.01, and ***P<0.001.*

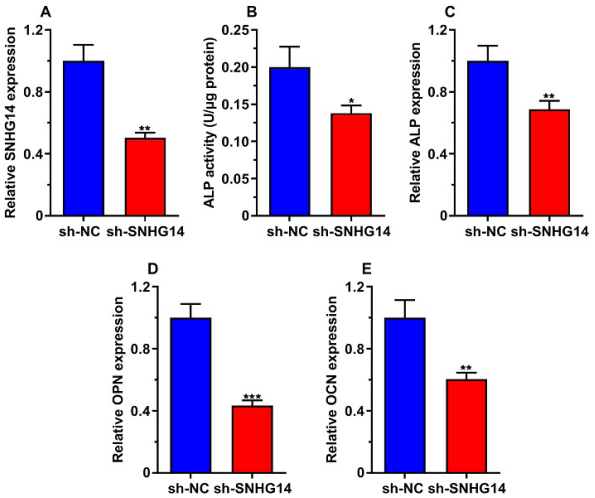


Fig. 2. *SNHG14 promotes the osteogenic differentiation of hBMSCs.* ***A****) SNHG14 expression was detected at 48 h after transfections of control shRNA (sh-NC) or SNHG14 shRNA (sh-SNHG14).* ***B****) The ALP activity was detected on the 7th day.* ***C, D****) The expression levels of ALP, OPN and OCN mRNA in hBMSCs tranfected with sh-NC or sh-SNHG14 were detected by qRT-PCR on the 3rd day. hBMSCs, human bone marrow-derived mesenchymal stem cells; shRNA, short hairpin RNA; ALP, alkaline phosphatase; qRT-PCR, quantitative real-time polymerase chain reaction. *P<0.05,**P<0.01, and ***P<0.001.*

patients, we used bioinformatics methods (http://starbase.sysu.edu.cn/) to predict the relationship between the two, and the results exhibited that there was a conserved binding site between SNHG14 and miR-185-5p (Fig. 3A). Thereafter SNHG14 wild type (SNHG14-WT) and SNHG14 mutant type (SNHG14-MUT) luciferase reporter vectors were constructed to investigate whether SNHG14 directly regulates miR-185-5p. Dual luciferase reporter assay displayed that miR-185-5p mimics significantly blocked the luciferase activity of SNHG14-WT, but had no effect on that of SNHG14-MUT, which validated the binding site between SNHG14 and miR-185-5p (Fig. 3B). Furthermore, RIP analysis showed that the expression of SNHG14 and miR-185-5p were significantly enhanced in the anti-Ago2 group compared with that in the anti-IgG group (Fig. 3C). Additionally, qRT-PCR results indicated that the expression of miR-185-5p was markedly increased in hBMSC with SNHG14 knockdown and decreased in hBMSCs with SNHG14 overexpression (Fig. 3D). The above results indicated that SNHG14 could directly target and negatively regulate miR-185-5p.

WISP2 is the direct target of miR-185-5p in hBMSCs

To ascertain the potential molecular mechanisms of miR-185-5p in regulating the phenotypes of hBMSC, we searched the potential target genes of miR-185-5p by Targetscan (http://www.targetscan.org/vert_72/). It was found that miR-185-5p and the 3'UTR of WISP2 have a possible binding site (Fig. 4A). It is reported that WNT1 mutation may alter cartilage turnover, and as a downstream molecule of WNT1, WISP2 may promote the osteogenesis (21). qRT-PCR showed that WISP2 expression was increased in OM-induced hBMSC (Fig. 4B). Furthermore, clinically, the

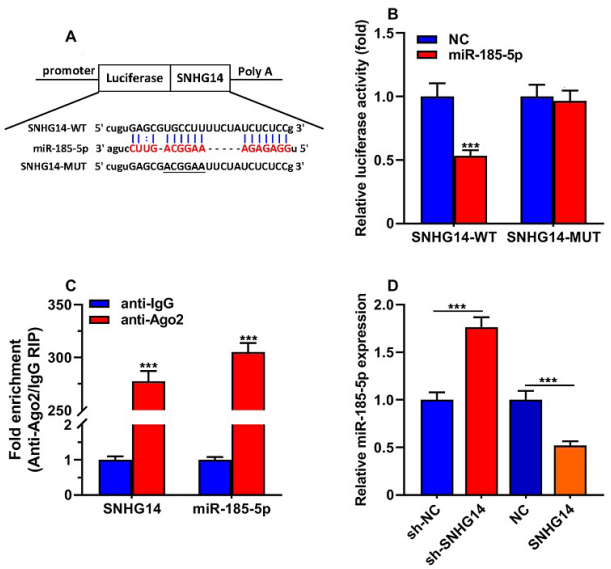


Fig. 3. *SNHG14 specifically binds to miR-185-5p.* ***A****) A binding site for SNHG14 and miR-185-5p was found through the StarBase database.* ***B****) The luciferase activity reporter gene assay was performed to verify the targeting relationship between SNHG14 and miR-185-5p.* ***C****) SNHG14 and miR-185-5p were enriched in the immunoprecipitated RNA containing Ago2, which is detected by RIP experiment.* ***D****) qRT-PCR was used to examine the effect of overexpression or knockdown of SNHG14 on the expression of miR-185-5p in hBMSCs. RIP, RNA binding protein immunoprecipitation; qRT-PCR, quantitative real-time polymerase chain reaction. ***P<0.001.*

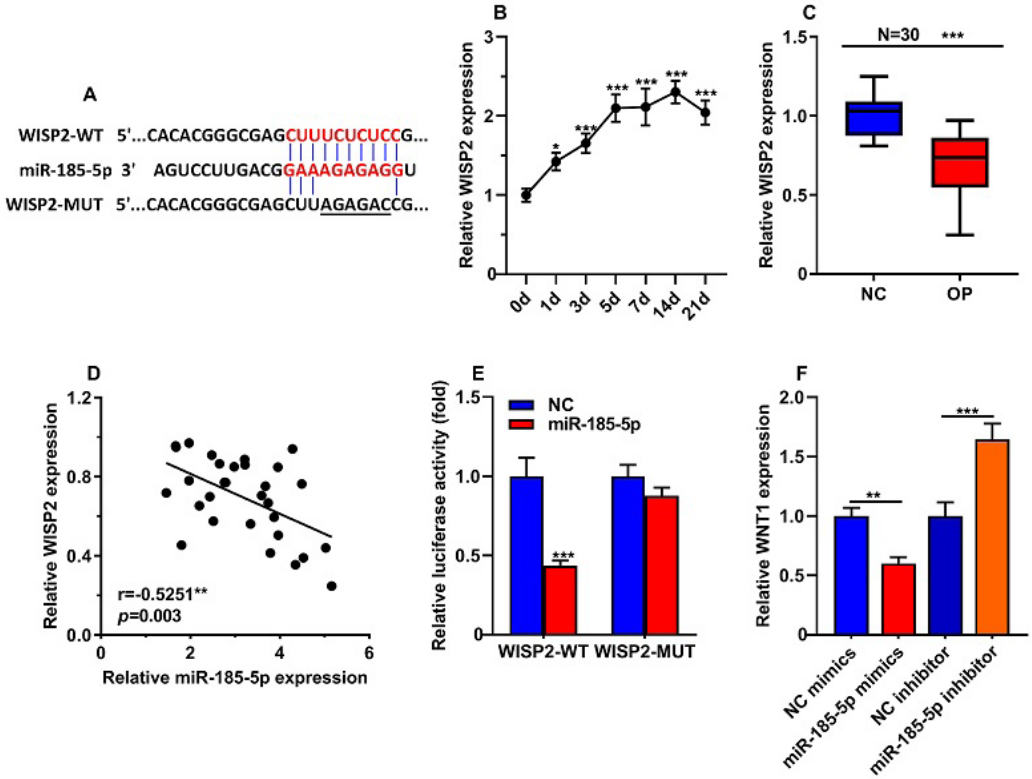


Fig. 4. *WISP2 is a direct target of miR-185-5p in hBMSCs.* ***A****) A binding site for WISP2 and miR-185-5p was found through the Targetscan database.* ***B****) The expression of WISP2 was detected by qRT-PCR after hBMSCs were treated with OM for 21 days.* ***C****) qRT-PCR was used to detect WISP2 expression in hBMSCs isolated from clinical samples (n=30).* ***D****) Correlations between WISP2 and miR-185-5p expression levels in hBMSCs (n=30).* ***E****) The luciferase activity assay was used to validate the targeting relationship between miR-185-5p and WISP2.* ***F****) qRT-PCR was used to detect the expression of WISP2 mRNA in hBMSCs treated with miR-185-5p mimics, inhibitors or NC. hBMSCs, human bone marrow-derived mesenchymal stem cells; OM, osteogenic medium; qRT-PCR, quantitative real-time polymerase chain reaction. *P<0.05, *P<0.01,and ***P<0.001.*

expression of WISP2 in the hBMSCs isolated from the patients with OP was significantly lower than that in the control group (Fig. 4C). Additionally, the study found a strong correlation between the expression levels of WISP2 and miR-185-5p in the hBMSCs in OP group (Fig. 4D). To work out whether miR-185-5p directly regulated WISP2, we constructed luciferase reporter vectors for WISP2 wild type (WISP2-WT) and mutant (WISP2-MUT) (Fig. 4A). As shown, miR-185-5p mimics significantly inhibited the luciferase activity of WISP2-WT in HEK-293T cells; while the luciferase activity of WISP2-MUT was not significantly affected (Fig. 4E). Additionally, after hBMSCs were transfected with miR-185-5p mimics, WISP2 expression was significantly inhibited, while transfection of miR-185-5p inhibitors worked oppositely. In short, miR-185-5p targeted WISP2 3'-UTR and blocked its expression.

SNHG14 regulates the osteogenic differentiation of hBMSCs by regulating miR-185-5p/WISP2 axis

Since SNHG14 could negatively target miR-185-5p expression in hBMSCs, and WISP2 was a direct target of miR-185-5p, we explored whether SNHG14 could up-regulate WISP2 expression via sponging miR-185-5p. As shown in Fig. 5A, knockdown of SNHG14 significantly inhibited WISP2 expression, but WISP2 mRNA level was restored after co-transfection with miR-185-5p inhibitors; overexpression of SNHG14 significantly increased WISP2 expression in hBMSCs, the miR-185-5p mimics reversed this effect (Fig. 5B).

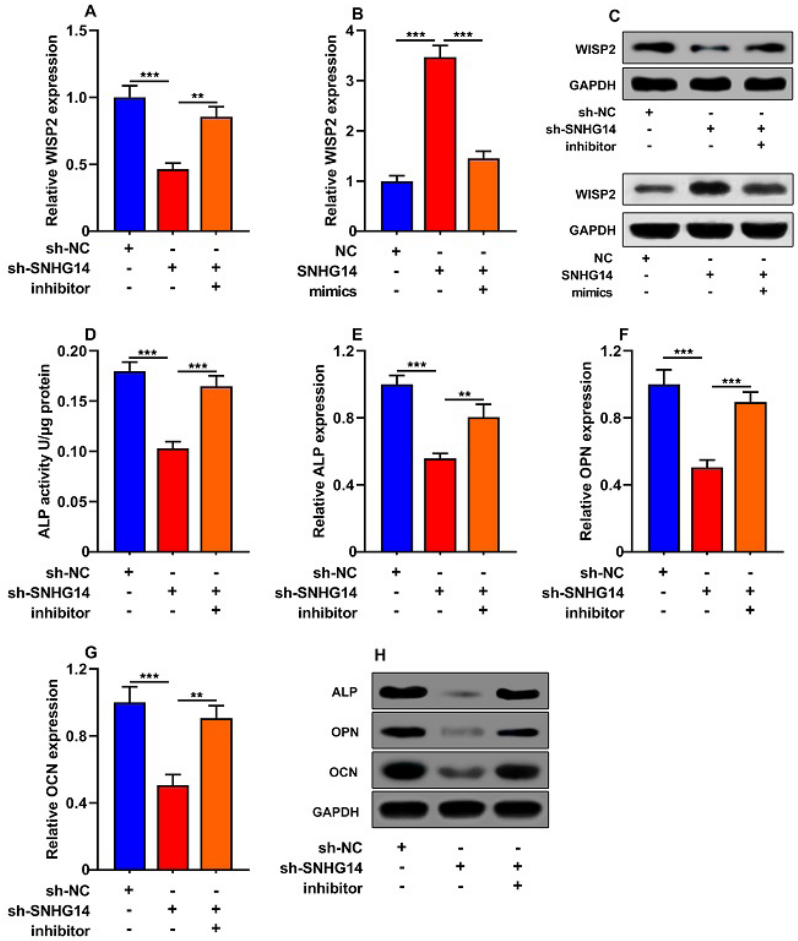


Fig. 5. *SNHG14 regulates the osteogenic differentiation of hBMSCs by specifically regulating miR-185-5p/WISP2axis. **A**) qRT-PCR was used to detect the expression of WISP2 in hBMSCs after transfection of sh-SNHG14 or/and miR-185-5p inhibitors. **B**) qRT-PCR was used to detect WISP2 expression in hBMSCs after transfection of SNHG14 overexpression plasmid or/and miR-185-5p inhibitors. **C**) Western blot analysis was used to detect WISP2 protein expression in hBMSCs after transfection. **D-H**) After transfection, the ALP activity (**D**), ALP, OPN, OCN mRNA expression (**E-G**) and protein level (**H**) were detected. qRT-PCR, quantitative real-time polymerase chain reaction; hBMSCs, human bone marrow-derived mesenchymal stem cells; ALP, alkaline phosphatase; OPN, osteopontin; OCN, osteocalcin. **P<0.01, and ***P<0.001.*

Western blot was adopted to further validate the aforementioned results at the protein level (Fig. 5C). Additionally, it was found that miR-185-5p inhibitors enhanced the ALP activity in sh-SNHG14 hBMSC (Fig. 5D); in addition, miR-185-5p inhibitors exerted the same effects on mRNA and protein levels of ALP, OPN and OCN (Fig. 5 E-H).

Moreover, a significant positive correlation between SNHG14 and WISP2 expression levels was found in the hBMSCs isolated from patients with OP (Fig. 6A). Furthermore, we inhibited WISP2 expression through transfection of WISP2 siRNA (si-WISP2). The results showed that WISP2 knockdown reduced enhancement of the ALP activity induced by the miR-185-5p inhibitors (Fig. 6B). In addition, qPCR results implied that knockdown of WISP2 reversed the effect of increased expression of ALP, OPN and OCN mRNA caused by miR-185-5p inhibitors (Fig. 6 C-E).

DISCUSSION

In the present work, we found that the expression of SNHG14 and WISP2 were continuously

Table I. *Primer sequences for RT-qPCR*

Gene	Primer sequence
SNHG14	F:5'- GGGTGTTTACGTAGACCAGAACC-3'
	R:5'- CTTCCAAAAGCCTTCTGCCTTAG-3'
miR-185-5p	F:5'- TCCGCTGGAGAGAAAGGC-3'
	R:5- ATGGAGGCTGAGGAGCACTG-3'
ALP	F:5'-AGAATCTGGTGCAGGAATGG-3'
	R:5'-TCGTATTTCATGTCTCCAGGC-3'
OPN	F:5'-GGAGTTGAATGGTGCATACAAGG-3'
	R:5'-CCACGGCTGTCCCAATCAG-3'
OCN	F:5'-GGCGCTACCTGTATCAATGG-3'
	R:5'-GTGGTCAGCCAACTCGTCA-3'
U6	R:5-CTCGCTTCGGCAGCACA-3'
	R:5'-AACGCTTCACGAATTTGCGT-3'
GAPDH	F:5'- GAAGGTGAAGGTC GGAGT-3
	R:5'- GAAGATGGTGATGGGATTTC-3'

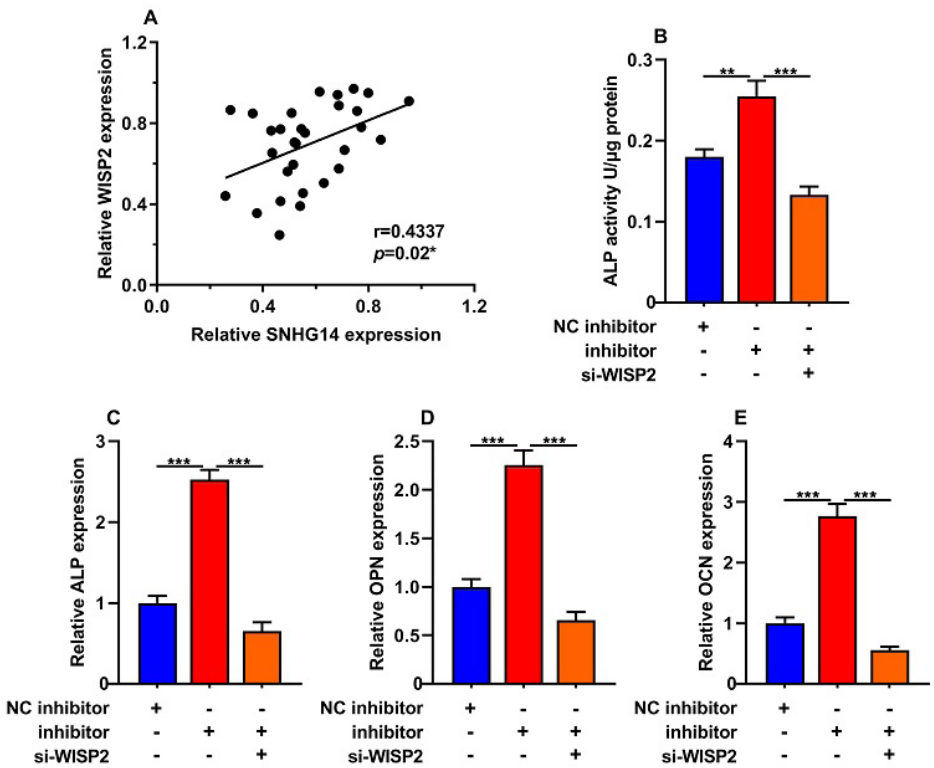


Fig. 6. *WISP2 knockdown reverses the osteogenic differentiation of hBMSCs, which is promoted by miR-185-5p inhibitors. **A**) Correlations between expression levels of SNHG14 and WISP2 in hBMSCs (n=30). **B**) The ALP activity in hBMSCs treated with miR-185-5p inhibitors or/and WISP2 siRNA was detected. **C-E**) qRT-PCR was used to detect ALP, OPN and OCN mRNA expression levels in hBMSCs treated with miR-185-5p inhibitors or/and WISP2 siRNA. hBMSCs, human bone marrow-derived mesenchymal stem cells; qRT-PCR, quantitative real-time polymerase chain reaction; siRNA, small interfering RNA; ALP, alkaline phosphatase; OPN, osteopontin; OCN, osteocalcin. **P<0.01 and ***P<0.001.*

increased during osteogenic differentiation, while the expression of miR-185-5p was inhibited. *In-vitro* experiments further proved that SNHG14 was capable of targeting miR-185-5p and promoting WISP2 expression, thus promoting osteogenic differentiation. The above results exhibited that SNHG14/miR-185-5p/WISP2 axis participated in regulating the osteogenic differentiation of hBMSCs.

Numerous studies have displayed that lncRNA is involved in the regulation of bone diseases and is considered as a new therapeutic target. For example, lncRNA HIF1α-AS1 activates the BMPs/TGF-β pathway in BMSCs and interferes with the expression of Sirtuin1, thereby promoting osteoblastic differentiation of human bone marrow stromal cells (22). LncRNA H19 mediates BMP9-induced osteogenic differentiation of hBMSCs via regulating Notch signaling (23). Growing studies have indicated that SNHG14 is at play in the progression of tumors such as pancreatic cancer, diffuse large B cell lymphoma, colorectal cancer and breast cancer (10-12, 24, 25), but its expression characteristics and biological functions in hBMSC are still not clear. For the first time, this study found that the expression of SNHG14 was significantly decreased in the hBMSCs of patients with OP, while in OM-induced hBMSCs, its expression was remarkably increased. Knockdown of SNHG14 significantly reduced osteogenic differentiation of hBMSCs. Our data indicate that SNHG14 promoted osteogenic differentiation of hBMSCs, and played a protective role in the pathogenesis of OP.

MicroRNA also participates in osteogenesis. For example, miR-335, which is regulated by the Wnt pathway, inhibit the proliferation, migration and osteogenesis of mesenchymal stem cells (26). The expression of miR-125b in hBMSCs is significantly upregulated in OP, and miR-125b inhibits the proliferation and osteogenic differentiation of hBMSCs through modulating the expression of osterix (OSX) (27). A recent study reports that blocking the expression of miR-185 enhances bone formation during OP by regulating Bgn expression and BMP/Smad signaling (28). It is well known that some lncRNAs can competitively bind with miRNAs to reduce its availability, thereby reducing the inhibitory effect of miRNAs on target genes (29). For example, lncRNA MALAT1 promotes OSX expression and regulates the osteogenic differentiation of hBMSCs through sponging miR-143 (30). In the present work, we observed a negative correlation between the expression levels of SHHG14 and miR-185-5p in the hBMSCs of OP patients. After knocking down SNHG14 in hBMSCs, miR-185-5p expression was significantly increased. Furthermore, we validated the targeting relationship between SNHG14 and miR-185-5p by luciferase reporter assay and RIP assay. Importantly, overexpression of miR-185-5p reversed the osteogenic differentiation of hBMSCs promoted by SNHG14 overexpression, but miR-185-5p inhibitors promoted the osteogenic differentiation of hBMSCs with SNHG14 knockdown, suggesting that SNHG14 directly targeted miR-185-5p to regulate osteogenic differentiation of hBMSCs.

WISP2 is also known as CCN5, whose gene is located on chromosome 20q12-20q13 and belongs to the CCN family (31). It is involved in regulating the proliferation, differentiation, migration and adhesion of cells (32). In recent years, WISP2 is reported to be related with the progression of some tumors, such as breast cancer and esophageal cancer (33, 34). WISP2 is also considered as a biomarker and regulator in chondrogenesis (35). However, there are few studies on its role in osteogenic differentiation of hBMSCs. This study found that WISP2 expression was significantly down-regulated in the hBMSCs of patients with OP, and it was also demonstrated that miR-185-5p could bind directly to the 3'-UTR of WISP2, so as to repress the WISP2 expression. Additionally, further experiments demonstrated that SNHG14 can regulate miR-185-5p/WISP2 axis to promote osteogenic differentiation of hBMSCs. Our data suggested that WISP2 was involved in the pathogenesis of OP. However, its detailed mechanism required more investigation in the future.

In summary, SNHG14 positively regulates osteogenic differentiation of hBMSCs by repressing miR-185-5p and up-regulating WISP2, indicating that SNHG14 is a key factor in osteogenesis and is expected to be a theraputic target for the treatment of OP.

ACKNOWLEDGEMENTS

The Authors thank Hubei Yican Health Industry Co., Ltd, for its linguistic assistance during the preparation of this manuscript.

This work was supported by a grant from the Key Specialty Construction Project of Pudong Health and Family Planning Commission of Shanghai (No. PWZzk201725).

REFERENCES

1. Seeman E, Delmas P D. Bone quality—the material and structural basis of bone strength and fragility. N Engl J Med 2006; 354:2250-61.
2. Zhou YL, Li YC, Luo DM, Ding YF, Hodgson P. Microstructures, mechanical and corrosion properties and biocompatibility of as extruded Mg–Mn–Zn–Nd alloys for biomedical applications. Mater Sci Eng C Mater Biol Appl 2015; 49:93-100.
3. Ensrud K E, Crandall C J. Osteoporosis. Ann Intern Med 2018; 168:306-7.
4. Zhao Y, Xue R, Shi N, et al. Aggravation of spinal cord compromise following new osteoporotic vertebral compression fracture prevented by teriparatide in patients with surgical contraindications. Osteoporosis Int 2016; 27: 3309-17.
5. Wang K C, Chang H Y. Molecular mechanisms of long noncoding RNAs. Mol Cell 2011; 43:904-14.
6. Qin W S, Li X Z, Xie L W, et al. A long non-coding RNA, APOA4-AS, regulates APOA4 expression depending on HuR in mice. Nucleic Acids Res 2016; 44: 6423-33.
7. Chan L H, Wang W, Yeung W, Deng Y, Yuan P, Mak K. Hedgehog signaling induces osteosarcoma development through Yap1 and H19 overexpression. Oncogene 2014; 33:4857-66.
8. Dong Y, Liang G, Yuan B, Yang C, Gao R, Zhou X. MALAT1 promotes the proliferation and metastasis of osteosarcoma cells by activating the PI3K/Akt pathway. Tumour Biol 2015; 36:1477-86.
9. Xia W, Zhuang L, Deng X, Hou M. Long noncoding RNA-p21 modulates cellular senescence via the Wnt/β-catenin signaling pathway in mesenchymal stem cells. Mol Med Rep 2017; 16:7039-47.
10. Deng PC, Chen WB, Cai HH, et al. LncRNA SNHG14 potentiates pancreatic cancer progression via modulation of annexin A2 expression by acting as a competing endogenous RNA for miR-613. J Cell Mol Med. 2019; 23:7222-32.
11. Zhao L, Liu Y, Zhang J, Liu Y, Qi Q. LncRNA SNHG14/miR-5590-3p/ZEB1 positive feedback loop promoted diffuse large B cell lymphoma progression and immune evasion through regulating PD-1/PD-L1 checkpoint. Cell Death Dis 2019; 10:1-15.
12. Di W, Weinan X, Xin L, Yu Z, Gu X, Tang J, Li M. Long noncoding RNA SNHG14 facilitates colorectal cancer metastasis through targeting EZH2-regulated EPHA7. Cell Death Dis 2019; 10:514.
13. Stroynowska-Czerwinska A, Fiszer A, Krzyzosiak W J. The panorama of miRNA-mediated mechanisms in mammalian cells. Cell Mol Life Sci 2014; 71:2253-70.
14. Friedman R C, Farh K K-H, Burge C B, Bartel D P. Most mammalian mRNAs are conserved targets of microRNAs. Genome Res 2009; 19:92-105.
15. Huang T C, Pinto S M, Pandey A. Proteomics for understanding miRNA biology. Proteomics 2013; 13(3-4):558-67.
16. Shenoy A, Blelloch R H. Regulation of microRNA function in somatic stem cell proliferation and differentiation. Nat Rev Mol Cell Bio 2014;15:565-76.
17. Lin Z, He H, Wang M, Liang J. MicroRNA-130a controls bone marrow mesenchymal stem cell differentiation towards the osteoblastic and adipogenic fate. Cell Prolif 2019;52: e12688-703.
18. Rodrigo-Muñoz J M, Cañas J A, Sastre B, et al. Asthma diagnosis using integrated analysis of eosinophil microRNAs. Allergy 2019; 74:507-17.
19. Huang Q, Sun Y, Ma X, et al. Androgen receptor increases hematogenous metastasis yet decreases lymphatic metastasis of renal cell carcinoma. Nat Commun 2017; 8:918-23.
20. Chang H, Wang Y, Liu H, et al. Mutant Runx2 regulates amelogenesis and osteogenesis through a miR-185-5p-Dlx2 axis. Cell Death Dis 2017; 8:3221-34.
21. Lehtovirta S, Mäkitie R, Casula V et al. Defective WNT signaling may protect from articular cartilage deterioration–a quantitative MRI study on subjects with a heterozygous WNT1 mutation. Osteoarthritis Cartilage 2019; 27:1636-46.

22. Xu Y, Wang S, Tang C, Chen W, Upregulation of long non-coding RNA HIF 1α-anti-sense 1 induced by transforming growth factor-β-mediated targeting of sirtuin 1 promotes osteoblastic differentiation of human bone marrow stromal cells. Mol Med Rep 2015; 12:7233-8.
23. Liao J, Yu X, Hu X et al. lncRNA H19 mediates BMP9-induced osteogenic differentiation of mesenchymal stem cells (MSCs) through Notch signaling. Oncotarget 2017; 8:53581-53601.
24. Ishaque N, Abba M L, Hauser C et al. Whole genome sequencing puts forward hypotheses on metastasis evolution and therapy in colorectal cancer. Nat Commun 2018; 9:4782-96.
25. Dong H, Wang W, Mo S, et al. Long non-coding RNA SNHG14 induces trastuzumab resistance of breast cancer via regulating PABPC1 expression through H3K27 acetylation. J Cell Mol Med 2018; 22:4935-47.
26. Tomé M, López-Romero P, Albo C, et al. miR-335 orchestrates cell proliferation, migration and differentiation in human mesenchymal stem cells. Cell Death Differ 2011;18:985-95.
27. Chen S, Yang L, Jie Q, et al. MicroRNA-125b suppresses the proliferation and osteogenic differentiation of human bone marrow-derived mesenchymal stem cells. Mol Med Rep 2014; 9:1820-26.
28. Cui Q, Xing J, Yu M, et al. Mmu-miR-185 depletion promotes osteogenic differentiation and suppresses bone loss in osteoporosis through the Bgn-mediated BMP/Smad pathway. Cell Death Dis 2019; 10: 172-86.
29. Tay Y, Rinn J, Pandolfi P P. The multilayered complexity of ceRNA crosstalk and competition. Nature 2014; 505:344-52.
30. Gao Y, Xiao F, Wang C, Wang C, Cui P, Zhang X, Chen X. Long noncoding RNA MALAT1 promotes osterix expression to regulate osteogenic differentiation by targeting miRNA-143 in human bone marrow-derived mesenchymal stem cells. J Cell Biochem 2018; 119:6986-96.
31. Frewer K A, Sanders A J, Owen S, Frewer N C, Hargest R, Jiang W G. A role for WISP2 in colorectal cancer cell invasion and motility. Cancer Genomics Proteomics 2013; 10: 187-96.
32. Katsube K, Sakamoto K, Tamamura Y, Yamaguchi A. Role of CCN, a vertebrate specific gene family, in development. Dev Growth Differ 2009; 51:55-67.
33. Das A, Dhar K, Maity G, et al. Deficiency of CCN5/WISP-2-Driven program in breast cancer promotes cancer epithelial cells to mesenchymal stem cells and breast cancer growth. Sci Rep 2017; 7:1220-33.
34. Chai D M, Qin Y Z, Wu S W, et al. WISP2 exhibits its potential antitumor activity via targeting ERK and E-cadherin pathways in esophageal cancer cells. J Exp Clin Cancer Res 2019; 38:102-17.
35. Schutze N, Noth U, Schneidereit J, Hendrich C, Jakob F. Differential expression of CCN-family members in primary human bone marrow-derived mesenchymal stem cells during osteogenic, chondrogenic and adipogenic differentiation. Cell Commun Signal 2005; 3:5-17.

Bone marrow mesenchymal stem cell-derived exosomal MiR-338-3p represses progression of hepatocellular carcinoma by targeting ETS1

Y.-H. Li[1], M.-F. Lv[2], M.-S. Lu[1] and J.-P. Bi[1]

[1]Department of Hepatobiliary Surgery, Jinan People's Hospital Affiliated to Shandong First Medical University, Jinan, China; [2]Department of Pharmacy, Jinan Second Maternal and Child Health Hospital, Jinan, China

Received November 3, 2020 – Accepted April 7, 2021

The present study aims to explore the function of human bone marrow mesenchymal stem cell (BMSC)-derived exosomal micro ribonucleic acid (miR)-338-3p in hepatocellular carcinoma (HCC) and further investigate its effect on HCC cell functions. Firstly, BMSCs were co-cultured with HCC cells, and BMSC-derived exosomes were identified. Next, Transwell assay and methyl thiazolyl tetrazolium (MTT) experiments were carried out to detect the effects of miR-338-3p and E26 transformation specific-1 (ETS1) on the viability, invasion, migration, and apoptosis of HCC cells through the exosomes derived from BMSCs. Furthermore, the targeting relationship between miR-338-3p and EST1 was verified via bioinformatics study and dual-luciferase reporter gene analysis. Additionally, Western blotting (WB) was carried out to measure the expression levels of EST1 and other proteins in HCC cells. It was found that BMSCs inhibited HCC cell proliferation, invasion and migration, and induced cell apoptosis, while the inhibitors of exosomes played the opposite roles. In addition, the up-regulation of exosomal miR-338-3p or the silencing of EST1 restrained HCC cell proliferation, invasion and migration, and induced cell apoptosis. In conclusion, BMSC-derived exosomal miR-338-3p delays the development of HCC by down-regulating EST1, providing a new promising treatment target for HCC.

As one of the most common malignant tumors in the world, hepatocellular cancer (HCC) has become the third leading cause of cancer-related deaths worldwide (1), and it is triggered by abnormal activation of proto-oncogenes and inactivation of tumor suppressor genes in liver cells (2). Clinically, HCC is characterized by invasiveness, poor prognosis and restricted treatment approaches. The 5-year survival rate of HCC patients remains very low although there is new understanding of its mechanism in clinical practice (3). Human bone marrow mesenchymal stem cells (hBMSCs) are adult stem cells with multi-directional differentiation potential, which have close associations with various kinds of cells in human liver tissues. Moreover, they can differentiate into oval cells, fibroblasts and myofibroblasts in the liver, thereby repairing damaged liver tissues (with bone marrow as a potential source of hepatic oval cells). HBMSCs not only have chemotactic and homing functions, but can also efficiently promote the immune system reconstitution,

Key words: human bone marrow mesenchymal stem cells; miR-338-3p; hepatocellular cancer

Corresponding Author:
Meifeng Lv, BM.
Department of Pharmacy,
Jinan Second Maternal and Child Health Hospital,
12 Fengcheng West Street, Laiwu District, Jinan, Shandong 271100, China
Tel.: +86 015063400428
e-mail: obbh05@163.com
Institutional e-mail: lvmeifeng@mail.sdufe.edu.cn

0393-974X (2021)
Copyright © by BIOLIFE, s.a.s.
This publication and/or article is for individual use only and may not be further reproduced without written permission from the copyright holder.
Unauthorized reproduction may result in financial and other penalties
DISCLOSURE: ALL AUTHORS REPORT NO CONFLICTS OF INTEREST RELEVANT TO THIS ARTICLE.

remove residual disease and prevent tumor recurrence and metastasis (4). Researchers transplanted hBMSCs into HCC animal models with high metastatic potential. After 3 weeks, they found that the metastasis of tumor cells was down-regulated, and the apoptosis of tumor cells was further induced by hBMSCs (5). More importantly, BMSC-derived exosomes can affect the development and progression of tumors by delivering micro ribonucleic acids (miRNAs) to tumor cells (6, 7). For instance, the BMSC-derived exosomal miR-9-3p is able to facilitate the apoptosis of bladder cancer cells and delay the disease progression by decreasing the expression level of ESM1 protein (8).

Exosomes are a kind of lipid bilayer vesicle secreted by almost all cells, with a diameter of 30-100 nm (9). More importantly, they can deliver various bioactive molecules from parental cells to recipient cells, including miRNAs, messenger RNA (mRNAs) and proteins (10). Among various contents of exosomes, the imbalance of miRNAs plays an important role in the occurrence and development of tumors (11). MiRNAs, a category of endogenous non-coding small RNAs, can negatively regulate gene expressions by inducing translational repression or mRNA decay (12). The changes in miRNA expressions are closely correlated with the occurrence and development of liver cancer (13-15). Studies have denoted that overexpressed miR-429 and miR-129-5p facilitate the apoptosis and inhibit the proliferation of HCC cells (16, 17). In addition, miR-338-3p represses the development of bladder cancer by adjusting the expression of E26 transformation specific-1 (ETS1) (18). As a member of the ETS family of transcription factors, ETS1 participates in cell metastasis. One study found that miR-129-5p targets ETS1 to suppress newly-occurring metastasis and invasion of liver cancer (19). However, the relationship between miR-338-3p and ETS1 in HCC cells has not yet been clarified. Therefore, the roles of BMSC-derived exosomal miR-338-3p and ETS1 in HCC cells were explored in this study.

MATERIALS AND METHODS

Cells lines

Human HCC HepG2 cells were purchased from American Type Culture Collection (ATCC) (Manassas, VA, USA). HBMSCs were purchased from Tongpai Biological Technology Co., Ltd (Shanghai, China). All cells were cultured with Dulbecco's modified Eagle medium (DMEM) (Beyotime, Shanghai, China) containing 10% fetal bovine serum (FBS) (Gibco, Grand Island, NY, USA) at 37°C under 5% CO_2.

Cell transfection

The HepG2 cells in the logarithmic growth phase were cultured with serum-free Opti-MEM at 1 d before transfection and then transfected according to the instruction of Lipofectamine 2000. The cells were then randomly divided into miR-338-3p negative control (NC) group, miR-338-3p mimic group, small interfering (si)-ETS1 group, and si-RGS17 NC group (GenePharma, Shanghai, China). Six hours later, the medium was replaced with DMEM containing 10% FBS for another 48 h of culture. After that, the cells in the logarithmic growth phase were collected for subsequent assays. Moreover, BMSCs in the logarithmic growth phase were transfected with mimic miR-NC and mimic miR-338-3p, separately. Finally, the corresponding exosomes (Exo-miR-NC and Exo-miR-338-3p) were extracted and isolated. All plasmids were provided by Beyotime (Beijing, China).

Co-culture of BMSCs and HepG2 cells

A system was constructed using a Transwell chamber for the co-cultivation of BMSCs and HepG2 cells. The HepG2 cells in the logarithmic growth phase (1.5×10^4 cells/well) were inoculated into the lower chamber of a 6-well plate. Following attachment of cells, the medium was discarded. BMSCs (4.5×10^4 cells/well) were inoculated in another chamber, which was then transferred to the plate with inoculated HepG2 cells. Subsequently, complete DMEM was added again for 24 h of culture. Subsequently, the cells in the upper chamber were removed, and those in the lower chamber were used for subsequent assays.

Isolation and identification of exosomes

The BMSCs were cultured in a 100-mm dish with exosomes-free medium until the cell density reached 50%, followed by continuous culture for 48 h with serum-free medium. After that, the cell supernatant was first centrifuged at 300 g for 10 min to pellet whole cells and 2,000 g for 30 min to separate cell debris. After filtration

by a 0.22 μm filter membrane, the filtrate was centrifuged at 120,000 g for consecutive 2 h to discard the supernatant. Then, the precipitate was re-suspended with an appropriate volume of Exo-free phosphate-buffered saline (PBS) and then centrifuged continuously at 120,000 g for 2 h again to obtain exosomes. Next, the exosomes were fixed with 2% uranyl acetate, and their morphology was observed with a transmission electron microscope (TEM) (Philips, Eindhoven, Netherlands). Western blotting (WB) was also adopted to analyze the expressions of exosome-specific proteins cluster of differentiation 81 (CD81), ALIX and heat shock protein 70 (HSP70). In addition, nanoparticle tracking analysis (NTA) was used to detect the size and concentration of exosomes.

Exosome uptake assay

PKH26 dye was bought from Sigma (Louis, MO, USA). To label exosomes, exosomes (200 μL) and Diluent C (500 μL) were mixed together, while 4 μL of PKH26 was mixed with Diluent C (500 μL) in another 1.5 mL Eppendorf (EP) tube. Thereafter, the two solutions were mixed in the dark for staining. After the staining was terminated using 1 mL of 10% FBS, 20 μg of exosomes were incubated at 37°C for 15 min and then centrifuged again at 120,000 g for 2 h to eliminate the residual dye. Later, the labeled exosomes and HepG2 cells were co-cultured for 24 h, and the uptake of exosomes was observed under a laser scanning confocal microscope.

Dual-luciferase reporter gene assay

The wild-type or mutant 3' untranslated region (3'-UTR) sequences of ETS1 were cloned into pmirGLO luciferase vectors for dual-luciferase reporter gene assay. Then, the wild-type or mutant luciferase reporter plasmids (ETS1-WT and ETS1-MUT) and miR-338-3p were co-transfected into HepG2 cells; 48 h later, the cells were harvested, and the luciferase activity was determined by a luciferase reporter gene assay kit (GenePharma, Shanghai, China).

4',6-diamidino-2-phenylindole (DAPI) staining

The cell suspension was heated and fixed at 50°C for 15 min and covered with 50 μL of DAPI solution (3 μg/mL). The mixture was incubated in the dark at room temperature for 10 min, and then rinsed twice in PBS. After that, the excess liquid on the slide was drained, and the sample was dried naturally in the dark. Finally, the cells were observed in a transmitted light mode, and a Leica TCS SP2 AOBS spectroscopic confocal microscope was utilized to excite DNA-DAPI specific fluorescence emission (461 nm) at 405 nm.

Quantitative real-time polymerase chain reaction (qRT-PCR) assay

Total RNAs, containing miRNAs, were isolated from cells and exosomes according to the TRIzol (Invitrogen, Carlsbad, CA, USA) methods in the instructions. The expressions of miR-338-3p and ETS1 mRNA were measured *via* qRT-PCR. Primers are shown in Table I. Complementary deoxyribose nucleic acid (cDNA) was synthesized according to the instructions and used for qRT-PCR, with U6 and glyceraldheyde 3-phosphate dehydrogenase (GAPDH) as controls for miR-338-3p and ETS1, respectively. Finally, the qRT-PCR results were analyzed with the $2^{-\Delta\Delta Ct}$ method.

Western blotting

The concentration of total protein extracted from cells and exosomes was detected by BCA assay (Beyotime, Shanghai, China). Next, the protein was separated through SDS-PAGE, and transferred to a membrane. Subsequently, the membrane was blocked with 5% milk, and added with primary antibodies against CD81 (1:1000), ALIX (1:1000), HSP70 (1:1000) and ETS1 (1:1000) (all from CST Danvers, MA, USA) in sequence for incubation at 4°C overnight,. After that, the membrane was washed with TBST and incubated with secondary antibodies at room temperature for 1 h. Thereafter, electrochemiluminescence (ECL) was adopted for image development, and ImageJ was employed to analyze the grayscale value of bands.

Methyl thiazolyl tetrazolium (MTT) assay

HepG2 cells were seeded into the 96-well plate at 5×10^4 cells/well. After attachment, the cells were grouped according to the requirements of the assay. The 96-well plate was cultured in an incubator with 5% CO_2 at 37°C for different lengths of time. Then, 20 μL of MTT solution (Beyotime, Shanghai, China) was added to each well and cultured in the incubator for 4 h, followed by discarding the supernatant and addition of 150 μL of DMSO solution in each well. The optical density (OD) at 570 nm was read using a microplate reader.

Transwell assay

HepG2 cells were inoculated into 6-well Transwell chambers (Millipore, Billerica, MA, USA) to test their migration and invasion. The HepG2 cells were trypsinized, counted and re-suspended in the serum-free medium. Then, they were inoculated into the upper chamber without a Matrigel-coated membrane at 4×10^4 cells/well, while 10% FBS was added in the lower chamber to induce the migration or invasion of HepG2 cells through the membrane. Next, the cells were placed in the upper chamber with a Matrigel-coated membrane for invasion analysis. Afterwards, they were incubated for cell migration and invasion. Finally, the cells were stained with crystal violet, and the migrating and invading cells were counted.

Statistical analysis

Statistical analysis was conducted using Statistical Product and Service Solutions (SPSS) 19.0. Differences between two groups were analyzed by the Student's *t*-test. One-way ANOVA test and Post Hoc Test (Least Significant Difference) were performed for comparison among multiple groups. $P<0.05$ indicated that the difference was statistically significant.

RESULTS

BMSCs inhibited the proliferation, invasion and migration and induced the apoptosis of HCC cells

To determine the influence of BMSCs on the functions of HepG2 cells, BMSCs and HepG2 cells were co-cultured. The results showed that the proliferation, invasion and migration abilities of HepG2 cells in the co-culture system were significantly inhibited, while the cell apoptosis rate was increased (Fig. 1 A-D). These results indicated that BMSCs exert inhibitory effects on HCC cells.

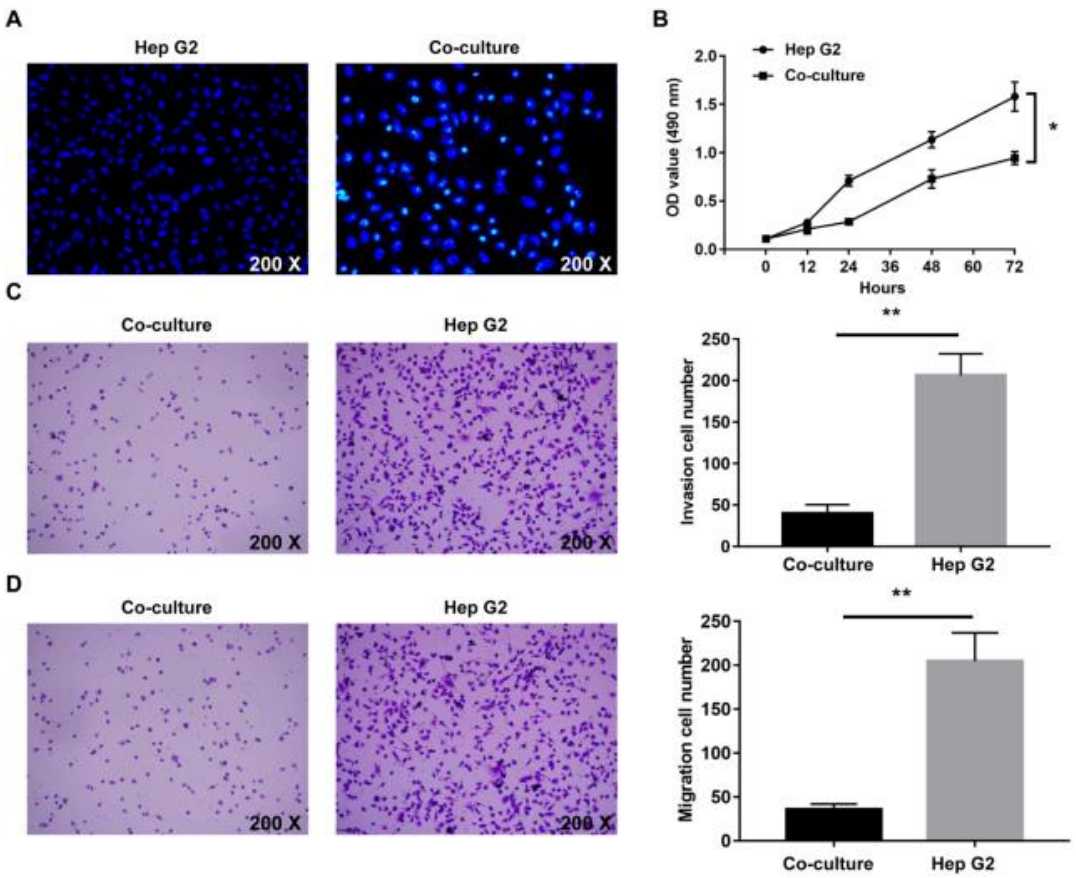


Fig. 1. *BMSCs inhibited tumor cell proliferation, cell invasion and cell migration and induced tumor cells apoptosis.* ***A)*** *Cell apoptosis of HepG2 measured by DAPI.* ***(B)*** *The viability of HepG2 detected by MTT assay.* ***C, D)*** *Cell invasion and cell migration determined by Transwell assay (magnification ×200). Data are shown as mean ± SD. **P<0.01.*

Identification and uptake results of exosomes

The morphology of the exosomes isolated was detected under the TEM after dilution. It was found that the exosomes exhibited a cup-shaped bilayer structure under the TEM (Fig. 2A). NTA was employed to further detect the size of exosomes. The results revealed that the average size of exosomes was about 110 nm (Fig. 2B). Exosome-specific proteins were identified through WB. It was discovered that the exosome-specific markers CD81, ALIX and HSP70 were positively expressed in exosomes, further proving that the substances isolated were exosomes (Fig. 2C). According to Fig. 2D, green fluorescence was clearly observed in HepG2 cells, suggesting that exosomes can be taken up by HepG2 cells.

BMSC-derived exosomes affected functions of HCC cells

To explore the effects of exosomes on the functions of HCC cells, the co-culture system for BMSCs and HepG2 cells was treated with the exosome inhibitor GW4869 (GW4869 group) and DMSO of the same concentration (DMSO group). The results

Table I. *The primer sequences*

List	F primer	R primer
miR-338-3p	5'-TGCGGTCCAGCATCAGTGAT-3'	5'-CCAGTGCAGGGTCCGAGGT-3'
ETS1	5'-TTCACTAAAGAACAGCAAC-3'	5'-TGTCCCCAACAAAGTCTG-3'
U6	5'-GCTTCGGCAGCACATATACTAAAAT-3'	5'-CGCTTCAGAATTTGCGTGTCAT-3'
GAPDH	5'-CGACCACTTTGTCAAGCTCA-3'	5-'ACTGAGTGTGGCAGGGACTC-3'

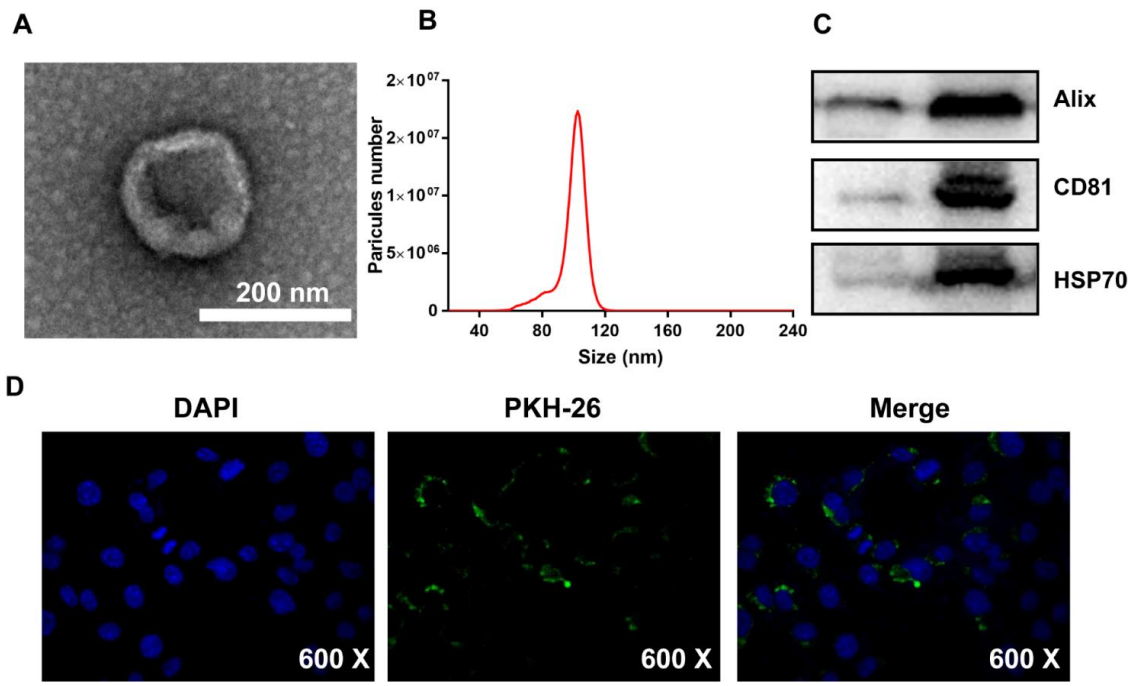


Fig. 2. *Identification and uptake results of exosomes. **A)** Representative photomicrographs exhibiting exosomes microstructure (scale bar=200 nm). **B)** The size and concentration of exosomes was detected by NanoSight Tracking Analysis. **C)** Western blot detected exosomal special protein Alix, CD81 and HSP70. (**D**) Exosomes were uptaken by HepG2 cells (magnification ×600).*

demonstrated that compared to DMSO group, the GW4869 group had increased the viability and promoted the invasion and migration of HCC cells (Fig. 3 A-D). Moreover, HepG2 cells were directly treated with the same concentration of GW4869 to further rule out the interference from other factors. It was found that GW4869 had no effects on HCC cell proliferation, invasion and migration (Fig. 3 A-D).

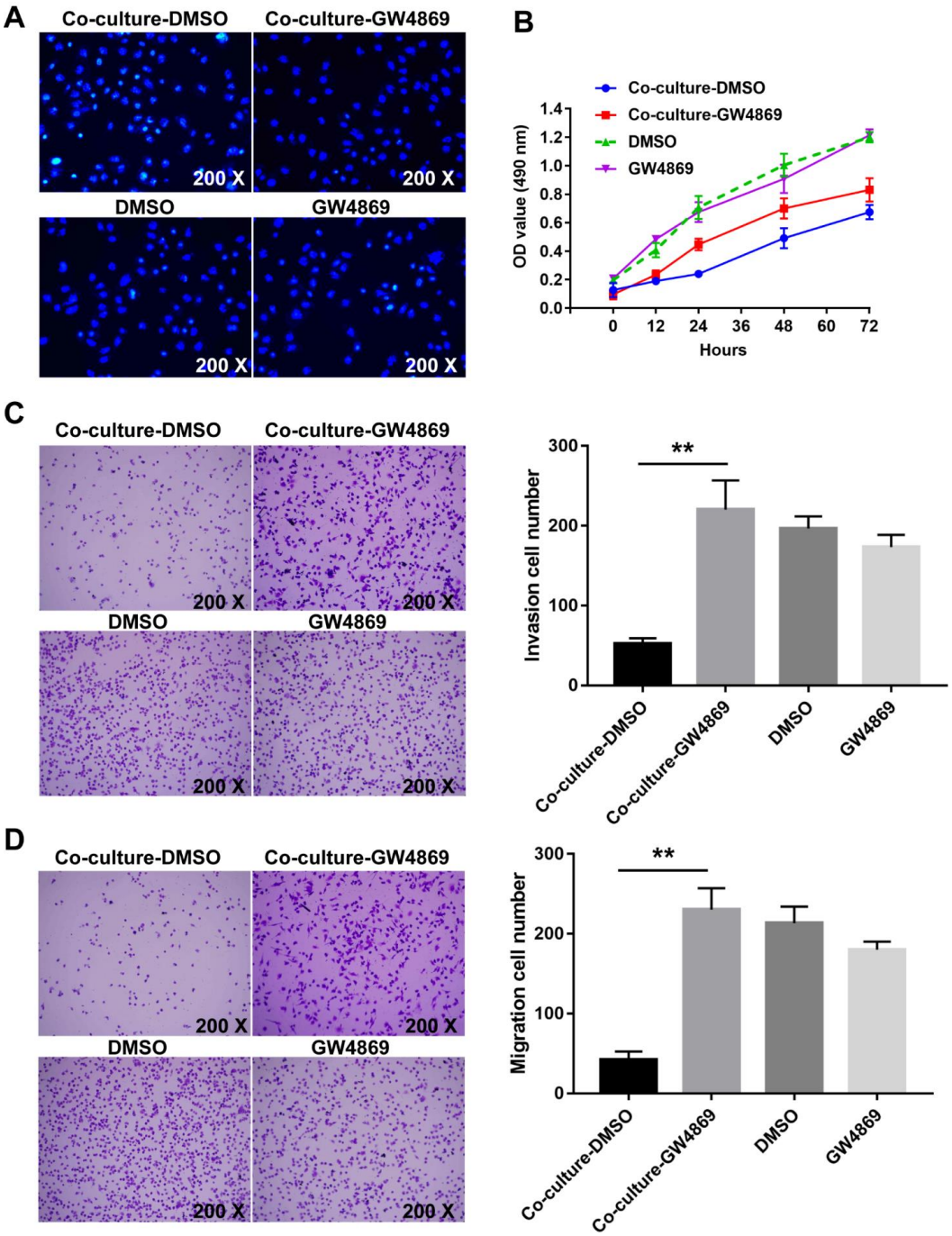


Fig. 3. *BMSC derived exosomes affected functions of HCC cells. **A)** Cell apoptosis of HepG2 measured by DAPI. **B)** The viability of HepG2 was determined with MTT. **C, D)** Tumor cell invasion and migration were determined through Transwell (magnification ×200). Data are shown as mean ± SD. **P<0.01.*

Exosomal miR-338-3p repressed the viability, invasion and migration and facilitated the apoptosis of HCC cells

miR-338-3p mimic was transfected to BMSCs to determine the impacts of exosomal miR-338-3p on the functions of HCC cells. BMSC-derived exosome (Exo-miR-338-3p) was then collected. The qRT-PCR results confirmed that compared with that in the Exo-miR NC group, the expression level of miR-338-3p was significantly increased in the transfection group (Fig. 4A, $p<0.05$). Moreover, the effects of exosomal miR-338-3p on the vitality, migration, invasion and apoptosis of HCC cells were assessed using a series of *in vitro* experiments such as MTT, DAPI and Transwell assays. Fig. 4 B-D denoted that after Exo-miR-338-3p treatment, the apoptosis rate of HCC cells rose, while the cell viability, migration and invasion were significantly reduced ($p<0.05$).

MiR-338-3p targeted ETS1

Based on the prediction with TargetScan website (http://www.targetscan.org/vert_71/), miR-338-3p had a specific binding region to ETS1 in its 3'-UTR (Fig. 5A). Hence, dual luciferase assay was conducted to verify whether miR-338-3p targetedly binds to ETS1 in its 3'-UTR as predicted. The results (Fig. 5B) revealed that compared to the NC group, the overexpressed miR-338-3p restrained the luciferase activity in the 3'-UTR of ETS1-WT ($p<0.05$). Nevertheless, no significant effect of miR-338-3p on the luciferase activity of ETS1-MUT was observed ($p>0.05$). It could be speculated that miR-338-3p can bind to ETS1 in the 3'-UTR and regulate its activity. Furthermore, the mRNA and protein expressions of ETS1 were determined via qRT-PCR and WB assays. In Fig. 5 C and D, it was shown that the mRNA and protein expressions of ETS1 declined when miR-338-3p was overexpressed. The above results further proved that ETS1 is a target gene of miR-338-3p.

Silencing of ETS1 restrained the proliferation, invasion and migration and facilitated the apoptosis of HCC cells

Subsequently, si-ETS1 was transfected to HepG2 cells to determine its role in HCC cells. It was discovered that after silencing ETS1, the

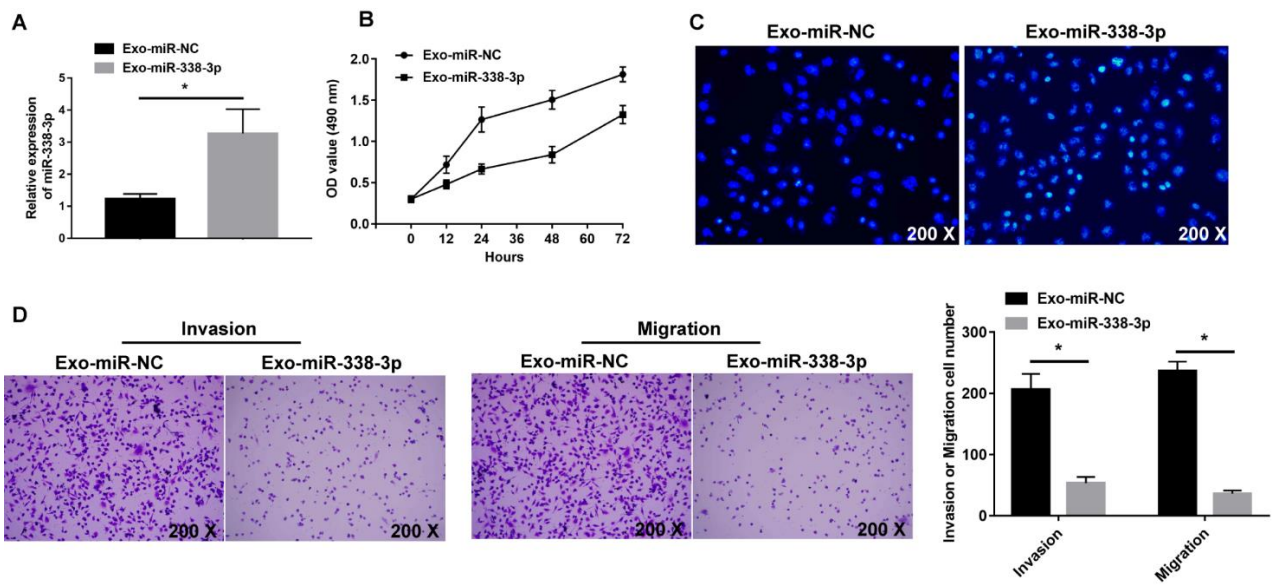


Fig. 4. *Exosomal miR 338 3p repressed tumor cell viability, cell invasion and cell migration and facilitated tumor cells apoptosis.* ***A)*** *RT PCR detected the expression level of miR 338 3p in exosomes.* ***B)*** *Cell proliferation was detected with MTT.* ***C)*** *Tumor cell apoptosis was determined through DAPI.* ***D)*** *The invasion and migration of HepG2 measured with Transwell assay (magnification ×200). *P<0.05.*

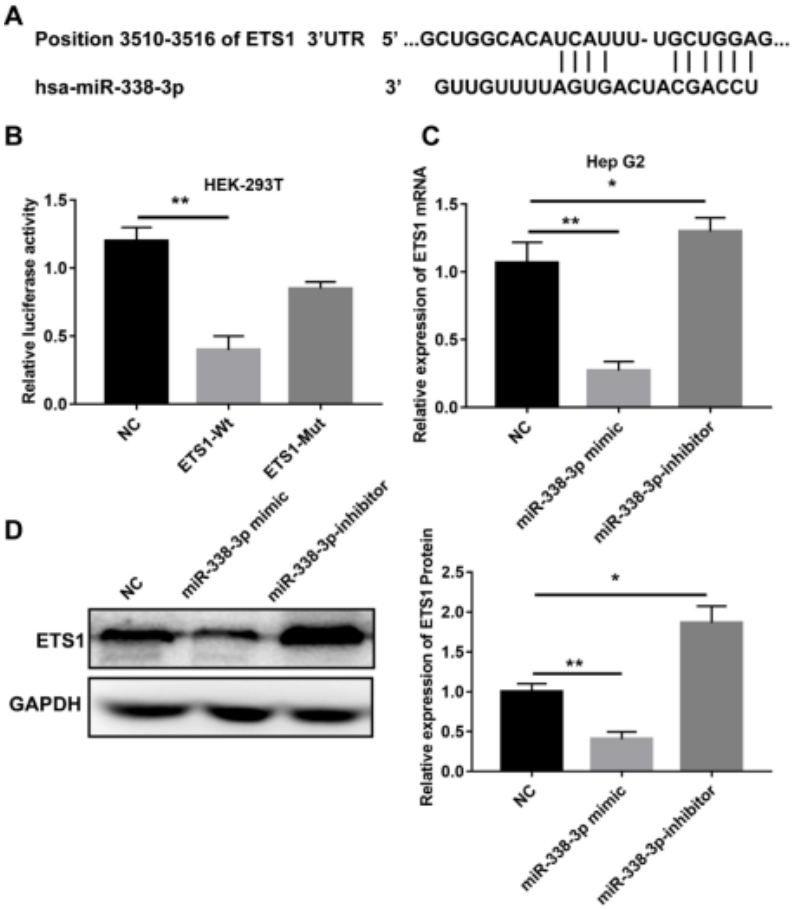


Fig. 5. *miR 338 3p targeted ETS1. **A)** miR 338 3p binds to EST1 at 3'UTR. **B)** Luciferase reporter. **C, D)** The expression of ETS1 were analyzed in HepG2. Data are shown as mean ± SD. *P<0.05, **P<0.01.*

apoptosis rate of HCC cells was raised, while their proliferation, migration and invasion abilities were inhibited (Fig. 6 A-D), hence, silencing ETS1 can repress the further progression of HCC.

DISCUSSION

HCC patients have a poor survival rate and prognosis partly due to recurrence and metastasis, therefore, elucidating the molecular pathogenesis of HCC is essential for developing effective treatment strategies and ameliorating the prognosis of such patients. A study found that exosomes containing miRNAs can act as markers assessing cancer aggressiveness and may be involved in the development of many human cancers (20). In view of this, the role and mechanism of BMSC-derived exosomes in HCC through delivering miR-338-3p were evaluated in the present study. The results showed that BMSC-derived exosomes could deliver miR-338-3p, down-regulate the expression level of ETS1, inhibit the proliferation, invasion and metastasis of HCC cells and facilitate their apoptosis. Hence, they are expected to become potential biomarkers for the treatment of HCC.

It was first found in the present study that BMSC-derived exosomes could be taken up by HCC cells, thereby inhibiting the viability, invasion and migration and inducing the apoptosis of HCC cells. According to reports, M1 macrophage-derived exosomes can enhance the anti-tumor effect of chemotherapeutic drugs by establishing a local inflammatory microenvironment (21). Moreover, researchers have confirmed that BMSC-derived exosomes can repress the proliferation, invasion and migration of bladder

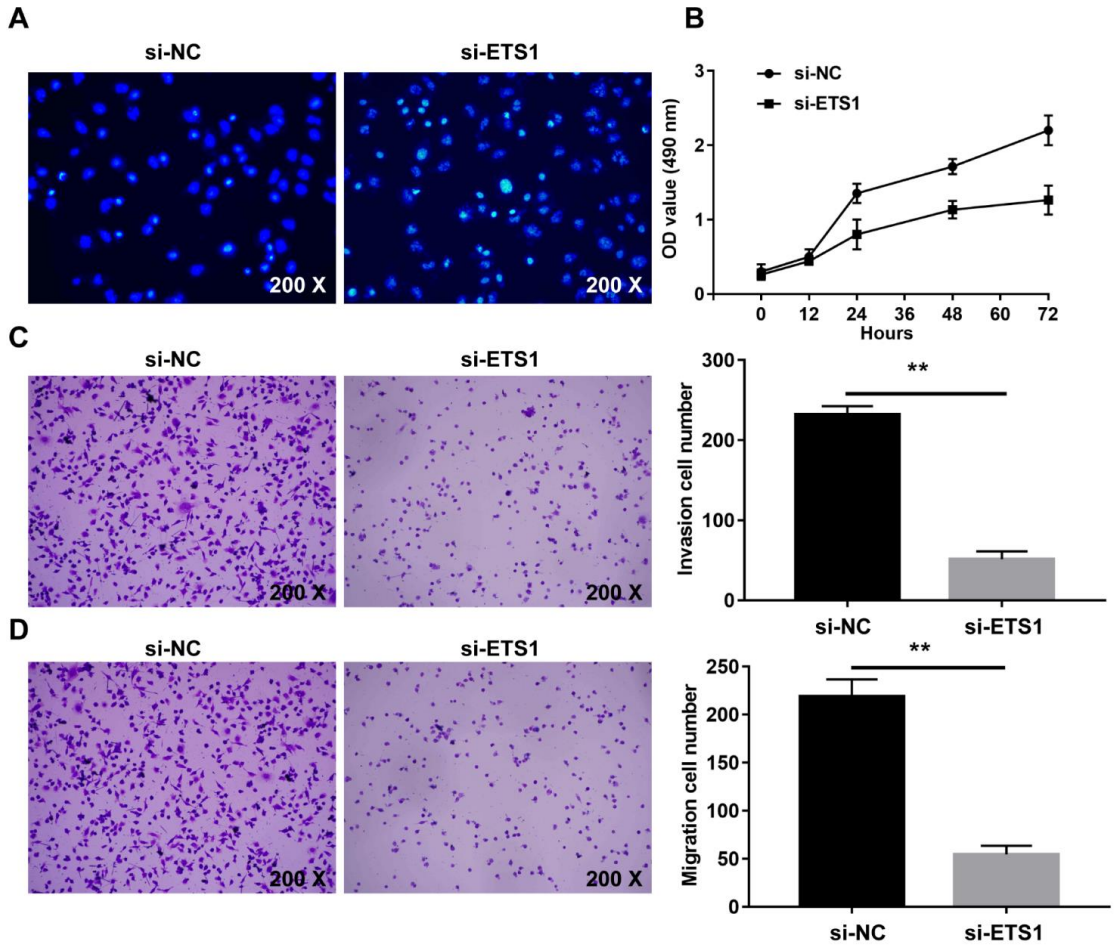


Fig. 6. *The function of ETS1 on HCC cells.* ***A)*** *Cell apoptosis of HepG2 measured by DAPI.* ***B)*** *The viability of HepG2 detected with MTT.* ***C, D)*** *Cell invasion and migration determined with Transwell (magnification ×200). Data are shown as mean ± SD. **P<0.01.*

cancer cells by carrying miRNAs (22). In this study, it was discovered that overexpressed and exosomal miR-338-3p inhibited the proliferation, invasion and migration of HCC cells. According to previous study results, miR-338-3p inhibited the progression and aggravation of various cancers. For example, miR-338-3p targets MACC1 to delay the proliferation, migration and invasion of malignant melanoma cells (23). Wang et al. corroborated that miR-338-3p impedes the growth and invasion of NSCLC cells by regulating IRS2 (24). Furthermore, the depletion of miR-338-3p expression is related to the clinical invasiveness of liver cancer (25). The results of this study revealed that BMSC-derived exosomes suppressed the viability, invasion and migration of HCC cells via delivering miR-338-3p

More importantly, it was also discovered in the present study that ETS1 was a target gene of miR-338-3p. Furthermore, the expression of ETS1 was lowered after the treatment of exosomes containing miR-338-3p inhibitors. It has been reported that miR-338-3p can inhibit the growth and metastasis of liver HCC cells through targeting the smoothened gene (26). Additionally, there is a specific binding site between miR-338-3p and the 3'-UTR of ETS1, and miR-338-3p impedes the progression of prostate cancer by targeting ETS1 (27), verifying the targeted connection between ETS1 and miR-338-3p. Similarly, the present study proved that BMSC-derived exosomal miR-338-3p exerted an anti-HCC effect by inhibiting ETS1.

The results of this study indicated that miR-

338-3p serves as an anti-cancer gene in HCC by inhibiting ETS1. More importantly, it was evidenced that delivering miR-338-3p to tumor cells through BMSC-derived exosomes can inhibit the progression and metastasis of the tumor, which may provide a theoretical basis for miRNA-based HCC treatment. However, the specific mechanism is still unclear, therefore further work is needed for improvement and consolidation

REFERENCES

1. Wallace MC, Preen D, Jeffrey GP, Adams LA. The evolving epidemiology of hepatocellular carcinoma: a global perspective. Expert Rev Gastroenterol Hepatol 2015; 9:765-79.
2. Hu MH, Ma CY, Wang XM, et al. MicroRNA-126 inhibits tumor proliferation and angiogenesis of hepatocellular carcinoma by down-regulating EGFL7 expression. Oncotarget 2016; 7:66922-66934.
3. Madkhali AA, Fadel ZT, Aljiffry MM, Hassanain MM. Surgical treatment for hepatocellular carcinoma. Saudi J Gastroenterol 2015; 21:11-17.
4. Aquino JB, Bolontrade MF, Garcia MG, Podhajcer OL, Mazzolini G. Mesenchymal stem cells as therapeutic tools and gene carriers in liver fibrosis and hepatocellular carcinoma. Gene Ther 2010; 17:692-708.
5. Li T, Song B, Du X, Wei Z, Huo T. Effect of bone-marrow-derived mesenchymal stem cells on high-potential hepatocellular carcinoma in mouse models: an intervention study. Eur J Med Res 2013; 18:34.
6. Shang S, Wang J, Chen S, et al. Exosomal miRNA-1231 derived from bone marrow mesenchymal stem cells inhibits the activity of pancreatic cancer. Cancer Med 2019; 8:7728-40.
7. Qin F, Tang H, Zhang Y, Zhang Z, Huang P, Zhu J. Bone marrow-derived mesenchymal stem cell-derived exosomal microRNA-208a promotes osteosarcoma cell proliferation, migration, and invasion. J Cell Physiol 2020; 235:4734-45.
8. Cai H, Yang X, Gao Y, et al. Exosomal MicroRNA-9-3p Secreted from BMSCs downregulates ESM1 to suppress the development of bladder cancer. Mol Ther Nucleic Acids 2019; 18:787-800.
9. Kibria G, Ramos EK, Wan Y, Gius DR, Liu H. Exosomes as a drug delivery system in cancer therapy: potential and challenges. Mol Pharm 2018; 15:3625-33.
10. Thongboonkerd V. Roles for Exosome in various kidney diseases and disorders. Front Pharmacol 2019; 10:1655.
11. Thind A, Wilson C. Exosomal miRNAs as cancer biomarkers and therapeutic targets. J Extracell Vesicles 2016; 5:31292.
12. Iwakawa HO, Tomari Y. The functions of MicroRNAs: mRNA decay and translational repression. Trends Cell Biol 2015; 25:651-65.
13. Murakami Y, Yasuda T, Saigo K, et al. Comprehensive analysis of microRNA expression patterns in hepatocellular carcinoma and non-tumorous tissues. Oncogene 2006; 25:2537-45.
14. Huang YS, Dai Y, Yu XF, et al. Microarray analysis of microRNA expression in hepatocellular carcinoma and non-tumorous tissues without viral hepatitis. J Gastroenterol Hepatol 2008; 23:87-94.
15. Varnholt H, Drebber U, Schulze F, et al. MicroRNA gene expression profile of hepatitis C virus-associated hepatocellular carcinoma. Hepatology 2008; 47:1223-32.
16. Huang XY, Yao JG, Huang HD, et al. MicroRNA-429 Modulates hepatocellular carcinoma prognosis and tumorigenesis. Gastroenterol Res Pract 2013; 2013:804128.
17. Ma N, Chen F, Shen SL, et al. MicroRNA-129-5p inhibits hepatocellular carcinoma cell metastasis and invasion via targeting ETS1. Biochem Biophys Res Commun 2015; 461:618-23.
18. Zhang L, Yan R, Zhang SN, et al. MicroRNA-338-3p inhibits the progression of bladder cancer through regulating ETS1 expression. Eur Rev Med Pharmacol Sci 2019; 23:1986-95.
19. Ma N, Chen F, Shen SL, et al. MicroRNA-129-5p inhibits hepatocellular carcinoma cell metastasis and invasion via targeting ETS1. Biochem Biophys Res Commun 2015; 461:618-23.
20. Kinoshita T, Yip KW, Spence T, Liu FF. MicroRNAs in extracellular vesicles: potential cancer biomarkers. J Hum Genet 2017; 62:67-74.
21. Wang P, Wang H, Huang Q, et al. Exosomes from M1-polarized macrophages enhance paclitaxel antitumor activity by activating macrophages-mediated

inflammation. Theranostics 2019; 9:1714-27.
22. Fu D, Liu B, Jiang H, Li Z, Fan C, Zang L. Bone marrow mesenchymal stem cells-derived exosomal microRNA-19b-1-5p reduces proliferation and raises apoptosis of bladder cancer cells via targeting ABL2. Genomics 2021 (Online ahead of print) (PMID: 33722655).
23. Zhang C, Li H, Wang J, Zhang J, Hou X. MicroRNA-338-3p suppresses cell proliferation, migration and invasion in human malignant melanoma by targeting MACC1. Exp Ther Med 2019; 18:997-1004.
24. Zhang P, Shao G, Lin X, Liu Y, Yang Z. MiR-338-3p inhibits the growth and invasion of non-small cell lung cancer cells by targeting IRS2. Am J Cancer Res 2017; 7:53-63.
25. Huang XH, Wang Q, Chen JS, et al. Bead-based microarray analysis of microRNA expression in hepatocellular carcinoma: miR-338 is downregulated. Hepatol Res 2009; 39:786-94.
26. Huang XH, Chen JS, Wang Q, et al. miR-338-3p suppresses invasion of liver cancer cell by targeting smoothened. J Pathol 2011; 225:463-72.
27. Zhang L, Yan R, Zhang SN, et al. MicroRNA-338-3p inhibits the progression of bladder cancer through regulating ETS1 expression. Eur Rev Med Pharmacol Sci 2019; 23:1986-95.

Pro-angiogenic effect of exosomal microRNA-103a in mice with rheumatoid arthritis via the downregulation of hepatocyte nuclear factor 4 alpha and activation of the JAK/STAT3 signaling pathway

M. Chen, MH. Li, N. Zhang, WW. Sun, H. Wang, YA. Wang, Y. Zhao and W. Wei

Department of Rheumatology and Immunology, Tianjin Medical University General Hospital, Tianjin, P.R. China

Received August 27, 2020 – Accepted April 7, 2021

Rheumatoid arthritis (RA) is characterized by inflammation of the synovial membrane, accompanied by hyperplasia and neo-angiogenesis, which promote local inflammation. Macrophage-derived exosomes have been reported to enhance inflammation and the immune response. In the present study, we identified a novel exosomal microRNA (miR)-103a, which aids in the regulation of inflammation and angiogenesis in mice with RA, and attempted to identify the underlying mechanism. Initially, a mouse model of RA was established. Thereafter, exosomes were isolated from macrophage RAW264.7 cells and evaluated through transmission electron microscopy and nanoparticle tracking analysis. After prediction and verification of the target genes of miR-103a, RT-qPCR was used to assess miR-103a and HNF4A expression in mice with RA. High expression of miR-103a and low expression of HNF4A were observed in mice with RA, thus, miR-103a was found to target and downregulate HNF4A. Exosomal miR-103a promoted inflammation and angiogenesis in mice with RA which was accompanied by an increase in the levels of factors associated with inflammation and angiogenesis. However, an opposite trend was observed upon HNF4A elevation. Exosomal miR-103a was also found to activate the JAK/STAT3 signaling pathway. In conclusion, exosomal miR-103a inhibited the expression of HNF4A to activate the JAK/STAT3 signaling pathway, thereby exacerbating RA in mice.

Rheumatoid arthritis (RA) is a chronic inflammation-associated disease of the joints. Patients with RA who do not received treatment are likely to suffer from joint deformity or even destruction and functionally progressive dysfunction (1). As a disorder typical in women and the elderly, half of the RA cases are attributable to genetic factors, with smoking being ranked as the leading environmental factor (2). The most common complications in patients with RA are atherosclerotic cardiovascular disease, atrial fibrillation, stroke, and eventually heart failure (3). Currently, the most common treatment methods include treatment-to-target strategy and disease-modifying anti-rheumatic drugs; however, many patients do not respond to the current therapies despite the favorable prospects for most patients (4). Angiogenesis is proposed to induce the nutrient supply of cytokines and inflammatory cells to the synovial membrane to exert pivotal functions in the progression of RA (5). Therefore, it

Key words: rheumatoid arthritis; MicroRNA; hepatocyte nuclear factor 4 alpha; Janus kinase/signal mammalian transducers and activators of transcription 3; inflammation; angiogenesis

Corresponding Author:
Dr Wei Wei,
Department of Immunology and Rheumatology,
Tianjin Medical University General Hospital,
No.154, Anshandao Road,
Heping District, Tianjin 300052, P.R. China
Tel./Fax: +86 022 60361332
e-mail: weiwei04061@163.com

0393-974X (2021)
Copyright © by BIOLIFE, s.a.s.
This publication and/or article is for individual use only and may not be further reproduced without written permission from the copyright holder.
Unauthorized reproduction may result in financial and other penalties
DISCLOSURE: ALL AUTHORS REPORT NO CONFLICTS OF INTEREST RELEVANT TO THIS ARTICLE.

is imperative to identify molecular factors that may inhibit angiogenesis in RA.

Extracellular vesicles are a group of subcellular cell-derived membrane vesicles that can be isolated from bodily fluids and cell sources and have various biological functions (6). Exosomes, nano-sized (30-100 nm) mammalian extracellular particles that can modulate biological processes by transferring proteins and genetic materials, have been implicated in various diseases, including autoimmune disorders such as RA (7). Exosomes have the potential to exert immunosuppressive or immunostimulatory effects depending on the cell type and cargo (8). A previous study proposed that macrophage-derived exosomes could enhance inflammation and immune responses (9). Exosomal microRNAs (miRs) also exert paramount functions in immune responses (10). Intriguingly, the ectopic expression of miR-103a was revealed in patients with RA, and serum miR-103a was identified to predict RA development in susceptible individuals (11). Based on the in silico analyses performed in the current study, miR-103a negatively targeted and inhibited hepatocyte nuclear factor 4 alpha (HNF4A) expression. HNF4A is located at the center of a complex transcriptional network, and its deficiency is directly related to glucose and lipid metabolism (12). HNF4A modulates leukocyte function and therapeutic response in juvenile idiopathic arthritis due to its presence in T lymphocytes and granulocytes (13). A prior study reported that the disruption of the Janus kinase (JAK)/signal mammalian transducers and activators of transcription 3 (STAT3) signaling pathway promotes apoptosis and inhibits proliferation in RA (14). Based on the aforementioned findings, we hypothesized that the exosomal miR-103a/HNF4A/JAK/STAT3 axis may be involved in RA development.

MATERIALS AND METHODS

Development of an RA mouse model

A total of 56 male DBA/1 mice (8 weeks old) were obtained from the Animal Center of Southern Medical University (Guangzhou, Guangdong, China) and kept in a specific-pathogen-free (SPF) animal laboratory at 22-24°C in a 12 h:12 h light/dark cycle. Animals were granted *ad libitum* access to water and food and were allowed to acclimatize for one week in the animal facility before the initiation of any intervention. The calf cartilage type II collagen acetic acid solution (4 mg/mL) was dissolved in Freund's complete adjuvant at a 1:1 ratio for complete emulsification. The 0.1-mL emulsion was injected into the base of the tail of 48 mice. As a booster injection, type II collagen from calf cartilage, dissolved and emulsified at 1:1 ratio with incomplete Freund's adjuvant (Difco Laboratories, Detroit, MI, USA), was injected into the hind limb 2 weeks later.

In the third week after modeling, mice were administered an intraperitoneal injection of either 100 μL PBS, 100 μL PBS containing 50 μg exo-miR-103a or 50 μg exo-miR-negative control (NC), or tail vein injection of 1×10^7 IU lentiviral particles containing oe-NC, oe-HNF4A, oe-HNF4A and NC mimic, or tail vein injection of 1×10^7 IU lentiviral particles containing oe-HNF4A and intraperitoneal injection of 100 μL PBS containing 50 μg exo-miR-103a (n = 8/group). All injections were administered twice per week. Immunofluorescence was used to track the DiO-labeled exosomes to validate whether exosomes entered the joint cavity via injection. Thereafter, paw thickness was assessed using calipers to determine RA severity, which was scored (0 = normal, 1 = slight edema and/or erythema, 2 = apparent edema, 3 = ankylosis), with 12 as the maximum score (i.e., total score of all four limbs). All animal studies were performed in strict accordance with the guidelines of the Institutional Animal Care and Use Committee of Tianjin Medical University General Hospital.

Cell transfection

Initially, 24 h prior to transfection, RAW264.7 macrophages (Zhongqiao Xinzhou Biotechnology Co., Ltd., Shanghai, China) were seeded into a 6-well plate containing DMEM with 10% fetal bovine serum (FBS). Upon 70% cell confluence, RAW264.7 cells were resuspended in serum-free DMEM and plated into 6-well plates. Thereafter, miR-103a mimic or NC mimic (Ribobio, Guangzhou, China) transfection with Lipofectamine 2000 (Invitrogen, Carlsbad, CA, USA) was implemented. Exo-miR-103a and exo-miR-NC were isolated from macrophages 24 h post-transfection.

Isolation and identification of exosomes

The exosomes were ultracentrifuged at 100,000 × g

and cultured in the medium in the presence of serum at 4°C overnight. RAW264.7 cells were cultured in DMEM containing 10% exosome-free serum for 48 h, and the cells in the supernatant in the logarithmic growth phase were collected to isolate the exosomes. The supernatants were centrifuged at 500 × g for 10 min at 4°C, followed by 2,000 × g for 30 min to remove cell debris, and finally, 10,000 × g for 20 min at 4°C to remove large vesicles. After filtering with a 0.22-μm filter, the supernatant was centrifuged at 110,000 × g for 70 min at 4°C, resuspended in PBS under the same conditions, resuspended in 100 μL sterile PBS, and finally frozen at -20°C for subsequent experiments.

The exosome suspension was ultracentrifuged, and the pellet was fixed in a mixture of 2% paraformaldehyde and 2.5% glutaraldehyde at 4°C for 1 h and washed thrice with PBS (15 min/time). The suspension was fixed with 1% osmic acid for 1.5 h, dehydrated with gradient alcohol, immersed, embedded in epoxy resin overnight, and finally polymerized at 35°C, 45°C, and 60°C for 24 h. After being cut into ultrathin-sections and lead- and uranium-stained sections, the sections were observed under a transmission electron microscope (TEM). Nanoparticle tracking analysis (NTA) was then conducted to determine the concentration and size distribution of exosomes using a nanoparticle tracking analyzer (Malvern, Worcestershire, UK). The diluted samples with concentrations of (1-9) × 10^8 particles/mL were added to the analyzer, and the movement trajectory of the particles was recorded to plot the concentration and particle size distribution. The concentration of exosomes was calculated based on the dilution factor.

Dual-luciferase reporter gene assay

Starbase (http://starbase.sysu.edu.cn/index.php) was used to assess the binding mRNA of miR-103a, which predicted that HNF4A is a target gene of miR-103a. The enzyme sites, SpeI and HindIII, were introduced into the pMIR-reporter (Huayueyang Biological Technology Co., Ltd., Beijing, China). Thereafter, the complementary sequence site of the HNF4A mutated (MUT) sequence was designed on the HNF4A4 wild-type (WT), and the target fragment was inserted into the pMIR-reporter reporter plasmid using T4 DNA ligase after restriction endonuclease cleavage. The correctly sequenced HNF4A4 WT and HNF4A MUT were co-transfected with miR-103a into HEK-293T cells (CRL-1415, Shanghai Xinyu Biotech Co., Ltd., Shanghai, China). After 48 h of transfection, the cells were collected and lysed. Luciferase activity was determined using a luciferase detection kit (RG005, Beyotime Biotechnology, Shanghai, China) on a Glomax20/20 luminometer fluorescence detector (Promega, Madison, WI, USA) with Rellina luciferase as a control.

Hematoxylin-eosin (HE) staining

Articular cartilage tissues were fixed with 4% paraformaldehyde, embedded in paraffin, and cut into paraffin sections (5 μm). After dewaxing and dehydration, the sections were stained with hematoxylin (Beyotime) for 5 min and eosin (Beyotime) for 2 min. The sections were then hydrated with 85% alcohol for 20 s, 95% alcohol for 1 min, anhydrous alcohol I for 2 min, anhydrous alcohol II for 2 min; mounted using neutral gum; and finally observed under a light microscope (DMI3000; Leica, Weztlar, Germany).

Safranine O staining

Articular cartilage tissues were fixed in 4% paraformaldehyde for 24 h and decalcified with 19% ethylenediaminetetraacetic acid. The specimens were dehydrated in an ascending series of alcohol and embedded in paraffin. The condyle was cut into 8-μm thick sections and de-paraffinized with xylene. After the sections were hydrated in alcohol at a reduced concentration, the cell nuclei were counterstained with hematoxylin for 1-3 min and rinsed with tap water for 1 min. The sections were differentiated with 1% hydrochloric acid and ethanol for 30 s, stained with 0.02% fast green solution for 3 min, and rinsed with 1% glacial acetic acid to remove residual fast green. Thereafter, the sections were stained with 1% safranin O for 3 min, washed with 95% ethanol, dehydrated with absolute ethanol, followed by xylene transparency, neutral gum sealing, and finally observed under a microscope.

Immunohistochemistry

Mouse synovial tissues were fixed with 10% neutral formalin, dehydrated with gradient alcohol, transparentized with xylene, and embedded in paraffin. All 4-μm sections were heated at 60°C for 1 h, deparaffinized, and hydrated using conventional gradient alcohol. Endogenous peroxidase activity was blocked with 0.3% hydrogen peroxide in distilled water and blocked with FBS for 15 min. The sections were incubated overnight with rabbit antibodies against vascular endothelial growth

factor (VEGF; ab39638, 1:100), CD31 (ab28364, 1:50), and matrix metalloproteinase 14 (MMP14; ab51074, 1:50) at 4°C and goat anti-rabbit immunoglobulin G (IgG; ab150077, 1: 500) at 37°C for 30 min. All antibodies were obtained from Abcam (Cambridge, UK). The sections were counterstained with hematoxylin for 2 min, dehydrated, transparentized, mounted using neutral gum, observed, and photographed under an inverted microscope with PBS as the NC instead of the primary antibody.

Immunoblotting

Total protein or exosomes were lysed using radioimmunoprecipitation assay lysis buffer (R0010, Solarbio, Beijing, China), and the protein concentration was determined using bicinchoninic acid kits (70-PQ0012, MultiSevoiences, Hangzhou, China). The proteins were separated by 10% sodium dodecyl sulfate polyacrylamide gel electrophoresis and transferred to a polyvinylidene fluoride membrane, followed by blocking with 5% skimmed milk powder at room temperature for 1 h. The membrane was probed with diluted primary antibodies against HNF4A (1:1000, ab219610), STAT3 (1:5000, ab119352), phosphorylated (p)-STAT3 (1: 2000, ab32143), rabbit polyclonal antibodies against the tumor susceptibility gene (TSG101; ab30871, 1:2000), polyclonal antibody CD63 (ab118307, 1:50), calnexin (ab75801, 1:2000), and glyceraldehyde-3-phosphate dehydrogenase (GAPDH; 1:2000, ab9485) at 4°C overnight. The membrane was then re-probed with secondary goat anti-mouse antibody against IgG labeled with horseradish peroxidase (HRP) (ab205719; 1: 2000) or HRP-labeled secondary antibody goat anti-rabbit IgG antibody (ab6721; 1:2000) for 1 h. All antibodies were obtained from Abcam. Thereafter, the same amount of liquid A and liquid B from the electrogenerated chemiluminescence (ECL) fluorescence detection kit (Cat. No. BB-3501, Amersham, Little Chalfont, UK) was mixed, placed on the membrane, and exposed for imaging. A Bio-Rad image analysis system (BIO-RAD, Laboratories, Hercules, CA, USA) was used for photography, and analysis was performed using Quantity One v4.6.2 software, with GAPDH as an internal reference.

Table I. *Primer sequences used for RT-qPCR.*

Target gene	Primer sequences (5'-3')
miR-103a	F: AGCAGCATTGTACAGGGCTATGA
	R: CACTCGCATAGAAGCATCTCACG
HNF4A	F: CATGGACATGGCCGACTACA
	R: CGTTGAGGTTGGTGCCTTCTGA
MMP14	F: GGCGGGTGAGGAATAACCAA
	R: GTACTCGCTAT CCACTGCCC
VEGF	F: ATCCAATCGAGACCCTGGTG
	R: TCTCTCCTATGTGCTGGCC
GAPDH	F: TGAACGGGAAGCTCACTGG

MiR-103a: MicoRNA-103a; HNF4A: hepatocyte nuclear factor 4 alpha; MMP14: matrix metalloproteinase 14; VEGF: vascular endothelial growth factor; GAPDH: glyceraldehyde-3-phosphate dehydrogenase.

Reverse transcription quantitative polymerase chain reaction (RT-qPCR)

Total RNA was extracted from cells using Trizol kits (Cat. No. 16096020, Thermo Fisher Scientific, New York, USA), and cDNA was synthesized according to the manufacturer's instructions (K1622; Fermentas Inc., Ontario, CA, USA). The synthesized cDNA was subjected to real-time PCR using the Fast SYBR Green PCR kit (Applied Biosystems, Foster City, CA, USA) and ABI PRISM 7300 RT-PCR system (Applied Biosystems). The $2^{-\Delta\Delta Ct}$ method was used to determine the relative transcription levels. The relative expression of mRNAs or miR-103a was relative to that of GAPDH or U6. The primers used are listed in Table I.

Statistical analysis

Statistical analysis was performed using IBM SPSS Statistics for Windows, version 21.0 (IBM Corp., Armonk, NY, USA). All measurement data are expressed as mean ± standard deviation. If the data conformed to the normal distribution and homogeneity of variance, the comparison of data between the two groups was carried out using the unpaired *t*-test. Data comparisons among multiple groups were analyzed using one-way analysis of variance (ANOVA), followed by Tukey's post hoc test. Statistical significance was set at $P < 0.05$.

RESULTS

Mice with RA exhibit elevated miR-103a and reduced HNF4A levels

We adopted a collagen-induced mouse model of RA with a successful modeling rate of 100%. Normal mice were in a good mental state and could move their joints normally without edema. However, mice with RA exhibited red paws, messy and sparse hair, abnormal gait, a certain degree of edema, thickening of the joints, and exudation of mucosa. At day 34 after modeling, we measured the thickness of the hind paws (Fig. 1A). Based on the findings, mice with RA exhibited markedly more obvious hind paw edema with thicker hind paws, accompanied by an RA score of 9.89±0.87, than normal mice, suggesting that the mouse model of RA was successfully induced.

Subsequently, RT-qPCR was used to assess miR-103a and HNF4A expression in serum and mouse synovial tissues. As shown in Fig. 1 B and C, potently elevated miR-103a and reduced HNF4A levels were observed in the serum and synovial tissues of mice with RA relative to normal mice.

Macrophage-derived exosomes are successfully isolated

A previous study proposed that macrophage-derived exosomes could enhance inflammation and immune responses (9). To clarify the effect of macrophage-derived exosomes on the occurrence of RA, we isolated exosomes from macrophages for validation. Exosomes were round and oval shaped with vesicle disc-like structures, complete membrane, and similar morphology, accompanied by a diameter of approximately 40-100 nm (Fig. 2A). NTA was then conducted to determine the concentration and size distribution of exosomes, which demonstrated a size distribution of 50-200 nm

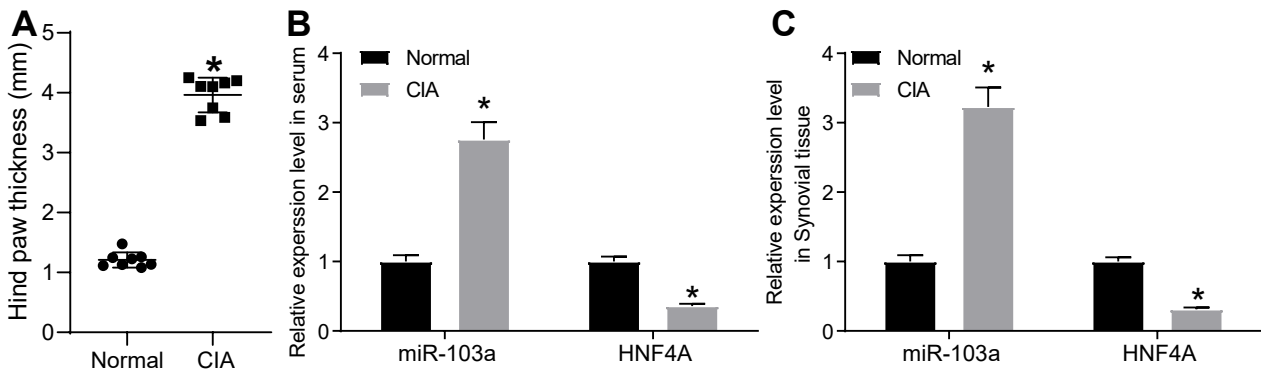


Fig. 1. *miR-103a expression is elevated while HNF4A level is reduced in RA mice compared to normal mice (n = 8/group). **A)** Thickness of the hind paw determined at day 34 after modeling; **B)** miR-103a expression and the mRNA expression of HNF4A in the serum determined using RT-qPCR; **C)** miR-103a expression and the mRNA expression of HNF4A in the mouse synovial tissues determined using RT-qPCR. * $p < 0.05$ vs normal mice.*

with an average size distribution of 113.6 nm. The size distribution of the highest concentration was 102.4 nm at a concentration of 8×10^7 particle/mL (Fig. 2B). Moreover, the exosomal markers, TSG101 and CD63, were observed in the isolated exosomes in the absence of the endoplasmic reticulum marker, calnexin (Fig. 2C), validating the successful isolation of exosomes from macrophages.

Exosomal miR-103a promotes angiogenesis to exacerbate disease in mice with RA

After the miR-103a mimic was transfected into macrophages, exo-miR-103a was collected and injected into mice with RA to assess its clinical potential, with PBS as the NC. Fig. 3A illustrates that exosomes entered the joint cavity. In fact, some exosomes reached the joint cavity and some of the synovial tissues, suggesting that the recipient cells for macrophage-derived exosomes are synovial fibroblasts. We used RT-qPCR to detect the expression of miR-103a in the exosomes derived from macrophages transfected with the miR-103a mimic or NC mimic. The expression in exo-miR-103a was found to be significantly higher than that in the exo-miR-NC (Fig. 3B). The results of RT-qPCR revealed the potent increase in MMP14 and VEGF levels in the synovial tissues of RA mice injected with exo-miR-NC relative to those injected with PBS. Mice injected with exo-miR-103a (Fig. 3C) exhibited even higher levels, accompanied by thicker hind paws and higher RA scores (Fig. 3 D, E).

H&E and safranin O staining of the ankle joint tissue in RA mice on day 35 revealed that exo-miR-103a treatment exacerbated ankle joint inflammation in RA mice compared to exo-miR-NC treatment (Fig. 3 F, G). As expected, immunohistochemistry identified increased expression of VEGF and CD31 in RA mice (Fig. 3H), suggesting that exosomal miR-103a effectively promoted angiogenesis. Similarly, a thicker lining layer and upregulated MMP14 levels were observed in RA mice treated with exo-miR-103a compared to exo-miR-NC-injected RA mice (Fig. 3 I, J). Collectively, exosomal miR-103a was found to increase MMP14 and VEGF levels to promote angiogenesis, thereby exacerbating RA.

miR-103a targets and negatively modulates HNF4A

Starbase (http://starbase.sysu.edu.cn/index.php) predicted the binding sites between miR-103a and HNF4A (Fig. 4A). The dual-luciferase reporter gene assay (Fig. 4B) confirmed that co-transfection of the miR-103a mimic and HNF4A-WT markedly reduced luciferase activity compared to the mimic NC, while HNF4A-MUT exhibited no significant changes in luciferase activity, indicating that miR-103a targeted HNF4A.

After the transfection efficiency of miR-103a overexpression was successfully validated in HEK-293T cells (Fig. 4C), RT-qPCR and immunoblotting results (Fig. 4C, D) showed that miR-103a elevation resulted in a reduction in HNF4A mRNA and protein expression compared to the mimic NC, suggesting that miR-103a targets HNF4A.

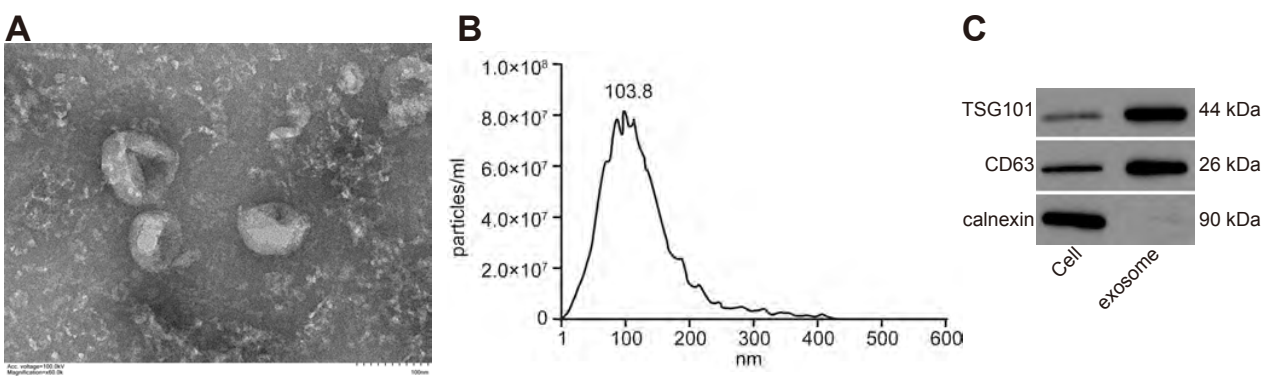


Fig. 2. *Exosomes are successfully isolated from macrophages.* ***A)*** *Ultrastructure of exosomes observed under a TEM (× 5000);* ***B)*** *concentration and size distribution of exosomes determined using NTA;* ***C)*** *levels of the exosomal markers, TSG101 and CD63, and endoplasmic reticulum marker, calnexin, assayed using immunoblotting.*

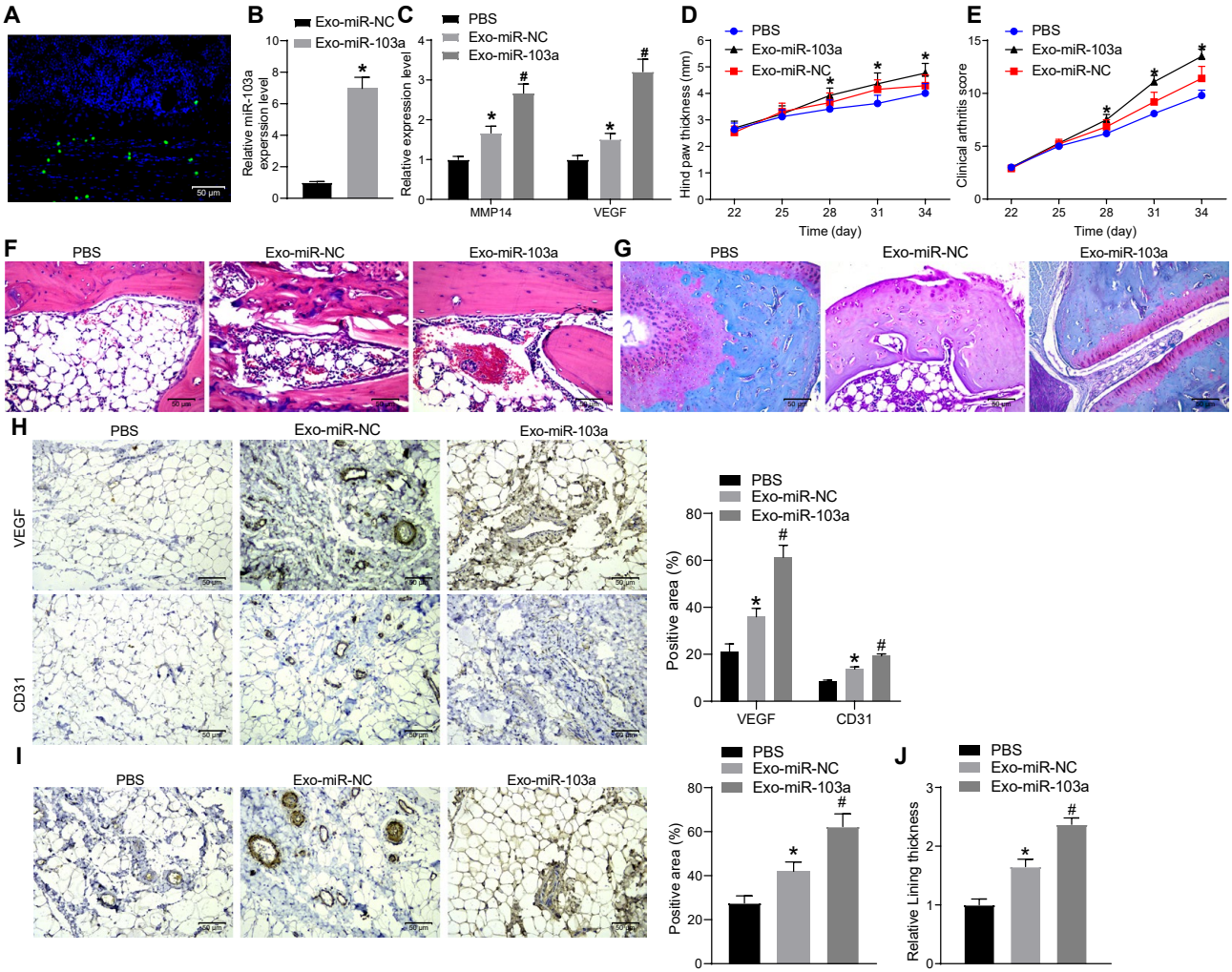


Fig. 3. *Exosomal miR-103a upregulates MMP14 and VEGF levels to promote angiogenesis, thereby exacerbating RA. RA mice were injected with PBS, exo-miR-103a, or exo-miR-NC (n = 8/group). **A)** Macrophage-derived exosomal miR-103a labeled by Dio in the joint cavity (× 100); **B)** the miR-103a expression in exosomes; **C)** MMP4 and VEGF expression in synovial tissues determined using RT-qPCR; **D)** Thickness of the hind paws of mice; **E)** Clinical RA scores of mice; **F)** HE staining of synovial tissues (× 100); **G)** Safranin O staining of synovial tissues (× 100); **H)** VEGF and CD31 expression in synovial tissues assayed using immunohistochemistry at day 35; **I)** MMP14 expression in synovial tissues assayed using immunohistochemistry at day 35; **J)** Thickness of the lining layer of the synovial tissue in mice. * $p < 0.05$ vs RA mice injected with PBS; # $p < 0.05$ vs RA mice injected with exo-miR-NC.*

Exosomal miR-103a rescues the alleviative effects of HNF4A elevation in RA mice

To better elucidate the effects of the exo-miR-103a/HNF4A axis on the occurrence of RA, we treated RA mice with oe-HNF4A and exo-miR-103a and verified that the delivery was successful (Fig. 5A). As shown in Fig. 5 B-D, oe-HNF4A transduction markedly reduced MMP14 and VEGF levels, accompanied by a less thick hind paw and lower RA score, whereas further treatment with exo-miR-103a reversed this trend compared to that observed in oe-HNF4A + NC mimic-treated RA mice.

HE, safranin O staining, and immunohistochemistry (Fig. 5E-G) showed that HNF4A elevation attenuated ankle joint inflammation in RA mice and decreased the expression of VEGF and CD31, which were reversed by exo-miR-103a treatment compared to mice treated with oe-HNF4A + NC mimic. As shown in Fig. 5H, I, a less thick lining layer and decreased MMP14 levels were observed in RA mice injected

with oe-HNF4A compared to those injected with oe-NC, whose trend was abrogated by exo-miR-103a treatment compared to oe-HNF4A + NC mimic-treated RA mice. Collectively, overexpression of HNF4A suppressed angiogenesis to attenuate RA, while the alleviative effects of HNF4A elevation were abrogated by exosomal miR-103a.

Exosomal miR-103a targets HNF4A to activate the JAK/STAT3 signaling pathway, thereby exacerbating RA

Prior studies have noted the involvement of the JAK/STAT3 signaling pathway in the pathogenesis of RA (14, 15). To determine the downstream mechanism of the miR-103a/HNF4A axis during RA, we determined the expression levels of miR-103a, HNF4A, and JAK/STAT3 signaling pathway-related factors in the synovial tissue (Fig. 6 A, B). A marked increase in miR-103a and p-STAT3 levels and reduced HNF4A expression were observed in RA mice treated with exo-miR-103a compared to those injected with PBS. Elevation of HNF4A induced upregulation of HNF4A and inhibited p-STAT3 levels accompanied by unchanged miR-103a expression, which was rescued by exo-miR-103a treatment with elevated miR-103a levels. Coherently, macrophage-derived exosomal miR-103a targets HNF4A to activate the JAK/STAT3 signaling pathway, thereby exacerbating RA.

DISCUSSION

RA is characterized by inflammation of the synovial membrane, hyperplasia, neo-angiogenesis, and immune cell infiltration, which promotes local inflammation (16). The abundant chemokines expressed in the synovial tissues promote the inflammatory cells to migrate into the inflamed joints, which contributes to the formation of new blood vessels (17). RA patients present with symmetric polyarthritis of the small joints of the hands and feet, accompanied by early morning stiffness and physical symptoms (18). Returning to the hypothesis posed at the beginning of this study, it is now possible to state that exosomal miR-103a activates the JAK/STAT3

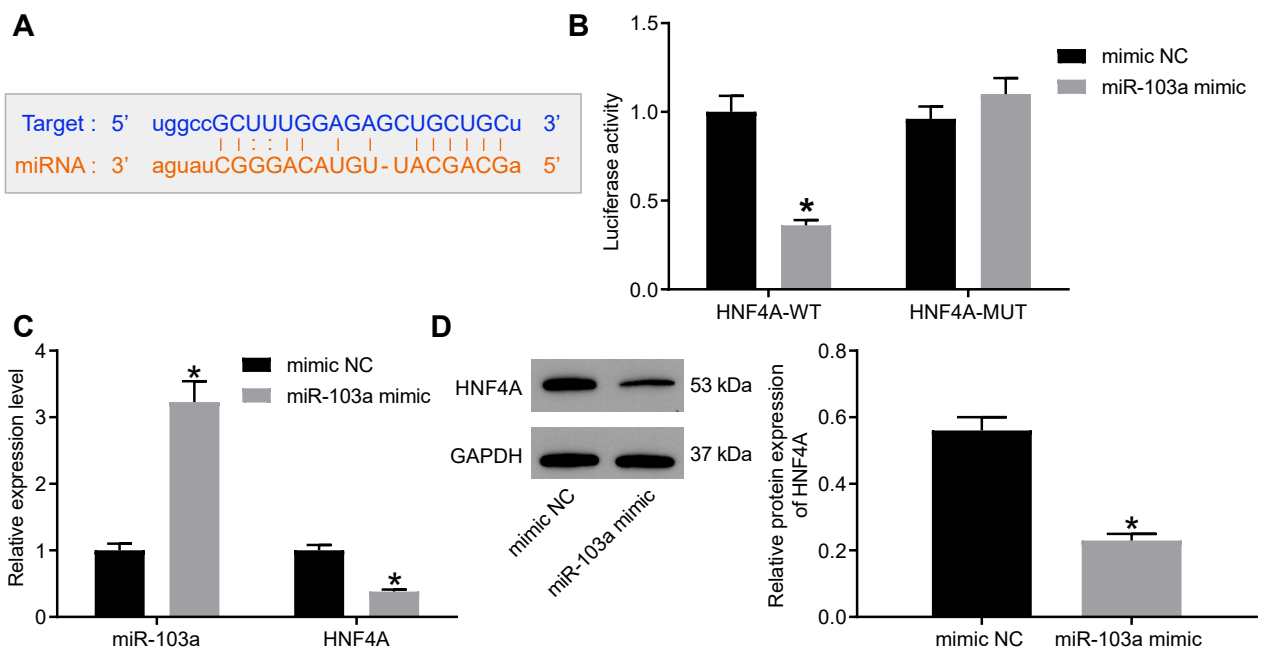


Fig. 4. *miR-103a targets HNF4A. **A**) the binding sites between miR-103a and HNF4A predicted by Starbase; **B**) the targeting relationship between miR-103a and HNF4A validated by a dual-luciferase reporter gene assay; **C**) miR-103a and HNF4A expression determined using RT-qPCR in response to the miR-103a mimic or mimic NC; **D**) HNF4A protein level assessed using immunoblotting in response to the miR-103a mimic or mimic NC. * $p < 0.05$ vs HEK-293T cells transfected with the mimic NC.*

signaling pathway by inhibiting HNF4A expression to exacerbate RA.

Initially, the mouse model of RA was successfully achieved in the current study, accompanied by thicker hind paws and reduced RA scores. In a mouse model of RA, the degree of paw swelling and arthritis index are important for evaluating the severity of RA (19). We also found that miR-103 levels were elevated in the synovial tissues and serum of the RA mice. Consistently, elevated levels of miR-103a-3p were observed in the

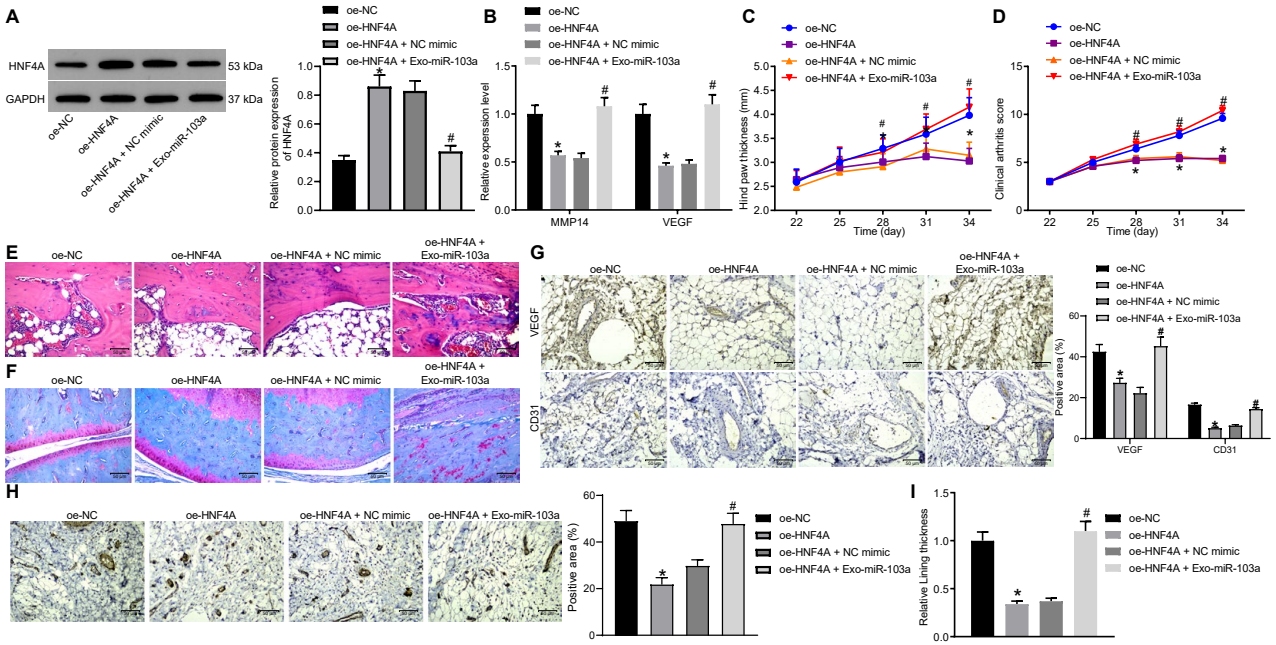


Fig. 5. *Exosomal miR-103a rescues the attenuative effects of HNF4A elevation on RA mice. RA mice were treated with oe-NC, oe-HNF4A, oe-HNF4A + NC mimic, or oe-HNF4A + Exo-miR-103a (n = 8/group).* ***A****) Protein expression of HNF4A in mice after treatment;* ***B****) MMP4 and VEGF expression in the synovial tissues determined using RT-qPCR;* ***C****) Thickness of the hind paws of mice;* ***D****) Clinical RA scores of mice;* ***E****) HE staining of synovial tissues (× 100);* ***F****) Safranin O staining of synovial tissues (× 100);* ***G****) VEGF and CD31 expression in the synovial tissues assayed using immunohistochemistry at day 35;* ***H****) MMP14 expression in the synovial tissues assayed using immunohistochemistry at day 35;* ***I****) thickness of the lining layer of the synovial tissue in mice. * p < 0.05 vs RA mice injected with oe-NC. # p < 0.05 vs RA mice injected with oe-HNF4A + NC mimic.*

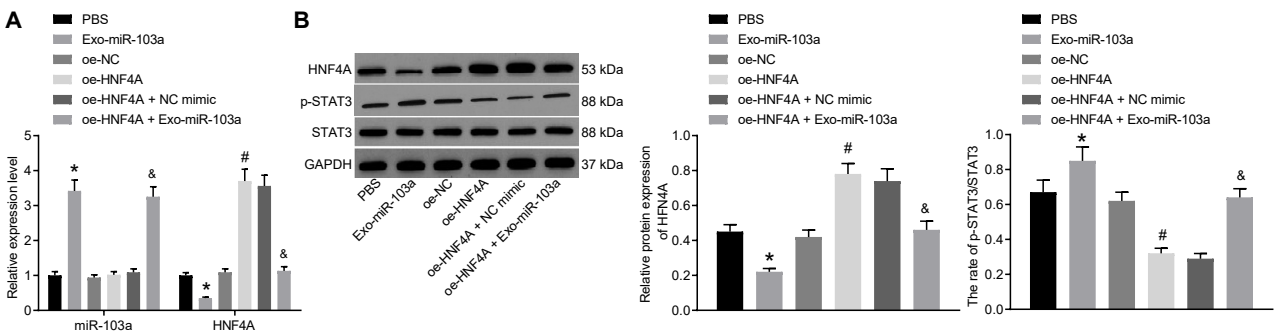


Fig. 6. *Exosomal miR-103a activates the JAK/STAT3 signaling pathway to exacerbate RA.* ***A****) miR-103a and HNF4A expression in the synovial tissue determined using RT-qPCR;* ***B****) Protein expression of HNF4A and the rate of p-STAT3/STAT3 in the synovial tissues based on immunoblotting. * p < 0.05 vs RA mice injected with PBS. # p < 0.05 vs RA mice injected with oe-NC. & p < 0.05 vs RA mice injected with oe-HNF4A + NC mimic (n = 8/group).*

peripheral blood mononuclear cells from patients with RA compared to disease-free healthy control subjects (20). The upstream mechanism of miR-103a overexpression might be caused by several factors, including transcriptional regulation and epigenetic modification regulation. For example, long noncoding RNA growth arrest-specific transcript 5 reduces miR-103 expression by binding to miR-103, thereby alleviating adjuvant-induced arthritis (21). Another study showed that HDAC1 promotes the exacerbation of RA symptoms by deacetylation modification of the miR-124 promoter, ultimately inhibiting miR-124 expression and activating the JAK/STAT signaling pathway (22). The underlying mechanism of miR-103a overexpression in RA may be the direction of our next investigation. In the subsequent analysis, we found that exosomal miR-103a induced marked increases in MMP14, VEGF, and CD31 expression to promote inflammation and angiogenesis in RA mice. A previous study proposed that macrophage-derived exosomes could enhance inflammation and immune responses (9). Likewise, macrophages that receive cancer-cell-secreted exosomal miR-103a further promote cancer progression and tumor angiogenesis, indicating that exosome inhibition may be effective for immunotherapy (23). Consistent with a previous study, remarkably increasing levels of MMP14 and VEGF were observed in the serum and synovial tissues of patients with RA compared to those with osteoarthritis, suggesting the promotion of angiogenesis (24). Similarly, miR-130a upregulated the protein expression of VEGF in endothelial progenitor cells (25).

Another important finding herein is the targeting and inhibition of HNF4A expression by miR-103a, as predicted by in silico analyses and validated by the dual-luciferase reporter gene assay, however, this has not yet been documented. HNF4A mRNA inhibition was induced by the cooperation of miR-34a and miR-21 in renal cell carcinoma (26). HNF4A modulates leukocyte function and therapeutic response in juvenile idiopathic arthritis due to its presence in T lymphocytes and granulocytes (13). The present study also revealed that reduced HNF4A levels in mice with RA and its elevation contributed to attenuated ankle joint inflammation and decreased expression of VEGF, CD31, and MMP14. Likewise, a reduction in HNF4A expression was also observed in dyslipidemia, accompanied by ethanol-induced liver dysfunction (27). Moreover, a decrease in HNF4A levels could be a secondary effect of epithelial cell loss that occurs during inflammation (28). We also found that exosomal miR-103a rescued the alleviative effects of HNF4A elevation in RA mice.

Furthermore, we revealed that exosomal miR-103a activates the JAK/STAT3 signaling pathway, as evidenced by the increased p-STAT3/STAT3 rate. Consistent with our study, hypoxic cancer cells-secreted exosomal miR-103a was found to promote the activation of AKT and STAT3 and the expression of VEGFA (23). As an important transcription factor in the liver, HNF4A coincides with the STAT5 binding sites in the liver (29). The activation of the JAK/STAT3 signaling pathway has been reported to exacerbate RA progression and enhance the secretion of different MMPs (15). The activation of the pathological pathway, JAK/STAT3, is associated with a higher risk of cancer, multiple sclerosis, and RA (30). In addition, repressed HNF4A expression during liver regeneration may be associated with the induction of STAT3 (31).

Altogether, we found that miR-103a was elevated in mice with RA and could be secreted from macrophage cell-derived exosomes. Furthermore, exosomal miR-103a inhibited the expression of HNF4A to activate the JAK/STAT3 signaling pathway, thereby exacerbating RA. HNF4A elevation was found to attenuate inflammation and angiogenesis in RA mice, however, this effect was abrogated by exosomal miR-103 treatment. Such finding may provide a further rational basis for the clinical use of available treatments for RA. Although our findings have significant implications in the inflammation and angiogenesis of RA treatment, the mechanism mediating the interaction among miR-103a, HNF4A, and JAK/STAT3 in RA still requires further elucidation in the clinical setting.

REFERENCES

1. Cheung TT, McInnes IB. Future therapeutic targets in rheumatoid arthritis? Semin Immunopathol

2017; 39:487-500.
2. Scott DL, Wolfe F, Huizinga TW. Rheumatoid arthritis. Lancet. 2010; 376:1094-108.
3. Semb AG, Ikdahl E, Wibetoe G, Crowson C, Rollefstad S. Atherosclerotic cardiovascular disease prevention in rheumatoid arthritis. Nat Rev Rheumatol 2020; 16:361-79.
4. Smolen JS, Aletaha D, McInnes IB. Rheumatoid arthritis. Lancet 2016; 388:2023-38.
5. Cheng WX, Huang H, Chen JH, et al. Genistein inhibits angiogenesis developed during rheumatoid arthritis through the IL-6/JAK2/STAT3/VEGF signalling pathway. J Orthop Translat 2020; 22:92-100.
6. Marton N, Kovacs OT, Baricza E, et al. Extracellular vesicles regulate the human osteoclastogenesis: divergent roles in discrete inflammatory arthropathies. Cell Mol Life Sci 2017; 74:3599-611.
7. Tavasolian F, Moghaddam AS, Rohani F, et al. Exosomes: Effectual players in rheumatoid arthritis. Autoimmun Rev 2020; 19:102511.
8. Tran TH, Mattheolabakis G, Aldawsari H, Amiji M. Exosomes as nanocarriers for immunotherapy of cancer and inflammatory diseases. Clin Immunol 2015; 160:46-58.
9. Cianciaruso C, Beltraminelli T, Duval F, et al. Molecular profiling and functional analysis of macrophage-derived tumor extracellular vesicles. Cell Rep 2019; 27:3062-80 e11.
10. Wang X, Yao X, Xie T, Chang Z, Guo Y, Ni H. Exosome-derived uterine miR-218 isolated from cows with endometritis regulates the release of cytokines and chemokines. Microb Biotechnol 2020; 13:1103-17.
11. Evangelatos G, Fragoulis GE, Koulouri V, Lambrou GI. MicroRNAs in rheumatoid arthritis: From pathogenesis to clinical impact. Autoimmun Rev 2019; 18:102391.
12. Huang KW, Reebye V, Czysz K, et al. Liver Activation of Hepatocellular Nuclear Factor-4alpha by Small Activating RNA Rescues Dyslipidemia and Improves Metabolic Profile. Mol Ther Nucleic Acids 2020; 19:361-70.
13. Jiang K, Frank M, Chen Y, Osban J, Jarvis JN. Genomic characterization of remission in juvenile idiopathic arthritis. Arthritis Res Ther 2013; 15:R100.
14. Zhang X, Feng H, Du J, et al. Aspirin promotes apoptosis and inhibits proliferation by blocking G0/G1 into S phase in rheumatoid arthritis fibroblast-like synoviocytes via downregulation of JAK/STAT3 and NF-kappaB signaling pathway. Int J Mol Med 2018; 42:3135-48.
15. Ni S, Li C, Xu N, et al. Follistatin-like protein 1 induction of matrix metalloproteinase 1, 3 and 13 gene expression in rheumatoid arthritis synoviocytes requires MAPK, JAK/STAT3 and NF-kappaB pathways. J Cell Physiol 2018; 234:454-63.
16. Rivellese F, Pontarini E, Pitzalis C. Tertiary lymphoid organs in rheumatoid arthritis. Curr Top Microbiol Immunol 2020; 426:119-41.
17. Khan MA, Khurana N, Ahmed RS, et al. Chemokines: A potential therapeutic target to suppress autoimmune arthritis. Curr Pharm Des 2019; 25:2937-46.
18. Ngian GS. Rheumatoid arthritis. Aust Fam Physician 2010; 39:626-8.
19. Sun M, Deng R, Wang Y, Wu H, Zhang Z, Bu Y, Zhang H. Sphingosine kinase 1/sphingosine 1-phosphate/sphingosine 1-phosphate receptor 1 pathway: A novel target of geniposide to inhibit angiogenesis. Life Sci 2020; 256:117988.
20. Anaparti V, Smolik I, Meng X, Spicer V, Mookherjee N, El-Gabalawy H. Whole blood microRNA expression pattern differentiates patients with rheumatoid arthritis, their seropositive first-degree relatives, and healthy unrelated control subjects. Arthritis Res Ther 2017; 19:249.
21. Chen H, He C, Liu Y, Li X, Zhang C, Qin Q, Pang Q. LncRNA-GAS5 inhibits expression of miR 103 and ameliorates the articular cartilage in adjuvant-induced arthritis in obese mice. Dose Response 2020; 18:1559325820942718.
22. Meng Q, Pan B, Sheng P. Histone deacetylase 1 is increased in rheumatoid arthritis synovium and promotes synovial cell hyperplasia and synovial inflammation in the collagen-induced arthritis mouse model via the microRNA-124-dependent MARCKS-JAK/STAT axis. Clin Exp Rheumatol 2020.
23. Hsu YL, Hung JY, Chang WA, et al. Hypoxic Lung-cancer-derived extracellular vesicle MicroRNA-103a increases the oncogenic effects of macrophages by targeting PTEN. Mol Ther 2018; 26:568-81.
24. Chen Z, Wang H, Xia Y, Yan F, Lu Y. Therapeutic potential of mesenchymal cell-derived miRNA-150-5p-expressing exosomes in rheumatoid arthritis mediated by the modulation of MMP14 and VEGF. J

Immunol 2018; 201:2472-82.
25. Meng S, Cao J, Zhang X, et al. Downregulation of microRNA-130a contributes to endothelial progenitor cell dysfunction in diabetic patients via its target Runx3. PLoS One 2013; 8:e68611.
26. Wirsing A, Senkel S, Klein-Hitpass L, Ryffel GU. A systematic analysis of the 3'UTR of HNF4A mRNA reveals an interplay of regulatory elements including miRNA target sites. PLoS One 2011; 6:e27438.
27. Shirpoor A, Heshmati E, Kheradmand F, et al. Increased hepatic FAT/CD36, PTP1B and decreased HNF4A expression contributes to dyslipidemia associated with ethanol-induced liver dysfunction: Rescue effect of ginger extract. Biomed Pharmacother 2018; 105:144-50.
28. Chahar S, Gandhi V, Yu S, et al. Chromatin profiling reveals regulatory network shifts and a protective role for hepatocyte nuclear factor 4alpha during colitis. Mol Cell Biol 2014; 34:3291-304.
29. Kang K, Robinson GW, Hennighausen L. Comprehensive meta-analysis of Signal Transducers and Activators of Transcription (STAT) genomic binding patterns discerns cell-specific cis-regulatory modules. BMC Genomics 2013; 14:4.
30. Kaur S, Bansal Y, Kumar R, Bansal G. A panoramic review of IL-6: Structure, pathophysiological roles and inhibitors. Bioorg Med Chem 2020; 28:115327.
31. Jiao H, Zhu Y, Lu S, Zheng Y, Chen H. An Integrated approach for the identification of HNF4alpha-centered transcriptional regulatory networks during early liver regeneration. Cell Physiol Biochem 2015; 36:2317-26.

High-fat diet exacerbates periodontitis: is it because of dysbacteriosis or stem cell dysfunction?

L. Li[1,2*], J. Bao[1,2*], M. Wang[1,2], B. Chen[1,2], B. Luo[1,2] and F. Yan[1,2]

[1]Department of Periodontology, Nangjing Stomatological Hospital, Medical School of Nanjing University, Nanjing, Jiangsu, P.R. China; [2]Central laboratory of Stomatology, Nangjing Stomatological Hospital, Medical School of Nanjing University, Nanjing, Jiangsu, P.R. China

Received October 28, 2020 – Accepted April 15, 2021

*These authors contributed equally to this work

Previous studies have shown that high-fat diet (HFD) may aggravate periodontitis, however the underlining mechanism remains to be further clarified. This study aims to explore whether HFD promotes periodontitis by inducing periodontal microbiota dysbiosis or stem cell dysfunction. A high-fat diet was given to four-week-old male Sprague-Dawley rats for 12 weeks. Periodontitis was induced during the latter 4 weeks. At the end of the 12th week, samples were collected after euthanasia. Maxillae were harvested for histological or microbial analysis. The microbial 16S rRNA gene sequencing was performed with the Illumina MiSeq platform. The data was analyzed through RDP Classifier against the SILVA database. The mandible molars were harvested for isolating periodontal ligament stem cells (PDLSCs). The protein level of p27, p21, and p16, which are negative regulators of the cell cycle, in PDLSCs were detected. Markers of osteogenic differentiation and pro-inflammatory mediators were detected by real-time polymerase chain reaction. Activation of pro-inflammatory signaling pathways was detected by Western blotting. We found that HFD significantly increased ligature-induced alveolar bone loss. HFD resulted in a less diverse periodontal microbiota, with increased proportions of *Lactococcus*, *Bacillus*, *Alloprevotella*, *Carnobacterium*, and *Exiguobacterium* and decreased proportion of *Nitrospira*. HFD increased the protein levels of p27, p16, and p21, and upregulated the expression of osteogenic biomarkers, IL-1β and IL-10 with the ERK1/2 signaling pathway activated in PDLSCs.

Periodontal disease is one of the most common diseases, affecting up to 90% of people globally (1), and is closely related to many metabolic disorders (2-5). Among the elements that promote development of periodontitis, dental plaque is the initial factor. Interestingly, studies have shown that hyperlipidemia is associated with a higher risk of periodontitis (6) and worse periodontal status (7), however, the mechanism underlying these associations remains to be identified further. Since dental plaque is the initial factor for periodontitis and periodontal ligament stem cells (PDLSCs) are crucial to maintain the homeostasis of periodontal tissue, the mechanism underlying the effects of hyperlipidemia on periodontitis was explored by evaluating these two aspects.

Mounting evidence suggests that dysbiosis of the periodontal microbiota plays a pivotal role in the development of periodontitis. Shift of a benign

Key words: high-fat diet; periodontitis; periodontal microbiota; periodontal ligament stem cells

Corresponding Author:
Dr Fuhua Yan,
Department of Periodontology,
Nanjing Stomatological Hospital,
Medical School of Nanjing University,
30 Zhongyang Road, Nanjing, Jiangsu 210008, P.R. China
Tel.: +86 25 83620253 - Fax: +86 25 83620202
e-mail: yanfh@nju.edu.cn

0393-974X (2021)
Copyright © by BIOLIFE, s.a.s.
This publication and/or article is for individual use only and may not be further reproduced without written permission from the copyright holder.
Unauthorized reproduction may result in financial and other penalties
DISCLOSURE: ALL AUTHORS REPORT NO CONFLICTS OF INTEREST RELEVANT TO THIS ARTICLE.

microbiota into a pathogenic one could initiate and promote the inflammatory procedure (8), therefore, diseases or conditions that could disturb the balance of periodontal microbiota may promote the development of periodontitis. To determine the effect of a high-fat diet (HFD) on periodontitis, it is essential to first identify the impact of HFD on periodontal microbiota.

PDLSCs are a unique population of somatic stem cells isolated from the periodontal ligament (9), and play an important role in maintaining homeostasis and facilitating wound healing (10). PDLSC dysfunction may increase the susceptibility to periodontitis, however, little attention has been paid to the impacts of HFD on PDLSCs. The status of PDLSCs could be influenced by the local environment, for example, a pro-inflammatory milieu, and an inflammatory microenvironment could impair the viability and differentiation potential of MSCs (11, 12). Pro-inflammatory cytokines may diminish the bone regeneration capacity of MSCs and promote bone resorption activity (13). Hyperlipidemia has been reported to increase the production of pro-inflammatory mediators in periodontal tissue (14), therefore, HFD may influence PDLSCs by promoting a pro-inflammatory environment.

This study demonstrated that HFD remodeled periodontal microbiota and induced PDLSC dysfunction, the latter perhaps being more closely related with the exacerbated periodontitis. Previous studies have not given due attention to the effect of HFD on PDLSCs, therefore the results of the present study may help to clarify how HFDs are associated with periodontitis, and additionally, may serve as evidence for diet control during periodontal treatment.

MATERIALS AND METHODS

Animals

Three-week-old male Sprague–Dawley rats were obtained from the Sino-British SIPPPR/BK Lab. Animal Ltd. and fed for 1 week before the formal experiment. The rats were maintained in a specific pathogen-free facility at 25°C. Throughout the experimental period, food intake and body weight were monitored weekly. All surgeries on animals were performed in accordance with the institutional protocol approved by the Animal Ethics Committee of Nanjing Agriculture University (No. PZ2019117, China).

Twenty-four rats were randomly divided into four groups (6 rats per group): the control group (ND), in which rats were fed a normal chow diet; the ND+Ligation group, in which rats were fed a normal chow diet and periodontitis was induced by ligature 8 weeks later; the high-fat diet group (HFD), in which rats were fed a high-fat diet containing 10% lard, 4% milk powder, 2% cholesterol, and 0.5% sodium cholate at the beginning of the experiment; the HFD+Ligation group, in which rats were fed a high-fat diet at the beginning of the experiment and periodontitis was induced 8 weeks later.

At the end of the twelfth week, the rats were sacrificed, and the mandibles were harvested for isolating PDLSCs. The right maxillae were harvested and stored in 4% paraformaldehyde for histological analysis. The left maxillae were harvested with sterile instruments with the supragingival and subgingival microbiota kept untouched, and kept in a sterile 1.5 mL Eppendorf tube at -80°C for microbial analysis.

Induction of periodontitis

Periodontitis was induced for 4 weeks beginning from the 9th week after the initiation of the experiment. Briefly, the rats were anesthetized by an intraperitoneal injection of pentobarbital sodium (40 mg/kg; Shandong Xiya Chemical Industrial Co., Ltd., Shandong, China) mixed with atropine sulfate monohydrate (0.1 mg/kg; Tianjin KingYork Pharmaceutical Co., Ltd., Tianjin, China). Periodontitis was induced by ligating the bilateral maxillary second molars with 5-0 silk thread (Jinghuan Medical Appliance, Yang Zhou, China). The thread on the palatal side was put into the gingival sulcus. After ligation, the ligatures were checked every other day. Once the thread fell off, the tooth would be re-ligated again immediately.

Histological examination of periodontal tissue

The right maxillae were processed for histological analysis. Briefly, after decalcification in 10% ethylenediaminetetraacetic acid solution (pH7.2, Servicebio, Wuhan, China) for 4 weeks, the tissues were embedded in paraffin and the 5-μm-thick sections were prepared for hematoxylin and eosin (HE) staining. The HE-stained sections were imaged with a scanner (Pannoramic Mid, 3DHISTECH, Hungary). The distance from the cemento-

enamel junction to the alveolar ridge crest was measured using CaseViewer (Version 2.2.0.85100, 3DHISTECH Ltd., Hungary) to evaluate alveolar bone loss.

16S rRNA gene sequencing and analysis of periodontal microbiota

Total periodontal microbial DNA was extracted from frozen left maxillae using the TIANamp Swab DNA Kit (TIANGEN Biotech, Beijing, China) according to the manufacturer's instructions. The V4-V5 region of the bacteria 16S rRNA gene was amplified with the 2×TransStart® FastPfu Fly PCR SuperMix (TransGen Biotech, Beijing, China). The microbiome primers-515F (5′-GTGCCAGCMGCCGCGGTAA-3′) and 907R (5′-CCGTCAATTCMTTTRAGTTT-3′) were used for amplification. The polymerase chain reaction (PCR) products were separated with 2% agarose gel electrophoresis and subsequently recovered using AxyPrep DNA Gel Extraction Kit (AXYGEN, America). The DNA concentration was determined with NanoDrop 2000 spectrophotometer (Thermo Scientific, Middlesex, MA, USA). The QuantiFluor™-ST kit (Promega, America) was used to quantify the PCR product according to the manufacturer's instructions. Amplicon sequencing was performed using Illumina MiSeq platform according to the standard protocols.

Sequence analysis and phylogenetic classification were performed as described previously (15). Briefly, the raw FASTQ files were demultiplexed and quality filtered using QIIME (version 1.9.1). The operational taxonomic units (OTU) were clustered with a threshold similarity of 97% using UPARSE (version 7.1; http://drive5.com/uparse/). The chimeric sequences were recognized and discarded using UCHIME. The taxonomy of the 16S rRNA gene sequences were analyzed with RDP Classifier (http://rdp.cme.msu.edu/) against the SILVA (SSU123) 16S rRNA database, using a confidence threshold of 70% (16).

Isolation and culture of PDLSCs

Rat PDLSCs were isolated as described previously (17, 18) with some modifications. Briefly, the mandibles were harvested and immediately transferred into phosphate-buffered saline (PBS) (pH7.4, Gibco, Suzhou, China) solution supplemented with 10% penicillin-streptomycin (Hyclone, Logan, UT, USA). Then, the mandibles were repeatedly washed with PBS for three times in a sterile operating station. After removing the gingiva around the molars, the exposed root surface above the alveolar ridge was thoroughly scaled using a mini-five curette (Hu-Friedy Co. Inc., Chicago, IL, USA) to completely remove the residual soft tissue and fibers. Then, the first and second molars were carefully extracted with vascular forceps. The molars with fractures were discarded.

Subsequently, the teeth were washed with PBS. The periapical tissue was removed with a mini-five curette. Thereafter, the teeth were immersed in a digesting solution containing 0.3% type I collagenase (Sigma-Aldrich) and 0.4% dispase II (Sigma-Aldrich) and incubated at 37°C for 2 h on a rotator. After incubation, the samples were centrifuged, and the digesting solution was discarded. The cells were resuspended and cultured in α-MEM (Invitrogen, Carlsbad, CA, USA) supplemented with 20% fetal bovine serum (Gibco, Melbourne, Australia), 1% penicillin-streptomycin solution (Hyclone, Logan, UT, USA) at 37°C in a humidified incubator with 95% air and 5% CO_2.

The culture medium was replenished every 3 days and the concentration of the fetal bovine was adjusted to 10%. When the cells reached approximately 70% confluence, homogeneous populations of PDLSCs were obtained using the limiting dilution technique. Single-cell-derived colonies were used in passages 3 to 5.

Real-time PCR

To detect the osteogenic biomarkers, the PDLSCs were cultured for 3 days in osteogenesis-inducing medium containing 50 mM L-ascorbic acid-2-phosphate, 1 nM dexamethasone, and 20 mM β-glycerolphosphate. Total RNA from the cultured cells was isolated using TRIzol reagent (Invitrogen, CA, USA). The concentration and quality of RNA was evaluated with a NanoDrop 2000 spectrophotometer. cDNA was synthesized using PrimeScript RT Master Mix (Takara Bio, Otsu, Japan) and amplified by real-time quantitative PCR using the SYBR® Select Master Mix (Applied Biosystems) according to the manufacturer's instructions. Primer sequences used are shown in Table I. Quantitative PCR was performed on the ViiA™ 7 Real-Time PCR System (Applied Biosystems). The relative mRNA expression was evaluated using the ΔΔCt method and normalized with the expression of *GAPDH* mRNA.

Western blotting

The cultured PDLSCs were washed with ice-cold

PBS and lysed in cell lysis buffer (Beyotime, China) containing protease and phosphatase inhibitor cocktail (Beyotime, China) for 30 min on ice. The lysate was then centrifuged at 12,000 ×g for 5 min at 4°C; the supernatant was collected. The protein samples were fractionated and separated by Sodium Dodecyl Sulfate Poly-Acrylamide Gel Electrophoresis (GenScript, Nanjing, China) and blotted onto a polyvinylidene difluoride (PVDF) membrane (Millipore, Bedford, MA, USA). After blocking the PVDF membrane with 5% bovine serum albumin for 1 hat room temperature, the membrane was incubated with appropriate primary antibody overnight at 4°C. The primary antibodies to p21, p16, and p27 were purchased from Proteintech (Illinois, USA). The primary antibodies to LC3, phosphorylated p38 MAPK, phosphorylated STAT3, and phosphorylated ERK1/2 were purchased from Cell Signaling Technology (Massachusetts, USA). GAPDH was used as the internal control. After incubation with primary antibodies, the membranes were washed with Tris-buffered saline containing 0.1% Tween-20 for 15 min and incubated with appropriate horseradish peroxidase-conjugated secondary antibody for 2 h at room temperature. The signals were produced using immobilon western chemilum HRP substrate (Millipore, Darmstadt, Germany) and visualized through a Tanon-5200 chemiluminescent imaging system (Tanon, Shanghai, China).

Statistical analysis

Data were analyzed with GraphPad Prism version 5.0 (GraphPad Software Inc., La Jolla, CA, USA). All data are presented as mean ± standard deviation (n = 4-6 rats/group). One-way analysis was used to determine the differences among groups. Student-Newman-Keuls tests were used for multiple comparisons. The enumeration data were analyzed with the Mann-Whitney test or Kruskal-Wallis test. *P*-values < 0.05 were considered statistically significant. *In vitro* experiments were repeated for three times.

Table I. *Primers used in RT-PCR.*

Name	Forward primer sequence (5'-3')	Reverse primer sequence (5'-3')
OCN	CAGTAAGGTGGTGAATAGACTCCG	GGTGCCATAGATGCGCTTG
Runx2	ATCCAGCCACCTTCACTTACACC	GGGACCATTGGGAACTGATAGG
BMP-2	GGAAAACTTCCCGACGCTTCT	CCTGCATTTGTTCCCGAAAA
BSP	AGAAAGAGCAGCACGGTTGAGT	GACCCTCGTAGCCTTCATAGCC
COL1	CTGCCCAGAAGAATATGTATCACC	GAAGCAAAGTTTCCTCCAAGACC
TGF-β	GAACCCCCATTGCTGTCC	TCCGTCTCCTTGGTTCAG
Periostin	TGCAAAAAGAGGTCTCCAAGGT	AGGTGTGTCTCCCTGAAGCAGT
IL-1β	CACCTCTCAAGCAGAGCACAG	GGGTTCCATGGTGAAGTCAAC
TNF-α	CCAGGTTCTCTTCAAGGGACAA	CTCCTGGTATGAAATGGCAAATC
IL-6	GTTGCCTTCTTGGGACTGATGTT	ACTGGTCTGTTGTGGGTGGTATC
MCP-1	GCTGCTACTCATTCACTGGCAAG	GGTCAAGTTCACATTCAAAGGTGC
IL-10	CACTGCTATGTTGCCTGCTCTTAC	GGGTCTGGCTGACTGGGAAG
GAPDH	CCTGCACCACCAACTGCTTA	GGCCATCCACAGTCTTCTGAG

RESULTS

HFD increased alveolar bone loss

Establishment of periodontitis was confirmed by HE-stained sections, which showed soft tissue recession, degradation of collagen fibers, inflammatory cell infiltration, and alveolar bone resorption in the ND+Ligation group. The distance from the cemento-enamel junction to the alveolar ridge crest was measured to quantify the alveolar bone loss. Compared with the ND group, the levels of alveolar ridge crest in the HFD group was significantly lower (One-way analysis and Student-Newman-Keuls tests, $P<0.05$). Furthermore, the levels of alveolar ridge crest in the HFD+Ligation group was significantly lower than that of the ND+Ligation group and the HFD group (One-way analysis and Student-Newman-Keuls tests, $P<0.05$) (Fig. 1).

HFD resulted in less diverse periodontal microbiota

The alpha diversity of the periodontal microbiota was evaluated through indices including OTU, Shannon, Simpson, ACE, and Chao indices. Compared with the ND group, the HFD group had significantly reduced values of OTU, Chao index, ACE index, and increased values of Simpson index (Mann-Whitney test, $P<0.05$). These results indicated that HFD decreased the diversity of the periodontal microbiota. Compared with the HFD group, the values of OTU, Chao index, and ACE index were significantly higher and the Simpson index was significantly lower in the HFD+Ligation group (Mann-Whitney test, $P<0.05$) (Fig. 2).

HFD altered the composition of periodontal microbiota

The composition of periodontal microbiota was altered by HFD. At the phylum level, the relative abundance of Firmicutes in the HFD group was significantly higher than that of the ND group (Mann-Whitney test, $P<0.05$). The relative abundance of Proteobacteria, Cyanobacteria, and Acidobacteria were significantly lower in the HFD group than those of the ND group (Mann-Whitney test, $P<0.05$) (Fig. 3). At the genus level, compared with the ND group, HFD increased the proportion of *Lactococcus*, *Bacillus*, *Alloprevotella*, *Carnobacterium*, and *Exiguobacterium* (Mann-Whitney test, $P<0.05$). The increase of *Veillonella*, *Porphyromonas*, and *Fusobacterium* in the HFD group were not statistically significant (Mann-Whitney test, $P>0.05$) (Fig. 4).

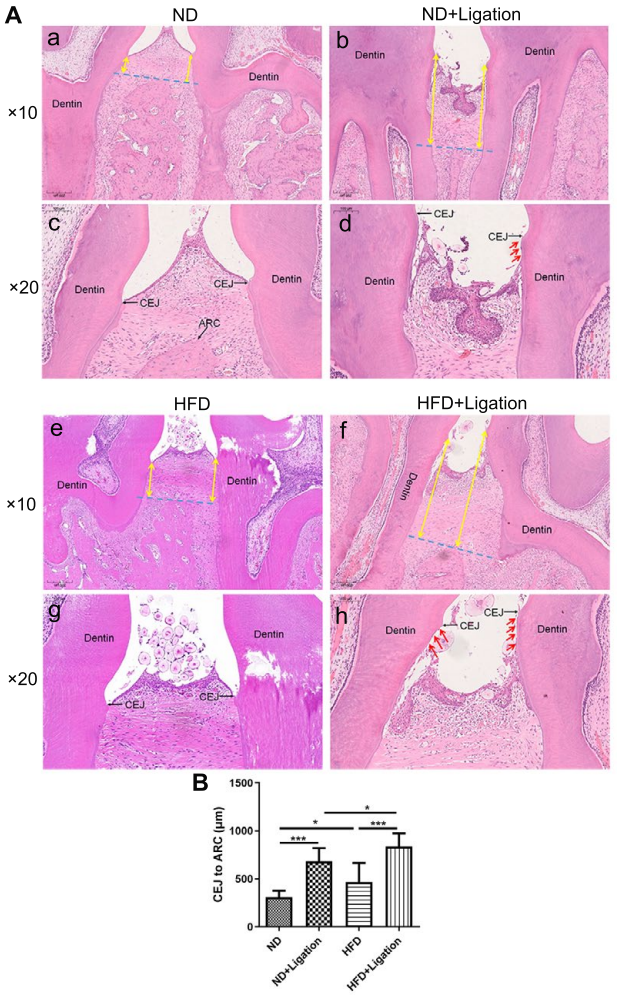


Fig. 1. *HFD aggravates the alveolar bone loss caused by periodontitis. **A)** Representative H&E-stained sections of periodontal tissue in each group. (Ab, f) show the alveolar bone loss in the ND+Ligation group and the HFD+Ligation group, respectively. (Ad, h) the amplified graphs showing the attachment loss, collagen fibers breakdown, and inflammatory cell infiltration in periodontal tissue of the ND+Ligation group and the HFD+Ligation group, respectively. The red arrows indicate attachment loss. The yellow arrows indicate alveolar bone loss. **B)** The distance from the CEJ to the ARC is measured to evaluate alveolar bone loss. Statistical significance is determined through One-way analysis and Student-Newman-Keuls tests. Data are shown as mean ± SD. * $P<0.05$, ** $P< 0.01$, *** $P < 0.001$. CEJ, Cemento-Enamel Junction. ARC, Alveolar Ridge Crest.*

Beta diversity analysis of periodontal microbiota in each group

In the beta diversity analysis, both phylogenetic tree analysis and the principal component analysis based on the Bray-Curtis distance showed that samples of the HFD group clustered separately from that of the ND group. Those results indicated that HFD changed the composition of periodontal microbiota in rats (Fig. 5 A, B). Bacteria enriched in the HFD group were mainly distributed among the phyla Firmicutes and Bacillus, while those enriched in the ND group were mainly distributed among Cyanobacteria, Deltaproteobacteria, Sphingobacteria, and Spirochaetes. The bacteria enriched in the ND+Ligation group were mainly distributed among the phyla Proteobacteria and Acidobacteria, while those enriched in the HFD+Ligation group were mainly distributed among Bacteroidetes and Planctomycetes (Fig. 5C).

HFD may promote osteogenic differentiation and decrease the proliferation of PDLSCs

The expression of osteogenic biomarkers in PDLSCs was detected to check whether HFD could affect the differentiation potential of PDLSCs. HFD significantly upregulated the expression of bone sialoprotein, Runx2, Collagen-1, TGF-β, and periostin (also called osteoblast-specific factor 2 [OSF-2]), but downregulated the expression of osteocalcin (OCN) as compared with the ND group (One-way analysis and Student-Newman-Keuls tests, $P<0.05$) (Fig. 6A). To investigate whether HFD would affect the proliferation of PDLSCs, we checked the protein expression of p27, p16 and p21 proteins in PDLSCs, which were negative regulators of cell cycle. We found that HFD increased the protein levels of p27, p16 and p21 in PDLSCs, which indicated a slow proliferation rate (Fig. 6B).

HFD increased IL-1β expression and activated the p38 and ERK1/2 signaling pathways in PDLSCs

The study investigated whether HFD could affect the immunomodulatory function of PDLSCs. Compared with the ND group, the expression levels of IL-1β and IL-10 were significantly higher, whereas TNF-α level was lower in the HFD group (One-way

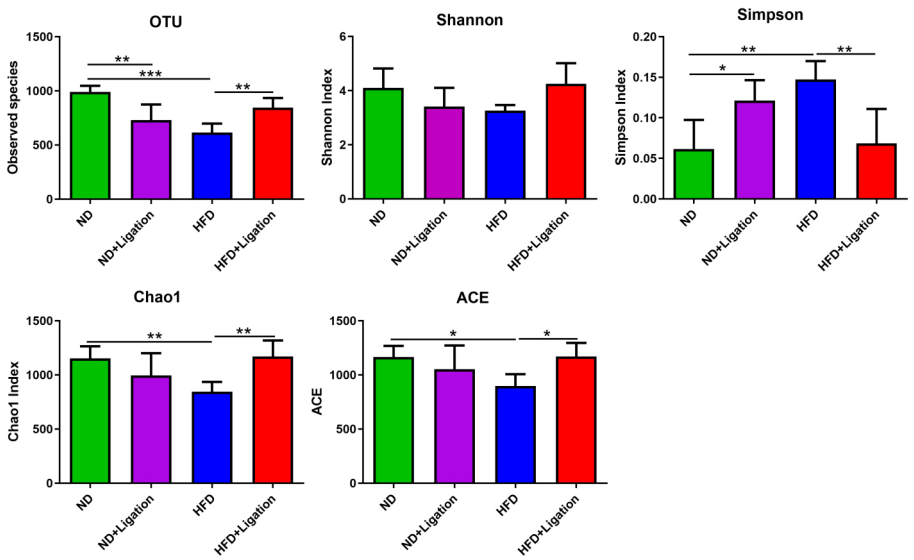


Fig. 2. *Alpha diversity of periodontal microbiota evaluated by OTU, Shannon, Simpson, ACE, and Chao index. The OTU, Chao and ACE indices are lower and the Simpson index is significantly higher in the HFD group than those of the ND group. Compared with the HFD group, the OTU, Chao and ACE indices increase and the Simpson index decreases significantly in the HFD+Ligation group. Data are shown as mean ± SD. Statistical significance is determined through Mann-Whitney test. * P<0.05, ** P<0.01, *** P<0.001.*

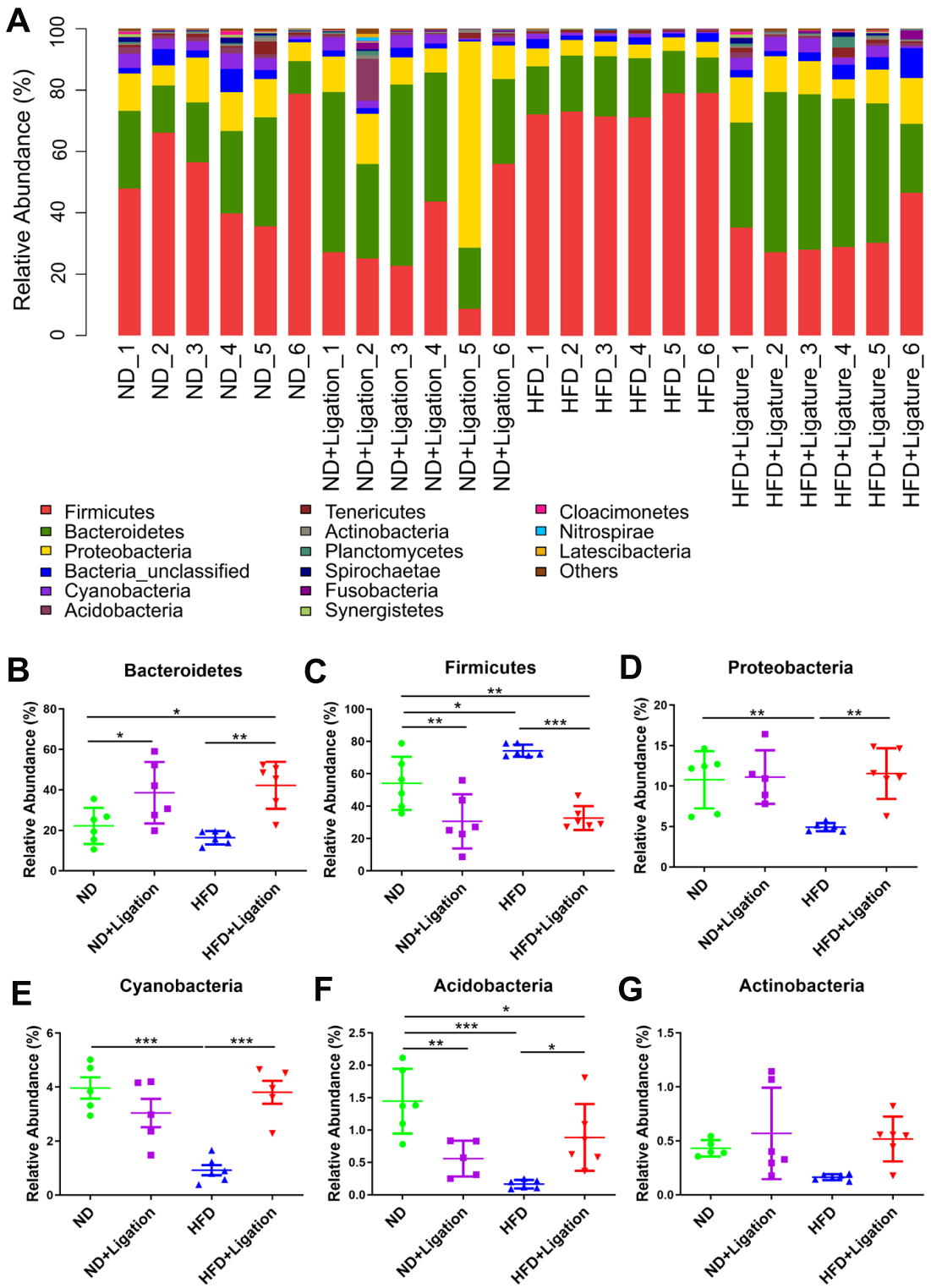


Fig. 3. *Comparison of the microbial composition on phylum level among groups. **A)** Relative abundance of bacterial composition on phylum level. **B)** High fat diet significantly increases the relative abundance of Firmicutes, while decreases the relative abundance of Proteobacteria, Cyanobacteria and Acidobacteria. Data are shown as mean ± SD. Statistical significance is determined through Mann-Whitney test. * P<0.05, ** P<0.01, *** P<0.001.*

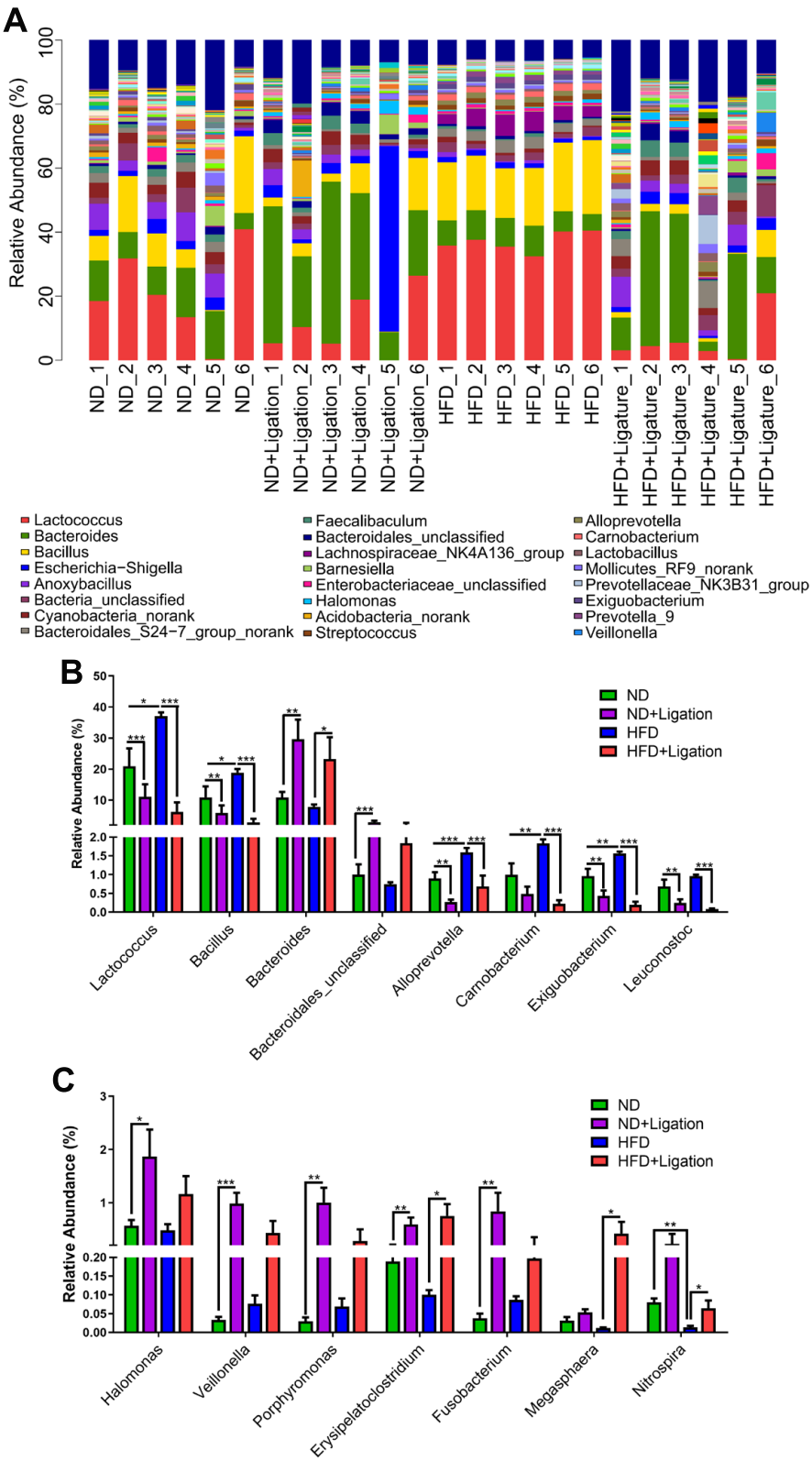


Fig. 4. *Comparison of the microbial composition on genus level among groups.* ***A****) Relative abundance of bacterial composition on genus level.* ***B, C****) Genera that changed significantly by HFD. Data are shown as mean ± SD. Statistical significance is determined through Mann-Whitney test. * P<0.05, ** P<0.01, *** P<0.001.*

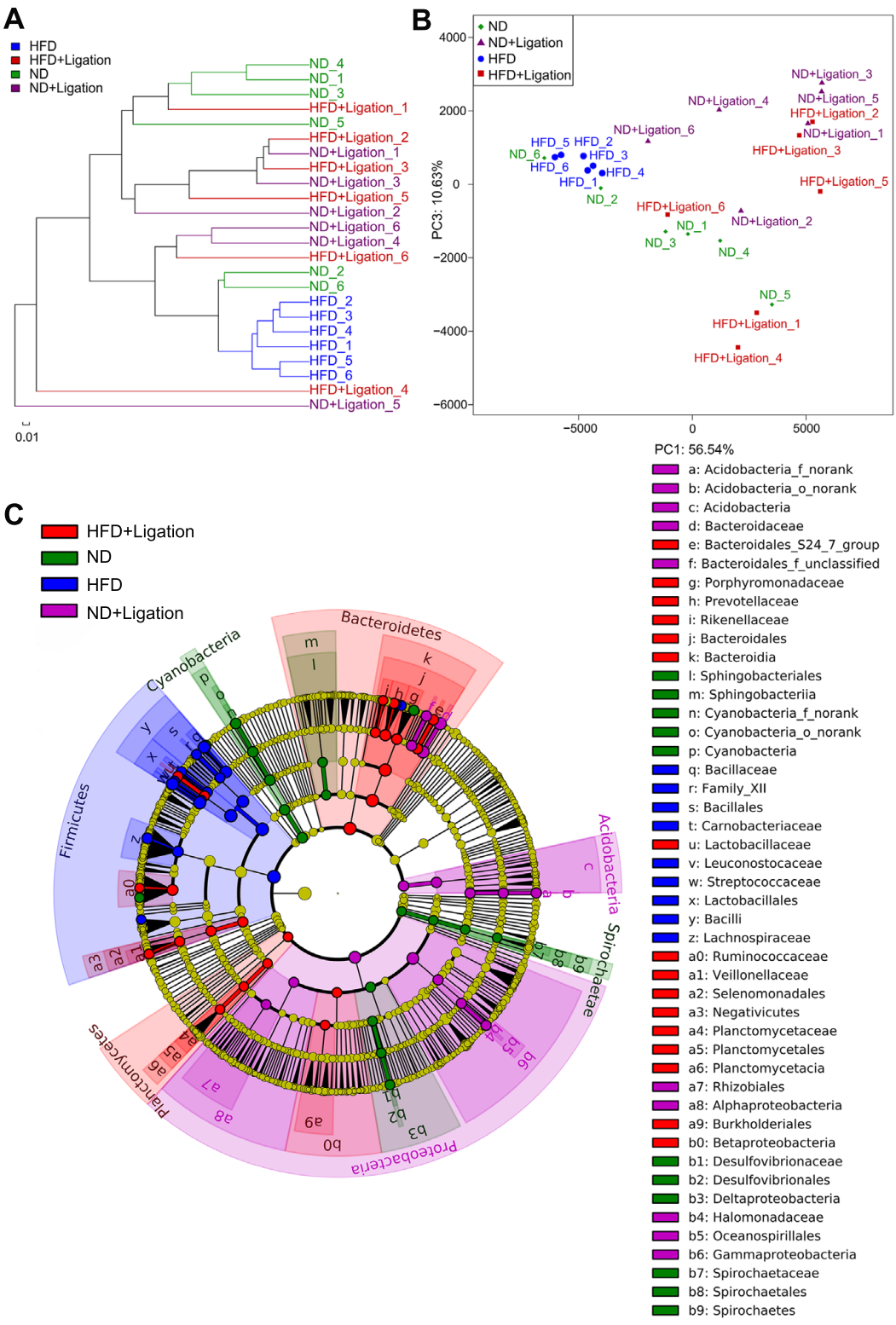


Fig. 5. *Beta diversity analysis of periodontal microbiota among each group. **A**) The phylogenetic tree shows that the samples of the HFD group clustered separately from the ND group. **B**) Principal component analysis shows that the samples of the HFD group (blue dot) clustered separately from the ND group (green dot). **C**) The cladogram based on linear discriminant analysis shows differentially enriched bacteria in each group.*

analysis and Student-Newman-Keuls tests, $P<0.05$) (Fig. 7A). Protein levels of phosphorylated p38 and phosphorylated ERK1/2 were elevated in the HFD group as compared with the ND group, which indicated that HFD may activate the p38/MAPK and ERK1/2 signaling pathways in PDLSCs. In both the HFD+Ligation group and the ND+Ligation group, the protein levels of phosphorylated STAT3 and LC3-II were higher than the ND group (Fig. 7B).

DISCUSSION

The present study explored whether HFD would promote periodontitis by inducing periodontal

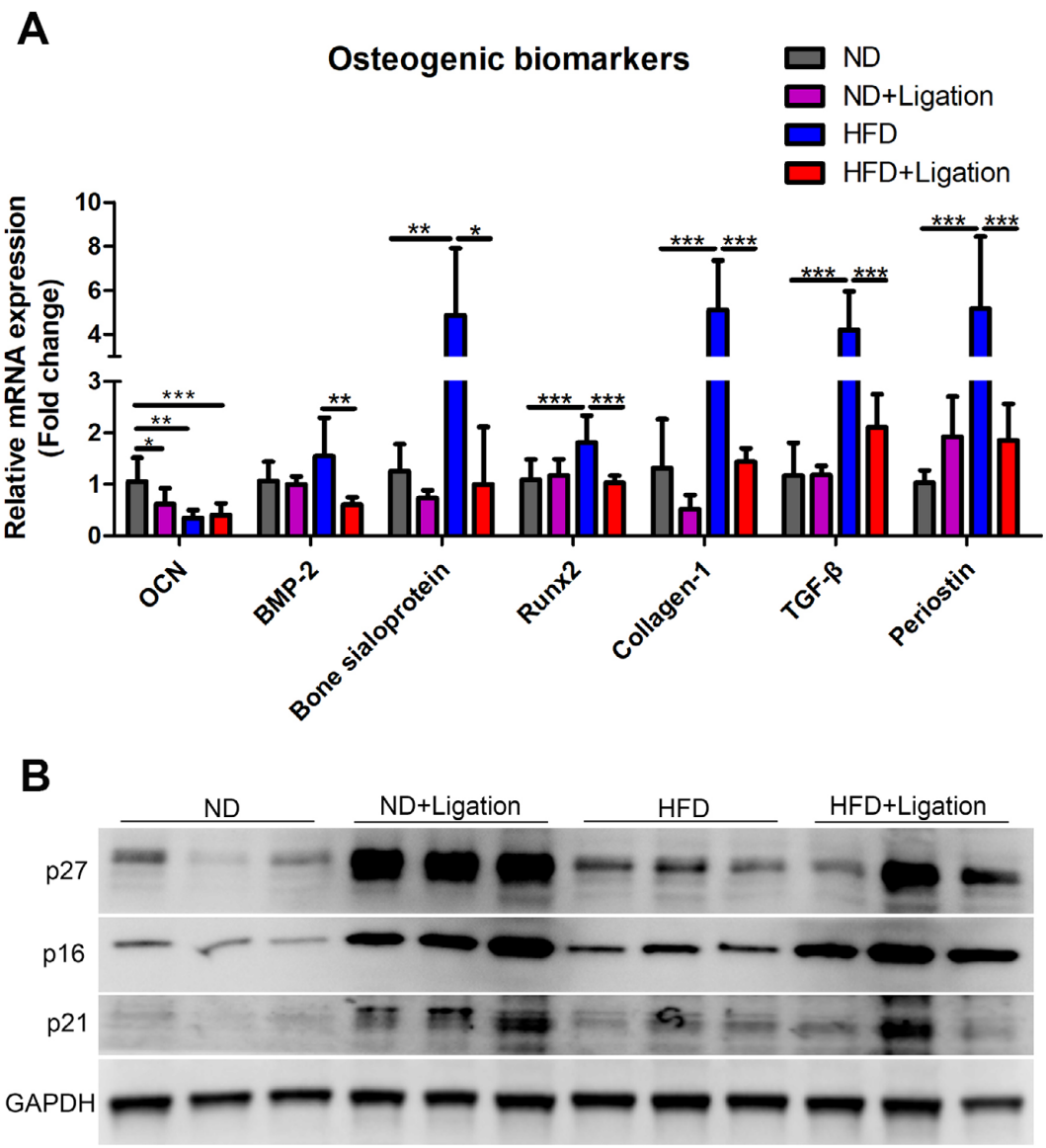


Fig. 6. *Effects of HFD on the expression of osteogenic biomarkers and cell cycle regulators of PDLSCs.* ***A****) Osteogenic biomarkers including BMP-2, Runx2, Collagen-1, TGF-β, bone sialoprotein and Periostin are up-regulated significantly by HFD.* ***B****) HFD up-regulated the protein level of p27, p16 and p21. Data are shown as mean ± SD. Statistical significance is determined through One-way analysis and Student-Newman-Keuls tests. * P<0.05, ** P<0.01, *** P<0.001.*

microbiota dysbiosis or stem cell dysfunction. We found that HFD remodeled periodontal microbiota. We also observed that HFD may decrease the proliferation, up-regulate the osteogenic gene expression, and activate the p38/MAPK and ERK signaling pathways in PDLSCs.

Periodontitis is an inflammatory disease induced by dental plaque. Shift of the periodontal microbial community to a predominantly pathogenic flora plays a pivotal role in the initiation and development of periodontitis. Hyperlipidemia has been associated with higher risk of the disease (6) and may promote its progression (7, 19), however, the mechanism underlying hyperlipidemia-associated periodontitis remains unclear. Previous studies have reported that hyperlipidemia may exacerbate periodontitis by elevating the serum levels of pro-inflammatory cytokines (20), thereby increasing the prevalence of periodontal pathogens (21), or by impairing innate immune response to periodontal pathogens (22), however, the involvement of HFD-associated periodontal microbiota remains unknown.

It was observed that HFD aggravated the alveolar bone loss caused by periodontitis, which was consistent with that reported previously (23). Generally, the damage and repair of tissues are well-

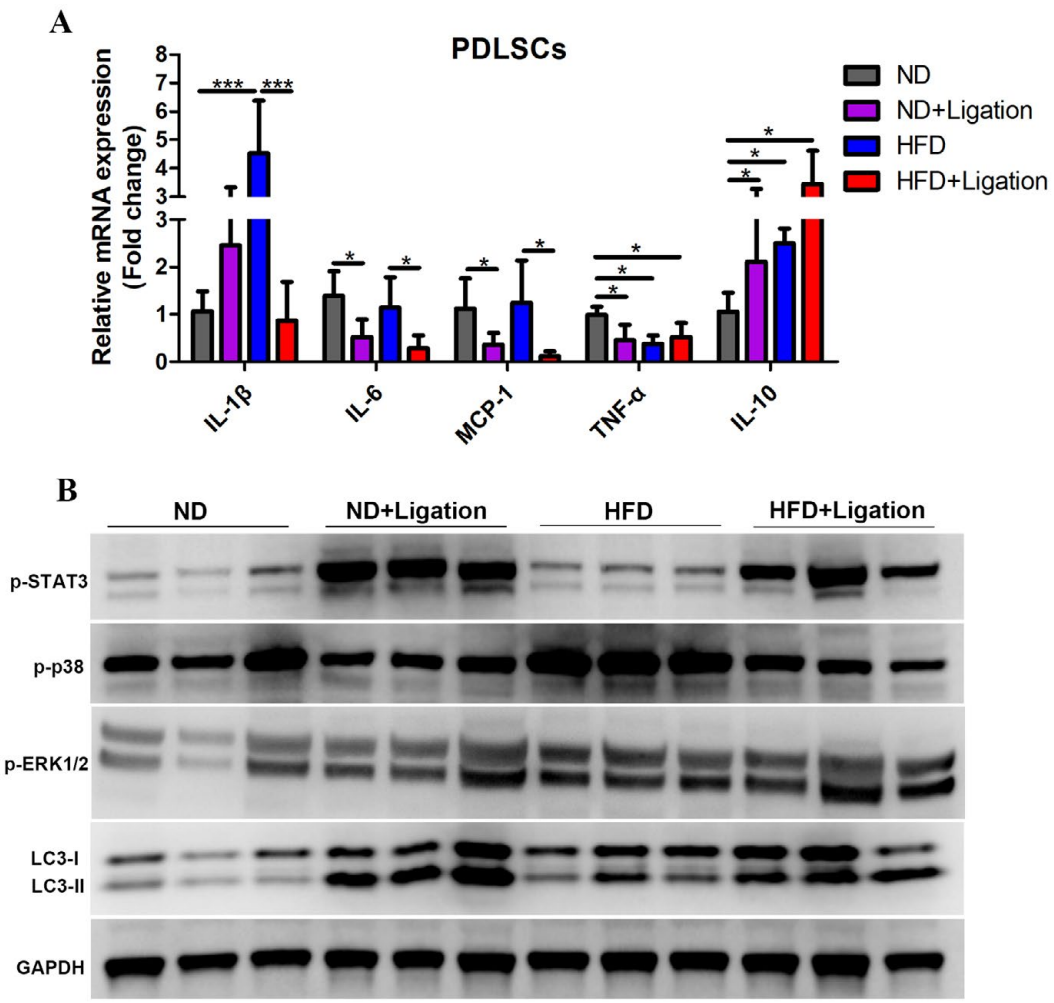


Fig. 7. *Impacts of HFD on the inflammation-related cytokines and signaling pathways in PDLSCs.* ***A****) HFD significantly up-regulates the expression of IL-1β and IL-10 in PDLSCs.* ***B****) HFD activates the p38 MAPK and ERK1/2 pathways in PDLSCs. GAPDH was used as loading control. Data are shown as mean ± SD. Statistical significance is determined through One-way analysis and Student-Newman-Keuls tests. * P<0.05, ** P< 0.01, *** P<0.001.*

balanced to maintain internal homeostasis. Both an excessive increase in tissue damage or impaired tissue repair could lead to tissue destruction, therefore we evaluated the impacts of HFD on periodontitis from these two aspects.

Dysbiosis of periodontal microbiota plays a pivotal role in the initiation of periodontitis (24), which could damage the periodontal tissue. We found that HFD changed the composition of the periodontal microbiota. The HFD-induced periodontal microbiota was obviously different from that of the periodontitis group because the microbial population of the HFD group clustered separately from those of the ND+Ligation and ND groups. Furthermore, HFD resulted in less diverse periodontal microbial flora; the proportion of *Lactococcus*, *Bacillus*, *Alloprevotella*, *Carnobacterium*, and *Exiguobacterium* increased significantly, whereas the proportion of *Nitrospira* decreased, and the proportion of *Veillonella*, *Porphyromonas*, and *Fusobacterium* tended to increase. *Veillonella*, *Porphyromonas*, and *Fusobacterium* are the major, aggressive periodontal pathogens and their populations were increased significantly because of periodontitis. These results indicated that HFD caused redistribution of the periodontal microbiota and that the HFD-induced periodontal microbiota was different from that present during periodontitis.

The difference between HFD-induced and periodontitis-associated periodontal microbiota was further analyzed. Interestingly, the proportion of most microbial genera that were reduced because of periodontitis was increased by HFD, except the relative abundance of *Veillonella*, *Porphyromonas*, and *Fusobacterium*. Similarly, the diversity of periodontal microbiota increased when periodontitis was accompanied with HFD as indicated by the OTU number, as well as Chao, ACE, and Simpson indices. These results indicated that HFD did in fact cause the periodontal flora to become more similar to that observed during periodontitis. These findings, however, cannot be interpreted as a beneficial shift because the results were obtained by the augmentation of some bacterial genera with very low abundance.

To evaluate whether HFD impairs the healing potential of periodontal tissue, the effect of HFD on PDLSCs was investigated, as these cells play an important role in tissue repair and homeostasis. Previous studies have reported that HFD increased the expression of pro-inflammatory cytokines in the periodontal tissue (25). Thus, HFD may also promote the formation of a pro-inflammatory milieu for PDLSCs, which consequently, might affect the status of PDLSCs. We observed that HFD reduced the proliferation rate and promoted the osteogenic differentiation of PDLSCs.

HFD led to an increase in the protein levels of p27, p16, and p21, all of which are negative regulators of cell cycle. We also observed the upregulation of IL-1β expression in PDLSCs, which may be related to cellular senescence (26). The decreased proliferation rate of PDLSCs may be due to the prolonged exposure of these cells to inflammation and the induction of NLRP3 inflammasome formation (26), both of which might increase the rate of senescence (27).

The analysis of osteogenic differentiation showed that HFD upregulated the expression of osteogenic biomarkers in PDLSCs. Previous studies could not achieve a consensus on the effect of HFD on the differentiation potential of mesenchymal stem cells. Some studies reported that HFD may inhibit the osteogenic differentiation of BMSCs (28-30), whereas others showed that HFD promoted the osteogenic differentiation of BMSCs (31). Another study reported that HFD impacted the differentiation potential of MSCs depending on the cell source. Wu et al. (32) showed that HFD decreased the osteogenic differentiation potential of bone marrow-derived MSCs, whereas it increased osteogenic differentiation potential of subcutaneous fat- and patellar fat pad-derived MSCs. In this study, HFD upregulated the expression of osteogenic biomarker in PDLSCs, which may be a cellular response to bone destruction.

PDLSCs also exerts immunomodulatory effects in response to pro-inflammatory stimulus (11, 33). Inflammatory condition increased the expression of VEGF, IL-1β, and IL-6 (34). The impaired PDLSCs may contribute to the disturbance of immune response and accelerate osteoclastogenesis (35). We observed that HFD increased the expression of IL-1β and IL-10 in PDLSCs and activated the inflammation-related p38 and ERK pathways. Notably, MSCs

produce the cytokines and chemokines needed for immunomodulation of inflammatory responses (36). IL-1β is a strong pro-inflammatory cytokine that is closely associated with inflammasomes (37). Previous studies have reported that IL-1β might inhibit osteogenic differentiation (38) and silencing of IL-1β in MSCs may promote osteogenesis (38). TNF-α could inhibit the osteogenic differentiation of bone marrow MSCs (39) and PDLSCs (40); both these findings were observed in this study. IL-10 was reported to promotes bone formation (41), which may be related to the suppression of osteoblast apoptosis and inhibition of osteoclast formation (42). IL-10 has also been shown to promote the osteogenesis of MSCs (43). In the present study, the increased expression of osteogenic biomarkers in PDLSCs derived from the HFD group was consistent with the upregulated expression of IL-10. Furthermore, increased IL-10 expression could activate the ERK1/2 signaling pathway (44), which was consistent with our results. The p38/MAPK signaling pathway is activated in response to inflammation and regulates the differentiation of stem cells (45, 46). Activation of the p38/MAPK signaling pathway may promote the osteogenic differentiation of MSCs (47) and PDLSCs (40). The activation of p38/MAPK signaling pathway in this study was consistent with HFD-induced increase in the expression of osteogenic biomarkers. The present study preliminarily explored the impacts of HFD on the status of PDLSCs, however, further studies are needed to confirm the specific details and mechanism of HFD on the function of PDLSCs.

In conclusion, this study demonstrated that HFD may aggravate alveolar bone loss caused by periodontitis. Compared with the HFD-remodeled periodontal microbiota, the increased expression of IL-1β in PDLSCs may play a more important role in HFD-induced alveolar bone loss. This study may not only help to clarify how HFDs are associated with periodontitis, but also serve as evidence for diet control during periodontal treatment.

ACKNOWLEDGEMENTS

This study was financially supported by the National Natural Science Foundation Project of China (No. 81970939), the Nanjing Clinical Research Center for Oral Diseases (No. 2019060009), and the Talent Foundation project of Nanjing Stomatological Hospital, Medical School of Nanjing University (2017-A2-420).

REFERENCES

1. Borgnakke WS. Does treatment of periodontal disease influence systemic disease? Dent Clin North Am 2015; 59(4):885-917.
2. Abraham S, Premnath A, Arunima PR, Kassim RM. critical appraisal of bidirectional relationship between periodontitis and hyperlipidemia. J Int Soc Prev Community Dent 2019; 9(2):112-8.
3. Bartova J, Sommerova P, Lyuya-Mi Y, et al. Periodontitis as a risk factor of atherosclerosis. J Immunol Res 2014; 2014:636893.
4. Oberti L, Gabrione F, Nardone M, Di Girolamo M. Two-way relationship between diabetes and periodontal disease: a reality or a paradigm?. J Biol Regul Homeost Agents 2019; 33(3 Suppl. 1):153-9.
5. Alakhali MS, Al-Maweri SA, Al-Shamiri HM, Al-Haddad K, Halboub E. The potential association between periodontitis and non-alcoholic fatty liver disease: a systematic review. Clin Oral Investig 2018; 22(9):2965-74.
6. Sangwan A, Tewari S, Singh H, Sharma RK, Narula SC. Periodontal status and hyperlipidemia: statin users versus non-users. J Periodontol 2013; 84(1):3-12.
7. Sayar F, Fallah S, Akhondi N, Jamshidi S. Association of serum lipid indices and statin consumption with periodontal status. Oral Dis 2016; 22(8):775-80.
8. Hajishengallis G, Darveau RP, Curtis MA. The keystone pathogen hypothesis. Nat Rev Microbiol 2012; 10(10):717-25.
9. Danijela M, Krzysztof Marek M, Naohisa W, et al. Periodontal-ligament-derived stem cells exhibit the capacity for long-term survival, self-renewal, and regeneration of multiple tissue types in vivo. Stem Cells Dev 2014; 23(9):1001-11.
10. Nagata M, Iwasaki K, Akazawa K, Komaki M, Yokoyama N, Izumi Y, Morita I. Conditioned medium from periodontal ligament stem cells enhances periodontal regeneration. Tissue Eng Part

A 2017; 23(9-10):367-77.
11. Barrachina L, Remacha AR, Romero A, et al. Priming equine bone marrow derived mesenchymal stem cells (eBM-MSCs) with pro-inflammatory cytokines: implications in immunomodulation-immunogenicity balance, cell viability and differentiation potential. Stem Cells Dev 2017; 26(1):15.
12. Crop MJ, Baan CC, Korevaar SS, et al. Inflammatory conditions affect gene expression and function of human adipose tissue-derived mesenchymal stem cells. Clin Exp Immunol 2010; 162(3):474-86.
13. Ansari S, Chen C, Hasani-Sadrabadi MM, Bo Y, Zadeh HH, Wu BM, Moshaverinia A. Hydrogel elasticity and microarchitecture regulate dental-derived mesenchymal stem cells-host immune system cross-talk. Acta Biomaterialia 2017; 60:181-9.
14. Xiaodong Z, Wenyi Z, Xiaoli L, Wu Z, Yiming L. Interrelationship between diabetes and periodontitis: role of hyperlipidemia. Arch Oral Biol 2015; 60(4):667-74.
15. Zhao D, Liu P, Pan C, Du R, Ping W, Ge J. Bacterial succession and metabolite changes during flax (Linum usitatissimum L.) retting with Bacillus cereus HDYM-02. Sci Rep 2016; 6:31812.
16. Christian Q, Elmar P, Pelin Y, et al. The SILVA ribosomal RNA gene database project: improved data processing and web-based tools. Nucleic Acids Res 2013; 41:590-6.
17. Sun J, Dong Z, Zhang Y, et al. Osthole improves function of periodontitis periodontal ligament stem cells via epigenetic modification in cell sheets engineering. Sci Rep 2017; 7(1):5254.
18. Tominaga N, Nakahara T, Nasu M, Satoh T. Isolation and characterization of epithelial and myogenic cells by "fishing" for the morphologically distinct cell types in rat primary periodontal ligament cultures. Differentiation 2013; 85(3):91-100.
19. Chen S, Lin G, Lei L, et al. Hyperlipidemia modifies innate immune responses to lipopolysaccharide via the TLR-NF-κB signaling pathway. 2013; 36(4):968-76.
20. Zhou X, Zhang W, Liu X, Zhang W, Li Y. Interrelationship between diabetes and periodontitis: role of hyperlipidemia. Arch Oral Biol 2015; 60(4):667-74.
21. Blasco-Baque V, Serino M, Vergnes JN, et al. High-fat diet induces periodontitis in mice through lipopolysaccharides (LPS) receptor signaling: protective action of estrogens. PLoS One 2012; 7(11):e48220.
22. Lei L, Li H, Yan F, Xiao Y. Hyperlipidemia impaired innate immune response to periodontal pathogen porphyromonas gingivalis in apolipoprotein E knockout mice. PLoS One 2013; 8(8):e71849.
23. Branchereau M, Reichardt F, Loubieres P, et al. Periodontal dysbiosis linked to periodontitis is associated with cardiometabolic adaptation to high-fat diet in mice. Am J Physiol Gastrointest Liver Physiol 2016; 310(11):G1091-101.
24. Curtis MA, Diaz PI, Van Dyke TE. The role of the microbiota in periodontal disease. Periodontol 2000 2020; 83(1):14-25.
25. Su Y, Chen C, Guo L, Du J, Li X, Liu Y. Ecological balance of oral microbiota is required to maintain oral mesenchymal stem cell homeostasis. Stem Cells 2018; 36(4):551-61
26. Shi L, Zhao Y, Fei C, et al. Cellular senescence induced by S100A9 in mesenchymal stromal cells through NLRP3 inflammasome activation. Aging (Albany NY) 2019; 11(21):9626-42.
27. Wu W, Fu J, Gu Y, Wei Y, Ma P, Wu J. JAK2/STAT3 regulates estrogen-related senescence of bone marrow stem cells. J Endocrinol 2020; 245(1):141-53.
28. Liu F, Wang ZF, Liu FF, Xu JZ, Liu Q, Lan J. MicroRNA-29a-3p regulates osteoblast differentiation and peri-implant osseointegration in a rat model of hyperlipidemia by modulating Frizzled 4 expression. Hua Xi Kou Qiang Yi Xue Za Zhi 2019; 37(2):200-7.
29. Choudhary D, Adhikary S, Gautam J, et al. Detrimental effects of atherogenic and high fat diet on bone and aortic calcification rescued by an isoflavonoid Caviunin beta-d-glucopyranoside. Biomed Pharmacother 2017; 92:757-71.
30. Qian C, Zhu C, Yu W, Jiang X, Zhang F. High-fat diet/low-dose streptozotocin-induced type 2 diabetes in rats impacts osteogenesis and Wnt signaling in bone marrow stromal cells. PLoS One 2015; 10(8):e0136390.
31. Lv S, Wu L, Cheng P, et al. Correlation of obesity and osteoporosis: Effect of free fatty acids on bone marrow-derived mesenchymal stem cell differentiation. Exp Ther Med 2010; 1(4):603-10.
32. Wu CL, Diekman BO, Jain D, Guilak F. Diet-induced

obesity alters the differentiation potential of stem cells isolated from bone marrow, adipose tissue and infrapatellar fat pad: the effects of free fatty acids. Int J Obes (Lond) 2013; 37(8):1079-87.
33. Barrachina L, Remacha AR, Romero A, et al. Effect of inflammatory environment on equine bone marrow derived mesenchymal stem cells immunogenicity and immunomodulatory properties. Vet Immunol Immunopathol 2016; 171:57-65.
34. Park MJ, Lee SH, Moon SJ, et al. Overexpression of soluble RAGE in mesenchymal stem cells enhances their immunoregulatory potential for cellular therapy in autoimmune arthritis. Sci Rep 2016; 6:35933.
35. Liu D, Xu J, Liu O, et al. Mesenchymal stem cells derived from inflamed periodontal ligaments exhibit impaired immunomodulation. J Clin Periodontol 2012;39(12):1174-82
36. Kovach TK, Dighe AS, Lobo PI, Cui Q. Interactions between MSCs and immune cells: implications for bone healing. J Immunol Res 2015; 2015(248):1-17.
37. Latz E, Xiao TS, Stutz A. Activation and regulation of the inflammasomes. Nat Rev Immunol 2013; 13(6):397-411.
38. Hu K, Jiang W, Sun H, Li Z, Rong G, Yin Z. Long noncoding RNA ZBED3-AS1 induces the differentiation of mesenchymal stem cells and enhances bone regeneration by repressing IL-1beta via Wnt/beta-catenin signaling pathway. J Cell Physiol 2019; 234(10):17863-75.
39. Wang N, Zhou Z, Wu T, Liu W, Yin P, Pan C, Yu X. TNF-alpha-induced NF-kappaB activation upregulates microRNA-150-3p and inhibits osteogenesis of mesenchymal stem cells by targeting beta-catenin. Open Biol 2016; 6(3):150258.
40. Yan W, Cao Y, Yang H, et al. CB1 enhanced the osteo/dentinogenic differentiation ability of periodontal ligament stem cells via p38 MAPK and JNK in an inflammatory environment. Cell Prolif 2019:e12691.
41. Cui K, Chen Y, Zhong H, Wang N, Zhou L, Jiang F. Transplantation of IL-10-Overexpressing Bone Marrow-Derived Mesenchymal Stem Cells Ameliorates Diabetic-Induced Impaired Fracture Healing in Mice. Cell Mol Bioeng 2020; 13(2):155-63.
42. Yi L, Li Z, Jiang H, Cao Z, Liu J, Zhang X. Gene Modification of Transforming Growth Factor beta (TGF-beta) and Interleukin 10 (IL-10) in suppressing Mt sonicate induced osteoclast formation and bone absorption. Med Sci Monit 2018; 24:5200-7.
43. Mahon OR, Browe DC, Gonzalez-Fernandez T, et al. Nano-particle mediated M2 macrophage polarization enhances bone formation and MSC osteogenesis in an IL-10 dependent manner. Biomaterials 2020; 239:119833.
44. Yu ZY, Ma D, He ZC, et al. Heme oxygenase-1 protects bone marrow mesenchymal stem cells from iron overload through decreasing reactive oxygen species and promoting IL-10 generation. Exp Cell Res 2018; 362(1):28-42.
45. Ma N, Teng X, Zheng Q, Chen P. The regulatory mechanism of p38/MAPK in the chondrogenic differentiation from bone marrow mesenchymal stem cells. J Orthop Surg Res 2019; 14(1):434.
46. Bost F, Aouadi M, Caron L, Binetruy B. The role of MAPKs in adipocyte differentiation and obesity. Biochimie 2005; 87(1):51-6.
47. Xu FF, Zhu H, Li XM, et al. Intercellular adhesion molecule-1 inhibits osteogenic differentiation of mesenchymal stem cells and impairs bio-scaffold-mediated bone regeneration in vivo. Tissue Eng Part A 2014; 20(19-20):2768-82.

LETTER TO THE EDITOR

Glenohumeral osteoarthritis treatment with a single hyaluronic acid administration: clinical outcomes

G. Di Giacomo and N. de Gasperis

Dipartimento di Ortopedia, Concordia Hospital for "Special Surgery", Rome, Italy

Received July 17, 2020 – Accepted February 16, 2021

To the Editor,

Glenohumeral osteoarthritis (OA) is a very common joint disease characterized by pain and functional limitation, which, particularly in the elderly, may compromise overall health and quality of life. The treatment of this pathology generally includes the use of oral analgesics, physical therapy and intra-articular injections with corticosteroids or hyaluronic acid (HA) aimed at reducing the pain and restoring the range of motion (ROM) of the shoulder, but no standardized protocol is available in clinical practice and literature data are contrasting (1-3). Analgesics and non-steroidal anti-inflammatory drugs are not always effective and may be associated with substantial side effects, particularly in elderly patients (4), whereas intra-articular injections of HA have gained consensus in the treatment of OA thanks to their outcomes in pain reduction and joint function improvement, without relevant side effects (5-7). HA therapeutic activity has been attributed to its high viscosity, which has a shielding effect on the articular surface (visco-supplementation), whereas the long-term efficacy is better explained by normalization of endogenous HA synthesis and chondroprotection (visco-induction) (8). The aim of this randomized, prospective, open-label clinical study was to assess the efficacy in terms of improvement in functional status, daily activities and pain, and safety of a single administration of high molecular weight (HMW) HA (HyalOne® 60mg/4ml) combined with a physical exercise program (PEP) in patients suffering from mild to moderate glenohumeral OA (degree II and III according to the Kellgren-Lawrence classification), and to compare these results with a control group of patients treated with the only PEP.

MATERIALS AND METHODS

In this open-label study, 60 consecutive patients with glenohumeral OA degree II or III were prospectively enrolled in our clinic from September 2018 to March 2019. The study was approved by the Ethics Committee of the Concordia Hospital for Special Surgery Rome (approval n° 4/2018) and performed according to ISO and the Declaration of Helsinki. Informed written consent was obtained from each patients prior to the inclusion in the study. All patients were carefully evaluated and selected based on inclusion and exclusion criteria. As per inclusion criteria patients with good general conditions and glenohumeral OA (KL degree II or III) quantified through the standard X-ray views were included, while patients with concomitant rotator cuff lesions evaluated through MRI, previous shoulder surgery, previous humeral head fracture or shoulder trauma, metabolic diseases, poor general conditions and OA degree IV with surgical indications (shoulder arthroplasty) were excluded from the study.

Key words: hyaluronic acid; glenohumeral osteoarthritis; shoulder

Corresponding Author:
Nicola de Gasperis MD,
Dipartimento di Ortopedia,
Concordia Hospital for "Special Surgery",
Via delle Sette Chiese 90, 00145 Rome, Italy
Tel.: +39 06 5126439
e-mail: nicola.degasperis@gmail.com

0393-974X (2021)
Copyright © by BIOLIFE, s.a.s.
This publication and/or article is for individual use only and may not be further reproduced without written permission from the copyright holder.
Unauthorized reproduction may result in financial and other penalties
DISCLOSURE: ALL AUTHORS REPORT NO CONFLICTS OF INTEREST RELEVANT TO THIS ARTICLE.

The "Constant score" functional scoring systems and ROM were calculated for all 60 patients before treatment. Patients were then randomly allocated to two different homogeneous groups, 30 patients in the treatment group and 30 patients in the control group. Of the 30 patients allocated to the treatment group 21 were male and 9 female. The mean age of the patients was 67.1 years (range 55 to 83 years). The dominant side was treated in 22 patients (73.3%). All patients referred to have had shoulder pain for many months (average 10.3 months); they all had moderate-to-severe pain (17 patients [56.7%] had moderate pain and 13 [43.3%] severe pain). All the patients had a reduced ROM: mean active forward elevation was 136.2°±12.3°, mean external rotation with the arm at the side was 21.5°±5.7°. The mean Constant Score was 69.3±4.2.

Of the 30 patients allocated to the control group 18 were male and 12 female. The mean age of the patients was 64.2 years (range 52 to 81 years). The dominant side was treated in 23 patients (76.7%). All patients had shoulder pain for several months (average 11.2 months); 2 of the patients (6.7%) had mild pain, 18 (60%) had moderate pain and 10 (33.3%) severe pain. All the patients had a reduced ROM: mean active forward elevation was 138.8°±12.2°, mean external rotation with the arm at the side was 22°±3.6°. The mean Constant Score was 69.9±4.4.

Patients in the treatment group received a single intra-articular injection with a HMW HA (HyalOne® 60mg/4ml 1.500-2.000.000 Da) in combination with PEP. Patients in the control group were treated with PEP only. PEP program for both groups was performed with a professional therapist for a 3months duration with a frequency of 3 days every week. The PEP program consisted of passive capsular stretching for recovery of ROM, isometric exercises for deltoid, rotator cuff and scapulo-thoracic muscles, isotonic exercises for scapulo-thoracic muscles (closed kinetic chain), and hydrokinesis therapy. Study follow-up examination was performed after 3 months and 6 months from the beginning of the therapy for both groups.

At the study follow-up visits the Constant Score was analyzed to recorder functional status, daily activities and pain of the treated shoulder and the ROM values of elevation and external rotation of the shoulder were collected. A safety evaluation of intra-articular injection with HyalOne® 60mg/4ml was further performed collecting the adverse events (AEs) that had occurred during the entire duration of the study.

Statistical analysis was performed by STATISTICA 10 software (StatSoft Inc, 1984-2011). Database was constituted of 60 patients with glenohumeral OA defined by the ROM (forward elevation and external rotation) and by the Constant score functional scoring systems (scale 0-100). The distribution of subjects along the three variables (forward elevation, external rotation and Constant score) before the treatment, verged on normality ($p>0.05$; Shapiro-Wilk = 0.974, 0.985 and 0.964, respectively). Therefore, patients were divided into two different groups of treatment and were evaluated before and after the two different kinds of treatments. Sample size was calculated setting the p value at <0.05 and the minimum power of the study at 80%. Considering a mean difference of 5.5 points on Constant score and a standard deviation of 7.5 between the treatment group and the control group, it was estimated that 30 patients per arm had to be recruited. Variables were considered as continuous and a oneway ANOVA for repeated measures was performed. Post-hoc tests (Tukey's test; $p<0.05$) were scheduled between the two groups and within the same group.

RESULTS

Patients were randomized in two different groups and were evaluated before and after the treatment. Means and standard deviations of the outcome measures are reported in Table I. At the three month follow-up, the mean active forward elevation was 159.6°±8.9° (gain of 23.8°), and the mean external rotation with the arm at the side was 28.5°±3.0° (gain of 7°) for patients belonging to the treatment group. The patients also showed a relevant reduction in level of pain and a significant improvement in daily activities ($p<0.05$). The mean Constant score after the treatment with HyalOne® 60mg/4ml increased by 15.8 points to a mean value (±SD) of 85.1±3.4 points (Table I). For patients belonging to the control group the mean active forward elevation was 149.5°±9.7 (gain of 10.7°), and the mean external rotation with the arm at the side was 27°±2.2 (gain of 5°). The patients also showed a lower level of pain and moderate improvement in the daily activities. The mean Constant score after the only PEP was

81.5±3.5 points, 11.6 points more than the initial score (Table I).

At the six month follow-up, the mean active forward elevation was 156.6°±8.8° (gain of 20.4° from baseline), and the mean external rotation with the arm at the side was 26.9°±3.1° (gain of 5.4° from baseline) for patients belonging to the treatment group. The patients also showed a long-lasting pain relief (p<0.05). The mean Constant score after the treatment with HyalOne® 60mg/4ml was 82.7±4.5 points, 13.4 points more than the initial score (Table I). In the control group the mean active forward elevation was 143.8°±10.5° (gain of 5°), and the mean external rotation with the arm at the side was 22.9°±2.8° (gain of 0.9°). This group also had no long-lasting reduction in level of pain. The mean Constant score after PEP alone was 78.8±3.1 points, 8.9 points more than the initial score (Table I).

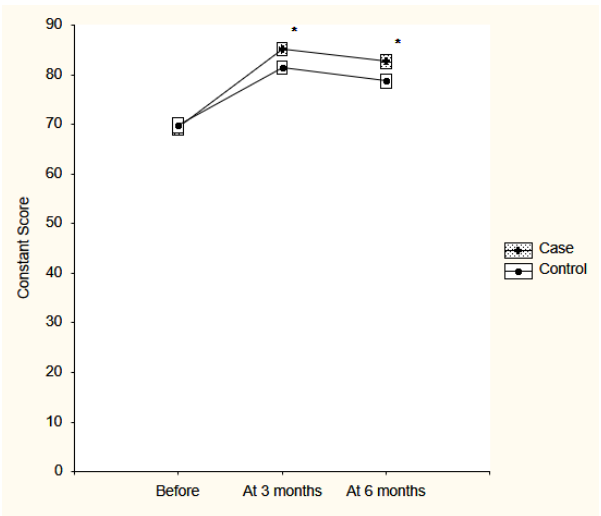


Fig. 1. *Constant score means for treatment and control group at baseline and after 3 and 6 months. Boxes indicate the confidence interval (95%). *p<0.05 (Post Hoc Tukey's Test).*

The ANOVA for repeated measures for the Constant score revealed a significant effect of the treatment ($F_{1,58}$= 7.080; p<0.05) and as function of the length of this ($F_{2,116}$= 19.310; p<0.05). As shown in Fig. 1, there was no difference between groups at baseline in the Constant score (69.3±4.2 and 69.9±4.4 for the treatment group and control group, respectively), while there was a significant effect at three months (85.1±3.4 and 81.5±3.5 for the treatment group and control group, respectively) and at six months after the treatment (82.7±4.5 and 78.8±3.1 for treatment and control group, respectively).

Similar results were obtained for the forward elevation movement. In this case, the ANOVA for repeated measure showed a significant effect of the treatment alone ($F_{1,58}$= 7.120; p<0.05) and over time between groups ($F_{2,116}$= 48.870; p<0.05). As shown in Fig. 2, there was no difference at baseline between the two groups (136.2±12.3 and 138.8±12.2 for treatment and control groups, respectively), while

Table I. *Means and standard deviation for treatment and control group, at baseline and after 3 and 6 months of therapy.*

	Baseline	3 months	6 months
Constant score			
Treatment	69.3± 4.2	85.1±3.4	82.7±4.5
Control	69.9±4.4	81.5±3.5	78.8±3.1
Elevation			
Treatment	136.2±12.3	159.6±8.9	156.6±8.8
Control	138.8±12.2	149.5±9.7	143.8±10.5
External Rotation			
Treatment	21.5±5.7	28.5±3.0	26.9±3.1
Control	22.0±3.6	27.0±2.2	22.9±2.8

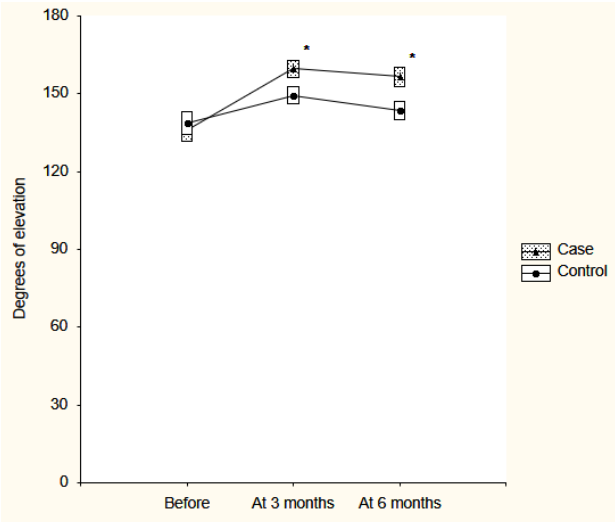


Fig. 2. *Means of the elevation's grades for treatment and control group at baseline and after 3 and 6 months. Boxes indicate the confidence interval (95%). *p<0.05 (Post Hoc Tukey's Test).*

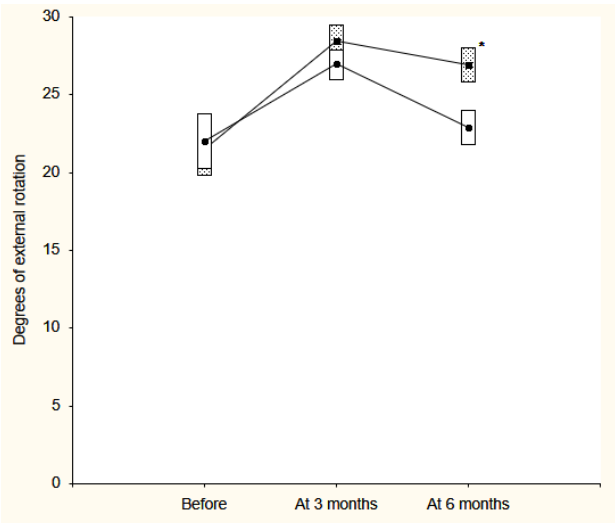


Fig. 3. *Means of the external rotation's grades for treatment and control group at baseline and after 3 and 6 months. Boxes indicate the confidence interval (95%). *p<0.05 (Post Hoc Tukey's Test).*

there was a significant difference between groups at three months (159.6±8.9 for the treatment group and 149.5±9.7 for the control group, respectively) and at six months (156.6±8.8 for the treatment group and 143.8±10.5 for the control group, respectively).

Evaluation of the external rotation movement, also showed a significant effect of the treatment over time ($F_{2,116}$= 28.006; p<0.05). In particular, there was a significant difference at six months after the treatment (26.9±3.1 and 22.9±2.8 for the treatment group and the control group, respectively). The effect is reported in Fig. 3.

No side effects occurred in patients treated with HyalOne® 60mg/4ml intra-articular injection.

DISCUSSION

The aim of this study was to evaluate the effects of the treatment with a single intra-articular injections of HMW HA combined with PEP in patients affected by shoulder OA degree II or III. We evaluated two different kind of therapies: a single intra-articular injection with a HMW HA (HyalOne® 60mg/4ml) associated with PEP *versus* PEP alone. The role of HA in patients affected by shoulder OA is controversial in literature (9-12). Patients treated with a single HyalOne® 60mg/4ml intra-articular injection in addition to PEP demonstrated to have a significantly higher decrease of shoulder pain in comparison to patients of the control group at the 3 and 6 month follow-ups (p<0.05). This result supports the concept that these patients benefit from a greater and long-lasting positive effect compared to patients who underwent PEP alone. Moreover, this study reported a significant long-term improvement in ROM between the two groups (p<0.05) and in daily activities. These results could be probably associated to the large reduction of shoulder pain. This study has some limitations. The first limitation is the possible concomitant inflammation of the long head of the biceps or the rotator cuff, very frequent in patients affected by glenohumeral OA, that could influence the results of the treatment in terms of pain. In addition, the second limitation is that we did not consider the scapular morphology that could partially influence the shoulder ROM. The present study demonstrates that patients affected by mild-to-moderate glenohumeral OA (KL degree II-III) treated with a single injection of HA (HyalOne® 60mg/4ml) combined with a physical exercise program had better results and longer duration, in terms of reduction of shoulder pain and improvement in daily activities, compared to patients treated with physical therapy alone. The great advantage of HyalOne® 60mg/4ml is also represented by the

single administration. Further studies are needed to better assess a standardized conservative protocol of treatment for shoulder OA.

REFERENCES

1. Andrews JR. Diagnosis and treatment of chronic painful shoulder: review of nonsurgical interventions. Arthroscopy 2005; 21:333-47.
2. Blaine T, Moskowitz R, Udell J, et al. Treatment of persistent shoulder pain with sodium hyaluronate: a randomized, controlled trial. J Bone Joint Surg Am 2008; 90:970-9.
3. Brander VA, Gomberawalla A, Chambers M, Bowen M, Nuber G. Efficacy and safety of hylan G-F 20 for symptomatic glenohumeral osteoarthritis: a prospective, pilot study. PM R 2010; 2:259-67.
4. American College of Rheumatology. Recommendations for the medical management of osteoarthritis of the hip and knee: 2000 update. American College of Rheumatology Subcommittee on Osteoarthritis Guidelines. Arthritis Rheum 2000; 43:1905-15.
5. Iannitti T, Rottigni V, Palmieri B. A pilot study to compare two different hyaluronic acid compounds for treatment of knee osteoarthritis. Int J Immunopathol Pharmacol 2012; 25:1093-8.
6. Henrotin Y, Raman R, Richette P, et al. Consensus statement on viscosupplementation with hyaluronic acid for the management of osteoarthritis. Semin Arthritis Rheum 2015; 45:140-9.
7. Maheu E, Rannou F. Reginster JY. Efficacy and safety of hyaluronic acid in the management of osteoarthritis: Evidence from real-life setting trials and surveys. Semin Arthritis Rheum 2016; 45(S4):S28-33.
8. Abate M, Pulcini D, Di Iorio A, Schiavone C. Viscosupplementation with intra-articular hyaluronic acid for treatment of osteoarthritis in the elderly. Curr Pharm Des 2010; 16:631-40.
9. Di Giacomo G, de Gasperis N. Hyaluronic acid intra-articular injections in patients affected by moderate to severe glenohumeral osteoarthritis: a prospective randomized study. Joints 2017; 5:138-42.
10. Di Giacomo G, De Gasperis N. The role of hyaluronic acid in patients affected by glenohumeral osteoarthritis. J Biol Regul Homeost Agents 2015; 29:945-51.
11. Frizziero A, Vittadini F, Oliva F, et al. I.S.Mu.L.T. hyaluronic acid injections in musculoskeletal disorders guidelines. Muscle, Ligaments and Tendons Journal 2018; 8(3):364-98.
12. Colen S, Geervliet P, Haverkamp D, Van Den Bekerom MP. Intra-articular infiltration therapy for patients with glenohumeral osteoarthritis: A systematic review of the literature. Int J Shoulder Surg 2014; 8:114-21.

LETTER TO THE EDITOR

Effects of kangaroo mother care on immune function and prognosis of premature infants in the neonatal intensive care unit

N. Yao[1*], J. Xie[1*], Z-Y. Li[1] , J. Zheng[1], A. Jiang[1], Y-F. Wang[1] and M-W. Liu[2]

[1]Department of Pediatrics, The First People's Hospital of Kunming, Xishan District, Kunming, China; [2]Department of Department of Emergency Medicine, the First Affiliated Hospital of Kunming Medical University, Wuhua District, Kunming, China

Received January 25, 2021 – Accepted February 16, 2021

[*]These Authors contributed equally to this work.

To the Editor,

Kangaroo mother care (KMC), also known as skin-to-skin contact care, is a way of caring for infants by kangaroos or marsupials. The newborn baby is placed on the mother's chest to keep it in contact with the mother's skin, which provides warmth and a sense of security (1). As early as 2003, the World Health Organization (WHO) promulgated the KMC implementation guidelines, which suggest that KMC should start after the baby is born up to 40 weeks of gestational age or when the baby's weight reaches 2500 g (2). According to the WHO report, 15 million premature infants are born every year globally, and the incidence of premature infants in China ranks second in the world (2). KMC is easy to implement and has obvious effects; it can enhance the physical fitness and immunity status of premature infants (3-6). Studies have shown that the immunity status of premature infants is lower than that of full-term infants, especially in the neonatal intensive care unit (NICU), and they are more prone to infection, which could increase their hospitalization time (7, 8). In this study, 140 cases of premature infants hospitalized in the NICU of The First People's Hospital of Kunming between April 2015 and October 2019 were taken as the study subjects to observe whether KMC could improve physical fitness, immune status, and milk intake of premature infants in NICU and whether KMC could reduce their infection status and hospitalization expenses.

MATERIALS AND METHODS

General information

From April 2015 to October 2019, 140 premature infants were hospitalized in the NICU of The First Hospital of Kunming for inpatient observation and discharge follow-up. The subjects included 75 males and 65 females. According to the time of admission, they were divided into two groups, 70 cases in the conventional nursing group (Control group), and 70 cases in the KMC group. Inclusion criteria: *Premature infants*: gestational age at birth approximately 31–33^{+} 6 weeks; birth weight ≥1500 g; single or twins; stable hemodynamic status; and with at least 4 heel blood samples expected within 2 weeks. *Mother*: age ≥ 18 years; agreement to participate in this study and sign the informed consent form; and with good communication skills. Exclusion criteria: *Premature infants*: suffering from severe congenital diseases and malformations; suffering from neurological diseases or

Key words: kangaroo mother care (KMC), T cell subsets, Infection, hospitalization expenses

Corresponding Author:
Dr Ming-wei Liu,
Department of Emergency Medicine,
the First Affiliated Hospital of Kunming Medical University,
295 Xichang Road, Wuhua District,
Kunming, 650032, China
e-mail: lmw2004210@163.com

0393-974X (2021)
Copyright © by BIOLIFE, s.a.s.
This publication and/or article is for individual use only and may not be further reproduced without written permission from the copyright holder.
Unauthorized reproduction may result in financial and other penalties
DISCLOSURE: ALL AUTHORS REPORT NO CONFLICTS OF INTEREST RELEVANT TO THIS ARTICLE.

having obvious neurological symptoms; administered with analgesics, tranquilizers, or muscle relaxants within 24 hours before the outcome index measurement; requiring intubation and mechanical ventilation; and with heel tissue damage or with signs of inflammation. *Mother*: refused to participate in this study; and with critical illness, infectious disease, or mental illness.

The study was approved by the First People's Hospital of Kunming Research Ethics Boards, and written informed consent for participation in the study was obtained from parents or relatives of participants.

Nursing methods

Control group: Conventional nursing methods were used as previously described (9). *KMC Group***:** In the implementation of KMC, the newborn only wears a diaper and lies prone between the mother's bare breasts. The mother lies on the bed inclined at an angle of 45–60°. The specific operation of KMC is shown in the literature (10).

*Observation indicators***:** After 28 days of nursing, the body mass and length, milk intake, leukocytes and neutrophils, hospitalization time, hospitalization expenses, infection rate, and mortality of premature infants were measured for the two groups of children. Their $CD3^+$, $CD4^+$, $CD8^+$, $CD4^+/CD8^+$ and $CD19^+$ indexes were measured by flow cytometry (Abcam, Cambridge, MA, USA), their peripheral blood tumor necrosis factor-α (TNF-α), interleukin (IL)-6, C-reaction protein (CRP), IL-4, IL-2, and interferon (IFN)-γ indexes were measured by ELISA (R&D Systems, Inc. Minneapolis, MN, USA), all according to the manufacturer's instructions.

Statistical analysis

The measurement data were described by the mean± standard deviation, and the group *t*-test was used for the comparison between groups. The number of cases and percentage [n(%)] were used for the description of count data, and the *Chi*-squared test was used for comparison between groups. $P<0.05$ was used for statistical differences.

RESULTS

Results of KMC treatment after 28 days

After 28 days of KMC treatment, the head circumference, body length, body weight growth, and milk intake of the newborns in the KMC group were significantly higher than those in the control group ($P<0.05$) (Table I). The total number of white blood cells, TNF-α, CRP, and IL-6 in the KMC group were significantly lower than those of the control group ($P < 0.05$) (Table II). The values of T-cell subsets, IFN-γ, IL-4, and IFN-γ/IL-4 in the KMC group were significantly higher than those in the control group, and the differences were statistically significant ($P < 0.05$) (Table III).

The incidence of neonatal necrotizing

Table I. *Influence of KMC on the body mass and length of premature infants*

Groups	Weight gain (kg)	Height growth (cm)	Head circumference growth (cm)	Milk intake comparison (ml/d)
Conventional nursing group	1.02± 0.16	5.33±1.29	3.17±1.65	211.38±30.62
Kangaroo Mother Care (KMC)group	2.14±0.47*	6.37±2.08*	4.35±1.22*	241.12±31.32*

*After 28 days of KMC treatment, the head circumference, body length, body mass growth, and milk intake of the newborns in the KMC group and control group were measured. The results were expressed as mean ± standard deviation. Compared with control group: *P< 005.*

Table II. *Comparison of total number of leukocytes, TNF-α, CRP, and IL-6 in peripheral blood between the two groups before and after the study*

Groups	TNF-α (mg/L)	TWBC ($\times 10^9$/L)	CRP (mg/L)	IL-6 (mg/L)
Conventional nursing group	57.42±17.62	11.34±4.45	17.65±4.72	67.38±17.62
Kangaroo Mother Care (KMC) group	38.42±9.62*	7.78±2.54*	14.32±3.65*	41.12±14.32*

*After 28 days of KMC treatment, the total number of peripheral blood leukocytes, TNF-α, CRP, and IL-6 of the two groups were measured before and after the test, and the results were expressed as mean ± standard deviation. Compared with control group: *P<0 05.*

Table III. *Comparison of T cell subsets expression levels, IFN-γ and IL-4, of the two groups*

Project	Conventional nursing group	Kangaroo Mother Care (KMC)group
Interferon-γ (pg/ml)	376.75±97.98	516.79±115.67*
Interleukin 4 (pg/ml)	643.87±138.64	528.67±105.90*
Interleukin 2 (pg/ml)	109.18±39.48	167.54±51.84*
IFN-γ/IL-4	0.73±0.27	0.91±0.34*
$CD3^+$ (%)	49.73±6.89	66.87±8.50*
$CD4^+$ (%)	40.6±5.65	50.70±7.98*
$CD8^+$ (%)	29.3±3.72	25.67±3.65*
$CD4^+/CD8^+$	1.23±0.34	2.62±0.74*
$CD16^+CD56^+$ (%)	12.40±1.76	19.6±1.54*
$CD19^+$ (%)	6.67±0.71	8.54±0.94*

*After 28 days of KMC treatment, the $CD3^+$, $CD4^+$, $CD8^+$, $CD4^+/CD8^+$, and $CD19^+$ levels of the peripheral blood T cell subsets of the two groups were measured by flow cytometry, and the levels of IFN-γ, IL-4, and IFN-γ/IL-4 in peripheral blood were measured by ELISA. The results are expressed as mean ± standard deviation. Compared with control group: *P<00.*

enterocolitis (NEC), sepsis, pneumonia, feeding intolerance, and other complications in the KMC group were significantly lower than those in the control group (1.35% *vs* 4%, p=0.02; 9% *vs* 17.65%, P=0.034; 14% *vs* 20.65%, P=0.037; 34% *vs* 51.5%, P=0.007). Statistical differences were found between the groups (Table IV).

The hospitalization days of the KMC group were less than those of the control group, and the average discharge weight and weight gain of premature infants were higher than those of the control group, with significant differences (P < 0.05) (Table V).

DISCUSSION

In the current study, premature infants in the NICU showed reduced levels of $CD3^+$, $CD4^+$, $CD8^+$, $CD4^+/CD8^+$, and $CD19^+$, indicating that their cellular immune function was low. KMC can increase the breast milk intake of premature infants. Through the

Table IV. *Comparison of infection rate and mortality rate of premature infants*

Groups	Complications					Complication rate	Fatality rate
	NEC	Septicemia	Pneumonia	Feeding intolerance	Skin ulceration or swelling		
Conventional nursing group	3 (4)	14 (17.65)	16 (20.65)	41 (51.5)	3 (4)	7 (21.54)	1 (2.92)
Kangaroo Mother Care (KMC) group	1 (1.35)*	7 (9)*	11 (14)*	27 (34)*	0 (0.00)*	1 (1.35)*	0 (0.00)*

*After 28 days of KMC treatment, the incidence of neonatal NEC, sepsis, pneumonia, and feeding intolerance complications in the KMC group were measured. The results were expressed as mean ± standard deviation. Compared with control group: *P < 0.05*

Table V. *Comparison of length of hospitalization and reduction of hospital expenses of premature infants*

Project	Conventional nursing group	Kangaroo Mother Care (KMC)group
Hospitalization days (d)	44.5±10.8	40.3±12.8*
Hospitalization expenses (w)	7.74±2.75	5.14±1.78*

*After 28 days of KMC treatment, the length of hospitalization of the newborn and the reduction of hospitalization expenses were determined, and the results were expressed as mean ± standard deviation. Compared with control group: *P < 0.05.*

detection of peripheral blood T lymphocyte subsets, the immunosuppression status of premature infants in the KMC group was improved, and the improved levels of T cell subsets, $CD3^+$, $CD4^+$, $CD4^+/CD8^+$, $CD16^+$, $CD56^+$, and $CD19^+$ in the KMC group were significantly higher than those of conventional nursing. The results suggest that KMC can increase the cellular immunity of premature infants. The conventional nursing group showed a decrease in Th1/Th2, IFN-γ, and IFN-γ/IL-4, and a decrease in their immune functions. KMC can increase the levels of IFN-γ and IFN-γ/IL-4 in peripheral blood of premature infants. Compared with conventional nursing, KMC can significantly increase the cellular immune function of premature infants. In the present study, premature infants in the NICU had a reduced level of IL-2 secretion, and their immunity was also low. KMC can increase the body's secretion of IL-2, which can improve the immunodeficiency of premature infants in the NICU. After KMC treatment, the incidence of complications, such as sepsis, pneumonia, and feeding intolerance, in premature infants was significantly reduced, and the total number of peripheral blood leukocytes, TNF-α, CRP, and IL-6 values were also reduced, thereby decreasing their hospitalization time, reducing their hospitalization expenses, and significantly decreasing their mortality rate.

Based on the above studies, early administration of KMC to premature infants in NICU can promote the growth and development, increase immunity, reduce mortality and infection rate, decrease hospitalization time, and reduce hospitalization expenses.

ACKNOWLEDGEMENTS

This research received funding via a grant provided by the National Natural Science Foundation(Grant No. 81960350), Kunming City Health Science and Technology Talent Training Project and Technical Center Construction Project(Grant No. 2020-SW (Technical)-05) and Kunming Science and Technology Bureau (Grant No. 2020-14-04-112). The authors are grateful for the excellent technical

assistance provided by the medical and nursing staff of our hospital's Pediatrics department.

REFERENCES

1. Dawar R, Nangia S, Thukral A, et al. Factors impacting practice of home kangaroo mother care with low birth weight infants following hospital discharge. J Trop Pediatr 2019; 65(6):561-68.
2. Chan GJ, Valsangkar B, Kajeepeta S, Boundy EO, Wall S. What is kangaroo mother care? Systematic review of the literature. J Glob Health 2016; 6(1):010701.
3. Shah RK, Sainju NK, Joshi SK. knowledge, attitude and practice towards kangaroo mother care. J Nepal Health Res Counc 2018; 15(3):275-81.
4. Charpak N, Tessier R, Ruiz JG, et al. Twenty-year follow-up of kangaroo mother care versus traditional care. Pediatrics 2017; 139(1):e20162063.
5. Taneja S, Sinha B, Upadhyay RP, Mazumder S, Sommerfelt H, Martines J, Dalpath SK, Gupta R, Kariger P, Bahl R, Bhandari N, Dua T; ciKMC development study group. Community initiated kangaroo mother care and early child development in low birth weight infants in India-a randomized controlled trial. BMC Pediatr 2020; 20(1):150.
6. Bigelow AE, Power M. Mother-infant skin-to-skin contact: short- and long-term effects for mothers and their children born full-term. Front Psychol 2020; 11:1921.
7. Mazumder S, Taneja S, Dalpath SK, et al. Impact of community-initiated kangaroo mother care on survival of low birth weight infants: study protocol for a randomized controlled trial. Trials 2017; 18(1):262.
8. Kadambari S, Whittaker E, Lyall H Postnatally acquired cytomegalovirus infection in extremely premature infants: how best to manage? Arch Dis Child Fetal Neonatal Ed 2020; 105(3):334-39.
9. Ortega Barco MA, Muñoz de Rodríguez L Evaluation of the nursing care offered during the parturition process. Controlled clinical trial of an intervention based on swanson's theory of caring versus conventional care. Invest Educ Enferm 2018; 36(1):e05.
10. Yilmaz F, Küçükoğlu S, Aytekin Özdemir A, Oğul T, Aşki N. The effect of kangaroo mother care, provided in the early postpartum period, on the breastfeeding self-efficacy level of mothers and the perceived insufficient milk supply. J Perinat Neonatal Nurs 2020; 34(1):80-87.

LETTER TO THE EDITOR

IgE reactivity to house dust mite allergen components in sensitized asymptomatic subjects: a role for Der p 20

A. Conti[1], G.J. Burastero[1], B.J. Hales[2], D. Breda[1], M. Alessio[1] and S.E. Burastero[3]

[1]Proteome Biochemistry, IRCCS - San Raffaele Scientific Institute, Milan, Italy; [2]Telethon Kids Institute, Center for Child Health Research, University of Western Australia, Perth, Australia; [3]Cellular and Molecular Allergology Unit, IRCCS - San Raffaele Hospital, Milan Italy

Received January 11, 2021 – Accepted March 1, 2021

To the Editor,

Whether the presence of allergen specific IgE translates into clinically significant symptoms and signs of allergy depends on the interplay of multiple factors. These include genetics, the ratio of total versus allergen-specific IgE, epitope-specificity and clonality of IgE (1) and IgE sialylation (2). The balance of T regulatory cells (Treg) and Th1/Th2 cells, the polymorphisms of the high affinity receptor for IgE (Fc-epsilon RI) and other factors regulating the activation of Fc epsilon RI-bearing cells may also play relevant roles. In this scenario, component-resolved diagnosis (CRD) may help clinicians in distinguishing between symptomatic and asymptomatic sensitized patients, particularly in the case of house dust mite allergy (3). In patients with house dust mite sensitization, different patterns of reactivity to mite allergen components have been reported (4) and polysensitization to multiple house dust mite (HDM) allergens have been variably correlated with the allergic phenotype (5).

Here, we analysed IgE reactivity to HDM allergens available to the clinical lab (Der p 1, Der p 2, Der p 10, Der p 23) in a cohort of patients with a positive prick test to HDM, who did not report symptoms of respiratory allergic rhinitis triggered by environmental house dust. HDM-sensitized patients who experienced allergic rhinitis and/or conjunctivitis and/or asthma when environmentally exposed to house dust served as controls. In one patient IgE did not react to any of these components and IgE to Der p 20 was the only sensitizing allergen. Reactivity to Der p 20 was compared in symptomatic versus asymptomatic subjects.

MATERIALS AND METHODS

This is a retrospective, observational study based on electronic records of patients in the outpatient Allergology clinic of the San Raffaele Hospital, Milan, filed between January 2018 and December 2019 during routine clinical activity. All patients included in the analysis performed prick test with a standard panel of inhalant allergens according to GA2LEN recommendations (6). Reagents for prick testing were from ALK Abello (Horsholm, DK). Answers to questions about circumstances when patients observed symptoms of rhinitis (indicated as sneezing, rhinorrea and/or nasal occlusion), if any, were recorded during the collection of the clinical history. Evidence of correlation between symptoms and positive skin prick test (SPT) to tested inhalant allergens was methodically registered.

Key words: allergy; component resolved diagnosis; allergen sensitization; house dust mite proteome

Corresponding Author:
Dr Samuele E. Burastero,
San Raffaele Scientific Institute,
Division of Immunology, Transplantation and Infectious Diseases,
58, via Olgettina, Milano, MI, 20132, Italy
Tel.: +39 0226434730
e-mail: burastero.samuele@hsr.it

0393-974X (2021)
Copyright © by BIOLIFE, s.a.s.
This publication and/or article is for individual use only and may not be further reproduced without written permission from the copyright holder.
Unauthorized reproduction may result in financial and other penalties
DISCLOSURE: ALL AUTHORS REPORT NO CONFLICTS OF INTEREST RELEVANT TO THIS ARTICLE.

Sixty-two subjects with a positive SPT to *D. pteronyssinus* and/or *D. farinae* extract were preliminarily identified. They were assigned to the symptomatic or asymptomatic group based on their positive or negative answer to specific questions about the elicitation of nasal symptoms (sneezing, rhinorrea or nasal occlusion), ocular symptoms (itchy eye, red eyes, lachrymation) and/or asthma symptoms (cough, dyspnoea, wheezing) in the presence of house dust in an indoor environment.

The following exclusion criteria were applied: urticaria, atopic dermatitis, allergen-specific immunotherapy in the previous 5 years, co-sensitization to perennial and/or indoor allergens other than HDM (animal dander, Alternaria, pellitory). Seventeen patients were excluded due to allergen-specific immunotherapy in the previous 5 years (7 patients) or sensitization to perennial and/or indoor sensitizing allergens other than HDM (10 patients). Based on these criteria, thirty patients were provisionally allocated to the symptomatic group and 15 to the asymptomatic group, respectively. These subjects were re-contacted by telephone to obtain their consent to participate anonymously to this study. In case this was granted, patients were attributed consecutive number identification codes and asked to confirm the answers they gave to questions related to the elicitation of symptoms in the presence of house dust within indoor environment. Twelve patients who could be re-contacted and confirmed the correlation of symptoms with exposure to house dust were allocated to the symptomatic group. Eleven subjects with positive skin prick test to house dust mite who denied any relevant symptom in the presence of house dust were allocated to the asymptomatic group. Specific IgE to Der p 1, Der p 2, Der p 10 and Der p 23 (ImmunoCAP, Thermo Fisher) in sera were measured from all patients included in the study, according to the manufacturer's instruction. Sera were either available from stored frozen samples, or from blood freshly redrawn. The flow chart of study subjects is presented in Fig. 1.

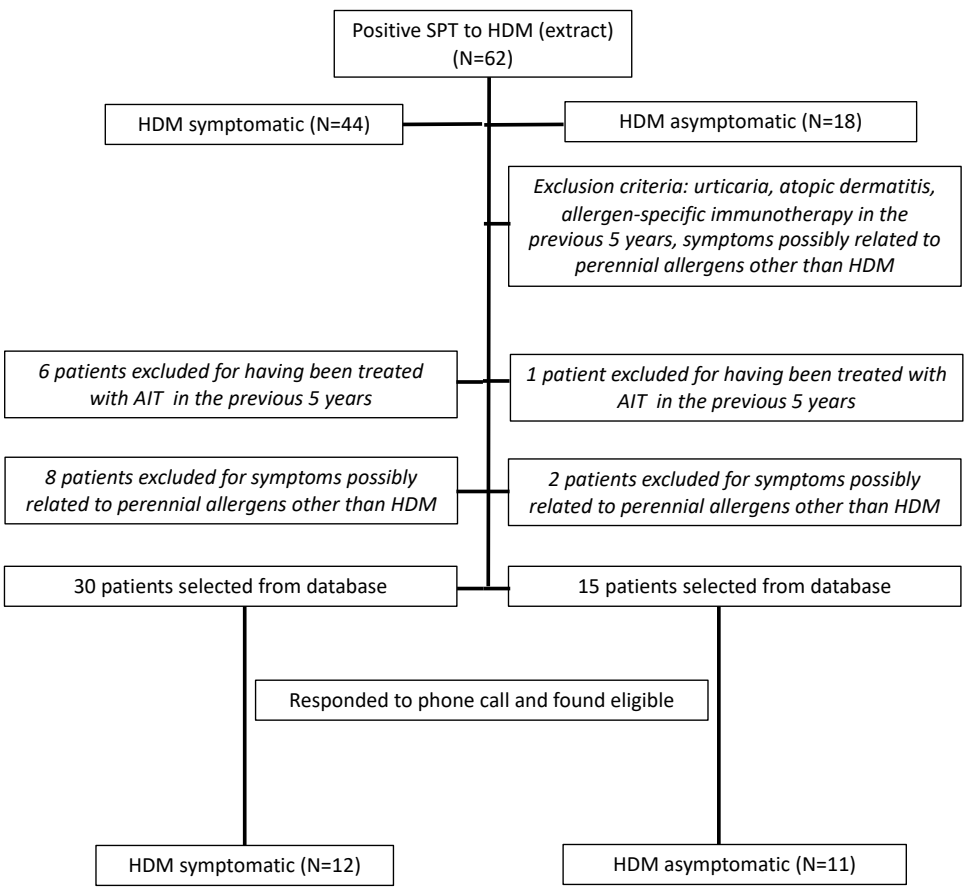


Fig. 1. *Flow chart of patient inclusion. HDM, house dust mite; SPT, skin prick test; AIT, Allergen-specific Immunotherapy*

Informed consent was obtained from all patients, according to the study protocols [BIO-IMMUNO-ALL CE 05.12.2002, rev. CE 02/12/04 (privacy) Vers. 04/10/2005], which were approved by the Ethics Committee of the IRCCS-San Raffaele Scientific Institute. Stored frozen samples were stocked in the San Raffaele institutional biobank (Biorep, Milan, Italy) until use.

Allergen extract for proteome analysis

Dermatophagoides pteronyssinus raw extract was purchased from Allergon/Thermo Fisher Scientific (Angelhom, Sweden) and used for the identification of IgE-reacting proteins as representative species of the mite allergen source.

Two-dimensional electrophoresis (2DE)

Serum from one patient (patient code: 310) was used as a probe for the evaluation of IgE reactivity to the mite proteome. For 2DE analysis, control serum was obtained from another patient allergic to HDM (patient code: 301). 2DE was performed as described in a previous study (7). In brief, 200 µg of total protein extracts were applied to 7-cm IPG strips (pH 3-10 NL; GE-Healthcare) by in-gel rehydration. Focusing was performed with an IPGphor system (GE-Healthcare) (50 mA/strip maximum; gradient voltage, max 5,000 V; 25 kVh total). Strips were reduced and alkylated by sequential incubation in equilibration buffer (50mmol/L Tris-HCl, pH 8.8; 6mol/L urea; 30% glycerol; 2% sodium dodecyl sulphate) containing 2% dithiothreitol or 2.5% iodoacetamide, respectively. Then, strips were transferred onto a 4-20% gradient or 12% sodium dodecyl sulphate polyacrylamide gel electrophoresis [SDS-PAGE] for the second-dimension separation. Preparative 2DE gels for protein spot excision (see below) were generated by loading 700 µg of total protein.

Western blot (WB) analysis

Total protein mite extracts or histidine-tag purified recombinant allergen Der p 20 (8) resolved by SDS-PAGE were transferred onto nitrocellulose membranes and incubated for 12 h at 4°C with patients' sera diluted 1/250 in tris-buffered saline containing 1% tween-20. Immunoreactivity was revealed by incubation with polyclonal goat anti-human IgE, conjugated with horseradish peroxidase (Sigma), followed by electro-chemo-luminescence (GE-Healthcare) reaction and film exposure. Images were acquired using a G:BOX Chemi XX6 System (Syngene, Cambridge, UK) and 2-DE protein patterns were analysed using Progenesis P240 software (NonLinear Dynamics, Newcastle, United Kingdom). Relative mass was estimated by comparison with reference markers (Precision, Bio-Rad) and isoelectric point values were assigned to the detected spots according to GE-Healthcare guidelines.

Protein identification by mass spectrometry analysis

Preparative gel was stained with Coomassie colloidal blue, images were acquired at high resolution and analysed as described above. Spots of interest were excised from the gel, reduced, alkylated, and in-gel digested with bovine trypsin (Roche Diagnostics Corp). Liquid chromatography electron spray ionization tandem mass spectrometry [LC-ESI-MS/MS] analysis was performed as previously described (7). In brief, 5 µL of digested sample were injected into a capillary chromatographic system (Agilent 1100 Series) equipped with a Nano Pump (Agilent) and peptide separation occurred in an RP C18 nanocolumn. The eluting peptides were ionized by a nano-ESI online source and analysed on an API QStar PULSAR (AB-Sciex, Toronto, Ontario, Canada) mass spectrometer. Full-scan mass spectra (range m/z 350-1,600) were collected, and for each spectrum, the 2 most intense doubly- and triply-charged ion peaks were selected for fragmentation. Tandem MS data files from chromatographic runs were combined and converted to MASCOT files using MASCOT.dll 2.2.07 through Analyst QS 1.1 (AB Sciex). All MS/MS samples were analysed using the MASCOT engine to search the Swiss Prot, Other Metazoa 2016_10 (10510 sequences) database. Peptide mass tolerances of 200 ppm and 0.3 Da were used for precursor and fragment ions, respectively. The other search parameters were 2 allowed missing cleavages, oxidation of methionine as a variable modification, and carbamide methylation as a fixed modification.

Determination of IgE specific to Der p 20

His-tag recombinant full length Der p 20 was obtained as described (8). An experimental Der p 20 ImmunoCAP test was developed by biotinylation of Der p 20 using EZ-link sulfo-NHSLC-biotin (Thermo Scientific) according to the manufacturer's instructions. Results were presented as kilounits of allergen per liter (kAU/l) (cut-off for positivity 0.10 kAU/L).

Statistical analysis

Patients' main characteristics were described as median (interquartile range, IQR) for continuous variables or proportions for categorical variables. Continuous variables were compared using the Wilcoxon rank sum test. Differences between proportions were tested by the *chi*-squared or Fisher exact test. Multivariate logistic regression models were performed to identify factors associated with the risk of symptoms. The multivariate model was performed in a stepwise manner with entry and removal criteria at 0.05 level. All analyses were conducted using SAS statistical software version 9.4 (Statistical Analyses System Inc, Cary, NC, USA).

RESULTS

Symptoms following exposure to mite dust and sensitization to inhalant allergens in HDM-sensitized symptomatic and asymptomatic patients

In a group of 62 reports of consecutive patients with positive skin prick test for HDM, 18 (29%) did not describe any symptoms of rhinitis when environmentally exposed to house dust, based on clinical records. The correlation between allergen exposure and triggering of symptoms could not be re-assessed in all patients, following a dedicated telephone call, due to no answer and/or unwillingness

Table I. *Results of skin prick test and diagnosis of study subjects*

			Skin Prick Test				
Symptomatic (12)	**sex**	**age**	***HDM***	***grass***	***trees***	***ragw***	**diagnosis**
S0301	*m*	*15*	*pos*	*pos*	*neg*	*neg*	*AR+AA*
S0315	*m*	*54*	*pos*	*neg*	*neg*	*neg*	*AR*
S0308	*f*	*45*	*pos*	*neg*	*neg*	*neg*	*AR+AA*
S0304	*f*	*9*	*pos*	*pos*	*pos*	*neg*	*AR*
S0309	*f*	*22*	*pos*	*neg*	*neg*	*neg*	*AR*
S0311	*f*	*19*	*pos*	*pos*	*neg*	*neg*	*AR*
S0307	*m*	*22*	*pos*	*neg*	*neg*	*neg*	*AR+AA*
S0302	*f*	*45*	*pos*	*pos*	*neg*	*neg*	*AR*
S0303	*f*	*35*	*pos*	*pos*	*pos*	*neg*	*AR+AA*
S0304	*m*	*19*	*pos*	*pos*	*neg*	*neg*	*AR*
S0305	*f*	*21*	*pos*	*neg*	*neg*	*pos*	*AR+AA*
S0306	*f*	*19*	*pos*	*pos*	*neg*	*neg*	*AR*
Asymptomatic (11)							
A331	m	8	pos	neg	neg	neg	AR+AA
A332	f	16	pos	pos	pos	neg	AR
A333	m	19	pos	neg	neg	neg	no respiratory allergy
A334	f	19	pos	neg	neg	neg	no respiratory allergy
A335	m	24	pos	pos	pos	neg	AR
A336	f	45	pos	pos	neg	pos	AR
A337	f	35	pos	pos	neg	neg	AR
A338	m	38	pos	pos	neg	neg	AR+AA
A310	m	53	pos	neg	neg	neg	no respiratory allergy
A339	m	51	pos	pos	neg	neg	AR
A333	f	18	pos	neg	neg	neg	no respiratory allergy

AA: Allergic Asthma; AR: Allergic Rhinitis; ragw: ragweed; Grass, trees and ragweed: result of positive prick test to Phleum p., Betula v., Ambrosia a.

to participate in the study. Twenty-three patients, including 12 subjects who were symptomatic following exposure to house dust and 11 who were not, provided informed consent and could be further studied. Results of skin prick test and diagnosis of patients included in the present study are reported in Table I.

Diagnosis in the symptomatic group was allergic rhinoconjunctivitis (AR) (N=12, 100%), associated with allergic asthma (AA) in 5 patients (41%). In the house dust mite prick test positive, asymptomatic group diagnosis was AR in 7 patients (64%), associated with allergic asthma in 2 of them (18%). Four subjects (36%) who did not report any symptoms at all correlated to AR with or without AA were screened as family members of subjects with respiratory allergies. At categorical analysis, the higher frequency of AR (with or without AA) in the symptomatic group was non-significant (p=0.061). IgE to commercially available Der p 1, 2, 10 and 23 allergen components were measured in sera. One subject of the asymptomatic group (patient 0310) did not display measurable IgE reactivity to any of these allergens. He had a positive prick test to house dust mite, which was confirmed by specific IgE in serum (0.89 kAU/l), and by a positive patch test to house dust mite (Rapid Patch Test, ALK Abellò). Bronchial provocation test with methacholine scored negative.

Identification of Der p 20 as the only IgE reactive allergen from the house dust mite proteome in one patient

In order to identify the allergen recognized by IgE from patient 0310, a previously described approach based on the evaluation of reactivity to the relevant allergen proteome was used. One protein spot (#1) of ≅ 35.5 kDa of molecular weight specifically reacted with patient 0310 serum, but not with the anti-human secondary antibody used as a probe or with serum from HDM-allergic patient 0301 serving as control (Fig. 2A). The protein spot corresponding to IgE reactivity was excised from a preparative gel and analysed by MS for protein identification. At LC-ESI-MS/MS analysis, the spot with isoelectric point of 7.98 and relative mass of 35.5 (kDa) yielded unique identification consistent to protein Der p 20 allergen (sequence coverage 11% on 4 fragmented peptides and Mascot score 40) and belonging to the arginine kinase-like protein 2 family (accession B2ZSY4). Small differences between theoretical and experimental isoelectric point (8.42

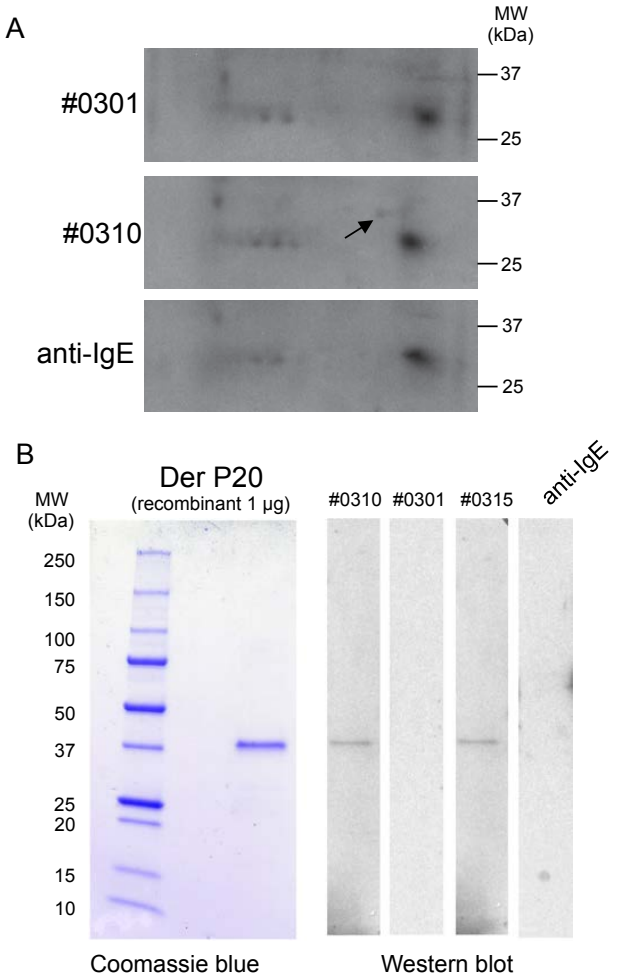


Fig. 2. ***A)*** *Reactivity of patient 0310 serum to the* Dermatophagoides pteronyssus *proteome.* D. pteronyssus *extracts were resolved by 2D-gel electrophoresis and then probed by WB with sera. IgE reactivity of patient 0310 serum was compared with the reactivity of another HDM-allergic patient (0301), and with the reactivity of the anti-human IgE secondary antibody as control. The arrow indicates the spot recognized by patient 0310 sera, that underwent to mass spectrometry analysis for protein identification.* ***B)*** *Reactivity of patient 0310 serum against recombinant Der p 20 allergen. The IgE reactivity of patient 0310 serum and of other two HDM allergic patient (0301, 0315) was tested against recombinant Der p 20 protein allergen resolved by SDS-PAGE. The anti-human IgE secondary antibody was used as control. Panel on the left shows the purity of the recombinant Der p 20 allergen resolved by SDS-PAGE and stained with blue Coomassie.*

vs 7.98) and relative mass (40.5 *vs* 35.5 kDa) could be due to protein fragmentation. However, the full-length recombinant Der p 20 allergen migrate in SDS-PAGE with an apparent relative mass below the 37 kDa reference standard (Fig. 2B on the left), suggesting that the 2DE reacting spot might represent the intact molecule.

Validation of IgE reactivity to Der p 20

His-tag recombinant full length Der p 20 expressed in *E. coli (8)* (1 μg) was used to test the reactivity with 0310 serum and with sera from 2 HDM allergic patients (0301 and 0315) serving as controls by mean of WB. IgE reactivity against the Der p 20 recombinant protein was observed with sera from patient 0310 and 0315 (Fig. 2B). In order to check allergen integrity, recombinant Der p 20 was resolved by SDS-PAGE and stained with Coomassie blue. There was no evidence of protein fragmentation (Fig. 2B). Titres of IgE levels to allergen components are individually reported in Table II and as median and interquartile range (IQR) in Table III.

IgE levels were unchanged in all the comparison, except for IgE to Der p 20, which was significantly higher in asymptomatic subjects (p=0.042). At categorical analysis (subjects considered positive when IgE > 010 kAU/l) no significant difference was observed with any allergen (not shown).

Table II. *Total and specific IgE levels to allergen components (individual values)*

Symptomatic	Der p 1	Der p 2	Der p 10	Der p 20	Der p 23	IgE to Dt. pt	total IgE
S0301	*0.45*	*2.12*	*0.35*	2.24	*1.12*	*2.35*	*56.00*
S0315	*3.20*	*7.22*	*0.00*	9.56	*0.00*	*5.12*	*46.00*
S0308	*1.23*	*1.20*	*0.00*	0.31	*2.45*	*3.45*	*34.00*
S0304	*0.00*	*42.03*	*0.00*	0.56	*0.00*	*22.45*	*220.00*
S0309	*0.00*	*5.56*	*0.00*	0.41	*0.56*	*1.52*	*157.00*
S0311	*2.23*	*2.12*	*0.00*	0.19	*1.23*	*6.45*	*159.00*
S0307	*0.00*	*2.22*	*0.00*	4.12	*0.00*	*9.53*	*42.00*
S0302	*5.78*	*3.96*	*0.00*	1.24	*0.00*	*12.45*	*45.00*
S0303	*2.45*	*5.12*	*0.00*	0.00	*1.11*	*2.23*	*424.00*
S0304	*1.05*	*1.23*	*0.00*	0.89	*0.85*	*7.89*	*350.00*
S0305	*4.02*	*19.45*	*0.00*	2.15	*2.12*	*12.56*	*442.50*
S0306	*5.56*	*7.45*	*0.00*	*0.00*	*1.22*	*4.98*	*33.00*
Asymptomatic							
A331	0.00	0.00	0.00	12.45	1.12	0.33	63.00
A332	0.00	1.45	0.00	4.56	0.56	0.98	78.00
A333	2.45	5.45	1.23	0.98	0.00	15.47	51.00
A334	0.00	3.45	0.00	1.23	0.59	3.32	68.00
A335	1.56	14.23	0.00	11.98	0.00	11.45	54.00
A336	1.23	7.45	0.00	6.23	0.00	1.68	78.00
A337	0.89	1.12	0.00	11.45	1.45	5.44	78.00
A338	0.89	1.25	0.00	0.78	0.00	0.98	89.00
A310	0.00	0.00	0.00	11.45	0.00	0.89	124.00
A339	4.45	6.41	0.00	0.98	0.00	7.55	94.00
A333	1.14	11.54	0.65	0.19	1.24	1.12	154.00

Results are expressed as AU/ml for allergens and IU/ml for total IgE

Table III. *Median and interquartile range of specific and total IgE values*

Vaariable	Category	Symptomatic	Aymptomatic	P-value
IgE to Der p 1	AU/ml	1.73 (0.23 - 3.61)	0.89 (0 - 1.56)	0.274
IgE to Der p 2	AU/ml	4.54 (2.12 - 7.34)	3.45 (1.12 - 7.45)	0.460
IgE to Der p 10	AU/ml	0.00 (0.00 - 0.00)	0.00 (0.00 - 0.00)	0.462
IgE to Der p 20	AU/ml	0.73 (0.25 - 2.20)	4.56 (0.98 - 11.45)	**0.042**
IgE to Der p 23	AU/ml	0.98 (0.00 - 1.23)	0.00 (0.00 - 1.12)	0.289
IgE D. pt. extract	AU/ml	5.79 (2.90 - 10.99)	1.68 (0.98 - 7.55)	0.079
total IgE	IU/ml	106.5 (43.5 - 285)	78 (63 - 94)	0.926

DISCUSSION

Up to 45% of subjects with a positive skin prick test (SPT) and/or positive level of serum sIgE for *D. pteronyssinus* do not suffer any allergic rhinitis (AR) symptoms (9). Here, we found that among patients with a positive skin prick test for HDM, 29% did not report any symptoms of rhinitis with or without conjunctivitis when environmentally exposed to house dust. Evaluation of reactivity to single allergen components in these subjects did not allow to highlight significant differences as compared to HDM-allergic subjects (1). One asymptomatic patient did not have any measurable IgE reactivity to the allergen components we analysed (Der p 1, Der p 2, Der p 10 and Der p 23). With a proteome-based approach, IgE to Der p 20 (arginine kinase) were identified in his serum. Arginine kinase allergens from different allergen sources show high sequence conservation and potential for cross reactivity. Notably, IgE to arginine kinase were previously correlated with mite sensitization not associated with allergy. Indeed, there is 75% and 80% identity to sequences of insects and crustaceans that have major inhalant (10) and food (11) arginine kinase allergens, respectively, but the HDM arginine kinases did not appear to be important HDM allergens (8). Der p 20 is a highly abundant protein in mites and, being the invertebrate equivalent of creatine kinase in muscle, is a candidate to induce high immune responses to a burrowing parasite. High levels of IgG and IgE to scabies were reported in patients with active infestation to this parasite (12). Along this line, in remote Australian Aboriginals IgE antibodies to Der p 20 reflected sensitisation to scabies mites and not to house dust mites (12). Our results suggest that non-species-specific, cross-reactive allergens, such as Der p 20, may act as markers of asymptomatic sensitization to house dust mite.

ACKNOWLEDGEMENTS

We thank Protein Microsequencing Facility (ProMiFa) at IRCCS-Ospedale San Raffaele for mass spectrometry analysis.

REFERENCES

1. Zidarn M, Robič M, Krivec A, et al. Clinical and immunological differences between asymptomatic HDM-sensitized and HDM-allergic rhinitis patients. Clin Exp Allergy 2019; 49:808-18.
2. Shade K-TC, Conroy ME, Washburn N, et al. Sialylation of immunoglobulin E is a determinant of allergic pathogenicity. Nature 2020; 582:265-70.
3. Fontanella S, Frainay C, Murray CS, Simpson A, Custovic A. Machine learning to identify pairwise interactions between specific IgE antibodies and their association with asthma: A cross-sectional analysis within a population-based birth cohort. Platts-Mills T,

editor. PLoS Med 2018; 15:e1002691.
4. Weghofer M, Thomas WR, Kronqvist M, et al. Variability of IgE reactivity profiles among European mite allergic patients. Eur J Clin Invest 2008; 38:959-65.
5. Kidon MI, Chiang WC, Chin CW, et al. Mite component-specific IgE repertoire and phenotypes of allergic disease in childhood: the tropical perspective. Pediatr Allergy Immunol 2011; 22:202-10.
6. Bousquet P-J, Burbach G, Heinzerling LM, et al. GA2LEN skin test study III: minimum battery of test inhalent allergens needed in epidemiological studies in patients. Allergy 2009; 64:1656-62.
7. Conti A, Ricchiuto P, Iannaccone S, et al. Pigment epithelium-derived factor is differentially expressed in peripheral neuropathies. Proteomics 2005;5: 4558-67.
8. Hales BJ, Martin AC, Pearce LJ, et al. IgE and IgG anti-house dust mite specificities in allergic disease. J Allergy Clin Immunol 2006; 118:361-7.
9. Droste JH, Kerhof M, de Monchy JG, Schouten JP, Rijcken B. Association of skin test reactivity, specific IgE, total IgE, and eosinophils with nasal symptoms in a community-based population study. The Dutch ECRHS Group. J Allergy Clin Immunol 1996; 97:922-32.
10. Sookrung N, Chaicumpa W, Tungtrongchitr A, Vichyanond P, Bunnag C, Ramasoota P, et al. Periplaneta americana arginine kinase as a major cockroach allergen among Thai patients with major cockroach allergies. Environ Health Perspect 2006; 114:875-80.
11. García-Orozco KD, Aispuro-Hernández E, Yepiz-Plascencia G, Calderón-de-la-Barca AM, Sotelo-Mundo RR. Molecular characterization of arginine kinase, an allergen from the shrimp Litopenaeus vannamei. Int Arch Allergy Immunol 2007;144(1):23-8.
12. Walton SF, Slender A, Pizutto S, et al. Analysis of IgE binding patterns to house dust mite allergens in scabies-endemic communities: insights for both diseases. Clin Exp Allergy 2016; 46:508-8.

LETTER TO THE EDITOR

LncRNA XIST is elevated in patients with chronic heart failure and has a regulatory role in cardiomyocyte function

ZL. Sun[1], MH. Chen[1], YN. Guo[2] and ZQ. Liu[1]

[1]Second Department of Cardiology, Changle People's Hospital, Shandong, China; [2]First Department of Cardiology, Changle People's Hospital, Shandong, China

Received December 18, 2020 – Accepted February 18, 2021

To the Editor,

Heart failure is a complex myocardial disease induced by diversified heart disorders of which chronic heart failure (CHF) is a common form (1). The incidence of heart failure has grown in the past decades, especially in the elderly with 23 million patients around the world (2). Hence, research focused on the mechanism underlying CHF is imperative.

LncRNA is a serious RNA with longer than 200 nt and exerts its function in many biological processes (3). The interaction between lncRNA and miRNA is a fundamental part in the mechanism of cardiovascular disease (4). Accumulating researchers have explored the essential functions of lncRNA XIST in heart diseases. The expression of XIST is increased in cardiomyocyte hypertrophy and can boost this process by directly targeting miR-101 (5). Hence, it was hypothesised that XIST could play a role in CHF and modulate cell viability and apoptosis by targeting a specific miRNA. In a microarray detection, the expression of miR-130a-3p is significantly reduced in the patient with coronary heart disease (6). In patients with deep vein thrombosis, the upregulation of miR-130a-3p facilitated the function recovery of endothelial progenitor cells and may be a probable target in the treatment of vein thrombosis (7). Nonetheless, the relationship between XIST and miR-130a-3p and the function of both in CHF remain unclear.

This study aimed to assess the expression levels of XIST and miR-130a-3p and their correlation in patients with CHF. The influence of XIST on cell viability and apoptosis was substantiated. Additionally, the direct target of XIST was validated and the function and mediation of miR-130a-3p were demonstrated.

MATERIALS AND METHODS

Patients and cells

Eighty-six CHF patients (48 males and 38 females; mean age 59.15±6.08 years) were included in the study. As controls, 81 healthy individuals (46 males and 35 females; mean age 59.77±5.59 years) were also randomly selected. No difference was found between CHF patients and healthy controls regarding age and gender. All these subjects were collected from Changle People's Hospital. The design and protocol of this study were approved by the Ethics Committee of the Changle People's Hospital, and written informed consent was obtained from all

Key words: lncRNA XIST; chronic heart failure; miR-130a-3p; cell viability; cell apoptosis

Corresponding Author:
Dr Yini Guo,
First Department of Cardiology,
Changle People's Hospital, 278 Limin Street,
Shandong, 262400, China
Tel.: +86 0536 6222822
e-mail: guoyinicl@163.com

0393-974X (2021)
Copyright © by BIOLIFE, s.a.s.
This publication and/or article is for individual use only and may not be further reproduced without written permission from the copyright holder.
Unauthorized reproduction may result in financial and other penalties
DISCLOSURE: ALL AUTHORS REPORT NO CONFLICTS OF INTEREST RELEVANT TO THIS ARTICLE.

participants. Five ml venous blood was collected from each subject and added into a tube with anticoagulants EDTA. The plasma was purified and obtained after centrifuging.

AC16 human cardiomyocyte cell lines were purchased from Longyue biological company (Beijing, China) and cultured in the DMEM (ThermoFisher Scientific, MA, USA) supplemented with 12% FBS and 1% antibiotics (Invitrogen, CA, USA) at 37°C. The CHF cell models were established by being incubated in a culture medium adding different concentrations of H_2O_2. The si-XIST and its negative controls (si-NCs) were purchased from Sangon (Shanghai, China). The miR-130a-3p mimic, anti-miR-130a-3p, and their negative control (miR-NC and anti-NC) were obtained from Sangon (Shanghai, China). The sequences obtained from Sangon were transfected into AC16 cells using lipofectamine 2000 reagent (Invitrogen, CA, USA), and ater transfection, the cells were incubated at 37°C for a further 48 h.

RNA isolation and quantitative real time polymerase chain reaction (qRT-PCR)

TRIzol reagent (Invitrogen, CA, USA) was applied to extract total RNA from plasma and cells based according to the manufacturer's instructions. cDNA was obtained by reverse transcription of total RNA in accordance with the procedure of SuperScript reverse transcription kit (ThermoFisher Scientific, MA, USA) for XIST or HyperScript III miRNA 1st Strand cDNA Synthesis Kit (NovaBio, Shanghai, China) for miR-130a-3p. The relative expression of XIST and miR-130a-3p was verified on the 7500 real-time system (ThermoFisher Scientific, MA, USA). PowerUp™ SYBR™ Green Master Mix (ThermoFisher Scientific, MA, USA) was mixed with the cDNA specimen following the manufacturer's suggestions. The expression of the GAPDH was used to normalize the relative expression of XIST, as was U6 for miR-130a-3p.

In vitro cell assay

The AC16 cell viability was assessed by MTT assay (Sigma. St Louis, USA). Collected cells were seeded into wells of a 96-well plate at a concentration of 1×10^5 cells/well. Twenty µl MTT were added into each well and the plate was stored at 37°C for 4 h. Then the supernatant was removed, and 150 µl DMSO were added into each well and mixed with cells. The absorption value was measured at 490 nm under an enzyme-linked immunometric meter.

Annexin V-EGFP Apoptosis Detection Kit (Kaiji, Jiangsu, China) was used to determine the cell apoptosis. Experimental cells were suspended using binding buffer after washing and collecting. Afterward, the cells were mixed with 5 µl Annexin V-EGFP and 5 µl Propidium Iodide, and were cultured in the dark for 20 min. The values of apoptotic cells were detected by flow cytometry (BD Biosciences, San Jose, USA).

The PCR products of XIST (WT-XIST) and mutation of XIST (MUT-XIST) were separately cloned into different pmirGLO vectors (Promega, Madison, USA). Then the vectors together with miR-NCs or miR-130a-3p mimics were co-transfected into AC16 cells. Dual-luciferase Reporter GeneAssay Kit was purchased from Yeasen company (Shanghai, China). Cells were cleaved by cell lysate from the kit and seeded into a black enzyme label plate. The diluted firefly luciferase buffer and renilla luciferase buffer were separately added into the plate, and the activity of luciferase was detected under a microplate reader.

Statistical analysis

The comparison of different groups was confirmed by Student's *t*-test and one-way ANOVA on GraphPad 7.0 and χ^2 test on the IBM SPSS. The correlation between the expression of miR-130a-3p and XIST levels was analyzed by Pearson's test.

RESULTS

Expression of XIST and miR-130a-3p and their correlation in plasma of patients with CHF

To ascertain the relative expression of XIST and miR-130a-3p in the plasma of CHF patients, 81 healthy individuals and 86 patients were enrolled in this study. The relative expression of XIST was significantly increased in the CHF group in contrast to the control group (Fig. 1A, $P < 0.001$). On the contrary, the relative expression of miR-130a-3p was significantly reduced in CHF patients (Fig. 1B, $P < 0.001$). The relative expression of XIST was negatively related to the levels of miR-130a-3p (Fig. 1C, $P < 0.001$).

Expression and function of XIST on H_2O_2-injured cell models

Compared with the 0 µM H_2O_2 group, the cell

viability was decreased with the different concentration gradients of H_2O_2, indicating that H_2O_2 leads to the injury of cells by reducing cell viability (Fig. 2A, $P < 0.01$). Moreover, with the increase of H_2O_2 concentration, the proportion of apoptosis gradually increased (Fig. 2B, $P < 0.01$). These findings indicate that the effect of H_2O_2 on cell viability and apoptosis depends on the concentration of H_2O_2.

As expressed in Fig. 2C, the relative expression of XIST was increased under H_2O_2 treatment of 100 μM, 150 μM, and 200 μM ($P < 0.01$) and, obviously, the relative expression of XIST was highest in the 150 μM group compared to the other concentration groups. Thus, 150 μM H_2O_2 was determined to be used in the following experiments.

The expression of XIST was decreased by artificially transfecting si-XIST into AC16 cell lines when compared with H_2O_2 group (Fig. 2D, $P < 0.001$). As seen in Fig. 2E, the result of viability of AC16 cells showed that the inhibition of XIST reversed the decline of cell viability induced by H_2O_2 ($P < 0.01$). In comparison with the raised apoptotic cells in the H_2O_2 group, the percentage of apoptotic cells was decreased in the H_2O_2 + si-XIST group (Fig. 2F, $P < 0.001$).

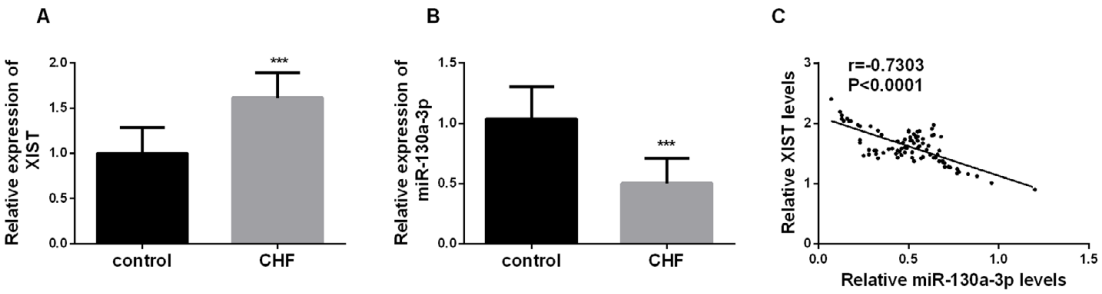


Fig. 1. ***A, B)*** *The relative expression of XIST was increased and the levels of miR-130a-3p were decreased in CHF patients compared with controls.* ***C)*** *The correlation between XIST and miR-130a-3p. ***P < 0.001.*

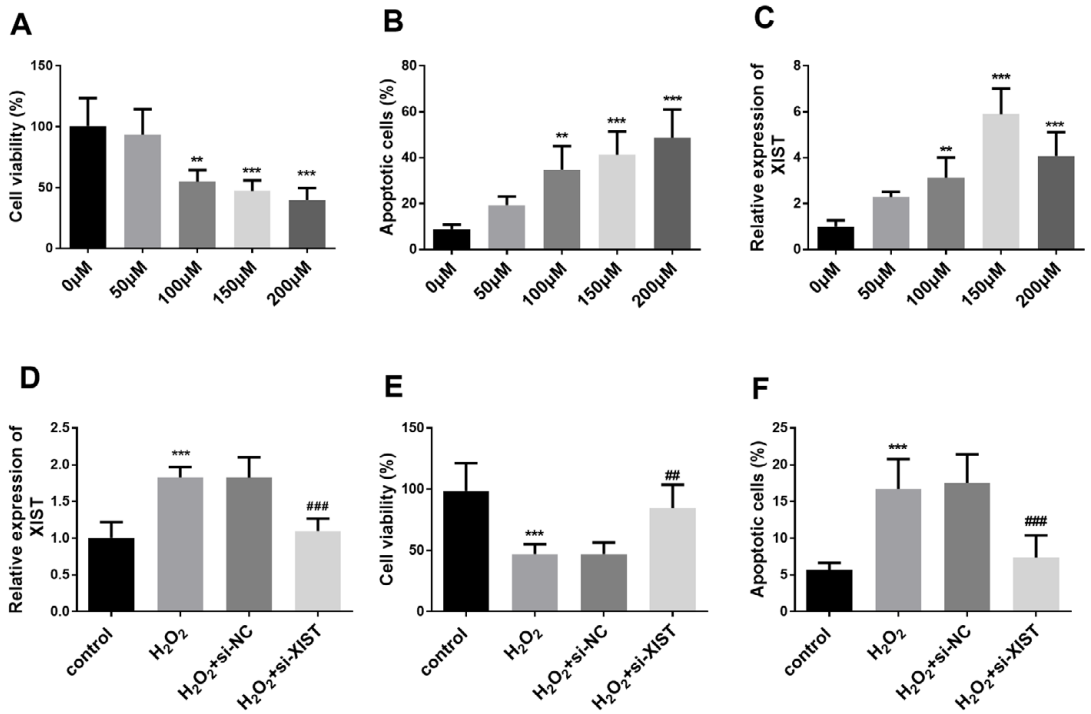


Fig. 2. *Influence of H_2O_2 on the (**A**) cell viability and (**B**) apoptosis.* ***C)*** *Function of H_2O_2 on the relative expression of XIST.* ***D)*** *The levels of XIST in the AC16 cells after being transfected with si-XIST. The function of H_2O_2 on the (**E**) cell viability and (**F**) apoptosis. **P < 0.01, ***P < 0.001, compared to controls; ##P < 0.01, ###P < 0.001, compared to the H_2O_2 group.*

miR-130a-3p was a target of XIST

The complementary bases among WT-XIST, miR-130a-3p, and MUT-XIST are shown in Fig. 3A. The dual-luciferase reporter assay shown in Fig. 3C verified that the luciferase activity was reduced after being transfected with miR-130a-3p mimics in the WT-XIST group ($P < 0.001$). Moreover, the targeted relationship was further verified by the relative expression of XIST being significantly increased in the si-XIST group when compared to the si-NC group (Fig. 3B, $P < 0.001$). The relative expression of miR-130a-3p was diminished in the100 μM and 150 μM groups ($P < 0.05$) (Fig. 3D), and 150 μM H_2O_2 was chosen for the following tests.

Impact of miR-130a-3p on cell viability and apoptosis

For further study on the function of miR-130a-3p, miR-130a-3p mimics were transfected into AC16 cardiomyocytes. The result showed the transfection of miR-130a-3p reversed the silenced expression of miR-130a-3p in the H_2O_2 group (Fig. 4A, $P < 0.001$). The viability of AC16 cells was decreased in the H_2O_2 group, whereas this trend was reversed by the overexpression of miR-130a-3p (Fig. 4B, $P < 0.001$). As shown in Fig. 4C, the proportion of apoptotic cells was inverted in the H_2O_2 + miR-130a-3p group when compared to the H_2O_2 group ($P < 0.001$).

Furthermore, the silenced XIST improved the expression of miR-130a-3p, and the anti-miR-130a-3p reversed the expression level of miR-130a-3p (Fig. 4D, $P < 0.01$). The co-translation of si-XIST and anti-miR-130a-3p reversed the heightened cell viability caused by si-XIST alone (Fig. 4E, $P < 0.001$). In comparison with H_2O_2 + si-XIST group, the cell apoptosis was enlarged in the H_2O_2 + si-XIST +anti- miR-130a-3p group (Fig. 4F, $P < 0.001$).

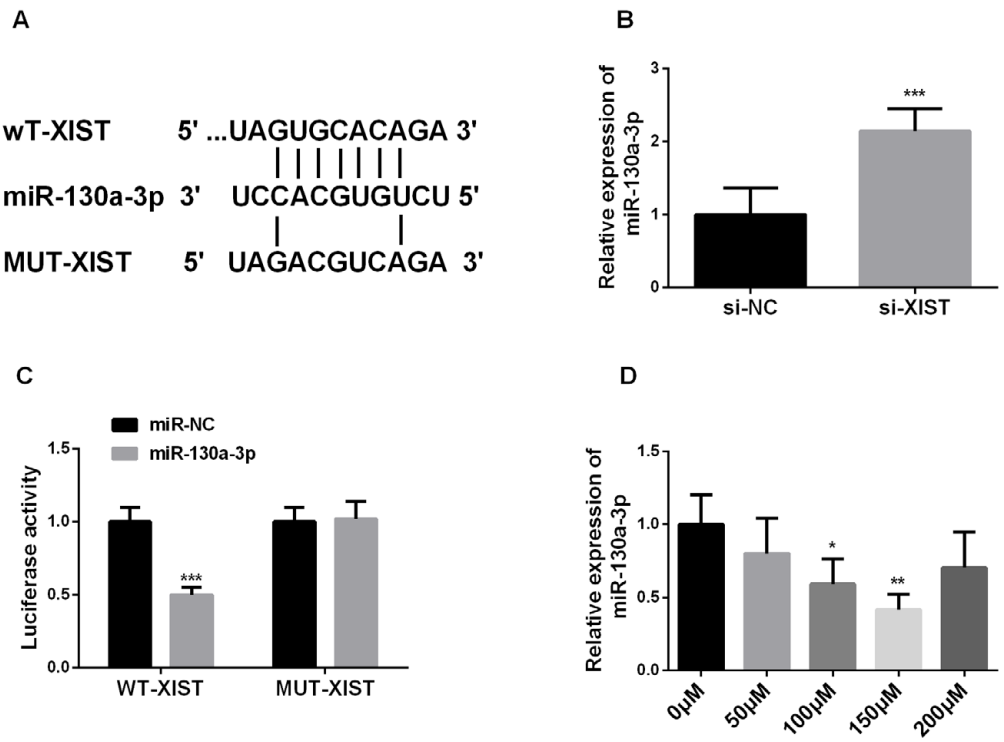


Fig. 3. ***A)*** *Complementary sequence among WT-XIST, miR-130a-3p, and MUT-XIST.* ***B)*** *The relative expression of miR-130a-3p was increased in the si-XIST group when compared with si-NC group.* ***C)*** *The luciferase activity.* ***D)*** *The function of H_2O_2 on the relative expression of miR-130a-3p. *P < 0.05, **P < 0.01, ***P < 0.001.*

DISCUSSION

In the present study, the expression of XIST was significantly increased in patients with CHF, indicating that the levels of XIST were associated with the progression of CHF. Consistently, the relative expression of XIST is elevated in newborn mouse cardiomyocytes (8). The expression of miR-130a-3p was decreased in CHF patients and was negatively correlated with the expression of XIST. In patients with coronary heart disease, the expression of miR-130a-3p is reduced, which is a further demonstration of our finding (9). Liu et al. discovered the expression of XIST is elevated in the cardiomyocyte models of myocardial infarction and the silenced XIST accelerates the cell viability and holds back cell apoptosis by sponging miR-101a-3p (10). In the present investigation, the expression of XIST was enhanced in the cell models induced by H_2O_2, which once again substantiated our previous finding. In addition, the inhibition of XIST suppressed the injury of AC16 cardiomyocytes on cell viability and cell apoptosis.

To further reveal the mechanism, we predicted and identified that miR-130a-3p was a direct target gene of XIST. A previous study demonstrated that XIST accommodated cell proliferation via miR-130a-3p in myocardial infarction (11). The expression of miR-130a-3p was lessened with the increased dosage of H_2O_2, which showed no difference in the levels of miR-130a-3p in CHF patients. More importantly, miR-130a-3p mediated the function of XIST on cell viability and apoptosis. A recent case reported by Wang et al. also supports the hypothesis that the expression of miR-130a-3p is reduced in hypertrophic cardiomyocytes and ameliorates cardiomyocyte hypertrophy (12).

In conclusion, upregulation of XIST and

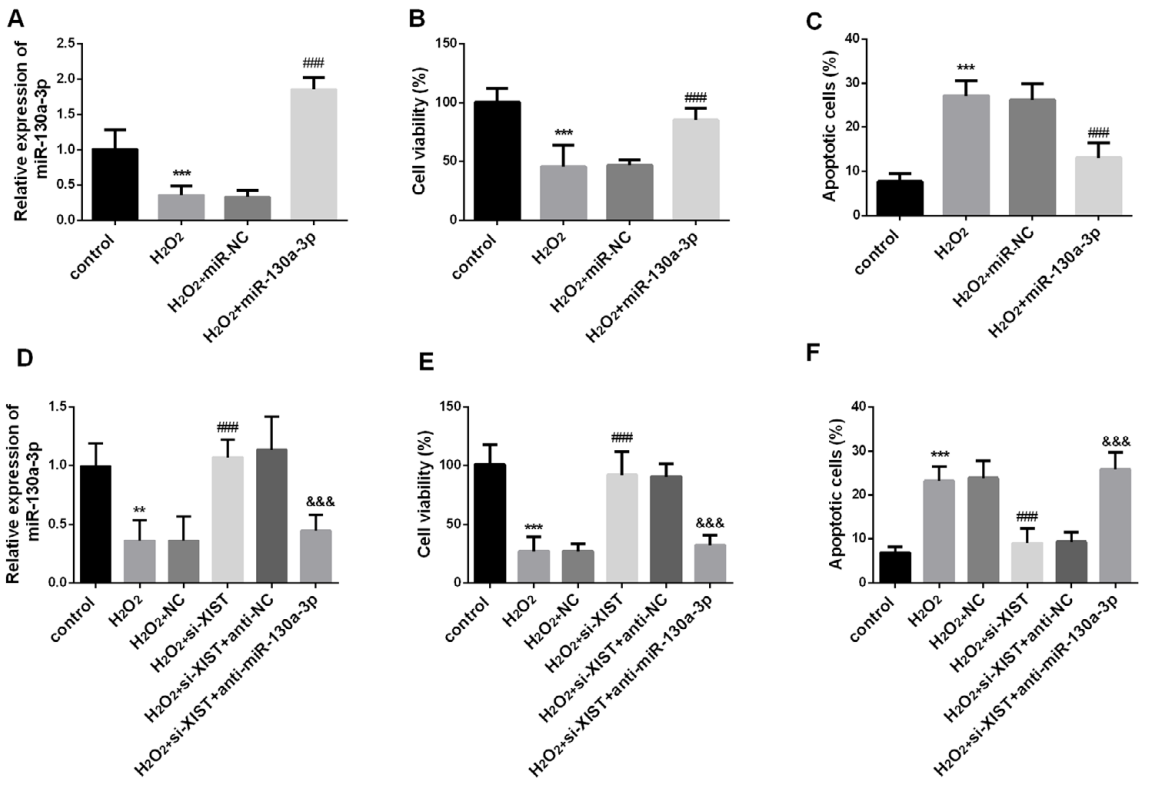


Fig. 4. *Effects of transfection with miR-130a-3p mimics on (**A**) the relative expression of miR-130a-3p, (**B**) cell viability, and (**C**) cell apoptosis. The function of co-transfection of si-XIST and anti-miR-130a-3p on (**D**) the relative expression of miR-130a-3p, (**E**) cell viability, and (**F**) cell apoptosis. **P < 0.01, ***P < 0.001, compared to controls; ###P < 0.001, compared to the H_2O_2 group; &&& P < 0.001, compared to the H_2O_2 + si-XIST group.*

downregulation of miR-130a-3p were found in CHF patients and cell models. Silenced XIST alleviated the influence of H_2O_2 on cell viability and apoptosis by upregualting the levels of miR-130a-3p.

REFERENCES

1. Liu L, Hu J, Wang N, et al. A novel association of CCDC80 with gestational diabetes mellitus in pregnant women: a propensity score analysis from a case-control study. BMC Pregnancy Childbirth 2020; 20(1):53.
2. Orso F, Fabbri G, Maggioni AP. Epidemiology of heart failure. Handb Exp Pharmacol 2017; 243:15-33.
3. Li M, Duan L, Li Y, Liu B. Long noncoding RNA/circular noncoding RNA-miRNA-mRNA axes in cardiovascular diseases. Life Sci 2019; 233:116440.
4. Huang CK, Kafert-Kasting S, Thum T. Preclinical and clinical development of noncoding RNA therapeutics for cardiovascular disease. Circ Res 2020; 126(5):663-78.
5. Xiao L, Gu Y, Sun Y, et al. The long noncoding RNA XIST regulates cardiac hypertrophy by targeting miR-101. J Cell Physiol 2019; 234(8):13680-92.
6. Pan RY, Liu P, Zhou HT, et al. Circular RNAs promote TRPM3 expression by inhibiting hsa-miR-130a-3p in coronary artery disease patients. Oncotarget 2017; 8(36):60280-90.
7. Cao M, Zhang L, Lin Y, et al. Differential mRNA and long noncoding RNA expression profiles in umbilical cord blood exosomes from gestational diabetes mellitus patients. DNA Cell Biol 2020; 39(11):2005-16.
8. Wang S, Lin Y, Zhong Y, et al. The long noncoding RNA HCG18 participates in PM2.5-mediated vascular endothelial barrier dysfunction. Aging (Albany NY) 2020; 12(23):23960-73.
9. Jia QW, Chen ZH, Ding XQ, et al. Predictive effects of circulating miR-221, miR-130a and miR-155 for coronary heart disease: a multi-ethnic study in China. Cell Physiol Biochem 2017; 42(2):808-23.
10. Lin B, Xu J, Wang F, Wang J, Zhao H, Feng D. LncRNA XIST promotes myocardial infarction by regulating FOS through targeting miR-101a-3p. Aging (Albany NY) 2020; 12(8):7232-47.
11. Zhou T, Qin G, Yang L, Xiang D, Li S. LncRNA XIST regulates myocardial infarction by targeting miR-130a-3p. J Cell Physiol 2019; 234(6):8659-67.
12. Wang Y, Wang H, Ruan J, Zheng W, Yang Z, Pan W. Long non-coding RNA OIP5-AS1 suppresses multiple myeloma progression by sponging miR-27a-3p to activate TSC1 expression. Cancer Cell Int 2020; 20:155.

LETTER TO THE EDITOR

Smell recovery in patients with COVID-19: an experience with nebulized nasal treatment

A. Varricchio[1], I. La Mantia[2], FP. Brunese[3] and G. Ciprandi[4]

[1]UOSD Video-Endoscopia delle VAS, P.O. San Gennaro – ASL Napoli 1-centro, Naples, Italy; [2]ENT Department, University of Catania, Catania, Italy; [3]Primary Care Paediatrics, ASL Caserta, Italy; [4]Allergy Clinic, Casa di Cura Villa Montallegro, Genoa, Italy

Received January 21, 2021 – Acepted February 18, 2021

To the Editor,

Since the initial notification of an unknown pneumonia hotspot in China, more than 80 million confirmed cases of COVID-19, including almost 2 million deaths, have been reported to WHO. COVID-19 is a multifaceted and pleiomorphic disease ranging from asymptomatic cases to severe acute respiratory syndrome, frequently lethal. Olfactory dysfunction is a key symptom in COVID-19 patients and is frequent, as reported by up to 78% of infected subjects (1, 2). Smell impairment may be total, named anosmia, partial, hyposmia, or distorted, cacosmia. Smell defect is very disturbing and could be dangerous. Post-viral smell dysfunction is longer in COVID-19 patients than in patients suffering from the common cold (3). However, anosmia/hyposmia duration is very variable, ranging from a few days to months to persistent.

The recovery of smell depends on different factors, including COVID-19 severity, pre-existing nasal disorders, and host immune response (4). However, a complete recovery of olfaction, such as before the infection, may require a long time. A very recent study reported a persistent loss in 32% of patients, partial recovery in 12%, and total recovery in 39% of patients at a 30-day follow-up (5). Smell impairment is therefore a relevant problem in a great number of COVID-19 patients. Moreover, no specific treatment is currently available. A recent viewpoint recommended nasal saline irrigation as a safe and beneficial remedy in patients with smell impairment dependent on COVID-19 (6). This consideration was derived from a study that demonstrated the ability of nasal irrigation with hypertonic saline (HS) for the common cold (7). HS nasal irrigation reduced illness duration by 22%, using symptomatic medications by 36%, and spreading contagion to the family by 35%. Consequently, the authors suggested that HS use could be a treatment option for COVID-19 (8). The rationale relies on the HS anti-inflammatory and decongestant activity, nasal irrigation removes mucus with entrapped pathogens, restores mucociliary clearance, and NaCl has an antiviral effect. In this regard, a medical device containing saline solution, high-molecular-weight sodium hyaluronate, and xylitol 5%, significantly reduced symptom perception, spotting, neutrophil, and bacteria count in children with acute rhinopharyngitis (9). Based on this background, the current preliminary study explored the possibility of shortening the duration of smell impairment, including anosmia, hyposmia, and cacosmia, in patients with COVID-19.

Key words: anosmia; hyposmia; cacosmia; COVID-19; nebulization; hyaluronic acid; hypertonic saline; xylitol

Corresponding Author:
Prof. Giorgio Ciprandi,
Allergy Clinic,
Casa di Cura Villa Montallegro,
Genoa, Italy
e-mail: gio.cip@libero.it

0393-974X (2021)
Copyright © by BIOLIFE, s.a.s.
This publication and/or article is for individual use only and may not be further reproduced without written permission from the copyright holder.
Unauthorized reproduction may result in financial and other penalties
DISCLOSURE: ALL AUTHORS REPORT NO CONFLICTS OF INTEREST RELEVANT TO THIS ARTICLE.

MATERIALS AND METHODS

The current study included 42 patients (22 males and 20 females, aged between 22 and 65 years) with COVID-19, confirmed by the nasal swab positive molecular testing. Inclusion criteria were: adulthood, COVID-19 diagnosis, and mild symptoms, including fever lasting no more than three days and lower than 37.5°C, and smell and taste impairment. Exclusion criteria were severe COVID-19, requiring hospitalization and pharmacological treatment, concomitant comorbidity, or current treatment that could interfere with the interpretation of the results. The study was performed according to the Helsinki Conference, and the internal review board approved the procedure. Each patient signed informed consent.

Treatment consisted of nasal nebulization of a solution containing hypertonic (3% NaCl) saline, high-molecular-weight sodium hyaluronate, and xylitol. This solution is available as a medical device (Aluneb® iper, Sakura Italia, Lonato del Garda, Italy). The solution was administered using a medical device (MAD Nasal™, Sakura Italia, Lonato del Garda, Italy). This device is a syringe with a needle able to nebulize particles with an aerodynamic diameter ranging from 30 to 100 mm, ideal for spreading into the upper airways. Namely, the dimensions of particles allows to reach an optimal deposition in the whole nasal cavity up to the nasopharynx.

The patients were evaluated at baseline, that is before initiating the treatment, and at the end of the course. Moreover, patients communicated the end of symptoms on the phone. Olfactory and taste dysfunction were self-reported. Treatment started within seven days after symptom onset. The medication was prescribed twice a day for seven days in patients with hyposmia and ten days in patients with anosmia.

RESULTS

All patients completed the treatment. Globally, 18 patients had hyposmia and hypogeusia, seven of them also had cacosmia; 24 patients had anosmia and ageusia, 10 of them also developed cacosmia during the smell recovery. All patients with hyposmia/hypogeusia improved after treatment and achieved normal sensory function ten days from treatment starting. Cacosmia completely disappeared between 10 and 30 days after the initial administration of Aluneb® iper. All anosmic/ageusic patients recovered normal smell and taste between 10 and 20 days after treatment; cacosmia resolved between 20 and 40 days after treatment onset. The treatment was safe and well-tolerated in all patients. No adverse events were reported during treatment.

DISCUSSION

COVID-19 pandemic is spreading worldwide, affecting many people and claiming many victims. COVID-19 very frequently impairs smell function and is commonly associated with taste impairment. Hyposmia/anosmia and hypogeusia/ageusia are annoying symptoms that severely impact the quality of life. Moreover, sensory alterations tend to persist for a long period. On the other hand, there is no specific treatment for COVID-19 and the cure of olfactory and taste disorders. Nasal irrigation with saline solution is currently the only modality that has been recommended. At present, only one ongoing study investigated the efficacy and safety of nasal irrigation in outpatients with COVID-19 (10). The study compared HS with HS plus 1% surfactant or no intervention. The interim analysis demonstrated that nasal irrigation significantly shortened symptom duration, mainly concerning nasal congestion and headache. The authors also hypothesized that HS could reduce viral shedding. The present experience showed that a medical device containing HS, hyaluronate, and xylitol, restored sensory function concerning smell and taste. Moreover, this treatment also improved cacosmia, which is usually challenging to be treated.

Hypertonic saline solution has many well-known advantages and can also improve viral clearance. Hyaluronic acid (HA) has many activities, including activation of innate immunity against viral pathogens, resolution of the inflammatory cascade, moistening respiratory mucosa, and cytoprotection of the epithelial barrier (9). In particular, the virus penetrates the central nervous system across the olfactory mucosa (11). The sustentacular cells play a relevant role in the pathogenic mechanism of smell impairment during viral infection. HA could repair

the viral damage and restore the integrity of the mucosal lining in the olfactory mucosa. Xylitol exerts an antiviral activity, modulates the immune system, and has decongestant and fluidifying upper airway activity (12). Therefore, these three components provide the beneficial effects of the medical device. Moreover, the MAD Nasal™ device used contributed to the effectiveness of successfully nebulizing the solution. In fact, MAD Nasal™ guaranteed an appropriate and effective distribution of the active components across the nasal cavity, allowing to also reach the olfactory mucosa. Moreover, this device was perceived by the patients as comfortable, faster, and easier to use than a traditional aerosol device, as it does not require a pneumatic pump and can be transported very conveniently.

These findings were consistent with three previous studies, investigating the efficacy and safety of hypertonic solution with high-molecular weight HA and xylitol in patients with upper airway disorders (9, 13, 14). Varricchio and colleagues evaluated 51 children with bacterial acute rhinopharyngitis who were randomly assigned to treatment with topical thiamphenicol diluted in isotonic saline alone or isotonic plus sodium hyaluronate with xylitol (9). Both regimens were effective, but the addition of HA and xylitol provided a greater effect on symptom perception, neutrophil count, and bacteria. The study of Cantone and colleagues included 126 children with recurrent respiratory infections (13). The patients were randomly allocated to different treatment groups: isotonic solution plus high-molecular weight HA, isotonic solution with high-molecular weight HA and xylitol, isotonic solution alone, or removing the principal components. The medical device containing HA and xylitol provided the most effective results, considering symptom severity, endoscopic parameters, use of antibiotics and antipyretics. Cioffi and colleagues enrolled 264 children with otitis media with effusion (14). Children were randomly treated with hypertonic solution plus high-molecular weight HA and xylitol or hypertonic solution alone. The medical device, containing the three components provided a significant improvement of the combined clinical score, considering both the intragroup and intergroup comparison.

The current outcomes suggest that nasal nebulization with HS, HA, and xylitol could recover smell and taste impairment in COVID-19 patients. On the other hand, the current experience has some limitations, including the open study design, the lack of a control group, and objective sensory defect measurements. Moreover, the number of cases was limited and severity of smell defects was not considered. Consequently, further studies should be conducted to answer these unmet needs.

In conclusion, the current preliminary experience showed that a medical device with HS, HA, and xylitol nebulized into the nose by a specific device could restore smell and taste in a short time and safely in patients with COVID-19, however, the lack of a control group requires further rigorous studies.

REFERENCES

1. Lechien JR, Chiesa-Estomba CM, De Siati DR, et al. Olfactory and gustatory dysfunctions as a clinical presentation of mild-to-moderate forms of the coronavirus disease (COVID-19): a multicenter European study. Eur Arch Otorhinolaryngol 2020; 277(8): 2251-61.
2. Mullol J, Alobid I, Marino-Sanchez F, et al. The loss of smell and taste in the COVID-19 outbreak: a tale of many countries. Curr Allergy Asthma Rep 2020; 20:61.
3. da Costa KVT, Lins Carnauba AT, Wanderley Rocha, de Andrade KC, Ferreira SMS, Menezes PL. Olfactory and taste disorders in COVID-19: a systematic review. Braz J Otorhinolaryngol 2020; 86(6):781-92.
4. Hoang MP, Kanjanaumporn J, Aeumjaturapat S, et al. Olfactory and gustatory dysfunction in COVID-19 patients: a systematic review and meta-analysis. Asian Pac J Allergy Immunol 2020; 38:162-9.
5. Chiesa-Estomba CM, Lechien JR, Radulesco T, et al. Patterns of smell recovery in 751 patients affected by the COVID-19 outbreak. Eur J Neurol 2020; 27(11):2318-21.
6. Farrell NF, Klatt-Cromwell C, Schneider JS. Benefits and safety of nasal saline irrigations in a pandemic-washing COVID-19 away. JAMA Otolaryngol 2020; 146(9):787-8.
7. Ramalingam S, Graham C, Dove J, Morrice L, Sheikh A. A pilot, open-labeled, randomized controlled trial

of hypertonic saline nasal irrigation and gargling for the common cold. Sci Rep 2019; 9:1015.
8. Ramalingam S, Graham C, Dove J, Morrice L, Sheikh A. Hypertonic saline nasal irrigation and gargling should be considered as a treatment option for COVID-19. J Glob Health 2020; 10:010332.
9. Varricchio A, Capasso M, Avvisati F, et al. Inhaled hyaluronic acid as ancillary treatment in children with bacterial acute rhinopharyngitis. J Biol Regul Homeost Agents 2014; 28(3):537-43.
10. Kimura KS, Freeman MH, Wessinger BC, et al. Interim analysis of an open-label randomized controlled trial evaluating nasal irrigations in non-hospitalized patients with coronavirus disease 2019. Int Forum Allergy Rhinol 2020; 10(12):1325-8.
11. Mori I, Nishiyama Y, Yokochi T, et al. Olfactory transmission of neurotropic viruses. J Neurobiol 2005; 11:129-37.
12. Salli K, Lehtinen MJ, Tiihonen K, et al. Xylitol's Health Benefits beyond Dental Health: A Comprehensive Review. Nutrients 2019; 11(8):1813.
13. Cantone E, Cavaliere E, Begvarfaj E, Motta S, Iengo M. New therapeutic strategies for the treatment of recurrent respiratory tract infections in children. J Biol Regul Homeost Agents 2020; 34(3):1185-91.
14. Cioffi L, Gallo P, D'Avino A, et al. Clinical improvement of subacute and chronic otitis media with effusion treated with hyaluronic acid plus hypertonic solution via nasal lavage: a randomized controlled trial. Global Pediatr Health 2017; 4:1-6.

LETTER TO THE EDITOR

miR-638 serves as an early diagnostic biomarker of acute kidney injury in intensive care units and indicates the clinical outcome of patients

C. Sun[1*], QT. Shi[2*] and HC. Liang[2]

[1]Department of Nephrology, Shanxian Dongda Hospital, Heze, Shandong, China; [2]Intensive Care Unit, Shanxian Dongda Hospital, Heze, Shandong, China

Received December 21, 2020 – Accepted February 19, 2021

[*]These authors contributed equally to this work

To the Editor,

Acute kidney injury (AKI) is a frequent serious complication in critically ill patients, especially in the intensive care unit (ICU), which is recognized as a significant risk factor for mortality (1). Although supportive care in ICU has been developed in the past decades, the clinical outcome of patients with AKI is still unacceptably unfavorable (2). The rise of serum creatinine and the reduction of urine output were considered as a major indicators for the detection of AKI, however, substantial kidney injury may have already occurred by the time creatinine increases and the urine flow decreases (3). The early diagnosis and risk predicting of AKI patients is therefore necessary to improve patient survival.

MicroRNAs (miRNAs) have been reported to be released into serum, urine, and other body fluids with high sensitivity and specificity (4). miRNAs are small single-stranded RNA sequences that regulate gene expression and play a role in disease (5). With the development of microarray analysis, numerous miRNA expression profiles in human biopsies and different types of AKI animal models have been reported. By comparing the miRNA expression profile of AKI patients and healthy age-matched controls, miR-638 was found to be upregulated in the plasma of AKI patients, which implied the potential clinical significance and functional role of miR-638 in AKI (6). Previously, miR-638 has been revealed to be involved in the development of glioma, oral squamous cell carcinoma, and many other diseases (7). The diagnostic and prognostic value of miR-638 in AKI was evaluated in this study to provided novel insight into the early detection and management of AKI patients in ICU.

MATERIALS AND METHODS

The protocol of this study was approved by the Shanxian Dongda Hospital Ethics committee. Fifty-seven AKI patients and 48 non-AKI patients were recruited from the ICU of Shanxian Dongda Hospital in the period 2018-2019, and 52 healthy controls who visited for usual health screenings were also included in the research. The AKI patients were included according to the Kidney Disease Improving Global Outcomes (KIDGO) criteria and had received renal replacement therapy. Patients diagnosed with diabetes, cancer, or pre-existing chronic kidney disease were excluded. Blood samples were collected from the participants after diagnosis, and isolated serum specimens were stored at -80°C for further research. Written informed consent from patients or their

Key words: acute kidney injury; intensive care unit; miR-638; diagnosis; prognosis

Corresponding Author:
Dr Houcai Liang,
Intensive Care Unit, Shanxian Dongda Hospital,
1, Shunshi East Road in Shan Country,
Heze, Shandong, 274300, China
Tel.: +86 0530 4633792
e-mail: lianghc_01@163.com
ORCID ID: 0000-0003-0954-5878

0393-974X (2021)
Copyright © by BIOLIFE, s.a.s.
This publication and/or article is for individual use only and may not be further reproduced without written permission from the copyright holder.
Unauthorized reproduction may result in financial and other penalties
DISCLOSURE: ALL AUTHORS REPORT NO CONFLICTS OF INTEREST RELEVANT TO THIS ARTICLE.

legal representatives were obtained before the sample collection. All patients were followed-up for 28 days to obtain survival information. The clinical data of patients and healthy controls are summarized in Table I.

Quantitative real-time PCR (qRT-PCR)

Total RNAs were extracted from collected serum samples with TRIzol reagent (Invitrogen, Carlsbad, CA, USA) and reverse transcribed to cDNA with PrimeScript RT Reagent Kit (Takara, Tokyo, Japan). The expression level of miR-638 was detected by SYBR Green I Master Mix Kit (Invitrogen, Carlsbad, CA, USA) and Applied Biosystems 7900 Real-Time PCR system (Applied Biosystems, Foster City, CA). The sequences of miR-638 primer were forward 5'-AGGGATCGCGGGCGGGT-3', reverse 5'-CAGTGCAGGGTCCGAGGT-3'. U6 (Forward 5'-CTCGCTTCGGCAGCACA-3, Reverse 5'-AACGCTTCACGAATTTGCGT-3') was used as the internal standard, and the relative expression of miR-638 was calculated based on the $2^{-\Delta\Delta Ct}$ method. The reaction conditions of PCR were 95°C for 15 s, 55°C for 45 s, 72°C for 1 min, then the final elongation at 72°C for 8 min.

Statistical analysis

Data are presented as mean±standard deviation (SD.) and analyzed by SPSS version 23.0 software (SPSS Inc., Chicago, IL) and GraphPad Prism 7.0 software (GraphPad Software, Inc., USA). The χ^2 test, Student's *t*-test, and one-way ANOVA followed by Turkey's post-hoc test were used to evaluate the differences between groups. The association between miR-638 level and creatinine and CRP of patients was estimated by Pearson's correlation analysis. Kaplan-Meier and multivariate Cox regression analysis were performed to assess the prognostic value of miR-638 in AKI. The diagnostic value of miR-638 for AKI patients was appraised by the receiver operating characteristic (ROC), and the value of area under the curve (AUC) with 95% confidence interval (95% CI) was calculated to evaluate the discrimination ability of miR-638. $P < 0.05$ was considered to be statistically significant.

RESULTS

Clinical features of the study population

Of the 57 AKI patients, there were 35 males and 22 females with an average age of 55.5±10.4. The 48 non-AKI patients from ICU included 26 males and 22 females with the average age of 54.6±8.6. The age, gender, BMI (body mass index), SBP (systolic blood pressure), and DBP (diastolic blood pressure) between AKI patients, non-AKI patients, and healthy controls showed no significant difference ($P > 0.05$). The ICU admission between AKI patients and non-AKI patients was also not significant ($P > 0.05$). The creatinine of AKI patients (134.3±21.1 μM) was significantly higher than that of non- AKI patients (101.0±20.1 μM) and healthy controls (77.4±18.9 μM), and the concentration of C-reactive protein (CRP) were also significantly different between healthy controls, non-AKI and AKI patients ($P < 0.001$).

Expression of miR-638 in AKI and its correlation with clinical features of patients

The expression of miR-638 in collected serum samples was evaluated with qRT-PCR. It was found that miR-638 showed a significant upregulation in non-AKI and AKI samples when compared with the expression in healthy controls ($P < 0.05$, $P < 0.001$, Fig. 1). While the expression level of miR-638 in AKI was also dramatically upregulated in relation to that in non-AKI samples ($P < 0.001$, Fig. 1). The dysregulation of miR-638 implied its potential functional role in the disease development of AKI.

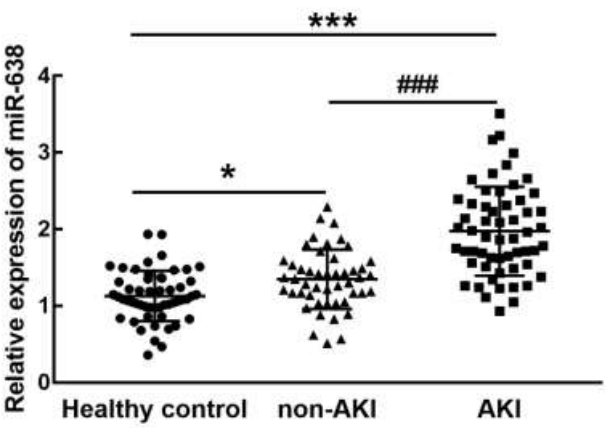


Fig. 1. *The expression level of miR-638 in serum samples of healthy controls, non-AKI patients, and AKI patients. miR-638 was significantly upregulated in AKI compared with healthy controls and non-AKI patients. The expression level of miR-638 was significantly higher than that in non-AKI patients. *P < 0.05, ***P < 0.001 relative to healthy controls. ###P < 0.001 relative to non-AKI patients.*

Table I. *Association between miR-638 expression and the clinicopathological features of AKI patients*

	Total patients (57)	Expression level of miR-638		*P* Value
		Low (22)	High (35)	
Age				0.776
< 55	22	9	13	
≥ 55	35	13	22	
Gender				0.784
Male	35	14	21	
Female	22	8	14	
BMI				0.847
< 24	38	15	23	
≥ 24	19	7	12	
ICU admission				0.618
Medicine	23	10	13	
General surgery	14	6	8	
Others	20	6	14	
AKI stage				0.040
Stage I	22	13	9	
Stage II	18	5	13	
Stage III	17	4	13	
Creatinine (μM)				0.039
< 130	24	13	11	
≥ 130	33	9	24	
CRP (mg/L)				0.034
< 100	19	11	8	
≥ 100	38	11	27	

AKI: acute kidney injury; BMI: body mass index; CRP: C-reactive protein

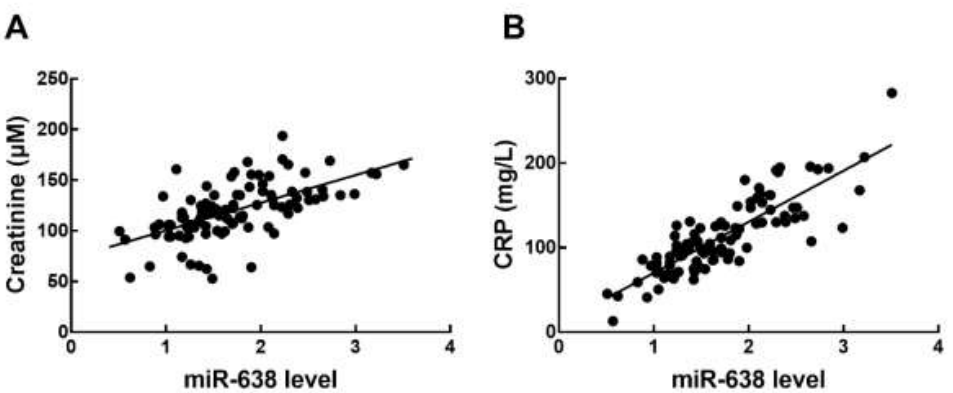


Fig. 2. *Correlation between serum miR-638 level and creatinine (**A**) and CRP (**B**). The serum miR-638 level was positively associated with the creatinine level (r = 0.607, P < 0.001) and CRP concentration of patients (r = 0.842, P < 0.001).*

Furthermore, the correlation between miR-638 and the clinical features of patients was evaluated. A total of 57 AKI patients were divided into two groups, including a low miR-638 expression group and a high miR-638 expression group, with the average expression level of miR-638 (2.301) in AKI serum samples as the cutoff. The low miR-638 expression group included 22 patients, while 35 AKI patients are included in the high miR-638 expression group. The expression level of miR-638 was closely associated with the AKI stage ($P = 0.040$), creatinine ($P = 0.039$), and CRP ($P = 0.034$) of patients, indicating the potential involvement of miR-638 in the development of AKI (Table I). Whereas, the other clinical features, including age, gender, BMI, and ICU admission of patients, showed no significant association with the expression level of miR-638 ($P > 0.05$, Table I). Consistently, the results of Pearson's correlation analysis showed that the serum miR-638 expression level was positively associated with the levels of creatinine ($r = 0.607$, $P < 0.001$, Fig. 2A) and the CRP concentration of patients ($r = 0.842$, $P < 0.001$, Fig. 2B).

Diagnostic value of miR-638 in AKI patients

With the help of the ROC curve, the diagnostic value of miR-638 in AKI patients was evaluated. As depicted in Fig. 3A, miR-638 could discriminate AKI patients from healthy controls with the AUC of ROC curve of 0.921, the sensitivity of 77.2%, and

Table II. *Cox regression analysis for the prognostic value of miR-638 and the clinicopathological features of AKI patients*

	HR factor	95% CI	*P* value
miR-638	6.444	1.557-26.664	0.010
Age	2.284	0.645-8.091	0.201
Gender	2.033	0.518-7.972	0.309
BMI	1.389	0.420-4.595	0.590
ICU admission	2.991	0.606-14.753	0.285
AKI stage	3.322	0.948-11.646	0.061
Creatinine	2.505	0.709-8.845	0.154
CRP	1.707	0.501-5.816	0.393

AKI: acute kidney injury; BMI: body mass index; CRP: C-reactive protein

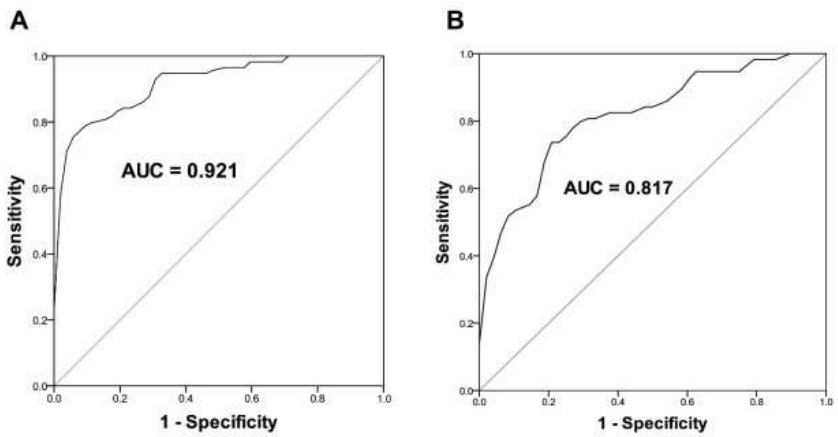


Fig. 3. *The diagnostic value of miR-638 was evaluated by ROC analysis. **A)** miR-638 could discriminate AKI patients from healthy controls with AUC of 0.932. **B)** miR-638 could distinguish AKI patients from non-AKI patients from ICU with AUC of 0.817.*

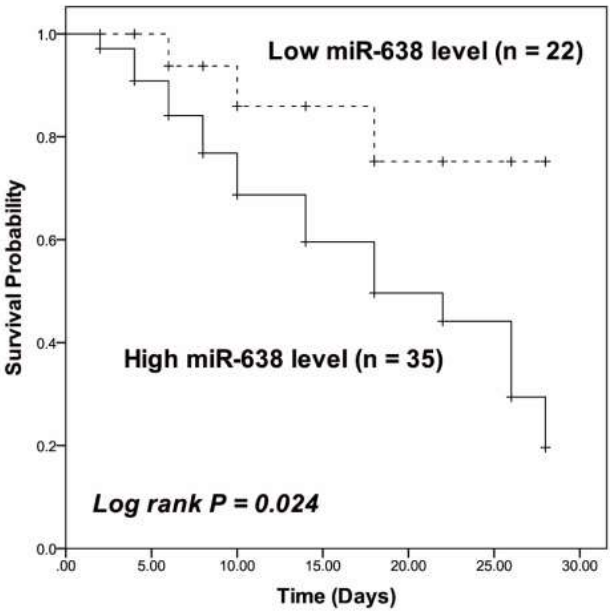


Fig. 4. *The prognostic value of miR-638 was assessed by the Kaplan-Meier analysis based on the differential expression of miR-638. The survival rate of patients with high miR-638 expression was significantly poorer than that of patients with low miR-638. Log-rank P = 0.024.*

the specificity of 94.2%. Meanwhile, miR-638 also had high sensitivity (73.7%) and specificity (81.2%) to distinguished AKI patients from non-AKI patients from ICU with the AUC of 0.817 (Fig. 3B). These results indicated that miR-638 served as diagnostic biomarker for AKI patients.

Prognostic value of miR-638 in AKI patients

The Kaplan-Meier cure based on the expression level of miR-638 showed the survival rate of patients with high miR-638 expression was much worse than that of patients with low miR-638 expression level (Log-rank P = 0.024, Fig. 4). Additionally, the prognostic value of miR-638 and the clinical characteristics of AKI patients was assessed by the Cox regression analysis. miR-638 (HR = 6.444, 95% CI = 1.557-26.664, P = 0.010) was identified as an independent prognostic factor for AKI (Table II).

DISCUSSION

miR-638 was found to be upregulated in AKI patients compared with non-AKI patients and healthy controls in this study, which is consistent with previous studies, indicating the potential functional role of miR-638 in the diagnosis and prognosis of AKI (6). miR-638 was reported to be alternatively expression in many diseases, such as breast cancer (8), hepatocellular carcinoma (9), and glioma (10), where miR-638 acts as oncogene or tumor suppressors. Previously, miR-638 was downregulated in the glomerulus and upregulated in the tubulointerstitial of lupus nephritis patients, which was correlated with the clinical disease severity (11). Here, the expression level of miR-638 showed a significant association with the AKI stage, serum creatinine level and CRP concentration of patients, which are important indicators in the development of AKI and are linked to the increased risk of AKI (12).

The results of the ROC curve demonstrated that miR-638 discriminated AKI patients from non-AKI patients and healthy controls with high sensitivity and specificity, and exhibited areas under the curve close to 1. Moreover, the expression level of miR-638 was demonstrated to be an independent indicator to predicate the prognosis of AKI patients.

In summary, the upregulation of miR-638 in AKI was associated with the development of AKI. Additionally, miR-638 was identified as a diagnostic and prognostic biomarker for the early detection and risk evaluation of AKI.

REFERENCES

1. Abd ElHafeez S, Tripepi G, Quinn R, et al. Risk, predictors, and outcomes of acute kidney injury in patients admitted to intensive care units in Egypt. Sci Rep 2017; 7(1):17163.
2. Pan HC, Chien YS, Jenq CC, et al. acute kidney injury classification for critically ill cirrhotic patients: a comparison of the KDIGO, AKIN, and RIFLE Classifications. Sci Rep 2016; 6:23022.
3. Bellomo R, Kellum JA, Ronco C. Defining acute renal failure: physiological principles. Intensive

Care Med 2004; 30(1):33-7.
4. Weber JA, Baxter DH, Zhang S, et al. The microRNA spectrum in 12 body fluids. Clin Chem 2010; 56(11):1733-41.
5. Bartel DP. MicroRNAs: genomics, biogenesis, mechanism, and function. Cell 2004; 116(2):281-97.
6. Lorenzen JM, Kielstein JT, Hafer C, et al. Circulating miR-210 predicts survival in critically ill patients with acute kidney injury. Clin J Am Soc Nephrol 2011; 6(7):1540-6.
7. Tang KL, Tang HY, Du Y, Tian T, Xiong SJ. MiR-638 suppresses the progression of oral squamous cell carcinoma through wnt/beta-catenin pathway by targeting phospholipase D1. Artif Cells Nanomed Biotechnol 2019; 47(1):3278-85.
8. Li M, Wang J, Liu H. Downregulation of miR-638 promotes progression of breast cancer and is associated with prognosis of breast cancer patients. Onco Targets Ther 2018; 11:6871-7.
9. Shi M, Jiang Y, Yang L, Yan S, Wang YG, Lu XJ. Decreased levels of serum exosomal miR-638 predict poor prognosis in hepatocellular carcinoma. J Cell Biochem 2018; 119(6):4711-6.
10. Zheng DH, Wang X, Lu LN, Chen DL, Chen JM, Lin FM, Xu XB. MiR-638 serves as a tumor suppressor by targeting HOXA9 in glioma. Eur Rev Med Pharmacol Sci 2018; 22(22):7798-806.
11. Lu J, Kwan BC, Lai FM, et al. Glomerular and tubulointerstitial miR-638, miR-198 and miR-146a expression in lupus nephritis. Nephrology (Carlton) 2012; 17(4):346-51.
12. Tang Y, Mak SK, Xu AP, Lan HY. Role of C-reactive protein in the pathogenesis of acute kidney injury. Nephrology (Carlton) 2018; 23(S4):50-2.

LETTER TO THE EDITOR

Dysregulation of lncRNA NRON in diabetic cardiomyopathy protects against high glucose-induced cardiomyocyte injury and inflammation

JZ. Li[1*], XH. Jin[1*], FM. Zhang[2] and QR. Guo[3]

[1]Department of Endocrinology, Caoxian People's Hospital, Shandong, China; [2]Department of Tuberculosis, Caoxian Tuberculosis Hospital, Shandong, China; [3]Department of Cardiology, Caoxian People's Hospital, Shandong, China

Received January 1, 2021 – Accepted February 22, 2021

[*]These authors contributed equally to this work

To the Editor,

Diabetic cardiomyopathy (DCM) is a form of heart disease with endocrine disorders that occurs independently of other cardiac risks (1). With increasing obesity and diabetes, the prevalence and mortality of DCM are emerging at an exceeding high rate (2). Thus, substantial research is needed to explore the molecular mechanisms of DCM and identify biomarkers to improve the management of DCM patients.

LncRNAs are recorded functionally well-characterized and exert heterogeneous biological functions through diverse molecular mechanisms, including the interaction with miRNA (3). Substantial research focuses on the effects of lncRNA in the pathogenesis of DCM. This is exemplified in the report written by Yang et al., lncRNA Kcnq1ot1 increasingly expresses in the AC16 cell models of DCM and participates in DCM by influencing miR-214-3p (4). LncRNA non-coding repressor of NFAT (NRON) is now receiving more attention and is identified as a protective role in the inflammatory responses and function of myocardial cells. A notable study written by Sun et al. proposes that the Lync inhibition of NRON facilitates the inflammation and atrial fibrosis in atrial myocytes (5). Another study indicates the expression of NRON was reduced in 34 patients with atrial fibrillation when compared with 20 patients with sinus rhythm, and represses fibroblast proliferation, which illustrates this point of view more clearly (6). In contrast to earlier studies, however, the expression level of NRON and its effects in DCM remains unsettled.

The purpose of this study was to detect the expression pattern of NRON in patients with DCM and its function in the clinical identification of DCM patients. Furthermore, the influence of NRON on viability, apoptosis, and inflammatory reaction of atrial myocyte models of DCM was validated.

MATERIALS AND METHODS

Patients and clinical samples

A total of 72 patients with DCM was randomly enrolled in our study from hospitalized patients in Caoxian People's Hospital. Another 65 patients with diabetes mellitus (DM) from the same hospital volunteered to participate in this study as control individuals. All these participants underwent myocardial biopsy suspected of

Key words: lncRNA NRON; diabetic cardiomyopathy; diagnosis; viability; apoptosis; inflammation

Corresponding Author:
Dr Qiurong Guo,
Department of Cardiology,
Caoxian People's Hospital,
Fumin Avenue, Shandong, 274400, China
Tel.: +86 0530 3490866 - Fax: +86 0530 3490866
e-mail: rong701102@163.com

0393-974X (2021)
Copyright © by BIOLIFE, s.a.s.
This publication and/or article is for individual use only and may not be further reproduced without written permission from the copyright holder.
Unauthorized reproduction may result in financial and other penalties
DISCLOSURE: ALL AUTHORS REPORT NO CONFLICTS OF INTEREST RELEVANT TO THIS ARTICLE.

heart disease. The patients were diagnosed as DCM by the myocardial biopsy and clinicopathological features, whereas the controls were excluded from the risk of DCM after all clinical examinations. Namely, DCM patients were identified by abnormal cardiac systolic function and a history of heart failure in the absence of coronary artery disease, hypertension, or valvular heart disease (7). The diagnosis of DM strictly followed the American Diabetes Association Standards published in 2014 (8). The inclusion criteria for the control group were: no complication of DM; no cancer or other severe diseases; no hypertension. All participants included in the study provided written informed consent. The protocols and design of this study were approved by the Ethics Committee of Caoxian People's Hospital.

RNA extraction and quantitative real-time PCR (qRT-PCR)

Total RNA was extracted from tissues of each individual by TRIzol Reagent (Invitrogen, USA). The concentration and quality of RNA were measured by Qubit 4 Fluorometer and NanoDrop 2000 (ThermoFisher, USA). The cDNA was synthesized from total RNA via SuperScript reverse transcription kit (ThermoFisher, USA) per the manufacturer's instructions.

The qRT-PCR was carried out to detect the relative expression of NRON and inflammatory cytokines on the 7500 system (ThermoFisher, USA). PowerUp™ SYBR™ Green Master Mix (ThermoFisher, USA) was used to assess the expression of NRON and inflammatory cytokines. The primers of NRON were as follows: forward 5'-CAAATCCAGTTGCAAGGACC-3', and reverse 5'-AGCTCAGTCCTAGGGTAGG-3'. GAPDH was used as a housekeeping gene and each experiment was performed three times.

In vitro cell assays

Human cardiomyocyte cell line AC16 was obtained from American Type Culture Collection (ATCC; Manassas, VA, USA). All cells were cultured in Dulbecco modified Eagle medium (Thermo Fisher Scientific, MA, USA) supplemented with 12% fetal bovine serum (FBS) and penicillin/streptomycin (Invitrogen, CA, USA) in an incubator of 5% CO_2 at 37°C. The cell models of DCM were established by a concentration (30 nM) of glucose for 48 h and controls were cultured with 5.5 nM glucose for 48 h. The overexpression vector of NRON and its negative control (NC) were purchased from IBSBIO (Shanghai, China). The transfected experiments were performed according to the recommended procedures of Lipofectamine 3000 (Invitrogen, CA, USA).

The cells were collected after 48-h incubation and seeded into a 6-well plate at an appropriate concentration. Lactate dehydrogenase activity assay Kit (Jiancheng, Nanjing, China) was used to measure the concentration of LDH in the culture medium of AC16. The AC16 cells were seeded into each well of a 96-well plate at a concentration of 1×10^4 cells/well. The plate was added with 20 µl MTT solution and incubated for further 4 h. After that, the supernate was discarded and 150 µl DMSO was added into each well. The absorption value was measured under

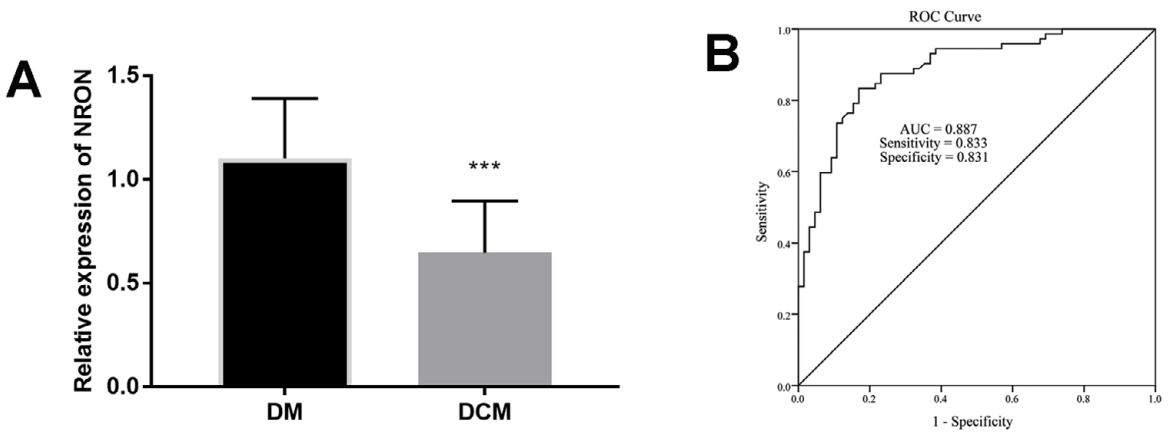


Fig. 1. *The expression and prognostic significance of NRON in DCM patients. **A)** The relative expression of NRON was reduced in DCM patients when compared with DM controls. **B**) The results of the ROC curve of NRON for DCM patients. ***P < 0.001.*

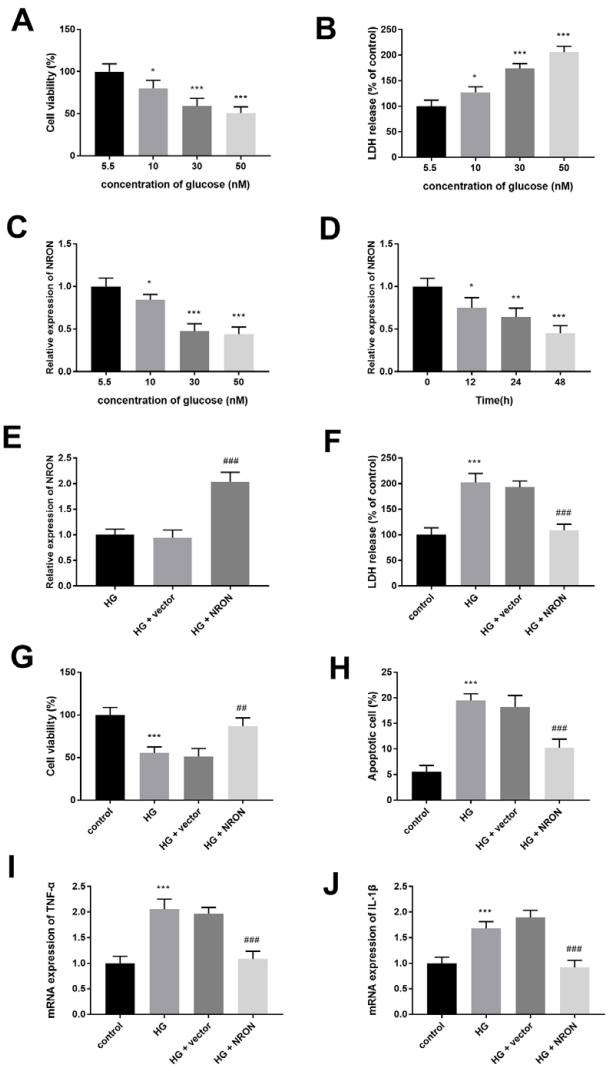


Fig. 2. *NRON protects cardiomyocyte cells from HG injury. **A**) The cell viability was decreased with the gradual increase of glucose. **B**) The LDH release was increased with the gradual increase of glucose. **C**) The relative expression of NRON was reduced with the gradual increase of glucose. **D**) The relative expression of NRON was detected after different processing times with glucose. **E**) The relative expression of NRON was detected by qRT-PCR. **F**) The release of LDH was increased in the HG group and upregulation of NRON reversed this adverse effect. **G**) The overexpression of NRON suppressed the inhabitation of cell viability caused by HG. **H**) The apoptotic cells were increased by HG and the abundance of NRON repressed this trend. **I, J**) The elevated expression of NRON attenuated the concentration inflammatory factors induced by HG. *P < 0.05, **P < 0.01, ***P < 0.001, compared to the control group; ##P < 0.01, ### P < 0.001, compared to the HG group.*

a microplate reader at 490 nm. AC16 cells growing in the logarithmic phase were washed with pre-cooled PBS and collected. 500 µl binding buffer was added to the cells and cells were cultured with 5 µl Annexin V-EGFP and 5 µl propidium iodide for 10 min at room temperature in the dark. A flow cytometer was used for observation and detection.

Statistical analysis

The data were calculated in the software of SPSS and GraphPad and demonstrated as mean ± standard deviation. The comparison of different groups was analyzed with a Student's *t*-test, *chi*-squared test, or one-way ANOVA. ROC was applied to predict the value of NRON in distinguishing DCM patients from DM patients.

RESULTS

As presented in Table I, no difference was found in the aspects of age, gender, BMI (all $P > 0.05$). The other characteristics, such as diabetes history, smoke, total cholesterol, triglyceride, HDL-C, LDL-C, EDLV, and LVEF had no difference between the control group and DCM patients (all $P > 0.05$). However, the values of E/E' and HbA1c were significantly higher in the DM controls than that in the DCM group (all $P < 0.001$).

Expression and diagnostic value of NRON in DCM patients

The result of qRT-PCR analysis is represented in Fig. 1A, which demonstrated that the relative expression of NRON was obviously decreased in the myocardial biopsy of DCM patients when compared with the DM patients ($P < 0.001$). This result proposed that NRON might participate in the development of DCM and play a protective role in the progression of DCM. The receiver operating characteristic (ROC) curve was applied to analyze the predictive value of NRON for DCM patients (Fig. 1B). The data showed the area under the curve of NRON was 0.887, the sensitivity was 0.833, and the specificity was 0.831 when the cutoff value was 0.856, suggesting that the levels of NRON might be an alternative diagnostic tool with high sensitivity and specificity.

Table I. *Clinical characteristics of DM controls and DCM patients*

Clinical features	DM controls (n = 65)	DCM patients (n = 72)	*P*-value
Age (years)	51.58±5.26	51.46±5.10	0.887
Gender			
Male	31	33	0.828
Female	34	39	
BMI (kg/m^2)	22.78±2.53	23.43±2.28	0.119
Diabetes history (months)	50.49±15.96	53.92±14.90	0.196
Smoke			0.249
Yes	38	35	
No	27	37	
Total cholesterol (mg/dl)	183.28±17.46	180.01±17.79	0.281
Triglyceride (mg/dl)	105.88±9.76	107.61±10.41	0.318
HDL-C (mg/dl)	37.78±4.18	38.71±4.75	0.231
LDL-C (mg/dl)	100.38±13.45	104.44±14.68	0.095
EDLV (mm)	4.98±0.19	5.04±0.25	0.143
LVEF (%)	57.48±3.45	56.08±3.92	0.057
E/E'	11.02±1.43	17.07±1.12	< 0.001
HbA1c	6.93±0.20	7.10±0.19	< 0.001

BMI: Body mass index; HDL-C: high density leptin cholesterol; LDL-C: low-density lipoprotein cholesterol; EDLV: left ventricular end diastolic diameter; LVEF: left ventricular ejection fractions; E/E': the ratio of early mitral velocity to tissue Doppler diastolic velocity.

Expression of NRON in AC16 cells

In order to simulate the injured cell by DCM, a series of concentration gradients of LDH was used to incubate AC16 cells. The cell viability and concentration of LDH were used to evaluate the result of establishing models after culturing for 48 h. As demonstrated in Fig. 2A, the cell viability was decreased was increased with the stimulated glucose ($P < 0.05$). Fig. 2B shows that the higher the glucose concentration, the higher the total LDH release ($P < 0.05$). Moreover, the relative expression of NRON in AC16 was detected under different glucose concentration and times. In Fig. 2 C and D, the data shows the relative expression of NRON was gradually decreased with the increasing dose of glucose and increasing time ($P < 0.05$).

NRON protects AC16 cells from the DCM injury

The NRON vectors were transfected into AC16 cells to adjust the relative expression of NRON artificially. The expression of NRON was significantly increased in the group of high glucose (HG) + NRON when compared with the HG group ($P < 0.001$) (Fig. 2E). The LDH release in different groups was further detected to show the protective effects of NRON in the cell models induced by HG. The overexpression of NRON reserved the high release of LDH induced by HG (Fig. 2F, $P < 0.001$).

The cell viability was significantly reduced in the HG group when compared with the control group, whereas the upregulation of NRON restored the cell viability (Fig. 2G, $P < 0.01$). The apoptosis of cells was prominently increased in the HG group and an elevated level of NRON reduced the number of apoptotic cells (Fig. 2H, $P < 0.001$). As shown in Fig. 2 I and J, the secretion of TNF-α and IL-1β was significantly elevated in the HG group, indicating that the inflammation was induced by the treatment of HG ($P < 0.001$). The transfection of vectors carrying NRON mitigated the reverse effects resulting from HG ($P < 0.001$).

DISCUSSION

In the present study, the expression of NRON was diminished in patients with DCM. Moreover, the ROC results substantiated that NRON could function as up-and-coming indicators. In a project about atrial fibrosis, the expression of NRON was decreased in patients (6). Another finding indicated that NRONwas downregulated in a group of cases with multiple sclerosis. Collectively, the expression of NRON was obviously reduced in DCM patients and could differentiate DCM patients in the clinical diagnosis.

The cardiomyocyte cell models were established in our study to indicate the function of NRON in DCM. The findings proposed that the expression of NRON was decreased in the cardiomyocyte cells, which was in accordance with previous results. The expression of NRON is reduced in the tissues of triple-negative breast cancer patients and the upregulation of NRON inhibits the proliferation of tumor cells (10). The inflammatory reaction is common in patients with DCM, and numerous cytokines become part of this feedback (11). In our study, the up-regulation of NRON was propitious to the amelioration of damaged cells in terms of viability and apoptosis. The overexpression of NRON attenuated the expedited concentration of TNF-α and IL-1β induced by HG, indicating NRON might protect the cell from inflammatory damage by reducing the secretion of TNF-α and IL-1β. The above-mentioned results implied that NRON played an inflammatory factor in the progression of DCM. Takern together, the results elucidated that the NRON might be a protective factor in DCM by promoting cell viability and suppressing cell apoptosis.

In conclusion, the expression of NRON was significantly decreased in patients with DCM and cell models induced by HG. The level of NRON was verified to be a promising marker. Moreover, the overexpression of NRON inhibited cell injury by motivating cell viability, repressing cell apoptosis, and suppressing inflammatory impairment.

REFERENCES

1. Jia G, Whaley-Connell A, Sowers JR. Diabetic cardiomyopathy: a hyperglycaemia- and insulin-resistance-induced heart disease. Diabetologia 2018; 61(1):21-8.
2. Jia G, DeMarco VG, Sowers JR. Insulin resistance and hyperinsulinaemia in diabetic cardiomyopathy. Nat Rev Endocrinol 2016; 12(3):144-53.
3. Chen L, Zhou Y, Li H. LncRNA, miRNA and lncRNA-miRNA interaction in viral infection. Virus Res 2018; 257:25-32.
4. Yang F, Qin Y, Wang Y, et al. LncRNA KCNQ1OT1 mediates pyroptosis in diabetic cardiomyopathy. Cell Physiol Biochem 2018; 50(4):1230-44.
5. Sun F, Guo Z, Zhang C, et al. LncRNA NRON alleviates atrial fibrosis through suppression of M1 macrophages activated by atrial myocytes. Biosci Rep 2019; 39(11).
6. Wang Y, Xu P, Zhang C, Feng J, Gong W, Ge S, Guo Z. LncRNA NRON alleviates atrial fibrosis via promoting NFATc3 phosphorylation. Mol Cell Biochem 2019; 457(1-2):169-77.
7. Chen Y, Tan S, Liu M, Li J. LncRNA TINCR is downregulated in diabetic cardiomyopathy and relates to cardiomyocyte apoptosis. Scand Cardiovasc J 2018; 52(6):335-9.
8. Standards of medical care in diabetes--2014. Diabetes Care 2014; 37(S1):S14-80.
9. Rajesh M, Mukhopadhyay P, Bátkai S, et al. Cannabidiol attenuates cardiac dysfunction, oxidative stress, fibrosis, and inflammatory and cell death signaling pathways in diabetic cardiomyopathy. J Am Coll Cardiol 2010; 56(25):2115-25.
10. Niu L, Fan Q, Yan M, Wang L. LncRNA NRON down-regulates lncRNA snaR and inhibits cancer cell proliferation in TNBC. Biosci Rep 2019; 39(5).
11. Li Y, Zhao Y, Qiu C, et al. Role of eotaxin-1/CCL11 in sepsis-induced myocardial injury in elderly patients. Aging (Albany NY) 2020; 12(5):4463-73.

LETTER TO THE EDITOR

A new Italian chemical peel, based on *Oenanthe crocata* extract

P. Amori[1], G. Vitiello[1] and T. Lotti[2,3]

[1]Department of Dermatology, University of Rome G. Marconi, Rome, Italy; [2]University of Rome G. Marconi, Rome, Italy; [3]Department of Dermatology, I.M. Sechenov First Moscow State Medical University, Moscow, Russia

Received October 16, 2020 – Accepted February 23, 2021

To the Editor,

Chemical peeling is a technique commonly used to treat various skin alterations, such as age-induced damage, wrinkles, acne scars, and spots, and is based on a controlled destruction of the epidermis and dermis (1, 2). To obtain skin exfoliation or ablation, different acid solutions are applied to the skin surface, according to well-coded protocols (1). Chemical peeling is a procedure that allows a predictable and uniform ablation of the skin at a certain depth, to remove the layer of damaged skin and stimulate the formation of new tissue (3).

There are several categories of chemical peels, based on the depth of the ablation produced, and depending on the chemical properties of the acid employed (4). Furthermore, other factors, such as acid dilution, number of layers of application, time of exposure, skin type and the extent of the damage being treated, can affect the depth reached (4).

Recently, a new chemical peeling appeared on the market, classified as a Class 1 device, according to EU rules. It is made from a mix of three acids, namely azelaic, mandelic and pyruvic acid, plus ozonated olive oil, and mother tincture of Oenanthe, an extract of *Oenanthe crocata* (water dropwort), a plant pertaining to the *Apiaceae* family. The aim of this work is to evaluate the results obtained on several women by using Oenanthe peeling to treat facial aging.

MATERIALS AND METHODS

Ten women, aged 40 to 60, who presented aging and dry skin, wrinkles and a dull complexion were enrolled. These skin alterations indicated the possibility of treatment with a chemical peel. It was therefore decided to treat them with Oenanthe Peel®, by Harmony Progress, Italy.

Before the treatment, the skin of each patients was assessed using a hydration and sebometry test, with D-Squame™ and Sebutape™ adhesive patches (Difa Cooper, Spain). Photographs were taken with standard projection. Each patient underwent personalized cosmetic treatment for 15 days before the peeling in order to normalize the skin parameters evaluated by the previous tests.

The treatment was performed by applying Oenanthe Peel®, according to the protocol suggested by the manufacturer, i.e. apply on a well cleansed facial skin, for which pH Balance, a serum containing mostly mandelic, glycolic, kojic, pyruvic, and lactic acid, in order to balance the pH, was used. It was applied through a 2-3 min massage and rinsed with water. Oenanthe Peel® in drops (3-4 drops on the forehead, 5-6 on each cheek, 2 on each prolabium, 4-5 on the lower third, and 2 for each periocular area) was then applied and massaged vigorously, using nitrile gloves. This was repeated up to 3 times, as needed, followed by an application of Neutro Active serum, containing panthenol, resveratrol, thioctic acid, DMAE, etc., to normalize pH. The session was repeated after 15-21 days, for 4-6 times. At the end of the

Key words: chemical peeling; skin alterations; skin age-induced damages; wrinkles; acne scars; skin exfoliation; skin ablation

Corresponding Author:
Dr Paolo Amori,
Department of Dermatology,
University of Rome G. Marconi,
Via Plinio, 44, 00193 Roma, Italy
Tel.: +39 06 377251
e-mail: paoloamori@gmail.com

0393-974X (2021)
Copyright © by BIOLIFE, s.a.s.
This publication and/or article is for individual use only and may not be further reproduced without written permission from the copyright holder.
Unauthorized reproduction may result in financial and other penalties
DISCLOSURE: ALL AUTHORS REPORT NO CONFLICTS OF INTEREST RELEVANT TO THIS ARTICLE.

treatment, we again took photographs of all patients, at the same projections. The final evaluation of all photographs, both those before and after the treatment, was carried out independently by an operator other than the one who had performed the treatment. All patients enrolled in this clinical study had first signed an informed consent.

RESULTS

Consistent with other types of peelings, a temporary redness of the skin on the treated areas was observed immediately after each session. Skin appearance was smoother and tenser compared to the first session. None of the patients showed adverse effects. At the end of the treatment cycle, all the treated patients showed a shinier and firmer skin, a decrease in micro-roughness and an attenuation of the spots with consequently a more homogeneous skin appearance. Ultimately, the skin appeared smooth, compact and bright (Figs. 1-3).



Fig. 1. *Left before treatment. Right, after the first session.*



Fig. 2. *Left before treatment. Right, after the first session.*

DISCUSSION

As mentioned above, chemical peeling is a widespread technique, commonly employed to treat several skin alterations, such as age-induced damage, wrinkles, acne scars, spots (1, 2). Different acid solutions exist which, according to well-coded protocols, are applied to the skin surface for this purpose, to obtain a predictable and uniform exfoliation or ablation of the skin, removing the layer of damaged skin and stimulating the formation of new tissue (1, 3). Contraindications to the treatment are active infection, allergy to peeling components, topical or oral retinoid treatment within the previous 6 months, open wounds, pregnancy and the lactation period (4). Relative contraindications are inflammatory dermatosis, such as psoriasis, rosacea and atopic dermatitis, along with any recent facial surgery or radiation therapy (4). Irritation, burning, erythema, itching, edema, and blistering may occur, although infrequent. Other complications, due to an incorrect technique, consist of the development of acneiform eruptions, infections, persistent erythema, pigmentary changes, textural changes, scarring and increased pigmentation of nevi (4).

Recently, a new chemical peeling appeared on the market, classified as a Class 1 device, according to EU rules: Oenanthe Peel® which is made from a mix of three acids, namely azelaic, mandelic and pyruvic acid, plus ozonated olive oil, and mother tincture of Oenanthe, an extract of *Oenanthe crocata* (water dropwort). Azelaic acid is known to have good depigmenting properties, is bactericidal and inhibits the proliferation of keratinocytes (5); mandelic acid is a superficial peel and improves facial skin viscoelasticity (6, 7); pyruvic acid penetrates rapidly and deeply through the skin (8) and presents keratolytic, antimicrobial, and sebostatic properties as well as the ability to stimulate new collagen production and elastic fiber formation (4). Their simultaneous presence at low concentration in the formula allows them to act both on the surface and in depth. Ozonated olive oil is an antioxidant and antimicrobial which improves tissue oxygenation and promotes neovascularization, accelerating wound healing (9, 10).

The key ingredient of this formulation is however mother tincture of Oenanthe, namely an extract of *Oenanthe crocata*, a plant pertaining to the *Apiaceae* family, which grows spontaneously



Fig. 3. *Left before treatment. Right, after the first session.*

in Sardinia, is extremely poisonous, and resembles parsnip or carrot. This plant is identified as the "sardonic herb", a neurotoxic plant used in pre-Roman Sardinia for killing rituals (10). The sardonic herb induces contraction of facial musculature, mimicking a smile, hence the expression "sardonic smile", indicating a sinister smile. The poisonous constituents of Oenanthe species are a series of polyacetylene alcohols exemplified by oenanthotoxin (11). Polyacetylene neurotoxins seem to bind to the convulsant site of GABA receptors and cause death by inducing convulsions and respiratory paralysis (11). Furthermore, they seem to be responsible for the so-called "tightening effect" on the skin. In fact, this "tightening effect" is highly appreciated by patients, as the effect is immediately evident. It should be emphasized that the application performed through massage, according to the manufacturer's instructions (connective tissue massage) stimulates the papillary dermis by activating the production of collagen and elastin, thus obtaining maximum benefit with minimum cost (12).

The peculiarity of this peeling therefore consists in giving an immediate result, pleasing to the patient, and a long-term result due to stimulating the formation of new tissue. The results of our study have been very satisfactory. In fact, all patients showed an improvement after the first session both in the appearance of the skin, and a smoother aspect of the face. This appearance is obviously what the treatment aims for. More studies will be needed to confirm our results, which, however, seem to indicate effectiveness of this new peeling formula.

REFERENCES

1. Grajqevci-Kotori M, Kocinaj A. Exfoliative Skin-peeling, Benefits from This Procedure and Our Experience. Med Arch 2015; 69:414-6.
2. Castillo DE, Keri JE. Chemical peels in the treatment of acne: patient selection and perspectives. Clin Cosmet Investig Dermatol 2018; 11:365-72.
3. Soleymani T, Lanoue J, Rahman Z. A Practical Approach to Chemical Peels: A Review of Fundamentals and Step-by-step Algorithmic Protocol for Treatment. J Clin Aesthet Dermatol 2018; 11:21-8.
4. O'Connor AA, Lowe PM, Shumack S, Lim AC. Chemical peels: A review of current practice. Australas J Dermatol 2018; 59:171-81.
5. Schulte BC, Wu W, Rosen T. Azelaic Acid: Evidence-based Update on Mechanism of Action and Clinical Application. J Drugs Dermatol 2015; 14:964-8.
6. Jacobs SW, Culbertson EJ. Effects of Topical Mandelic Acid Treatment on Facial Skin Viscoelasticity. Facial Plast Surg 2018; 34:651-6.
7. Wójcik A, Kubiak M, Rotsztejn H. Influence of azelaic and mandelic acid peels on sebum secretion in ageing women. Postepy Dermatol Alergol 2013; 30:140-5.
8. Berardesca E, Cameli N, Primavera G, Carrera M. Clinical and instrumental evaluation of skin improvement after treatment with a new 50% pyruvic acid peel. Dermatol Surg 2006; 32:526-31.
9. Valacchi G, Fortino V, Bocci V. The dual action of ozone on the skin. Br J Dermatol 2005; 153:1096-100.
10. Kirkil C, Yiğit MV, Özercan IH, Aygen E, Gültürk B, Artas G. The Effect of Ozonated Olive Oil on Neovascularizatıon in an Experimental Skin Flap Model. Adv Skin Wound Care 2016; 29:322-7.
11. Appendino G, Pollastro F, Verotta L, et al. Polyacetylenes from Sardinian Oenanthe fistulosa: A Molecular Clue to risus sardonicus. J Nat Prod 2009; 72:962-5.
12. Nguyen HX, Puri A, Banga AK. Methods to simulate rubbing of topical formulation for in vitro skin permeation studies. Int J Pharm 2017; 519:22-33.

LETTER TO THE EDITOR

miR-520 predicates poor prognosis and inhibits the progression of cervical cancer

YX. Hou, CL. Min and LJ. Ma

Department of Laboratory Medicine, Weifang Yidu Central Hospital, Weifang, Shandong, China

Received December 23, 2020 – Accepted February 26, 2021

To the Editor,

Cervical cancer is one of the most common cancers in women with an increasing number of new cases (1). Despite developments in screening and early treatment, its occurrence is still common, and the mortality continues to be high. Recurrence and metastasis are two major causes of cervical cancer-related mortality(2), therefore, it is of great importance to explore novel therapeutic targets.

Carcinogenesis is a complicated process involving a variety of cellular hallmarks, such as resistance and uncontrolled cell growth, and promotes cell metastasis that can be regulated by aberrantly expressed microRNAs (miRNAs) (3). Studies in the literature have reported a series of dysregulated miRNAs that play roles in the progression of cervical cancer. For example, downregulated miR-424 was identified as a tumor suppressor of cervical cancer because of its suppressive role during tumor progression (4). miR-378 enhances migration and invasion by targeting autophagy-related protein 12 (5).

MiR-520 is a functional miRNA that has been demonstrated to play roles in the development of various cancers, including renal carcinoma, lung cancer, esophageal squamous cell cancer, and hepatoma cancer (6-9). In the miRNA expression profiling of cervical cancer, miR-520 has been identified as a downregulated miRNA, which makes it possible to participate in its progression of (10). Therefore, in this study, the function of miR-520 in the progression of cervical cancer and its function in the biological processes of were investigated.

MATERIALS AND METHODS

Tissues and cell lines

Cervical cancer tissues and corresponding non-cancerous tissues were obtained from 124 patients in Weifang Yidu Central Hospital during 2012-2014. None of the patients had received additional treatment prior to surgery. Specimens were obtained with informed consent and the study was approved by Weifang Yidu Central Hospital Ethics Committee. Collected tissues were frozen in liquid nitrogen and stored at –80°C until use. Survival data of patients were obtained with a follow-up time of 5 years.

Human cervical cancer cell lines (SiHa, C-33A, Caski, and Hela) and the normal cervical cell, ECT1/E6E7, were procured from American Type Culture Collection. Cells were cultured in Dulbecco's modified Eagle's medium (DMEM) with 10% fetal bovine serum (FBS; Gibco, Carlsbad, CA, USA) and maintained at 37°C with 5% CO2 in a humidified incubator.

Cell transfection

Cultured cell were transfected with miR-520 mimic (5'-CUACAAAGGGAAGCCCUUUC-3'), inhibitor (5'-GAAAGGGCUUCCCUUUGUAG-3'), mimic negative control (mimic NC), or inhibitor negative

Key words: cervical cancer; miR-520; prognosis; cell proliferation; migration; invasion

Corresponding Author:
Dr Lujuan Ma,
Department of Laboratory Medicine,
Weifang Yidu Central Hospital, No.4138, South Linglongshan Road,
Weifang 262500, Shandong, China
Tel.: +86 0536 3275532
e-mail: ydLjMa@163.com

0393-974X (2021)
Copyright © by BIOLIFE, s.a.s.
This publication and/or article is for individual use only and may not be further reproduced without written permission from the copyright holder.
Unauthorized reproduction may result in financial and other penalties
DISCLOSURE: ALL AUTHORS REPORT NO CONFLICTS OF INTEREST RELEVANT TO THIS ARTICLE.

control (inhibitor NC) to upregulate or downregulate the expression of miR-520, with untreated cells as control. The transfection was conducted with the help of Lipofectamine 2000 Reagent (Invitrogen; Thermo Fisher Scientific, Inc.) according to the manufacturer's instructions.

Quantitative Real-Time Polymerase Chain Reaction (qRT-PCR)

Total RNA was extracted from collected tissues and cells with TRIzol reagent (Thermo Fisher Scientific, Waltham, MA, USA) according to the manufacture's protocols. Relative expression of miR-520 was quantified by qRT-PCR with U6 as the control. cDNA was then synthesized by a Revert Aid First Strand cDNA Synthesis KIT (Thermo, Scientific, USA). qRT-PCR was performed with Applied Biosystems 7900 Real-Time PCR system (Applied Biosystems, Foster City, CA) and SYBR Green I Real-Time PCR Kit (GenePharma, Shanghai, China). Experiments were run in triplicate and the $2^{-\Delta\Delta Ct}$ method was used for quantification.

Cell proliferation, migration, and invasion

The proliferation of cervical cancer cells was evaluated by CCK8 assay. Cells were seeded into 96-well plates at 5×10^3 cells per well. Cell counting kit-8 (CCK-8) reagent (Dojindo, Kumamoto, Japan) were added into each well at 0, 24, 48, and 72 h of incubation and incubated for 1 h at 37°C with 5% CO_2. After incubation, the absorbance at 450 nm of each well was measured using a microplate reader (Thermo Fisher Scientific).

The migration and invasion of cervical cancer cells were assessed by Transwell assay in a 24-well Transwell chamber with a pore size of 8 μm. For the invasion assay, the wells were pre-coated with Matrigel (BD Biosciences, Franklin Lakes, NJ, USA) to form a barrier. Transfected cells (5×10^4) were seeded into upper chambers with FBS-free culture medium and the lower chamber was filled with the medium with 10% FBS as a chemoattractant. After an incubation of 24 h, migrated and invaded cells were stained with 0.1% crystal violet. The number of migrated and invasive cells was counted under a microscope.

Dual-luciferase reporter assay

The 3'-UTR of VEGF containing the binding sites of miR-520 was coned into the pmirGLO vector. The mutant vector was constructed with mutations in binding

Table I. *Association between miR-520 expression and the clinicopathological features of the patients (n = 124)*

	Total patients (n = 124)	miR-520 expression		*P* value
		Low (n = 69)	High (n = 55)	
Age				
≤ 45	58	34	24	0.644
> 45	66	35	31	
Tumor size (cm)				
≤ 4	61	36	25	0.287
> 4	63	33	30	
Differentiation				
Well + moderate	75	30	45	0.312
Poor	49	39	10	
Lymph node metastasis				0.178
Negative	87	45	42	
Positive	37	24	13	
FIGO stage				
I/II	84	50	34	0.016*
III/IV	40	19	21	

sites using a Quickchange Site-Directed Mutagenesis kit. Then, Hela cells were seeded into the 48-well plates and co-transfected with luciferase plasmids, pmirGLO -VEGF WT or pmirGLO -VEGF MT vector, and miR-520 mimic or inhibitor. The relative luciferase activity levels were detected with the Dual-luciferase Reporter Assay kit according to the manufacturer's instructions.

Statistial analysis

All statistical analyses were conducted by SPSS 20.0 (SPSS, Inc., Chicago, IL, USA) and GraphPad Prism 5.0 software (GraphPad Software, Inc., Chicago, USA). Student's paired *t*-test was performed to compare the differences between collected paired tissues. The expression of miR-520 was associated with the clinicopathological information of patients by the χ^2 test. Survival of patients was estimated by the Kaplan-Meier analysis and evaluated by the log rank test. The multivariate analysis of prognostic values was evaluated using the Cox proportional hazards model.

RESULTS

miR-520 expression in cervical cancer

miR-520 expression levels in cervical cancer tissues and noncancerous tissues were detected by qRT-PCR. Compared with the expression of miR-520 in normal tissues, miR-520 was significantly downregulated in cervical cancer tissues ($P < 0.001$, Fig. 1A). Moreover, the expression level of miR-520 was also investigated in cervical cancer cell lines. Compared with the normal cervical epithelial cell line ECT1/

Table II. *Multivariate Cox analysis of clinical parameters in relation to overall survival*

	HR factor	95% CI	P value
miR-520	2.598	1.041-6.489	0.041
Age	1.177	0.532-2.604	0.687
Tumor size	1.891	0.769-4.648	0.165
differentiation	1.997	0.826-4.830	0.125
Lymph node metastasis	2.302	0.773-6.855	0.134
FIGO stage	2.099	0.966-4.560	0.061

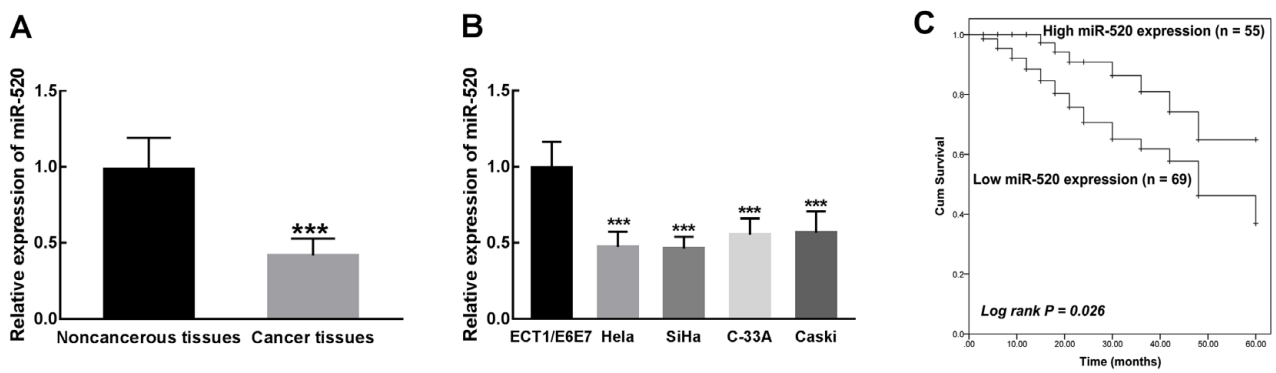


Fig. 1. *Expression of miR-520 in cervical cancer tissues and cells. **A**) The expression level of miR-520 was significantly lower in cervical cancer tissues than in noncancerous tissues ($P < 0.001$); **B**) The expression level of miR-520 was significantly lower in cervical cancer cells (SiHa, C-33A, Caski, and Hela) than in normal cervical epithelial cell line ECT1/E6E7 ($P < 0.001$). **C**) Kaplan-Meier curve of cervical cancer patients based on the expression of miR-520. Patients with low miR-520 expression had a poorer prognosis than patients with high miR-520 expression (Log rank P = 0.026).*

E6E7, miR-520 showed a decreased expression in cervical cancer cells (SiHa, C-33A, Caski, and Hela) ($P < 0.001$, Fig. 1B). Hela and SiHa cells showed a relatively lower miR-520 expression than C-33A and Caski cells, indicating the higher sensitivity of Hela and SiHa cells to the downregulation of miR-520. Therefore, Hela and SiHa cells were selected for following *in vitro* experiments.

Association between miR-520 expression and clinicopathological features of the patients

The recruited 124 cervical cancer patients were divided into two groups, an miR-520 low expression group and an miR-520 high expression group, according to the average expression level of miR-520 in cervical cancer tissues (0.417). The expression of miR-520 was associated with the clinicopathological information of the patients by the χ^2 test. As shown in Table I, miR-520 was closely associated with the FIGO stage of patients ($P = 0.016$) and other features did not show significant associations ($P > 0.05$).

Downregulation of miR-520 predicates poor prognosis of patients

The Kaplan-Meier curve of cervical cancer patients with low or high miR-520 expression showed that patients in the low miR-520 expression group showed a worse survival rate than that of patients with high expression of high miR-520 (Log rank $P = 0.026$, Fig. 1C). Moreover, the result of Cox regression analysis showed that miR-520 served as an independent indicator for the prognosis of cervical cancer patients with the HR factor value of 2.598 (95% CI = 1.041-6.489, $P = 0.041$, Table II).

Expression of miR-520 in cervical cancer cells regulated by cell transfection

After transfection with miR-520 mimic, miR-520 relative expression in Hela and SiHa cells was significantly upregulated compared with control and negative control groups ($P < 0.001$, Fig. 2A). On the other hand, the expression miR-520 significantly decreased in cells transfected with miR-520 inhibitor relative to untreated cells ($P < 0.001$, Fig. 2A). These results all illustrated that Hela and SiHa cells were successfully transfected.

Downregulation of miR-520 promoted the proliferation, migration, and invasion of cervical cancer cell

s

CCK8 assay showed that dramatically higher

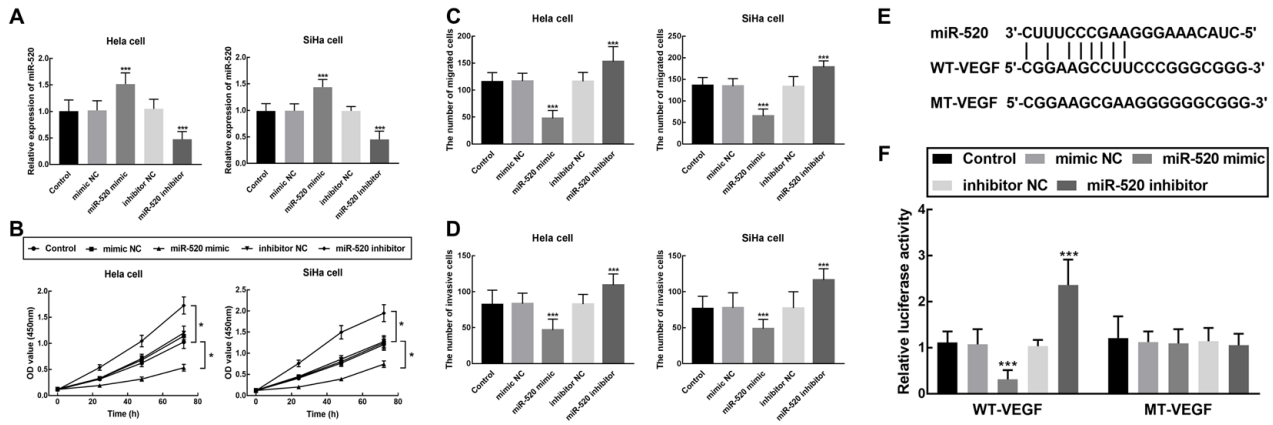


Fig. 2. *Effect of miR-520 on cell proliferation, migration, and invasion of cervical cancer.* ***A)*** *miR-520 mimic significantly increased the expression level of miR-520, while miR-520 inhibitor decreased the expression level of miR-520 in Hela and SiHa cells ($P < 0.001$);* ***B)*** *miR-520 upregulation inhibited the proliferation of Hela and SiHa cells, whereas it was promoted by the downregulation of miR-520 ($P < 0.05$);* ***C)*** *miR-520 overexpression suppressed the migration of Hela and SiHa cells, whereas it was enhanced by the knockdown of miR-520 ($P < 0.001$);* ***D)*** *miR-520 upregulation inhibited the invasion of Hela and SiHa cells, whereas it was enhanced by the downregulation of miR-520 ($P < 0.001$).* ***E)*** *The binding sites between miR-520 and the 3'UTR of VEGF.* ***F)*** *The overexpression of miR-520 significantly inhibited the relative luciferase activity of VEGF ($P < 0.001$).*

OD value at 450 nm was found in cells with the transfection of miR-520 inhibitor, indicating that miR-520 downregulation promoted cell proliferation of cervical cancer ($P < 0.05$, Fig. 2B). On the contrary, cells with the transfection of miR-520 mimic showed a lower OD value at 450 nm, which indicated the inhibitory effect of miR-520 upregulation on cell proliferation of cervical cancer ($P < 0.05$, Fig. 2B).

It was also found that the number of migrated and invasive cells in miR-520 mimic-transfected group was significantly lower than that of the control group. While the miR-520 inhibitor transfected group had enhanced migration and invasion compared with the control group, which revealed the promoter role of miR-520 downregulation in the migration and invasion of cervical cancer cells ($P < 0.001$, Fig. 2 C and D). Moreover, results of dual-luciferase reporter demonstrated that VEGF might be the direct target of miR-520. The relative luciferase activity of VEGF was significantly inhibited by the overexpression of miR-520 and enhanced by the knockdown of miR-520 ($P < 0.001$, Fig. 2 E and F).

DISCUSSION

The development of molecular markers could aid in the prevention, treatment and prognosis of cervical cancer. Accumulating evidence has demonstrated the vital roles of aberrant expression of miRNAs in the progression of multiple tumors, including cervical cancer. For example, miR-218 was downregulated and reduced cell viability by directly targeting IDO1 (11). miR-520 was evaluated as a dysregulated miRNA in cervical cancer (10), implying that it might be involved in the progression of cervical cancer.

The prognostic value of various miRNAs in different cancers have been widely reported. Aberrant expressed miR-153 in cervical cancer has been demonstrated to be associated with the poor prognosis of patients (12). In the present study, miR-520 was found to be downregulated and associated with the FIGO stage of cervical cancer patients, indicating its involvement in the progression of cervical cancer. In addition, MiR-520 was identified as an independent prognostic factor. Previously, miR-520 was demonstrated to suppress the proliferation and migration of lung cancer cells by regulating VEGF (7). The downregulation of miR-520 in renal carcinoma was involved in the tumor progression and provided a potential therapeutic target for the treatment of renal carcinoma (6). In hepatoma cancer, miR-520 was found to reduce the mutations of hepatoma cancer cells (9). In the present study, miR-520 served as a tumor suppressor that inhibited cell proliferation, migration, and invasion of cervical cancer. Additionally, VEGF was identified as the direct target of miR-520, suggesting that miR-520 might participate in the development of cervical cancer via targeting VEGF.

In conclusion, the downregulation of miR-520 in cervical cancer is associated with the FIGO stage and poor prognosis of patients. miR-520 serves as a tumor suppressor of cervical cancer via targeting VEGF.

REFERENCES

1. Ahmed NU, Rojas P, Degarege A. Knowledge of cervical cancer and adherence to pap smear screening test among female university students in a multiethnic institution, USA. J Natl Med Assoc 2020; 12(3):300-7
2. Rubin SC. Cervical cancer: successes and failures. CA: a cancer journal for clinicians 2001; 51:89-91.
3. Peters JM, Gonzalez FJ. The evolution of carcinogenesis. Toxicol Sci 2018; 165:272-6.
4. Xu J, Li Y, Wang F, Wang X, Cheng B, Ye F, et al. Suppressed miR-424 expression via upregulation of target gene Chk1 contributes to the progression of cervical cancer. Oncogene 2013; 32:976-87.
5. Tan D, Zhou C, Han S, Hou X, Kang S, Zhang Y. MicroRNA-378 enhances migration and invasion in cervical cancer by directly targeting autophagy-related protein 12. Mol Med Rep 2018; 17:6319-26.
6. Ding M, Lu X, Wang C, Zhao Q, Ge J, Xia Q, et al. The E2F1-miR-520/372/373-SPOP axis modulates progression of renal carcinoma. Cancer Res 2018; 78:6771-84.
7. Zhou W, Wu Y, Pan M, Liu D, Liu B. Proliferation and migration of lung cancer could be inhibited by oxymatrine through the regulation for miR-520/VEGF. Am J Chin Med 2019; 47:865-78.

8. Wu N, Song Y, Pang L, Chen Z. CRCT1 regulated by microRNA-520 g inhibits proliferation and induces apoptosis in esophageal squamous cell cancer. Tumour biology: the journal of the International Society for Oncodevelopmental Biology and Medicine 2016; 37:8271-9.
9. Miura N, Ishihara Y, Miura Y, Kimoto M, Miura K. miR-520d-5p can reduce the mutations in hepatoma cancer cells and iPSCs-derivatives. BMC Cancer 2019; 19:587.
10. Ye H, Yu X, Xia J, Tang X, Tang L, Chen F. MiR-486-3p targeting ECM1 represses cell proliferation and metastasis in cervical cancer. Biomed Pharmacother 2016; 80:109-14.
11. Zhu L, Tu H, Liang Y, Tang D. MiR-218 produces anti-tumor effects on cervical cancer cells in vitro. World J Surg Oncol 2018; 16:204.
12. Liu L, Lai X, Yuan C, et al. Aberrant expression of miR-153 is associated with the poor prognosis of cervical cancer. Oncol Lett 2018; 15:9183-7.

JOURNAL OF BIOLOGICAL REGULATORS & HOMEOSTATIC AGENTS Vol. 35, no. 2, 709-715 (2021)

LETTER TO THE EDITOR

Comparison of the effect of regular diet and low-fiber diet on bowel cleansing before colonoscopy

D. Liu*, H. Zhang*, D. Liu and T. Peng

Institute of Digestive Disease of Guangzhou Medical University, Department of Gastroenterology, The Sixth Affiliated Hospital of Guangzhou Medical University, Qingyuan, Guangdong, China

Received October 12, 2020 – Accepted February 26, 2021

+These authors contributed equally to this work

To the Editor,

Colonoscopy is a standard and valuable tool for screening colorectal precancerous and cancerous lesions. It is well-understood that the high quality of bowel preparation (BP) is critical for diagnostic accuracy and therapeutic safety of colonoscopy. BP regimens typically include dietary restrictions and oral cathartics. Traditionally, a clear liquid diet (CLD) is recommended for the day before the colonoscopy; however, patients' compliance is generally poor. Recent clinical data has demonstrated the superiority of a low-fiber diet (LFD) over CLD in improving BP quality (1). The European Society of Gastrointestinal Endoscopy Guideline recommends LFD with FDA-approved purgatives for BP (2). However, an LFD is considered too restrictive to provide enough calories, leading to starvation, fatigue, and hypoglycemia-induced side effects. In view of these facts, regular diet (RD) is being considered to increase patients' willingness to undergo colonoscopy. In a Korean multicenter, randomized study with healthy subjects with the avoidance of high-fiber food for 3 days before the colonoscopy, no significant difference in BP quality was observed between CLD and RD groups (3). A randomized, single-blind trial performed by the American University of Beirut Medical Center revealed a better BP quality with RD with split-dose of polyethylene glycol electrolyte (PEG) than LFD with the whole-dose of PEG (4). The present study was designed as a non-inferiority trial and aimed to test a hypothesis that the BP quality of RD is comparable to that of LFD.

MATERIALS AND METHODS

A randomized, non-inferiority, and single-blind prospective cohort trial was carried out at the Sixth Affiliated Hospital of Guangzhou Medical University from March 2019 to July 2019. Both outpatients and inpatients aged between 18-75 years who were scheduled for colonoscopy during that period were enrolled in this study. The exclusion criteria were as follows: patients under the age of 18 or over 75; acute abdominal disorders (such as acute pancreatitis, acute appendicitis, acute cholecystitis, gastrointestinal perforation, or acute intestinal obstruction), cirrhosis ascites, active inflammatory bowel disease, or other severe cardiopulmonary, cerebral, renal, and metabolic illnesses; colorectal cancer (CRC) on imaging; history of abdominal surgery, diabetes, or major psychiatric illness; females who were pregnant, menstruating, or breastfeeding.

The study was reviewed and approved by the

Key words: bowel preparation; colonoscopy; regular diet; low-fiber diet; diet satisfaction

Corresponding Author:
Dr Tieli Peng,
Institute of Digestive Disease of Guangzhou Medical University, Department of Gastroenterology, the Sixth Affiliated Hospital of Guangzhou Medical University, Qingyuan, Guangdong, China
Tel.: +86 18998986685
e-mail: pengtieli@126.com

0393-974X (2021)
Copyright © by BIOLIFE, s.a.s.
This publication and/or article is for individual use only and may not be further reproduced without written permission from the copyright holder.
Unauthorized reproduction may result in financial and other penalties
DISCLOSURE: ALL AUTHORS REPORT NO CONFLICTS OF INTEREST RELEVANT TO THIS ARTICLE.

Institutional Review Board of The Sixth Affiliated Hospital of Guangzhou Medical University. This study is registered at http://www.chictr.org.cn, with registration identification number ChiCTR1900021836. All study participants or their legal guardians provided informed written consent prior to enrollment.

Bowel preparation

Patients were randomized by a random number table to receive a split dose of 3L PEG preparation either with LFD (the LFD group) or RD (the RD group). On the day before the colonoscopy (until 8:00 PM), patients in the LFD group were instructed by oral notification and written notice to have an LFD (including rice, milk, noodles, eggs, meat, or other dairy products, excluding high-fiber food, such as vegetables, fruits, seaweeds, and mushrooms). Patients randomized to the RD group were allowed to have an RD without any restriction. All patients received three PEG sachets, each containing 59 g macrogol 4000, 1.46 g sodium chloride, 5.68 g anhydrous sodium sulfate, and 0.74 g potassium chloride, and1.68 g sodium bicarbonate. Those sachets were to be dissolved in 3 L water. 2 L PEG solution was consumed at 8:00 PM before the day of colonoscopy (250ml/15min), and the remaining 1 L PEG solution was consumed within 4 to 6 h before the procedure, and then, 5 g dimethicone powder mixed with 50 ml water was consumed 30 min later. All colonoscopies were performed between 9:00 AM and 12:00 PM.

Data collection

Before the colonoscopy, patient information was collected, such as age, gender, height, weight, body mass index (BMI), history of constipation and diarrhea, hypertension, history of smoking and alcohol, and family history of CRC. Before the procedure, all participants were interviewed by an independent investigator and asked to complete a questionnaire detailing their diet plan and overall preparation process (medicine and diet). All patients were informed of potential common adverse events (including hunger, sleep disturbance, dizziness, fatigue, vomiting, abdominal pain, nausea, acid regurgitation, anal orifice, bloating, palpitation, heartburn, cough, and dry mouth) during the preparation process. Endoscopists, who were blinded to the type of diet preparation, used the Boston Bowel Preparation Scale (BBPS) to assess the quality of the BP (5). Adequate bowel cleansing was defined as a BBPS score ≥ 2 in all three colon segments and ≥ 6 in the total colon. We measured the amount of foam and bubbles and their overall impact on mucosal visualization in each bowel segment (6). Moreover, we collected the results of colonoscopy and the histopathology of the polyps. The polyp detection rate (PDR) and adenoma detection rate (ADR) were defined as the proportion of procedures detecting at least one polyp and one adenoma, respectively. The indicators for clinical outcomes were the quality of BP, dietary satisfaction, PDR, and ADR. The colonoscopy withdrawal time was more than 6 minutes.

Statistical analysis

The sample size calculation was based on the assumption of a 90% adequate preparation in the LFD group *versus* 75% in the RD group. Using an α level of 0.05 and statistical power of 95%, considering a 10% dropout rate, the sample size was 180 patients per group. The software SPSS version 24 was used for statistical analyses. The normal distribution of data (BMI) was expressed as mean±SD and analyzed by the Student`s *t*-test, while the skew distribution of data (Age) was described by median and quartile spacing and tested by rank-sum test statistics. The *chi*-squared or Fisher's exact test was used to compare count data. Analyses on the clinical outcomes (the quality of bowel preparation, dietary satisfaction, PDR, and ADR) were made by both intention-to-treat (ITT) and per-protocol (PP) analyses. All other analyses were carried out on a PP cohort. *P*-value <0.05 was considered statistically significant. The primary endpoint was the rate of adequate BP, and the secondary endpoints included bubble scale, the rate of dietary satisfaction, PDR, ADR, and adverse events.

RESULTS

The flow chart of this study is shown in Fig. 1. A total of 400 patients were included and randomized to either the LFD group (n=200) or RD group (n=200). In the RD group, 25 patients were excluded from the per-protocol (PP) analysis for not taking laxatives as required (n=6), not following the diet preparation (n=18), or not finishing colonoscopy (n=1). In the LFD group, 18 patients were excluded from the PP analysis for not taking laxatives as required (n=14),

not following the diet preparation (n=2), or not finishing colonoscopy (n=2). Ultimately, 357 patients (175 in the RD group and 182 in the LFD group) remained who finished the complete procedure in PP population.

The demographic and clinic characteristics of patients in the two groups are listed in Table I. Among the 357 patients, 174 (48.7%) were males, and 183 (51.3%) were females. Patients' age ranged from 18 to 75 years, with a median age of 49 (40, 57). No significant differences were observed between the two groups in terms of gender, age, BMI, history of smoking and alcohol, family history of CRC, hypertension, constipation, diarrhea, and mixed bowel habits.

Comparison of clinical outcome

The clinical outcome of the two groups is shown in Table II. The BP quality was evaluated by the BBPS and the bubble scale. The RD group had a similar portion of adequate BP (PP analysis 97.1% *vs* 98.4%, *P*=0.440; ITT analysis 96.5% *vs* 99.6%, *P*=0.792) and 0 score in bubble scale with the LFD group (PP analysis 97.1% *vs* 98.4%, *P*=0.440; ITT analysis 97.1% *vs* 98.4%, *P*=1.000). The ADR in PP population was 17.1% (23.6% in men, 10.9% in women). No differences were observed in terms of dietary satisfaction (PP analysis 99.4% *vs* 99.9%, *P*=0.097; ITT analysis 97.0% *vs* 96.5%, *P*=0.778), PDR (PP analysis 25.6% *vs* 27.1%, *P*=0.641; ITT analysis 24.5% *vs* 23.0%, *P*=0.724), and ADR (PP analysis 16.0% *vs* 17.42%, *P*=0.619; ITT analysis 17.0% *vs* 16.5%, *P*=0.893) between the two groups.

The adverse events during the BP in the two groups are shown in Table III. There were no significant differences in adverse events between the two groups, except hunger, which in the RD group was significantly lower than the LFD group (*P*=0.010).

Evaluation of bowel preparation quality in different subgroups

We divided the patients into three subgroups according to their ages: young patients (18 to 40 years old), middle-aged patients (41 to 65 years old), and elderly patients (66 to 75 years old). In young patients, there were no differences in terms of the portion of adequate BP (PP analysis 100% *vs* 93.5%, *P*=0.233; ITT analysis 100% *vs* 94.2%, *P*=0.216), 0 score in bubble scale (PP analysis 95.7% *vs* 97.8%, *P*=1.000; ITT analysis 96.4% *vs* 98.1%, *P*=1.000), dietary satisfaction (100.0% *vs* 97.8%, *P*=0.991; ITT analysis 100% *vs* 98.4%, *P*=1.000), PDR (PP analysis 8.5% *vs* 10.9%, *P*=0.973; ITT analysis 8.9% *vs* 9.6%, *P*=1.000), and ADR (PP analysis

Table I. *Demographic data and indication for colonoscopy.*

	RD group (n=175)	**LFD group (n=182)**	***P-value***
Gender (Male/Female)	91/84	83/99	0.227
Age	48 (39, 56)	51 (40, 57)	0.177
BMI ($\bar{x}$±s)	22.46±0.21	22.36±0.24	0.742
History of smoking (n, %)	40 (22.9%)	39 (21.4%)	0.745
History of alcohol (n, %)	33 (18.9%)	27 (14.8%)	0.310
Family history of CRC (n, %)	10 (5.7%)	8 (4.4%)	0.569
Hypertension (n, %)	22 (12.6%)	23 (12.6%)	0.985
Constipation (n, %)	33 (18.9%)	36 (19.8%)	0.825
Diarrhea (n, %)	28 (16.0%)	29 (15.9%)	0.986
Mixed bowel habits (n, %)	11 (6.3%)	7 (3.8%)	0.292

RD: Regular diet, LFD: Low-fiber diet, BMI: Body mass index

Table II. *Clinical outcomes according to different diet types (n, %)*

	RD group	LFD group	*P-value*
PP analysis	**n=175**	**n=182**	
Adequate bowel preparation[a]	170 (97.1%)	179 (98.4%)	0.440
Bubble scale=0	170 (97.1%)	179 (98.4%)	0.440
Dietary satisfaction	174 (99.4%)	181 (99.5%)	0.978
PDR	39 (22.3%)	43 (23.6%)	0.763
ADR	29 (16.6%)	32 (17.6%)	0.800
ITT analysis	**n=200**	**n=200**	
Adequate bowel preparation[a]	193 (96.5%)	192 (96.0%)	0.792
Bubble scale=0	194 (97.0%)	194 (97.0%)	1.000
Dietary satisfaction	194 (97.0%)	193 (96.5%)	0.778
PDR	49 (24.5%)	46 (23.0%)	0.724
ADR	34 (17.0%)	33 (16.5%)	0.893

[a] *BBPS score ≥2 in all three colon segments and ≥6 in the total colon RD: Regular diet, LFD: Low-fiber diet, PP: Per-protocol, ITT: Intention-to-treat, PDR: Polyp detection rate, ADR: Adenoma detection rate.*

Table III. *Adverse events (n, %)*

	RD group (n=175)	LFD group (n=182)	*P-value*
Adverse event	107 (61.1%)	126 (69.2%)	0.109
Hunger	62 (35.4%)	89 (48.9%)	0.010[a]
Sleep disturbance	56 (32.0%)	70 (38.0%)	0.202
Abdominal pain	4 (2.3%)	4 (2.2%)	1.000
Bloating	8 (4.6%)	9 (4.9%)	0.868
Nausea	4 (2.3%)	2 (1.1%)	0.645
Acid regurgitation	1 (0.6%)	0 (0.0%)	0.984
Vomiting	3 (1.7%)	1 (0.5%)	0.588
Fatigue	1 (0.6%)	0 (0.0%)	0.984
Palpitation	0 (0.0%)	1 (0.5%)	1.000
Dizziness	1 (0.6%)	0 (0.0%)	0.984
Dry mouth	0 (0.0%)	1 (0.5%)	1.000

[a] *P<0.05 RD: Regular diet, LFD: Low-fiber diet*

8.5% *vs* 6.5%, *P*=1.000; ITT analysis 8.9% *vs* 5.8%, *P*=0.718) in the two groups (Table IV). Similar results were obtained in middle-aged patients and elderly patients. Hunger in the RD group was significantly lower than the LFD group in young patients (*P*=0.029).

According to recent studies, hospitalization status was an independent risk factor for inadequate BP; therefore, we divided patients into inpatient and outpatient subgroups to analyze the quality of BP. In inpatients, there were no significant differences between the RD group and the LFD group in terms of the portion of adequate BP (PP analysis 92.5% *vs* 100%, *P*=0.055; ITT analysis 91.0% *vs* 98.8%, *P*=0.072), 0 score in bubble scale (PP analysis 100% *vs* 97.4%, *P*=0.641; ITT analysis 100% *vs* 97.5%, *P*=0.556), dietary satisfaction (PP analysis 100.0% *vs* 98.7%, *P*=1.000; ITT analysis 100% *vs* 98.82%, *P*=1.000), PDR (PP analysis 34.0% *vs* 27.6%, *P*=0.441; ITT analysis 40.3% *vs* 27.5%, *P*=0.101), and ADR (PP analysis 28.3% *vs* 18.4%, *P*=0.186; ITT analysis 28.4% *vs* 18.8%, *P*=0.169). Similar results were found in the outpatients. Hunger in the RD group was significantly lower than the LFD group in inpatients (*P*=0.036).

DISCUSSION

The quality of BP plays a fundamental role in colonoscopy examination. A good BP requires a clean colon and good tolerability. A study by Aoun et al. demonstrated that colonic preparation without dietary restriction provided a better quality of colon cleansing than CLD (4). However, the dose of PEG between the two groups was different in their study. Accordingly, our study aimed to test the hypothesis that an RD on the day before colonoscopy has efficacy comparable to a traditional LFD in BP.

Our study confirmed that the quality of BP and ADR in the RD group was comparable to that in the LFD group. Without changing the eating habits, RD may provide sufficient energy and improve patients'

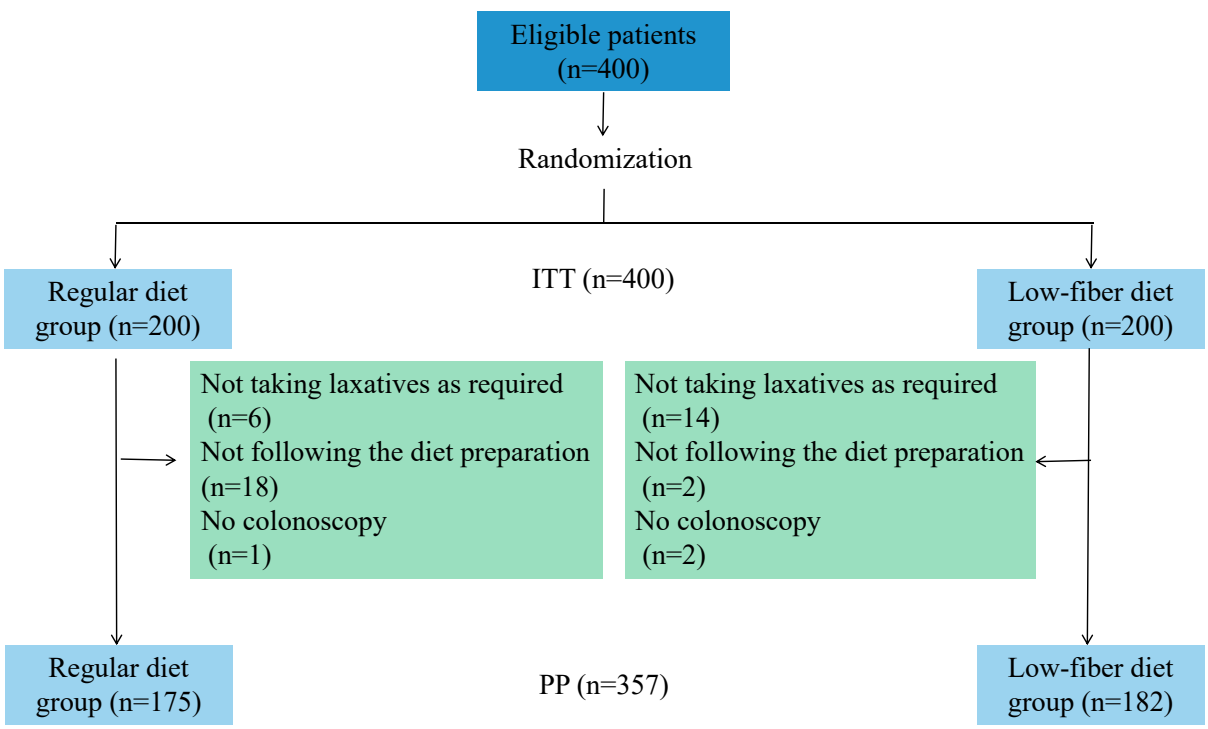


Fig. 1. *Enrolment flow chart*

Table IV. *Patients' bowel preparation quality in different ages (n, %)*

	RD group	LFD group	*P-value*
Young patients			
PP analysis	**n=47**	**n=46**	
Adequate bowel preparation[a]	47 (100%)	43 (93.5%)	0.233
Bubble scale=0	45 (95.7%)	45 (97.8%)	1.000
Dietary satisfaction	47 (100%)	45 (97.8%)	0.991
PDR	4 (8.5%)	5 (10.9%)	0.973
ADR	4 (8.5%)	3 (6.5%)	1.000
ITT analysis	**n=56**	**n=52**	
Adequate bowel preparation[a]	56 (100%)	49 (94.2%)	0.216
Bubble scale=0	54 (96.4%)	51 (98.1%)	1.000
Dietary satisfaction	56 (100%)	51 (98.1%)	0.970
PDR	5 (8.9%)	5 (9.6%)	1.000
ADR	5 (8.9%)	3 (5.8%)	0.718
Middle-aged patients			
PP analysis	**n=119**	**n=124**	
Adequate bowel preparation[a]	115 (96.6%)	124 (100%)	0.120
Bubble scale=0	117 (98.3%)	122 (98.4%)	1.000
Dietary satisfaction	118 (99.2%)	124 (100%)	0.984
PDR	32 (26.9%)	32 (25.8%)	0.848
ADR	22 (18.5%)	24 (19.4%)	0.863
ITT analysis	**n=133**	**n=136**	
Adequate bowel preparation[a]	127 (95.5%)	132 (97.1%)	0.720
Bubble scale=0	131 (98.5%)	131 (96.3%)	0.462
Dietary satisfaction	132 (99.2%)	136 (100%)	0.991
PDR	40 (30.1%)	36 (26.5%)	0.511
ADR	26 (19.5%)	25 (18.4%)	0.807
Elderly patients			
PP analysis	**n=9**	**n=12**	
Adequate bowel preparation[a]	8 (88.9%)	12 (100%)	0.429
Bubble scale=0	8 (88.9%)	12 (100%)	0.429
Dietary satisfaction	9 (100%)	12 (100%)	1.000
PDR	3 (33.3%)	6 (50.0%)	0.660
ADR	3 (33.3%)	5 (41.7%)	1.000
ITT analysis	**n=11**	**n=12**	
Adequate bowel preparation[a]	10 (90.9%)	12 (100%)	0.965
Bubble scale=0	10 (90.9%)	12 (100%)	0.965
Dietary satisfaction	10 (90.9%)	12 (100%)	0.965
PDR	5 (45.5%)	6 (50.0%)	0.827
ADR	3 (27.3%)	5 (41.7%)	0.667

[a] BBPS score ≥2 in all three colon segments and ≥6 in the total colon RD: Regular diet, LFD: Low-fiber diet, PP: Per-protocol, ITT: Intention-to-treat, PDR: Polyp detection rate, ADR: Adenoma detection rate.

compliance and tolerability. A significantly lower incidence of hunger was found in the RD group, especially in young patients and inpatients ($P<0.05$). Factors such as age and hospitalization status can also affect the quality of BP (7, 8). In our results, regardless of age or visits, no significant differences were observed between the two groups. Therefore, we suggest that RD should be recommended for BP.

As this is a single-center study with small sample size, further multicenter studies with a larger sample size are needed to confirm the efficacy and safety of RD for colonoscopy preparation.

ACKNOWLEDGEMENTS

The authors thank the investigators and patients for participating in this study. Kaihua Su, Fengling Liang, Ruyin Pan, Xixiang Qin from the Department of Gastroenterology, The Sixth Affiliated Hospital of Guangzhou Medical University, Yibo Ding from Department of Epidemiology, Second Military Medical University, Shanghai.

REFERENCES

1. Thukral C, Tewani SK, Lake AJ, et al. Results of a community-based, randomized study comparing a clear liquid diet with a low-residue diet using a magnesium citrate preparation for screening and surveillance colonoscopies. J Clin Gastroenterol 2019; 53:34-9.
2. Hassan C, East J, Radaelli F, et al. Bowel preparation for colonoscopy: European Society of Gastrointestinal Endoscopy (ESGE) Guideline - Update 2019. Endoscopy 2019; 51:775-94.
3. Jung YS, Seok HS, Park DI, et al. A clear liquid diet is not mandatory for polyethylene glycol-based bowel preparation for afternoon colonoscopy in healthy outpatients. Gut Liver 2013; 7:681-7.
4. Aoun E, Abdul-Baki H, Azar C, et al. A randomized single-blind trial of split-dose PEG-electrolyte solution without dietary restriction compared with whole dose PEG-electrolyte solution with dietary restriction for colonoscopy preparation. Gastrointest Endosc 2005; 62:213-8.
5. Calderwood AH, Jacobson BC. Comprehensive validation of the Boston Bowel Preparation Scale. Gastrointest Endosc 2010; 72:686-92.
6. Parente F, Vailati C, Bargiggia S, et al. 2-Litre polyethylene glycol-citrate-simethicone plus bisacodyl versus 4-litre polyethylene glycol as preparation for colonoscopy in chronic constipation. Dig Liver Dis 2015; 47:857-63.
7. Zhang YY, Niu M, Wu ZY, Wang XY, Zhao YY, Gu J. The incidence of and risk factors for inadequate bowel preparation in elderly patients: A prospective observational study. Saudi J Gastroenterol 2018; 24:87-92.
8. Almadi MA, Alharbi O, Azzam N, Altayeb M, Thaniah S, Aljebreen A. Bowel preparation quality between hospitalized patients and outpatient colonoscopies. Saudi J Gastroenterol 2018; 24:93-9.

LETTER TO THE EDITOR

Reliability of dental calcification compared to hand-wrist X-ray to evaluate skeletal maturation in growing subjects: a systematic review

M. Ferrillo[1], M. Migliario[2], C. Curci[3], A. Roccuzzo[4,5], M. Invernizzi[6,7] and A. de Sire[8]

[1]Dental School, Department of Surgical Sciences, University of Turin, Turin, Italy; [2]Department of Translational Medicine, University of Eastern Piedmont, Novara, Italy; [3]Physical Medicine and Rehabilitation Unit, Department of Neurosciences, ASST Carlo Poma, Mantova, Italy; [4]Department of Periodontology, School of Dental Medicine, University of Bern, Bern, Switzerland; [5]Department of Oral and Maxillofacial Surgery, Copenhagen University Hospital (Rigshospitalet), Copenhagen, Denmark; [6]Department of Health Sciences, University of Eastern Piedmont, Novara, Italy; [7]Infrastruttura Ricerca Formazione Innovazione (IRFI), Azienda Ospedaliera SS. Antonio e Biagio e Cesare Arrigo, Alessandria, Italy; [8]Department of Medical and Surgical Sciences, University of Catanzaro "Magna Graecia", Catanzaro, Italy

Received March 1, 2021 – Accepted March 24, 2021

To the Editor,

Skeletal maturation (SM) assessment is used in the common clinical practice of orthodontics, physiatrists, pediatrics, and orthopedics for the diagnosis of skeletal discrepancies to establish an optimal timing for intervention, and to monitor the treatment response in growing subjects (1-3). Moreover, bone maturation stages [prepubertal, peak growth spurt (PGS) or completed skeletal development] might help orthodontists in the choice between extraction or non-extraction, selection of orthodontic retention, and planning orthognathic surgery in case of skeletal malocclusions (4, 5). At the same time, physiatrists and orthopedics should start only from a clear SM evaluation in order to perform an adequate scoliosis screening and to provide a patient-tailored rehabilitative treatment aimed at reducing functional impairments and counteracting the potential disabling sequelae (6-9).

To date, SM is commonly evaluated through the hand wrist maturation (HWM), assessing the morphological changes shown by hand and wrist X-ray (1, 2). Although HWM is considered the gold standard, dental calcification assessment has been proposed as an innovative approach to avoid additional X-ray examinations (3). Dental maturity assessment could be used for evaluation of permanent teeth calcification degree, starting from periapical or panoramic radiographs routinely used for diagnosis in orthodontics (3, 4, 10). However, at the present time, although other SM assessment methods (i.e. cervical vertebral maturation) have been proposed (11), there is still no common agreement regarding the reliability of dental calcification compared to HWM for the assessment of SM (3, 4, 10).

This systematic review aimed to evaluate

Key words: growth and development; dental maturity; skeletal maturity; orthodontics; rehabilitation

Corresponding author:
Alessandro de Sire, MD
Associate Professor of Physical and Rehabilitative Medicine,
Department of Medical and Surgical Sciences,
University of Catanzaro "Magna Graecia",
Viale Europa, Località Germaneto, 88100 Catanzaro, Italy
Tel.: +390961369768
e-mail: alessandro.desire@gmail.com
https://orcid.org/0000-0002-5541-8346

0393-974X (2021)
Copyright © by BIOLIFE, s.a.s.
This publication and/or article is for individual use only and may not be further reproduced without written permission from the copyright holder.
Unauthorized reproduction may result in financial and other penalties
DISCLOSURE: ALL AUTHORS REPORT NO CONFLICTS OF INTEREST RELEVANT TO THIS ARTICLE.

the reliability of dental calcification according to Demirjian compared to HWM to assess SM in growing subjects and provide implications in the clinical management of a wide spectrum of pathological conditions.

Search strategy

This systematic review has been registered with PROSPERO number CRD42020220867 and was performed in accordance with the PRISMA statement. We systematically searched PubMed, Scopus, and Web of Science from inception until February, 1st, 2021 to recognize the papers published in literature, according to each specific thesaurus, adopting the following search strategy: ("hand-wrist") AND ("dental calcification" OR "dental age" OR "lateral cephalogram" OR "orthopantomography" OR "dental X-ray") AND ("skeletal maturation" OR "maturation" OR "skeletal maturity" OR "maturity" OR "growth peak" OR "growth spurt" OR "pubertal growth peak" OR "pubertal growth spurt" OR "ossification") AND ("pubertal stage" OR "growing age" OR "pubertal" OR "growth" OR "children" OR "adolescents").

Selection criteria

After the removal of duplicates, two reviewers independently screened articles for eligibility. In case of disagreement, a consensus was achieved by the decision of a third reviewer. All observational cross-sectional studies were screened and considered as eligible according to the following PICO model:

1. P) Participants consisted of growing subjects;
2. I) Intervention consisted of Demirjian method for the SM assessment;
3. C) Comparator consisted of HVM methods commonly used in clinical practice for SM assessment (i.e. Grave and Brown and Fishman);
4. O) Outcome measure consisted of the reliability of the Demirjian method compared to HWM for SM assessment.

The exclusion criteria were: studies investigating chronological, skeletal or dental age as primary outcomes; studies with cleft lip/palate patients; papers written in a language different from English; other study designs (e.g. case reports, case series, and reviews); full text unavailable (e.g. posters, conference abstracts, etc.); book chapters; animal studies.

Data extraction

Two reviewers independently extracted data from eligible full-text papers using a customized data extraction form in Microsoft Excel. Key data were extracted from each study relevant to the specific research questions. In case of disagreement, a consensus was achieved by the decision of a further experienced reviewer. The following data were extracted: authors; scientific journal; publication year; Nationality of study participants; population and number of patients; age of subjects; SM assessment methods; main findings.

Data synthesis

All the studies were synthetized describing both extracted data and main characteristics. Each study was then assessed for quality by a 10-item quality scoring according to a previous systematic review performed by our study group (11). The 10 criteria for the quality scoring of the studies included were the following: 1. Adequate presentation of study objective; 2. Adequate presentation of study design; 3. Clear description of eligibility criteria of study population; 4. Adequate presentation of methods of assessment; 5. Sample size calculation; 6. Presentation of demographic characteristics of the study population; 7. Adequate reliability assessment; 8. Appropriate statistical analysis; 9. Adequate reporting of results with tables and/or figures; 10. Declared p-values in the results. All of them could be scored as 0 (absence of the criterion) to 1 (presence of the criterion). Thus, the papers were classified as low-quality studies (0–4 points), medium-quality studies (5-7 points) or high-quality studies (8-10 points).

RESULTS

Out of 108 search results, 37 duplicates were removed, and 71 studies were considered as eligible for inclusion and screened for title and abstract,

of which, 25 papers were included for full-text screening. Sixteen articles not respecting eligibility criteria were excluded by the systematic review. Nine papers (12-20) were included in the synthesis, as depicted by PRISMA Flow Diagram in Fig. 1.

According to the above-mentioned 10-item quality scoring for the studies included, 4 studies (44.4%) were classified as high-quality studies (13-16) and 5 (55.6%) as medium-quality studies (12, 17-20). No low-quality studies were included in the present systematic review (further details about the quality scoring for each assessment criteria are depicted by Table I). A meta-analysis could not be performed due to the high clinical heterogeneity of the articles included in terms of variability of SM assessment and characteristics of study participants. The main characteristics of the 9 papers included (12-20) are shown in detail in Table II and described in the following paragraphs.

DM Demirjian vs HWM Grave and Brown. Three papers (12-14) compared the Demirjian method (3) with the HWM Grave and Brown method (1), reporting contrasting results: Camacho-Basallo et al. (12) showed no significant correlations ($p>0.05$) between the two methods; on the other hand, both Motghare et al. (13) and Uysal et al. (14) demonstrated significant correlations between Demirjian method and HWM Grave and Brown ($p<0.01$) method. More in detail, that the second molar showed the highest relationship (0.865 in female and 0.760 in male, and 0.826 in female and 0.706 in male, respectively). However, it was interesting to notice that canine showed a high significant relationship (0.808 in female and 0.768 in male) in one study (13) and a low significant relationship (0.691 in female; 0.633 in male) in another study (14).

DM Demirjian vs HWM Fishman. Seven papers (12, 15-20) compared the Demirjian method (3) with the HWM Fishman method (2). Günen Yılmaz et al. (15) divided the 11 SM indexes (SMI) of HWM Fishman method into three phases: pre-peak (SMI 1–2–3), peak (SMI 4–5–6–7), and post-peak (SMI 8–9–10–11); they reported a statistically significant correlation ($p<0.01$) between dental calcification and the 3 HWM Fishman groups (prepeak stages: CC=0.478; peak stages: CC=0.605; postpeak stages: CC=0.387).

Another 4 studies (16, 17, 19, 20) reported statistically significant correlations ($p<0.05$) between the Demirjian (3) and HWM Fishman (2) methods. However, the studies showed differences in terms of highest correlation (expressed as CC) with teeth involved: Krailassiri et al. (16) reported second premolars in both sexes (0.69 in female; 0.66 in male);

Table I. *Quality assessment of the studies included in the present systematic review.*

Articles	*Criteria for the quality scoring*										*Score*	*Quality level*
	1	*2*	*3*	*4*	*5*	*6*	*7*	*8*	*9*	*10*		
Camacho-Basallo et al. (2017) [12]	1	0	1	0	0	1	1	1	1	1	7	Medium quality
Motghare et al. (2016) [13]	1	0	1	1	0	1	1	1	1	1	8	High quality
Uysal et al. (2004) [14]	1	1	1	1	0	1	1	1	1	1	9	High quality
Günen Yılmaz et al. (2019) [15]	1	0	1	1	0	1	1	1	1	1	8	High quality
Krailassiri et al. (2002) [16]	1	1	1	1	0	1	1	1	1	1	9	High quality
Lecca-Morales et al. (2017) [17]	1	0	0	0	1	1	1	1	1	1	7	Medium quality
Mustafa et al. (2015) [18]	1	0	1	0	0	0	1	1	1	1	6	Medium quality
Ojha et al. (2018) [19]	0	0	1	1	0	0	1	1	1	1	6	Medium quality
Yadav et al. (2017) [20]	1	0	1	1	0	0	1	1	1	1	7	Medium quality

Criteria for the quality scoring of the studies included performed according to Ferrillo et al. [11] were: 1. Adequate presentation of study objective; 2. Adequate presentation of study design; 3. Clear description of eligibility criteria of study population; 4. Adequate presentation of methods of assessment; 5. Sample size calculation; 6. Presentation of demographic characteristics of the study population; 7. Adequate reliability assessment; 8. Appropriate statistical analysis; 9. Adequate reporting of results with tables and/or figures; 10. Declared p-values in the results.

Lecca-Morales et al. (17) reported second molars in both sexes (0.792 in female; 0.800 in male); both Ojha et al. (19) and Yadav et al. (20) reported second molars in female (0.882 and 0.845, respectively) and canines in male (0.835 and 0.755, respectively). Nevertheless, Mustafa et al. (18) showed low significant correlations ($p<0.05$) between the DM Demirjian method and HWM Fishman method for male and not statistically significant ($p>0.05$) for female. Lastly, Camacho-Basallo et al. (12) reported significant correlations ($p<0.001$) between the two methods with the exception of the first molars that

Table II. *Main characteristics of the articles included in the present systematic review*

Authors	Journal	Publication year	Nationality	Population (M/F)	Age (years)	Dental calcification assessment method	HWM assessment method	Main findings
Camacho-Basallo et al. [12]	Acta Odontol Scand	2017	Spain	202 (104 M/98 F)	11-14	Demirjian [3]	Grave and Brown [1]	No significant correlations were found between Demirjian method and HWM Grave and Brown method ($p>0.05$).
Motghare et al. [13]	J Forensic Dent Sci	2016	India	300 (150 M/150 F)	7-20	Demirjian [3]	Grave and Brown [1]	All the correlations between Demirjian and HWM Grave and Brown stages were statistically highly significant ($p<0.0001$). The CC indicates that the second molars showed the highest relationship (0.865 in female; 0.760 in male) and the first molars showed the lowest correlation (0.461 in female and 0.480 in male).
Uysal et al. [14]	Angle Orthod	2004	Turkey	500 (215 M/285 F)	7-20	Demirjian [3]	Grave and Brown [1]	All the correlations between Demirjian and HWM Grave and Brown stages were statistically significant ($p<0.01$). The CC indicates that the second molars showed the highest relationship (0.826 in female; 0.706 in male) and the canines showed the lowest correlation (0.691 in female; 0.633 in male).
Günen Yılmaz et al. [15]	Acta Odontol Scand	2019	Turkey	717 (334 M/383 F)	10-15	Demirjian [3]	Fishman [2]	Authors divided the 11 SMI of HWM Fishman method into three phases: pre-peak (SMI 1–2–3), peak (SMI 4–5–6–7), and post-peak (SMI 8–9–10–11). All the correlations between Demirjian and the 3 groups of HWM Fishman method were statistically significant ($p<0.01$) (pre-peak stages: CC=0.478; peak stages: CC=0.605; post-peak stages: CC=0.387).
Krailassiri et al. [16]	Angle Orthod	2002	Thailand	361 (139 M/222 F)	7-19	Demirjian [3]	Fishman [2]	All the correlations between Demirjian method and HWM Fishman method were statistically significant ($p<0.01$). The CC indicates that the second premolar showed the highest correlation (0.69 in female; 0.66 in male) and the third molars showed the lowest correlation (0.31 in female; 0.47 in male).
Lecca-Morales et al. [17]	Dental Press J Orthod	2017	Peru	78 (44 M/34 F)	7-17	Demirjian [3]	Fishman [2]	All the correlations between Demirjian method and HWM Fishman method were statistically significant ($p<0.001$). The strongest correlation between DM stages and HWM stages was with second molars (CC=0.792 in female; 0.800 in male).
Mustafa et al. [18]	Asian Biomed	2015	Saudi Arabia	60 (45 M/15 F)	8-16	Demirjian [3]	Fishman [2]	All correlations between Demirjian method and HWM Fishman method were statistically significant ($p<0.05$) for male and not statistically significant ($p>0.05$) for female. However, the Spearman's CC were low also in male, ranging from 0.44 to 0.51 for the male.
Ojha et al. [19]	J Forensic Dent Sci	2018	India	50 (25 M/25 F)	8-14	Demirjian [3]	Fishman [2]	All correlations between Demirjian method and HWM Fishman method were statistically significant ($p<0.05$). R-value CC ranged from 0.676 to 0.835 for males and from 0.812 to 0.882 for females. Authors concluded that canines reported the highest correlation in male (CC=0.835) and the second molars in female (CC=0.882).
Yadav et al. [20]	Natl J Maxillofac Surg	2017	India	120 (60 M/60 F)	7-13	Demirjian [3]	Fishman [2]	All the correlations between Demirjian method and HWM Fishman method were statistically significant ($p<0.001$). The Spearman's rank CC indicates that the second molars showed the highest correlation in female (CC=0.845) and canines in male (0.755).
Camacho-Basallo et al. [12]	Acta Odontol Scand	2017	Spain	202 (104 M/98 F)	11-14	Demirjian [3]	Fishman [2]	All the correlations between Demirjian method and HWM Fishman method were statistically significant ($p<0.001$), with the exception of the first molars that showed a low significant correlation in female (CC=0.263; $p<0.05$) and not significant correlation in male (CC=0.187; $p>0.05$). The CC indicates that the highest correlation was showed with second molars in female (CC=0.711) and second premolars in male (CC=0.594).

Abbreviations: CC: Correlation coefficient; F: female; HWM: hand–wrist maturation; M: male; SM: skeletal maturation; SMI: skeletal maturation index. The paper by Camacho-Basallo et al. [12] assessed more two HWM methods and was described in two lines, accordingly.

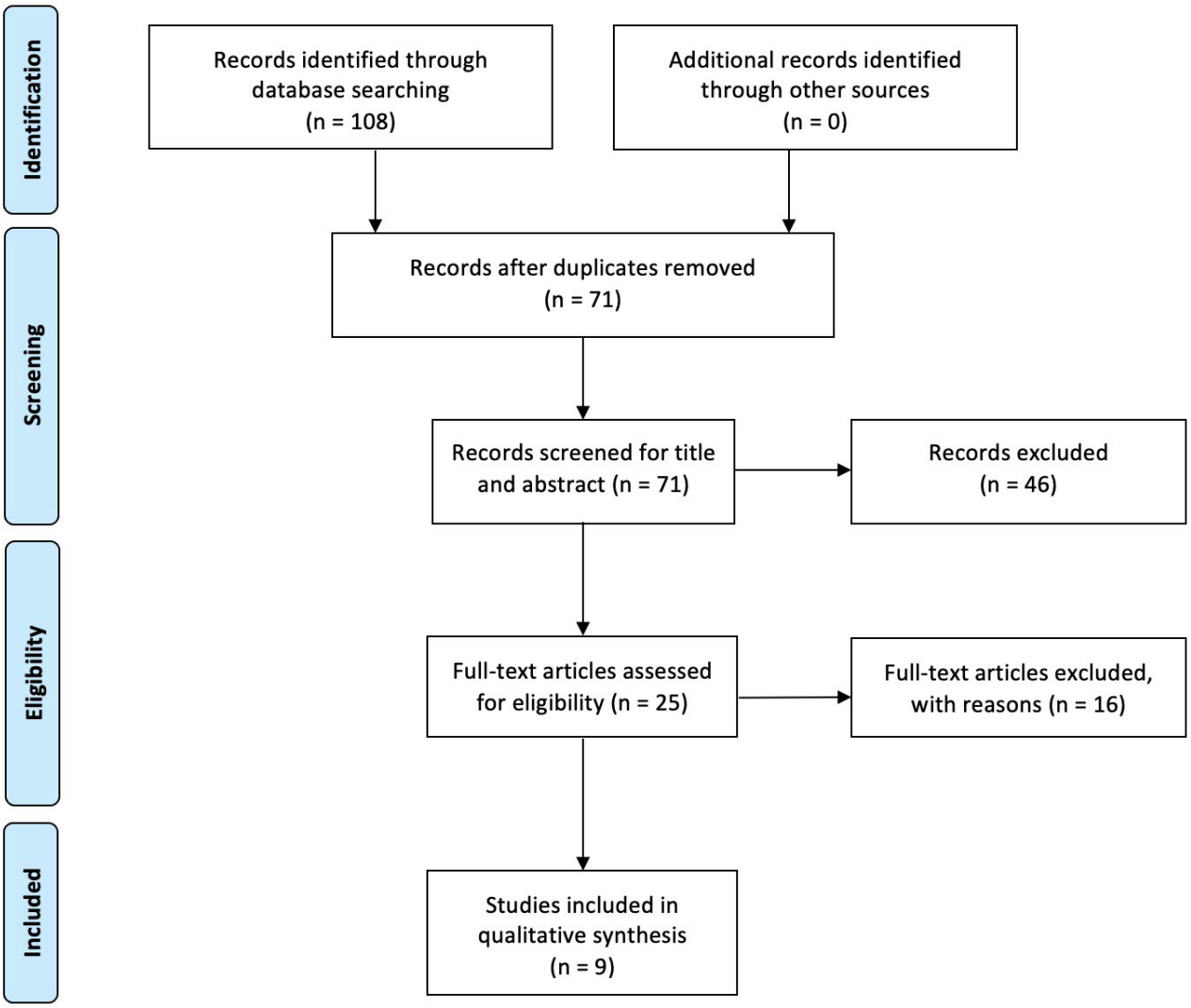


Fig. 1. *PRISMA 2009 Flow diagram*

showed a low significant correlation in female (CC=0.263; $p<0.05$) and not significant correlation in male (CC=0.187; $p>0.05$).

DISCUSSION

The present systematic review summarized the level of evidence behind the reliability of DM, showing substantial correlations between this method compared to HWM for the SM assessment in growing subjects. All nine studies (12-20) showed a statistically significant correlation between Demirjian (3) and HWM methods (1-2). However, two studies (12, 18) reported that Demirjian (3) was not significantly correlated with HWM Grave and Brown (in both sexes) (12) and HWM Fishman (in female) (18). Günen Yılmaz et al. (15) compared Demirjian to HWM Fishman stages, showing that mandibular second molar was categorized according to the different peak phases. Moreover, Lecca-Morales et al. (17) confirmed that the PGS was found in approximately the stage G in the mandibular second molar. Similarly, Motghare et al. (13) found that the second molar stage G for both sexes was indicative of a very high rate of growth acceleration. These findings were confirmed by Krailassiri et al.

(16), reporting that the mandibular second molar development was highly concentrated in stage G, during the stage at middle phalanx of the third finger when the epiphysis caps its diaphysis (MP3cap). According to the previous results about mandibular molars, an interesting remark was that two papers included in this systematic review (19, 20) reported a high correlation between Demirjian and HWM in the canines in male (0.835 and 0.755, respectively). Indeed, Ojha et al. (19). showed that the canine stage F had shown the highest percentage distribution in male (92%), during the stage of middle phalanx of the third finger, when the epiphysis equals its diaphysis (MP3 stage), suggesting the onset of a period of accelerating growth in the MP3 stage. Also, Yadav et al. (20) concluded that canine stage G and H could represent the peak of the PGS in male. Accordingly, a recent longitudinal study (4) confirmed that Demirjian applied to mandibular second molars could be considered as a plausible predictor of the occurrence of the distance to growth peak according to their findings; they stated that developmental stages of the mandibular second molar most closely observed to the PGS onset were stage F for female and stage G for male.

This review had some limitations, as the absence of a meta-analysis that could not be performed due to the high clinical heterogeneity, and the inclusion of only cross-sectional studies hindering to obtain data on growth analysis. However, this is the first systematic review that assessed the reliability of the Demirjian method compared to HWM methods to evaluate SM in growing subjects, from inception to February 2021 in the main scientific databases.

Taken together, the findings of this systematic review showed the reliability of the Demirjian dental calcification method compared to HWM in growing subjects, highlighting the potential role of the mandibular second molar calcification as a plausible indicator of SM to monitor conservative intervention in orthodontics clinical practice.

ACKNOWLEDGEMENT

The Authors thank Lorenzo Lippi for his support in this work.

REFERENCES

1. Grave KC, Brown T. Skeletal ossification and the adolescent growth spurt. Am J Orthod 1976; 69:611-9.
2. Fishman LS. Radiographic evaluation of skeletal maturation; a clinically oriented method based on hand wrist films. Angle Orthod 1982; 52:88-12.
3. Demirjian A, Goldstein H, Tanner JM. A new system of dental age assessment. Hum Biol 1973; 45:211-27.
4. Oyonarte R, Sánchez-Ugarte F, Montt J, et al. Diagnostic assessment of tooth maturation of the mandibular second molars as a skeletal maturation indicator: A retrospective longitudinal study. Am J Orthod Dentofacial Orthop 2020; 158:383-90.
5. Bizzarro M, Generali C, Maietta S, et al. Association between 3D palatal morphology and upper arch dimensions in buccally displaced maxillary canines early in mixed dentition. Eur J Orthod 2018; 40(6):592-6.
6. Scaturro D, de Sire A, Terrana P, et al. Adolescent idiopathic scoliosis screening: Could a school-based assessment protocol be useful for an early diagnosis? J Back Musculoskelet Rehabil 2020; doi: 10.3233/BMR-200215.
7. Lippi L, de Sire A, Desilvestri M, et al. Can scoliosis lead to spinal cord ischaemia? Early diagnosis and rehabilitation: A paradigmatic case report and literature review. J Back Musculoskelet Rehabil 2021; 34:43-7.
8. Masiero S, Sarto F, Cattelan M, et al. Lifetime prevalence of non-specific low back pain in adolescents: a cross-sectional epidemiological survey. Am J Phys Med Rehabil. 2021. doi: 10.1097/PHM.0000000000001720.
9. Paolucci T, Agostini F, Mangone M, et al. Sagittal spine alignment and postural balance in pre-puberty age: a multidisciplinary and multi-professional rehabilitative point of view. J Biol Regul Homeost Agents. 2021; 35(1):367-72.
10. Bittencourt MV, Cericato G, Franco A, et al. Accuracy of dental development for estimating the pubertal growth spurt in comparison to skeletal development: a systematic review and meta-analysis. Dentomaxillofac Radiol 2018; 47:20170362.
11. Ferrillo M, Curci C, Roccuzzo A, Migliario M, Invernizzi M, de Sire A. A Reliability of cervical vertebral maturation compared to hand-wrist for skeletal maturation assessment in growing subjects: a systematic review. J Back Musculoskelet Rehabil

2021; doi: 10.3233/BMR-200XXX.

12. Camacho-Basallo P, Yáñez-Vico RM, Solano-Reina E, Iglesias-Linares A. Five radiographic methods for assessing skeletal maturity in a Spanish population: is there a correlation? Acta Odontol Scand 2017; 75:106-12.
13. Motghare PC, Bedia AS, Degwekar SS, Indurkar AD, Bedia S. Correlation of calcification of permanent mandibular canine, mandibular premolars, and permanent mandibular first and second molars with skeletal maturity in Indian population. J Forensic Dent Sci 2016; 8:67-73.
14. Uysal T, Sari Z, Ramoglu SI, Basciftci FA. Relationships between dental and skeletal maturity in Turkish subjects. Angle Orthod 2004; 74:657-64.
15. Günen Yılmaz S, Harorlı A, Kılıç M, Bayrakdar İŞ. Evaluation of the relationship between the Demirjian and Nolla methods and the pubertal growth spurt stage predicted by skeletal maturation indicators in Turkish children aged 10-15: investigation study. Acta Odontol Scand 2019; 77:107-13.
16. Krailassiri S, Anuwongnukroh N, Dechkunakorn S. Relationships between dental calcification stages and skeletal maturity indicators in Thai individuals. Angle Orthod 2002; 72:155-66.
17. Lecca-Morales RM, Carruitero MJ. Relationship between dental calcification and skeletal maturation in a Peruvian sample. Dental Press J Orthod 2017; 22:89-96.
18. Mustafa S, Raj AC, Anekar J, et al. Evaluation of dental and skeletal maturity using digital panoramic radiographs and digital cephalograms. Asian biomedicine 2015; 9:335-42.
19. Ojha A, Prasanth MA, Singh V, et al. Assessment of correlation between dental calcification stages and skeletal maturity indicators. J Forensic Dent Sci 2018; 10:132-6.
20. Yadav V, Loomba A, Autar R. A comparative evaluation of dental calcification stages and skeletal maturity indicators in North-Indian children. Natl J Maxillofac Surg 2017; 8:26-33.

JOURNAL OF BIOLOGICAL REGULATORS & HOMEOSTATIC AGENTS Vol. 35, no. 2, 725-728 (2021)

LETTER TO THE EDITOR

Evaluation and efficiency of curcumin against periodontal bacteria: an *in vitro* study

R. Pulcini[1], F. Avolio[1], B. Sinjari[1], I. Robuffo[2], V. Flati[3], L. Pignatelli[4], S. Martinotti[1] and E. Toniato[1]

[1]Department of Innovative Technologies in Dentistry and Medicine, University of Chieti; [2]Molecular Genetic Institute (CNR), Chieti, Italy; [3]Department of applied clinical Science and Biotechnology, University of L'Aquila. L'Aquila, Italy: [4]Vitalex-hc, Sulmona Science Park, Sulmona, Italy

Received September 15, 2020 – Accepted January 13, 2021

To the Editor,

The effects of turmeric in the medical-scientific field are increasingly cited in literature. Turmeric has a long history as a medical herb within Ayurvedic medicine, and for its anti-inflammatory, antioxidant and antibacterial properties, it shows a therapeutic potential for various diseases (1-3). The aim of this study is to evaluate the effect of turmeric in the oral area, which has a very complex microbiome represented by 200 different organisms and 700 taxa. In recent years, there has been increasing interest in studies related to the oral microbiome which confirm the importance of oral health in the individual health. The correlations of the oral microbiome with other pathologies, such as fibrous cystic (fc), oral cavity tumors, esophageal tumors, lung tumors, prostate cancer, hematological tumors, colorectal cancer (CRC), rheumatoid arthritis and Alzheimer's disease, has been increasingly studied in the last decade, thanks also to the new analysis technologies.

The oral microbiome is something complex that interacts with the other microbiomes present in our body. The microbiome is made up of a sum of different microorganisms, and is a highly regulated ecosystem that involves different surfaces of the oral cavity (4, 5). Dysbiosis is an alteration of the homeostasis of the mouth, it can be determined by several factors such as oral hygiene, age, diet, smoking, hormonal changes and pathologies present in the body. In cases of dysbiosis, the balance of microbiome is interrupted leading to several alterations that may result in dental caries, gingivitis and periodontitis.

Gingivitis affects about 80% of the population and is due to the accumulation of bacterial plaque. The gold standard for its treatment is chlorhexidine. Chlorhexidine is a widely studied antiseptic, which has antimicrobial effects on gram-negative and gram-positive bacteria, fungi and viruses. In this study, the quantitative and qualitative profile of a sample of bacterial plaque were traced through molecular analysis. The aim of this study is to demonstrate how turmeric can be a possible bacteriostatic and bactericidal modulator in the oral cavity.

MATERIALS AND METHODS

The study was conducted in accordance with the Declaration of Helsinki, and the protocol was approved by the CAST (Center for Advanced Studies and Technology)

Key words: curcumin; turmeric; oral health; bacteria; periodontal disease

Corresponding author:
Dr Riccardo Pulcini,
Department of Medical, Oral and Biotechnological Sciences,
University of Chieti,
Via Dei Vestini 31, 66100 Chieti, Italy
Tel.: +39 3409767298
e-mail: riccardopulcini@outlook.com

0393-974X (2021)
Copyright © by BIOLIFE, s.a.s.
This publication and/or article is for individual use only and may not be further reproduced without written permission from the copyright holder.
Unauthorized reproduction may result in financial and other penalties

of Chieti. The patient was selected from the dental clinic of Chieti University. The patient gave consent for the study of the extracted genetic material.

Molecular genetic test

The molecular genetic test for the identification of the 11 bacterial species of periodontal-pathogenic bacteria (*aggregatibacter actinomycetemcomitans AA, porphyromonas gingivalis PG, prevotella intermedia PI, tannerella forsythia TF, treponema denticola TD, parvimonas micra PM, fusobacterium nucleatum FN, campylobacter rectus CR, eubacterium nodatum EN, eikenella corrodens EC, capnocytophaga CSP*) is highly specific (Fig. 1) (6). The test used I-Dent® plus11 (Hain Lifescience - Bruker) and provides data on the quality and quantity of 11 periodontal-pathogenic species and on their affiliation with "bacterial complexes". The test results represent an optimal control for an individual therapy for the support of mechanical therapy and possible antibiotic therapy. The test draws a threshold line between non-surgical periodontal treatment and antibiotic therapy. The threshold concentrations are:

AA	(+)	corresponding to $< 10^3$
PG	+	corresponding to 10^4
TF	+	corresponding to $< 10^5$
TD	+	corresponding to $< 10^5$
PI	+	corresponding to $< 10^5$
PM	++	corresponding to $< 10^6$
FN	+++	corresponding to $> 10^7$
CR	++	corresponding to $< 10^6$
EN	++	corresponding to $< 10^6$
EC	+++	corresponding to $> 10^7$
CS	+++	corresponding to $> 10^7$

DNA extraction of collected samples from bacterial plaque were taken using sterile paper cones. The cones were placed in a 1.5 ml tube, avoiding possible causes of contamination. A magnetic stir bar was added to the 5% Chelex 100 Resin solution in 10 mM Tris pH 8.4/8.5 and shaken on a magnetic stirrer. During the stirring, 100 µl of Chelex solution were removed using a 1000 µl pipette and then incubated for 15 min at 60°C in an ultrasonic bath and for 15 min at 100-105°C in a thermal block. After vortexing the lysate for 30 s, it was centrifuged for 1 min at 12,000 rpm in a benchtop centrifuge, and 2.5 µl of the supernatant was used for the amplification reaction. Two amplification reactions were prepared for each sample using the kit (AM-A1, AM-A2 and AM-B).

Broth culture of dental plaque

For the growth of an aliquot of periodontal bacteria a solution consisting of: urea broth enriched with mineral salts and yeast extract was used. The bacteria were collected directly from the patient using a sterile paper cone and placed in the culture broth and subsequently in the orbital incubator at 37°C overnight.

Preparation of the agar media

For the preparation of the agar media, 10 cm Petri dishes containing LB broth 1.5% agar were used. In particular, in 800 ml of distilled water were dissolved by stirring for 3 h at room temperature, 10 g of tryptone, 5 g of yeast extract and 10 g of NaCl. Subsequently the solution was brought to pH 7.2 dispensed in 100 ml autoclaved bottles for 1 h at 121°C 1.5 atm. For the solid culture plates, liquid LB was complemented by adding 1.5% of agar, in turn dissolved in a microwave oven.

Preparation of curcumin solution on media for evaluation in vitro

Firstly, 0.8 g of turmeric root was dissolved in 40 ml of 100% ethanol and left to stir overnight at 37°C. The following day the insoluble residue was left to settle and the ethanolic part containing curcumin was diluted in an equal volume (40 ml) tris mM, and DTA 1 mM,

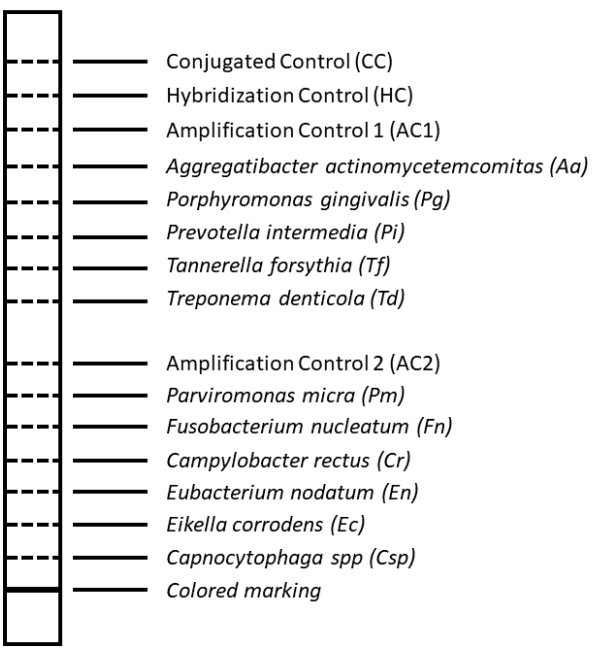


Fig. 1. *data strip*

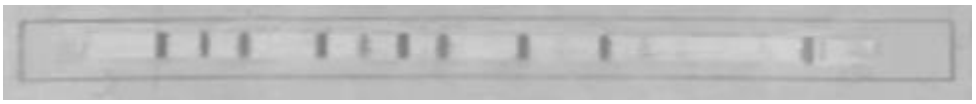
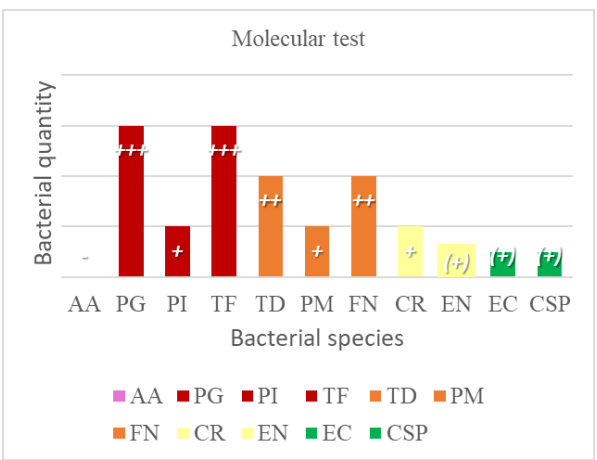


Fig. 2. *Strip of molecular test*

pH 7.8 in order to have a solution of 1% curcumin and 50% of ethanol. The agar plates supplemented with 100 μL of the curcumin solution were subsequently used, pre-adsorbing curcumin on the LB agar surface; after spreading, the plates were incubated for 30 min before bacterial sowing. Adequate controls of the LB agar plates were set up in control for the standard growth of the bacterial preparation. The experiment was conducted in triplicate for the analysis of the plaque. At the end of the preparation of the plates, an aliquot of the bacteria was plated with sterile loop, leaving them in an overnight incubator at 37°C.

RESULTS

The patient had 10 out of 11 bacterial species present in his oral cavity (Figs. 2, 3). More bacterial clusters were involved. Some bacterial strains exceeded the threshold value for antibiotic treatment



- = <10^4 (exception AA: 10^3)
(+) = 10^4 (exception AA: 10^3)
+ = <10^5 (exception AA: 10^4)
++ = <10^6 (exception AA: 10^5)
+++ = >10^7 (exception AA: 10^6)

Fig. 3. *Analysis of periodontal bacteria*

Table I. *Control group plates and added plate of 0.01% curcumin*

	Plate 1	Plate 2	Plate 3	Average
Control Group	28	32	40	33.3
Curcumin 0.1%	18	19	30	22.3
% bacterial inhibition	35.71%	40.63%	25%	33.03%

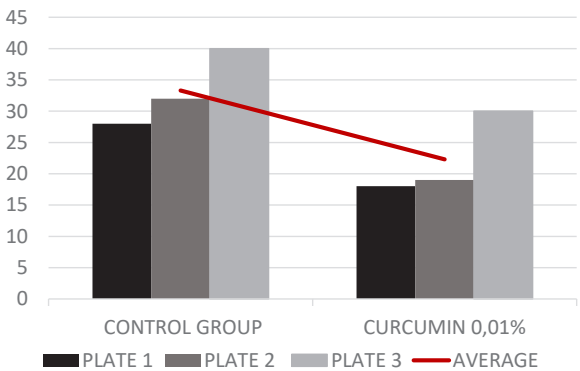


Fig. 4. *Bar graphs of control group and added plate of 0.1% curcumin*

as PG, TF and TD. These bacteria had a high pathogen load. After this analysis, the patient, was treated with mechanical therapy (scaling and root planing). The bacterial plaque sample was amplified with the described techniques, after conducting an *in vitro* study in triplicate. In the plates with the 0.01% curcumin solutions an inhibition of bacterial growth could be observed (Table I and Fig. 4) due to the properties of the curcuminoid polyphenols.

DISCUSSION

Numerous studies have been conducted on curcumin, and a PubMed research with the word

"curcumin" highlighted 15,326 articles. The properties of turmeric have been largely studied with findings also in the oral cavity. Mouthwashes, topical gels, subgingival irrigations, and sealants have been tested, and turmeric has also been used for the treatment of precancerous lesions (7, 8). In all these experiments, its properties have been demonstrated (9-11). Our intention was to also demonstrate its antibacterial properties. In this preliminary study we demonstrated that a 0.01% curcumin solution, prepared as previously described, can produce a bacteriostatic effect. Further studies are needed to observe a possible modulation of some specific bacterial strains, repeating a PCR analysis after the addition of the curcumin solution and repeating the PCR analysis several times in order to compare any bacterial modulations in the different phases of bacterial plaque formation in the oral cavity.

Turmeric, with its properties, could represent a valid support for the modulations of the dysbiosis of the oral microbiome. The *in vitro* result could anticipate the effect *in vivo*, however further in depth studies are needed to better understand the dynamics of curcumin as antibacterial and bactericidal mediator of the oral cavity.

REFERENCES

1. Jurenka JS. Anti-inflammatory properties of curcumin, a major constituent of Curcuma longa: a review of preclinical and clinical research [published correction appears in Altern Med Rev 2009; 14(3):277. Altern Med Rev 2009; 14(2):141-53.
2. Gupta SC, Patchva S, Aggarwal BB. Therapeutic roles of curcumin: lessons learned from clinical trials. AAPS J 2013; 15(1):195-218. doi:10.1208/s12248-012-9432-8.
3. Moghadamtousi SZ, Kadir HA, Hassandarvish P, Tajik H, Abubakar S, Zandi K. A review on antibacterial, antiviral, and antifungal activity of curcumin. Biomed Res Int 2014; 2014:186864. doi:10.1155/2014/186864
4. Willis JR, Gabaldón T. The human oral microbiome in health and disease: from sequences to ecosystems. Microorganisms 2020; 8(2):308. Published 2020 Feb 23. doi:10.3390/microorganisms8020308
5. Kilian M, Chapple IL, Hannig M, et al. The oral microbiome - an update for oral healthcare professionals. Br Dent J 2016; 221(10):657-66. doi:10.1038/sj.bdj.2016.865
6. MacLean D, Jones JD, Studholme DJ. Application of 'next-generation' sequencing technologies to microbial genetics. Nat Rev Microbiol 2009; 7(4):287-96. doi:10.1038/nrmicro2122
7. Fonseca-Santos B, Bonifácio BV, Baub TM, Gremião MPD, Chorilli M. In-situ gelling liquid crystal mucoadhesive vehicle for curcumin buccal administration and its potential application in the treatment of oral candidiasis. J Biomed Nanotechnol 2019; 15(6):1334-44. doi:10.1166/jbn.2019.2758
8. Schaffer M, Schaffer PM, Bar-Sela G. An update on Curcuma as a functional food in the control of cancer and inflammation. Curr Opin Clin Nutr Metab Care 2015; 18(6):605-11. doi:10.1097/MCO.0000000000000227
9. Nagpal M, Sood S. Role of curcumin in systemic and oral health: An overview. J Nat Sci Biol Med 2013; 4(1):3-7. doi:10.4103/0976-9668.107253
10. Mali AM, Behal R, Gilda SS. Comparative evaluation of 0.1% turmeric mouthwash with 0.2% chlorhexidine gluconate in prevention of plaque and gingivitis: A clinical and microbiological study. J Indian Soc Periodontol 2012; 16(3):386-91. doi:10.4103/0972-124X.100917
11. Waghmare PF, Chaudhari AU, Karhadkar VM, Jamkhande AS. Comparative evaluation of turmeric and chlorhexidine gluconate mouthwash in prevention of plaque formation and gingivitis: a clinical and microbiological study. J Contemp Dent Pract 2011; 12(4):221-24. doi:10.5005/jp-journals-10024-1038.

LETTER TO THE EDITOR

Atrial natriuretic peptide differentiates between primary submandibular gland squamous cell carcinoma and oral squamous cell carcinoma: preliminary data

W. Arancio[1,2*], A. Ahmed[3*], C. Basset[4], A. Jurjus[5], I. Miletich[3] and A. Leone[4]

[1]Department of Biological, Chemical and Pharmaceutical Sciences and Technologies (STEBICEF), University of Palermo, Palermo, Italy; [2]Advanced Data Analysis Group, Fondazione Ri.MED, Palermo, Italy; [3]Centre for Craniofacial and Regenerative Biology, Faculty of Dentistry, Oral and Craniofacial Sciences, King's College London, Guy's Hospital, London, UK; [4]Department of Biomedicine, Neuroscience and Advanced Diagnostic, Bi.N.D, School of Medicine, Institute of Anatomy and Histology, University of Palermo, Palermo, Italy; [5]Department of Anatomy, Cell Biology and Physiology, American University of Beirut, Beirut, Lebanon

Received January 12, 2021 - Accepted March 24, 20-21

*These Authors share the first authorship

To the Editor,

The natriuretic peptide (NP) family is composed of atrial natriuretic peptide (ANP), brain natriuretic peptide (BNP) and C-type natriuretic peptide (CNP). ANP and BNP are synthetized prevalently in the heart, although their expression has also been reported in other organs and tissues, while CNP is synthetized mainly by the vascular endothelium. NPs act through specific receptors, which have been identified as NPRA, NPRB and NPRC, possessing different affinities for each NP, with NPRA showing the highest affinity for ANP.

NPs act mainly as homeostatic agents, and are secreted in response to pressure and stress on myocardial walls. They exert diuretic and vasodilatory functions regulating the water–salt balance and consequently blood volume. In addition to endocrine actions involved in blood pressure regulation, NPs can also exert local functions through paracrine and autocrine mechanisms. Indeed, several studies have pointed to the presence of non-canonical (*i.e.* extracardiac) sites for the production of ANP including the brain, gastrointestinal tract, peripheral cells of pancreatic islets, testis, macrophages (1) and, of particular interest for this study, the salivary glands (SGs) (2-4).

NP system alterations have been correlated with a wide panel of diseases including congenital heart disease, heart failure, dyspnea, sepsis, cirrhosis, leading to NPs and their receptors being used as diagnostic and prognostic markers, in particular for cardiovascular diseases. Components of the NP system have also been identified as potential targets in cancer therapy, one example being NPRA, which is documented as being involved in tumor angiogenesis (5, 6). Based on previously published data in which we recently showed that ANP is expressed in intralobular ducts of both murine and human submandibular glands (SMGs) (4), we conducted a small exploratory study to investigate expression levels of *NPPA* and *NPR1*, encoding respectively for ANP and its receptor NPRA, in primary benign pleomorphic adenoma (PA), and malignant squamous cell carcinoma (SCC) SMG

Key words: NPA; NPPA; submandibular gland; oral squamous cell carcinoma

Corresponding Author:
Dr Angelo Leone,
Plesso di Anatomia Umana e Istologia,
Policlinico Universitario "Paolo Giaccone",
Via del Vespro, 129, 90127 Palermo, Italy
Tel.: +39 389 584 6341
e-mail: angelo.leone@unipa.it
ORCID ID: https://orcid.org/0000-0001-6904-5141

0393-974X (2021)
Copyright © by BIOLIFE, s.a.s.
This publication and/or article is for individual use only and may not be further reproduced without written permission from the copyright holder.
Unauthorized reproduction may result in financial and other penalties
DISCLOSURE: ALL AUTHORS REPORT NO CONFLICTS OF INTEREST RELEVANT TO THIS ARTICLE.

tumors and in primary oral squamous cell carcinoma (OSCC). Our data show that expressions of *NPPA* and *NPR1* are respectively significantly increased and abrogated in SMG SCC compared to OSCC. Primary SMG SCC, being rare and easily confused with SCC from distant sites that have spread to the SMGs via metastasis, emanating data suggest *NPPA* and *NPR1* expression could be used as diagnostic markers to help discriminate between primary and secondary SMG SCC.

MATERIALS AND METHODS

Human salivary gland tissues were obtained from patients who had undergone surgery at the Division of Surgery of the Medical School within the University of Palermo (Italy). Informed consent was obtained from all patients. The study protocol was approved by the Institutional Research Board and is in line with the ethical guidelines of the 1975 Declaration of Helsinki.

Salivary gland tissues

Human SMG tissues embedded in paraffin were selected from the archives of the Department of Pathology of the University of Palermo. Human biopsies used in this study comprised three normal submandibular salivary glands (SMGs) (median age 50 years), three SMG pleomorphic adenomas (PA, median age 34.5 years), three oral squamous cell carcinomas of non-salivary gland origin (OSCC, median age 55.5years) and three SMG SCC (median age 64.5 years). Tumor cases presented a history of variable size of primary tumors as well as variable presence of metastasis in draining lymph nodes and were reviewed by a pathologist who confirmed the initial diagnosis.

Immunohistochemical analysis

Immunohistochemistry was performed using a polymer detection method. Briefly, tissue samples were fixed in 10% buffered formalin and paraffin embedded. Four-micrometers-thick tissue sections were deparaffinized and rehydrated. The antigen unmasking technique was performed using Novocastra Epitope Retrieval Solutions pH 6 and pH 9 and in PT Link Dako at 98°C for 30 minutes. Subsequently, the sections were brought to room temperature and washed in PBS. After neutralization of the endogenous peroxidase with 3% H2O2 and Fc blocking by a specific protein block (Novocastra UK) the samples were incubated overnight with the primary antibodies Mouse anti-human ANP 1/50 pH 6 (Clone M622709; Abcam Cod. 2093); Rabbit Polyclonal anti-human ANP 1/100 pH 9 (Abcam Cod.76743); Rabbit Polyclonal anti-human ANP receptor A 1/50 pH 6 (Abcam Cod.70848) at 4°C. Staining was revealed by polymer detection kit (Novocastra) and AEC (3-amino-9-ethylcarbazole) substrate-chromogen. The slides were counted with Harris hematoxylin (Novocastra). All the slides were analyzed under AXIO Scope A1 optical microscope (Zeiss) and micrographs were collected using an Axiocam 503 Color digital camera (Zeiss). Negative control stainings were performed by using mouse and rabbit immune sera instead of the primary antibodies.

RNA extraction and RT-qPCR

RNA was extracted using the RNeasy FFPE kit (Qiagen) from 4 paraffin-embedded tissue sections of 5 μm each, following the manufacturer's instructions. Purified RNA was quantified using the Qubit 3.0 fluorometer (Life technology). cDNA synthesis was carried out with the Quantinova reverse transcription Kit (Qiagen) following the manufacturer's instructions. Real-time quantitative polymerase chain reactions (qPCR) were performed with the Quantinova SYBR green PCR kit (Qiagen) in triplicate on a Rotor-Gene Q system (Qiagen) following the manufacturer's instructions. QuantiTech Primer assay (Qiagen) was used with Hs_NPR1_1_SG QT00081963, Hs_NPPA_1_SG QT00203322, and Hs_ACTB_1_SG QT00095431 primers, for the quantification of human *NPR1*, *NPPA* and *ACTB* (normalizer) transcripts, respectively. Data were analyzed using the $2^{-\Delta\Delta CT}$ method using an external independent reference tissue (7).

Statistical analysis

One-tailed Mann-Whitney test was carried out to analyze the RT-qPCR data with *P< 0.05 considered as statistically significant.

RESULTS

This preliminary study investigated whether levels of *NPPA* expression in the SMG could be subjected to significant changes in neoplasia. Quantitative PCR was used to compare *NPPA* expression levels

in SMG tissue resected from patients diagnosed with SMG primary benign PA and malignant SCC tumors and either normal SMG tissues or malignant tumors of the buccal mucosa OSCC. PA is the most common benign tumor affecting the SMG, representing 40 to 60% of all SMG neoplasia. While SMG primary SCCs constitute a rare occurrence, OSCC, which can spread to the SMG, is a common cancer in humans that represents 90% of oral cancers and constitutes an important global health concern.

In this exploratory study we analyzed *NPPA* expression levels in three biopsies obtained from three independent patients for each type of neoplasms. The *ACTB* gene was used to normalize mRNA levels between samples. *NPPA* expression levels were not statistically different between normal SMG, PA and OSCC (Fig. 1A). In contrast, all SMG primary SCC studied exhibited an increase in *NPPA* expression, which was significant when compared to OSCC *NPPA* levels (Fig. 1A), suggesting SMG SCC have specific molecular characteristics compared to OSCC, and increased *NPPA* expression represents one of these features.

We complemented this study by analyzing expression levels of *NPR1* encoding the major ANP receptor in the nine cases of neoplasms studied. We found that *NPR1* expression was below the level of detection in all cases of primary SMG SCC studied, while *NPR1* was expressed at similar levels in SMG PA and OSCC (Fig. 1B), further illustrating primary SMG SCC and OSCC are molecularly distinct entities. Histochemical analysis of NPRA, confirmed

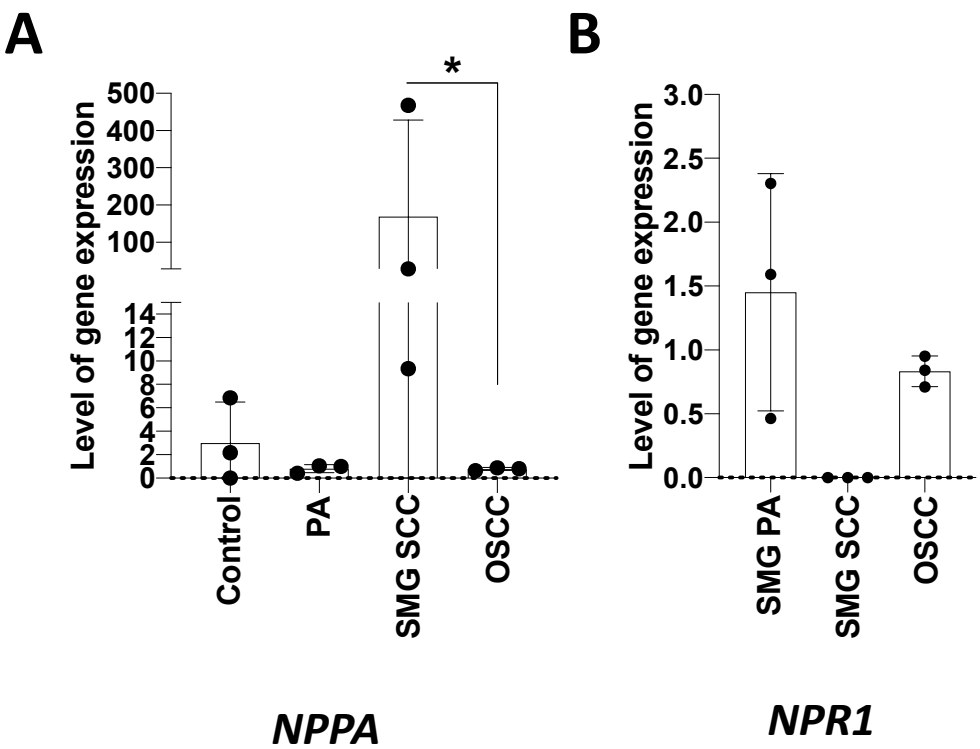


Fig. 1. *Expression of NPPA (**A**) and NPR1 (**B**) in normal salivary submandibular glands (SMGs) (Control), SMG pleomorphic adenomas (SMG PAs), SMG squamous cell carcinomas (SMG SCCs), and oral squamous cell carcinomas (OSCCs) of non-salivary gland origin originating in the buccal mucosa (OSCCs). NPPA and NPR1 expression are significantly increased and absent, respectively, in SMG SCCs in comparison with OSCCs. One-tailed Mann-Whitney test was carried out with *P< 0.05 considered as statistically significant.*

the PCR data by showing an elevated expression of this receptor in the SMG-SCC compared to the other categories (Fig. 2).

In summary, primary SMG SCC are characterized by increased expression of *NPPA*, the coding gene for ANP, and absence of expression of *NPR1*, encoding ANP major receptor, compared to OSCC.

DISCUSSION

Major salivary gland malignancies are rare, accounting for 0.2% of all malignant neoplasms and 9% of head and neck cancers. While SCC is the most common type of malignant neoplasm in other head and neck locations, it is a rare type of primary SMG malignancy. As the SMG is anatomically close to head and neck structures, such as the skin and oral mucosa that exhibit a higher incidence of SCC, SCC of the skin or the oral mucosa can easily spread to the SMG by direct invasion. Furthermore, SCC originating from distant sites can also spread to the salivary glands via metastasis. Hence, a proportion of malignant tumors found in the SMG are not primary tumors that have arisen in the SMG. Combined with the rarity of SMG primary SCC, these considerations illustrate the complexity of diagnosing SMG SCC. While it is currently recommended that primary SMG SCC are diagnosed by exclusion of other metastatic cancers, it is undeniable that molecular markers specific to SMG SCC would help diagnose this pathology. We have shown here that *NPPA* and *NPR1* expression levels may help discriminate between SMG primary SCC and OSCC. Indeed, *NPPA* is significantly increased in SMG SCC compared to OSCC. Furthermore, *NPR1* is expressed in OSCC, while *NPR1* expression is undetectable in SMG SCC. Despite the small number of primary SMG SCC analyzed, mostly due to the rarity of this malignant neoplasm, the preliminary results of this study warrant further investigations using a larger sample set.

The combined increase in *NPPA* expression and absence of *NPR1* expression identified in SMG SCC raises the question of the significance of a potential increase in ANP production in SMGs developing primary SCC. *NPR1* encodes NPRA, characterized as the main receptor for ANP. ANP has also been shown to bind - albeit with a lower affinity - to the NPRB receptor, which is structurally related to NPRA and exhibits similar guanylyl cyclase activity to NPRA following ligand binding (8). ANP binds as well with high affinity to the NPRC receptor, which is believed to function as a clearance receptor, by removing natriuretic peptides from the extracellular compartment (9). The lack of *NPR1* expression, in all SMG SCC analyzed, strongly suggests abnormal ANP production does not have a local role in neoplastic SMG. Future studies should investigate whether there is increased ANP concentration in the saliva of SMG SCC patients, in which case salivary ANP could also be used as a diagnostic tool to discriminate between primary SMG SCC and OSCC. Furthermore, increased ANP production in SMG SCC could be associated to increased plasma ANP concentration and a potential risk of hyponatremia (low blood sodium),

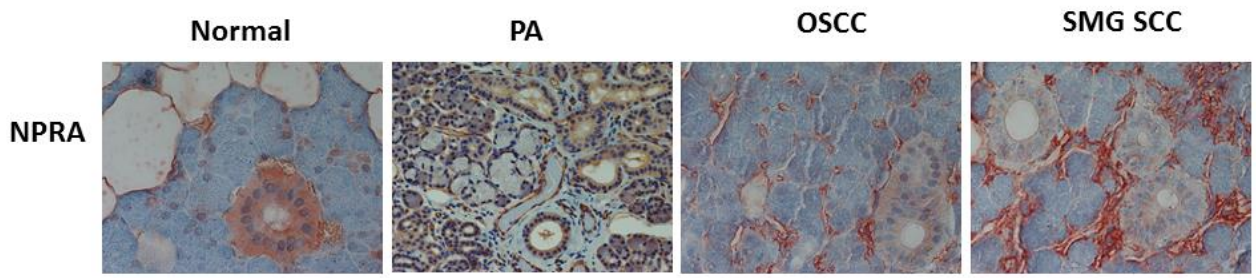


Fig. 2. *NPRA expression in a subset of human submandibular glands from patients with normal SMGs, Pleomorphic adenoma (PA), Oral squamous cell carcinoma (OSCC) and SMG squamous cell carcinoma (SMG-SCC). Note the high expression of NPRA in the periacinar regions of SMG-SCC compared to other categories of tissues.*

an important clinical problem with symptoms ranging from vomiting to confusion, seizures and coma. While a number of small cell lung cancers have been shown to ectopically produce ANP (10, 11) and exhibit hyponatremia, such clinical manifestation has not yet been reported for cases of SMG SSC.

Characterizing the cells expressing *NPPA* and *NPR1* in SMG SCC and OSCC respectively, should help understand the differences between these SCC of distinct origin at the molecular level. Modulation of the NP system in SMG SCC versus OSCC could take place within any of the cell types present within the tumor: neoplastic or non-neoplastic resident cells, endothelial cells or infiltrated immune cells. Macrophages, which are key players in malignant tumors, may be good candidates for *NPPA* upregulation in SMG SCC. Indeed, murine macrophages secrete ANP, and ANP expression in mouse macrophages has been shown to be regulated by compounds affecting macrophage function (1) - could this be happening also in humans? More work is needed in this direction before arriving at a final conclusion.

ACKNOWLEDGEMENTS

This research was partially funded by LEONPLAST of Diego Leone, Palma di Montechiaro AG, Italy, as a liberal contribution.

REFERENCES

1. Vollmar AM, Schulz R. Gene expression and secretion of atrial natriuretic peptide by murine macrophages. J Clin Invest 1994; 94:539-45.
2. Bansal AK, Bindal R, Kapoor C, Vaidya S, Singh HP. Current concepts in diagnosis of unusual salivary gland tumors. Dent Res J (Isfahan) 2012; 9(S1):S9-19.
3. Bianciotti LG, Elverdín JC, Vatta MS, Fernández BE. Atrial natriuretic factor modifies the composition of induced-salivary secretion in the rat. Regul Pept 1996; 65:139-43.
4. Ahmed A, Gulino A, Amayo S, et al. Natriuretic peptide system expression in murine and human submandibular salivary glands: a study of the spatial localisation of ANB, BNP, CNP and their receptors. J Mol Histol 2020; 51:3-13.
5. Kong X, Wang X, Xu W, et al. Natriuretic peptide receptor A as a novel anticancer target. Cancer Res 2008; 68:249-56.
6. Wang X, Raulji P, Mohapatra SS, et al. Natriuretic peptide receptor a as a novel target for prostate cancer. Mol Cancer 2011; 10:56.
7. Livak KJ, Schmittgen TD. Analysis of relative gene expression data using real-time quantitative PCR and the 2-ΔΔCT method. Methods 2001; 25:402-8.
8. Bennett BD, Bennett GL, Vitangcol RV, Jewett JR, Burnier J, Henzel W, Lowe DG. Extracellular domain-IgG fusion proteins for three human natriuretic peptide receptors. Hormone pharmacology and application to solid phase screening of synthetic peptide antisera. J Biol Chem 1991; 266:23060-7.
9. Matsukawa M, Grzesik WJ, Takahashi N, Pandey KN, Pang S, Yamauchi M, Smithies O. The natriuretic peptide clearance receptor locally modulates the physiological effects of the natriuretic peptide system. Proc Natl Acad Sci U S A 1999; 96:7403-8.
10. Campling BG, Sarda IR, Baer KA, Pang SC, Baker HM, Lofters WS, Flynn TG. Secretion of atrial natriuretic peptide and vasopressin by small cell lung cancer. Cancer 1995; 75:2442-51.
11. Shimizu K, Nakano S, Nakano Y, Ando M, Seki K, Kameda N. Ectopic atrial natriuretic peptide production in small cell lung cancer with the syndrome of inappropriate antidiuretic hormone secretion. Cancer 1991; 68:2284-8.

LETTER TO THE EDITOR

Correlation of STAT6 expression and gene polymorphism with chronic obstructive pulmonary disease

M.-F. Zhu[1#], L.-X. Chen[1,#], F. Gao[1], D.-Y. Sheng[1], M.-J. Xu[1], J.-R. Zhang[1] and W.-X. Qian[1*]

[1]*Department of Respiratory Diseases, The First People's Hospital of Zhangjiagang City, Soochow University, Zhangjiagang, China*

Received October 29, 2020 – Accepted March 16, 2021

[#]These Authors contributed equally to this work

To the Editor,

Chronic obstructive pulmonary disease (COPD) is a respiratory disease characterized by chronic inflammation of the airway and emphysema, resulting in persistent airflow restriction (1). The pathogenesis of COPD may be related to airway inflammation caused by T cell-mediated immune imbalance resulting from toxic and harmful gases or particles such as cigarette smoke (2). Signal transducer and activator of transcription 6 (STAT6) is located on chromosome 12q13.3 and plays an important role in the regulation of T lymphocytes (3). SATA6 was confirmed to be associated with chronic inflammation of the airway (4, 5).

As a member of the STAT family of Janus kinase (JAK) signal transduction pathway, STAT6 is a specific transcription factor in T-helper 2 (Th2) cell differentiation, which can promote Th2 cell proliferation and differentiation and secrete cytokines such as interleukin (IL)-4, IL-10 and IL-13 (6). Previous studies on the correlation between STAT6 and COPD are relatively few, therefore, this study adopted a case-control design to discuss the relationships of the two loci (rs1059513 and rs841718) on STAT6 gene with COPD.

A total of 150 COPD patients were randomly selected as the case group and 180 healthy adults were selected as the control group. There were no significant differences in gender (male: n=89 (59.3 %) *vs* n=96 (53.3%); female: n=61 (40.7%) *vs* n=84 (46.7%)), age (42.5±18.1 *vs* 38.0±11.1 years), and living habits [Smoking: n=65 (43.3%) *vs* n=71 (39.4); drinking: n=75 (50%) *vs* n=83 (46.1)] between the two groups (P>0.05). This study was approved by the Ethics Committee of The First People Hospital of Zhangjiagang City. Signed written informed consents were obtained from all participants prior to the study.

Deoxyribonucleic acid (DNA) extraction and typing. In the morning, 3 to 5 mL of fasting peripheral venous blood samples were taken from patients and placed in an anticoagulated vacuum blood collection tube containing ethylenediaminetetraacetic acid. Whole blood genomic DNA extraction was performed using the QIAamp DNA Blood Midi Kit (nucleic acid extraction kit) supplied by Qiagen, Germany in strict accordance with the instructions of the kit. Two single-nucleotide polymorphisms (SNPs) in the STAT6 gene, rs1059513 and rs841718, were genotyped by Taqman probe method. The

Key words: COPD, STAT6 gene, gene polymorphism, correlation

Corresponding Author:
Wenxia Qian, BM,
Department of Respiratory Diseases,
The First People's Hospital of Zhangjiagang City,
Soochow University, No. 68 Jiyang West Road,
Zhangjiagang, Jiangsu 215600, China
Tel.: +86 013952440813
e-mail: lroetz@163.com

0393-974X (2021)
Copyright © by BIOLIFE, s.a.s.
This publication and/or article is for individual use only and may not be further reproduced without written permission from the copyright holder. Unauthorized reproduction may result in financial and other penalties
DISCLOSURE: ALL AUTHORS REPORT NO CONFLICTS OF INTEREST RELEVANT TO THIS ARTICLE.

reaction conditions were as follows: denaturation at 95°C for 5 min, and annealing at 95°C for 15 s and 60°C for 30 s with 40 cycles. The primer sequences are shown were: rs1059513: Forward: 5'-ATGTGGTTACTAGTACAGGT-3'; Reverse: 5'-CATGTTCTATGTGGTCATGC-3'; HEX: 5'-AGTACAAGGGCTGAGATTC-3'; FAM: 5'-AGTACAAGGGCTGAGATTC-3'; rs841718: Forward: 5'-TCCGGAGCCACTACAAGCG-3'; Reverse: 5'-GGAAGTAAGAGAAGCACAGC-3'; HEX: 5'-TGCCCGCGTGTCATCCTGATG-3'; FAM: 5'-TGCCCGTGTGTCATCCTGATG-3'.

Table I. *Frequency distribution of genotypes*

Genotype	Control group (n=150)		Case group (n=180)		χ^2	P
	n	%	n	%		
rs1059513						
AA	130	86.7	152	84.4	0.681	0.325
AG	18	12	26	14.4	0.871	0.334
GG	2	1.3	2	1.2	0.014	0.901
A	278	92.7	330	91.7	0.226	0.618
G	22	7.3	30	8.3		
rs841718						
GG	71	47.3	84	46.7	0.172	0.653
AG	63	42	79	43.9	0.53	0.451
AA	16	10.7	17	9.4	3.156	0.074
G	205	68.3	247	68.6	0.698	0.397
A	95	31.67	113	31.4		

Table II. *Analysis of COPD risk in different rs1059513 models*

Model		Genotype	Control group (n=150)	Case group (n=180)	OR (95%Cl)	P
	Dominant model	AA	130 (86.7)	152 (84.4)	1	-
		AG+GG	20 (13.3)	28 (15.6)	0.814 (0.645-1.061)	0.129
	Recessive model	AA+AG	148 (98.7)	178 (68.9)	0.618 (0.219-1.738)	0.368
		GG	2 (1.3)	2 (1.2)	-	
Additive model		AA	130 (86.7)	152 (84.4)	-	-
		GG	2 (1.3)	2 (1.2)	0.817 (0.654-1.039)	0.107

Table III. *Analysis of COPD risk in different rs841718 models*

Model	Genotype	Control group (n=150)	Case group (n=180)	OR (95%Cl)	P
Dominant model	GG	71 (47.3)	84 (46.7)	-	-
	AG+AA	79 (43.9)	96 (53.3)	0.963 (0.801-1.118)	0.564
Recessive model	GG+AG	134 (89.3)	163 (90.6)	-	-
	AA	16 (10.7)	17 (9.4)	1.103 (0.832-1.387)	0.418
Additive model	GG	71 (47.3)	84 (46.7)	-	-
	AA	16 (10.7)	17 (9.4)	0.984 (0.865-1.129)	0.925

Table IV. *Frequency distribution and OR values of the combined genotypes of rs841718 and rs1059513*

Genotype n (%)		Control group n (%)	Case group	OR (95%CI)	P
rs1059513	rs841718				
A	G	75	97	1.689 (1.451-1.915)	0.048
A	A	85	41	0.563 (0.316-0.608)	0.142
G	G	45	28	0.352 (0.281-0.399)	0.059
G	A	44	56	1.711 (1.452-1.818)	0.047

Statistical analysis. Statistical Product and Service Solutions (SPSS) 23.0 (IBM, Armonk, NY, USA) was used for statistical analysis. The measurement data were expressed as mean ± standard deviation ($\bar{\chi}\pm s$), and the *t*-test was adopted for comparison between groups, the enumeration data were described as frequency, and the χ^2 test was chosen to verify differences between the groups. The genetic equilibrium was tested by the Hardy-Weinberg equilibrium method. All tests were two-sided and the test level $\alpha=0.05$. $P<0.05$ indicated that the difference was statistically significant.

Genotyping results and frequency distribution of rs1059513 and rs841718 polymorphic loci. A total of 150 patients with COPD and 180 healthy controls were included in this study. The basic information of the two SNP loci is presented below: rs1059513: mutation type: A>G; minimum allele frequency=0.06; Hardy-Weinberg p=0.584; rs841718: mutation type: G>A; minimum allele frequency=0.32; Hardy-Weinberg p=0.251. In the study objects, the genotypes (AA, AG and GG) of rs1059513 as well as genotypes (GG, AG and AA) of rs841718 had no obvious difference in genotype frequency between the case group and the control group (P>0.05), as shown in Table I. The distribution was consistent with the Hardy-Weinberg equilibrium law ($P_{rs1059513}=0.57$, $P_{rs841718}=0.22$).

The OR value of dominant model (AG+GG/AA), recessive model (GG/AA+AG) and additive model (GG/AA) of rs1059513 was 0.814 (P=0.129), 0.618 (P=0.368) and 0.817 (P=0.107), respectively (Table II). The OR value was 0.963 (P=0.564) of the dominant model (AG+AA/GG), 1.103 (*p*=0.418) of the recessive model (AA/GG+AG), and 0.984 (P=0.925) of the additive model (GG/AA) (Table III).

Analysis of linkage disequilibrium between two SNPs on STAT6 gene. When COPD patients carried both type A of rs841718 and type G of rs1059513, the risk of the disease was 1.689 (P=0.048), as presented in Table IV.

STAT6 gene, firstly identified and cloned by Hou et al. (7), is located on human chromosome 12. A large number of studies have illustrated that it participates in inflammatory reactions. Studies have denoted that its gene polymorphism is related to such diseases as periodic psychosis (8), schistosomiasis (9), asthma (10). STAT6 mediates IL-4 production through the JAK-STAT signaling pathway and is directly involved in the pathogenesis of COPD with the help of the activation of the IL-4/STAT 6 signaling pathway and its accompanying inflammatory mediators and inflammatory factors (11, 12). In this study, a novel multiplex enzyme linkage reaction genotyping technology was used to perform STAT6 genotyping on COPD patients and healthy controls, and the correlations of rs1059513 and rs1059513 alleles with COPD were investigated *via* case comparison. To sum up, this study found that the rs1059513 and rs1059513 alleles in the STAT6 gene are related to the pathogenesis of COPD. The frequencies of three genotypes at two loci in the case group were not significantly different from those in the control group. The dominant, recessive and additive genetic models of the two loci exhibited no marked relationship with the incidence rate of COPD. However, when COPD patients carry both type A of rs841718 and type G of rs1059513, the risk of the disease was 1.689.

In conclusion, the polymorphism of the STAT6 gene is somewhat related to COPD. However, as the pathogenesis of COPD is affected by heredity, environment, living habits and other factors, it has always been a research hotspot. The results of studies in different periods are different, which may be related to the small sample size and the limitations of research technology. Therefore, in the future, it depends on a larger sample size to confirm the genetic factors of COPD onset, thus developing targeted therapy for COPD patients.

REFERENCES

1. Riley CM, Sciurba FC. Diagnosis and outpatient management of chronic obstructive pulmonary disease: a review. JAMA 2019; 321: 786-97.
2. Lilholt PH, Witt UF, Ehlers L, Hejlesen OK. Telehealthcare for patients suffering from chronic obstructive pulmonary disease: effects on health-related quality of life: results from the Danish 'TeleCare North' cluster-randomised trial. Bmj Open 2017; 7:e14587.
3. Nagarkatti R, Ghosh B. Identification of single-nucleotide and repeat polymorphisms in two candidate genes, interleukin 4 receptor (IL4RA) and signal transducer and activator of transcription protein 6 (STAT6), for Th2-mediated diseases. J Hum Genet 2002; 47:684-7.
4. Tamura K, Arakawa H, Suzuki M, et al. Novel dinucleotide repeat polymorphism in the first exon of the STAT-6 gene is associated with allergic diseases. Clin Exp Allergy 2001; 31:1509-14.
5. Nagarkatti R, B-Rao C, Vijayan V, Sharma SK, Ghosh B. Signal transducer and activator of transcription 6 haplotypes and asthma in the Indian population. Am J Respir Cell Mol Biol 2004; 31:317-21.
6. Lee S, Shan J, Aldossary H, et al. STAT6 inhibitory peptide reduces dendritic cell migration to the lymph nodes to control Th2 adaptive immunity in the mouse lung. Eur J Immunol 2019; 49: 157-169.
7. Hou J, Schindler U, Henzel WJ, Ho TC, Brasseur M, McKnight SL. An interleukin-4-induced transcription factor: IL-4 Stat. Science 1994; 265:1701-6.
8. Kawashige S, Kanazawa T, Tsutsumi A, et al. An association study of the signal transducer and activator of transcription 6 gene with periodic psychosis. Psychiatry Investig 2008; 5:41-4.
9. He H, Isnard A, Kouriba B, et al. A STAT6 gene polymorphism is associated with high infection levels in urinary schistosomiasis. Genes Immun 2008; 9: 195-206.
10. Kavalar MS, Balantic M, Silar M, et al. Association of ORMDL3, STAT6 and TBXA2R gene polymorphisms with asthma. Int J Immunogenet 2012; 39: 20-5.
11. Nofziger C, Vezzoli V, Dossena S, et al. STAT6 links IL-4/IL-13 stimulation with pendrin expression in asthma and chronic obstructive pulmonary disease. Clin Pharmacol Ther 2011; 90: 399-405.
12. Yew-Booth L, Birrell MA, Lau MS, et al. JAK-STAT pathway activation in COPD. Eur Respir J 2015; 46: 843-5.

LETTER TO THE EDITOR

Photo-crosslinking of hyaluronic acid with low-level laser therapy device: a new combined and innovative approach

F. Rinaldi[1*], A. Trink[2], A. Sparavigna[3] and D. Pinto[1]

[1]Giuliani SpA, Milan, Italy; [2]IHRF, International Hair Research Foundation, Milan, Italy; [3]Derming, Clinical Research and Bioengineering Institute, Monza, Italy

Received January 25, 2021 – Accepted March 24, 2021

To the Editor,

Skin aging is a naturally occurring process characterized by degenerative changes in skin appearance and functionality; both intrinsic and environmental-linked aging factors are involved and, more recently, specific microbiome signatures have been associated with skin aging (1). One of the most common changes characterizing the skin aging process is the significant reduction of the epidermal hyaluronic acid (HA) (2). In recent years, HA has been used as a filler to partially revert wrinkling and to give the skin a "younger" look (3, 4). The use of cross-linked HA has been linked to several side-effects (5). In this sense, the use of light as a catalyst for the cross-linking of HA without incurring chemical substances such as methacrylate could represent a valid and safer alternative. Another increasingly popular approach for treating skin aging is low-level laser therapy (LLLT) (6). The use of LLLT allows to overcome the limitations of other commonly used skin-rejuvenations interventions and is also safer and more effective, as well as requiring minimum postoperative care. Ip and collaborators (7) reported on the usefulness of the combined use of HA injection and LLLT in the prolongation of the longevity of degenerative knee joints.

In the present work, we combined LLLT and a medium-size HA, used as bio-revitalizing agent, to achieve its photo-crosslinking and demonstrate its efficacy *in vitro*. A biorevitalizing gel with HA (Giuliani SpA) was used for photo-crosslinking and *in vitro* and *in vivo* tests. The product consists of medium-chain (1.0-1.5x106 Da) HA, obtained from *Streptococcus equi* bacteria, formulated to a concentration of 20mg/mL in a physiologic buffer. A medium-chain HA from Sigma Aldrich (Milan, Italy) was used for *in vitro* assays.

Cross-linking of HA in 3D skin models

3D Phenion® full-thickness skin models were purchased from Henkel (Phenion® FT; Düsseldorf, Germany) and cultured in 3.5 cm Petri dishes filled with 4 mL pre-warmed air-liquid-interface (ALI) medium, provided by the manufacturer. The medium was refreshed once after an initial overnight equilibration period. Tissues were subjected to experiments after the overnight equilibration at 37°C and 5% CO_2. 0.1 mL of HA was injected into the tissues. A 4 Lights laser (Monodermà Tech, Giuliani SpA, Milan, Italy) was used for tissue irradiation. The laser allows the emission of three different wavelengths, 450nm, 650nm, and 1064nm, simultaneously. Total irradiated energy was 2400 mj/min. After HA injection, the tissues were exposed for 1 min to the emission of the three different wavelengths. Tissues not injected with HA and not

Key words: hyaluronic acid; LLLT; photocrosslinking; biorevitalization

Corresponding Author:
Dr Fabio Rinaldi,
Viale Bianca Maria, 19
20122, Milan, Italy
Tel.: +39 02 76006089
Fax: +39 02 2054307
e-mail: fabio.rinaldi@studiorinaldi.com

0393-974X (2021)
Copyright © by BIOLIFE, s.a.s.
This publication and/or article is for individual use only and may not be further reproduced without written permission from the copyright holder. Unauthorized reproduction may result in financial and other penalties

exposed to laser treatment were used as negative control. Immediately after the 24-h exposure period, 4 biopsy punches (2 mm) were collected and maintained at -80°C until further analysis.

Tandem mass spectrometry (MS/MS)

SANIST platform was used for Tandem Mass Spectrometry analysis as described by Albini and coll. (8) with minor modification. Briefly, prior to LC/MS analysis, samples were treated with a triple extraction procedure using three specific solvents with different polarities (H2O, CH3OH, and CH3CN). This procedure makes it possible to maximize the extraction efficiency of both modified and non-modified hyaluronic acid.

Before mass spectrometric analysis, the samples were separated by liquid chromatography by Ultimate 3000 UPLC (Thermofisher, San Jose, CA, USA) using a Phenomenex reverse-phase C-18 chromatographic column (50 x 2.1 mm; particle size, 5 µm; pore size, 100 Å; San Jose, USA). The mobile phases were: A) 0.2% (v/v) HCOOH(aq) and B) CH3CN. The composition of the elution gradient was 2% (v/v) B between 0 and 2 min; 2 to 30% B between 2 and 7 min; 30 to 80% between 7 and 9 min; 80% B between 9 and 12 min; 80 to 2% B between 12 and 12.1 min; and the column was equilibrated with 2% B between 12.1 and 17 min. The eluent flow was 0.25 mL/min. The injection volume was 15 µL. A mass spectrometer operating in SACI/ESI condition and positive ion mode was employed. Following ion, the source parameters used were: ESI capillary voltage 2750 V, drying gas: 12 L/min, nebulizer gas: 60 psi, and temperature: 350°C. The data were acquired in data-dependent scan mode (auto-fragmentation).

Changes in interleukin-1 beta, hyaluronan synthetase and metalloproteinase-12 gene expressions

Normal human keratinocyte NCTC 2544 (National Institute on Cancer Research, Italy) were cultured in 5% CO_2, at 37°C on RPMI medium containing 2 mM l-glutamine, 1% of penicillin (100U/ml)/streptomycin (100U/ml) supplemented with 10% Fetal Bovine Serum (FBS) (basal medium). Mouse fibroblasts (Balb 3 T3, clone CCL-163™) were purchased from ATCC Culture Collection (Middlesex, UK), and were cultured under humidified atmosphere (5% CO_2, 37°C), using Dulbecco's Modified Eagle Medium (DMEM), which was supplemented with 10% (w/v) calf bovine serum (CBS), 1% penicillin (10,000 U/mL)/ streptomycin (10,000 U/mL) mixture, and 1% non-essential amino acid solution (NEAA). Both cell types were incubated in 25 cm^2 surface culture flasks at 37°C with 5% CO_2 until ca. 80% of confluence was reached. Cells were then harvested with trypsin/ EDTA and seeded at a density of 1×10^6 cells per well into 12-well plates for qRT-PCR.

Twenty-four hours after seeding on 12-well plates, NCTC2544 and BALB3T3 80% confluent cells were exposed to 1 mM hydrogen peroxide (100 µl/well) for 2 h and 30 min, respectively. After the treatment medium was removed, cells were washed and exposed to 200µg/mL of HA followed by irradiation with the three different wavelengths (450, 650, and 1064nm), simultaneously. RNA for qRT-PCR analysis was extracted 24 h after the treatment. Tri Reagent (Sigma Aldrich) method, as described by Chomczynski and Mackey (9), was used and the cDNA was then synthesized from 2 µg RNA template in a 20 µl reaction volume, using the PrimeScript RT-PCR Kit (Takara, Japan). The cDNA was amplified and detected by the Stratagene Mx3000P Real-Time PCR System (Agilent Technologies Italia S.p.A., Milan, Italy). The amplification of cDNA from NCTC cells was conducted using the following Taqman gene expression assays: Hs01555410_m1 (interleukin-1 beta, IL-1β,) andHs999999 m1 (human glyceraldehyde-3-phosphate dehydrogenase, GAPDH). The following genes were used for BALB3T3 cell: Mm03048195_m1 (hyaluronan synthetase, HAS1), Mm00500554_m1 [metalloproteinase-12 (MMP-12)] and Mm00466519ml (beta-actin, β-actin). GAPDH and β-actin were used as housekeeping genes, respectively. PCR amplifications were carried out in 20 µl of total volume. The mixture of reaction contained 10 µl of 2X Premix Ex Taq (Takara, Japan), 1 µl of 20× TaqMan gene expression assay, 0.4 µl of RoX Reference Dye II (Takara, Japan), 4.6 µl of water, and 4 µl of DNA. PCR conditions were the following: 95°C for 30 s followed by 40 cycles

Table I. *Over-expressed signals (m/z) m/z signals in samples injected with HA and irradiated with the combination of the three wavelengths (Combo-x), compared to the negative control (injected HA/no laser)*

	m/z
Combo-1	768.1016084
Combo-2	631.577331
Combo-3	695.0770477
Combo-4	483.223441
Combo-5	404.986113
Combo-6	203.6698455

of 95°C for 5 s, 60°C for 20 s. PCR reactions were performed in duplicate using an MX3000p PCR machine (Stratagene, La Jolla, CA, USA). Δ cycle threshold was used for the calculation of the relative abundance in the expression of each gene.

RESULTS

The photo-crosslinking of HA was tested on 3D Full Thickness skin models through Tandem Mass Spectrometry Analysis (MS/MS). Samples irradiated with the combination of the three different wavelengths (450-650-1064nm) were compared with the negative control sample (not irradiated). The analyte m/z value, retention time, and their peak chromatographic area are shown in Fig. 1. The following over-expressed signals (m/z) were found in samples injected with HA and irradiated with the combination of the three wavelengths, compared to the negative control (injected HA/no laser): 768.10, 631.58, 695.08, 483.22, 404.99, 203.67. Each over-expressed signal corresponds to a different chemical structure. The identification of each unknown structure was made through a library-search procedure (National Institute for Standard and Technology-NIST). This search is based on the criterion of similarity and allows the identification of the structural features of an unknown compound from its electron-ionization mass spectrum. SANIST software was used for this purpose (8). Following data acquisition, the software automatically proceeds to data elaboration using a proprietary (ISB - Ion Source & Biotechnologies S.r.l., Bresso, Italy) Bayesian elaboration model.

The presence of over-expressed signals (m/z) (Table I) in irradiated samples and the analysis of similarity confirmed the photo-crosslinking of HA. The analysis also revealed that the photo-crosslinking of HA takes place on the glycosidic bonds present in free linear polymer or fragment of

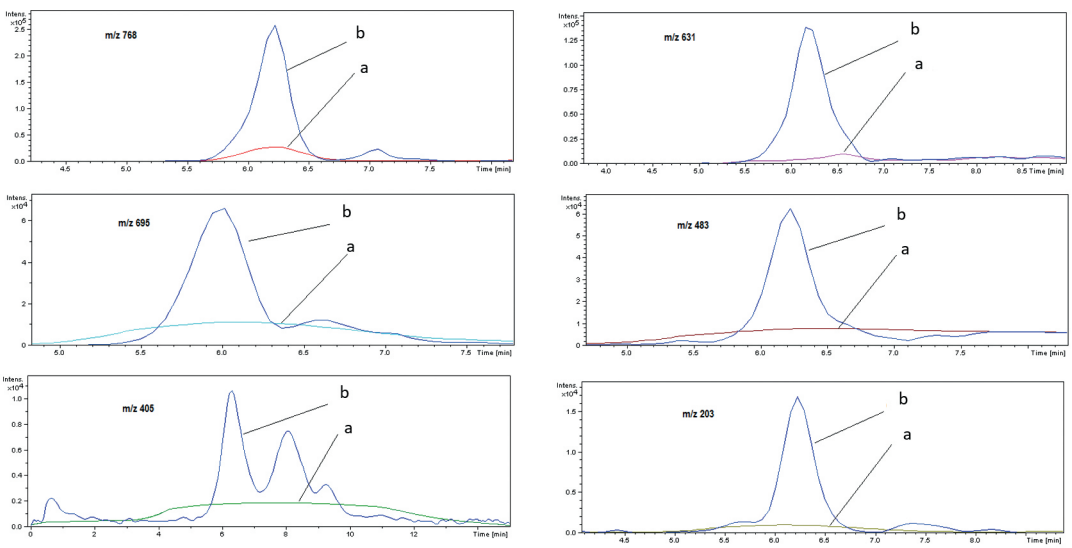


Fig. 1. *Representative full scan (base peak) extracted ion 'SANIST' mass chromatograms.* ***a)*** *HA injected Full-thickness 3D model.* ***b)*** *HA injected and LLLT irradiated (450,650 and 1064nm, combined) Full-thickness 3D model.*

HA and other species inside the tissues and is able to create such bonds. The comparative analysis (expressed in counts/s) carried out on the average of the abundance of ions collected in the samples shows a higher Area (count/s) in the sample irradiated compared with negative control, and confirms the photo-crosslinking of injected HA.

In vitro activity of photo-crosslinked hyaluronic acid

In the present work, linear HA was combined with LLLT (450-650-1064nm, combined). After the injection of linear HA, LLLT was applied by means of a 3-wavelengths LLLT device. This leads to a rearrangement of linear HA in a self-aggregate natural cross-linked system. The intra- and inter-chain interactions via glycosidic bonds are responsible for the formation of a temporary network structure also capable of incorporating free circulating HA. Coupling linear HA to LLLT results in a volumizing and filling effect of the skin without incurring the use of chemical substances. We evaluated the anti-aging efficacy of the combined treatment with HA and LLLT by means of qRT-PCR, examining gene expression profiles associated with skin aging on human keratinocytes NCTC 2544 and murine fibroblast BALB3T3.

Even though the injection of the medium-size HA alone did not reduce the expression of *IL-1β* gene in human keratinocytes NCTC2544, compared to negative control (Fig. 2a) the combined use of LLLT laser (3 combined wavelengths, 450/650 e 1064nm) produced a significant ($p<0.05$) decrease of *IL-1β* gene (Fig. 2a). *HAS-1* gene expression was significantly ($p<0.05$) decreased after the combined treatment of HA and LLLT devices (Fig. 2b). The exposition of fibroblast BALB3T3 to the combination of 3 wavelengths of LLLT device after HA injection produced a significant ($p<0.05$) decrease of *MMP-12* compared to the sample injected with HA alone and negative control (Fig. 2c).

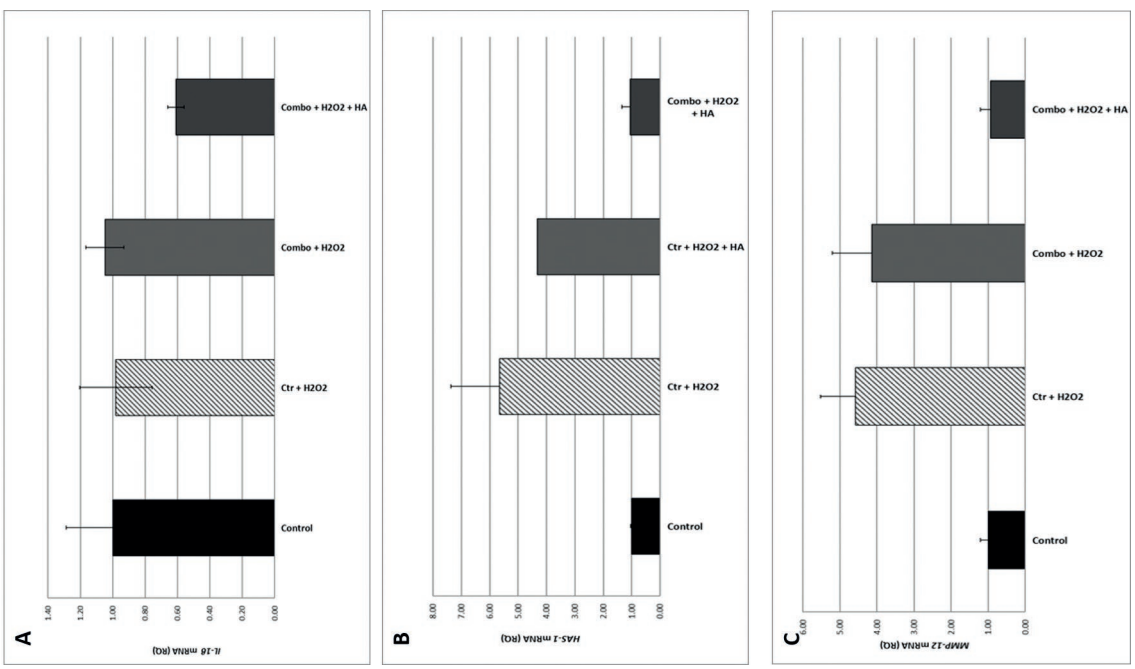


Fig. 2. *Expression of the interleukin 1 beta (IL-1β) (**a**), hyaluronan synthetase 1 (HAS-1) (**b**), and matrix metalloproteinase 12 (MMP-12) (**c**) genes as determined by RT-PCR. NCTC or BALB3T3 cells were treated with: medium alone (control); medium and 1mM hydrogen peroxide (Ctr+H2O2); LLLT laser (3 combined wavelengths, 450/650 e 1064nm) and 1mM hydrogen peroxide (Combo+H2O2); LLLT laser (3 combined wavelengths, 450/650 e 1064nm), hyaluronic acid and 1mM hydrogen peroxide (Combo+H2O2+HA). Analyses were carried out after incubation at 37°C for 24 h, under 5% CO2. Data are the means±SD of three separate experiments performed in triplicate. Statistical differences between mean values were determined with Tukey's HSD test. The asterisk indicates a significant difference (P < 0.05) to the control.*

DISCUSSION

Photo-crosslinking is a chemical reaction that takes advantage of some specific wavelengths to catalyze a chemical reaction. In the present work, we tested the hypothesis that the polymerization of HA could be obtained intradermally via LLLT irradiation.

As a complex process, skin aging is regulated both from endogenous and exogenous factors (1). This leads to progressive changes in pathways related to energy metabolism, inflammation, epidermal barrier and oxidative stress (10). Nowadays, the use of biorevitalizing agents such as HA has acquired importance due to its great versatility and efficacy (3, 4). The main limitation of HA, used in its linear form (not cross-linked), is its rapid enzymatic degradation, and for this reason, HA is often subjected to cross-linking by means of chemical substances (mainly Butanediol diglycidyl ether, divinyl sulfone and methacrylate). Moreover, the use of LLLT represents a useful tool to reverse dermal and epidermal signs of aging (6).

The aging process of the skin is characterized by a chronic progressive increase of the proinflammatory response of the cells (11). "Inflamm-aging" is the term coined in 2000 to described this process and while the causes are not completely understood, the involvement of a dysregulation of the inflammatory cytokine network has been reported (11), including the stimulation of NF-κB and the IL-1β-mediated inflammatory cascade (11). The aging process is also reported to increase the expression of hyaluronidase 1 and 2 and metalloproteinases (2, 12). An increased level of HAS genes means more availability of HA, even in the photo-crosslinked form, and improvement of the skin rejuvenation process. Other proteases strictly involved during the aging process of the skin are metalloproteinases that can enzymatically accelerate the aging process from decades to hours (12). MMPs produced by different skin cell types have different functions and roles during aging. In particular, MMP-12 secreted by macrophages and fibroblasts is responsible for elastin degradation.

The present findings on the effect of LLLT-photocrosslinked HA on *IL-1β, HAS1, MMP-12* genes corroborate the usefulness of LLLT for reducing inflammation in many skin conditions, including skin aging, and suggest a role of photo-crosslinked HA in reducing inflammatory cascade caused by the aging process.

In conclusion, in the present work, we confirmed by MS/MS the cross-linking of HA by LLLT. Data from *in vitro* assays on human keratinocytes and murine fibroblasts also reported that the ability of photo-crosslinked HA effectively counteracts skin aging by reducing inflamm-aging, HA, elastin, and collagen degradation. Future clinical work should be aimed at investigating the *in vivo* safety and efficacy of LLLT photo-crosslinked hyaluronic acid.

ACKNOWLEDGEMENT

This study was supported by Giuliani SpA.

CONFLICTS OF INTEREST: F. Rinaldi, A. Trink and A. Sparavigna serve as consultants for Giuliani S.p.A. D. Pinto is employed by Giuliani S.p.A.

REFERENCES

1. Khmaladze I, Leonardi M, Fabre S, Messaraa C, Mavon A. The skin interactome: a holistic "genome-microbiome-exposome" approach to understand and modulate skin health and aging. Clin Cosmet Investig Dermatol 2020; 13:1021-40.
2. Papakonstantinou E, Roth M, Karakiulakis G, Hyaluronic acid A key molecule in skin aging. Dermatoendocrinol 2012; 4:253-8.
3. Longas MO, Russell CS, He XY. Evidence for structural changes in dermatan sulfate and hyaluronic acid with aging. Carbohydr Res 1987; 159:127-36.
4. Fallacara A, Baldini E, Manfredini S, Vertuani S. Hyaluronic acid in the third millennium. Polymers (Basel) 2018; 10:701.
5. Ranneva E. The use of hyaluronidase to treat the excess of cross-linked hyaluronic acid following aesthetic medicine procedures: a practical point of view. Emerg Med (Los Angel) 7:357.
6. Sorbellini E, Rucco M, Rinaldi F. Photodynamic and photobiological effects of light-emitting diode (LED) therapy in dermatological disease: an update. Lasers Med Sci 2018; 33:1431-9.
7. Ip D, Fu NY. Can combined use of low-level lasers

and hyaluronic acid injections prolong the longevity of degenerative knee joints? Clin Interv Aging 2015; 10:1255-8.
8. Albini A, Briga D, Conti M, et al. SANIST: a rapid mass spectrometric SACI/ESI data acquisition and elaboration platform for verifying potential candidate biomarkers. Rapid Commun Mass Spectrom 2015; 29:1703-10.
9. Chomczynski P, Mackey K. Modification of the TRI reagent procedure for isolation of RNA from polysaccharide- and proteoglycan-rich sources. Biotechniques 1995; 19:942-5.
10. Kim M, Park HJ. Molecular Mechanisms of Skin Aging and Rejuvenation. In Molecular Mechanisms of the Aging Process and Rejuvenation. InTech. 2016 31 Aug. Available from: https://www.intechopen.com/books/molecular-mechanisms-of-the-aging process-and-rejuvenation/molecular-mechanisms-of-skin-aging-and-rejuvenation
11. Maeve Rea I, Gibson DS, McGilligan V, McNerlan SE, Alexander DH, Ross AH. Age and age-related diseases: role of inflammation triggers and cytokines. Front Immunol 2018; 9:586.
12. Xia S, Zhang X, Zheng S, et al. An update on inflamm-aging: mechanisms, prevention, and treatment. J Immunol Res 2016; 2016:8426874.

LETTER TO THE EDITOR

Overexpression of miR-522 facilitates gastric cancer progression and predicts poor prognosis

S. Wang[1], YC. Wang[2] and KL. Dong[3]

[1]Department of Second Ward of Gastroenterology, Yidu Central Hospital of Weifang, Weifang, Shandong, China; [2]Department of First Ward of Gastroenterology, Yidu Central Hospital of Weifang, Weifang, Shandong, China; [3]Department of Anorectal Surgery, Zhucheng People's Hospital, Weifang, Shandong, China

Received December 7, 2020 – Accepted March 26, 2021

To the Editor,

Gastric cancer (GC) is one of the most common malignant tumors. Most patients are diagnosed in the advanced stage, leading to a low survival rate (1). It is necessary to further clarify the molecular biological mechanisms underlying the occurrence and development of GC and to find new effective molecular biological markers for the diagnosis and treatment of GC, which will contribute to improving the prognosis and survival quantity of GC.

MicroRNA (miR) can directly bind to the 3'-untranslated region (3'-UTR) of the mRNA to regulate the expression of target mRNA molecules or cause their degradation (2). miR affects cell development, differentiation, proliferation, and apoptosis, and is involved in biological processes of various diseases and tumors, such as GC, breast cancer, and lymphoma (2-4).

In recent years, an increasing number of studies have been focused on the relationship between the expression of miR-522 and the progression of tumors, such as in non-small cell lung cancer (5) and hepatocellular carcinoma (6). One study screened the regulatory mechanism of miR typing on GC cells in GC tissues and displayed that miR-522 was overexpressed in GC cells (7), however, they did not follow up on this research.

In the present study, the expression levels of miR-522 in GC cells and tissues, and its role in the proliferation, migration, and invasion of GC cells were investigated. The clinicopathologic characteristics of GC patients were also evaluated.

MATERIALS AND METHODS

Patients and tissue samples

One hundred and twenty-five patients with GC who underwent resection were selected in Zhucheng People's Hospital from 2013 to 2015. The GC tissues and matched adjacent normal tissues (4 cm away from the cancer tissues) with a diameter of 0.5 cm were were used as samples. The fresh specimens were immediately frozen in liquid nitrogen after surgical excision and stored at -80°C until use. All GC specimens were confirmed by pathological diagnosis. All the included patients signed informed consent. This study was approved by the Ethics Committee of Zhucheng People's Hospital. To further analyze the survival status of GC patients, the 5-year follow-up information of all patients in this study was also collected.

Cell culture and transfection

GC cell lines (HGC-27, NCI-N87, AGS, MKN45, and

Key words: miR-522; gastric cancer; progression; prognosis

Corresponding Author:
Dr Kunlun Dong,
Department of Anorectal Surgery, Zhucheng People's Hospital,
58 South Outer Ring Road, Zhucheng, Weifang, Shandong, 262200, China
Tel.: +86 18765133237
e-mail: DklDong@163.com
Zhucheng People's Hospital does not have
an institutional e-mail address but can be found at:
https://www.zchosp.com/index.php?c=show&id=968

0393-974X (2021)
Copyright © by BIOLIFE, s.a.s.
This publication and/or article is for individual use only and may not be further reproduced without written permission from the copyright holder.
Unauthorized reproduction may result in financial and other penalties
DISCLOSURE: ALL AUTHORS REPORT NO CONFLICTS OF INTEREST RELEVANT TO THIS ARTICLE.

KATO III) and human normal epithelial cells (GES-1) were all purchased from the Cell Bank of the Chinese Academy of Sciences (Shanghai, China). All cells were cultured in RPMI-1640 medium (Hyclone) supplemented with 10% fetal bovine serum (FBS, Gibco) in 5% CO_2 at 37°C.

The cells were inoculated into a six-well plate one day before transfection and cultured in a CO_2 incubator. When the cell coverage rate reached 60~70%, the cell transfection experiment was conducted. For miRNA transfection, miR-522 mimic (5'- AAAAUGGUUCCCUUUAGAGUGU-3'), mimic negative control (mimic NC; 5'-UUCUCCGAACGUGUCACGUTT-3'), miR-522 inhibitor(5'-ACACUCUAAAGGGAACCAUUUU-3'),and inhibitor NC (5'-CAGUACUUUUGUGUAGUACAA-3'), were purchased from GenePharma (Shanghai, P.R. China). Lipofectamine 2000 transfection reagent (Invitrogen; Thermo Fisher Scientific, Waltham, USA) was used for cell transfection according to the manufacturer's instructions (untreated cells as blank control).

RNA extraction and quantitative real-time PCR

Total RNA was extracted from tissues and cells by the Trizol method (Invitrogen; Thermo Fisher Scientific, Waltham, USA). NanoDrop 2000 (Thermo Fisher Scientific, Waltham, USA) was used to quantify the RNA. The reverse transcription was in strict accordance with the instructions provided by the PrimeScript RT reagent kit (Takara, Otsu, Japan). Quantitative real-time PCR analysis (qRT-PCR, Thermo Fisher Scientific, Waltham, USA) was used to detect the expression of miR-522 on a 7900 Real-time PCR system with an SYBR-Green I Master mix kit, and the $2^{-\Delta\Delta Ct}$ method was used to calculate the relative expression level of miR-522 normalized to U6. The sequences for PCR were as follows: miR-522, 5'-GGGAAAATGGTTCCCTTTA-3' (forward) and 5'-CTCAACTGGTGTCGTGGA-3' (reverse); U6, 5'-GCTTCGGCAGCACATATACTAAAAT-3' (forward) and 5'-CGCTTCACGAATTTGCGTGTCAT-3' (reverse).

Cell proliferation assay

After RNA extraction and quantitative real-time PCR analysis, the CCK-8 kit was used to measure cell activity (Dojindo, Kumamoto, Japan). Transfected HGC-27 and MKN45 cells were collected and seeded in 96-well plates with a density of 2×10^3 cells/well. The conventional culture was conducted in a constant temperature incubator (37°C, 5% CO_2); 10 μL CCK-8 solution was added to each well during detection, and the absorbance was determined at the wavelength of 450 nm after continued incubation in the incubator for 1 h. Each experiment was carried out three times in parallel.

Cell migration and invasion assays

Cell invasion experiment: HGC-27 and MKN45 cells was mixed with serum-free RPMI 1640 medium, respectively. Then 200 μL cell suspension was added to the Transwell upper chamber (Corning, NY, USA) with matrigel (BD Biosciences, San Jose, CA, USA) and 500 μL medium containing 10% fetal bovine serum was added in the lower compartment (FBS, Thermo Fisher Scientific, Waltham, USA).

In the Transwell cell migration assay, matrigel was not added in the chamber, and the other steps were the same as the cell invasion assay.

Fixation staining method: cells were cultured in an incubator for 48 h at 37°C, 5% CO_2 and then fixed with 1% formaldehyde. After 0.1% crystal violet staining, the matrix glue and cells on the upper surface of the chamber were wiped off. The cells were observed and photographed under an inverted microscope and counted.

Each experiment was carried out three times in parallel.

Statistical analysis

SPSS 22.0 (SPSS, Inc., Chicago, IL, USA) and GraphPad Prism 5.0 software (GraphPad, Inc., La Jolla, CA, USA) were used for statistical analysis, and Student's *t*-tests or one-way analysis of variance (ANOVA) were used for comparison of measurement data between the two groups or among three or more groups, respectively. Kaplan-Meier analysis and Cox regression analysis were performed to explore the prognostic significance of miR-522. Experimental data were expressed as mean ± standard deviation. $P < 0.05$ was considered statistically significant.

RESULTS

Expression of miR-522 in GC tissues and cell lines

In order to determine whether the progression of GC is related to the miR-552 expression, qRT-PCR was used to analyze the miR-522 expression in tumor tissues and para-carcinoma tissues. The results showed that miR-522 expression in tumor

tissues was significantly higher than that in para-carcinoma tissues ($P < 0.001$, Fig. 1A). Then the miR-522 expression in GC cells was also examined. The results showed that miR-522 expression was up-regulated in GC cells compared with normal human epithelial GES-1 cells ($P < 0.01$, Fig. 1B). Among the GC cells, HGC-27 and MKN45 cells had relatively higher miR-522 expression levels, which were chosen for subsequent experiments.

Relationship between clinicopathological characteristics and miR-522 expression in GC patients

According to the median expression level of miR-522 in GC cells, the patients were divided into a high-expression combination goup (n = 63) and a low-expression group (n = 62). Then the relationship between clinicopathological characteristics and miR-522 expression in GC patients was studied. As shown in Table I, miR-522 was obviously correlated with lymph node metastasis ($P = 0.013$) and TNM stage ($P = 0.010$), and there was no data to prove the correlation between miR-522 and other clinicopathological characteristics such as age, gender, tumor size, and differentiation.

Upregulation of miR-522 is associated with poor prognosis in GC patients

The relationship between miR-522 expression level and patients' overall survival was investigated by Kaplan-Meier survival curves and log-rank tests as shown in Fig. 1C. The results showed that the overall survival of patients in the high expression group was significantly lower than that in the low expression group (log-rank test $P = 0.019$). The univariate and multivariate Cox regression analyses were then carried out for independent risk factors of overall survival. Results of both the univariate and multivariate Cox regression analyses showed

Table I. *Correlation between miR-522 expression and clinical characteristics of gastric cancer patients*

Clinical characteristics	Cases (n = 125)	Tissue miR-522 expression		*P*-value
		Low (n = 62)	High (n = 63)	
Age (years)				
≤ 50	67	34	33	0.783
>50	58	28	30	
Gender				
female	49	22	27	0.399
male	76	40	36	
Tumor size (cm)				
≤ 2	77	42	35	0.161
> 2	48	20	28	
Differentiation				
Well-moderate	86	40	46	0.305
Poor	39	22	17	
Lymph node metastasis				
No metastasis	88	50	38	0.013
metastasis	37	12	25	
TNM stage				
I-II	92	52	40	0.010
III	33	10	23	

that miR-522 expression (HR = 2.166, 95%CI: 1.093 - 4.292, $P = 0.027$ for univariate analysis and HR = 2.236, 95%CI: 1.0733 –4.661, $P = 0.032$ for multivariate analysis, respectively), lymph node metastasis (HR = 2.136, 95%CI: 1.128 - 4.044, $P = 0.020$ for univariate analysis and HR = 1.996, 95%CI: 1.027 - 3.878, $P = 0.041$ for multivariate analysis, respectively) and TNM stage (HR = 2.169, 95%CI: 1.144 - 4.115, $P = 0.018$ for univariate analysis and HR = 1.995, 95%CI: 1.022 – 3.894, $P = 0.043$ for multivariate analysis, respectively) were associated with overall survival and can be independent prognostic factors for GC.

Upregulation of miR-522 promotes GC cell proliferation, migration, and invasion

To investigate the regulatory role of miR-522 in GC cells, miR-522 mimic, mimic NC, miR-522 inhibitor, and inhibitor NC were respectively transfected into HGC-27 and MKN45 cells. The qRT-PCR result showed that miR-522 mimics can upregulate the miR-522 expression, and the miR-522 inhibitor can downregulate the miR-522 expression, while mimic NC and inhibitor NC have no effect on miR-522 expression ($P < 0.001$, Fig. 2A). Next, the CCK-8 assay results show that the overexpression of miR-522 promotes GC cell proliferation and downregulation of miR-522 expression inhibits GC cell proliferation ($P < 0.05$, Fig. 2B). As shown in Fig. 3 A, B, the ectopic expression of miR-522 also affects the migration and invasion of GC cells using Transwell assays. Specifically, the upregulation of miR-522 promoted GC cell migration, and invasion, while down-regulated miR-522 inhibited the migration and invasion of GC cells, compared with control ($P < 0.01$).

DISCUSSION

In previous research, miR-522 was shownto play an important role in human colorectal cancer, osteosarcoma, and hepatocellular carcinoma (6, 8, 9). Previous studies showed that the upregulation of miR-522 promoted the growth of cancer cells, and miR-522 could be used as a tumor predictor (5, 9-12). Consistent with previous research, in the present study, the miR-522 expression was upregulated in GC tissues and cell lines, compared with adjacent normal tissues and cells, respectively, which suggests miR-522 might promote GC progression. Furthermore, miR-522 expression correlates with lymph node metastasis and TNM stage. Kaplan-Meier results

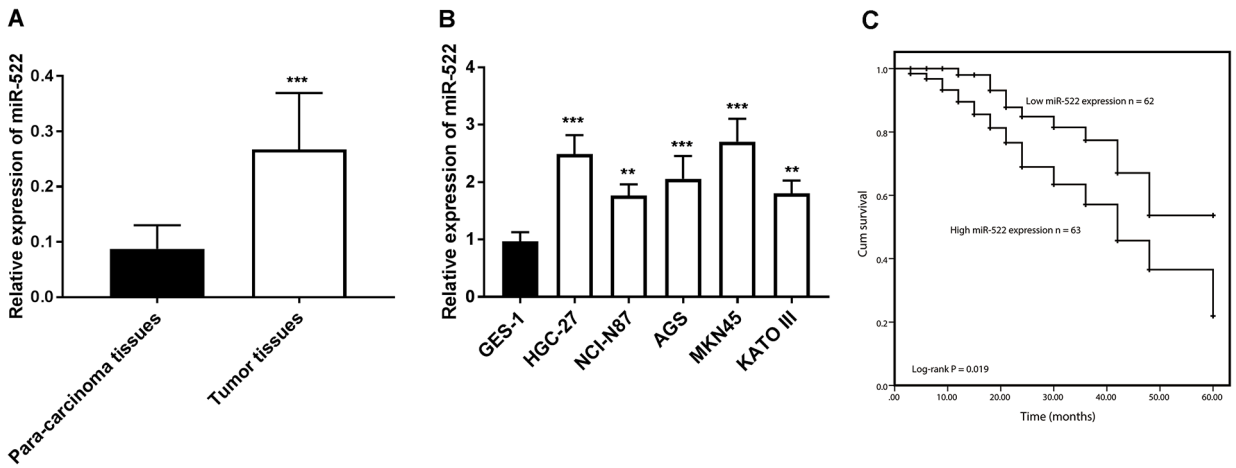


Fig. 1. *The expression and clinical significance of miR-522 in GC.* ***A)*** *Expression levels of miR-522 were examined in GC tissue samples and para-carcinoma tissues. ***P < 0.001.* ***B)*** *Expression levels of miR-522 were detected in 5 GC cell lines and a normal epithelial cell line. ***P < 0.001.* ***C)*** *Kaplan-Meier survival curve in relation to the miR-522 expression level in patients with GC. Log-rank test P = 0.019.*

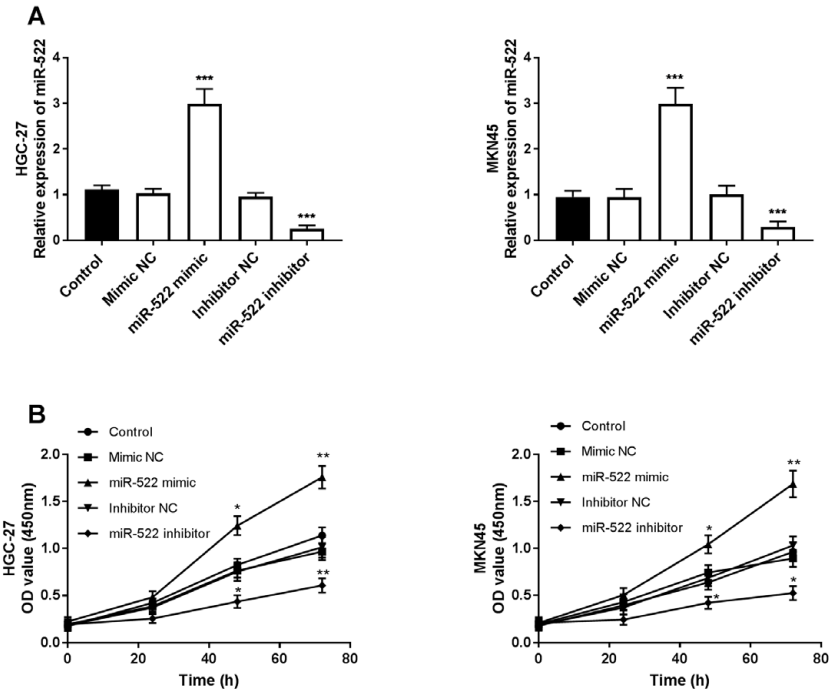


Fig. 2. *Effects of miR-522 expression levels on proliferation in HGC-27 and MKN45 cells. **A**) Expression level of miR-522 was verified by qRT-PCR after transient transfection with miR-522 mimic/inhibitor (or mimic/inhibitor NC). **B**) CCK-8 assay was performed to examine cell proliferation. *P < 0.05, **P < 0.01, ***P < 0.001.*

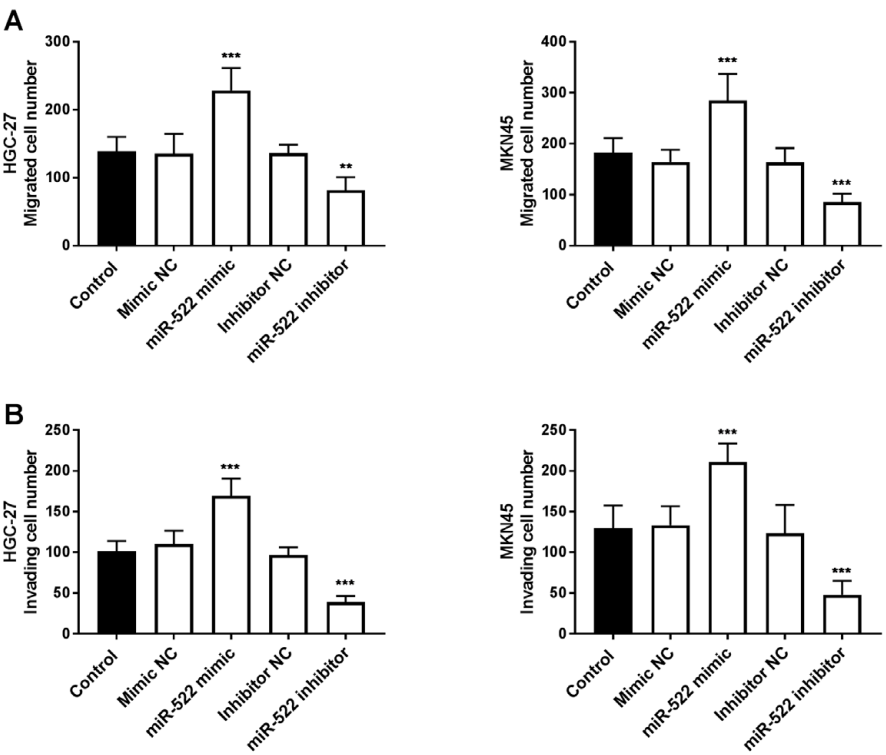


Fig. 3. *Effects of miR-522 on cell migratory and invasive abilities in HGC-27 and MKN45 cells. **A**) Cell migratory and (**B**) invasive abilities were assessed with Transwell assay. **P < 0.01, ***P < 0.001.*

showed that patients with high expression of miR-522 had shorter overall survival rates, which suggests that miR-522 may be involved in the development of GC and may be used as a potential prognostic marker. Moreover, overexpression of miR-522 promotes cell proliferation, migration, and invasion of GC cell lines. It seems reasonable to speculate that miR-522 may be a GC promoter and may serve as an oncogene in GC, however, the targeted genes and specific mechanisms of miR-522 will be studied in our future work.

In summary, miR-522 was significantly upregulated in GC tissues and cell lines compared to respective controls. Patients with high expression of miR-522 had short survival, suggesting that miR-522 may be a prognostic predictor. Overexpression miR-522 promotes proliferation, metastasis, and invasion of GC cells. This may provide new therapeutic targets for the treatment of GC.

REFERENCES

1. Dong X, Liu Y. Expression and significance of miR-24 and miR-101 in patients with advanced gastric cancer. Oncol Lett 2018; 16(5):5769-74.
2. Wei W, Cao W, Zhan Z, Yan L, Xie Y, Xiao Q. MiR-1284 suppresses gastric cancer progression by targeting EIF4A1. Onco Targets Ther 2019; 12:3965-76.
3. Wang YW, Zhao S, Yuan XY, et al. miR-4732-5p promotes breast cancer progression by targeting TSPAN13. J Cell Mol Med 2019; 23(4):2549-57.
4. Takashima Y, Kawaguchi A, Iwadate Y, et al. MicroRNA signature constituted of miR-30d, miR-93, and miR-181b is a promising prognostic marker in primary central nervous system lymphoma. PLoS One 2019; 14(1):e0210400.
5. Zhang T, Hu Y, Ju J, et al. Downregulation of miR-522 suppresses proliferation and metastasis of non-small cell lung cancer cells by directly targeting DENN/MADD domain containing 2D. Sci Rep 2016; 6:19346.
6. Shi YH, Qi BB, Liu XB, Ding HM. Upregulation of miR-522 is associated with poor outcome of hepatocellular carcinoma. Eur Rev Med Pharmacol Sci 2016; 20(15):3194-8.
7. Yang O, Huang J, Lin S. Regulatory effects of miRNA on gastric cancer cells. Oncol Lett 2014; 8(2):651-6.
8. Shuai F, Wang B, Dong S. miR-522-3p Promotes tumorigenesis in human colorectal cancer via targeting Bloom syndrome protein. Oncol Res 2018; 26(7):1113-21.
9. Xu X, Liu M. miR-522 stimulates TGF-β/Smad signaling pathway and promotes osteosarcoma tumorigenesis by targeting PPM1A. J Cell Biochem 2019; 120(10):18425-34.
10. Zhang H, Yu C, Chen M, Li Z, Tian S, Jiang J, Sun C. miR-522 contributes to cell proliferation of hepatocellular carcinoma by targeting DKK1 and SFRP2. Tumour Biol 2016; 37(8):11321-9.
11. Zhang HC, Han YY, Zhang XM, et al. miR-522 facilitates the prosperities of endometrial carcinoma cells by directly binding to monoamine oxidase B. Kaohsiung J Med Sci 2019; 35(10):598-606.
12. Zhang S, Zhang H, Zhu J, Zhang X, Liu Y. MiR-522 contributes to cell proliferation of human glioblastoma cells by suppressing PHLPP1 expression. Biomed Pharmacother 2015; 70:164-9.

JOURNAL OF BIOLOGICAL REGULATORS & HOMEOSTATIC AGENTS Vol. 35, no. 2, 751-756 (2021)

LETTER TO THE EDITOR

Efficacy of transcutaneous electrical nervous stimulation in patients with somatosensory tinnitus and cervicofacial myalgia

D. Cavagnetto*, M. Carossa*, A. Deregibus, M. Lacilla, A. Albera, P. Ceruti and S. Carossa

Department of Surgical Science, University of Torino, Italy

Received November 7, 2020 – Accepted March 30, 2021

*These authors contributed equally to this work

To the Editor,

Tinnitus can be defined as the involuntary perception of a sound in the absence of an auditory stimulus. The pathogenesis originates in the brain, and tinnitus has been associated with a worsening of quality of life. In terms of diagnosis, it is defined as "subjective" or "idiopathic," if it cannot be detected by the examiner. It can be continuous or intermittent, its intensity can be stable or variable, and it can have a sensorineural or middle ear origin (1). The overall annoyance of tinnitus is a result of its characteristics and of the psychological make up of each individual patient (2). Several parts of the brain are involved in the representation of tinnitus and of the reactions to it. Treatments can be focused on reducing tinnitus (e.g. pills) or on reducing the reactions to the tinnitus (e.g. Counseling). Approximately 1–2% of the population in industrialized areas suffers from clinically relevant tinnitus (3, 4). Pezzoli et al. (5) suggested that among the types of facial pain, only myogenic pain is significantly related to tinnitus, although migraine may also have a role. Transcutaneous electrical nerve stimulation (TENS) is recognized as an effective treatment for chronic musculoskeletal pain. Although the neurophysiological mechanisms of TENS-induced tenderness reduction have not been fully defined, it is known that it activates supraspinal opioid receptors (6). When the electrodes are placed near the ear (at the level of the temporomandibular joint and close to the insertion of the masseter muscle), TENS seems to increase the activation of the dorsal cochlear nucleus by somatosensory stimulation and augment its role in auditory stimuli selection, possibly leading to a reduction of tinnitus intensity and frequency (7). There has been a lack of trials investigating the influence of TMD therapy on tinnitus. Previous studies have mainly focused on TMD therapy with occlusal splints, as well as selective grinding and laser therapy. Thus, the aim of this study was to evaluate the efficacy of TENS in effecting changes in quality of life, perceived tinnitus intensity, and audiometric and tinnitometric values, among patients with craniofacial myalgia and tinnitus with somatic modulation.

MATERIALS AND METHODS

The study sample was selected from a pool of 168 patients (45 males, 123 females, average age 42.08±20.4 years) consecutively assessed over an 18-month period, at the Department of Gnathology of the Dental School, University of Turin, Italy. The inclusion criteria comprised

Key words: quality of life; tinnitometry; tinnitus; transcutaneous electrical nerve stimulation

Corresponding Author:
Ass. Prof. Paola Ceruti,
C.I.R. Dental School, Via Nizza 230,
10126 Torino (TO), Italy
Tel.: +39 0116708367
Fax: +39 0116708389
e-mail: paola.ceruti@unito.it

0393-974X (2021)
Copyright © by BIOLIFE, s.a.s.
This publication and/or article is for individual use only and may not be further reproduced without written permission from the copyright holder.
Unauthorized reproduction may result in financial and other penalties
DISCLOSURE: ALL AUTHORS REPORT NO CONFLICTS OF INTEREST RELEVANT TO THIS ARTICLE.

adults with cervicofacial myalgia (111 patients out of the initial 168) who also complained of persistent somatic tinnitus (27 patients out of 111) for at least 6 months (21 patients out of 27). The latter criterion was instituted in order to limit the potential bias associated with the physiological reduction of tinnitus intensity in the first 6 months after its onset.

The exclusion criteria included the following: hearing loss (a hearing loss of up to 20 decibels below the hearing threshold is still considered to be normal hearing, the aforementioned information has been added to the text); pregnancy; presence of either psychiatric, neurological, or rheumatological comorbidity; cardiological pathology; pathology or sequelae of a past pathology that affects the middle or inner ear; and risk of depression or anxiety disorder as assessed with the Hospital Anxiety and Depression Scale (HADS). Patients whose HADS score was 11 or higher were excluded, in accordance with the generally accepted cut-off for high risk depression/anxiety disorder (15 patients).

All subjects provided written informed consent to the inclusion of material pertaining to themselves, and acknowledged that they would not be identified via the paper. All subjects were fully anonymized. The study was approved by the local Ethical Committee (# 3742015), and conducted in accordance with the principles of the Declaration of Helsinki.

Primary and secondary outcomes were recorded at T0 and T1 (10 weeks of TENS treatment). The primary outcomes included tinnitus effects on quality of life [Tinnitus Handicap Inventory (THI) questionnaire], perceived tinnitus intensity, and audiometric and tinnitometric values. The 25-item THI questionnaire 26 evaluates the influence of tinnitus on quality of life, with each item being given a score of 4 (if the answer is yes), 2 (if the answer is sometimes), or 0 (if the answer is no). The maximum score is 100 points. Perceived tinnitus intensity comprises four individual components, with each being assessed with visual analog scale (VAS) consisting of a 100-mm horizontal line to be crossed between 0 and maximum bearable intensity and to be read using a ruler to quantify patient's perceived intensity. These comprise; perceived tinnitus volume (0 = absence of tinnitus, 10 = maximum intensity); patient anxiety level (0 = maximum serenity, 10 = maximum anxiety); state of mind (0 = maximum tranquility, 10 = maximum insecurity); and tinnitus tolerability (0 = absent, 10 = intolerable).

For the determination of audiometric values, audiological evaluation was conducted with pure tone audiometry performed in a soundproof booth at 5 dB intervals, with audiometer 455 Amplaid Audiometers (Amplifon, Milan). Tinnitometry was performed with the same machine to assess tinnitus intensity. The test was performed contralateral to the most affected ear. The initial pitch or frequency of tinnitus was determined by asking patients to indicate to the examiner when they realized that the sound presented was similar to their tinnitus frequency. Loudness was determined at the same frequency indicated by the patients as being similar to their tinnitus. The stimulus was presented with an initial intensity 10 dB below the patient's hearing threshold, and then increased in steps of 1 dB. The final intensity was recorded and subtracted from the individual hearing threshold to obtain each patient's level of sensation.

The secondary outcome of this study comprised: cervical tenderness score (CTS) and pericranial tenderness score (PTS) on palpation; perceived muscle pain intensity VAS; and range of movement (ROM). For the PTS, the pericranial muscles examined were the masseter, lateral pterygoid, medial pterygoid, temporalis at the mandibular insertion, and temporalis at the cranial insertion. For the CTS, assessments were performed for the sternocleidomastoid (belly and cranial insertion), trapezius, and sub-occipital muscles. Tenderness on palpation was scored in each location from 0 to 3 (0 = normal tone; 1 = mild; 2 = moderate; 3 = severe tenderness). Pericranial and nuchal muscles were palpated (i.e., small rotational movements with pressure) with the second and third finger. The other cervical muscles were pinched delicately. The palpation of each site lasted 3–4 seconds. The scores for pericranial muscles and cervical muscles were added separately, and the total obtained was divided by the number of sites examined. Thus, a PTS and CTS (range 0–3) was calculated for each patient.

The assessment of perceived muscle pain intensity comprised three components, with each being assessed with VAS. These included the maximum intensity of muscle pain (0 = absent, 10 = intolerable), average intensity of muscle pain (0 = absent, 10 = intolerable), and intensity of muscle pain at the time of the visit (0 = absent, 10 = intolerable). A tongue blade was held against the maxillary anterior teeth, with the mesioincisal embrasures between

the mandibular central incisors being used as a reference point to record maximum right and left laterotrusion, maximum protrusion, and maximum opening.

Home therapy with TENS (NeuroTracTM TENS, Verity Medical Ltd., Farley Lane, Braishfield, Hampshire, UK) was administrated according to the protocol published by the University of Turin (8) (Figs. 1 and 2), which specified the following properties and settings: double channel TENS with individually isolated circuits; amplitude (0–80 mA in 500 Ω); waveform (asymmetric biphasic); type (direct current); pulse frequency (50 Hz); pulse duration (50 μs); pulse pattern (continuous); and electrodes (self-adhesive 50 mm x 50 mm).

Each subject performed the first TENS session with the clinician in the clinic, in order to set the pulse frequency and pulse duration, and to learn how and where to place the electrodes. A pair of electrodes was placed on the trapezium between the acromion and the C7 vertebra. The remaining pair was placed on the long axis of the muscular belly of the masseter, on the line between the gonial angle and the canthus, 1 cm above the gonial angle. At home, patients performed a continuous 60-minute daily TENS session for 10 weeks. At the end of the intervention period, all primary and secondary outcomes (THI, VAS, ROM, CTS, PTS, audiometry, tinnitometry) were assessed again, and compared with pre-therapy values. Primary and secondary outcomes were presented as descriptive statistics, and compared before and after therapy.

RESULTS

A total of 15 patients (12 females and 3 males, mean age 53.2±18.19 years) with persistent tinnitus of constant intensity was selected. Three patients refused to be included in the study, and 3 patients were unable to complete the treatment cycle (one due to financial reasons, two due to a missed follow-up appointment). Thus, a total of 9 patients (7 women and 2 men, mean age 55.3±16.89 years) were included in the analysis. In terms of tinnitus onset, 8 patients had experienced symptoms for more than 1 year, and a single patient had symptoms for over 8 months. A range of sound types [pure tone, 7 patients; noise (comprised of multiple sounds), 2 patients] and descriptions [whistle, 5 patients; sizzle, 3 patients; hiss (like a gas leak), 1 patient] were documented. Seven patients reported that their tinnitus was more often perceived at night.

At the 10-week follow-up, the mandibular ROM had improved in all patients. Increases were observed for average active jaw opening (from 43.2±6.6 mm to 45.9±7 mm), passive jaw opening (from 47.7±6.9 mm to 49.5±8.7 mm), protrusion (from 7.2±1 mm to 8.1±1.8 mm), right laterotrusion (from 11.3±2.4 mm to 12.3±3.3 mm), and left laterotrusion (from 10.1±3.6 mm to 11±2.4 mm). PTS and CTS values were lower after therapy (PTS, 18±0.86; CTS, 1.24±0.89) compared to baseline (PTS, 1.86±1; CTS, 2.07±1.05).

In terms of cervicofacial muscle pain, decreases in scores at the end of therapy were observed for average muscular pain (from 5.43±1.98 to 2.81±1.91, percentage decrease of 48.26%), maximum muscle pain (from 6.67±2.05 to 3.67±2.49, percentage

Table I. *Tinnitometric data (expressed in dB) obtained before and after 10 weeks of transcutaneous electrical nerve stimulation therapy.*

	Hearing threshold	Tinnitus intensity
SUBJECT	BEFORE	AFTER
1	52	51
2	25	54
3	76	72
4	20	20

decrease of 45%), and muscle pain at the time of the assessment (from 4.18±3.16 to 2.7±2.36, percentage decrease of 35.37%) (Fig. 3A). In terms of perceived tinnitus intensity, scores were decreased at the end of therapy for perceived volume of tinnitus (from 6.1±1.36 to 5±1, average percentage decrease of 18.18%), level of anxiety connected to tinnitus (from 6.3±1 to 6.1±2.20, percentage decrease of 3.17%), and tolerability of tinnitus (from 6.3±1.14 to 6±1.80, percentage decrease of 5.26%). In terms of the influence of tinnitus on mood, scores after therapy (5.2±1.99) were higher than before therapy (4.4±2.07, an increase of 18.18%) (Fig. 3 B,C).

Improvements in quality of life were observed. The mean pre-therapy THI score of 31.1 was higher than the mean post-therapy score of 23.8, yielding a mean difference of 7.3 points. Six patients had improvements of at least 6 points, reflecting significant improvements following treatment (Fig 3D). Tinnitometric data are shown in Table I. The mean reduction in level of sensation values after therapy was 4.44 Db, which equated to a percentage reduction of 44.4%.



Fig. 2. *Electrode placement on the trapezium between the acromion and the C7 vertebra.*



Fig. 1. *Electrode placement on the long axis of the muscular belly of the masseter, on the line between the gonial angle and the canthus, 1 cm above the gonial angle.*

DISCUSSION

The purpose of this study was to evaluate whether TENS therapy could be beneficial to patients complaining of somatic tinnitus. Comparing the results of the present study with previously published data is difficult, as each study has used different sample selection protocols and assessment methods. Many authors have highlighted the need for placebo-controlled studies to evaluate the placebo effect in treatment protocols for tinnitus (9, 10). The perceived intensity of tinnitus changed from a mean score of 6.1 to 5 (percentage reduction of 18.18%). A reduction of this value occurred in 66.67% of the patients evaluated. This result is in agreement with the study by Bonaconsa et al. (11) which reported a reduction of 1.45 points among 53% of patients. The article by Lee et al. (12)

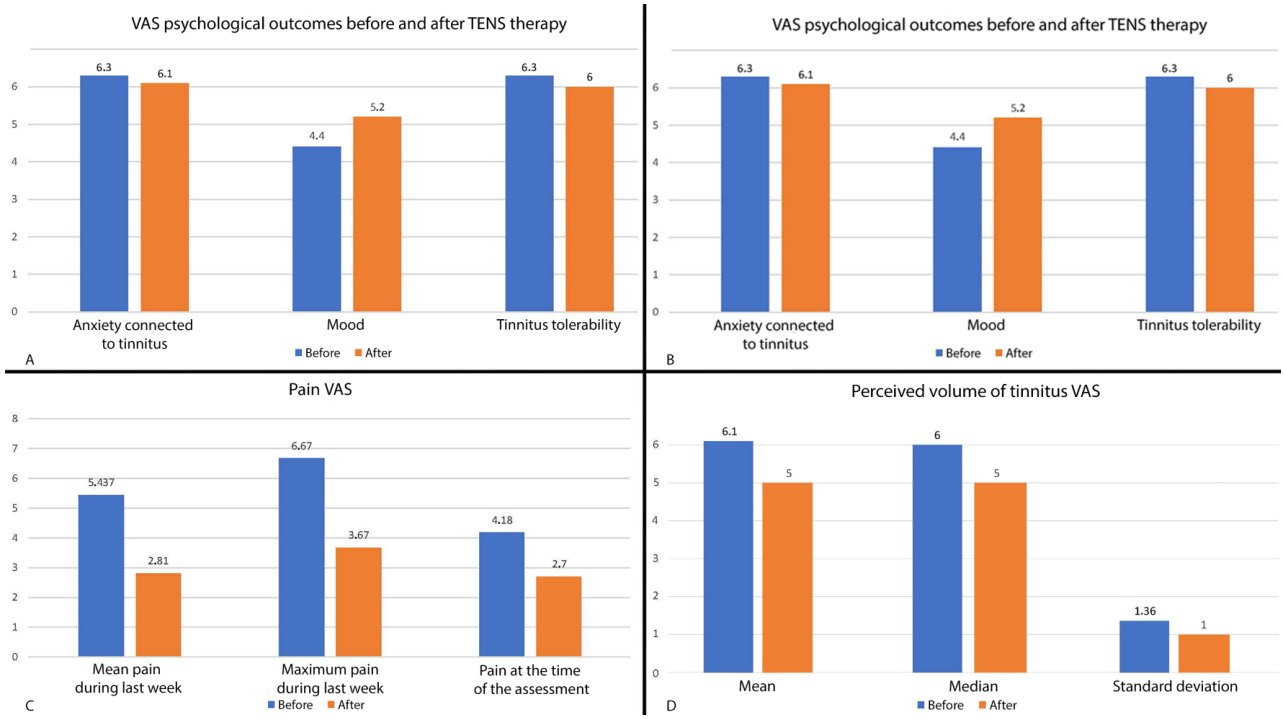


Fig.3. ***A)*** *Cervicofacial muscle pain assessed with a visual analogue scale (VAS, 0 – 10 scale), before and after 10 weeks of transcutaneous electrical nerve stimulation therapy.* ***B)*** *Perceived volume of tinnitus, as assessed with a visual analogue scale (VAS, 0 – 10 scale), before (SD = 1.36) and after 10 weeks of transcutaneous electrical nerve stimulation therapy (SD = 1.00).* ***C)*** *Visual analogue scale scores (VAS, 0 – 10 scale) for level of anxiety connected to tinnitus, tinnitus influence on mood, and tolerability of tinnitus, before and after 10 weeks of transcutaneous electrical nerve stimulation therapy.* ***D)*** *Tinnitus Handicap Inventory (THI) questionnaire scores before (SD = 11.5) and after 10 weeks of transcutaneous electrical nerve stimulation therapy (TENS) (SD = 12.3).*

provided similar data, identifying a mean reduction of 0.9 points in perceived intensity. On the other hand, Herraiz (2007) found an improvement in 46% of the participants performing TENS for two weeks at home. That study, however, did not distinguish between somatosensory tinnitus, and tinnitus associated with otolaryngologic pathology. All patients had significant tinnitometric improvements (mean decrease was from 10 dB to 5.6 dB, 44.44% reduction). Nevertheless, comparisons with existing literature could not be made, as no studies have used a similar research protocol to assess this outcome.

It is interesting to consider that a significant reduction in tinnitus intensity, as assessed with tinnitometry, does not imply a similar improvement in VAS assessments tailored to assess self-perception of tinnitus intensity, or quality of life as assessed by THI (10, 14). Confirmation of the efficacy of this therapeutic protocol would require a larger sample size, as well as an extension of the follow-up period to evaluate whether the reduction in intensity of tinnitus that appears after 10 weeks corresponds to a progressive improvement in patients' quality of life.

It is important to investigate possible occult pathologies that may not have a dental cause. For this reason, it would be appropriate to approach the treatment of a patient with tinnitus with an interdisciplinary team specialized in the various aspects of diagnosis and therapy (otolaryngologists, neurologists, psychiatrists and psychologists). A lack of knowledge in somatosensory tinnitus etiology leaves little option but to consider and use all possible therapies validated by the literature to find one that, for a specific patient, is effective, at least in part. Clinicians must have the ability to make a differential diagnosis between different types of tinnitus in order to successfully manage these patients, or refer the patient to the appropriate specialist.

REFERENCES

1. Bentler RA, Tyler RS. Tinnitus management. ASHA 1987; 29(5):27-32.
2. Tyler RS, Aran, J-M, Dauman R. Recent advances in tinnitus. Am J Audiol 1992; 1(4):36-44. doi: 10.1044/1059-0889.0104.36.
3. Ralli M, Greco A, Turchetta R, Altissimi G, de Vincentiis M, Cianfrone G. Somatosensory tinnitus: Current evidence and future perspectives. J Int Med Res 2017; 45(3):933-47. doi:10.1177/0300060517707673
4. Tyler RS. Tinnitus Treatment : Clinical Protocols. Ed Thieme; 2006.
5. Pezzoli M, Ugolini A, Rota E, et al. Tinnitus and its relationship with muscle tenderness in patients with headache and facial pain. J Laryngol Otol 2015; 129(7):638-43. doi:10.1017/S0022215115001425
6. Johnson M, Martinson M. Efficacy of electrical nerve stimulation for chronic musculoskeletal pain: a meta-analysis of randomized controlled trials. Pain 2007; 130(1-2):157-65. doi:10.1016/j.pain.2007.02.007
7. Herraiz C, Toledano A, Diges I. Trans-electrical nerve stimulation (TENS) for somatic tinnitus. Prog Brain Res 2007; 166:389-94. doi:10.1016/S0079-6123(07)66037-3
8. De Giorgi I, Castroflorio T, Sartoris B, Deregibus A. The use of conventional transcutaneous electrical nerve stimulation in chronic facial myalgia patients. Clin Oral Investig 2017; 21(1):275-280. doi:10.1007/s00784-016-1787-2
9. Tyler R S, Noble WG, Coelho C. Considerations for the design of clinical trials for tinnitus. Acta Oto-Laryngologica, 2006; 126: 44-49.
10. Tyler RS, Oleson J, Noble W, Coelho C, Ji H. Clinical trials for tinnitus: Study populations, designs, measurement variables, and data analysis. Prog Brain Res 2007; 166:499-509.
11. Amanda B, Manuela M, Antonia M, Claudio M, Gregorio B. Posturography measures and efficacy of different physical treatments in somatic tinnitus. Int Tinnitus J 2010; 16(1):44-50. http://www.ncbi.nlm.nih.gov/pubmed/21609913. Accessed December 8, 2018.
12. Lee SK, Chung H, Chung JH, Yeo SG, Park MS, Byun JY. Effectiveness of transcutaneous electrical stimulation for chronic tinnitus. Acta Otolaryngol 2014; 134(2):159-67. doi:10.3109/00016489.2013.844854
13. Kapkin O, Satar B, Yetiser S. Transcutaneous electrical stimulation of subjective tinnitus. A placebo-controlled, randomized and comparative analysis. ORL J Otorhinolaryngol Relat Spec 2008; 70(3):156-61. doi:10.1159/000124288
14. Tyler R, Perreau A, Mohr AM, Ji H, Mancini PC. An exploratory step toward measuring the 'meaning of life' in patients with tinnitus and in cochlear implant Users. J Am Acad Audiol 2019; doi: 10.3766/jaaa.19022.

LETTER TO THE EDITOR

Nickel sensitization influence on microbiota in allergic and non-allergic disorders: what's up?

L. Ricciardi, F. Furci and S. Gangemi

Allergy and Clinical Immunology Unit, Department of Clinical and Experimental Medicine, University Hospital G.Martino, University of Messina, Messina Italy

Received September 18, 2020 – Accepted March 31, 2021

To the Editor,

Nickel (Ni) is a chemical element that causes clinical manifestations such as allergic contact dermatitis (ACD) and systemic nickel allergy syndrome (SNAS), in nickel sensitized patients. ACD is the most common form, due to contact with any objects containing nickel (buttons, jewellery, belt buckles etc.) in sensitized subjects. The most common routes of exposure and sensitization to nickel are skin, and oral ingestion. The oral route represents not only a route of sensitization but also of tolerance; indeed, it has been reported that exposure to nickel released from dental braces, prior piercing, can reduce the appearance of nickel allergy (1).

The human microbiome refers to collective genetic information of microorganisms that inhabit the body. These microorganisms, classified as beneficial (symbiotic) or dangerous (pathogenic), account for 90% of cells. They inhabit the gut predominantly and may be important in health or disease conditions such as obesity, irritable bowel syndrome (IBS) or atopic dermatitis (AD), so much so that they can be defined as the "second genome" (2). Gastrointestinal microbiota variations may interrupt mucosal immunological tolerance, mainly through the gut microbiota, its metabolic products, dietary factors, epithelial cells, DCs, IgA antibodies, and regulatory T cells, leading to allergic conditions such as food allergy (3). Some studies reported that the introduction of nickel with a specific diet can induce changes in the equilibrium of the symbiotic intestinal microbiota.

The role of nickel sensitization and its influence on microbiota in patients with allergic and non-allergic diseases is still under investigation. In the present study, we report on the microbiota changes in some allergic and non-allergic disorders where the role of nickel in diet has been taken into consideration. The knowledge of the impact of nickel on microbiota could play a role in possible and new therapeutic approaches.

Nickel sensitization and microbiota in allergic disorders

ACD. In nickel allergy, ACD is the most common clinical expression of sensitization to nickel, and skin microbiota, which is closely related to gut microbiota, plays a fundamental role (4). Although there is no general agreement on the efficacy of a low nickel treatment, some studies have reported an improvement of dermatitis after a nickel-free or low nickel diet for a minimum period of 4 weeks (up to a maximum of 6 months) in nickel sensitized patients (1).

AD. Among patients with Ni-ACD there is a subgroup that experience concomitant AD. The role of the microbiota in skin immune responses of subjects

Key words: nickel allergy; microbiota; atopic dermatitis; IBS

Corresponding Author:
Luisa Ricciardi, MD, PhD
Allergy and Clinical Immunology Unit,
Department of Clinical and Experimental Medicine,
G.Martino University Hospital, University of Messina,
Via Consolare Valeria, 1, 98124 - Messina, Italy
e-mail: lricciardi@unime.it

0393-974X (2021)
Copyright © by BIOLIFE, s.a.s.
This publication and/or article is for individual use only and may not be further reproduced without written permission from the copyright holder.
Unauthorized reproduction may result in financial and other penalties
DISCLOSURE: ALL AUTHORS REPORT NO CONFLICTS OF INTEREST RELEVANT TO THIS ARTICLE.

with AD, with or without nickel sensitization, and the role of *Staphylococcus aureus* in the pathogenesis of AD is currently under further investigation (2). Various studies reported that infants with AD have a lack of bacterial diversity, low quantities of Bifidobacterium and Bacteroides and high levels of Enterobacteriaceae (5). Fujimura et al. reported that infants with higher risk of atopic diseases present low levels of Akkermansia, Bifidobacterium, and Faecalibacterium and high quantities of Candida and Rhodotorula (6); in particular, bacterial colonization of the intestines and establishment of gut flora in infancy are related to the development of the immune system. Limited data are available about nickel allergy and gut microbiota in infants with or without AD or nickel sensitization.

SNAS. Approximately 5% of patients with nickel-ACD develop SNAS; in this case nickel ingestion and absorption induces systemic symptoms, in particular gastrointestinal symptoms (i.e. nausea, pyrosis, meteorism, abdominal pain, diarrhoea, constipation), associated with immune system dysregulation with massive infiltration of pro-inflammatory $CD4^+$ T lymphocytes in the duodenal lamina propria and epithelium, with the involvement of Th2-cytokines such as interleukin (IL)-5 and IL-13 (1). Considering the effects of nickel on the gastrointestinal tract, investigations on the nickel-induced intestinal microbiota modifications could be relevant. Various studies reported the role of a low nickel diet in improving typical symptoms in patients affected by SNAS, with associated increased skin and oral nickel tolerance levels, however, few studies have analysed the role of probiotics in nickel allergy, in particular in SNAS. As reported in the work of Lombardi et al., as well as a low nickel diet, the addition of probiotic therapy, according to urinary dysbiosis markers in subjects with SNAS, obtains better results characterized by improved intestinal dysbiosis than with the use of a low-nickel diet alone (7). In particular, while a low nickel diet induces a reduction of nickel sensitivity and the level of dysbiosis, the use of probiotics leads to a shift to a lower dysbiosis grade, or eubiosis, in many patients, with restoration of physiological mechanisms of immune tolerance that are altered in some conditions such as SNAS or IBS**.** The use of probiotics may have a beneficial influence on the restoration of the altered gut microbiota, increasing beneficial bacteria, such as Bifidobacteria and Lactobacilli and decreasing the inflammation associated with the proliferation of pathogenic bacteria. Zhou et al. (8) evaluated the community composition of intestinal flora in mice after nickel administration, comparing it with a control group that had not received nickel. The feedback, in the oral nickel group, of a greater presence of Bacteroides, Intestinimonas and a lower ratio of Firmicutes/Bacteroides, according to the results of real time quantitative PCR, confirmed that oral nickel induces modifications in the interaction between the host and the intestinal flora. These results highlight the impact of nickel on the microbiota, in terms of composition and functions. Dysregulation of the intestinal microbiota, known as dysbiosis, has a clinical impact in immunological, metabolic, and intestinal diseases.

Nickel sensitization and microbiota in non-allergic disorders

Non-allergic gastrointestinal diseases. A high prevalence of nickel sensitization has been reported in patients with non-allergic gastrointestinal disorders such as IBS, lactose intolerance and Coeliac Disease (CD). Management of these patients using a low nickel diet, induces improvement in gastrointestinal symptoms and in the general physical health in patients with concomitant Ni allergy. Clinical suspicion is correlated to persistent IBS or unresponsiveness to either a lactose-free or gluten-free diet, respectively, and improvement only after also following a low nickel diet. Likely this occurs through a reduction of a pro-inflammatory nickel-induced state which might be related to dysregulation of the microbiota. Not only IBS but also IBS-like disorders can be induced by nickel sensitization with the appearance of similar clinical features (chronic diarrhoea, bloating, abdominal pain). A correct differential diagnosis is therefore of great importance in the work-up of these disorders, often with an integrated approach (9).

Obesity. An increased presence of nickel allergy, both ACD and SNAS, was also reported in obese

patients, assuming that nickel has a role in the genesis of the metabolic and inflammatory profile typical of obese individuals. As in patients with SNAS, also in obese individuals, a therapeutic approach based on the use of probiotics can modulate gut microbiota, in particular with three mechanisms of action: antimicrobial activity, barrier function regulation and modulation of the gastrointestinal immune system (10).

Pathophysiology of nickel influence on microbiota

The gastrointestinal tract plays a crucial immune role in inducing effector or tolerant responses to different antigens by balancing the functions of Th1 and Th2 cells as well as regulating Th17 and T regulatory (Treg) cells in the lamina propria. Increased IL-22 serum levels, a cytokine from the Th17 family, were found in Ni-allergic patients with gastrointestinal symptoms, improving after a low-nickel diet. Furthermore, it has been shown that the differentiation of naïve T cells into Th1, Th2, and Th17 or Forkhead box P3 (Foxp3)+ Treg cells is related to gut flora. Treg cells play a crucial role controlling inflammation by downregulating cellular activities of mast cells, eosinophils, and basophils, suppressing IgE production and inducing IgG4

Bifidobacterium, Lactobacillus, Clostridium, Bacteroides, Streptococcus and their metabolic products, butyric acid and propionic acid, are important due to their capacity to induce Treg cells. Th17 cells produce IL-17, IL-17F, and IL-22, having a crucial role in the barrier function of the GI tract, contributing to pathogen clearance at the mucosal surface. The interaction between Th1 and Th2 is important for homeostasis as skewing can lead to chronic inflammation and autoimmune or allergic conditions (11).

Gut and skin microbiota are probably linked, as indeed short-chain fatty acids (SCFAs), i.e. propionate, acetate, butyrate, which are end products of dietary fibre fermentation in the gut, play a crucial role in inducing the composition of the skin microbiota. Acetate and propionic acid, produced in the gut by Cutibacterium, are SCFAs. Propionic acid and its esterified derivatives block the growth of methicillin-resistant *Staphylococcus aureus* USA300 (*in vitro* study). Cutaneous commensals such as *S.epidermidis* and *C. acnes* tolerate wider SCFA shifts than others. Together, these results highlight the presence of mutual interaction between the gut and skin (12).

Conclusions and perspectives

Changes in the microbiota of patients with nickel sensitization appear to be correlated to the immune dysfunction typical of allergic diseases. Host-related factors such as age, diet, and environmental conditions may also influence these changes with differences in the various digestive tracts, such as in the oral cavity, stomach, intestine. A greater localization of aerobic species is present in the upper small intestine, while anaerobic species is present in the colon. Several studies reported the positive effects of the use of probiotics on various allergic conditions, such as AD, respiratory allergic diseases, milk protein allergy, with enhancement of Treg cells as well as suppression of Th2 and Th17 responses.

The use of a specific probiotic based on the type of dysbiosis could be investigated in a multi-omic study in subjects with Nickel sensitization and either skin or gastrointestinal diseases which improve after a low nickel diet. This could lead to a consequent personalized approach, as microbiome is highly individual, with a relevant role in a future diagnostic and therapeutic application of precision medicine in clinical conditions where nickel allergy is involved.

Underlying pathophysiological mechanisms have been found to be common to nickel sensitization with gastrointestinal and microbiota involvement and allergic and non-allergic disorders. Existing clinical evidence suggests the need for therapeutic manipulation of the intestinal microbiota to prevent or treat obesity and other disorders characterized by dysbiosis and nickel sensitization.

REFERENCES

1. Ricciardi L, Furci F, Isola S, Minciullo L, Saitta S, Gangemi S. Systemic nickel allergy syndrome: tips and tricks on how to be suspected and treated. J Biol Regul Homeost Agents 2019; 33:1289-92.
2. Yamazaki Y, Nakamura Y, Nunez G. Role of the microbiota in skin immunity and atopic

dermatitis. Allergol Int 2017; 66:539-44.
3. Aitoro R, Paparo L, Amoroso A, et al. Gut microbiota as a target for preventive and therapeutic intervention against food allergy. Nutrients 2017; 9:672.
4. Pascal M, Perez-Gordo M, Caballero T, et al. Microbiome and allergic diseases. Front Immunol 2018; 9:1584.
5. Nylund L, Nermes M, Isolauri E, Salminen S, de Vos WM, Satokari R. Severity of atopic disease inversely correlates with intestinal microbiota diversity and butyrate-producing bacteria. Allergy 2015; 70:241-4.
6. Fujimura KE, Sitarik AR, Havstad S, et al. Neonatal gut microbiota associates with childhood multisensitized atopy and T cell differentiation. Nat Med 2016; 22:1187-91.
7. Lombardi F, Fiasca F, Minelli M, et al. The Effects of low-nickel diet combined with oral administration of selected probiotics on patients with Systemic Nickel Allergy Syndrome (SNAS) and gut dysbiosis. Nutrients 2020; 12:1040.
8. Zhou X, Li J, Sun JL. Oral nickel changes of intestinal microflora in mice. Current Microbiology 2019; 76:590-96
9. Borghini R, Donato G, Alvaro D, Antonio Picarelli. New insights in IBS-like disorders: Pandora's box has been opened; a review. Gastroenterol Hepatol Bed Bench Spring 2017; 10:79-89.
10. Abenavoli L, Scarpellini E, Colica C, et al. Gut microbiota and obesity: a role for probiotics. Nutrients 2019; 11:2690.
11. Akdis M. Healthy immune response to allergens: T regulatory cells and more. Curr Opin Immunol. 2006; 18:738-44.
12. Salem I, Ramser A, Isham N, Ghannoum MA. The gut microbiome as a major regulator of the gut-skin axis. Front Microbiol 2018; 9:1459.

LETTER TO THE EDITOR

Angiogenic effect of the application of radial shock waves on the integral musculature of the Wistar rat quadriceps - a new perspective for muscle physiology

RS. Almeida[1], RI. Ferreira[2], DAA. Galdino[3], IGGF. Mariano[2], NF. Silveira[4], PL. Almeida[2] and MAP. Andrade[1]

[1]School of Medicine of the Federal University of Minas Gerais, Brazil; [2]School of Medicine of the University of Barbacena, Minas Gerais, Brazil; [3]School of Medicine of the University of Barbacena, Minas Gerais, Brazil; [4]Institute of Orthopedics and Traumatology of Barbacena, Minas Gerais, Brazil

Received October 20, 2020 – Accepted March 31, 2021

To the Editor,

Shock waves consist of high-energy, high-pressure mechanical sound pulses that are applied in a short time to a specific part of the body (1, 2). The use of extracorporeal shockwave therapy (ESWT) in medicine began in 1980 with lithotripsy in urolithiasis (1). Later studies demonstrated the benefits of ESWT in bone ailments such as delayed fracture healing and pseudoarthrosis (1). The osteogenic effect of ESWT is well defined in medical literature due to the fact that the activation of the integrin-cytoskeleton-nucleus protein system acts in the conversion of the mechanical to biological stimulus and promotes the release of growth factors (3).

Although several articles describe the benefits of ESWT in muscle diseases, assessments of its histological effect in the process of cell regeneration are lacking (3). It is known that in the recovery of skeletal muscle there is a period of degradation and inflammation, followed by an extensive repair phase and, finally, a period of maturation and redevelopment (4). The main histological changes that indicate the success of this process are neovascularization and the proliferation and activation of satellite cells (4, 5).

Taking these aspects into consideration, the objective of this study was to verify whether the stimulus produced by electrohydraulic shock waves is capable of inducing histological changes compatible with the cell recovery process in the quadricep muscle of Wistar rats: in particular, angiogenesis and the proliferation of satellite cells. The confirmation of muscular changes induced by ESWT may therefore permit its recommendation in improving the muscular conditions of professional and amateur athletes, the rehabilitation of patients undergoing osteoarticular procedures by reducing the effects of disuse, and in neurological injuries with intact musculature, such as spasticity (6).

MATERIALS AND METHODS

This is a prospective experimental study to evaluate the histological effects of shockwave therapy on the whole quadricep muscles of Wistar rats. The study was approved by the Ethics Committee on Animal Use (CEUA - FAME Barbacena) with protocol number 01/2017, and followed current regulations on animal research.

The sample size was estimated using a 5% confidence interval and 80% power. The variable used to estimate sample size was the existence of blasts. Assuming that no control sample has blasts and that 50% of the test samples do, it would be necessary to have a sample of 8 animals

Key words: shock waves; neovascularization; satellite cells

Corresponding Author:
Ms Raquel Ida Ferreira,
Praça Presidente Antônio Carlos, 08,
São Sebastião, Barbacena,
Minas Gerais, Brazil
Fax: +32 3339 2966
e-mail: raquelferreiraida@yahoo.com

0393-974X (2021)
Copyright © by BIOLIFE, s.a.s.
This publication and/or article is for individual use only and may not be further reproduced without written permission from the copyright holder.
Unauthorized reproduction may result in financial and other penalties
DISCLOSURE: ALL AUTHORS REPORT NO CONFLICTS OF INTEREST RELEVANT TO THIS ARTICLE.

in Fischer's exact test. A sample consisting of 12 animals (12 right test members and 12 left control members) was chosen so that, even if an evaluation of 1/3 of the samples was not feasible, the minimum sample size was respected.

Twelve male healthy Wistar rats, provided by the Biology Reproduction Center of the Federal University of Juiz de Fora, Minas Gerais, were evaluated in the vivarium of the Faculty of Medicine of Barbacena. The average age of the animals was 8 weeks. The animals were kept under stable temperature conditions in a ventilated unit at 22°C in controlled light/dark cycles of 12 h, with open access to water and *ad libitum* food. The right legs of the 12 animals were used as test legs and the 12 left legs were used as control legs. There were no exclusions of animals during the study. As all animals were tested (right paws) it was not necessary to use methods of separating the animals between the test group and the control group.

The researchers' blinding methods were not used during the applications of extracorporeal shock waves. The animals were anesthetized with ketamine (75mg/kg) and xylazine (10mg/kg) in order to produce a dissociative effect with the cerebral cortex and a state of deep analgesia without a loss of protective reflexes. Both drugs were administered intraperitoneally. Water-based contact gel was then applied to the right lower limb. The quadriceps were then subjected to a stimulus of 2000 pulses at 4.0 bar of air output pressure and a frequency of 20 Hz through the SwissDolorclastSmart® 20 device with the Evo Blue® air gun. After the procedure, the rats were placed in collective cages for 3 animals. The second application was performed with the same criterion after 7 days, and the third after 14 days.

The protocol used followed the recommendations of the manufacturer of the Swiss Dolorclast Smart® device in use for muscle tissues and in articles by different authors for use in skeletal muscle (4). The general data of the animals' health, behavior, and gait were evaluated daily and changes were noted. Prior to the start of the shock wave therapy sessions and after the end of the anesthesia effect, the animals were observed with an emphasis on changes in the test paws. One week after the third shock wave application, the animals were euthanized by way of increasing intraperitoneal anesthetic, using thiopental (45mg / kg).

After the loss of foot and corneal reflexes, trichotomy of the right and left lower limbs was performed and, with the aid of a scalpel and Metzenbaum scissors, part of the quadricep muscle was removed. The conservation of biological material was carried out in a previously designated plastic container containing 10% formaldehyde solution. Animal carcasses were then disposed of in accordance with current regulations for biological waste.

The histological blades were made by a qualified professional in a specialized laboratory. In order to standardize the depth of the cut of the muscles to be studied, 5 microtomy cuts were made in each paraffin block, which were disregarded. The following microtomy cut was used to make the histological blade to be studied: for each paw evaluated, two histological blades were made, one stained in hematoxylin and eosin and the other stained by Gomori's trichrome.

Histological analysis was performed in the pathology laboratory at the College of Medicine of Barbacena, Minas Gerais and in the angiogenesis sector of the Institute of Biological Sciences at the Federal University of Minas Gerais. The review was carried out at the TECSA Laboratory - Technology in Animal Health, where the reading was made by two distinct pathologists in a blind system with diagnostic agreement on all slides.

The microscopic reading of the histological blades was divided into: i) in the 10x increase, the existence of gross changes suggestive of malignant transformation was evaluated, as well as the general appearance of the muscle fibers; ii) in the 40x increase, the size and width of muscle fibers, the morphology and number of nuclei, the existence of inflammatory infiltrate, the number of satellite cells, and blood vessels were measured; iii) in the 100x increase with immersion oil, the presence of blasts was investigated. In each phase, five random histological fields were evaluated.

Statistical analysis

The data obtained were transcribed into the database and an Excel spreadsheet was made with the data, identifying the animals in regard to the results of the test and control paws. All statistical calculations were performed using the software R-3.5.2, using non-parametric methods, continuous variables regarding the legs of the same animal were compared using the Wilcoxon paired test (signed-rank). Discrete variables were compared using Fisher's exact test with mid-p correction. Statistical significance was considered when $p < 0.05$. Boxplot charts

were used to illustrate the distribution of data between different subgroups. Continuous variables were described as median (interquartile range) and binary variables as absolute number (%). The results were calculated considering the 95% confidence interval.

RESULTS

The average weight of the animals studied was 173 grams. After the three shockwave therapy sessions, the right quadriceps presented a hematoma with a pattern similar to all animals studied. It is worth noting that during the reapplications, there was no initial hematoma in any animal. During the 21 days of evaluation, beginning with the first application, no changes in the animals' behavior, gait, and general condition were observed.

Histological analysis was performed, comparing the test and control paw of the same animal. Vascular proliferation, an increase in the number of fibers and satellite cells in the test paws was shown, with a statistically significant difference ($p < 0.05$, Table I). Right paws showed an increase of 40% in the number of satellite cells and 66% in the number of vessels when compared to the left paw of the same animal. (Figs. 1-3). There was no statistical difference in the number of blasts, interstitial edema, and in the integrity of the muscle fibers. Additionally, both groups studied showed no signs of malignant tissue transformation.

Table I. *Comparison of the results obtained in the study of the right legs (test) and left legs (control).*

	Control	Test	P-value
Nuclei per fiber	3 (3 - 3.25)	4 (3.75 - 5)	**0.0206**
Fiber cores	3 (2 - 4)	5 (4.75 - 6.25)	**0.0105**
Blasts	0 (0%)	3 (25%)	0.1087
Vessels	2 (2 - 3.25)	6 (5 - 6.25)	**0.0024**

Statistical difference was admitted when $p < 0.05$. In brackets is the 95% confidence interval.

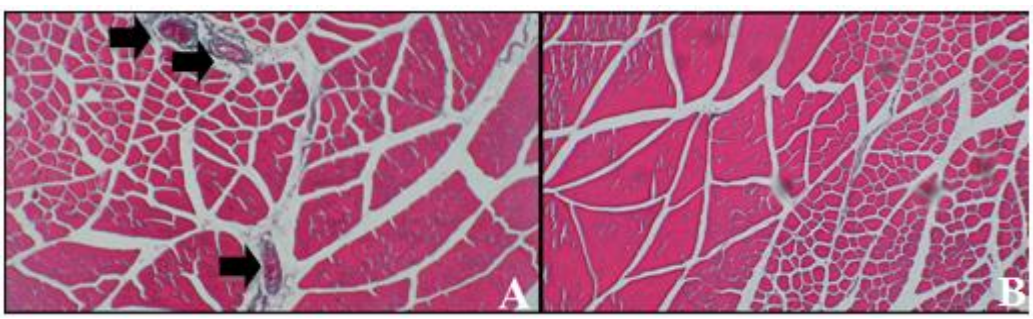


Fig. 1. *Histological slides stained in hematoxylin and eosin comparing the findings of the right (**A**) and left (**B**) paws of animal 1. The presence of vessels in A and absence in B is evident.*

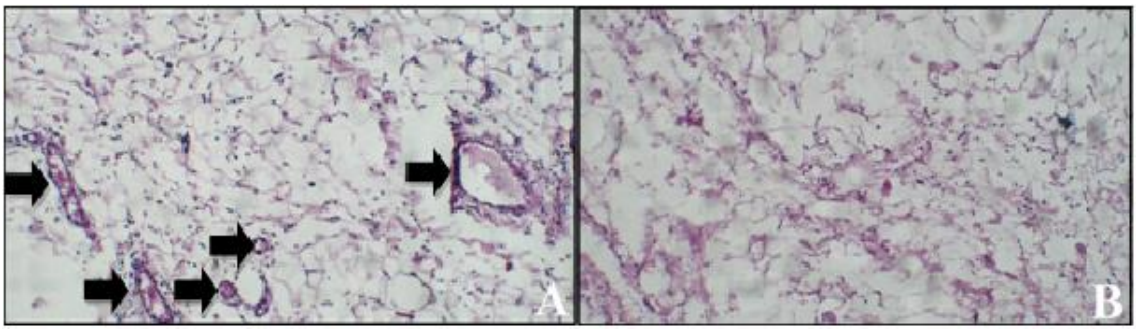


Fig. 2. *Histological slides stained by Gomori trichomium showing the connective tissue of the right (**A**) and left (**B**) paws of animal 1 with a clear difference in the count and dimensions of the vessels, corroborating the assessment of neovascularization in the test paw (A).*

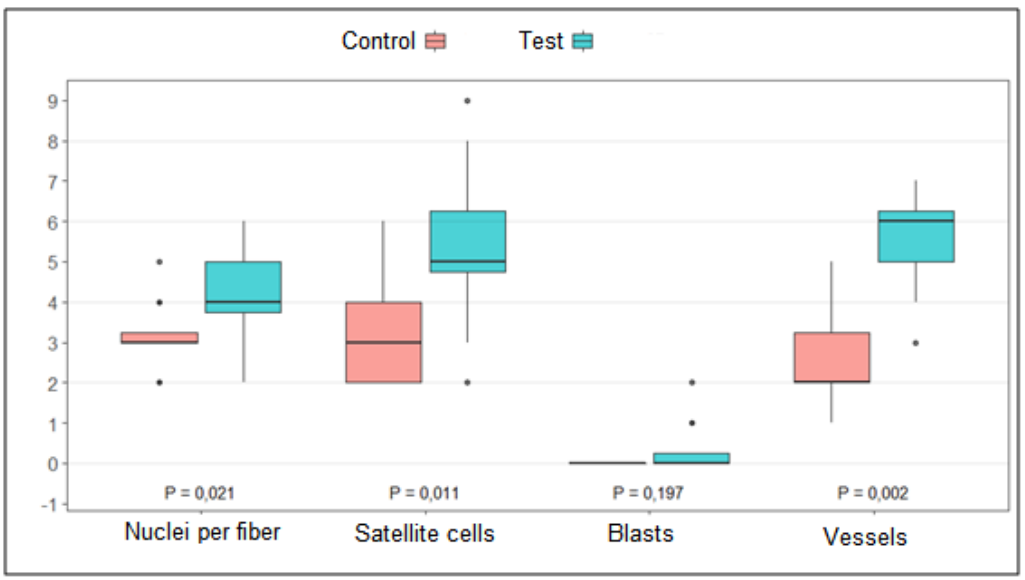


Fig. 3. *Boxplot comparing the variables studied in test paws and control paws.*

DISCUSSION

The regeneration process of muscle injuries is a complex process that includes the formation of new vessels and proliferation of satellite cells, which represent the muscle reserve (1, 5, 7). In spite of the lack of specific studies on skeletal muscle, the literature points out that the use of radial ESWT is capable of stimulating the proliferation of endothelial cells and satellite cells similar to that which occurred in the injury (8). The capacity of radial ESWT accelerates the signaling pathways of muscle regeneration can be especially important among athletes, seeing that injuries are commonly associated with pain and functional loss that impact the competitor's performance (5, 8). In healthy muscles, the increase of vascularization can improve the tissue oxygenation (4, 8). The therapy could therefore help to reduce muscle fatigue and improve the performance of professional athletes (4).

Other applications of neovascularization induced by radial ESWT are the improvement of muscle pain, hyperreflexia, and strength recovery after injury. In painful muscle syndromes and in the hyperreflexia after stroke, the neoangiogenic effect of ESWT can reduce muscle stiffness and tension (10, 11). In patients with tendinopathies, the demonstration of satellite cell proliferation after the use of radial ESWT can aid in the recovery of muscle strength (12).

In tissue injuries, neovascularization and the proliferation of satellite cells are the main processes that promote tissue regeneration. In the present study, the evaluation of the effect of radial shock waves on the skeletal muscle of Wistar rats demonstrated the capacity of the method to stimulate the proliferation of vessels and satellite cells, which can be applied to assist in the restoration of muscle integrity in several muscular pathologies. Thus, there were no other factors that could stimulate the proliferation of vessels and satellite cells, with this effect being attributed only to radial shock waves.

It is worth noting that the results may present some bias since, only one model of radial equipment was tested, and future studies are necessary for a better understanding of the effect on integral musculature. Additionally, the histological evaluation technique must be complemented with electron microscopy and VEGF protein research in order to deepen the knowledge of the effects of ESWT on skeletal muscle.

REFERENCES

1. Wang CJ. Extracorporeal shockwave therapy in musculoskeletal disorders. J Orthop Surg Res 2012; 7(1):2-8.
2. Kertzman P, Lenza M, Pedrinelli A, et al. Shockwave treatment for musculoskeletal diseases and bone consolidation: qualitative analysis of the literature. Rev Bras Ortop 2015; 50(1):3-8.
3. Cargnello M, Roux PP. Activation and function of the MAPKs and their substrates, the MAPK-activated protein kinases. Microbiol Mol Biol Rev 2011; 75(1):50-83.
4. Notarnicola A, Covelli I, Maccagnano G, et al. Extracorporeal shockwave therapy on muscle tissue: the effects on healthy athletes. J Biol Regul Homeost Agents 2018; 32(1):185-93.
5. Zissler A, Steinbacher P, Zimmermann R, et al. extracorporeal shock wave therapy accelerates regeneration after acute skeletal muscle injury. Am J Sports Med 2016; 45(3):676-84.
6. Lee JY, Kim SN, Lee IS, et al. Effects of extracorporeal shock wave therapy on spasticity in patients after brain injury: a meta-analysis. J Phys Ther Sci 2014; 26:1641-7.
7. Brandão D, Costa C, Mansilha A. Angiogenesis e arteriogenesis nin peripheral arterial disease. Angiol Circ Vasc 2012; 8(2):53-9.
8. Sundaram S, Sellamuthu K, Nagavelu K, et al. Stimulation of angiogenesis using single-pulse low-pressure shock wave treatment. J Mol Med 2018; 96(11):1177-87
9. Wang HJ, Cheng JH, Chuang YC. Potential applications of low-energy shock waves in functional urology. Int J Urol 2017; 24(8):573-81.
10. Jeon JH, Jung YJ, Lee JY, et al. The effect of extracorporeal shock wave therapy on myofascial pain syndrome. Ann Rehabil Med 2012; 36(5):665-74.
11. Guo P, Gao F, Zhao T, et al. Positive effects of extracorporeal shock wave therapy on spasticity in poststroke patients: a meta-analysis. J Stroke Cerebrovasc Dis 2017; 26(11):2470-6.
12. Notarnicola A, Quagliarella L, Sasanelli N, et al. Effects of extracorporeal shock wave therapy on functional and strength recovery of handgrip in patients affected by epicondylitis. Ultrasound Med Biol 2014; 40(12):2830-40.

LETTER TO THE EDITOR

Dual-wavelength high-power laser therapy and neuromuscular manual therapy in chronic neck pain: a randomized clinical trial

G. Barassi[1], M. Supplizi[1], L. Prosperi[1], G. Irace[1], A. Younes[1], M. Della Rovere[1], A. Rabini[2], A. Colombo[2] and A. Di Iorio[3]

[1]Center for Physiotherapy, Rehabilitation and Re-education (CeFiRR) Training Center, "G. d'Annunzio" University of Chieti-Pescara, Chieti, Italy; [2]Department of Cardiovascular Pathologies, University Hospital "A. Gemelli", Campobasso, Italy;[3]Department of Aging Sciences, "G. d'Annunzio" University of Chieti-Pescara, Chieti, Italy

Received January 26, 2021 – Accepted April 1, 2021

To the Editor,

Chronic Myofascial Neck Pain (CMNP) is one of the main manifestations of musculoskeletal disorders and frequently requires the intervention of the physiotherapist (1). In particular, CMNP constitutes a frequent cause of pain, disability, absence from work and reduced quality of life. About two-thirds of the population declared to have experienced Neck Pain (NP) during their lifetime, with an increase of prevalence during adulthood and in the elderly (2). The annual prevalence of the problem reaches 30% of the general population and 50% of acute NP cases tend not to undergo spontaneous resolution, creating a relapsing and highly invalidating problem for the people concerned (2, 3) and assuming, over time, the characteristics of chronic pain (4).

Recently, the clinical relevance of the duration of NP has been questioned, as it seems to be a poor indicator of disability when the intensity of NP tends to be low (5). A strong correlation between NP intensity and disability has been observed (5), which may be a problem in presence of chronic NP, due to the fact that, when the NP intensity reaches moderate to high levels, the lengthening of the problem can lead to an equally long-lasting disability condition for the patient.

Several studies have been carried out, demonstrating the effectiveness of Manual Therapy (MT) in the treatment of Myofascial Trigger Points (MTrPs) responsible for NP. Simons highlighted, in his study, an important correlation between the development of Myofascial Trigger Points (MTrPs) in muscles such as the sternocleidomastoideus, the levator scapula, the upper trapezius and the splenius capitis and the genesis of pain at the cervical level, known as NP (6).

Bodes-Pardo et al. (7), in a randomized pilot clinical study, experienced how MT, targeting on MTrPs of the sternocleidomastoid muscle, was able to reduce NP and headache, compared to a sham therapy. Javier et al. (8) in their case report on a girl with NP, showed how ischemic compression of MTrPs responsible for NP was able to determine improvements in pain and mobility after just a single treatment session. Ischemic compression has been shown to be as effective as hydrocortisone phonophoresis and ultrasound therapy in the treatment of MTrPs of the upper trapezius muscle (9).

Key words: musculoskeletal manipulations; manual therapy; laser therapy; neck pain; physical therapy modalities; rehabilitation; trigger points

Corresponding Author:
Dr Giovanni Barassi,
Center for Physiotherapy,
Rehabilitation and Reeducation (CeFiRR) Training Center,
Gabriele d'Annunzio University of Chieti-Pescara,
Chieti, 66013, Italy
e-mail: coordftgb@unich.it

0393-974X (2021)
Copyright © by BIOLIFE, s.a.s.
This publication and/or article is for individual use only and may not be further reproduced without written permission from the copyright holder.
Unauthorized reproduction may result in financial and other penalties
DISCLOSURE: ALL AUTHORS REPORT NO CONFLICTS OF INTEREST RELEVANT TO THIS ARTICLE.

Generally, the most recent scientific evidence has supported the use of MT as a moderately effective approach in the management of NP, particularly in association with other types of treatment such as exercise and instrumental methods (10). Among the instrumental methods used for NP, a relevant role could be assumed by High-Power Laser Therapy (HPLT), which differs from the typical Low-Level Laser Therapy (LLLT) for a clearly higher power application (expressed in units of W instead of hundreds of mW), able to guarantee a stronger and deeper biological stimulation at the application site level.

Recent studies have highlighted the ability of HPLT to improve the symptoms deriving from NP, improving the functional limitation of the cervical tract, increasing mobility and reducing the pain perceived by patients (11-12), in particular with the use of Neodymium-doped Yttrium Aluminum Garnet (Nd:YAG) type lasers with a wavelength of 1064 nm (11). However, it must be considered that also other type of laser, characterized by wavelengths in the order of 810 nm and administered with low power (≤500 mW), have proven to be effective in the management of pain (13), advancing the idea that a multiple-wavelength radiation could represent a valid therapeutic option in the treatment of pain at the level of the spine. A therapeutic window of effectiveness of laser therapy has been defined, falling in a range between approximately 600 nm and 1200 nm (14). Specifically, in the rehabilitation field, it is generally assumed that a laser working at 810 nm acts on a more superficial level, thus defining a mainly analgesic effect in terms of nociceptive inhibition; conversely 1064 nm lasers are characterized by greater penetration into tissues as well as biostimulating-reparative, decontracting and anti-inflammatory effects, especially at the muscle level (14).

Taking into consideration these premises, the present study aimed to compare two methods, namely Dual-Wavelenght High-Power Laser Therapy (DWHPLT) and Neuromuscular Manual Therapy (NMT), in the treatment of CMNP.

MATERIALS AND METHODS

This study was conducted at the Center for Physiotherapy, Rehabilitation and Re-education (Ce. Fi.R.R.), located at the University "Gabriele d'Annunzio" of Chieti-Pescara as part of the Centre of Sports Medicine. A clinical parallel study was performed in accordance with the Helsinki Declaration and Good Clinical Practice standards (15). All participants signed the informed consent for the experimental procedures, complying with ISO 9001-2015 standards for "Research and experimentation". The study was conducted, as far as possible, according to the CONSORT guidelines. All the evaluation and treatment methods used for this study, as well as the actual application procedures, are commonly used in the clinical-rehabilitative practice of the private rehabilitation center where the study was carried out, therefore, the normal ethics committee clearance was not required (16).

The study sample consisted of 20 subjects, diagnosed with CMNP associated to MTrPs present in the Upper Trapezius (UT) and in the Splenius Capits (SC). The diagnosis was carried out by a medical doctor specialized in physical medicine and rehabilitation, who was not involved in the study. The study sample consisted of 10 male and 10 female subjects, aged between 19 and 82 years (average 54.29 years).

The subjects were randomly divided into two study groups, with a 1:1 allocation ratio. The randomization was carried out by an operator different from the ones responsible for the assessments, for the treatments or for the statistical analysis of data. The random allocation of patients was carried out through the "List Randomizer" online tool of the website www.random.org. To randomize patients, also taking into account the distribution of the sample by gender, two list of 10 elements were made, one for male patients and one for female patients, with each list in turn comprising 5 nominal elements A and 5 nominal elements B, with reference to the treatment groups to which the subjects were assigned. The total 10 values for each list were then randomly sequenced by the tool used, providing a random list used to allocate suitable patients either to the A or B treatment group, following the order of admission. By creating two separate lists for male and female patients, an equal gender distribution was obtained for each treatment group. While it was impossible to blind the therapist and the patients in terms of treatment provided/received, due to completely different procedures adopted, it was

provided a blinding of evaluations, that were carried out by a different person then the one performing the treatment. Moreover, data analysis was blinded, making sure that the analyst was not informed of which treatment corresponded to the two groups.

Patients diagnosed with CMNP, associated to MTrPs present in the central belly of the UT and of the SC, were considered eligible for the study. Patients affected by infections, neurological symptoms, cancer and specific contraindications to NMT or DWHPLT were excluded from the selection. Patients were required to abstain from taking painkillers during the study.

Group A (10 patients) underwent NMT treatments of the cervical area, twice a week for 3 weeks, for a total of 6 treatments. Group B (10 patients) underwent DWHPLT treatments on the cervical area, twice a week for 3 weeks, for a total of 6 treatments.

Outcome measures and intervention

The selected subjects underwent an initial evaluation, at time T0, and a final evaluation, at time T1, at the end of the therapeutic protocol.

Assessments were conducted with the use of:

- Neck Disability Index (NDI) assessment questionnaire, recommended for the assessment of the disability of patients suffering from NP (17). This scale includes 10 items regarding activities of daily living; each question provides 6 possibilities of answer (from 0 = no disability to 5 = complete disability) based on the degree of functional limitation manifested by the examined subjects;
- Pressure Algometer on the MTrPs identified at the level of the UT and SC muscles on both the left and right side of the body (18), using an F-Meter (Storz Medical AG, Tägerwilen, Switzerland). The value read on the display of the instrument, expressed in pure numbers, with each unit corresponding to 200g, expresses the objective pressure pain threshold of the assessed point.

Patients in Group A were treated through 6 sessions of NMT, that is a global and advanced system of soft tissue manipulations that mainly deals with chronic myofascial pain and pain syndromes. This technique restores the homeostatic balance of the central nervous system and of the musculoskeletal system, using various massage therapy methods such as "brushing", "kneading" and "deep transverse friction", through which deactivation of MTrPs is obtained in muscles and their fascia, in tendons and in ligaments. A pressure on MTrPs, known as finger pressure technique, is used to rebalance the MTrPs themselves present in soft tissues. The relaxation of MTrPs frees patients from local and referred pain.

Patients in group A were treated with NMT techniques at the level of the cervical area, focusing, in particular, on the UT and SC muscles, concentrating the treatment at the level of MTrPs located in the area. The treatment consisted in the sequential use of touch, kneading, friction, ischemic compression (lasting about 30 seconds for each MTrP) and stretching techniques, for a total duration of treatment of approximately 30 minutes.

Patients in Group B were treated with 6 sessions of DWHPLT. The device used for this study was the Medilaser 15 ED (Medisport Srl, Latina, Italy), a Nd: YAG instrument for HPLT (maximum average power 15 W, class IV), capable of operating with two different wavelengths, in a ratio of 25% for 810 nm and 75% for 1064 nm, guaranteeing potentially greater therapeutic efficacy.

The effects provided by the device, which can be modulated in all emission parameters, include:

- analgesic effect, determined by the modulation of peripheral nervous system activity through the administration of pulsed stimuli, characterized by peak power and duration varying below the thermal stimulation threshold of the tissues (defined as "Stochastic emission" mode);
- anti-inflammatory and anti-edema effect, related to the deep cellular biological stimulation of the tissues, accompanied by phenomena vasodilation, due to the controlled release of nitric oxide, increased oxygen supply to the tissues and neoangiogenesis;
- biostimulating effect, related to the facilitation of cellular processes of collagen production and cellular ATP regeneration, in particular for pulses lasting more than 100 ms ("continuous" or "long-pulse" emission);
- muscle relaxant effect, due to the local increase in temperature and the release of oxygen from hemoglobin in muscle fibers in a state of hypoxic contraction.

The MTrPs present in the muscles of the cervical tract (UT and SC) of patients in group B were treated by applying a 3-step program, to combine an intense analgesic activity with biostimulating and decontracting

actions, according to the following application scheme:

- Phase 1: analgesic application in "Stochastic emission" (a randomly pulsed mode) on the right cervical tract between the trapezius and the sternocledomastoid muscle, focusing the application on MTrPs of UT and SC, with an average power of 10 W and a duration of 3 minutes, with a manual scanning movement using a pen applicator in contact with the skin, with prolonged stops (about 5-7 seconds) in the areas of MTrPs;
- Phase 2: analgesic application in "Stochastic emission" mode on the left cervical tract between the trapezius and the sternocledomastoid muscle, using the same modalities exploited in Phase 1 for the right hemisome;
- Phase 3: biostimulating/decontracting application in "Continuous" mode on the entire cervical tract between the trapezius and the sternocledomastoid muscle, with average power of 8 W and energy density of 60 J/cm^2 (with a variable duration depending on the personal extension of the cervical tract to be treated, considered as an isosceles triangle with the base corresponding to the distance between the two acromions and the height corresponding approximately to the distance between the C7-T1 spinal tract and the upper nuchal line) manually applied with a scanning movement using a pen in contact with the skin, with enough rapid movements to avoid the local overheating perceived by the patient.

The total cervical treatment through the DWHPLT lasted between 7 and 10 minutes, depending on the duration of the phase 3.

RESULTS

Differences in the outcome measures between groups, at baseline and at follow-up, were tested by mixed models analysis of covariance. The advantage of this statistical approach is improvement in the precision of the effects estimate by using all available information and, at the same time, allow for handling missing data. For brevity, only the *p*-value for the fully adjusted model with the interaction term between time and type of intervention was reported. Classical Akaike's Information Criterion (AIC) and Bayesian Information Criterion (BIC) were used to examine improvement in model fit. All statistical analysis were carried out with SAS software (release 9.4). The significance for the *p*-value was set at ≤0.05.

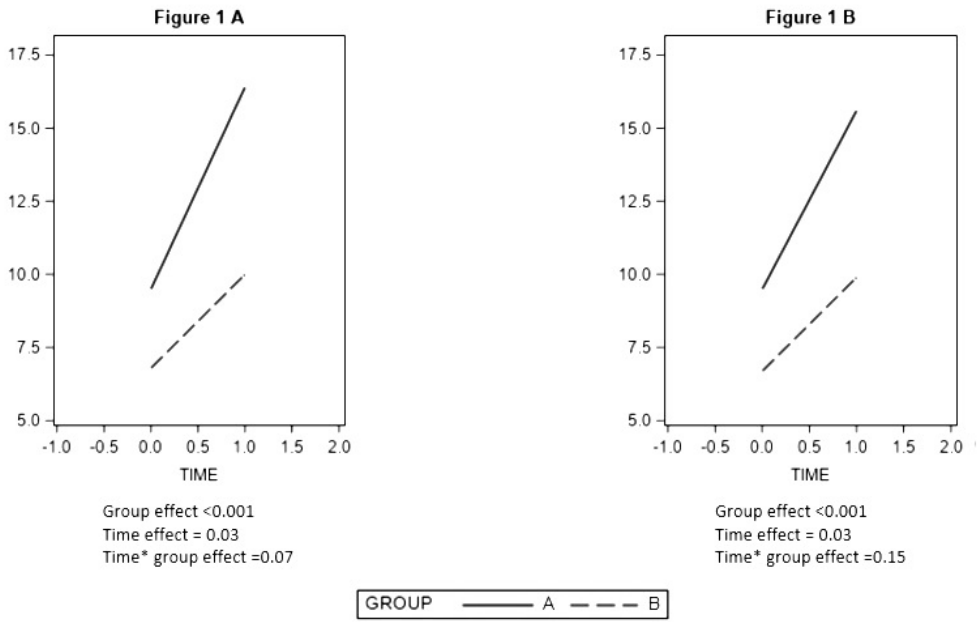


Fig. 1. *Linear Mixed Model. Variation of nociceptive level through study times (p value shown), according to algometric measurements on the UT in study groups.* ***A****)Right hemisome;* ***B****) left hemisome; 1 unit ≈ 200g).*

Regarding the algometric measurements of the UT, a general significance was detected for data variations in terms of group effect and time effect, but not for the time*group effect of both sides. As a matter of fact, a pressure pain reduction could be demonstrated of 72.6% in the right side and 64.2% in the left side for Group A and a pressure pain reduction of 47.1% in the right side and 47.8% in the left side for Group B.

With regard to algometric measurements of the SC, a general significance was detected for data variations in terms of group effect and time*group effect, while no significant variations were detected for time effect of the two hemisomes. A pressure pain reduction of 98.3% on the right side and 98.4% on the left side was calculated for Group A, and of 57.1% on the right side and 31.4% on the left side for Group B.

Finally, observing the NDI assessment questionnaire, a significant reduction was observed, in terms of time effect but not in terms of group effect and time*group effect, in the level of subjectively perceived disability both in group A (-60.2%) and in group B (-75.2%), with DWHPLT highlighting

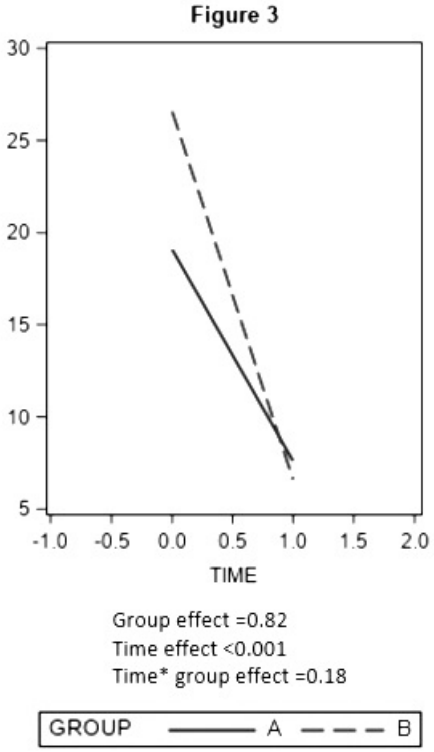


Fig. 3. *Linear Mixed Model. Variation of NDI score through study times (p value shown), according to study groups.*

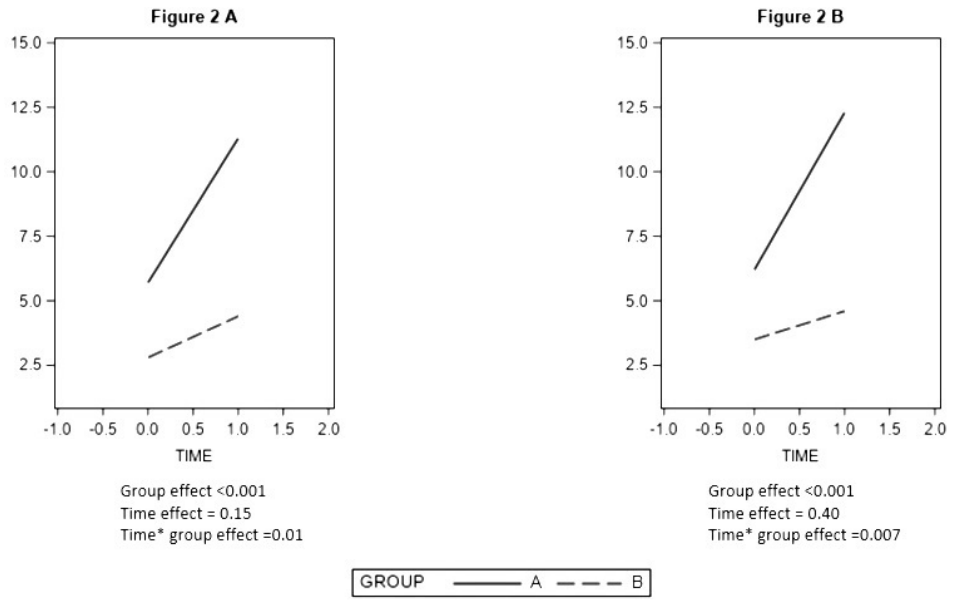


Fig. 2. *Linear Mixed Model. Variation of nociceptive level through study times (p value shown), according to algometric measurements on the SC in study groups. **A**) Right hemisome; **B**) left hemisome; 1 unit ≈ 200g).*

a superior effect, compared to NMT, in reducing disability related to CMNP.

DISCUSSION

Algometric measurements showed an improvement of pain tolerance with both the rehabilitation protocols, highlighting the effectiveness of NMT and DWHPLT in improving pressure related hyperalgesia associated with CMNP. More specifically, NMT showed a superior efficacy, especially for the SC. As already reported in a previous study, manual ischemic compression on MTrPs is able to increase the pain pressure threshold (8). The reason for this reaction should be found in the ischemic compression ability to promote a rapid acceleration of local blood flow after its release, therefore causing an increase in blood perfusion of the treated area and in tissue healing (20). It is also possible to hypothesize that NMT may have guaranteed a greater analgesic effect in terms of pressure pain due to a more intense stimulation of Aβ fibers and a subsequent inhibition of pain perception induced by Aδ and C fibers (10), which would explain the more instantaneous and intense effect of NMT on pain modulation compared to DWHPLT. However, it can be highlighted that this superiority of NMT in the inhibition of pressure pain appears completely in contrast with the perception of pain and disability in daily life by patients enrolled in our study.

Indeed, the DWHPLT-treated group showed a greater reduction in the NDI score, related to the reduction of the complications determined by NP in everyday life of patients. This condition identifies the DWHPLT as an instrument that induces an improvement in terms of influence of pain on daily life, as well as being capable of inducing improvement of functional limitations induced by NP. Several scientific studies showed that laser therapy, both low and high power, could be successfully used in the treatment of painful myofascial syndromes because of its therapeutic effects (21, 22). Furthermore, several studies have shown a great efficacy of different wavelengths in the treatment of pain syndromes of myofascial nature, in particular wavelengths of 1064 nm (11, 12, 14) and 810 nm (14) which, based on current knowledge, would seem to be the most effective light emissions for the control of myofascial pain, probably related to the biostimulating and neuromodulating properties of these types of laser radiation (11, 12, 14). Specifically, DWHPLT may be able to provide tissues with a more effective analgesic and reparative stimulus due to the combination of different levels of stimulation, (14) which mainly combines analgesic and superficial effects of the 810 nm wavelength with the predominantly biostimulating and anti-inflammatory effect of the 1064 nm wavelength, (14) thus obtaining a contemporary analgesic and reparative effect, not limiting the treatment to a short-term therapeutic efficacy, but promoting an actual healing and resolution process of somatic musculoskeletal dysfunctions, in the specific case in patients with CMNP.

In conclusion, the results demonstrated that both NMT and DWHPLT have proven to be effective methods in the treatment of CMNP. In the future, it would be desirable to further explore the proposed topic, with the assumption of a numerically larger and homogeneous study sample in terms of age and basal level of disability from NP, in order to reduce the influence of potential confounders or epidemiological bias. Furthermore, the hypothesis of prospectively evaluating the duration of the benefits and results obtained in both treatments, achievable by increasing the number of sessions and by inserting a follow-up assessment, could be really important to identify variability in response times of biological tissues, particularly in biostimulant therapies, such as DWHPLT, compared to other mechanical approaches, such as NMT.

The main limitations of this study are represented by the small dimension of the study sample, by the impossibility to blind operative procedures to the operator and to the patient, due to the completely different nature of the two proposed approaches, and, finally, by the lack of registration of the following trial in the clinicaltrials.gov registry.

REFERENCES

1. Zimoli A, Testa M. Il Dolore Cervicale: Guida alla

valutazione e al trattamento. Edra Masson. Milano, 2015.
2. Cohen SP. Epidemiology, diagnosis, and treatment of neck pain. In Mayo Clinic Proceedings, Elsevier. Amsterdam, 2015; Vol. 90, No. 2, pp. 284-99.
3. Falla D. Unravelling the complexity of muscle impairment in chronic neck pain. Man Ther 2004; 9(3):125-33.
4. Merskey HE. Classification of chronic pain: descriptions of chronic pain syndromes and definitions of pain terms. Pain 1986.
5. Fejer R, Hartvigsen J. Neck pain and disability due to neck pain: what is the relation? Euro Spine J 2008; 17(1):80-8.
6. Simons DG. Myofascial pain syndrome due to trigger points. J Rehabil Med 1988; 686-723.
7. Bodes-Pardo G, Pecos-Martín D, Gallego-Izquierdo T, Salom-Moreno J, Fernández-de-las-Peñas C, Ortega-santiago R. Manual treatment for cervicogenic headache and active trigger point in the sternocleidomastoid muscle: a pilot randomized clinical trial. J. Manip Physiol Ther 2013; 36(7):403-11.
8. Montañez-Aguilera FJ, Valtueña-Gimeno N, Pecos-Martín D, Arnau-Masanet R, Barrios-Pitarque C, Bosch-Morell F. Changes in a patient with neck pain after application of ischemic compression as a trigger point therapy. J Back Musculoskelet 2010; 23(2):101-4.
9. Sarrafzadeh J, Ahmadi A, Yassin M. The effects of pressure release, phonophoresis of hydrocortisone, and ultrasound on upper trapezius latent myofascial trigger point. Arch Phys Med Rehabil 2012; 93(1):72-7.
10. Hidalgo B, Hall T, Bossert J, Dugeny A, Cagnie B Pitance L. The efficacy of manual therapy and exercise for treating non-specific neck pain: A systematic review. J Back Musculoskelet Rehabil 2017; 30(6):1149-69.
11. Dundar U, Turkmen U, Toktas H, Solak O, Ulasli AM. Effect of high-intensity laser therapy in the management of myofascial pain syndrome of the trapezius: a double-blind, placebo-controlled study. Lasers Med Sci 2015; 30(1):325-32.
12. Pekyavas NO, Baltaci G. Short-term effects of high-intensity laser therapy, manual therapy, and Kinesio taping in patients with subacromial impingement syndrome. Lasers Med Sci 2016; 31(6):1133-41.
13. Cotler HB, Chow RT, Hamblin MR, Carroll J. The use of low level laser therapy (LLLT) for musculoskeletal pain. MOJ Orthop Rheumatol, 2015; 2(5).
14. Notarnicola A, Solarino G, Covelli I, Rifino F, Moretti B. Temperature controlled high energy adjustable multi-mode emission laser therapy in the treatment of the chronic low back pain. Am J Arthritis 2018; 2(1):1010.
15. World Medical Association. WMA Declaration of Helsinki–Ethical principles for medical research involving human subjects, 2018. Internet: https:// www. wma. net/policies-post/wma-declaration-of-helsinki-ethical-principles-for-medical-research-involving-human-subjects.
16. Winter EM, Maughan RJ. Requirements for ethics approvals. J Sports Sci 2009; 27:985.
17. Vernon H. The Neck Disability Index: state-of-the-art, 1991-2008. J Manipulative Physiol Ther 2008; 31(7):491-502.
18. Fischer AA. Pressure algometry over normal muscles. Standard values, validity and reproducibility of pressure threshold. Pain 1987; 30(1):115-26.
19. Oliveira-Campelo NM, de Melo CA, Alburquerque-Sendín F, Machado JP. Short-and medium-term effects of manual therapy on cervical active range of motion and pressure pain sensitivity in latent myofascial pain of the upper trapezius muscle: a randomized controlled trial. J Manipulative Physiol Ther 2013; 36(5):300-9.
20. Vigotsky AD, Bruhns RP. The role of descending modulation in manual therapy and its analgesic implications: a narrative review. Pain Res Treat 2017; 2017:1535473.
21. Simunovic Z. Low level laser therapy with trigger points technique: a clinical study on 243 patients. Lasers Surg Med 1996; 14(4):163-7.
22. Ceccherelli F, Altafini L, Lo Castro G, Avila A, Ambrosio F, Giron GP. Diode laser in cervical myofascial pain: A doubleblind study versus placebo. Clin J Pain 1989; 5(4):301-4.

LETTER TO THE EDITOR

Hyaluronidase use before rhinoplasty in noses previously injected with hyaluronic acid: is it always necessary?

R. Rauso[1], GF. Nicoletti[2], R. Fragola[1], N. Zerbinati[3], E. Nikolli[1], P. Bove[4] and G. Tartaro[1]

[1]Maxillo-Facial Surgery, "Luigi Vanvitelli" University Hospital, Naples, Italy; [2]Plastic Surgery, "Luigi Vanvitelli" University Hospital, Naples, Italy. [3]Dermatology, University of Insubria, Varese, Italy, [4]Private practice, Milan, Italy

Received March 5, 2021 – Accepted April 7, 2021

To the Editor,

Filler rhinoplasty with hyaluronic acid (HA) has been a fast growing procedure during recent years due to the possibility of nasal reshaping without surgery (1, 2). Although filler rhinoplasty has shown to be effective, nasal injections may be challenging especially when accidental vascular compromise occurs. In medical literature, serious complications such as skin necrosis, visual loss or impairment have been described following this procedure (3). In order to reduce nasal filling risk and to have the possibility to reverse vascular embolization or compression, the use of HA is widely recommended, instead of other substances, because it is the only filler that can be reversed thanks to the use of hyaluronidase (HYAL) (4). Several HYAL injection protocols have been suggested in order to solve vascular problems following nasal injections, moreover, also delayed injections of HYAL have shown to be effective in order to reverse vascular compromise (5). However, patients who have received nose injections with filler may decide to undergo a surgical rhinoplasty, either for esthetic correction or respiratory improvement, which HA is unable to provide, because of the limited or temporary esthetic results from the injectable procedure. Concerns regarding the approach to previously injected noses in patients looking for further surgical nasal modification has recently arisen (6).

HA fillers are the most used fillers worldwide, mainly because of their high safety profile. However, degradability of HA has 2 aspects: HA fillers exhibit an excellent safety profile as any unfavorable HA effect is temporary; on the other hand, virtually, the only downside of HA fillers is that any beneficial HA effect is also temporary (7, 8). Many HA products officially indicate that the materials are resolved within 6–12 months (7, 8). In the authors routine practice, patients looking for surgical rhinoplasty who had received nasal HA injections within the 12 months prior to the planned surgery are injected with HYAL at least 3 weeks before surgery, while HYAL injection is not performed if nasal HA injections were performed more than 12 months earlier. The authors present a case of surgical rhinoplasty where HA bolus was identified during surgical dissection, although HA injections were performed more than 18 months before surgery.

Case presentation

A 32-yearold female patient, unhappy with her nasal appearance, was scheduled for rhinoplasty. Her

Key words: rhinoplasty; filler rhinoplasty; hyaluronic acid; hyaluronidase

Corresponding Author:
Prof. Raffaele Rauso,
Maxillofacial Surgery Complex Unit,
University of Campania "Luigi Vanvitelli",
Piazza Miraglia,
80138 Naples, Italy
e-mail: raffaele.rauso@unicampania.it

0393-974X (2021)
Copyright © by BIOLIFE, s.a.s.
This publication and/or article is for individual use only and may not be further reproduced without written permission from the copyright holder.
Unauthorized reproduction may result in financial and other penalties
DISCLOSURE: ALL AUTHORS REPORT NO CONFLICTS OF INTEREST RELEVANT TO THIS ARTICLE.

nasal tip had been injected with HA filler (Revofill plus, 23 mg/mL HA) by another physician more than 18 months before the planned surgery. Due to this long time frame, pre-operative HYAL injection was not performed.

The surgical procedure was carried out under general anesthesia, and an open rhinoplasty approach was performed. After trans-columellar incision, supra-perichondral tip cartilage dissection was performed. Once the supra-tip area was reached, between the passage from LLC to ULC, a bolus of HA placed in the subcutaneous tissue came out (Fig. 1). Once the HA was removed, the whole rhinoplasty procedure was performed and the patient healed without any problem.

DISCUSSION

Non-surgical rhinoplasty with filler, in selected cases, is an excellent alternative to surgical rhinoplasty in order to ameliorate nasal appearance with no down time (1, 2). On the other hand, the filling procedure can be challenging due to the high vascular network present in a triangle shape on the middle of the face; this triangle is centered on the nose (3). Vascular compromise can arise for 2 main reasons: vascular embolization or vascular compression (9). In order to avoid vascular embolization, perpendicular injections above the bones or the cartilages have been suggested (1, 2); on the other hand, to avoid vascular compression it is mandatory to use a filler with the right rheology: in order to prevent vascular compression the use of an HA filler with a high G' should be avoided (9).

In a recent paper, Ramos and colleague evaluated the management of patients with previous nasal injections of HA seeking surgical rhinoplasty, and they proposed an algorithm based on the layer of HA injection (6). HYAL injection was suggested only when the HA injection layer was not represented by the supra-periosteal or the supra-perichondrial one, while in these cases direct surgical approach was suggested. Nevertheless, they concluded that once the surgeon has confirmed that the injected product



Fig. 1. *Surgical field after supra-perichondral tip cartilage dissection. Black arrow points out the HA bolus identified during the dissection.*

is HA and has established that a surgical procedure is the best option, he/she can inject HYAL before surgery or proceed directly to rhinoplasty (6).

In 2013, Mashiko et al. showed that long lasting results with HA injection, from 1 to several years, can be achieved in some facial sites, such as forehead, nasal root, chin, when the injection is performed on the periosteum.The Authors sustain that HA injection on the periosteum induces persisting inflammatory changes around the injected HA particles, which are expected to activate periosteal stem cells and contribute to the induction of tissue neogenesis, thus causing the formation of capsule/fibrosis during the process of HA absorption (7). Mashiko et al. concluded that, although volumizing effects by HA injections are typically temporary and repeated injections with an interval of 6–12 months are usually required for maintaining the cosmetic effects, the injection of an absorbable HA filler onto the bone only, instead of conventional intradermal or subcutaneous injection methods, led to long lasting results (7).

Another issue regarding previously injected noses with filler is the possibility to have a more challenging intra-operative dissection; this, of course, can be more evident with filler inducing neocollagenogenesis such as CaHA-based fillers. In the present case and in the Authors' experience, previous HA injection does not induce fibrotic tissue growth or, at least, does not require a more demanding surgical dissection.

In the present case, a subcutaneous HA bolus, injected more than 18 months earlier, was found during nasal dissection. This shows that also injection of the nasal subcutaneous layer, just like bone-only injection technique, induces a longer resorption time. Based on the presented finding, we started to inject HYAL to all planned rhinoplasties who refer previous nasal HA injections. To date, there is no consensus or recommendation on the optimum time to apply the enzyme before surgery. It is known that application of HYAL has an immediate action when injected into the skin and lasts between 24 and 48 hours with a half-life of only a few minutes, and it is metabolized by the liver and kidneys (9). However, after HYAL injection, an inflammatory process develops and, in order to avoid operating on an "inflammatory" field, we empirically started to inject HYAL at least 3 weeks before the planned surgery. Further studies, such as blinded non-randomized controlled clinical trials, are mandatory to support the authors' hypothesis regarding the frame of time to wait between HYAL injection and surgical procedure to be performed in the same anatomical area.

REFERENCES

1. Rauso R, Tartaro G, Chirico F, Zerbinati N, Albani G, Rugge L. Rhinofilling with hyaluronic acid thought as a cartilage graft. J Craniomaxillofac Surg 2020; 48(3):223-8.
2. Rauso R, Colella G, Zerbinati N, Salti G. Safety and early satisfaction assessment of patients seeking nonsurgical rhinoplasty with filler. J Cutan Aesthet Surg 2017; 10(4):207-14.
3. Rauso R, Sesenna E, Fragola R, Zerbinati N, Nicoletti GF, Tartaro G. Skin necrosis and vision loss or impairment after facial filler injection. J Craniofac Surg 2020; 31(8):2289-93.
4. Rauso R, Colella G, Franco R, et al. Is hyaluronidase able to reverse embolism associated with hyaluronic acid filler? An anatomical case study. J Biol Regul Homeost Agents 2019; 33(6):1927-30.
5. Wibowo A, Kapoor KM, Philipp-Dormston WG. Reversal of post-filler vision loss and skin ischaemia with high-dose pulsed hyaluronidase injections. Aesthetic Plast Surg 2019; 43(5):1337-44.
6. Ramos HHA, Freire L, Cavallieri F, Frota AE, Ragazzo R, Jurado JRP. Management of patients seeking surgical rhinoplasty with previous nasal injections of hyaluronic acid. Aesthetic Plast Surg 2021. doi: 10.1007/s00266-021-02136-3.Online ahead of print.
7. Mashiko T, Mori H, Kato H, et al. Semipermanent volumization by an absorbable filler: onlay injection technique to the bone. Plast Reconstr Surg Glob Open 2013; 1(1):e4-e14.
8. Zerbinati N, D'Este E, Farina A, Rauso R, Cherubino M, Calligaro A. Morphological evidences following pegylated filler treatment in human skin. J Biol Regul Homeost Agents 2017; 31(2 Suppl 2):79-85.
9. Rauso R, Zerbinati N, Franco R, et al. Cross-linked hyaluronic acid filler hydrolysis with hyaluronidase: Different settings to reproduce different clinical scenarios. Dermatol Ther 2020; 33(2):e13269.

LETTER TO THE EDITOR

Primary CD5$^+$ diffuse large B-cell lymphoma with hyperlactatemia as the first manifestation

K. Lian[1], J. Cui[1], L. Li[2], Y. Li[2] and QH. Zhang[1]

[1]Department of Oncology, Shanxi Academy of Medical Sciences and Shanxi Bethune Hospital, Shanxi Bethune Hospital affiliated to Shanxi Medical University, Taiyuan, China; [2]Department of Pathology, Shanxi Academy of Medical Sciences and Shanxi Bethune Hospital, Shanxi Bethune Hospital affiliated to Shanxi Medical University, Taiyuan, China

Received August 17, 2020 – Accepted April 8, 2021

To the Editor,

CD5 positive (CD5$^+$) diffuse large B-cell lymphoma (DLBCL) is rare in clinics, and accounts for 5–10% of all patients with DLBCL (1). Compared with CD5$^-$ DLBCL, CD5$^+$ DLBCL has unique clinical and pathological characteristics, with high invasion and poor prognosis. Hyperlactatemia is a rare, serious complication of this disease. This study reports a case of primary CD5$^+$ DLBCL with hyperlactatemia as the first manifestation.

Case report

A 44-year-old female patient visited a local hospital on August 20, 2018, complaining of intermittent fever for over a month and progressive aggravation of dyspnea for a week. The results of the arterial blood gas analysis were as follows: pH 7.45; partial pressure of carbon dioxide (PCO_2), 33.5 mmHg; oxygen partial pressure (PO_2), 95.7 mmHg; bicarbonate, 10.8 mmol/L; anion gap, 12.5 mmol/L; serum lactate, 7.1 mmol/L (normal reference range 0.5–1.6 mmol/L). Her serum lactate level was significantly high. The patient was therefore diagnosed with hyperlactatemia and treated with anti-infection, hydration, alkalization, and hemodialysis, however, the dyspnea and other symptoms did not diminish, and the lactate level failed to decrease after treatment. The color ultrasound revealed enlarged lymph nodes on both sides of the neck and groin, with the largest one being about 0.7 × 0.2 cm. The positron emission tomography–computed tomography (PET–CT) (Fig. 1) revealed infiltration in the liver, bone, lungs, and spleen (liver SUV_{max} = 13.4, bone SUV_{max} = 3.8, and spleen SUV_{max} = 8.4). The results of bone marrow biopsy revealed that the diagnosis of the patient was consistent with CD5$^+$ DLBCL, hence, a cycle of R-CHOP chemotherapy regimen was carried out (Rituximab injection, 300 mg/d 0; Cyclophosphamide, 600 mg/d 1 and 3; Epirubicin, 60 mg/d 1 and 3; Vindesine, 2 mg/d 1 and 3; and Prednisone, 100 mg/d 1–5). At the end of one chemotherapy cycle, the serum lactate and lactate dehydrogenase (LDH) were decreased to 3.7 mmol/L and 1,068 U/L, respectively. Consequently, the patient received three cycles of R-MTX-CHOP chemotherapy regimen, sequentially (Rituximab injection, 300 mg/d 0; Methotrexate, 1.6 g civ 4 h d 2; Cyclophosphamide, 1,200 mg/d 3; Epirubicin,

Key words: diffuse large B-cell lymphoma; hyperlactatemia; CD5

Corresponding Author:
Dr QiaoHua Zhang,
Department of Oncology, Shanxi Academy of Medical Sciences and Shanxi Bethune Hospital, Shanxi Bethune Hospital affiliated to Shanxi Medical University, No.99 of Longcheng Street, Xiaodian District, Taiyuan 030032, China
Tel.: +86 18734125658
e-mail: zhqiaohua523@163.com
The hospital does not have an institutional e-mail address but can be reached through the following link:
http://www.sxbqeh.com.cn/zhongliuzhongxin.html

0393-974X (2021)
Copyright © by BIOLIFE, s.a.s.
This publication and/or article is for individual use only and may not be further reproduced without written permission from the copyright holder.
Unauthorized reproduction may result in financial and other penalties
DISCLOSURE: ALL AUTHORS REPORT NO CONFLICTS OF INTEREST RELEVANT TO THIS ARTICLE.

120 mg/d 3; Vindesine, 4 mg/d 3; and Prednisone, 100 mg/d 1–5). After three cycles of R-MTX-CHOP chemotherapy, the patient achieved complete remission, with the serum lactate and lactate dehydrogenase reduced to 1.5 mmol/L and 247 U/L, respectively.

On September 27, 2019, the patient was admitted to our hospital. The imaging, including computerized tomography (CT), revealed lymphomatous lesions on both sides of the neck, mediastinum, and retroperitoneal lymph nodes, together with liver and spleen infiltration. Blood tests demonstrated normochromic normocytic anemia and thrombocytopenia. The results of the arterial blood gas analysis were as follows: pH, 7.327; PCO_2, 21.2 mmHg; PO_2, 80.7 mmHg; serum lactate, 17.5 mmol/L; bicarbonate, 10.8 mmol/L; and anion gap, 25.8 mmol/L (normal reference range 12–20 mmol/L). Lactate dehydrogenase was 3941.2 U/L. The right cervical lymph node pathological tissue taken from the patient in September 2019 was re-examined in our hospital. The results were consistent with $CD5^+$ DLBCL and inclined toward the germinal center origin.



Fig. 1. *Examination results of the patient's PET–CT*

After admission, hyperlactatemia was considered. Sodium bicarbonate was infused intravenously to correct acidosis. The dyspnea symptoms were visibly relieved, and the serum lactate level gradually dropped to 7 mmol/L. The R-DEP chemotherapy regimen was carried out for two cycles (Rituximab, 600 mg/d 0; Pirarubicin liposome, 20 mg/d 1 and 2; Etoposide, 0.1 mg/d 1–5; Methylprednisolone, 30 mg, bid, d 1–5). The enlarged lymph nodes shrank in size, and the patient achieved partial remission, with the serum lactate level reduced to 2.3 mmol/L.

This study was conducted with approval from the Ethics Committee of Weifang People's Hospital, and was conducted in accordance with the declaration of Helsinki, Written informed consent was obtained from the patient.

DISCUSSION

In the present case, the patient was diagnosed with $CD5^+$ DLBCL with hyperlactatemia as the first manifestation. To the best of our knowledge, this special case has not been reported previously.

CD5 is a type of transmembrane glycoprotein expressed on the surfaces of T cells and a few B cells with a relative molecular weight of 67 kD. $CD5^+$ is common in chronic lymphocytic leukemia and mantle cell lymphoma but rare in DLBCL (2). CD5 can promote the occurrence and development of tumors by changing the tumor microenvironment and regulating the immune response (3). Large-scale research in Japan showed that $CD5^+$ DLBCL accounts for 5–10% of all patients with DLBCL (4-5). The international prognostic index score of $CD5^+$ DLBCL is high, suggesting these patients have a poor prognosis (6).

Usually, hyperlactatemia occurs in the recurrence or progression of DLBCL (7), however, the present case suggests that hyperlactatemia could also occur in the early stage of DLBCL, accompanied by fluctuations in the disease development. Regular monitoring of the serum lactate level and pH value is therefore recommended in the diagnosis and treatment of patients with hematological tumors.

In conclusion, we report a case of primary $CD5^+$ DLBCL with hyperlactatemia as the first

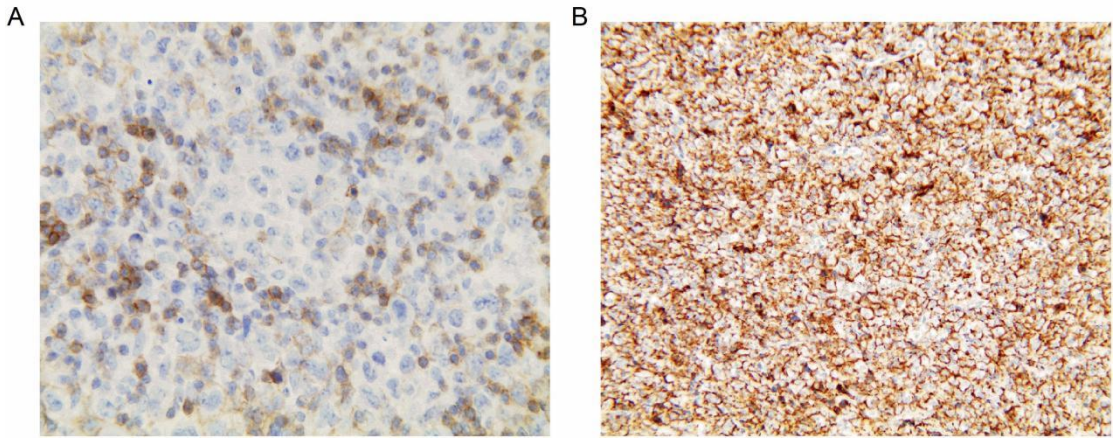


Fig. 2. *Immunohistochemistry results of the right cervical lymph node pathological tissue taken from the patient.* ***A****) CD5 staining results show that most of the tumor cell membranes are positive (about 80%), and a few are negative. Magnification 400×.* ***B****) CD20 shows that tumor cells are diffusely positive in cell membranes 200×.*

manifestation. Both hyperlactatemia and $CD5^+$ in patients with DLBCL indicate a poor prognosis. However, the relationship between hyperlactatemia and $CD5^+$ DLBCL has not been clearly revealed previously. More studies are needed to detect the characteristics of this special case.

ACKNOWLEDGEMENTS

We would like to acknowledge the hard and dedicated work of all the staff that implemented the intervention and evaluation components of the study.

REFERENCES

1. Thakral B, Medeiros LJ, Desai P, et al. Prognostic impact of CD5 expression in diffuse large B-cell lymphoma in patients treated with rituximab-EPOCH-Eur J Haematol 2017; 98(4):415-21.
2. Xu Y, Sun W, Li F. De novo CD5+ diffuse large B-Cell lymphoma: biology, mechanism, and treatment advances. clin lymphoma myeloma Leuk 2020; 20(10):e782-90.
3. Burgueño-Bucio E, Mier-Aguilar CA, Soldevila G. The multiple faces of CD5. J Leukoc Biol 2019; 105(5):891-904.
4. Yamaguchi M, Nakamura N, Suzuki R, et al. De novo CD5+ diffuse large B-cell lymphoma: results of a detailed clinicopathological review in 120 patients. Haematologica 2008; 93(8):1195–202.
5. Hyo R, Tomita N, Takeuchi K, et al. The therapeutic effect of rituximab on CD5-positive and CD5-negative diffuse large B-cell lymphoma. Hematol Oncol 2010; 28 (1):27–32.
6. Jain P, Fayad LE, Rosenwald A, Young KH, O'Brien S. Recent advances in de novo CD5+diffuse large B cell lymphoma. Am J Hematol 2013; 88(9):798-802.
7. He Y, Ong J, Ong S. Refractory lactic acidosis and an approach to its management - a case report. J Crit Care Med (Targu Mures) 2019; 5(2):60-65.

LETTER TO THE EDITOR

SARS-CoV-2 infection *versus* the body immune defenses: the role of immune responses and mechanism of action of dexamethasone

I.Z. Sadiq[1], A. Muhammad[1,2], F. Sadiq Abubakar[1] and M.N. Shuaibu[1, 2]

[1]Department of Biochemistry, Faculty of Life Sciences, Ahmadu Bello University, Zaria, Kaduna State, Nigeria; [2]Africa Center of Excellence in Neglected Tropical Diseases and Forensic Biotechnology, Ahmadu Bello University, Zaria-Nigeria

Received September 30, 2020 – Accepted April 12, 2021

To the Editor,

Severe acute respiratory syndrome coronavirus virus, SARS-CoV-2, an agent of coronavirus disease 2019 (COVID-19) constitutes the primary scientific, medical, and economic challenges globally. COVID-19 was first reported in Wuhan as an unknown etiology, characterized by fever and pneumonia-like symptoms with human-to-human transmission. Response to this infection is largely through innate/non-specific immune response and adaptive immune response (1). Basically, SARS-CoV-2 enters cells through endocytosis by binding its spike glycoprotein to Angiotensin-Converting Enzyme receptor 2 (ACE-2) in respiratory epithelial cells, releasing RNA into the cytoplasm and translating it into pp1a and pp1ab, forming NSPs, replication, and transcription complex. This ultimately leads to the synthesis of sub-genomic RNAs that encode structural proteins and accessory proteins (1).

Several cytokines were clinically implicated in COVID-19 (2), triggering multi-organ damage via a cytokines storm (Fig. 1). Viral RNA is detected via pattern recognition receptors (PRRs) mostly through toll-like receptors (TLRs) such as TLR-3, TLR-7, and TLR-8, amplifying the signals to downstream effectors, eventually responding to SARS-CoV-2 infection (Fig. 1). Coronaviruses also trigger AP-1 and NF-κB signaling pathways, which cause multiple target cells to produce pro-inflammatory cytokines as well as chemokines (Fig. 1). The inflammatory cytokines such as IL-1, TNF, and IL-6 are also released by leukocytes, which increase the hypothalamic set point, resulting in fever (Fig. 2).

One of the activated pathways in COVID-19 is the complement system composed of distinct plasma proteins synthesized by the liver and accordingly consisting of three different pathways – classical, lectin, and alternative. Activation of the complement system by SARS-CoV-2 occurs in multiple organs of COVID-19 patients via complement activator MASP-2 (3) and initiation of lectin pathway (Fig. 3). Activating each of the three pathways leads to the cleavage of inactive C3 protein into the functional C3a and C3b fragments. C3a is an inflammatory mediator, and C3b is an opsonin, which can covalently bind and tag any surface near its generation site. In COVID-19 patients, excess deposition of tubular renal protein may directly lead to tubular necrosis, which in turn is linked to acute renal failure (4). Moreover, an elevated serum level of 5a has been reported in some patients suffering from COVID-19

Key words: COVID-19; SARS-CoV-2; immunopathology; innate immune; adaptive immune; dexamethasone

Corresponding Author:
Idris Zubairu Sadiq,
Department of Biochemistry,
Ahmadu Bello University,
Zaria-Nigeria
Tel.: +23 048038041910
e-mail: izsadiq@abu.edu.ng

0393-974X (2021)
Copyright © by BIOLIFE, s.a.s.
This publication and/or article is for individual use only and may not be further reproduced without written permission from the copyright holder.
Unauthorized reproduction may result in financial and other penalties
DISCLOSURE: ALL AUTHORS REPORT NO CONFLICTS OF INTEREST RELEVANT TO THIS ARTICLE.

(5) (Fig. 3). C5b-9 levels were significantly elevated in both moderate and severe COVID-19 patients compared to healthy controls (6).

Adaptive immunity during COVID-19 infections includes a tightly regulated interplay between antigen-presenting cells, T and B-lymphocytes, that facilitates pathogen-specific immune effector pathways, immunological memory generation, and host immune homeostasis control. By activating T-dependent B cells, the CD4 T cells promote viral-specific antibody production, thus blocking SARS-CoV-2. CD8 T cells play a key role in clearing viral

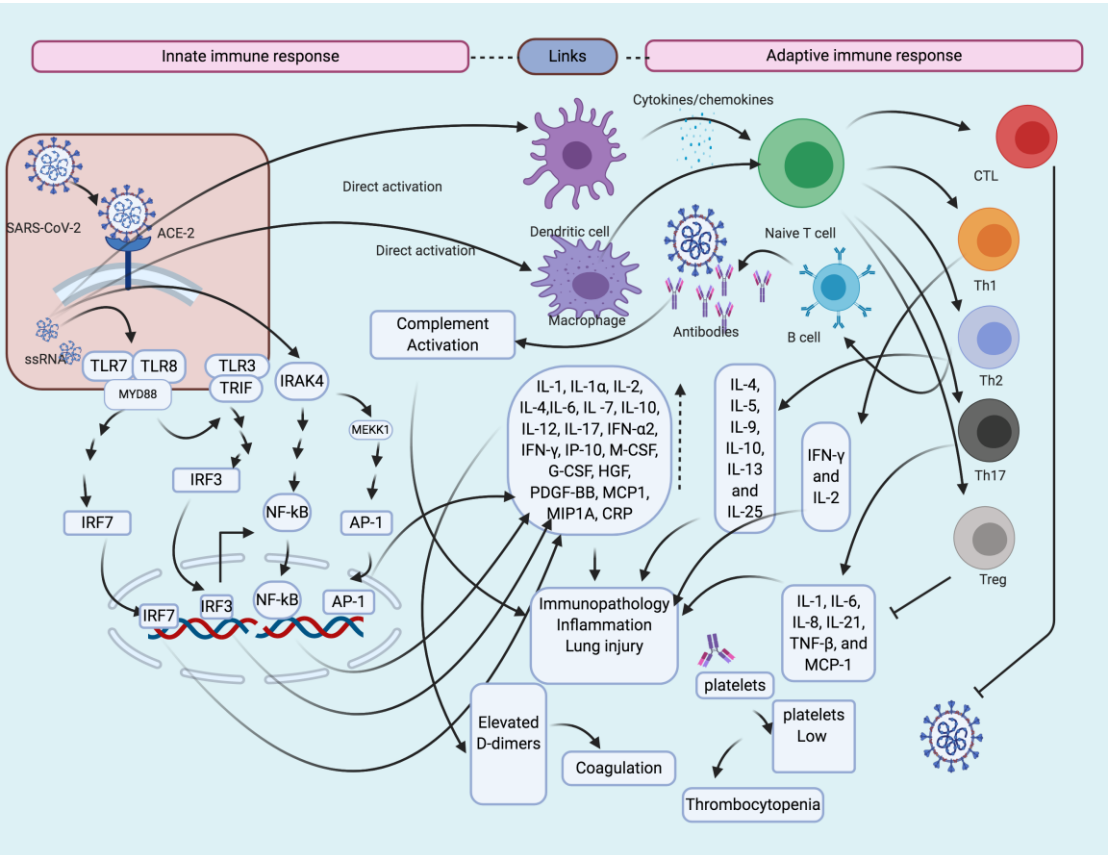


Fig. 1. *Hallmark of innate and adaptive responses during COVID-19 infection. Coronavirus enters the respiratory epithelial cell via ACE-2 by endocytosis and releases its genetic material into the cytoplasm. The viral RNA is then recognized by the TLR 7 and 8 receptors and sends signals downstream. The adapter protein MyD88, connects the receptors to the protein that transmits signals within the cell. Upon activation, the interferon regulatory transcription factors (3 and 7) can cross the nuclear membrane and activate the transcription of interferons essential for controlling viral infections. In the nucleus, NF-kB and AP-1 induce transcription of pro-inflammatory cytokines. The innate immune response also induces increased D-dimer and low platelets, causing coagulation and thrombocytopenia. Bridging the gap between innate and adaptive immunity function, the antigen-presenting cells (dendritic cell and macrophage), activate naïve T cell to generate CTL, Th1, Th2, Th17, and Treg. CTL is responsible for killing virall- infected cells via cytokines, chemokines, granzyme B, and perforin. Th1 leads to increased response mediated by cells through the activity of their effector cytokines IFN-γ and IL-2. Th2 responds to infections via humoral immunity by secreting effector cytokines IL-4, IL-5, IL-9, IL-10, IL-13, and IL-25 which helps in clearing infections as well as contributing to cytokine storm. The Th17 cells play a part in adaptive immunity to protect the body from pathogens via its effector cytokines IL-17A, IL-17F, IL-21, IL-22, and GCSF. Three T cell subsets are capable of affecting the myeloid component of the immune system, which is primarily responsible for innate pathogen response. Tregs are a highly specialized subpopulation of T cells, which act to suppress the immune response and thus maintain self-tolerance and homeostasis. Increases in cytokines (hypercytokinemia) lead to immunopathology, inflammation, and lung injury.*

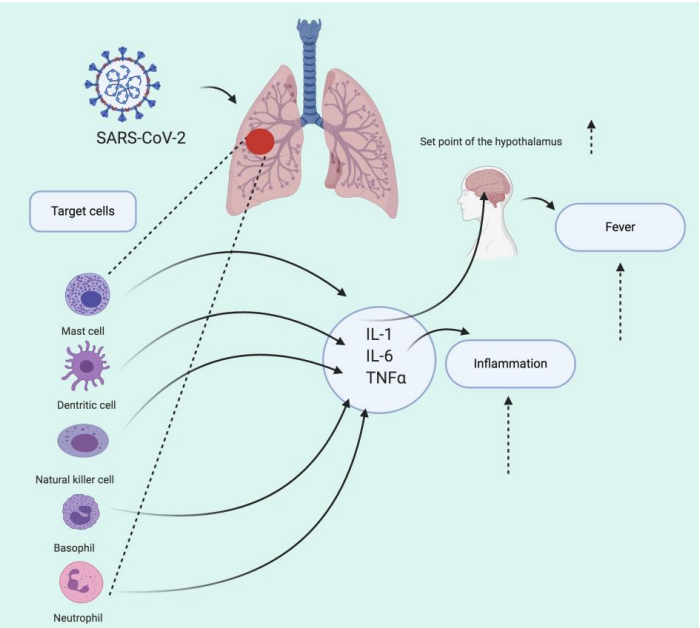


Fig. 2. *Mechanism of inflammation and fever during COVID-19 infection. As the virus enters the lungs, it causes the target cells to release cytokines (IL-1, TNFα, and IL-6). The released cytokines mediate inflammation. These cytokines enter circulation and travel to endothelial cells of the hypothalamus of the brain where they causes fever via an elevation in the set point of the hypothalamus.*

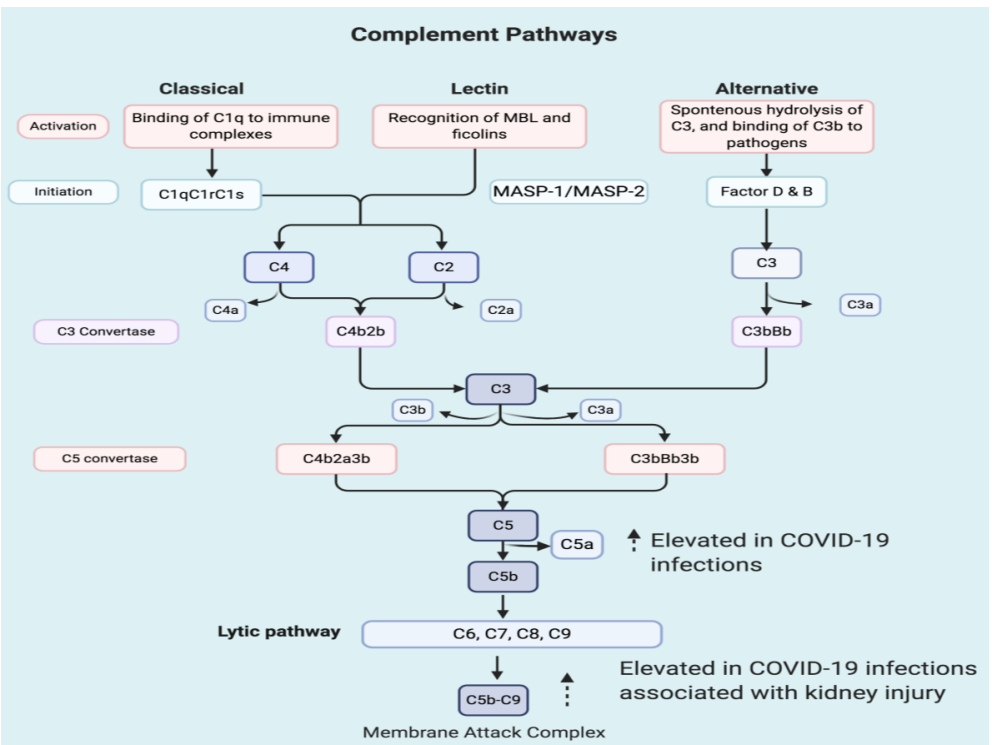


Fig. 3. *Complement pathways in COVID-19 infections. The complement pathways consist of three interconnected pathways - classical, alternative, and lectin. These three pathways lead to a final common pathway called the lytic pathway. During COVID-19 infection, complement cascades are activated via complement activator MASP-2 and initiation of the lectin pathway. C5a and C5b-C9 have been reported to be elevated in COVID-19. The C5b-C9, commonly called the membrane attack complex, in particular, has been implicated in kidney dysfunction.*

infection in SARS-CoV-2 patients, accounting for roughly 80% of all inflammatory cells. (7).

The humoral immune pathway in COVID-19 infections begins as soon as viral antigen binds to the cell surface receptor of B cell. Soon after, the viral antigen is internalized and processed by MHC-II proteins. The processed viral antigen is then displayed on the surface of the B cell. The helper T cell then binds to the complex, becomes activated, and releases cytokines that induce B cells to divide rapidly, resulting in thousands of identical B cell clones. Immunoglobulin (Ig)M is the first to respond to SARS-CoV-2, followed by IgA, and finally IgG production (1-14 days) (8).

As SARS-CoV-2 sets in**,** dendritic cells in the lungs acquire and process antigen, and display the processed antigen in the form of MHC I to naïve circulating T-cells. As the T-cell receptor interacts with MHC, T cells are activated, vigorously proliferate, and migrate to the infection site (9). When at the infection site, antiviral cytokines (IFN-π TNF-α, IL-2) are produced by activated virus-specific T cells (Fig. 1). Targeting these inflammatory pathways could therefore be a game changer in the management of COVID-19 patients, and to this end, dexamethasone is currently being utilized. The probable mechanism of action of dexamethasone as regards its anti-inflammatory activity in COVID-19 infections involves inhibition of leukocyte infiltration into the inflammatory site (10), adhesion to receptor molecules of nuclear steroids, as well as impairment with NF-κB signaling, AP-1, and cell death pathways (11). Other mechanisms of action include inhibition of Toll-like receptor activation, phosphorylation suppression, and DNA-binding activity of IκB to up-regulate the synthesis of IκBα (12). Accordingly, deciphering host-immune responses as it relates to innate and adaptive immunity in COVID-19 will provide a guide to arresting cytokine storms and possible vaccine development, leading to a decrease in terms of viral infection, mortality, and morbidity.

REFERENCES

1. Guo YR, Cao QD, Hong ZS, et al. The origin, transmission and clinical therapies on coronavirus disease 2019 (COVID-19) outbreak - an update on the status. Mil Med Res 2020; 7(1):11.
2. Liu Y, Zhang C, Huang F, et al. 2019-novel coronavirus (2019-nCoV) infections trigger an exaggerated cytokine response aggravating lung injury. 2020. http://www.chinaxiv.org/abs/202002.00018. Accessed 15 May 2020.
3. Wilk C.M. Coronaviruses hijack the complement system. Nat Rev Immunol 2020; 20(6):350
4. Pei G, Zhang Z, Peng J, et al. Renal Involvement and Early Prognosis in Patients with COVID-19 Pneumonia. J Am Soc Nephrol 2020; 31(6):1157-65.
5. Carvelli J, Demaria O, Vély F, et al. Association of COVID-19 inflammation with activation of the C5a-C5aR1 axis. Nature 2020; 588(7836):146-50.
6. Cugno M, Meroni P, Gualtierotti R, et al. Complement activation in patients with covid-19: a novel therapeutic target. J Allergy Clin Immunol 2020; https://doi.org/10.1016/j.jaci.2020.05.006
7. Maloir Q, Ghysen K, von Frenckell C, Louis R, Guiot J. Acute respiratory distress revealing antisynthetase syndrome. Rev Med Liege 2018; 73(7-8):370-5.
8. Sokolowska M, Lukasik Z, Agache I, et al. Immunology of COVID-19: mechanisms, clinical outcome, diagnostics and perspectives - a report of the European Academy of Allergy and Clinical Immunology (EAACI). Allergy 2020; 75(10):2445-76
9. Channappanavar R, Zhao J, Perlman S. T cell-mediated immune response to respiratory coronaviruses. Immunol Res. 2014; 59(1-3):118-28.
10. Tsurufuji S, Kurihara A, Ojima F. Mechanisms of anti-inflammatory action of dexamethasone: blockade by hydrocortisone mesylate and actinomycin D of the inhibitory effect of dexamethasone on leukocyte infiltration in inflammatory sites. J Pharmacol Exp Ther. 1984; 229(1):237-43.
11. National Center for Biotechnology Information. PubChem Database. Dexamethasone, CID=5743, https://pubchem.ncbi.nlm.nih.gov/compound/dexamethasone (accessed on June 24, 2020)
12. Mogensen TH, Berg RS, Paludan SR, Østergaard L. Mechanisms of dexamethasone-mediated inhibition of Toll-like receptor signaling induced by Neisseria meningitidis and Streptococcus pneumoniae. Infect Immun 2008; 76(1):189-97.

LETTER TO THE EDITOR

Bruxism, perceived anxiety and stress in university students

G. Laganà[1], A. Malara[1], A. Koumoulis[1], M. Tepedino[2], N. Venza[1] and P. Cozza[1]

[1]Department of Systems Medicine, University of Rome 'Tor Vergata', Rome, Italy;
[2]Department of Biotechnological and Applied Clinical Sciences, University of L'Aquila, L'Aquila, Italy

Received September 29, 2020 – Accepted April 12, 2021

To the Editor,

Bruxism is defined as a repetitive jaw-muscle activity characterized by clenching or grinding of the teeth and/or by bracing or thrusting of the mandible (1). In particular, two distinct circadian manifestations of bruxism can be identified: Awake Bruxism (AB), a repetitive or sustained tooth contact and/or by bracing or thrusting of the mandible; Sleep Bruxism (SB), a rhythmic (phasic) or a non-rhythmic (tonic) masticatory muscle activity (1). These two different types of bruxism may overlap (2). Several classification schemes have been proposed for bruxism based on different criteria, the most accepted being: i) Possible, based on a positive self-report only; ii) Probable, based on a positive clinical inspection, with or without a positive self-report; iii) Definite, based on a positive instrumental assessment, with or without a positive self-report and/or a positive clinical inspection (1). A large variety of cases is present in the literature regarding the prevalence of bruxism, between 6–91% (2). Although widely distributed among the population and extensively investigated, bruxism remains an enigmatic condition requiring further scientific evaluation (3). It is considered a multifactorial disorder and its etiology is not well defined. Bruxism is much more than just tooth wearing as it is currently linked to orofacial pain, headaches, sleep disorders, sleep breathing disorders, behavior disorders, or those associated with the use of medications (4). While morphological and pathophysiological factors are thought to be related to bruxism, the importance of psychosocial factors, such as anxiety and stress, in its etiology is becoming clearer, particularly in the case of awake bruxism (5). University students may experience an important amount of stress and anxiety, resulting in negative outcomes (6) in terms of academic performance and personal, emotional or health consequences. One of the main manifestations of these situations is bruxism or grinding teeth occurring without a functional purpose (7). The aim of the current study was to verify the correlation between possible bruxism and perceived anxiety and stress in university students by using questionnaires.

MATERIALS AND METHODS

The study project was approved by the Ethics Committee of the University of Rome "Tor Vergata" (protocol n.139/2019), and informed consent was obtained from all subjects. All procedures performed in studies involving human participants were in accordance with the ethical standards of the institutional and/or national research committee and with the 1964 Helsinki declaration and its later amendments or comparable ethical standards. The sample included pre- and post-graduate Italian students enrolled in the Department of Orthodontics

Key words: sleep bruxism; sleep surveys and questionnaires; psychological factors

Corresponding Author:
Dr Giuseppina Laganà,
Department of Systems Medicine,
University of Rome 'Tor Vergata',
Viale Oxford 81, 00133 Rome, Italy
e-mail: giuseppinalagana@libero.it

0393-974X (2021)
Copyright © by BIOLIFE, s.a.s.
This publication and/or article is for individual use only and may not be further reproduced without written permission from the copyright holder.
Unauthorized reproduction may result in financial and other penalties
DISCLOSURE: ALL AUTHORS REPORT NO CONFLICTS OF INTEREST RELEVANT TO THIS ARTICLE.

of the University of Rome "Tor Vergata" from January to December, 2019. Participation was on a voluntary basis and all participants signed an informed consent before the study onset. The inclusion criteria considered for the study were: age over 18 years, sufficient cognitive and mental capacity to fill out a questionnaire and willingness to participate in the study. The exclusion criteria were: severe systemic diseases, secondary bruxism induced by systemic diseases and/or drugs, use of medicines that could significantly affect the function of the nervous and muscular systems, severe mental illness or significant mental disorders.

From an initial group of 567 subjects, 65 were excluded according to the exclusion criteria or for incomplete records. The final sample was composed of 502 students (304 females, 198 males, mean age of 26.5±8.4 years).

Data collection

Each member of the sample submitted three questionnaires in order to verify the incidence of sleep or awake bruxism and the possible association with sleep and psychological factors such as anxiety and stress. All three surveys were prepared by Google Drive application, so the subjects were able to fill in the forms comfortably on smartphone, tablet or PC, without being conditioned by the presence of an operator, and the results were directly accessible on the Google Sheets app.

Oral Behaviors Checklist (OBC)

The first completed questionnaire was the Oral Behaviors Checklist (OBC), a 21-item self-reporting survey to quantify the frequency of observable and non-observable oral behaviors (e.g. grinding, clenching, biting, chewing) (8). Five response options (scored 0-4) based on the last 30 days (https://buffalo.app.box.com/s/2czrz7hjl0jynpgcfiqjvxj40wo1b1u3) were prepared. The five response options are: none of the time =0, <1 time/month =1, 1-3 times/month =2, 1-3 times/week =3 and 4-7 times/week =4. The OBC includes 2 items regarding sleep bruxism and 19 items investigating the frequency of different wake-time oral behaviors. A total score of 0 suggests no reported parafunctions, scores ranging from 1 to 24 and from 25 to 84 denote low and high parafunctions respectively, as indicated by the scoring manual for self-Report Instruments of Diagnostic Criteria for Temporomandibular Disorders (DC/TMD) (8).

Symptom Checklist 90 questionnaire (SCL-90)

Perceived anxiety and anxiety symptoms were assessed and reduced to 10 specific items from the version of the Symptom Checklist 90 questionnaire (SCL-90, Derogatis 1975). SCL-90 is a self-report measure for persons aged at least 13 years. The SCL items assess psychopathological or somatic disturbances on a 4-point scale ranging from 0 (absence of the symptom) to 4 (maximum disturbance). The General Severity Index (GSI) is the average score for all responded items and serves as an overall measure of psychiatric distress. GSI considered interest scores equal to or greater than 1. Lower scores indicate a low level of anxiety while higher scores a high level of anxiety.

Perceived Stress Scale (PSS)

Stress, a conditions where an environmental demand exceeds the natural regulatory capacity of an organism in particular situations that include unpredictability and uncontrollability (9), was determined and reduced to a four-item version of Perceived Stress Scale (PSS, Cohen 1988). In this study, the 4-item PSS version was used, each item was scored on a 5-point scale: never (0), almost never (1), sometimes (2), fairly often (3), very often (4). In the 4-item PSS, two items are negative (e.g., ''in the last month, how often have you felt that you were unable to control the important things in your life?''; ''in the last month, how often have you felt difficulties were piling up so high that you could not overcome them?''; Cohen et al., 1983; Cohen & Williamson, 1988) and two items are positive (e.g., ''in the last month, how often have you felt confident about your ability to handle your personal problems?''; ''how often have you felt that things were going your way?''). In scoring the stress measure, positive items are reversed scored, and then all items are summed (scores ranging from 0 to 16 for the 4-item scale, and from 0 to 40 for the 10-item scale). Higher scores indicate greater stress.

Statistical analysis

All statistical analyses were performed using SPSS statistical software (Statistical Package for Social Sciences, version 23.0, SPSS Inc., Chicago, USA). Descriptive statistics were used to describe the studied sample. Correlation analysis between sleep behaviors and psychological factors such as anxiety and stress were performed using Pearson correlation coefficient. *t*-test for unpaired data was applied for assessing the comparison of the quantitative variables. All reported p-values are two-sided and a value of $p<0.05$ was considered statistically significant.

RESULTS

The sample was composed of 502 subjects (198 females, 304 males) between 18 and 34 years of age with a mean age of 26.5±8.4 years. The answers to the OBC questionnaire were used to classify the participants of the study into three groups: No parafunctions (n=4, 0.8%), Low level of parafunctions (n=158, 31.5%) and High level of parafunctions (n=340, 6.7%). Perceived anxiety and anxiety symptoms were perceived in 29.1% of the sample while not in the other 70.9%. Stress was recorded in mean of 7.4±2.6 (Table I).

Table II shows the relationship among high levels of parafunction, perceived anxiety and stress. Specifically, a significative correlation was highlighted between high level of parafunction and stress (p=0.02) and between perceived anxiety and stress (p=0.02).

Table I. *Descriptive analysis of the study group*

Study Group n = 502 (198 M, 304 F)			
	Min	**Max**	**Mean (SD)**
Age	18.1	34.9	26.5±8.4
OBC	0	67	31.4±12.7
SCL-90	0	38	8.3±7.4
PSS	2	15	7.4±2.6

Table II. *OBC, SCL-90 and PSS correlation*

	OBC	**SCL-90**	**PSS**
OBC	1	0.35	0.02*
SCL-90	0.35	1	0.02*
PSS	0.02*	0.02*	1

Level of significance $p<0.05$

DISCUSSION

The purpose of the present investigation was to verify a correlation between possible bruxism and perceived anxiety and stress in university students by using questionnaires. Literature on bruxism etiology and regarding the role of psychosocial factors in the multifactorial bruxism generator pattern has not been conclusive due to the lack of homogeneity in the diagnostic criteria adopted in most studies (10). There is emerging evidence showing that both sleep and awake bruxism often mirror psychological conditions in individuals with certain personality features (i.e. trait anxiety, stress sensitivity, avoidance pattern) (11). The duration of sleep-time MMA is associated with trait anxiety and less with state anxiety or with other psychological symptoms (8). In other words, personality features seem to be more important than acute episodes of anxiety in the aetiology of sleep-time MMA and to explain muscle activity (emotional overload) (11).

The correlation between stress and bruxism is reported in the current literature (8) and, more specifically in university students, stress can lead to neuromuscular alterations in the mouth and jaw, increasing the overall prevalence of temporomandibular disorders (12). Psychosocial factors such as anxiety and stress are as important as somatic causes in the onset and maintenance of bruxism (5). The present study emphasized that subjects with a high score in the OBC-it had a high or medium level of stress. Regarding perceived anxiety, no correlation with bruxism was found, however, further studies are needed to confirm our finding in a larger cohort with more varied psychosocial determinants.

The limitation of the study is a subjective evaluation of the disorders that should be investigated in depth and objectified by diagnostic tests. In fact, the current study is based on possible sleep bruxism since risk of bruxism and psychological factors were subjectively determined using a questionnaire.

In conclusion, associations between oral parafunctional behaviours and perceived stress have been observed in the investigations. These associations show that the analysis of psycho-social-economic factors is essential to better appraise the impact of these conditions on the quality of life.

REFERENCES

1. Lobbezoo F, Ahlberg J, Raphael KG, et al. International consensus on the assessment of bruxism: Report of a work in progress. J Oral Rehabil 2018; 45(11):837-44.
2. Lobbezoo F, Ahlberg J, Manfredini D, Winocur E. Are bruxism and the bite causally related? J. Oral Rehabil 2012; 39:489-501.
3. Laganà G, Osmanagiq V, Malara A, Venza N, Cozza P. Sleep bruxism and SDB in Albanian growing subjects: a cross-sectional study. Dent J (Basel) 2021; 9(3):25.
4. Firmani M, Reyes M, Becerra N, Flores G, Weitzman M, Espinosa P. Bruxismo de sueño en niños y adolescentes [Sleep bruxism in children and adolescents]. Rev Chil Pediatr 2015; 86(5):373-9.
5. Przystańska A, Jasielska A, Ziarko M, et al. Psychosocial predictors of bruxism. Biomed Res Int 2019; 2019:2069716.
6. Marshall LL, Allison A, Nykamp D, Lankea S. Perceived stress and qual- ity of life among doctor of pharmacy students. Am J Pharm Educ 2008; 72(6):137-45.
7. Cavallo P, Carpinelli L, Savarese G. Perceived stress and bruxism in university students. BMC Res Notes 2016; 9(1):514.
8. Donnarumma V, Cioffi I, Michelotti A, Cimino R, Vollaro S, Amato M. Analysis of the reliability of the Italian version of the Oral Behaviours Checklist and the relationship between oral behaviours and trait anxiety in healthy individuals. J Oral Rehabil 2018; 45(4):317-22.
9. Koolhaas JM, Bartolomucci A, Buwalda B, et al. Stress revisited: a critical evaluation of the stress concept. Neurosci Biobehav Rev 2011; 35(5):1291-301.
10. Manfredini D, Fabbri A, Peretta R, Guarda-Nardini L, Lobbezoo F.Influence of psychological symptoms on home-recorded sleep- time masticatory muscle activity in healthy subjects. J Oral Rehabil 2011; 38:902-11.
11. Manfredini D, De Laat A. Why not stop looking at bruxism as a black/white condition? Aetiology could be unrelated to clinical consequences. J Oral Rehabil 2016; 43(10):799-801.
12. Akhter R, Morita M, Esaki M, Nakamura K, Kanehira T. Development of temporomandibular disorder symptoms: a 3-year cohort study of university students. J Oral Rehabil 2011; 38(6):395403.

LETTER TO THE EDITOR

Custom-made cementless revision total knee arthroplasty in a patient with metal and bone cement hypersensitivity

N. Logoluso[1*], R. Ciliberto[2*], I. Morelli[3*], G.M. Peretti[4,5#] and A.V. Pellegrini[1#]

[1]IRCCS Istituto Ortopedico Galeazzi, Centre for Reconstructive Surgery and Osteoarticular Infections (C.R.I.O. Unit), Milan, Italy; [2]University of Milan, Residency Program in Orthopaedics and Traumatology, Milan, Italy; [3]U.O.C. Ortopedia e Traumatologia, ASST Ovest Milanese, Ospedale di Legnano, Legnano (MI), Italy; [4]Department of Biomedical Sciences for Health, University of Milan, Milan, Italy; [5]IRCCS Istituto Ortopedico Galeazzi, EUORR Unit, Milan, Italy

Received December 7, 2020 – Accepted April 13,2021

*Equally contributed and share the position as first author
#Equally contributed and share the position as senior author

To the Editor,

Total knee arthroplasty (TKA) is the gold standard to treat end-stage knee osteoarthritis, with excellent long-term functional outcomes, but along with the increasing demand for this procedure, the number of revision total knee arthroplasties (RTKA) is rising (1). The most common causes of TKA failure are infection, aseptic loosening, periprosthetic fractures, implant instability, patellar maltracking and residual pain (2). Hypersensitivity to metals and polymethylmethacrylate (PMMA) bone cement has been reported in patients undergoing RTKA without other evident reasons, such as possible uncommon cause of pain, but its role as causative factor or consequence of a TKA loosening is still debated (3-6). Nevertheless, RTKA with hypoallergenic components is required in these cases (4). We herein report the first case of a 74-year old patient who had an aseptic loosening of TKA with bone cement and metal hypersensitivity, treated with RTKA using a custom-made hypoallergenic cementless condylar-constrained implant. This report has been written according with the CARE guidelines for case reports. The patient gave his informed consent to use his anonymized clinical data for scientific purposes.

Clinical case

A 74-year old male who had undergone a TKA on the left knee in 2012 for end-stage knee osteoarthritis, came to our department in July 2018 presenting left knee pain, major instability, and impossibility to weight-bearing. The symptoms had started six months after the left TKA procedure. During consultation, clinical examination revealed an antalgic gait with limping, 10° varus alignment and 10° fixed flexion contracture of the left knee. Diffuse skin rashes had appeared after TKA surgery, and edema were also seen around the knee. Range of motion was 10° to 90°. In addition, there were clinical signs of moderate laxity of the medial collateral ligament. The patient's

Key words: revision total knee arthroplasty; revision total knee replacement; metal allergy; metal hypersensitivity; PMMA allergy; bone cement hypersensitivity; custom-made cementless hypoallergenic TKA; TKA failure; metaphyseal sleeves; antibacterial coatings

Corresponding Author:
Ilaria Morelli, M.D.
U.O.C. Ortopedia e Traumatologia, Ospedale di Legnano,
ASST Ovest Milanese, via Papa Giovanni Paolo II,
20025, Legnano, MI, Italy
Tel.: +39 3331266580
e-mail: ilaria.morelli90@gmail.com

0393-974X (2021)
Copyright © by BIOLIFE, s.a.s.
This publication and/or article is for individual use only and may not be further reproduced without written permission from the copyright holder.
Unauthorized reproduction may result in financial and other penalties
DISCLOSURE: ALL AUTHORS REPORT NO CONFLICTS OF INTEREST RELEVANT TO THIS ARTICLE.

Table I. *Panel of the haptens tested through skin patch test.*

Hapten	Patch test positivity at 72 h	Hapten	Patch test positivity at 72 h
Benzoyl peroxide	-	Mercaptobenzothiazole Mix	-
Bisphenol A-glycidyl methacrylate	-	2-mercaptobenzothiazole	-
1,4 Butandiol diacrylate	-	Molybdenum	-
Butylacrylate	+ - -	Methyl methacrylate	-
Butyl methacrylate	+ - -	Pyrogallol	-
Carba mix	-	Paraphenylenediamine Mix	-
Dibutyl phthalate	-	Resorcin	-
Diethyl phthalate	-	Tetraethylene glycol dimethacrylate	-
N,N-dimethyl P-toluidine	-	Thiuram mix	-
Di-N-Octyl phthalate	-	Tricresyl phosphate	-
1,6-Hexanediol diacrylate	-	Triethylene glycol dimethacrylate	-
Ethyl acrylate	-	Triphenyl phosphate	-
Ethyl methacrylate	-	Trimethylolpropane triacrylate	-
Ethylene glycol dimethacrylate	-	Diurethane dimethacrylate	-
2-ethylhexyl acrylate	-	Titanium dioxide	-
Hydrazine hydrate	-	Potassium dichromate	-
Hydroquinone monobenzyl ether	-	**Cobalt(II) chloride hexahydrate**	+ - -
2-hydroxyethylmethacrylate	-	Nickel(II) sulfate hexahydrate	-
Hydroxypropyl methacrylate	-	Aluminium chloride	-
Isobutyl acrylate	+ - -	Chromium(III) chloride	-

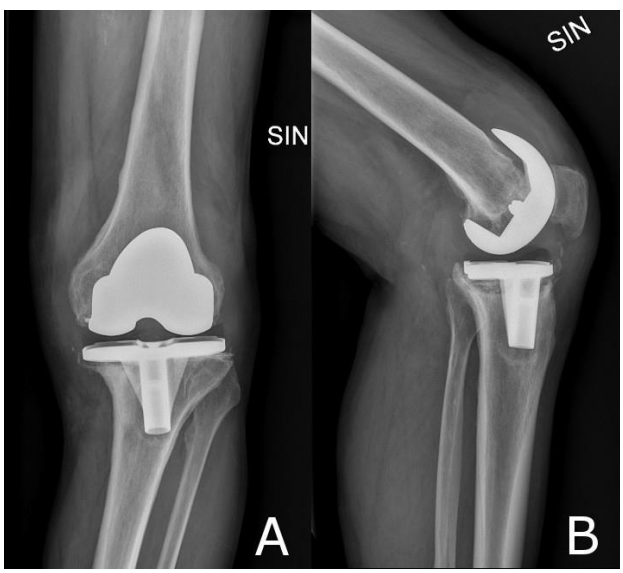


Fig. 1. *Preoperative X-rays showing TKA loosening.*

medical history was positive for asthma and restless leg syndrome. Patient-reported outcomes (PROs) on knee function revealed very low scores (WOMAC 76%, Oxford Knee Score 9/48). Knee Injury and Osteoarthritis Outcome Score (KOOS) resulted: symptoms 35.71%, pain 27.78%, daily function 23.53%, sport-related function 0%, quality of life 6.25%. SF-36 questionnaire showed very low results in the physical, emotional and social areas.

Plain radiographs revealed a severe loosening of the tibial tray with massive bone resorption involving the tibial metaphysis. The distal femur showed also diffuse radiolucency at the bone-implant interface (Fig. 1). The periprosthetic bone loss was classified as type 2a according to the Anderson Orthopaedic Research Institute (AORI) (Fig. 2). Computed

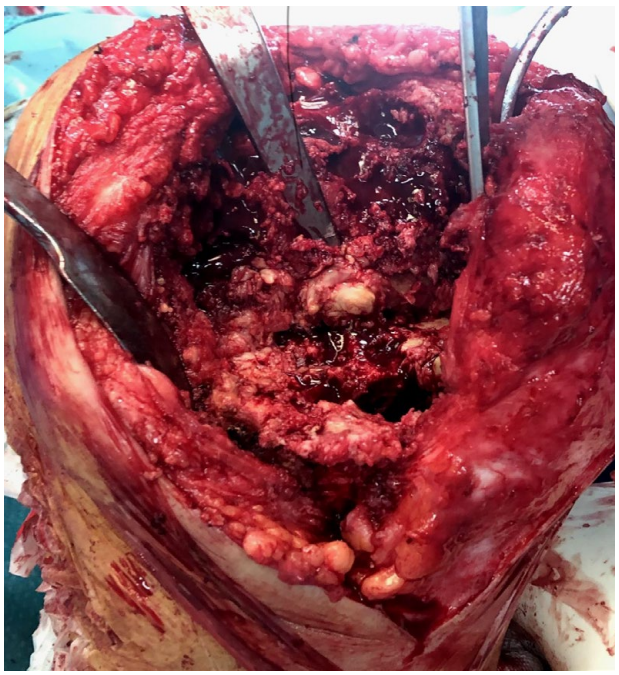


Fig. 2. *The periprosthetic bone loss.*

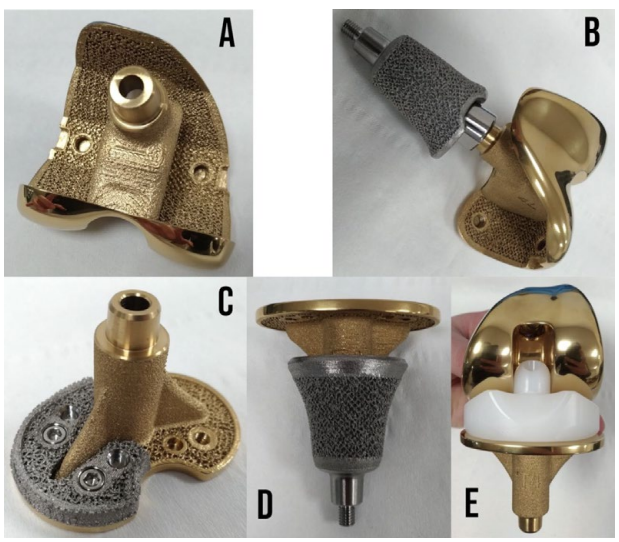


Fig. 3. *3D custom-made cementless condylar-constrained implant with meta-diaphyseal fixation (Adlerortho S.p.A, Cormano, Milano, Italy) (**E**). The femoral component was made of a zirconium alloy (97.5% zirconium- 2.5% niobium) (**A**) with a titanium metaphyseal sleeve (**B**) and a femoral stem that allowed for meta-diaphyseal fixation. Titanium tibial tray with a 5 mm medial wedge (**C**) was used to address the bone loss, and a metaphyseal sleeve (**D**) with a short stem was chosen to guarantee bone fixation and ingrowth.*

Tomography (CT) scans indicated a diffuse area of osteolysis around the implant, which was completely loosened, and a fluid collection of 5 x 3 cm in the subquadricipital recess.

Periprosthetic joint infections were excluded according to the Musculoskeletal Infection Society criteria (7). A complete laboratory workup was made, including: complete blood count with white blood cells 7.4 x 10^9/L (reference value 5-10 x 10^9/L), normal eosinophil count, C-reactive protein 1.2 mg/L (reference range, 0-10 mg/L), erythrocyte sedimentation rate 30 mm/h, and negative cultures and biochemical analysis of the synovial fluid. Blood exams were repeated preoperatively with similar results. Bone scans (three-phase scintigraphy) revealed an abnormally high uptake of the radiotracer around the medial tibial tray and medial femoral condyle, and ^{99m}Tc-HMPAO-labeled leukocyte scintigraphy excluded a possible infectious etiology.

Due to the local presence of skin rashes, hypersensitivity to implant components was suspected. The patient underwent Patch testing, focused on the most common allergens contained in orthopaedic implants and cement (Table I). Patch testing was moderately positive to butylacrylate, butyl methacrylate, isobutyl acrylate, and cobalt (II) chloride hexahydrate. Subsequently, a diagnosis of TKA aseptic loosening with acrylates and cobalt hypersensitivity was made.

After meticulous preoperative planning, an RTKA was performed. Both the components of the prosthesis were loose. Five samples of periprosthetic tissue were sent for both cultural and histological examination (less than five neutrophils per high-power field; presence of chronic inflammation and foreign body giant cell reaction). Given the bone loss and the double hypersensitivity issue, a hypoallergenic 3D custom-made cementless condylar-constrained implant with meta-diaphyseal fixation (Adlerortho S.p.A, Cormano, Milano, Italy) was chosen. The femoral component was made of a zirconium alloy (97.5% zirconium, 2.5% niobium) with a titanium metaphyseal sleeve and a femoral stem that allowed for meta-diaphyseal fixation (Fig. 3). On the tibial side, a titanium tibial tray with a 5 mm medial wedge was used to address the

bone loss, and a metaphyseal sleeve with a short stem was chosen to guarantee bone fixation and ingrowth. Implant surfaces facing the bone were coated with an antibacterial hydrogel loaded with Vancomycin 500 mg and Meropenem 500 mg at 5% dilution (Defensive Antibacterial Coating – DAC®, Novagenit S.R.L, Mezzolombardo, Trento, Italy) just before implantation. At the end of the surgery, the implant was stable.

Postoperatively, plain radiographs were performed and confirmed the correct alignment. For the first six weeks after surgery, the patient was instructed to walk with partial weight-bearing. He completed the rehabilitation process without problems. At 1-year follow-up he could walk with full bearing and no pain, range of motion was 0°-110° and there were no radiological signs of osteolysis around the implant (Fig. 4). The skin rashes around the knee had fully disappeared. We observed an improvement in all the SF-36 items, especially in the physical and social areas, as well as in all the knee PROs (WOMAC 42.7%, Oxford Knee Score 33/48, KOOS: symptoms 67.86%, pain 69.44%, daily function 70.59%, sport-related function 30%, quality of life 31.25%). The patient himself said to be very satisfied with the surgery.

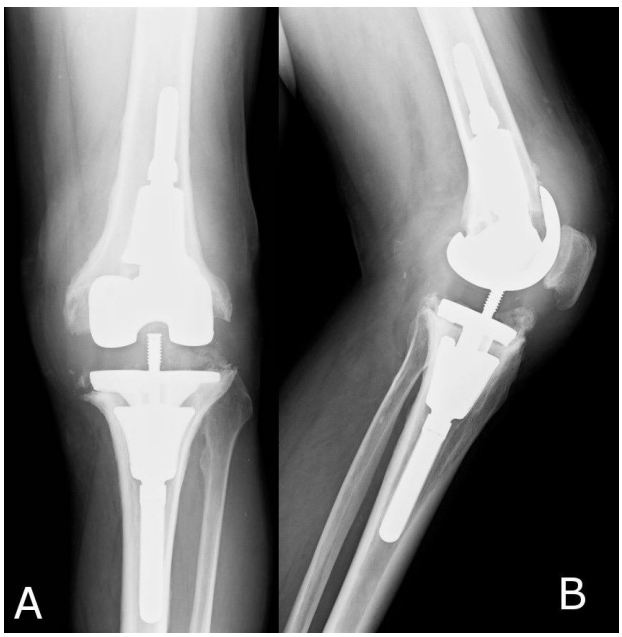


Fig. 4. *1-year follow-up X-rays showing no signs of implant loosening.*

DISCUSSION

To our knowledge, this is the second case in the English literature of aseptic TKA loosening associated with hypersensitivity to both acrylates and cobalt, and the first treated with a custom-made cementless hypoallergenic RTKA to face this uncommon double issue. Stathopoulos et al. reported a case of a patient who had an aseptic loosening with hypersensitivity to metals and bone cement components treated successfully with a hypoallergenic implant fixated with a cement to which the patient was not sensitized (5).

Allergy-related implant failure is an exclusion diagnosis. Skin patch testing is useful, inexpensive, and represents the first line diagnostic test, but the response may vary from subject to subject and the overall sensitivity reported for acrylates is only 46.2-61.5% (4, 8). Other promising tests, such as the Lymphocyte Transformation Test (LTT), the Leukocyte Migration Inhibition test and the Memory Lymphocyte Immunostimulation Assay (MELISA), are not yet routinely available in several hospitals (4). Recently, Saccomanno et al. proposed an algorithm to guide diagnosis and implant choice in case of hypersensitivity (9). In our case, MELISA and LTT were not performed, as they are not available at our institution.

Nowadays, two options mainly exist for RTKA in case of metal hypersensitivity: cobalt-chrome implants, coated with inert substances, and revision systems with an oxidized zirconium femoral component and titanium tibial tray and stem (4, 10). Regarding hypersensitivity to bone cement, cementless replacements should be considered (10). Modern knee revision systems include osseo-integrative metal sleeves with a specially structured surface supporting bone ingrowth and enhancing durable stable fixation by a cementless technique. The femoral and tibial implants can be placed independently of where the sleeve is placed, so that the sleeve itself could be rotated to the best bone stock, and the components to the appropriate orientation (11). These implants showed up to 98% survival rate after 5 years (12). We opted for a 3D-customized condylar-constrained implant with meta-diaphyseal cementless fixation through

sleeves. Results were very satisfying after 1 year, although a longer follow-up is needed to test the long-term implant stability.

REFERENCES

1. Khan M, Osman K, Green G, et al. The epidemiology of failure in total knee arthroplasty: avoiding your next revision. Bone Joint J 2016; 98-B:105-112. doi: 10.1302/0301-620X.98B1.36293
2. Postler A, Lutzner C, Beyer F, et al. Analysis of Total Knee Arthroplasty revision causes. BMC Musculoskelet Disord 2018; 19:55. doi: 10.1186/s12891-018-1977-y
3. Hallab N, Merritt K, Jacobs JJ. Metal sensitivity in patients with orthopaedic implants. J Bone Joint Surg Am 2001; 83:428-436. doi: 10.2106/00004623-200103000-00017
4. Innocenti M, Vieri B, Melani T, et al. Metal hypersensitivity after knee arthroplasty: fact or fiction? Acta Biomed 2017; 88:78-83. doi: 10.23750/abm.v88i2 -S.6517
5. Stathopoulos IP, Andrianopoulos N, Paschaloglou D, et al. Revision total knee arthroplasty due to bone cement and metal hypersensitivity. Arch Orthop Trauma Surg 2017; 137:267-71. doi: 10.1007/s00402-016-2614-6
6. Carulli C, Villano M, Bucciarelli G, et al. Painful knee arthroplasty: definition and overview. Clin Cases Miner Bone Metab 2011; 8:23-5.
7. Parvizi J, Gehrke T, International Consensus Group on Periprosthetic Joint I. Definition of periprosthetic joint infection. J Arthroplasty 2014; 29:1331. doi: 10.1016/j.arth.2014.03.009
8. Spencer A, Gazzani P, Thompson DA. Acrylate and methacrylate contact allergy and allergic contact disease: a 13-year review. Contact Dermatitis 2016; 75:157-64. doi: 10.1111/cod.12647
9. Saccomanno MF, Sircana G, Masci G, et al. Allergy in total knee replacement surgery: Is it a real problem? World J Orthop 2019; 10:63-70. doi: 10.5312/wjo.v10.i2.63
10. Faschingbauer M, Renner L, Boettner F. Allergy in total knee replacement. does it exist?: Review Article. HSS J 2017; 13:12-19. doi: 10.1007/s11420-016-9514-8
11. Burastero G, Cavagnaro L, Chiarlone F, et al. A Case report: custom made porous titanium implants in revision: a new option for complex issues. Open Orthop J.2018; 12:525-35. doi: 10.2174/1874325001812010525
12. Wirries N, Winnecken HJ, Lewinski GV, et al. Osteointegrative Sleeves for Metaphyseal Defect Augmentation in Revision Total Knee Arthroplasty: Clinical and Radiological 5-Year Follow-Up. J Arthroplasty 2019; 34:2022-9. doi: 10.1016/j.arth.2019.04.024

LETTER TO THE EDITOR

Factors associated with the synovial membrane thickness of wrist detected by ultrasonography in rheumatoid arthritis patients: a retrospective study

L. Xiao[1], Z. Yang[1] and G. Li[2]

[1]Department of Rheumatology, Hainan General Hospital, Hainan Affiliated Hospital of Hainan Medical University, Hainan, China; [2]Department of Radiology, Hainan General Hospital, Hainan Affiliated Hospital of Hainan Medical University, Hainan, China

Received September 22, 2020 – Accepted April 14, 2021

To the Editor,

Rheumatoid arthritis (RA), a chronic autoimmune disorder, leads to the formation of tumor-like tissue, i.e., the pannus, resulting in irreversible joint damage and destruction of cartilage and bone (1). Nowadays, musculoskeletal ultrasonography (US) is applied in clinical practice to detect early changes and inflammation of joints. US achieves high agreement with magnetic resonance imaging (MRI) for assessing active inflammation and bone erosions in patients with RA and can directly visualize soft tissue pathologies (2). Furthermore, US has been tested to be a valid method for demonstrating the thickness of synovium by comparison with MRI (2). Recently, synovial tissue analysis has attracted increasing interest for basic research on disease pathobiology. The two major cell types in the synovium lining of patients with RA include the macrophage-like synoviocytes and the fibroblast-like synoviocytes (3). Synovitis plays a potential role in future joint damage. Additionally, bone destructions of patients with RA are mediated by osteoclasts activated under the influence of cytokines produced by synovium (4). The quantity of synovial cells may therefore directly relate to the degree of joint damage. Considering that US can demonstrate the thickness of synovium and that power doppler (PD) signals represent active inflammation, investigating factors that may affect the thickness of synovium via US is practicable and meaningful in studying the disease activity. To our knowledge, research focusing on this topic is limited. Consequently, our study aims to identify potential factors that may affect the synovial membrane thickness of patients with RA by US detection.

MATERIALS AND METHODS

Study subjects

Patients who fulfilled the following criteria were included: i) met the 2010 American College of Rheumatology/European League Against Rheumatism Classification and Scoring Criteria for the diagnosis of RA; ii) under 65 years of age; iii) within 24 months of symptom onset; and iv) had not undergone RA treatments, including glucocorticoid, disease-modifying antirheumatic drugs (DMARDs), or biological DMARDs (5). Patients with histories of surgery of the wrist, bacterial infection (such as purulent arthritis) in the wrist, or wrist joint trauma were excluded from the study. Forty patients in Hainan General Hospital who fulfilled the above criteria between July 2019 to January 2020 were enrolled in the study. Informed consents were obtained from all participating patients and

Key words: rheumatoid arthritis; ultrasonography; rheumatoid factors; synovitis

Corresponding Author:
Dr Lu Xiao,
Department of Rheumatology, Hainan general hospital,
Hainan Affiliated Hospital of Hainan Medical University,
Hainan, 570311, China
ORCiD iD: http://orcid.org/0000-0001-6791-3726
Tel.: +86 0898 68622128 - Fax: +86 0898 68681196
e-mail: xiaolu_230@163.com

0393-974X (2021)
Copyright © by BIOLIFE, s.a.s.
This publication and/or article is for individual use only and may not be further reproduced without written permission from the copyright holder.
Unauthorized reproduction may result in financial and other penalties
DISCLOSURE: ALL AUTHORS REPORT NO CONFLICTS OF INTEREST RELEVANT TO THIS ARTICLE.

the study was approved by the Ethics Committee of Hainan General Hospital (ethic approval number: MED-Eth-RE [2020]11).

For each patient, demographic data, including age, sex, and disease duration, were collected. Blood samples were obtained from an antecubital vein in the morning. The levels of rheumatoid factor (RF), C-reactive protein (CRP), erythrocyte sedimentation rate (ESR), anticyclic citrullinated peptide antibody (ACPA), RF–immunoglobulin (Ig) A, RF–IgM, RF–IgG, antikeratin antibody (AKA), and antiperinuclear antibody (APF) were recorded.

US data

PHILIPS high-grade color ultrasonic diagnostic apparatus and an 18 MHz linear array probe were used for ultrasonic inspection. Three radiologists, who had more than five years of experience and were blinded to the clinical diagnosis and treatment, carried out the inspection. A fixed protocol following the technical guidelines of the European Society of Musculoskeletal Radiology for hand scanning was performed (6). For each patient, the average result of synovial thickness values measured by three radiologists was recorded. The US classification standards of different pathologies was according to the Outcome Measures in Rheumatoid Arthritis Clinical Trials US group definitions (7). Inflammatory, structural changes, and PD signal were graded (0, absent; 1, present).

Statistical analysis

The statistical software SPSS 20.0 was used to analyze data. Quantitative clinical and demographic variables were reported as mean±standard deviation. The comparison of the quantitative values was performed using Student's *t*-test. The McNemar test was applied to compare qualitative values. US findings, except the thickness of synovium, were considered as dichotomous

Table I. *Demographics and clinical characteristics of the patients*

Patient characteristics	Results
Gender(male/female)	6/34
Mean age(years)	52.08± 10.67
Mean duration of disease (months)	11.33±9.53
CRP (mg/L)	45.66±40.29
ESR (mm/h)	68.75±35.08
RF (IU/ml)	200.03±278.33
ACPA(IU/ml)	89.12±80.61
RF-IgG (IU/ml)	14.27±18.95
RF-IgA (IU/ml)	143.14±18.95
RF-IgM (IU/ml)	165.59±68.09
AKA (positive/negative)	13/27
APF (positive/negative)	10/30
Thickness of synovium(mm)	2.81±1.53
Power doppler signal(positive/negative)	40/0

Data presented as means±SD or number of patients; CRP: C-reactive protein; ESR: erythrocyte sedimentation rate; RF: rheumatoid factor; ACPA: anti-cyclic citrullinated peptide antibody; AKA: Anti-keratin antibody; APF: Antiperinuclear antibody

data depending on absence/presence. Linear correlation analysis was used to determine the association between synovial thickness and different factors, including ESR, CRP, RF–IgA, RF–IgM, RF–IgG, ACPA, RF, and US findings. P value < 0.05 was considered significant.

RESULTS

Demographic characteristics of patients

Forty patients with RA (6 males and 34 females) were included in our retrospective study. Demographic data are summarized in Table I. The mean age was 52.08±10.67 years. The mean disease duration was 11.33±9.53 months. The mean levels of CRP, ESR, RF–IgA, RF–IgM, RF–IgG, ACPA, and RF were 45.66±40.29 mg/l, 68.75±35.08 mm/h, 143.14±18.95 IU/ml, 165.59±68.09 IU/ml, 14.27±18.95 IU/ml, 89.12±80.61 IU/ml, and 200.03±278.33 IU/ml, respectively. A total of 13 and 10 patients were found positive to AKA and APF, respectively.

US findings in wrists of patients with RA

The six most common US pathologies are listed in Fig.1. Synovitis, joint effusion, tenosynovitis, soft tissue swelling, bone erosion, and joint space narrowing were included in our analysis. The percentages of patients having the above-mentioned six lesions were 97.5%, 22.5%, 12.5%, 7.5%, 30%,

Table II. *Correlation between the thickness of synovial synovium in US and different parameters*

Clinical and laboratory parameters	β	P value	F value	P value
Constant	2.37	0.00	4.67	0.03
RF (IU/ml)	0.02	0.04		
RF-IgA (IU/ml)	0.08	0.01		
Joint space narrowing in US	-1.43	0.02		

RF: rheumatoid factor; US: ultrasonography

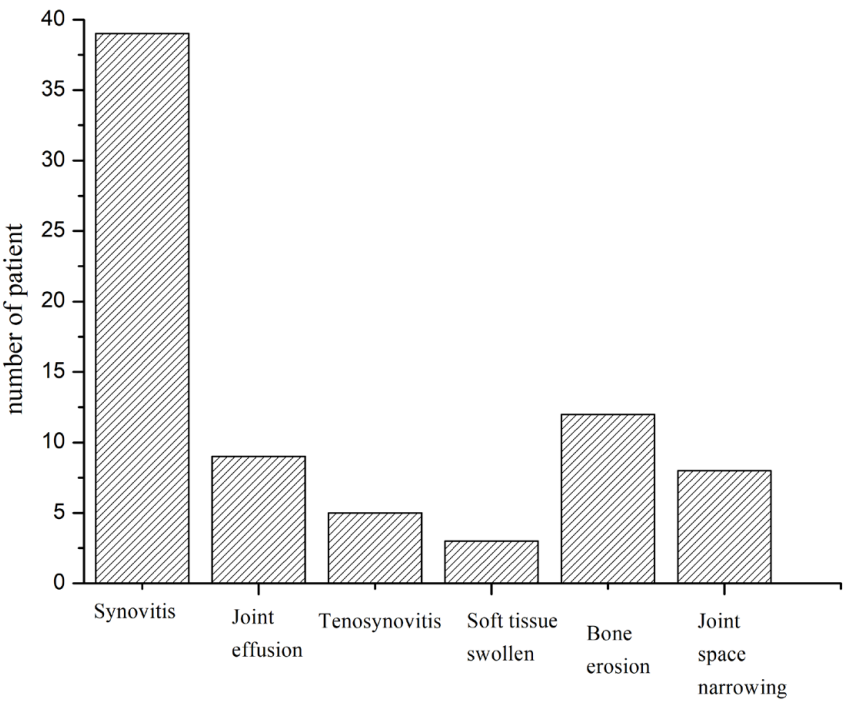


Fig. 1. *US findings of RA patient*

and 20%, respectively. The mean thickness of synovium was 2.81±1.53 mm. All enrolled patients were found positive to the PD signal.

Correlation between the synovium thickness detected using US and different factors

The linear correlation analysis was performed to clarify the relationship between the average synovial thickness and different factors, including ESR, CRP, RF–IgA, RF–IgM, RF–IgG, ACPA, RF, and US findings. The results are demonstrated in Table II. Statistically positive associations were found between the levels of RF, RF–IgA and the thickness of synovium. A negative relationship was discovered between the synovium thickness and US detecting joint space narrowing.

DISCUSSION

This retrospective study was designed to ***identify possible factors associated with*** synovial membrane thickness measured using US in patients with RA. In our research, the most common change revealed by US was synovitis. This result had been proven more than once in previous studies (8, 9). Our investigation drew the conclusion that the synovial thickness ***was associated with RF and RF–IgA levels.*** Several studies are in agreement with ours, indicating that the high level of RF is related to joint damage and unfavorable prognosis (10). The early onset of RF is linked to a severe condition, highlighting a possible contribution of this antibody to exacerbate the disease. B cells with RF specificity can migrate into the synovium, presenting a variety of complex antigens to relevant T cells, leading to the perpetuation of local inflammatory responses and may be the reason for synovium thickening (8, 11). We also found that joint space narrowing in US imaging was negatively related to the thickness of synovium. In 2001, Kirwan and his colleagues demonstrated that there may be a relationship between joint space narrowing and synovitis. The joint space narrowing represents a late-stage pathological change in RA (12), however, synovitis with positive PD signal usually happens in the early course of the disease (12); this may therefore be the reason for negative link between joint space narrowing and synovium thickness. In summary, our study found that the synovial membrane thickness was positively related to RF and RF–IgA levels. Patients with high RF and RF–IgA levels may therefore need intensive treatment to keep the disease from progressing.

ACKNOWLEDGEMENTS

This study was supported by the Hainan Provincial Natural Science Foundation of China (820QN386) and the project of Hainan General Hospital (QN 202009).

REFERENCES

1. Wakefield RJ, Gibbon WW, Conaghan PG, et al. The value of sonography in the detection of bone erosions in patients with rheumatoid arthritis: A comparison with conventional radiography. Arthritis Rheum 2000; 43:2762-70.
2. Platzgummer H, Schueller-Weidekamm C. [Radiological imaging in early diagnosis of rheumatoid arthritis. The role of ultrasound and magnetic resonance imaging]. Radiologe 2012; 52:124-31.
3. Valencia X, Higgins JM, Kiener HP, et al. Cadherin-11 provides specific cellular adhesion between fibroblast-like synoviocytes. J Exp Med 2004; 200:1673-9.
4. Scher JU, Sczesnak A, Longman RS, et al. Expansion of intestinal prevotella copri correlates with enhanced susceptibility to arthritis. eLife 2013; 2:e01202.
5. Aletaha D, Neogi T, Silman AJ, et al. 2010 rheumatoid arthritis classification criteria: An american college of rheumatology/european league against rheumatism collaborative initiative. Arthritis Rheum 2010; 62:2569-81.
6. Martinoli C. Musculoskeletal ultrasound: Technical guidelines. Insights into imaging 2010; 1:99-141.
7. Wakefield RJ, Balint PV, Szkudlarek M, et al. Musculoskeletal ultrasound including definitions for ultrasonographic pathology. J Rheumatol 2005; 32:2485-7.
8. Filippucci E, Iagnocco A, Meenagh G, et al. Ultrasound imaging for the rheumatologist vii. Ultrasound imaging in rheumatoid arthritis. Clin Exp

Rheumatol 2007; 25:5-10.
9. Sagawa A, Henmi M, Narita A, Hagiwara H, Matsuhashi M. Ultrasonographic assessment of joints in rheumatoid arthritis. Nihon Rinsho 2005; 63 Suppl 1:400-4.
10. Jansen LM, van der Horst-Bruinsma IE, van Schaardenburg D, Bezemer PD, Dijkmans BA. Predictors of radiographic joint damage in patients with early rheumatoid arthritis. Ann RheumDis 2001; 60:924-7.
11. Michael VV, Alisa KE. Cell cycle implications in the pathogenesis of rheumatoid arthritis. Front Biosci 2000; 5:D594-601.
12. Rubin DA. Mri and ultrasound of the hands and wrists in rheumatoid arthritis. I. Imaging findings. Skeletal Radiol 2019; 48:677-95.

LETTER TO THE EDITOR

IL-35 suppresses epileptiform burst activity in primary hippocampal neurons

L-M. Zhang[1,2], L. Chen[2], Y-J. Chen[3] and M-W. Liu[4]

[1]Institute of Primate Translational Medicine, Kunming University of Science and Technology, Kunming, Yunnan; [2]Department of Neurology, the First Affiliated Hospital of Kunming Medical University, Kunming, Yunnan, China; [3]Department of Neurology, Nanhua Affiliated Hospital, University of South China, Hengyang, Hunan, China; [4]Department of Emergency, The First Affiliated Hospital of Kunming Medical University, Kunming, Yunnan, China

Received December 2, 2020 – Accepted April 19, 2021

To the Editor,

Epilepsy is a relatively common neurological condition that can severely adversely impact the quality of life of affected individuals. Mechanisms associated with the pathology of epilepsy include inflammation, genetic factors, and apoptosis (1), although further research is required to precisely clarify the etiology of this disease. A number of antiepileptic drugs have been designed to date, but they are only able to control seizures in about 60% of epilepsy patients, while approximately 30% of patients exhibit progressive uncontrolled epilepsy (2).

At the molecular level, epilepsy triggers a series of inflammatory immune responses linked to neuroinflammatory mediator and chemokine production (3). Several inflammatory factors have been shown to be relevant in the context of epilepsy, including interleukin (IL)-6 and IL-1β, both of which can aggravate the disease (3).

IL-35 is an anti-inflammatory member of the IL-1B2 cytokine family, and it has been shown to regulate the progression of autoimmune diseases such as experimental autoimmune encephalomyelitis, uveitis, multiple sclerosis, and diabetes (4). The specific functional role of IL-35 in primary hippocampal neurons remains uncertain. As such, in this study, the impact of IL-35 on organotypic hippocampal neuron excitability and apoptosis was investigated. The analyses revealed the ability of IL-35 to suppress spontaneous discharges and epileptiform burst activity, with this suppression being most pronounced in response to 100 ng/mL of IL-35. Treatment with IL-1β abolished the neuroprotective activity of IL-35. Overall, the results suggest that inflammatory cytokines serve a vital role as regulators of normal neuronal excitability.

MATERIALS AND METHODS

Organotypic hippocampal culture

Organotypic hippocampal samples were obtained from 7-day old male mice, as discussed previously (2). Briefly, 10% chloral hydrate (i.p.) was used to euthanize mice, after which brain samples were collected and transferred to chilled artificial cerebrospinal fluid (ACSF) supplemented with 124 mM NaCl, 5 mM KCl, 26 mM NaHCO3, 1.6 mM MgCl2, 2.0 mM CaCl2, and 10 mM D-glucose (14). Coronal hippocampal sections

Key words: IL-35, apoptotic death, epileptiform burst activity, hippocampal neurons

Corresponding Author:
Dr Ming-wei Liu,
Department of Emergency, The First Affiliated Hospital of Kunming Medical University,
Kunming, Yunnan 650032, China
e-mail: lmw2004210@163.com
Institutional e-mail address: liumingwei.92233@ydyy.net.cn

0393-974X (2021)
Copyright © by BIOLIFE, s.a.s.
This publication and/or article is for individual use only and may not be further reproduced without written permission from the copyright holder.
Unauthorized reproduction may result in financial and other penalties
DISCLOSURE: ALL AUTHORS REPORT NO CONFLICTS OF INTEREST RELEVANT TO THIS ARTICLE.

were prepared using a Vibratome (Leica, Germany) prior to transfer into a Transwell insert (Cell Signaling Technology, Inc., Danvers, MA, USA) in a 6-well plate. To each well, 1 mL of neural culture medium (9.7 mM Neurobasal, 100 mM NEAA, 50 mM N2, 100 mM B27, and 100 mM GlutaMax) was added, with half of the media being replaced twice per week. Samples were incubated at 37°C in a 5% CO_2 incubator.

Epileptiform discharge model

To induce epileptiform discharges, hippocampal sections were exposed to a Mg^{2+}-free solution for 3 h, as detailed previously (5). Briefly, samples were washed thrice with 1.5 mL of sterile ACSF (with or without Mg^{2+}) following neural culture medium removal, after which samples were incubated for 3 h in ACSF at 37°C in a 5% CO2 incubator. Samples were then washed thrice with 1.5 mL of sterile ACSF and returned to neural culture medium.

Sample treatment

After 3 h culture in Mg^{2+}-free solution, the organotypic hippocampal samples were returned to neural culture medium containing a range of concentrations of IL-35 (0, 1, 50, 100 ng/ml) or IL-1β (1 nM) for 48 h.

Following a 48-h treatment with IL-35 or IL-1B, neuron patch-clamping was performed. Briefly, organotypic hippocampal samples were assessed at room temperature in a solution containing 125 mM NaCl, 2.5 mM KCl, 2 mM $CaCl_2$, 5 mM $MgCl_2$, 26 mM $NaHCO_3$, and 15 mM Glucose. A Sutter P-97 pipette puller (Sutter Instruments, CA, USA) was used to pull soft-glass recording pipettes with 2-5 MΩ resistance. These pipettes were filled with a solution containing 140 mM KCl, 9 mM NaCl, 1 mM $MgCl_2$, 1 mM EDTA, and 10 mM HEPES. Whole-cell recordings of pyramidal neurons were conducted using a MultiClamp 700B amplifier (Axon Instruments, CA, USA). Pyramidal neurons were recorded while held at a -70mV membrane potential in current-clamp mode. Normal spontaneous discharges were defined as single or double action potentials firing spontaneously on top of EPSPs. A large depolarization shift was defined as a membrane potential upshift of ≥10 mV for ≥300 ms. An epileptiform burst was defined by five or more consecutive action potentials overlaying this large depolarization shift. Current clamp traces used for data analysis were averaged from 10-15 recordings. Epileptiform burst activity was defined by a minimum of two repeated bursts within 10 min of recording.

RT-PCR

Hippocampal tissue sections were collected from the control group, the Mg^{2+}-free group, and the IL-35-treated (50, 100, or 200 ng/mL) groups. Total RNA was extracted from these samples with TRIzol (Invitrogen, Carlsbad, CA, USA), and the expression of IL-1β, IL-6, and IL-35 was detected with SYBR Green Quantitative RT-PCR Kit (Sigma-Aldrich, MO, USA). GAPDH served as a normalization control. Primers were as follows: GAPDH, 5'-AAATGGTGAAGGTCGGTGTGAAC-3' (forward) and 5'-CAACAATCTCCACTTTGC CACTG-3' (reverse); IL-1β, 5'-TCCAGGATGAGGACATGAGCAC-3' (forward)and5'-GAACGTCACACACCAGCAGGTTA-3' (reverse); IL-6, 5'-CAGTTGCCTTCTTGGGACT-3'

Table I. *IL-35 suppresses cultured organotypic hippocampal slice neuron burst activity*

group	Bursting neurons(n)	Burst frequency(episodes/30 min)	Burst duration(
Control	1/12	1.2±1.4	0.025±0.01
Mg^{2+}-free	12/12**	8.2±2.7**	150.1±10.73**
IL-35 (50ng/ml)	5/12*##	3.4±1.5*##	75.1±10.71**##

*IL-35 suppressed the percentage of bursting neurons, burst frequency, and burst duration in response to different IL-35 doses (0, 10, 50,100, 200ng/ml). Recordings are representative of 60 hippocampal slice neurons. Data from three independent experiments are presented as mean±SEM. *P<0.05, **P<0.01, vs control group; #P<0.05, ##P<0.01, vs Mg^{2+}-free group*

(forward), 5'-TCTGACAGTGCATCATCGCT-3' (reverse); p35, 5'-CATCGATGAGCTGATGCA GT-3' (forward), 5'-CAGATAGCCCATCACCCTGT-3' (reverse); EBI3, 5'-TCTTCCTGTCACTTGCCCTCTG-3' (forward), 5'-AGTTGGGAGCCTGGAGAGGAGT-3' (reverse). PCR products were evaluated via 1.2% agarose gel electrophoresis with ethidium bromide under UV light.

TUNEL staining

Organotypic hippocampal slices were fixed overnight with 4% paraformaldehyde, after which they were cut into 10-μm-thick sections that were subsequently dehydrated with an ethanol gradient, rinsed with PBS, and heated for 5 min in sodium citrate buffer (0.1 mol/L) in a 350-W microwave. Sections were then washed again, after which they were treated with a prepared Terminal deoxynucleotidyl transferase-mediated dUTP nick-end labeling (TUNEL) reaction mixture for 1 h at 37°C while protected from light. Sections were then washed with PBS and were incubated for 30 min with Converter-POD at 37°C in the dark, followed by an additional PBS wash. Sections were then treated for 15 min with the 3,3'-diaminobenzidine (DAB) substrate, washed, counterstained using hematoxylin, and rinsed under running water. An ethanol gradient was then used to dehydrate sections, which were treated with xylene and mounted using neutral balsam. The presence of brown particles within neuronal nuclei was considered indicative of TUNEL positivity.

Statistical analysis

A MultiClamp 700B amplifier (Systat Software, Inc., San Jose, CA, USA) was used to record all data, which are given as means ± SEM and were analyzed with SPSS 17.6 (SPSS Inc., IL, USA). Data were compared via unpaired Student's *t*-tests and *chi*-squared tests with $P < 0.05$ as the significance threshold.

RESULTS

Impact of IL-35 on cultured organotypic hippocampal neuron discharges

While IL-35 is well known to play important regulatory roles in the context of infectious disease and autoimmunity, its impact on cultured neurons remains to be assessed. We began by comparing organotypic hippocampal slice neuron discharges when these cells were cultured in the presence or absence of IL-35. When treated with Mg^{2+}-free medium, all neurons (12/group, 6 total culture plates) exhibited epileptiform burst activity in current mode regardless of the presence or absence of IL-35. However, the culturing of these neurons in media containing IL-35 (50 ng/mL) for 48 h resulted in a significant decrease in epileptiform burst activity (41.6%, 5/12, $P<0.05$) relative to the Mg^{2+}-free group (100%, 12/12). IL-35 was also associated with

Table II. *Index changes in the control group relative to the Mg^{2+}-free group and the IL-35 treatment group.*

Groups	IL-1β mRNA	IL-6 mRNA	p35 mRNA	EBi3 mRNA	Apoptosis rate%
Control	1.00±0.03	1.00±0.03	1.00±0.03	1.00±0.03	8.91±2.79
Mg^{2+}-free	3.35±0.06*	2.27±0.05*	0.52±0.05*	0.83±0.03	39.11±12.36**
IL-35 (50ng/ml)	2.35±0.04$^{*\#}$	1.82±0.05$^{*\#}$	1.21±0.02$^{\#}$	1.63±0.04$^{\#}$	30.46±9.90**
IL-35 (100ng/m)	1.75±0.06$^{\#\#}$	1.35±0.07$^{\#\#}$	2.15±0.04$^{*\#\#}$	3.15±0.04$^{**\#\#}$	19.72±5.91$^{*\#\#}$
IL-35 (200ng/m)	2.04±0.05$^{*\#}$	1.55±0.04$^{\#}$	2.55±0.06$^{**\#\#}$	3.81±0.03$^{**\#\#}$	21.53±6.73$^{*\#\#}$

*The apoptotic death and levels of inflammatory cytokine gene expression of neurons following a 3 h treatment in Mg^{2+}-free medium in the presence or absence of IL-35 (100 ng/mL) was assessed. Data from three independent experiments are presented as means ± SEM. *P<0.05, **P<0.01, vs control group; # P<0.05, ##P<0.01, vs Mg^{2+}-free group*

a significant reduction in such burst activity relative to culture in IL-35-free medium ($P<0.05$). The burst frequency in the Mg^{2+}-free group was 8.2±2.7 episodes/30 min, whereas this frequency was reduced to 3.4±1.5 episodes/30 min in the IL-35 treatment group. Similarly, the average burst duration was reduced from 150.1±10.73 s in the Mg^{2+}-free group to 75.1±10.71 s and 0.025±0.01s in the IL-35 and control groups, respectively. IL-35 treatment was thus associated with significant reductions in burst frequency and burst duration ($P<0.05$, $P<0.001$). Neurons in the control group, the Mg^{2+}-free group, and the IL-35 treatment group (50ng/ml) exhibited mean membrane potential values of -65.3±2.1 mV, -62.4±1.1 mV, and -61.5±3.2 mV, respectively, and mean input resistance values of 129.5±5.17 mΩ, 131.7±4.65 mΩ, and 134.5±2.81 mΩ, respectively. These values did not differ significantly from one another (n =12 each).

IL-35 treatment suppresses cultured organotypic hippocampal neuron epileptiform burst activity in a dose-dependent manner

The impact of IL-35 on cultured organotypic hippocampal slice neuron epileptiform burst activity was evaluated, revealing a dose-dependent suppression of this activity following a 48-h culture period in the presence of IL-35 (0, 10, 50, 100, or 200 ng/mL) (Fig. 2A) (12 neurons/group, 6 culture plates). We found that an IL-35 dose of 100 ng/mL was optimal to suppress this activity (Fig. 2B), resulting in a significant decrease in the percentage of neurons exhibiting burst activity (25%, 3/12; $P < 0.001$) relative to the Mg^{2+}-free group, whereas at IL-35 doses of 0, 10, 50, and 200 ng/ml these percentages were 100% (12/12), 83.3% (10/12), 41.6% (5/12), and 75% (9/12), respectively (Fig. 2B). Burst frequencies in the 0, 10, 50, 100, and 200 ng/mL IL-35 treatment groups were 8.2±2.7, 6.7±2.1, 3.4±1.5, 2.1±0.8, and 5.9±1.7

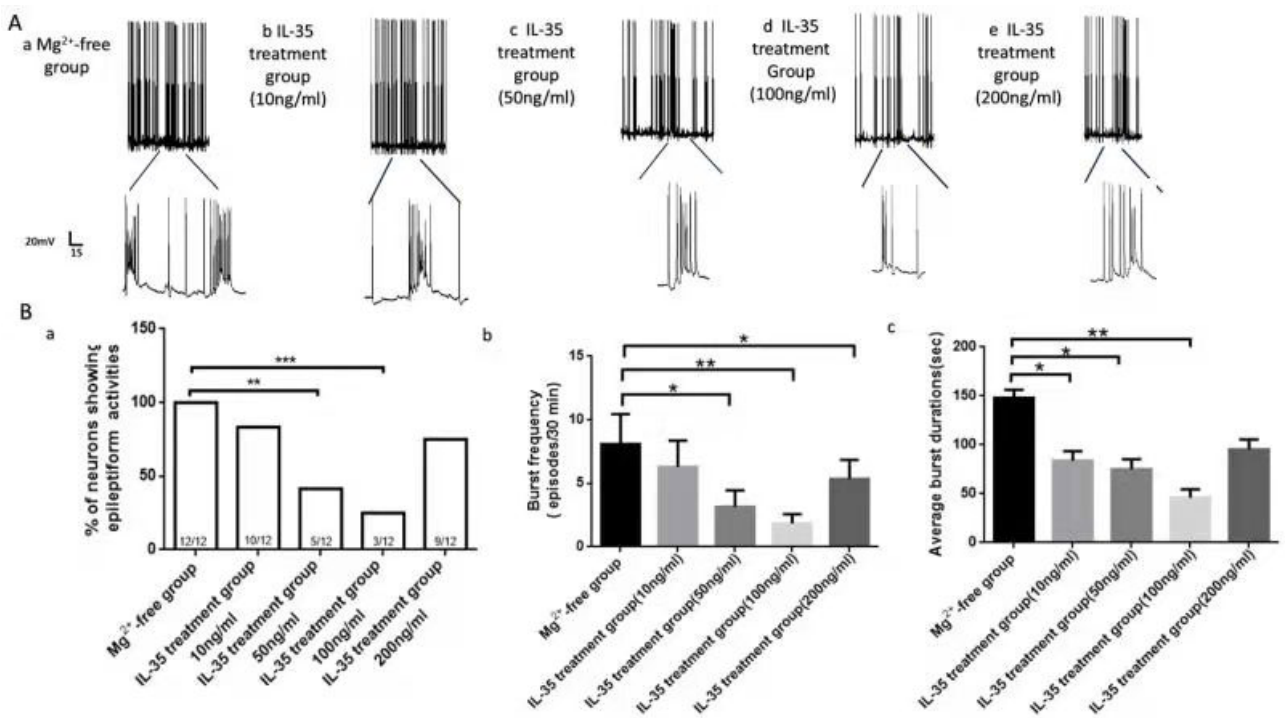


Fig. 1. *IL-35 inhibits cultured organotypic hippocampal slice neuron epileptiform burst activity.* ***A)*** *Current clamp traces from pyramidal hippocampal neurons in culture medium containing a range of IL-35 doses (0, 10, 50,100, 200ng/ml) revealed the dose-dependent suppression of epileptiform burst activity.* ***B)*** *IL-35 suppressed the percentage of bursting neurons (a), burst frequency (b), and burst duration (c) in response to different IL-35 doses (0, 10, 50, 100, 200ng/ml). Recordings are representative of 60 hippocampal slice neurons. *P<0.05,**P<0.01, vs control group; # P<0.05, ##P<0.01, vs Mg^{2+}-free group.*

episodes/30 min, respectively. These frequencies were significantly reduced in the 50 and 100 ng/mL groups compared to other groups (P<0.05, P<0.001). Average bust durations in these five treatment groups were 150.1±10.73 s, 84.4±9.17 s, 75.1±10.71 s, 46.3±8.92 s, and 95.9±10.34 s, respectively, and these burst durations were significantly decreased in the 50 and 100 ng/mL treatment groups in relation to the other treatment groups (P<0.05, P<0.001). Neurons in the Mg^{2+}-free group, the IL-35 treatment group (10ng/ml), the IL-35 treatment group (50ng/ml), the IL-35 treatment group (100ng/ml), and the IL-35 treatment group (200ng/ml) exhibited mean membrane potential values of -62.4±1.1 mV, -65.1±4.6 mV, -61.5±3.2 mV, -64.7±5.4 mV, and -61.3±2.8 mV, respectively, with respective mean input resistance values of 131.7±4.65 mΩ, 135.2±3.17 mΩ, 134.5±2.81 mΩ, 134.1±1.24 mΩ, and 136.2±5.15 mΩ. These values did not differ significantly from one another (n =12 each).

Impact of IL-1β on IL-35-mediated changes in the activity of cultured organotypic hippocampal slice neurons

Given that IL-35 is an anti-inflammatory cytokine that plays important roles in the context of autoimmunity, the ability of pro-inflammatory IL-1β to modulate the suppressive effects of IL-35 on cultured organotypic hippocampal neuron epileptiform burst activity was next explored. For these experiments, cells were treated with IL-35 (100 ng/mL) and/or IL-1β (50 ng/mL), and recordings were made for 12, 12, 14, 15, and 12 neurons in the control, Mg^{2+}-free, IL-1β, IL-1β + IL-35, and IL-35 treatment groups, respectively. This analysis revealed that IL-1β treatment significantly inhibited the ability of IL-35 to suppress epileptiform burst activity in these neurons (P<0.001; Fig. 3A). When treated with IL-35 alone, only 25% of neurons (3/12) exhibited burst activity, whereas 35.7% (5/14) and 66.7% (10/15) of neurons in the IL-35 + IL-1β and

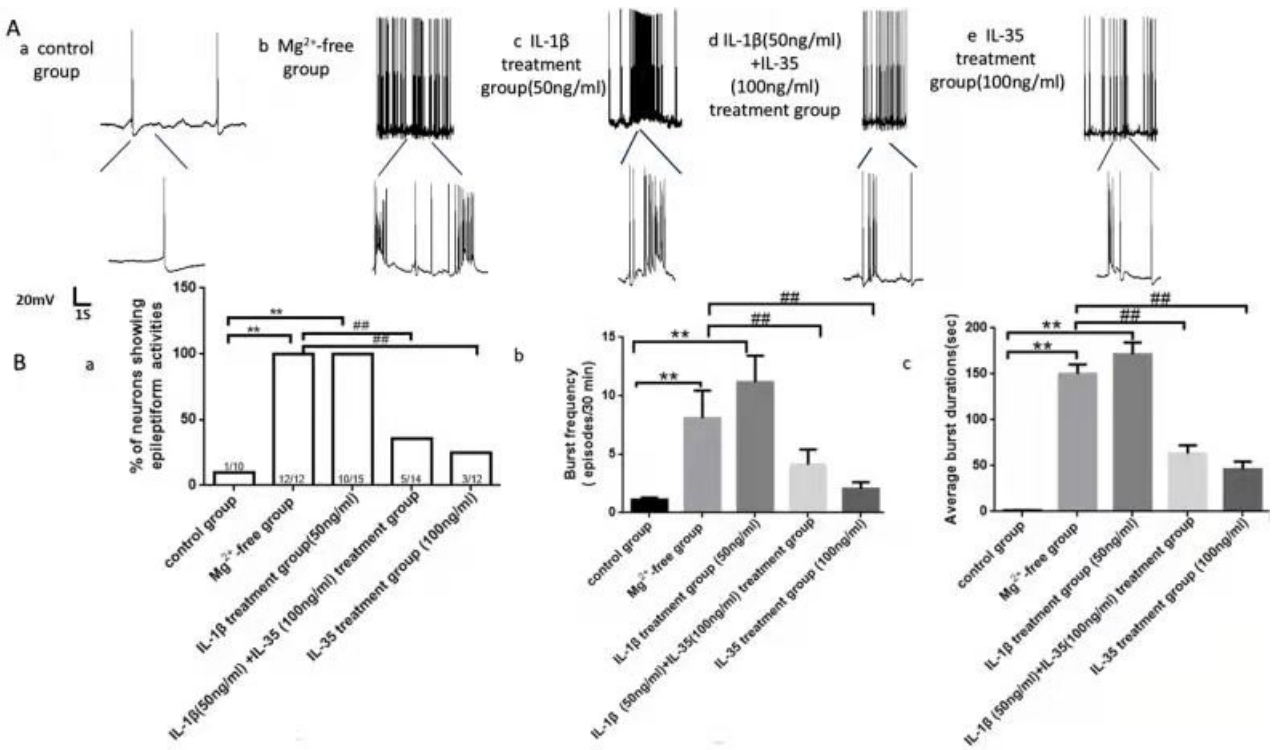


Fig. 2. *IL-1β disrupts the ability of IL-35 to suppress cultured organotypic hippocampal slice neuron epileptiform burst activity.* ***A)*** *Current clamp traces exhibiting firing patterns in the Mg^{2+}-free group (a), the IL-35 treatment group (b), the IL-35 + IL-1β treatment group (c), and the IL-1β (50ng/ml) treatment group (d). IL-35 and IL-1β were administered at respective doses of 100 ng/mL and 50 ng/mL.* ***B)*** *IL-1β co-treatment significantly (P<0.001) inhibited decreases in the frequency of bursting neurons (b) and average burst durations (c) relative to IL-35 treatment alone. Recordings are representative of 63 hippocampal slice neurons. *P<0.05, **P<0.01, vs control group; # P<0.05, ##P<0.01, vs Mg^{2+}-free group*

IL-1β treatment groups exhibited burst activity (Fig. 3B). Burst frequencies in the Mg^{2+}-free, IL-35, IL-35 + IL-1β, and IL-1β treatment groups were 8.2±2.7, 2.1±0.8, 4.1±1.7, and 11.4±2.5 episodes/30 min, respectively. Following IL-35 treatment, burst frequency decreased significantly ($P<0.05$). Similarly, the average burst durations in these treatment groups were 150.1±10.73 s, 46.3±8.92 s, 63.7 ± 9.16 s, and 171.5±13.17 s, respectively, with IL-35 having significantly reduced the average burst duration ($P<0.001$). Overall, these data suggest that the ability of IL-35 to suppress epileptiform burst activity in culture neurons is likely attributable to its anti-inflammatory activity. Neurons in the Mg^{2+}-free, IL-35, IL-35 + IL-1β, and IL-1β treatment groups had mean membrane potential values of -62.4±1.1 mV, -64.7±5.4 mV, -62.4±2.1 mV, and -63.7±2.1 mV, respectively, and mean input resistance values of 131.7±4.65 mΩ, 134.1±1.24 mΩ,133.7±2.61 mΩ, and 132.4±5.21 mΩ, respectively. These values did not differ significantly between groups (n =12 each)

IL-35 attenuates neuronal inflammation

To explore the potential anti-inflammatory properties of IL-35, we next assessed neuronal inflammation following a 3 h treatment in Mg^{2+}-free medium in the presence or absence of IL-35 (100 ng/mL). As shown in Table I, compared with the control group, the Mg^{2+}-free group exhibited significantly increased IL-1β and IL-6 mRNA expression, and significantly decreased p35 and EBi3 mRNA expression. Relative to the Mg^{2+}-free group, the IL-35 treatment group (50 ng/ml, 100 ng/ml, 200 ng/ml) exhibited significantly decreased IL-1β and IL-6 mRNA expression, and significantly increased p35 and EBi3 mRNA expression. As such, IL-35 can function as an anti-inflammatory cytokine to prevent Mg^{2+}-free media-induced neuronal inflammation.

IL-35 functions as a neuroprotective cytokine

To explore the potential neuroprotective activity of IL-35, the apoptotic death of neurons following a 3 h treatment in Mg^{2+}-free medium in the presence or absence of IL-35 (100 ng/mL) was then assessed. As shown in Table II, neurons in the control group, the Mg^{2+}-free group, and the IL-35 treatment groups (50 ng/ml, 100 ng/ml, 200 ng/ml) (n=6 each) exhibited apoptosis rates of 8.91%, 39.11%, 30.46%, 19.72%, and 21.53%, respectively. As such, IL-35 can function as a neuroprotective factor to prevent apoptotic neuronal death.

DISCUSSION

Herein, we found that IL-35 can suppress burst activity in cultured organotypic hippocampal slice neurons. This suppression is likely linked to the anti-inflammatory properties of this cytokine, given that the pro-inflammatory cytokine IL-1β was able to partially reverse these effects.

IL-35 has previously been shown to function as a key regulator of immune status in the context of neurological disease (6-9). Moreover, low IL-35 concentrations had little impact on epileptiform burst activity in cultured hippocampal neurons, whereas this activity was reduced in response to higher levels of this cytokine (200 ng/mL), while intermediate levels (100 ng/mL) suppressed such epileptiform activity.

IL-1β was able to block the suppressive effects of IL-35 in the culture system, confirming that IL-35 can disrupt epileptiform burst activity owing to its anti-inflammatory properties. IL-1β enhances NMDA-mediated neuronal Ca^{2+} influx (10) and reduces A-type K^+ currents, thereby causing neuronal network hyper-excitability (11). However, we did not assess the channels whereby IL-35 mediates its protective functions, and further research will therefore be required to clarify the mechanistic basis for this activity.

Apoptosis is the primary driver of neuronal damage following brain injury (12). As such, we evaluated the impact of IL-35 on neuronal apoptosis under Mg^{2+}-free treatment conditions via TUNEL staining, revealing the ability of this cytokine to suppress neural apoptosis. This is consistent with data from Xu et al. demonstrating the protective role of IL-35 in the context of murine ischemic brain injury (9). Overall, these data suggest that IL-35 is an important neuroprotective cytokine, although further work will be necessary to elucidate the mechanisms whereby it prevents neuronal death.

In summary, we found that IL-35 is a key mediator of normal neuronal firing, exhibiting an

ability to suppress epileptiform burst activity in a dose-dependent manner that can be disrupted by IL-1β treatment. From a mechanistic perspective, IL-35 was able to prevent neuronal apoptosis, thus functioning as a neuroprotective cytokine.

Ethics statement

The Committee on the Use of the Laboratory Animals, Kunming Medical University approved the present study, which was conducted in a manner consistent with the Chinese National Nature Science Foundation animal research regulations.

ACKNOWLEDGEMENTS

This study was supported by grants from the Nature Science Foundation of China (82060252, 81760243 and 81960350) and Yunnan Basic Research Projects (2018FB115) and the Yunnan health training project of high-level talents (H-2018058).

REFERENCES

1. Auvin S, Shin D, Mazaratia A, Sankar R. Inflammation induced by LPS enhances epileptogenesis in immature rat and may be partially reversed by IL1RA. Epilepsia 2010; 51(Suppl 3):34-8.
2. Li Q, Han Y, Du J, et al. Alterations of apoptosis and autophagy in developing brain of rats with epilepsy: Changes in LC3, P62, Beclin-1 and Bcl-2 levels. Neurosci Res 2018; 130:47-55.
3. Sookyong Koh. Role of neuroinflammation in evolution of childhood epilepsy. J Child Neurol 2018; 33(1):64-72.
4. Collison LW, Workman CJ, Kuo TT, et al. The inhibitory cytokine IL-35 contributes to regulatory T-cell function. Nature 2007; 450:566
5. Zhang LM, Liang ZR, Zhu PP, et al. Altered intrinsic properties and bursting activities of neurons in layer IV of somatosensory cortex from Fmr-1 knockout mice. Exp Neurol 2016; 280:60-9.
6. Shen P, Roch T, Lampropoulou V, et al. IL-35-producing B cells are critical regulators of immunity during autoimmune and infectious diseases. Nature 2014; 507:366.
7. Dambuza IM, He C, Choi JK, et al. IL-12p35 induces expansion of IL-10 and IL-35-expressing regulatory B cells and ameliorates autoimmune disease. Nat Commun. 2017; 8(1):719.
8. Jafarzadeh A, Jamali M, Mahdavi R, et al. Circulating levels of interleukin-35 in patients with multiple sclerosis: evaluation of the influences of FOXP3 gene polymorphism and treatment program. J Mol Neurosci 2015; 55:891-7.
9. Xu C, Zhu H, Shen R, Feng Q, Zhou H, Zhao Z. L-35 is a Protective Immunomodulator in Brain Ischemic Injury in Mice, Neurochemical Research 2018; 43:1454-63.
10. Yang S, Liu ZW, Wen L, Qiao HF, Zhou WX, Zhang YX. Interleukin-1beta enhances NMDA receptor-mediated current but inhibits excitatory synaptic transmission. Brain Res 2005; 1034:172-9.
11. Tabarean IV, Korn H, Bartfai T. Interleukin-1beta induces hyperpolarization and modulates synaptic inhibition in preoptic and anterior hypothalamic neurons. Neuroscience 2006; 141: 1685-95.
12. Du G, Zhao Z, Chen Y, et al. Quercetin attenuates neuronal autophagy and apoptosis in rat traumatic brain injury model via activation of PI3K/Akt signaling pathway. Neurol Res 2016; 38:1-8.

LETTER TO THE EDITOR

Combining the platelet-to-albumin ratio with serum and pathologic variables to establish a risk assessment model for lymph node metastasis of gastric cancer

C. Huang, YQ. Xia, L. Xiao, J. Huang and ZM. Zhu

Department of Gastrointestinal Surgery, The Second Affiliated Hospital of Nanchang University, Nanchang, Jiangxi, China

Received October 29, 2020 – Accepted April 26, 2021

To the Editor,

Gastric cancer (GC) is a common malignant tumor, and its incidence ranks fifth among all cancers. Lymph node metastasis (LNM) is the most common form of metastasis in GC. LNM is the main factor affecting the prognosis of GC, so regional lymph node dissection is recommended in routine radical surgery for GC (1). Determining a reasonable range of lymph node dissection is a key step and an important factor to improve the prognosis. Relevant studies have found that tumor markers are related to LNM in GC (2). In addition, the host's systemic inflammatory response (SIR) is an important component of tumor progression. Recently, studies have confirmed that platelets play an important role in tumor progression (3). A large sample of studies reported that preoperative platelet counts were associated with increased LNM rates in GC (4), but the mechanism of the influence of platelets on the invasion and proliferation of GC cells remains to be further studied. Moreover, serum albumin (Alb) is used as an indicator of nutritional status, and low Alb levels have been related to poor survival of GC patients (5). Accurate evaluation of LNM before surgery is therefore of great significance for determining the scope of lymph node dissection and evaluating the prognosis. The aim of this study was to determine the independent risk factors for LNM in GC and to establish a risk assessment model that incorporated platelet-to-albumin ratio (PAR) for LNM, which would provide a reference for the determination of lymph node dissection scope during surgery.

MATERIALS AND METHODS

This is a retrospective study and was performed according to the guidelines of the Helsinki Declaration. The study was approved by the Ethics Committee of the Second Affiliated Hospital of Nanchang University and written informed consent was obtained from all patients.

The clinical data of 314 patients with GC diagnosed by postoperative pathology in The Second Affiliated Hospital of Nanchang University were collected from May 2017 to May 2019. According to whether there was LNM in the pathological specimens from the surgery, the patients were divided into a group without LNM and a group with LNM. There were 143 patients in the group without LNM (113 males, females), including 26 complicated with hypertension, 4 with diabetes and 42 who were smokers. The group with LNM consisted of 171 patients (114 males, 57 females), including 34 complicated with hypertension, 5 with diabetes and 32 who were smokers. There were no statistically significant differences in age (P=0.919), body

Key words: gastric cancer; lymph node metastasis; platelet-to-albumin ratio; serum tumor markers; risk factors; nomogram model

Corresponding Author:
Dr Zhengming Zhu,
Department of Gastrointestinal Surgery,
The Second Affiliated Hospital of Nanchang University,
No. 1 Minde Road, Nanchang, Jiangxi Province
Tel.: +86 0791 86312170
e-mail: yjsy@ncu.edu.cn

0393-974X (2021)
Copyright © by BIOLIFE, s.a.s.
This publication and/or article is for individual use only and may not be further reproduced without written permission from the copyright holder.
Unauthorized reproduction may result in financial and other penalties
DISCLOSURE: ALL AUTHORS REPORT NO CONFLICTS OF INTEREST RELEVANT TO THIS ARTICLE.

mass index (BMI) (P=0.315), hypertension (P=0.703), diabetes (P=0.947),neutrophil-to-lymphocyte ratio (NLR) (P=0.667), platelet-to-lymphocyte ratio (PLR) (P=0.213) or carcinoembryonic antigen (CEA) (P=0.229) between the two groups (Table I).

The inclusion criteria for patients were: treated with surgery; did not have neoadjuvant radiotherapy or chemotherapy before surgery; and a complete pathological report after surgery. Patients with bleeding, hyperthyroidism or hypothyroidism, acute infection, no radical resection, and incomplete data were excluded.

Surgical methods and postoperative pathology

Laparoscopically-assisted radical gastrectomy or open radical gastrectomy was performed. Distal gastric resection or total gastrectomy was performed according to the location of the tumor. The range of lymph node dissection was D2. In the group without LNM, there were 48 cases of low differentiation, 41 of medium-low differentiation, 52 of medium differentiation, and 2 of medium-high differentiation. There were 63, 18, 11 and 51 cases in T1, T2, T3 and T4, respectively. In the group with LNM, there were 99 cases of low differentiation, 41 of medium-low differentiation, 31 of medium differentiation, and 0 of medium-high differentiation. There were 8, 15, 32 and 116 cases in T1, T2, T3 and T4, respectively.

Statistical analysis

The single-sample Kolmogorov-Smirnov test was used for the normality of the data. If the quantitative data had a normal distribution, they are described as the mean ± standard deviation; otherwise, they are described as the median and interquartile range. Categorical variables were expressed as rate with 95% confidence intervals (CI). Univariate analysis between the two groups was performed using the Mann-Whitney U test. The indicators that were meaningful in univariate analysis were put into the logistic regression model. A classification tree is a nonlinear discriminant method that uses a set of independent variables to gradually decompose the sample into smaller subgroups. This procedure iterates on each branch of the tree, and selects the independent variable with the strongest correlation with the dependent variable according to specific criteria. The random forest algorithm was used to extract the important risk factors affecting the LNM of GC, and the mean decrease Gini (MDG) was used to rank the important indicators. The optimal cut-off value of important risk factors was determined by plotting the receiver operating characteristic (ROC) curve. The R software "rms" package was used to construct the nomogram model of risk assessment for LNM in GC. A *P* value less than 0.05 was considered statistically significant. Data were analyzed using SPSS 22.0 for Windows (SPSS Inc., Chicago, IL, USA) and R (version x64 3.5.1).

RESULTS

Univariate analysis showed that factors associated with LNM of GC were sex (P=0.032), smoking (P=0.027), lesion size (P=0.000), pathological type (P=0.001), differentiation degree (P=0.000), infiltration depth (P=0.000), PAR (P=0.005), carbohydrate antigen (CA) 19-9 (P=0.017), CA125 (P=0.000), and CA72-4 (P=0.005). The differences between the two groups were statistically significant (Table I).

The 10 variables with statistically significant differences in univariate analysis were gender, smoking, lesion size, pathological type, differentiation degree, infiltration depth, PAR, CA19-9, CA125, and CA72-4. The threshold values of 5 of these variables were calculated by ROC curve analysis. The area under the curve (AUC) of the lesion size was 0.758, the 95% CI was 0.705 to 0.811, the sensitivity was 86.5%, and the specificity was 53.8%. The AUC of the PAR was 0.592, the 95% CI was 0.529 to 0.655, the sensitivity was 79.5%, and the specificity was 36.4%. The AUC of CA19-9 was 0.578, the 95% CI was 0.515 to 0.642, the sensitivity was 42.1%, and the specificity was 77.6%. The AUC of CA125 was 0.618, the 95% CI was 0.556 to 0.680, the sensitivity was 69%, and the specificity was 51%. The AUC of CA72-4 was 0.593, the 95% CI was 0.530 to 0.655, the sensitivity was 60.8%, and the specificity was 56.6%. These data indicate that the accuracy, sensitivity and specificity of individual indicators to determine LNM were generally good (Table II). The ROC curve in Fig. 1 shows the accuracy, sensitivity and specificity of lesion size, PAR, CA19-9, CA125, CA72-4 and LNM of GC. By ROC curve evaluation, the cut-off values of lesion diameter, PAR, CA19-9, CA125 and CA72-4 were 2.65 cm, 4.61, 18.865 U/ml, 7.45 U/ml, and 1.655 IU/ml, respectively.

Table I. *General characteristics of patients with GC and comparison of the relevant factors between the two groups (n=314).*

Factors	Without LNM (n=143)	LNM (n=171)	*P* value
Age (years)	63(54,68)	62(54,69)	0.919
Sex (n)			0.032
Male	111	114	
Female	32	57	
BMI (kg/m^2)	21.48(19.78,23.62)	21.45(19.13,23.53)	0.315
Hypertension (n)			0.703
Yes	26	34	
No	117	137	
Diabetes (n)			0.947
Yes	4	5	
No	139	166	
Smoking (n)			0.027
Yes	42	32	
No	101	139	
Lesion size (cm)	2.5(1.5,4.0)	4.5(3.0,7.0)	0.000
Location(n)			0.886
Fundus of stomach	34	32	
Body of stomach	14	31	
Antrum of stomach	95	108	
Pathological type (n)			0.001
Ulcerative type	122	121	
Nodular bulge type	20	25	
Diffuse infiltration type	1	25	
Differentiation degree (n)			0.000
Low	48	99	
Medium-low	41	41	
Medium	52	31	
Medium-high	2	0	
Infiltration depth (n)			0.000
T1	63	8	
T2	18	15	
T3	11	32	
T4	51	116	
Detection indicators			
NLR	2.59(1.77,3.56)	2.43(1.72,3.60)	0.667
PLR	152.73(109.77,202.38)	160.61(118.44,214.71)	0.213
PAR	5.44(4.14,7.17)	5.99(4.71,7.80)	0.005
CEA (ng/ml)	2.83(1.90,4.87)	3.12(1.79,6.40)	0.229
CA19-9 (U/ml)	11.66(7.24,18.11)	14.94(7.76,28.38)	0.017
CA125 (U/ml)	7.40(5.60,11.30)	10.0(6.70,15.70)	0.000
CA72-4 (IU/ml)	1.51(0.97,2.90)	1.86(1.23,4.51)	0.005

Table II. *Relevant results of indicators.*

Factors	AUC	SE	*P* value	95% CI	Sensitivity	Specificity	Cut-off value
Lesion size	0.758	0.027	0.000	(0.705,0.811)	86.50%	53.80%	2.65
PAR	0.592	0.032	0.005	(0.529,0.655)	79.50%	36.40%	4.61
CA19-9	0.578	0.032	0.017	(0.515,0.642)	42.10%	77.60%	18.865
CA125	0.618	0.032	0.000	(0.556,0.680)	69.00%	51.00%	7.45
CA72-4	0.593	0.032	0.005	(0.530,0.655)	60.80%	56.60%	1.655

The above 10 variables with statistically significant differences in univariate analysis were analyzed by logistic stepwise regression, the results of which showed that the independent risk factors for LNM of GC were: lesion size (OR: 1.322; P = 0.000), differentiation degree (OR: 0.582; P = 0.001), and infiltration depth (OR: 1.734; P = 0.000). The accuracy, sensitivity, and specificity of the prediction of LNM in GC were 80.3%, 80.7%, and 69.2%, respectively.

Classification tree analysis to obtain decision rules affecting LNM in GC

The above 10 variables with statistically significant differences in univariate analysis were analyzed by using a classification tree to obtain decision rules affecting LNM in GC (Fig. 2). Six variables (infiltration depth, differentiation degree, CA125, size, CA19-9, and PAR) were selected through the classification tree program. The accuracy, sensitivity, specificity, positive predictive value and negative predictive value of the decision rules for detecting LNM in GC were 76.9, 71.4, 81.8, 77.8 and 76.3%, respectively, indicating that the decision rules were effective in the determination of LNM in GC.

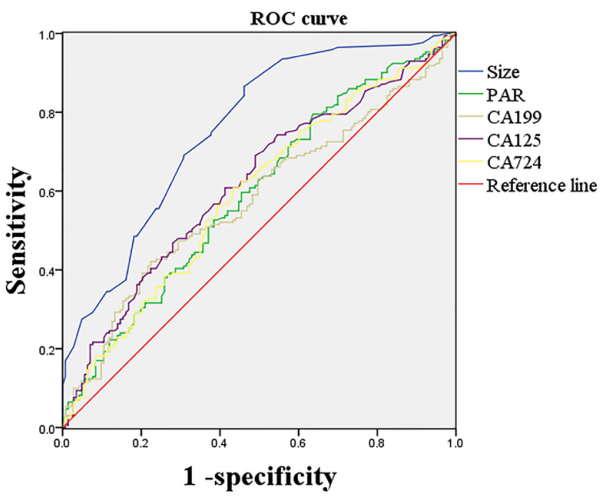


Fig. 1. *ROC curve of lesion size, PAR, CA19-9, CA125 and CA72-4.*

Random forest algorithm for extracting important risk factors of LNM in GC

The above 10 variables with statistically significant differences in univariate analysis were analyzed using a random forest algorithm to obtain the importance ranking of the variables. The larger the mean decrease Gini was, the more important the indicator was. The first was lesion size, followed by infiltration depth, CA125, CA19-9, PAR, CA72-4, differentiation degree, pathological type, sex and smoking.

Nomogram model for risk assessment of LNM in GC

Quantification assignments were based on the cut-off values for NLR, serum CEA, CA19-9, CA125, and CA72-4. A score of 1 was given if a lesion was greater than or equal to 2.65 cm and 0 if less than 2.65 cm; 1 if CA125 was greater than or equal to 7.45 U/ml and 0 if less than 7.45 U/ml; 1 if CA19-9 was greater than or equal to 18.865 U/ml and 0 if less than 18.865 U/ml; 1 if PAR was greater than or equal to 4.61 and 0 if less than 4.61; and 1 if CA72-4 was greater than or equal to 1.655 IU/ml and 0 if less than 1.655 IU/ml. After the assignment, the "rms" package of the R language was used to construct a logistic regression model combining PAR, lesion size, infiltration depth, CA125, CA19-9, CA72-4, and differentiation degree, and the C statistic of the evaluation was 0.827, which indicated that the prediction model had good accuracy. Then, the plotting function was constructed, and the

nomogram was plotted (Fig. 3). The score of lesions greater than or equal to 2.65 cm was 57 points, while the score of lesions less than 2.65 cm was 0 points; the score of CA125 greater than or equal to 7.45 U/ml was 31 points, while the score of CA125 less than 7.45 U/ml was 0 points; the score of CA19-9 greater than or equal to 18.865 U/ml was 27 points, while the score of CA19-9 less than 18.865 U/ml was 0 points; the score of PAR greater than or equal to 4.61 was 14 points, while the score of PAR less than 4.61 was 0 points; the score of CA72-4 greater than or equal to 1.655 IU/ml was 39 points, while the score of CA72-4 less than 1.655 IU/ml was 0 points; the score of T1 was 0 points; the score of T2 was 25 points; the score of T3 was 51 points; the score of T4 was 76 points; the score of low differentiation was 100 points; the

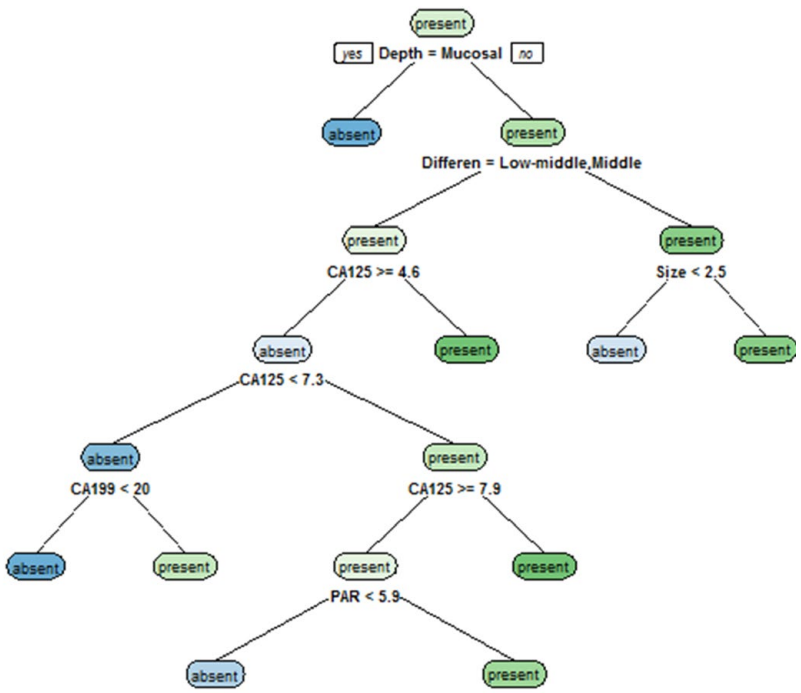


Fig. 2. *Classification tree for detecting undiagnosed LNM in GC.*

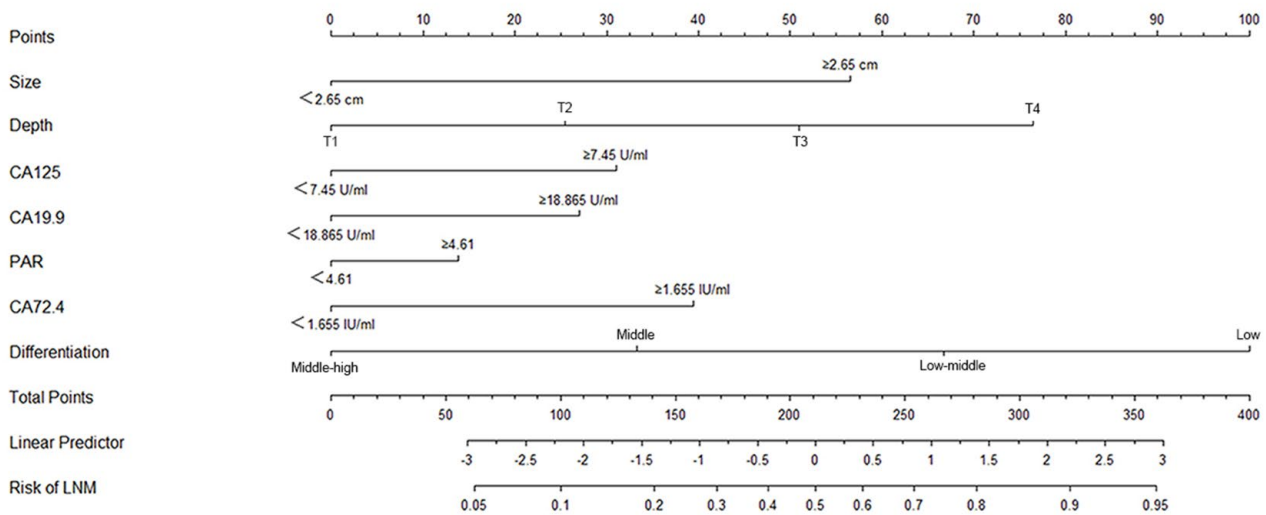


Fig. 3. *Nomogram of the logistic regression model.*

score of low-medium differentiation was 67 points; the score of medium differentiation was 33 points; the score of medium-high differentiation was 0 points. The risk of LNM in GC can be predicted based on the total points (Fig. 3). The area under the ROC curve of the combined factors was 0.827, the 95% CI was 0.782 to 0.873, the sensitivity was 77.2%, and the specificity was 74.8%, indicating that the prediction model had good accuracy, sensitivity and specificity.

DISCUSSION

LNM is an important indicator for judging the prognosis of GC (1). LNM rate of tumors invading the mucosa was 2.5%, while that of tumors invading the submucosa was 20.2%, suggesting that the depth of tumor invasion was closely related to LNM of GC (6). Poor tumor differentiation is an independent risk factor for LNM (7). Moreover, tumor markers were related to LNM in GC (2). Serum CA19-9 level was correlated with LNM in patients with GC (8). CA72-4 was the best predictor for progression of GC (9). Serum CA125 was an effective indicator for the clinical diagnosis of GC, as it could not only evaluate the efficacy of chemotherapy but also predict the prognosis of patients with peritoneal diffusion (10). Platelet levels can not only reflect tumor-related inflammatory response status but also predict the prognosis of some tumor patients, so the increase in platelet count is one of the signs of a poor prognosis of a tumor (11). Moreover, hypoalbuminemia can impair cellular immune function and ultimately lead to poor prognosis. Therefore, the Alb concentration is not only a nutritional indicator but also an indicator of the inflammatory response. Serum Alb level before treatment and tumor-node-metastasis (TNM) stage were the most important prognostic factors associated with survival in patients with GC (12).

In conclusion, lesions larger than 2.65 cm, poor differentiation and deep infiltration were high-risk factors for LNM in GC. The nomogram model constructed by PAR, lesion size, invasion depth, CA125, CA19-9, CA72-4, and differentiation degree, can well predict the risk of LNM in GC, providing a certain reference value for determining the range of intraoperative lymph node dissection.

ACKNOWLEDGEMENTS

This present study was supported by the National Natural Science Foundation of China (Grant Number: 81560389) and Key Research and Development Program of Jiangxi Province (Grant Number: 20181BBG70015).

REFERENCES

1. Guo J, Yu W, Su H Pang X. Genomic landscape of gastric cancer: molecular classification and potential targets. Sci China Life Sci 2017; 60:126-37.
2. Wang J, Yu JC, Kang WM, Wang WZ, Liu YQ Gu P. The predictive effect of cadherin-17 on lymph node micrometastasis in pN0 gastric cancer. Ann Surg Oncol 2012; 19:1529-34.
3. Goubran HA, Stakiw J, Radosevic M Burnouf T. Platelet-cancer interactions. Semin Thromb Hemost 2014; 40:296-305.
4. Hwang SG, Kim KM, Cheong JH, et al. Impact of pretreatment thrombocytosis on blood-borne metastasis and prognosis of gastric cancer. Eur J Surg Oncol 2012; 38:562-7.
5. Crumley AB, Stuart RC, McKernan M McMillan DC. Is hypoalbuminemia an independent prognostic factor in patients with gastric cancer? World J Surg 2010; 34:2393-8.
6. Shimada S, Yagi Y, Honmyo U, Shiomori K, Yoshida N Ogawa M. Involvement of three or more lymph nodes predicts poor prognosis in submucosal gastric carcinoma. Gastric Cancer 2001; 4:54-9.
7. Leers JM, DeMeester SR, Oezcelik A, et al. The prevalence of lymph node metastases in patients with T1 esophageal adenocarcinoma a retrospective review of esophagectomy specimens. Ann Surg 2011; 253:271-8.
8. Tsirlis TD, Kostakis A, Papastratis G, Masselou K, Vlachos I, Papachristodoulou A, Nikiteas NI. Predictive significance of preoperative serum VEGF-C and VEGF-D, independently and combined with Ca19-9, for the presence of malignancy and lymph node metastasis in patients with gastric cancer. J Surg Oncol 2010; 102:699-703.
9. Cidon EU Bustamante R. Gastric cancer: tumor markers as predictive factors for preoperative

staging. J Gastrointest Cancer 2011; 42:127-30.
10. Emoto S, Ishigami H, Yamashita H, Yamaguchi H, Kaisaki S Kitayama J. Clinical significance of CA125 and CA72-4 in gastric cancer with peritoneal dissemination. Gastric Cancer 2012; 15:154-61.
11. Tomimaru Y, Eguchi H, Gotoh K, et al. Platelet count is more useful for predicting posthepatectomy liver failure at surgery for hepatocellular carcinoma than indocyanine green clearance test. J Surg Oncol 2016; 113:565-9.
12. Onate-Ocana LF, Aiello-Crocifoglio V, Gallardo-Rincon D, et al. Serum albumin as a significant prognostic factor for patients with gastric carcinoma. Ann Surg Oncol 2007; 14:381-389.

LETTER TO THE EDITOR

Long non-coding RNA FGD5-AS1 is an inducer of cisplatin chemoresistance in gastric cancer cells by sponging miR-195

KH. Tong and J. Qian

Department of Gastrointestinal Surgery, The Affiliated People's Hospital of Ningbo University, Ningbo, Zhejiang Province, China

Received November 12, 2020 – Accepted January 25, 2021

To the Editor,

As a common gastrointestinal tumor, gastric cancer (GC) is the second leading cause of cancer-related deaths worldwide (1). GC patients are often diagnosed at an advanced stage, and their clinical outcomes remain largely unfavorable (2). Cisplatin (DDP) is still recognized as a first-line chemotherapy drug for GC patients, but unfortunately, chemoresistance largely limits its clinical application (3). Therefore, there is an urgent need to explore the etiology and detailed molecular mechanisms underlying DDP resistance in GC.

Long non-coding RNAs (lncRNAs) are characterized as a group of transcripts that are longer than 200 nucleotides. Although lncRNAs lack the potential of protein coding, recent studies have delineated that they may exert oncogenic or anti-oncogenic effects in several types of human cancers, including GC (4). FGD5 antisense RNA 1 (FGD5-AS1), which is located on human chromosome 3p25.1, is a well-studied oncogenic lncRNA in colorectal cancer (5), non-small cell lung cancer (6) and esophageal squamous cell carcinoma (7). The aim of this study was to evaluate the expression profile of FGD5-AS1 in GC samples, and uncover its potential involvement in DDP resistance.

MATERIALS AND METHODS

Patients and tissue samples

A total of 127 pairs of GC tissue samples and neighboring non-cancerous tissues (>2 cm from tumor border) were obtained from patients who underwent surgical resection at The Affiliated People's Hospital of Ningbo University (Ningbo, China). These patients had not received radiotherapy or chemotherapy prior to surgery. All fresh tissues were immediately frozen in liquid nitrogen and then stored at −80°C. The study was approved by the EthicsCommittee of The Affiliated People's Hospital of Ningbo University, and all participants provided written informed consent for sample collection in accordance with the Declaration of Helsinki.

Cell culture and treatments

GC cell lines (BGC-823, SGC-7901, MGC-803, MKN-45, HGC-27), human gastric mucosa cell line GES-1, and human embryonic kidney cell line HEK-293 were obtained from American Type Cell Collection (Manassas, VA, USA). GES-1 and HEK-293 cells were cultured in Dulbecco's modified Eagle's medium (DMEM; HyClone, Logan City, UT, USA); other cell lines were cultured in RPMI-1640 medium (HyClone), containing 10% fetal bovine serum (FBS; HyClone) and 1% penicillin/

Key words: gastric cancer; cisplatin chemoresistance; lncRNA FGD5-AS1; miR-195; exosomes

Corresponding Author:
Dr Kehui Tong,
Department of Gastrointestinal Surgery,
The Affiliated People's Hospital
of Ningbo University, Ningbo,
315040, Zhejiang Province, China
e-mail: kehuitong8848@sina.com

0393-974X (2021)
Copyright © by BIOLIFE, s.a.s.
This publication and/or article is for individual use only and may not be further reproduced without written permission from the copyright holder.
Unauthorized reproduction may result in financial and other penalties
DISCLOSURE: ALL AUTHORS REPORT NO CONFLICTS OF INTEREST RELEVANT TO THIS ARTICLE.

streptomycin at 37°C in a humidified atmosphere of 95% air and 5% CO_2.

To establish DDP-resistant GC cells, BGC-823 and SGC-7901 cells were exposed to incremental doses (from 0.05 μg/ml to 1 μg/ml) of DDP (Sigma-Aldrich, St. Louis, MO, USA) for 1 year. Before the experiments, DDP-resistant cells were cultured without DDP for one week.

Small interfering RNA (siRNA) targeting FGD5-AS1 (si-FGD5-AS1), non-targeting scrambled siRNA (si-NC), miR-195 mimic, mimic control (NC mimic), miR-195 inhibitor and inhibitor control (NC inhibitor) were designed and synthesized by Guangzhou RiboBio Co., Ltd. (Guangzhou, China). To overexpress FGD5-AS1, the full-length sequence of FGD5-AS1 cDNA was cloned into the mammalian expression vector pcDNA3.1(+) (Invitrogen, Carlsbad, CA, USA), and an empty pcDNA3.1 vector served as a negative control. Cell transfection was performed by Lipofectamine 2000 reagent (Invitrogen).

RT-qPCR analysis

Total RNA was extracted using Trizol reagent (Invitrogen), and first-strand cDNA was synthesized from 1 μg of total RNA by the PrimeScript RT reagent kit (TaKaRa, Dalian, China). Thereafter, qPCR analysis was performed using a SYBR Green PCR Kit (TaKaRa) on a 7500 Fast Real-Time Sequence detection system (Applied Biosystems, Foster City, CA, USA). The primer sequences were listed as follows: FGD5-AS1, 5′-AGAAGCGGAGGGGTGAAAAT-3′ (forward) and 5′-CCGCCTTATAGTTGGCCCTC-3′ (reverse); miR-195, 5′-TAGCAGCACAGAAATATTGGC-3′ (forward) and 5′-TGCTGTGCCAGCTGCAGT-3′ (reverse); GAPDH, 5′-GTCAAGGCTGAGAACGGGAA-3′ (forward) and 5′-AAATGAGCCCCAGCCTTCTC-3′ (reverse); U6, 5′-CTCGCTTCGGCAGCACA-3′ (forward) and 5′-AACGCTTCACGAATTTGCGT-3′ (reverse). The $2^{-\Delta\Delta Ct}$ method was used to calculate the relative gene expression (8). Data were normalized to GAPDH or U6 expression.

MTT assay

The sensitivity of cells to DDP was determined by MTT assay. Cells (3,000 cells/well) were seeded into 96-well plates, and treated with different doses of DDP for 48 h. Then 20 μl MTT (5mg/ml; Sigma-Aldrich) solution was added to each well. After incubation for additional 4 h, the culture medium was removed, and 150 μl DMSO was added to fully dissolve the crystal. A microplate reader (MultiskanEX, Lab systems, Helsinki, Finland) was used to detect the absorbance at 570 nm.

Exosomes separation and identification

The isolation of exosomes from culture medium was performed using the Total Exosome Isolation Reagent (Invitrogen). Exosome markers, including TSG101 and CD63, were detected by western blot analysis, and exosomal morphology was observed by a transmission electron microscope (TEM).

Western blot analysis

Total protein was extracted using RIPA buffer (Beyotime, Shanghai, China) containing protease inhibitor cocktail, and the concentration was detected using a BCA assay kit (Pierce Biotechnology, Inc., Rockford, IL, USA). Equal amounts of protein samples were separated by gel electrophoresis, and transferred onto PVDF membranes (Millipore, Bradford, MA, USA). After blocking in 5% nonfat milk for 1 h, the membranes were then incubated with the specific primary antibodies against CD63 (1:1000 dilution; cat. No. ab59479; Abcam, Cambridge, MA, USA) and TSG101 (1:500 dilution; cat. No. ab125011; Abcam) overnight at 4°C, followed by incubation with HRP-conjugated secondary antibody (1:5000 dilution; cat. No. sc-516102; Santa Cruz Biotechnology, Inc., Dallas, TX, USA) for 2 h at room temperature. The bands were then visualized by using an enhanced chemiluminescence reagent (Beyotime).

Dual-luciferase reporter assay

The fragment of FGD5-AS1 encompassing the putative target sites for miR-195 was amplified by PCR and then subcloned into the psiCHECK-2 luciferase reporter vector (Promega, Madison, WI, USA). The binding sites were mutated using the GeneTailor™ Site-Directed Mutagenesis System (Invitrogen). HEK-293 cells were seeded into 24-well plates and co-transfected with the recombinant plasmids and miR-195 mimic or mimic control. The cells were harvested at 48 h after transfection, and the luciferase activity was measured with the Dual-Luciferase Reporter Assay system (Promega).

RNA immunoprecipitation (RIP) assay

EZ-Magna RIP™ RNA-Binding Protein

Immunoprecipitation Kit (Millipore) was used for RIP assay. Cells were lysed in RIP lysis buffer, and incubated with magnetic beads conjugated with anti-Ago2 or IgG antibody. The immunoprecipitated RNA samples were then subjected to RT-qPCR analysis.

Statistical analysis

All statistical analyses were performed by using GraphPad Prism 6.0 software (GraphPad Software Inc., San Diego, CA, USA) and SPSS 18.0 software (IBM Corporation, Armonk, NY, USA). All experiments were repeated three times, and continuous data are expressed as mean ± standard deviation (SD). Comparison between groups was performed by Student's *t*-test or one-way ANOVA. The enumeration data were analyzed by *Chi*-squared test. The correlation between FGD5-AS1 and miR-195 expression was analyzed by Pearson correlation coefficient. *P* values were calculated and those less than 0.05 were considered significant.

RESULTS

FGD5-AS1 is upregulated in GC samples

Through RT-qPCR analysis, we observed that the expression level of FGD5-AS1 in GC tissues was obviously higher compared to neighboring non-cancerous tissues (Fig. 1A). Moreover, overexpressed FGD5-AS1 was also found in a series of GC cell lines (BGC-823, SGC-7901, MGC-803, MKN-45, HGC-27), compared to normal GES-1 cells (Fig. 1B).

The association between FGD5-AS1 expression and clinicopathological characteristics of GC patients was then examined. Based on the cut-off value of intratumoral FGD5-AS1 expression, 127 GC patients were allocated to High expression group (N=55) and Low expression group (N=72). As shown in Table I, GC patients with high FGD5-AS1 expression tended to have larger tumor size (*P*=0.046) and advanced TNM stage (*P*=0.033).

Table I. *Association between FGD5-AS1 expression and clinicopathological characteristics of GC patients.*

Characteristics	Total number (N=127)	FGD5-AS1 expression		*P* value
		High (N=55)	Low (N=72)	
Age (years)				0.284
≥55	67	32	35	
<55	60	23	37	
Gender				0.653
Male	78	35	43	
Female	49	20	29	
Tumor size (cm)				0.046
≥5	52	28	24	
<5	75	27	48	
Location				0.352
Cardia+body	82	38	44	
Pylorus	45	17	28	
Distant metastasis				0.098
Yes	43	23	20	
No	84	32	52	
Lymph node invasion				0.185
Yes	70	34	36	
No	57	21	36	
TNM stage				0.033
I-II	78	31	47	
III-IV	49	24	25	

FGD5-AS1 is upregulated in DDP-resistant GC cells

The involvement was evaluated of FGD5-AS1 in DDP resistance of GC cells. As shown in Fig. 1C, BGC-823/DDP and SGC-7901/DDP cells showed more powerful resistance to DDP than their parental cells. Moreover, FGD5-AS1 expression was remarkably increased in BGC-823/DDP and SGC-7901/DDP cells, compared to their parental cells (Fig. 1D). FGD5-AS1 expression was then effectively silenced by transfecting si-FGD5-AS1 into BGC-823/DDP and SGC-7901/DDP cells (Data not shown), and MTT assay indicated that FGD5-AS1 knockdown markedly weakened the DDP resistance (Fig. 1E). Furthermore, FGD5-AS1 was overexpressed in BGC-823 and SGC-7901 cells (Data not shown), and the chemosensitivity of these cells to DDP was notably reduced (Fig. 1F).

Exosome-mediated transfer of FGD5-AS1 disseminates DDP resistance in GC cells

The exosomes in the culture medium of DDP-resistant GC cells and parental cells were then isolated, and the morphological characteristics of these exosomes are shown in Fig.2A. Their size was 50–200 nm. Western blot analysis further confirmed the expression of exosome markers, including TSG101 and CD63 (Fig. 2B). As anticipated, exosomal FGD5-AS1 expression was markedly higher in BGC-823/DDP and SGC-7901/DDP cells than in parental cells (Fig. 2C). Then the exosomes of DDP-resistant GC cells were used to treat parental cells, and it was observed that BGC-823 and SGC-7901 cells became insensitive to DDP (Fig. 2D).

FGD5-AS1 directly interacts with miR-195 in GC

FGD5-AS1 was mainly distributed in the cytoplasm of BGC-823 and SGC-7901 cells (Fig. 3A), indicating the post-transcriptional regulation of FGD5-AS1 in GC. Then, the potential binding sites of FGD5-AS1 and miR-195 were predicted by Starbase database (http://starbase.sysu.edu.cn/index.php), as shown in Fig. 3B. Dual-luciferase reporter

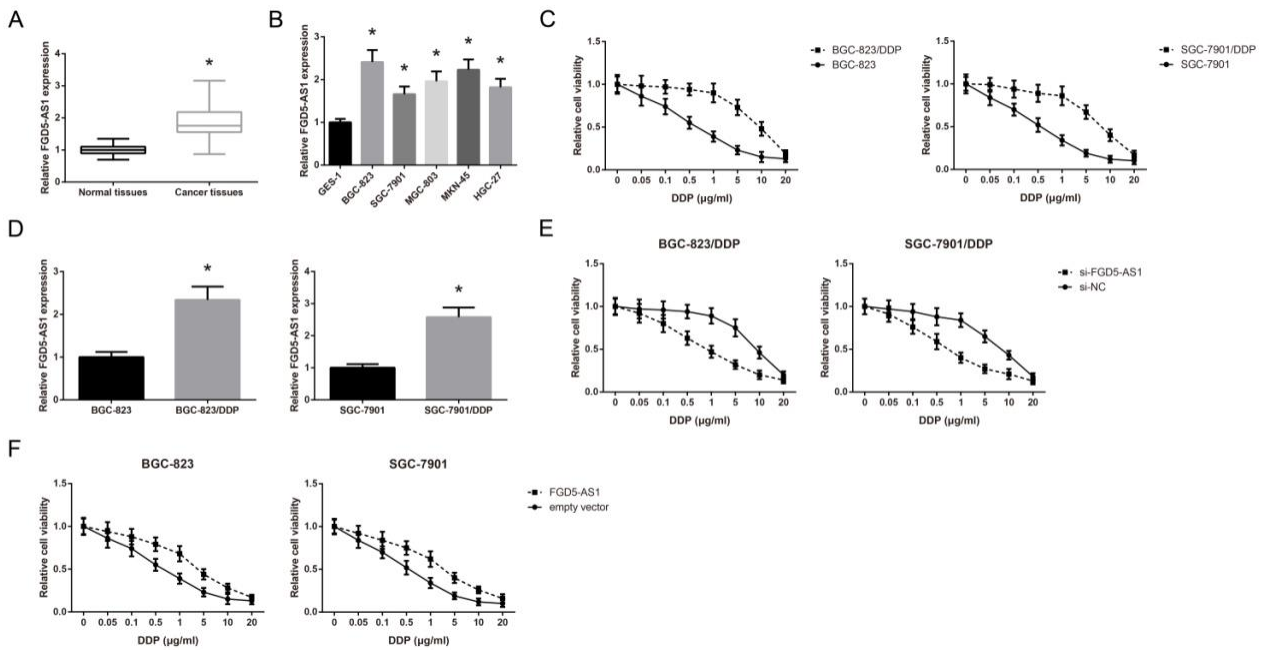


Fig. 1. *FGD5-AS1 is upregulated in GC samples and DDP-resistant GC cells. **A)** Expression levels of FGD5-AS1 in GC tissues and neighboring normal tissues, detected by RT-qPCR analysis. **B)** Expression levels of FGD5-AS1 in GC cell lines and normal GES-1 cells. **C)** Chemosensitivity of DDP-resistant cells and their parental cells to DDP. **D)** Expression levels of FGD5-AS1 in DDP-resistant cells and their parental cells. **E)** The effect of FGD5-AS1 knockdown on the chemosensitivity of DDP-resistant cells to DDP. **F)** Effect of FGD5-AS1 overexpression on the chemosensitivity of parental cells to DDP. *P<0.05 vs normal tissues, GES-1 cells or parental cells.*

assay was then carried out, and the luciferase activity of FGD5-AS1-WT reporter was markedly decreased by miR-195 mimic in HEK-293 cells; however, it failed to suppress the luciferase activity when the binding sites were mutated (Fig. 3C). In addition, RIP assay indicated that miR-195 could be co-immunoprecipitated with FGD5-AS1 by Ago2 antibody in BGC-823 and SGC-7901 cells (Fig. 3D).

The decreased expression levels of miR-195 in BGC-823/DDP and SGC-7901/DDP cells were notably restored by si-FGD5-AS1 (Fig. 3E), while FGD5-AS1 overexpression markedly reduced miR-195 expression in BGC-823 and SGC-7901 cells (Fig. 3F). The downregulation was also confirmed of miR-195 in clinical GC tissues and cell lines (Fig.3 G-H). The negative correlation between FGD5-AS1

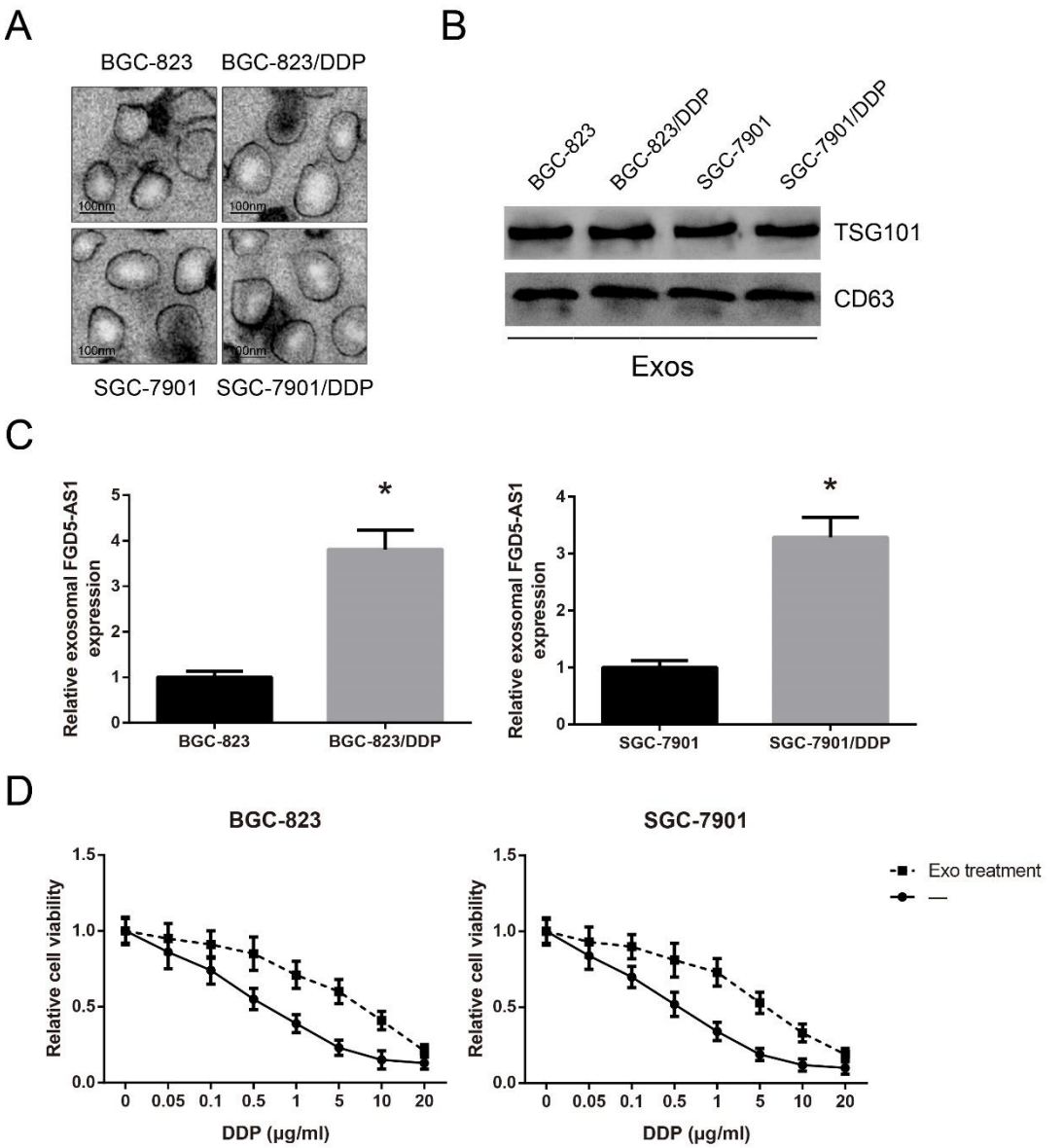


Fig. 2. *Exosome-mediated transfer of FGD5-AS1 disseminates DDP resistance in GC cells.* ***A****) Morphological characteristics of exosomes, detected by TEM.* ***B****) Expression levels of exosome markers, detected by western blot analysis.* ***C****) Expression levels of FGD5-AS1 in the exosomes of DDP-resistant cells and their parental cells.* ***D****) Chemosensitivity of parental cells to DDP after exosome-mediated transfer of FGD5-AS1. *P<0.05 vs parental cells.*

and miR-195 levels was then observed in GC tissues (r=−0.212, *P*=0.017; Fig. 3I).

miR-195 inhibition blocks the effect of FGD5-AS1 knockdown on DDP resistance in GC cells

We also observed that restoration of miR-195 overcame DDP resistance in BGC-823/DDP and SGC-7901/DDP cells (Fig. 4A). To further confirm whether FGD5-AS1 exerted its function partly via miR-195, DDP-resistant GC cells were co-transfected with si-FGD5-AS1 and miR-195 inhibitor. MTT assay demonstrated that the suppressive role of FGD5-AS1 knockdown against DDP resistance was notably abrogated by miR-195 inhibition (Fig. 4B). Moreover, as shown in Fig. 4C, the enhanced DDP resistance of BGC-823 and SGC-

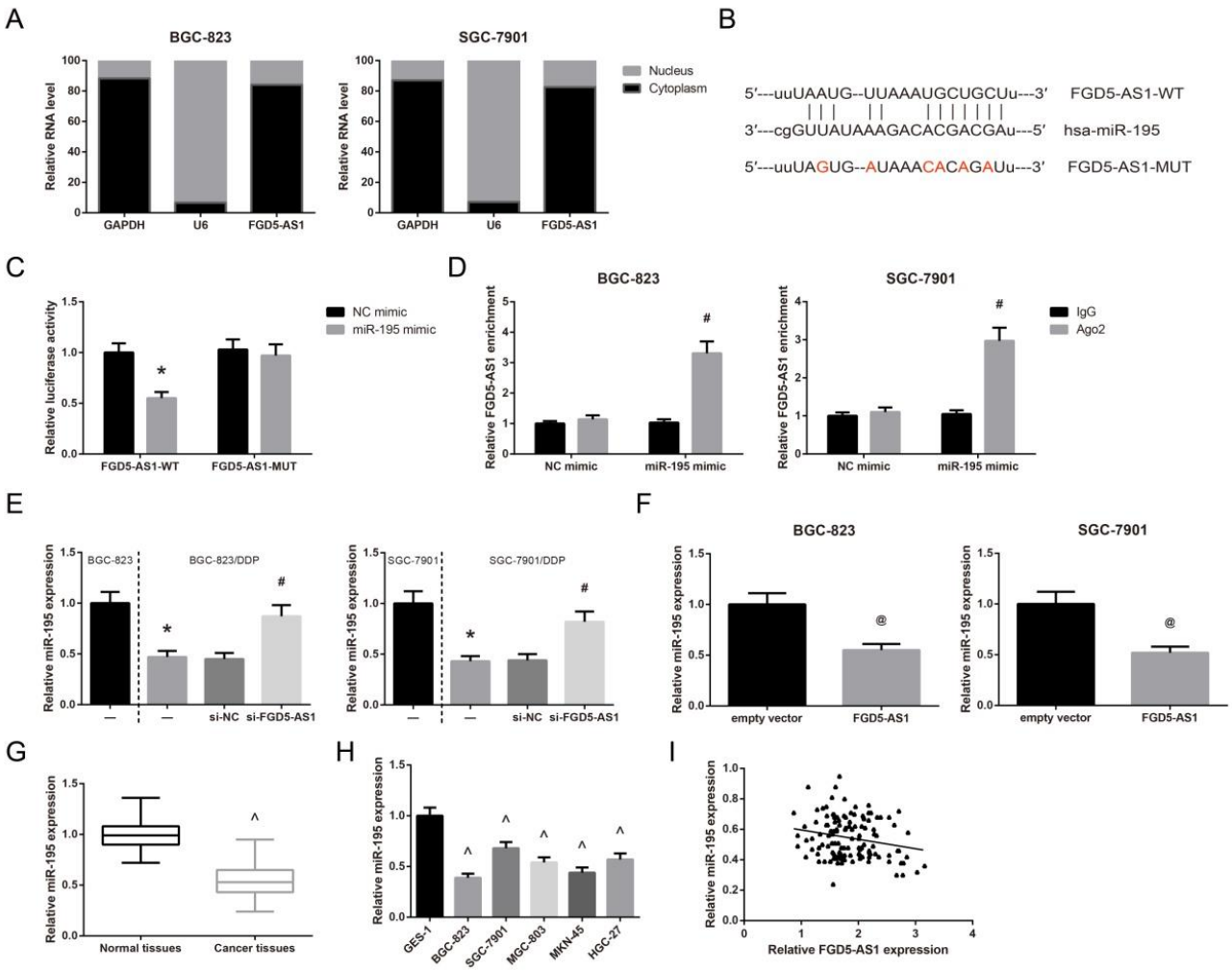


Fig. 3. *FGD5-AS1 directly interacts with miR-195 in GC. **A**) Subcellular distribution of FGD5-AS1 in GC cells. B) Putative binding sites of miR-195 in FGD5-AS1 fragment. **C**) The luciferase activity of recombinant plasmids in HEK-293 cells after transfection. **D**) The immunoprecipitated FGD5-AS1 and miR-195 in GC cells. **E**) Expression levels of miR-195 in DDP-resistant cells after transfection. **F**) Expression levels of miR-195 in parental cells after transfection. **G**) Expression levels of miR-195 in GC tissues and neighboring normal tissues. **H**) Expression levels of miR-195 in GC cell lines and normal GES-1 cells. **I**) Correlation between the expression levels of FGD5-AS1 and miR-195 in GC tissues. *P<0.05 vs NC mimic-transfected cells or parental cells; #P<0.05 vs IgG group or si-NC-transfected cells; @P<0.05 vs empty vector-transfected cells; ^P<0.05 vs normal tissues or GES-1 cells.*

7901 cells with FGD5-AS1 overexpression was markedly diminished by miR-195 restoration.

DISCUSSION

LncRNAs have gained increasing attention in the field of cancer biology in recent years. The development of DDP resistance in GC is known as a multistep process, and some relevant lncRNAs have been reported. For instance, Li et al. showed that knockdown of lncRNA CASC2 weakened the response of GC cells to DDP (9). In addition, lncRNA SNHG5 was found to promote DDP resistance in GC by inhibiting cell apoptosis.

The present study confirmed that FGD5-AS1 is upregulated in clinical GC samples. Moreover, it was shown that FGD5-AS1 is upregulated in DDP-resistant GC cells, and knockdown of FGD5-AS1 notably reduced the drug resistance. Exosomes, a subclass of extracellular vesicles, could mediate cell-cell crosstalk in cancer progression and drug resistance by transferring bioactive factors, including lncRNAs

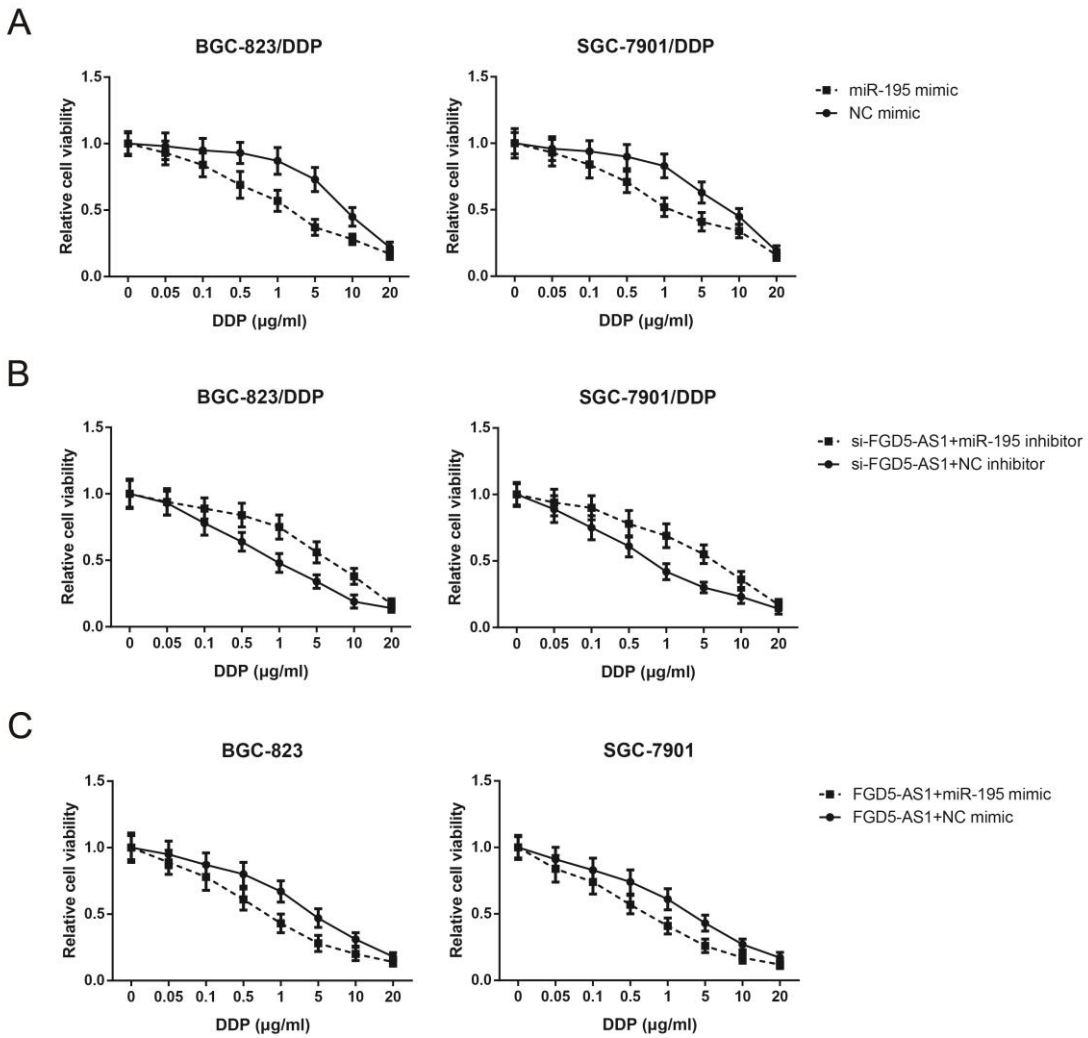


Fig. 4. *miR-195 inhibition blocks the effect of FGD5-AS1 knockdown on DDP resistance in GC cells.* ***A****) Effect of miR-195 restoration on the chemosensitivity of DDP-resistant cells to DDP.* ***B****) Effect of miR-195 inhibition on the chemosensitivity of DDP-resistant cells with FGD5-AS1 knockdown to DDP.* ***C****) Effect of miR-195 restoration on the chemosensitivity of parental cells with FGD5-AS1 overexpression to DDP.*

(10). Wang et al. reported that exosome-mediated transfer of lncRNA HOTTIP promotes DDP resistance in GC cells (11). Our study showed that DDP-resistant cells secreted high levels of exosomal FGD5-AS1, and transmitted these exosomes to parental cells, thus inducing DDP resistance.

A ceRNA hypothesis, proposed by Salmena et al. in 2011, indicated that lncRNAs may function as ceRNAs to interact with miRNAs, thereby reducing their expression and function (12). In this study, miR-195 was selected for further analysis because it was widely reported as a tumor suppressor in GC. miR-195 overexpression also enhanced the chemotherapy sensitivity of DDP in GC cells. Our study indicated that FGD5-AS1 could bind directly to miR-195 and suppress its expression in GC. Furthermore, rescue experiments showed that inhibition of miR-195 diminished the suppressive role of FGD5-AS1 knockdown on DDP resistance.

In conclusion, this study may be the first direct report to show that overexpressed FGD5-AS1 induces DDP resistance in GC cells partly by sponging miR-195, providing a novel insight to understanding the DDP resistance in GC.

REFERENCES

1. Sitarz R, Skierucha M, Mielko J, Offerhaus GJA, Maciejewski R, Polkowski WP. Gastric cancer: epidemiology, prevention, classification, and treatment. Cancer Manag Res 2018; 10:239-48.
2. Yoon H, Kim N. Diagnosis and management of high risk group for gastric cancer. Gut Liver 2015; 9(1):5-17.
3. Dasari S, Tchounwou PB. Cisplatin in cancer therapy: molecular mechanisms of action. Eur J Pharmacol 2014; 740:364-78.
4. Wang Y, Yang F, Yang Q. The regulatory roles and potential prognosis implications of long non-coding RNAs in gastric cancer. Histol Histopathol 2020; 35(5):433-42.
5. Li D, Jiang X, Zhang X, Cao G, Wang D, Chen Z. Long noncoding RNA FGD5-AS1 promotes colorectal cancer cell proliferation, migration, and invasion through upregulating CDCA7 via sponging miR-302e. In Vitro Cell Dev Biol Anim 2019; 55(8):577-85.
6. Fan Y, Li H, Yu Z, Dong W, Cui X, Ma J, Li S. Long non-coding RNA FGD5-AS1 promotes non-small cell lung cancer cell proliferation through sponging hsa-miR-107 to up-regulate FGFRL1. Biosci Rep 2020; 40(1):BSR20193309.
7. Gao J, Zhang Z, Su H, Zong L, Li Y. Long Noncoding RNA FGD5-AS1 Acts as a Competing Endogenous RNA on microRNA-383 to Enhance the Malignant Characteristics of Esophageal Squamous Cell Carcinoma by Increasing SP1 Expression. Cancer Manag Res 2020; 12:2265-78.
8. Livak KJ, Schmittgen TD. Analysis of relative gene expression data using real-time quantitative PCR and the 2(-Delta Delta C(T)) method. Methods 2001; 25(4):402-8.
9. Li Y, Lv S, Ning H, Li K, Zhou X, Xv H, Wen H. Down-regulation of CASC2 contributes to cisplatin resistance in gastric cancer by sponging miR-19a. Biomed Pharmacother 2018; 108:1775-82.
10. Dragomir M, Chen B, Calin GA. Exosomal lncRNAs as new players in cell-to-cell communication. Transl Cancer Res 2018; 7(Suppl 2):S243-S252.
11. Wang J, Lv B, Su Y, Wang X, Bu J, Yao L. Exosome-Mediated Transfer of lncRNA HOTTIP Promotes Cisplatin Resistance in Gastric Cancer Cells by Regulating HMGA1/miR-218 Axis. Onco Targets Ther 2019; 12:11325-38.
12. Salmena L, Poliseno L, Tay Y, Kats L, Pandolfi PP. A ceRNA hypothesis: the Rosetta Stone of a hidden RNA language? Cell 2011; 146(3):353-58.

LETTER TO THE EDITOR

Beyond pre-analytical and analytical concerns in the study of synovial fluid proteome: description of an optimized Gel-based protocol

D. Bizzoca[1*], M. T. Rocchetti[2*], S. Scacco[3], F. Taurino[3], G. Vicenti[1], F. Spadaccino[3], L. Moretti[1], E. Ranieri[2], L. Gesualdo[4], F. Moretti[5], G. Peretti[6,7], G. Banfi[8], B. Moretti[1#] and A. Gnoni[2#]

[1]Orthopaedics and Trauma Unit, Department of Basic Medical Sciences, Neuroscience and Sense Organs, University of Bari "Aldo Moro", Bari, Italy; [2]Center of Molecular Medicine, Department of Medical and Surgical Sciences, University of Foggia, Foggia, Italy; [3]Section of Clinical Biochemistry, Department of Basic Medical Sciences, Neuroscience and Sense Organs, University of Bari "Aldo Moro", Bari; [4]Department of Emergency and Organ Transplantation, University of Bari "Aldo Moro", Bari; [5]National Center For Chemicals, Cosmetic Products And Consumer Protection, National Institute of Health, Rome, Italy; [6]Department of Biomedical Sciences for Health, University of Milan; [7]IRCCS Istituto Ortopedico Galeazzi, Milan; [8]University Vita-Salute San Raffaele, School of Medicine, Milano.

**These authors contributed equally to this work (co-first authors)*
#These authors contributed equally to this work (co-last authors)

To the Editor,

Synovial fluid (SF) is a highly viscous and mucinous substance, whose viscosity mainly depends on its high concentration of hyaluronic acid. SF is produced by the synovium, a specialized connective tissue that lines diarthrodial joints. SF mainly aims to lubricate joints, but it also allows the circulation of nutrients and catabolites between the avascular articular cartilage and the vascularized synovial membrane (1). SF is an ultrafiltrate of plasma, thus synovial proteome includes both plasmatic proteins and proteins secreted from the surrounding tissues (e.g. the articular cartilage and synovium) (1-3).

As SF is in the closest proximity with the joint tissues, which are primarily altered during articular diseases, it could provide relevant information in orthopaedic and rheumatologic diseases (4,5). However, the lack of normal SF samples is a big concern in the study of this biologic fluid.

Proteome analysis or "proteomics" is the large-scale protein-based systematic analysis of the protein content, from a cell, tissue or entire organism (5), Proteomic plays a key role in the search for disease-specific biomarkers, which could be also selectively modulated with specific drugs (5,6).

Several studies have focused on the study of SF fluid proteome in joint diseases, however, the lack of consensus arises on the preanalytical issues, including i) the SF collection (e.g. several studies have analyzed *post-mortem* SF samples or animal samples), ii) its storage, iii) the treatment to overcome its viscosity (e.g. SF is treated with different concentrations of hyaluronidase, that breaks down hyaluronic acid and chondroitin sulfate) and analytical, issues mainly related to the strategies used to obtain highly abundant SF proteins depletion (6). Hence, SF has a large protein concentration dynamic range (3), that

Keywords: synovial fluid; proteomics; two-dimensional electrophoresis (2DE); hyaluronidase

Corresponding Author:
Dr Antonio Gnoni
Section of Clinical Biochemistry,
Department of Basic Medical Sciences,
Neuroscience and Sense Organs,
University of Bari "Aldo Moro", AOU Consorziale Policlinico.
Piazza Giulio Cesare 11, 70124 Bari, Italy
e-mail: antonio.gnoni@uniba.it

0393-974X (2021)
Copyright © by BIOLIFE, s.a.s.
This publication and/or article is for individual use only and may not be further reproduced without written permission from the copyright holder.
Unauthorized reproduction may result in financial and other penalties
DISCLOSURE: ALL AUTHORS REPORT NO CONFLICTS OF INTEREST RELEVANT TO THIS ARTICLE.

could mask the detection of low abundant proteins thus compromising SF proteome analysis (7).

This study aims to define an optimized sample processing protocol for human synovial fluid proteome analysis, employing a gel-based proteomics approach.

MATERIAL AND METHODS

Patient selection

In the present study, 16 SF samples were collected from patients undergoing knee arthroscopy for acute meniscal (mean age: 24.65 years old) at the Orthopaedic and Trauma Unit, University of Bari "Aldo Moro", between January 2019 and January 2020. Exclusion criteria: diabetes mellitus; coagulopathies; rheumatoid arthritis or other autoimmune arthritis; chronic inflammatory diseases; previous surgery of the affected knee; previous intra-articular injections in the last 12 months; osteoarthritis; obesity; the history of joint infection.

All the patients underwent a preoperative clinical, radiographic and laboratory evaluation, following the current clinical practice standards. During enrolment, anthropometric data, drugs assumption and comorbidities were recorded.

Ethical clearance was obtained from our centre's clinical research ethics as per the 1964 Declaration of Helsinki (code: SINOVIALE-20), all participants signed a consent form before enrollment in the study.

Synovial fluid sample collection

The patient underwent local anaesthesia and then was positioned in supine decubitus with a pneumatic tourniquet applied to the thigh and set at 100 mmHg over the systolic pressure, to avoid blood contamination. The SF samples were obtained through knee joint arthrocentesis, before starting the arthroscopic surgical procedure. A heparinized syringe with an 18 gauche needle was inserted into the suprapatellar pouch of the knee and 2-4 mL of synovial fluid were aspirated and aliquoted into 500µl amounts. Each 500 µl aliquoted sample was centrifuged at 400´g at 4°C for 5 min to remove cells and debris. The aliquoted samples were then stored at -80°C in liquid nitrogen until analysis. A single frozen sample was thawed and used only once.

Experimental Protocol 1: the search for the optimal hyaluronidase concentration

Cell-free SF samples from non-arthritic patients (i.e. patients undergoing knee arthroscopy for acute meniscal injury) were treated with 1 µg/mL hyaluronidase (Sigma-Aldrich, Gillingham, UK) at 37°C for 1 h, or with 1 mg/mL hyaluronidase (Sigma-Aldrich, Gillingham, UK) at 37°C for 1 h, to assess the optimal hyaluronidase concentration. All samples were then centrifuged at 10.000´g, at 5°C for 10 min. The total protein concentration of SF was measured by a colourimetric assay based on the Bradford dye-binding method (BioRad Protein assay) yielding a mean of 13µg/µL (±1.4).

Experimental Protocol 2: the search for the optimal high-abundance protein depletion technique

The SF samples treated with 1 µg/mL hyaluronidase underwent two different high-abundance protein depletion techniques. All the samples were divided into two aliquots, one of which was treated with affinity columns (ProteoPrep® Immunoaffinity Albumin and IgG Depletion Kit, Sigma-Aldrich, Gillingham, UK) and processed according to the manufacturer's instructions.

The remaining SF aliquot was concentrated by 3-kDa cut-off Amicon filter devices (Millipore, Billerica, MA) to reach the concentration of about 25 µg/µL and treated with ProteoMiner™ Small Capacity beads (Bio-Rad Laboratories, Hercules, California, USA). 5 mg of SF proteins were appropriately adapted to its spin column and processed according to the manufacturer's instructions.

Following both the high-abundance protein depletion techniques, all SF samples were then centrifuged (10.000´g, at 5°C for 10 min) and the protein concentration was determined by Bradford assay.

Two-dimensional gel electrophoresis (2DE)

SF proteins enriched with the two different methods were then analyzed by 2D-PAGE, as previously described by Taurino et al.(6), with minor modifications. Briefly, isoelectrofocusing (IEF) was carried out using 7 cm pH 3-10 NL gradient Immobiline IPG strips, previously rehydrated with 125µL IEF buffer overnight at 20°C. Forty µg of SF proteins were loaded onto rehydrated IPG strips and focused for a total of 22 kVh produced by overnight run (PROTEAN IEF cell, Bio-Rad) and then stored at -70°C.

After strips equilibration, the second-dimension run was carried out using NuPAGE™ 4-12% Bis-Tris ZOOM™ Protein Gels (Thermo Fisher Scientific Waltham, Massachusetts, USA). Both NuPAGE™

Table I. *Patients' data.*

Patients (n)	16
Age	
Mean ±SD	24.65±4.73
Range	19-34
Gender	
Male, n (%)	11 (68.75%)
Female, n (%)	5 (31.25%)
BMI (Kg/m^2)	
Mean ±SD	22.16 ±1.7
Smoking status	
# of smokers, n (%)	2 (12.5%)

BMI= Body Mass Index; CRP= C-Reactive Protein; SD= Standard Deviation.

MES SDS Running Buffer and NuPAGE™ MOPS SDS Running Buffer were used. Gels were stained with SYPRO® Ruby (Invitrogen™, Carlsbad, CA) according to the manufacturer's protocol and acquired with a PROXPRESS 2D scanner (Perkin ElmerLife Sciences, Cambridge, UK). Image Master Platinum 2D software was used for image analysis of analytical 2D gels as previously described (7). 2DE gels of all SF samples were run at the list in duplicate.

Statistical analysis

The results of the quantitative variables were expressed as mean ± SD. Statistical analysis was performed using SPSS software (version 23; IBM Corp, Armonk, NY). The Mann-Whitney U test was used. Statistical significance was set at $p<0.05$ level of confidence.

RESULTS

The demographic and clinical data of the patients enrolled in the study are summarized in Table I. Sixteen patients were recruited, with a mean age of 24.65 years old; 31.5% of patients were females and 68.75% males.

First, we evaluate the impact of two very different hyaluronidase concentrations on SF samples, and we found that 1 µg/mL was enough to reduce the viscosity of SF, making it suitable for subsequent proteomic analysis.

Table II shows the mean protein spots number in samples treated with different hyaluronidase concentrations. Image analysis provided a significantly lower protein spots number with 1mg/mL compared with 1 µg/mL hyaluronidase-treated SF ($p=0.001$; black arrows in Figure-1A). Subsequently, we evaluated the efficacy of two major methods for abundant plasma proteins depletion in SF. Specifically, we assessed the effect of albumin and IgG depletion kit and ProteoMiner™ on the number of protein spots identified in the 2DE proteomic map of SF.

Table III shows the mean protein spots number in SF samples without depletion, in SF samples treated with affinity columns or ProteoMiner™. A significantly higher protein spots number was obtained in SF samples treated with ProteoMiner™, compared with albumin and IgG-depleted kit ($p= 0.001$). The non-depleted SF samples shared 56.6% protein spots with immune-depleted samples (mean=215) and 59.8% protein spots with ProteoMiner™ treated samples (mean=277, Table III). Moreover, 273 mean protein spots were shared between immune-depleted and ProteoMiner-treated SF samples and 171 mean protein spots were shared among the three differently treated SF aliquots.

Table II. *Mean protein spots number in samples treated with different concentrations of hyaluronidase: comparison between groups (Mann-Whitney U test).*

	Samples treated with 1µg/mL hyaluronidase	Samples treated with 1mg/mL hyaluronidase	***p*-value**
Protein spots number (Mean ±SD)	418±57	288±40	**0.001***

*significant p-value

Table III. *Mean protein spots number in samples without depletion, treated with affinity columns (ProteoPrep® Immunoaffinity Albumin and IgG Depletion Kit) or treated with ProteoMiner™.*

	Samples without depletion	Samples treated with affinity columns only (ProteoPrep®)	Sample treated with ProteoMiner™	*p*-value§	Contrasts *p*-value°
Protein spots number (Mean ±SD)	367±50	351±47	611±70	**0.003***	0.783 undepleted samples vs ProteoPrep **0.001*** undepleted samples vs ProteoMiner **0.001*** ProteoPrep vs ProteoMiner
Number of protein spots shared with untreated samples Mean (%)	-	215 (56.6%)	277 (59.8%)	-	-

*§Kruskal-Wallis test; °Mann-Whitney U test; *significant p-value*

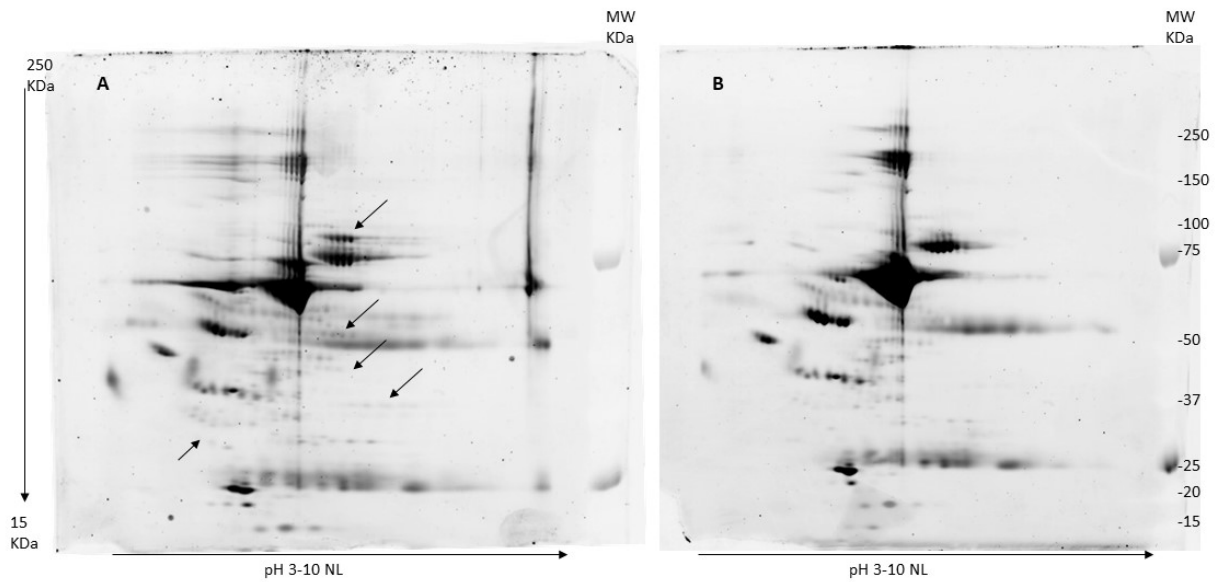


Fig. 1. *Two-dimensional gels of two SF aliquots of the same sample, stained with SYPRO Ruby. Representative 2D gel of SF diluted (1:1, v/v) with solubilization buffer containing **A)** 1 µg/mL of hyaluronidase or **B)** 1 mg/mL of hyaluronidase. MW markers: Precision Plus dual colour (Bio-Rad). The arrows indicate protein spots more expressed in the 2D gel of SF proteome obtained treating the sample with a lesser amount of hyaluronidase.*

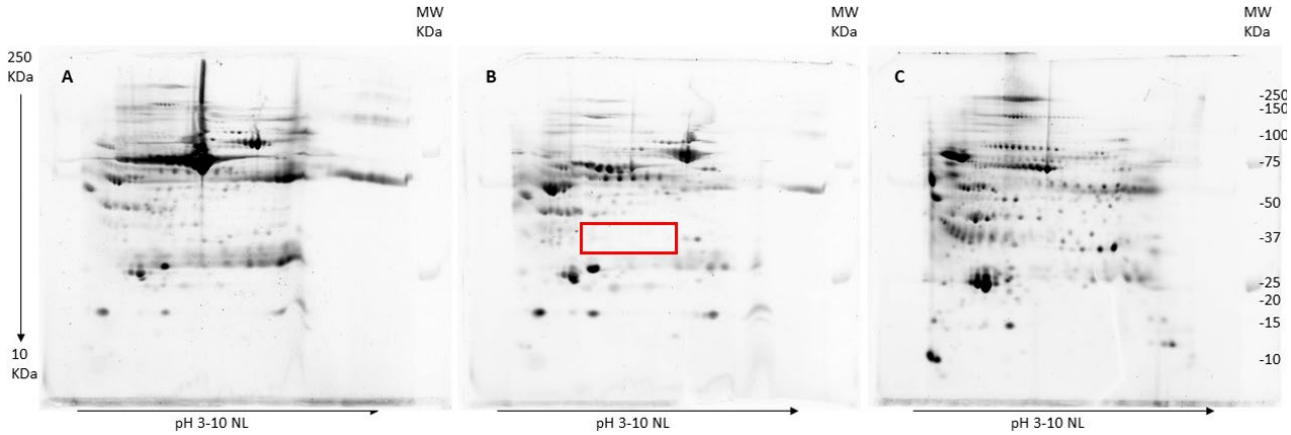


Fig. 2. *Two-dimensional gels of three aliquots of the same SF samples, stained with SYPRO Ruby.* ***A)*** *Representative 2D gel of SF;* ***B)*** *albumin depleted SF by ProteoPrep;* ***C)*** *SF treated by ProteoMiner™. MW markers: Precision Plus dual colour (Bio-Rad, Hercules, California, USA). The red box indicates protein spots less expressed in the 2D gel of SF proteome albumin and IgG depleted by affinity column.*

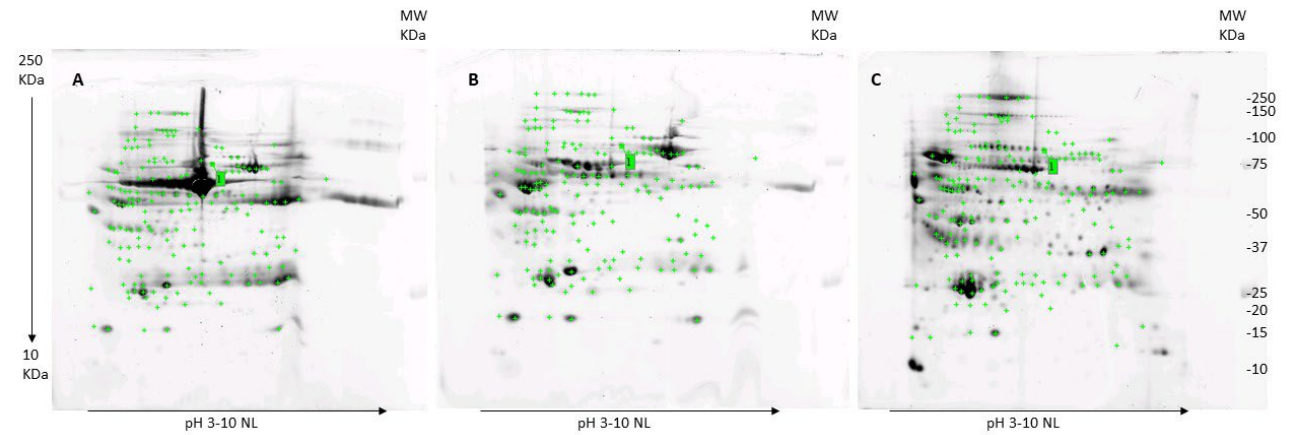


Fig. 3. *Two-dimensional gels of three aliquots of the same SF sample, stained with SYPRO Ruby.* ***A)*** *Representative 2D gel of SF;* ***B)*** *albumin depleted SF by ProteoPrep (Sigma);* ***C)*** *SF treated by ProteoMiner™ (Bio-Rad). MW markers: Precision Plus dual colour (Bio-Rad, Hercules, California, USA). The green crosses indicate the protein spots shared (pairs) among the three maps.*

Figure 2 and Figure 3 show representative 2D gels of three differently treated SF aliquots of the same sample: without depletion (Figure 2A and 3A); treated with the Immunoaffinity Albumin and IgG Depletion Kit (Figure 2B and 3B); treated with the ProteoMiner™ (Figure 2C and 3C).

DISCUSSION

The study of the synovial fluid proteome has been gaining importance in recent years, since it has shown the up-regulation of several components of the classic complement pathway in osteoarthritic knee SF (1-3, 8-10). To the best of our knowledge, this is the first study aiming at describing an optimized protocol for SF analysis, using a proteomic gel-based approach.

SF sample selection plays a key role in SF proteome analysis, spanning from animal-derived SF samples, *post-mortem* SF samples, purchased samples to pathological samples – i.e., samples from OA or RA patients – (1, 8-10). In the current study,

16 SF samples from non-OA knees were analyzed.

Reducing SF viscosity with hyaluronidase is mandatory, but there is no consensus about the optimal hyaluronidase concentration. Therefore, in the present study, we compared the 2DE proteome profiles of SF samples treated with two different hyaluronidase concentrations (11). We found hyaluronidase 1 μg/mL is the best concentration to reduce SF viscosity, while a high hyaluronidase concentration (i.e. 1mg/mL) may have proteolytic activity.

The next steps aimed to solve one of the major concerns in SF proteome analysis, i.e. high-abundant proteins (e.g. albumin and IgG) depletion, since these proteins may mask the detection of low-abundant ones, on a 2DE gel. We tested two different strategies to overcome this problem, namely affinity depletion and ProteoMiner™. We found a significantly higher protein spots number in ProteoMiner™-enriched SF samples providing 334 unique mean protein spots; these findings are consistent with those reported by Pisanu et al. in serum proteomics (12). The optimized standard sample processing protocol for human SF proteome analysis described in the present paper could be helpful also in the gel-free proteome approach of SF analysis (i.e. shotgun analysis).

Our findings are relevant in light of the increasing interest in SF study in orthopaedics and rheumatology, to improve the diagnosis and the management of several joint diseases, including osteoarthritis, rheumatoid arthritis, other autoimmune non-rheumatoid arthritis, osteochondrosis, articular infection and periprosthetic joint infection.

REFERENCES

1. Vicenti G, Bizzoca D, Carrozzo M, Solarino G, Moretti B. Multi-omics analysis of synovial fluid: a promising approach in the study of osteoarthritis. J Biol Regul Homeost Agents 2018; 32(6 Suppl. 1):9–13.
2. Vicenti G, Bizzoca D, Nappi V, et al. Serum biomarkers in the diagnosis of periprosthetic joint infection: consolidated evidence and recent developments. Eur Rev Med Pharmacol Sci 2019; 23(2 Suppl):43–50. doi:10.26355/eurrev_201904_17473
3. Balakrishnan L, Nirujogi RS, Ahmad S, et al. Proteomic analysis of human osteoarthritis synovial fluid. Clin Proteomics 2014; 11(1):6. doi:10.1186/1559-0275-11-6
4. Salari P, Grassi M, Cinti B, Onori N, Gigante A. Synovial fluid calprotectin for the preoperative diagnosis of chronic periprosthetic joint infection. J Arthroplasty 2020; 35:534–7. doi:10.1016/j.arth.2019.08.052
5. Corigliano A, Preianò M, Terracciano R, et al. C3f is a potential tool for the staging of osteoarthritis. J Biol Regul Homeost Agents 2017; 31(4 Suppl. 1):29–35.
6. Taurino F, Stanca E, Siculella L, et al. Mitochondrial proteome analysis reveals depression of the Ndufs3 subunit and activity of complex I in diabetic rat brain. J Proteomics 2012; 75(8):2331–41.
7. Rocchetti MT, Alfarano M, Varraso L, et al. Two dimensional gel phosphoproteome of peripheral blood mononuclear cells: comparison between two enrichment methods. Proteome Sci 2014; 12(1):46. doi:10.1186/s12953-014-0046-1
8. Peffers MJ, McDermott B, Clegg PD, Riggs CM. Comprehensive protein profiling of synovial fluid in osteoarthritis following protein equalization. Osteoarthr Cartil 2015; 23:1204–13. doi:10.1016/j.joca.2015.03.019
9. Fernández-Puente P, Calamia V, González-Rodríguez L, et al. Multiplexed mass spectrometry monitoring of biomarker candidates for osteoarthritis. J Proteomics 2017; 152:216–25. doi:10.1016/j.jprot.2016.11.012
10. Yamagiwa H, Sarkar G, Charlesworth MC, McCormick DJ, Bolander ME. Two-dimensional gel electrophoresis of synovial fluid: Method for detecting candidate protein markers for osteoarthritis. J Orthop Sci 2003; 8(4):482–90. doi:10.1007/s00776-003-0657-3
11. Anderson JR, Phelan MM, Rubio-Martinez LM, et al. Optimization of synovial fluid collection and processing for NMR metabolomics and LC-MS/MS proteomics. J Proteome Res 2020; 19(7):2585-97. doi:10.1021/acs.jproteome.0c00035
12. Pisanu S, Biosa G, Carcangiu L, Uzzau S, Pagnozzi D. Comparative evaluation of seven commercial products for human serum enrichment/depletion by shotgun proteomics. Talanta 2018; 185:213–20. doi:10.1016/j.talanta.2018.03.086